Chemical and Physical Modifications of Semicrystalline Gels to Achieve Controlled Heterogeneity

Lindsey Jane Anderson

Dissertation submitted to the faculty of the Virginia Polytechnic Institute and State University in partial fulfillment of the requirements for the degree of

Doctor of Philosophy
In
Chemistry

Robert B. Moore, Chair
Timothy E. Long
Judy S. Riffle
Guoliang Liu

December 5, 2018
Blacksburg, VA

Keywords: proton exchange membrane, post-polymerization functionalization, poly(ether ether ketone), semicrystalline ionomer, blocky copolymer

Chemical and Physical Modifications of Semicrystalline Gels to Achieve Controlled Heterogeneity

Lindsey Jane Anderson

ABSTRACT

Sulfonated polyaromatic hydrocarbon membranes have emerged as desirable candidates for proton exchange membranes (PEMs) due to their excellent mechanical properties, high thermal and chemical stability, and low cost. Specifically, sulfonated multiblock copolymers are attractive because their phase-separated morphologies aide in facile proton transport. In this work, the functionalization of semicrystalline gels of poly(ether ether ketone) (PEEK) is explored as a novel post-polymerization method to prepared blocky copolymers, and the effect of copolymer architecture on membrane physical properties, structure, and performance is extensively investigated. First, the blocky sulfonation of PEEK was explored to prepare blocky copolymers (SPEEK) with densely sulfonated domains and unfunctionalized, crystallizable domains. Compared to random SPEEK ionomers at similar ion content, blocky SPEEK exhibited enhanced crystallizability, decreased melting point depression, and faster crystallization kinetics. Phase separation between the hydrophilic sulfonated blocks and hydrophobic PEEK blocks, aided by polymer crystallization, resulted in enhanced water uptake, superior proton conductivity, and more closely associated ionic domains than random SPEEK.

Furthermore, the random and blocky bromination of PEEK was investigated to prepare PEEK derivatives (BrPEEK) with reactive aryl-bromides. Spectroscopic evidence revealed long domains of unfunctionalized homopolymer for blocky BrPEEK, and this translated to an increased degree of crystallinity, higher melting temperature, and more rapid crystallization kinetics than random BrPEEK at similar degrees of bromination. The

subsequent sulfonation of blocky BrPEEK resulted in a hydrophilic-hydrophobic blocky copolymer with clear multi-phase behavior. The phase-separated morphology contributed to decreased water uptake and areal swelling compared to random SPEEK and resulted in considerably higher proton conductivity at much lower hydration levels (λ). Moreover, Ullmann coupling introduced superacidic perfluorosulfonic acid side chains to the BrPEEK backbone, which yielded membranes with less water content and less dimensional swelling than random SPEEK. Superior proton transport than random SPEEK was observed due to the superacid side chain and wider hydrophilic channels within the membranes, resulting in more continuous pathways for proton transport.

Overall, this work provided a novel platform for the preparation of functionalized PEEK membranes using a simple post-polymerization functionalization procedure. The established methods produced blocky-type copolymers with properties reminiscent of multiblock copolymers prepared by direct polymerization from monomers/oligomers.

Chemical and Physical Modifications of Semicrystalline Gels to Achieve Controlled Heterogeneity

Lindsey Jane Anderson

GENERAL AUDIENCE ABSTRACT

Block copolymers are an important class of polymers that are composed of two or more blocks of distinct polymeric segments covalently tethered to one another. Dissimilarity in the chemical nature of the blocks leads to self-organization into well-defined structures, and this unique structural order imparts material properties that are different from (and often superior to) the properties of the individual blocks alone. Thus, block copolymers are advantageous for a diverse array of applications including membranes, gas separation, water purification, medical devices, etc. Although considerable synthetic progress has been made towards discovering novel methods to prepare block copolymers, their widespread use is somewhat limited by the complex, energy-intensive procedures necessary to precisely control the block sequencing during polymerization. In this dissertation, a straightforward, inexpensive physical procedure is explored to synthesize blocky copolymers with controlled sequencing from commercially available polymers. This process relies on performing reactions in the gel state, whereby segments of the polymer chain are effectively shielded from the functionalizing chemistry. In particular, the gel state sulfonation and bromination of poly(ether ether ketone), a high performance polymer, is investigated to develop novel, blocky materials for membrane applications. This work not only expands the methodology towards the synthesis of block copolymers, but alaso provides critical insight into the effect of copolymer architecture on membrane physical properties, structure, and performance. Furthermore, this work provides an economically feasible method to prepare blocky copolymers from

commercially derived materials, thereby providing a means to progress the widespread use of block copolymers in industry.

Acknowledgements

First, I would like to sincerely thank my Ph.D. advisor, Dr. Robert B. Moore, for his constant support, encouragement, and guidance throughout my time at Virginia Tech. His enthusiasm for research was contagious, and I am forever grateful for the invaluable lessons he taught me. Who knew you could learn so much from an Aggie. I would also like to thank my committee members Dr. Timothy E. Long, Dr. Judy S. Riffle, Dr. Guoliang Liu, and Dr. Mark Van Dyke (former committee member) for their critical insight and discussions during my many graduate milestones.

I was lucky enough to have incredible labmates in the Moore group, many of whom I also consider to be great friends. Christina Orsino, Samantha Talley, and Kristen Felice Noble – thank you for sharing your knowledge, encouragement, and kindness with me. Not only did you push me to be a better scientist, but you also taught me what it means to be a good teammate. I would also like to thank the entire Moore group, both past and present, including Greg Fahs, Lin Ju, Melissa Novy, Xijing Yuan, Dr. Theodore Canterbury, Dr. Jeremy Beach, Dr. Elise Naughton, and Dr. Amanda Hudson. I couldn't have asked for a better group to spend each day with and to learn from.

I would be nowhere in life without the love and support of my family. To my parents and sister (Scott, Cindy, and Kendall), thank you for always encouraging me to be the best version of myself. You've wholeheartedly supported me in every endeavor, and I consider myself extremely blessed to have had your encouragement throughout graduate school and throughout life in general. Mom and Dad, your love and generosity mean more to me than you will ever know. I am also grateful for my Virginia family including my Grandma Judy, Aunt Michelle, Uncle Gary (Curly), Lauren, and Brooke. Thank you for giving me a home away from home. Gary and Michelle, thank you for the many tailgates,

brewery visits, and LakeFest trips – your kindness towards me, Ryan, and our many tag-a-long friends will never be forgotten.

Last, but certainly not least, I would like to express my deepest gratitude to Ryan Mondschein and the best pup around, Athena. There is no way I could have made it through graduate school without you both. Thank you for always keeping me sane, for picking me up when I'm down, and for being the best life partners I could ask for. Ryan, there is no better person I could have gone on this crazy journey with, you're the best.

Table of Contents

List of Figures

List of Tables

List of Abbreviations

4-CP = 4-chlorophenol

AFC = alkaline fuel cell

ATR = attenuated total reflectance

BrPEEK = brominated poly(ether ether ketone)

BrSPEEK = brominated sulfonated poly(ether ether ketone)

BrsPS = brominated syndiotactic polystyrene

dBragg = Bragg spacing

DCA = dichloroacetic acid

DCE = 1,2-dichloroethane

DMA = dynamic mechanical analysis

DMAc = dimethylacetamide

DMEM = Dulbecco's modified eagle medium

DMSO = dimethylsulfoxide

DPS = 4,4'-dichlorophenyl sulfone

DS = degree of sulfonation

DSBr = degree of bromination

DSC = differential scanning calorimetry

ECM = extracellular matrix

EGF = epidermal growth factor

EHM model = Eisenberg-Hird-Moore model

ES = equilibrium swelling

EW = equivalent weight

FTIR = fourier-transform infrared

FWHM = full width half maximum

HFB = hexafluorobenzene

IEC = ion exchange capacity

KT = Kinning-Thomas

la = amorphous thickness

lc = lamellar thickness

Lp = long period

MCFC = molten carbonate fuel cell

NBS = N-bromosuccinimide

NMR = nuclear magnetic resonance

PAFC = phosphoric acid fuel cell

PBS = phosphate buffered saline

PEEK = poly(ether ether ketone)

PEG = poly(ethylene glycol)

PEK = poly(ether ketone)

PEM = proton exchange membrane

PEMFC = proton exchange membrane fuel cell

PEO = poly(ethylene oxide)

PES = poly(ether sulfone)

PETA = pentaerythritol triacrylate

PFS = perfluoro sulfonate

PFS-PEEK = perfluorosulfonated PEEK

PFSA = perfluoro sulfonic acid

PPO = poly(phenylene oxide)

PTFE = poly(tetrafluoroethylene)

R = radius

Rca = radius of closest approach

Rg = radius of gyration

RH = relative humidity

Rip = inter-particle radius

SAXS = small angle x-ray scattering

SDCDPS = 3,3'-disulfonated-4,4'-dichlorophenyl sulfone

SEM = scanning electron microscopy

SOFC = solid oxide fuel cell

SPEEK = sulfonated poly(ether ether ketone)

SsPS = sulfonated sydiotactic polystyrene

STEM = scanning transmission electron microscopy

t1/2 = crystallization half time

Tc = crystallization temperature

TEM = transmission electron microscopy

TFAS = trifluoroacetyl sulfate

Tg = glass transition temperature

TGA = thermogravimetric analysis

Tm = melting temperature

USAXS = ultra small angle x-ray scattering

UV = ultraviolet

WAXD = wide angle x-ray diffraction

XA = mol fraction of crystallizable segments

Xc = degree of crystallinity

XRD = x-ray diffraction

ΔH_c = enthalpy of crystallization

ΔH_m = enthalpy of melting

σ = conductivity

Attributions

Chapter 2:

Xijing Yuan: This coauthor is from Virginia Tech in the department of chemistry. Xijing helped develop the method for the solution state and gel state sulfonation of PEEK and developed the solvent suppression ^{1}H NMR characterization method utilized to determine the degree of sulfonation.

Gregory B. Fahs: This coauthor is from Virginia Tech in the department of chemistry. Greg performed the USAXS/SAXS shown in Figure 2.14.

Robert B. Moore: This coauthor is a professor at Virginia Tech in the department of chemistry. Dr. Moore is the author's advisor and oversaw the project completion.

Chapter 1

Hydrocarbon Alternatives for High Performance Proton Exchange Membranes (PEMs)

1.1 Introduction and Motivation

Due to growing concerns about the depletion of fossil fuels and rising greenhouse gas emissions, the development of clean, sustainable energy sources has been widely recognized as a global necessity. Currently fossil fuels, such as oil, coal, and natural gas, account for 78% of total primary energy production.[1] Not only does the use of these resources produce harmful carbon dioxide (CO_2) emissions, but also the finite nature and geographic confinement of these resources provides a clear problem for future energy security due to political, economic, and environmental factors. As global energy demands continue to rise (1.8% projected increase per year), significant efforts are thus necessary to provide sustainable energy sources with limited environmental impact.

The establishment of the Paris Climate Agreement of 2015, in which 148 nations committed to reducing greenhouse gas emissions and adopting practices to restrict global temperature rise this century to less than 2 ºC, is one step in the shift towards alternative energy practices.[2] This widespread initiative towards the use of clean, renewable energy sources is demonstrated when examining the projected global energy consumption. Based off of current laws, regulations, and stated targets, nonhydroelectric renewables, including solar and wind power, are projected to be the fastest growing energy source in the next 30 years.[1] Despite this projected growth, these renewable energy sources currently account for only 3.6 % of global primary energy consumption.[3] Therefore, to ensure a future of sustainable energy practices, continued development of these existing practices as well as research into alternative fuel sources such as hydrogen power will be necessary.

1.2 Hydrogen Power as a Clean Energy Source

Recently, a large emphasis has been placed on the concept of the hydrogen economy, in which conventional fossil fuels used for transportation and energy are replaced with hydrogen.[4] Hydrogen is a useful energy carrier with a high energy content by weight, almost 3 times the energy density of conventional hydrocarbon-based fuels, as shown in **Table 1.1**.[5] Energy is generated through the oxidation of hydrogen in a fuel cell, which produces water and heat as the only byproducts. This process converts the chemical energy of hydrogen into electrical energy capable of supporting transportation, stationary, or mobile applications with no harmful emissions.

Table 1.1. Energy density of hydrogen compared to conventional hydrocarbon fuels.[5] Reprinted from Renewable and Sustainable Energy Reviews, Volume 16, Mazloomi, K.; Gomes, C., Hydrogen as an energy carrier: Prospects and challenges, 3024-3033, Copyright (2012), with permission from Elsevier.

Fuel	Energy Density (MJ/kg)
Hydrogen	143
Natural gas	53.6
Methane	55.6
Gasoline	46.4
Diesel	45.4

Hydrogen is the most abundant element in the universe, however it is not found free in nature. To utilize hydrogen, it must first be extracted from hydrocarbon sources, such as fossil fuels, or produced from nuclear energy or the electrolysis of water. By developing renewable practices such as water electrolysis powered by solar and wind energy, both the production and use of hydrogen can be carbon-free, thereby reducing CO_2 emissions and lessening the dependence on nonrenewable fossil fuels.[6] The key technology to enable the success of the hydrogen economy is the fuel cell, which will be discussed in **Section 1.3**.

1.3 Hydrogen Fuel Cells

Fuel cells are electrochemical devices that convert the chemical energy stored in fuels (such as hydrogen) to electrical energy that may be used to as power for vehicles, generators, etc .[7] Fuel

cells themselves are very similar to batteries in the electrochemical nature of their energy production; however, unlike batteries fuel cells do not need to be recharged and can be run as a continuous energy supply as long as fuel is supplied. A fuel cell consists of three main components: an anode, a cathode, and an electrolyte, as shown in **Figure 1.1**.

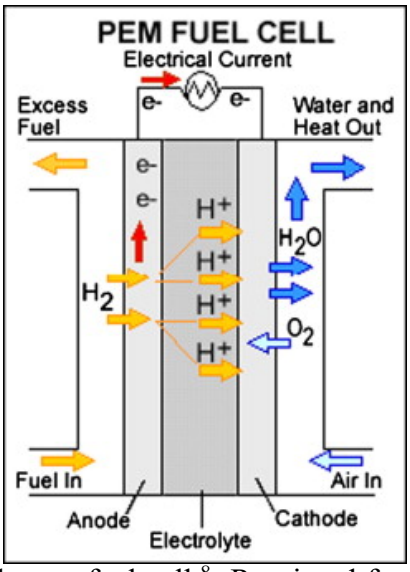

Figure 1.1. Schematic of a hydrogen fuel cell.[8] Reprinted from Applied Energy, Volume 88, Wang, Y.; Chen, K.S.; Mishler, J.; Cho, S.C.; Adroher, X.C., A review of polymer electrolyte membrane fuel cells: Technology, applications, and needs on fundamental research, 981-1007, Copyright (2011), with permission from Elsevier.

The fuel (hydrogen, methanol, natural gas, etc.) is supplied to the anode, where it is oxidized to produce protons and electrons. The protons travel across the electrolyte, while the electrons travel via an external circuit to the cathode. At the cathode, oxygen from the air is supplied and reacts with the protons and electrons to form water, heat, and energy. Unreacted oxygen is expelled from the exhaust along with the vaporized water formed. The half reactions for the reactions that occur at the anode and the cathode are displayed in **Equations 1.1** and **1.2**, respectively, and the overall reaction of the hydrogen fuel cell is displayed in **Equation 1.3**.

$$H_2 \rightleftharpoons 2H^+ + 2e^- \quad \textbf{(1.1)}$$

$$\frac{1}{2}O_2 + 2H^+ + 2e^- \rightleftharpoons H_2O \quad \textbf{(1.2)}$$

$$\frac{1}{2}O_2 + H_2 \rightleftharpoons H_2O \quad \textbf{(1.3)}$$

Fuel cells are advantageous due to their pollution-free byproducts, high efficiency, flexibility of fuel, and design variability. Furthermore, they may be used for both low power and high power applications including transportation, stationary devices, and portable applications.[8] There are five major categories of fuel cells that utilize hydrogen as fuel: (1) proton exchange membrane fuel cells (PEMFCs), (2) alkaline fuel cells (AFCs), (3) phosphoric acid fuel cells (PAFCs), (4) solid oxide fuel cells (SOFCs), and (5) molten carbonate fuel cells (MCFCs).[9] A summary of the key characteristics of each type of fuel cell is shown in **Table 1.2**.

Table 1.2. Comparison of the most common types of fuel cells.

Type	Full Name	Electrolyte	Fuel	Charge Carrier	Catalyst	Operating Temperature (°C)	Efficiency (%)
PEM	Proton Exchange Membrane Fuel Cell	Proton conducting polymer membrane	H_2	H^+	Pt/Pt Alloy	50-120	40-60
AFC	Alkaline Fuel Cell	Potassium hydroxide	H_2	OH^-	Pt, Ni	150-200	60
PAFC	Phosphoric Acid Fuel Cell	Concentrated phosphoric acid	H_2	H^+	Pt	150-220	35-45
SOFC	Solid Oxide Fuel Cell	Yttria stabilized zirconia	H_2, CO, CH_4	O^{2-}	Ni, Sr	650-1000	50-60
MCFC	Molten Carbonate Fuel Cells	Sodium, magnesium, and/or lithium carbonate	H_2, CO, CH_4	CO_3^{2-}	NiO	600-700	40-55

Several key differences are evident among the main types of fuel cells including electrolyte used, operating temperature, and fuel used. Thus, unique operating environments and materials requirements are necessary depending on the fuel cell utilized. In particular, our research focuses on PEMFCs due to their low temperature, quick startup, high power density, and high efficiency.[7, 9]

1.4 Proton Exchange Membrane Fuel Cells

PEMFCs utilize proton exchange membranes (also known as polymer electrolyte membranes) to transport protons from the anode to the cathode in a fuel cell. The PEM is a solid electrolyte that is semipermeable – allowing for the transport of ions between the electrodes, but acting as a barrier for the hydrogen/oxygen reactants and electrons. For successful use in fuel cells, PEMs must exhibit several key features: (1) good proton conductivity, (2) low electronic conductivity, (3) minimal permeability to fuel and oxidants, (4) chemical and electrochemical stability in the fuel cell environment, (5) oxidative and hydrolytic stability, (6) dimensional and morphological stability with swelling and deswelling, (7) suitable water transport, (8) mechanically robust, (9) long lifetime under fuel cell operating conditions, and (10) low cost.[7, 10-11] The current standard for PEMs is the perfluorinated ionomer Nafion®, which exemplifies many of these required properties.

1.5 Perfluorinated Ionomers for PEMs

Perfluorinated sulfonic-acid (PFSA) ionomers are a class of materials based on poly(tetrafluoroethylene) (PTFE) backbones bearing perfluoroether side chains with a terminal sulfonic acid group.[12] The hydrophobic PTFE backbones combined with the hydrophilic sulfonated perfluoroether side chains result in the unique properties of PFSA ionomers such high proton conductivity, ion perm-selectivity, and good chemical and thermal stabilities. The first perfluorinated ionomer, Nafion®, was developed by Dupont in the 1960's, and has since inspired

the development of numerous other PFSA ionomers with similar chemical architectures, such as Aquivion® by Solvay and 3M's PFSA and PFIA. The excellent transport properties and interesting morphologies have led to the extensive investigation of PFSA ionomers in numerous applications, including PEMFCs.

1.5.1 Properties of Nafion®

Nafion® is the most widely investigated PEM, and it is considered the benchmark material for use in fuel cells due to its excellent proton transport and remarkable thermal and mechanical stability.[13] Nafion® is a random copolymer of perfluorinated vinyl ether and tetrafluoroethylene (TFE) comonomers prepared by free radical polymerization. The chemical structure of Nafion® is shown in **Figure 1.2**.[14]

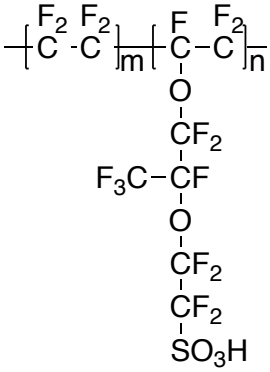

Figure 1.2. Chemical structure of Nafion®.

Due to the polymerization process, the ion content of Nafion® may theoretically be varied by changing the ratio of comonomers used during polymerization. Nafion® is often described by its equivalent weight (EW), i.e. the number of grams of dry polymer per moles of sulfonic acid group. Thus, the value of m in **Figure 1.2** is obtained using the equation EW = 100m + 446 and yields an estimate of the average separation of the sulfonic acid functionalities.[14] Furthermore, the EW value is easily related to the ion exchange capacity (IEC) of the membrane using the equation IEC = 1000/EW. A variety of EWs for Nafion® have been prepared and are available

commercially, including 900, 1100, 1200 g/mol, etc. Useful EWs prepared for Nafion® generally lie in the range of 800-1,500 g/mol.

The chemical structure of Nafion® also affords a unique phase-separated morphology due to ionic aggregation of the sulfonate groups.[14-16] Thus, the microstructure of Nafion® consists of at least two distinct morphological phases: a hydrophobic domain comprised of the PTFE backbone and a hydrophilic domain containing the sulfonated side chains. The hydrophobic PTFE domains are semicrystalline, thereby imparting mechanical integrity to the membrane. The hydrophilic domains, on the other hand, consist of ionic aggregates of the sulfonate functionalities, enabling proton transport and contributing to membrane perm-selectivity.[17-18] The morphology of Nafion® is shown in **Figure 1.3**. Phase separation between the hydrophobic backbone and the hydrophilic side chains is further enhanced upon hydration, which amplifies the dissimilarities and produces continuous hydrophilic nanodomains through which proton and water transport occur.[13, 19] In fact, the water content of Nafion® membranes is key to control the formation, dimensions, and connectivity of the hydrophilic channels and thereby plays a key role in the ability of the membrane to transport protons.[7]

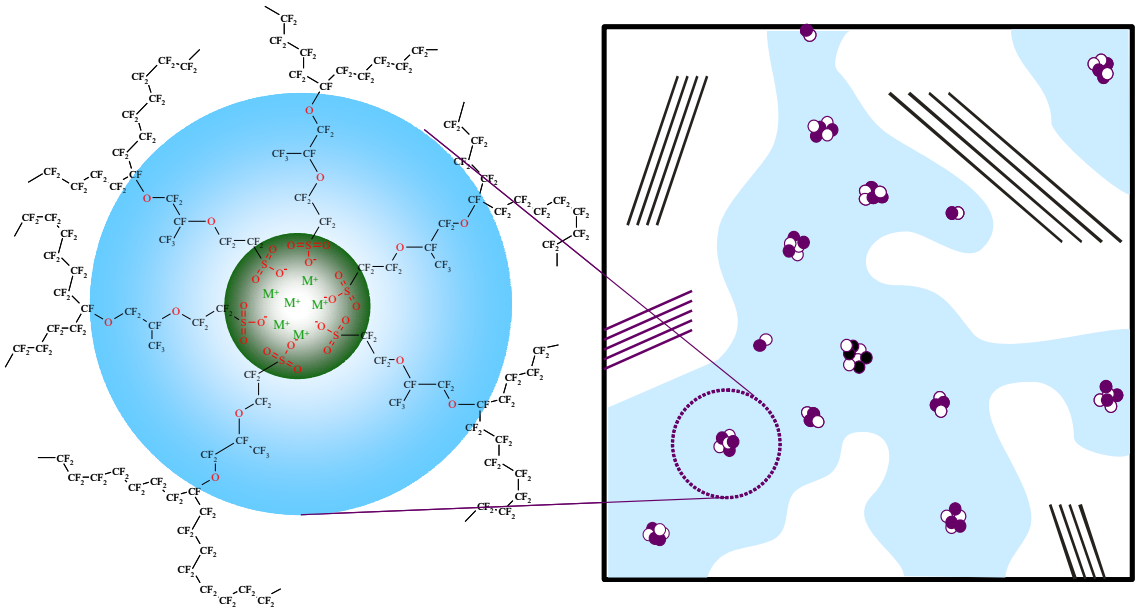

Figure 1.3. Morphology of Nafion®. White areas show the hydrophobic domains, consisting of a semi-crystalline matrix of the PTFE backbone. Blue, shaded areas show the hydrophilic domains, consisting of ionic aggregates. A zoomed in view of the ionic aggregate is also displayed.

Overall, the proton conductivity of Nafion® depends on the combination of many features: polymer structure, EW (i.e. number of charge carriers), hydration number (λ, number of water molecules/sulfonic acid group), membrane morphology, and temperature. First, the chemical structure is key because the perfluoroether sulfonated side chain has a $pK_a \sim -6$, qualifying it as a superacid catalyst.[20] This allows the sulfonic acid site to readily dissociate into its ionic form and transport protons. The EW influences the number of these acidic sites which may act as charge carriers, and thus as EW decreases (higher number of charge carriers), proton conductivity increases. Hydration is also crucial for proton conductivity, as it promotes the dissociation of the sulfonic acid groups and provides a mechanism of proton transport by the diffusion of hydrated protons. Furthermore, hydration number heavily influences membrane morphology, and it has been shown that as hydration increases, proton conductivity increases. At very high levels of hydration, however, overswelling of the membrane may occur, resulting in diminished mechanical properties, dilution of charge carriers, and electro-osmotic drag which slows oxidation at the

cathode.[21] Temperature also influences thermal energy (faster proton hopping kinetics) and water content and thereby changes the proton conductivity. Thus, the reconciling of these various attributes leads to Nafion®'s high proton conductivity.

1.5.2 Alternative Perfluorinated Ionomers

With the success of Nafion®, novel PFSA ionomers have emerged bearing unique sulfonated perfluoroether side chains. Two examples of these PFSA ionomers are Aquvion® and 3M's PFSA, whose structures are shown in **Figure 1.4**. These PFSA ionomers differ from Nafion® in their side chain length and lack of pendant CF_3 group along the side chain, and differ from one another in the length of their perfluoroether side chain.[19, 22] Often, the side chains are shorter than Nafion® and thus, these PFSA ionomers have lower molecular weight per repeat unit and exhibit lower EWs than Nafion® at similar ion contents. The shorter side chains also contribute to more facile crystallization of the PTFE backbone in these PFSA ionomers, and thus Aquivion® has a higher heat of fusion (i.e. greater crystallinity) than Nafion® at similar EW.

Furthermore, the difference in side chain composition and length contributes to a difference in thermal transitions from Nafion®. As the side chain decreases in size, the glass transition temperature (T_g) increases. For example, Nafion® exhibits a T_g around 100 ºC while the 3M PFSA has a T_g around 125 ºC and Aquivion® has a T_g around 140 ºC.[22] The increase in T_g permits the use of these membranes at higher and higher operating temperatures. Despite these changes in structure and thermal transitions, these PFSA ionomers exhibit similar hydrophobic-hydrophilic phase separation to Nafion®, contributing to their high proton conductivity and excellent chemical and mechanical stabilities.

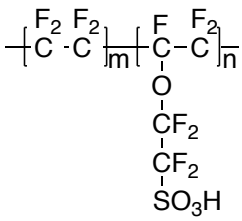

A

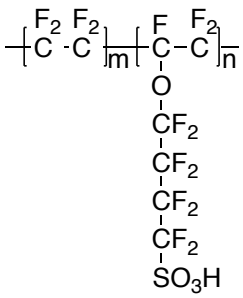

B

Figure 1.4. Chemical Structures of the perfluorinated ionomers Aquivion® (A) and 3M PFSA (B).

1.5.3 Advantages and Disadvantages of Perfluorinated Ionomers

As stated previously, perfluorinated ionomers such as Nafion® are widely used as proton exchange membranes due to their excellent proton conductivity that arises from the phase-separated morphology. Furthermore, they are chemically, electrochemically, and thermally stable, enabling them to withstand many cycles within the oxidizing environment of the fuel cell. In fact, PFSA ionomers are capable of withstanding >60,000 h in the fuel cell environment.[23]

Although Nafion® and related PFSA ionomers are the primary choice for proton exchange membranes, there are several disadvantages that many researchers are trying to overcome. First, Nafion® is quite costly (~ $700/m^2).[21] As the membranes are one of the primary expenses in the PEMFC stack, the high cost of Nafion® prohibits the widespread commercialization of fuel cells. Furthermore, Nafion® does not perform well at temperatures above 80 ºC and/or at low humidity due to extensive dehydration.[24-25] Finally, the chemical synthesis of Nafion® is difficult and has the potential to result in toxic byproducts.[26] Due to these limitations, novel hydrocarbon membranes have been explored as potential inexpensive alternatives to Nafion®.

1.6 Hydrocarbon Membranes for Alternative PEMs

To replace Nafion® and other PFSA ionomers, researchers have turned to sulfonated hydrocarbon membranes, primarily focusing on high performance aromatic polymers due to their

thermal, mechanical, and chemical stabilities. In particular, emphasis has been placed on developing membrane materials that are inexpensive and can perform at elevated temperatures (~120 ºC) and at low humidity (50% R.H.). In this section, a variety of aromatic polymers bearing an ion-conducting sulfonic acid group will be explored as potential alternative PEMS.

1.6.1 Materials for Hydrocarbon PEMs

The most widely recognized candidates for hydrocarbon proton exchange membranes are wholly aromatic polymers due to their availability, high mechanical and chemical stability, and wide variety of chemical compositions. The high glass transition temperatures afforded by these copolymers also provide the thermal stability necessary to operate at high temperatures within the fuel cell. A variety of aromatic polymers including poly(arylene ether ketone)s, poly(arylene ether sulfone)s, poly(benzimidazole)s, and poly(imides) have been extensively explored as potential PEM materials, and examples of these commonly employed polymer classes are displayed in **Figure 1.5**.

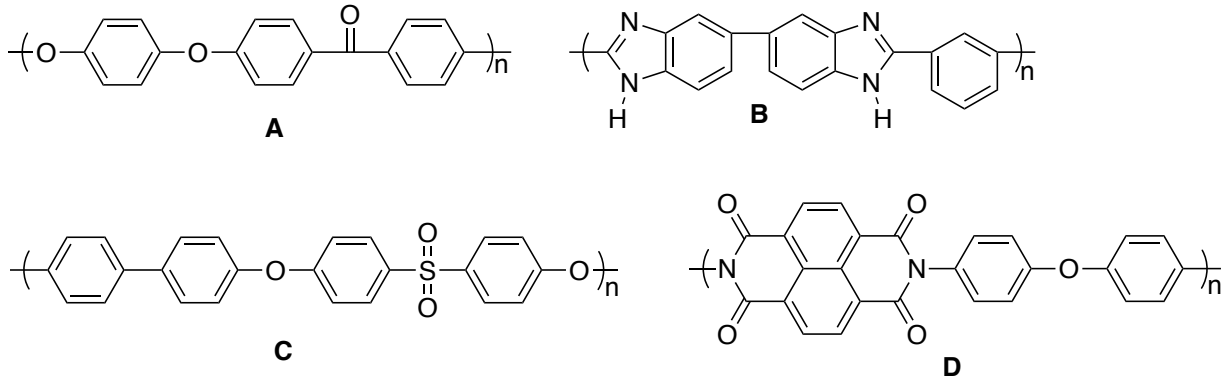

Figure 1.5. Several classes of aromatic hydrocarbons used in PEMs including poly(arylene ether ketones) (A), poly(benzimidazoles) (B), poly(arylene ether sulfones) (C), and poly(imides) (D).

Of these wholly aromatic hydrocarbon materials, poly(arylene ether)s provide a versatile platform due to the breadth of chemical functionalities composing the backbone, as shown in **Figure 1.6**. These slight modifications in backbone can vastly alter polymer properties. For example, the incorporation of more flexible bridging units (e.g. SO_2 vs. CO or $C(CF_3)_2$ vs a direct aryl-aryl bond) improves the solubility and processability of the materials. Incorporating more

rigid, periodic structures, on the other hand, results in crystallizable polymers. To prepare sulfonated hydrocarbon materials suitable for proton transport in PEMs, two main methods exist: post-polymerization sulfonation and the direct synthesis of materials using sulfonated monomers. Both routes will be discussed in detail below.

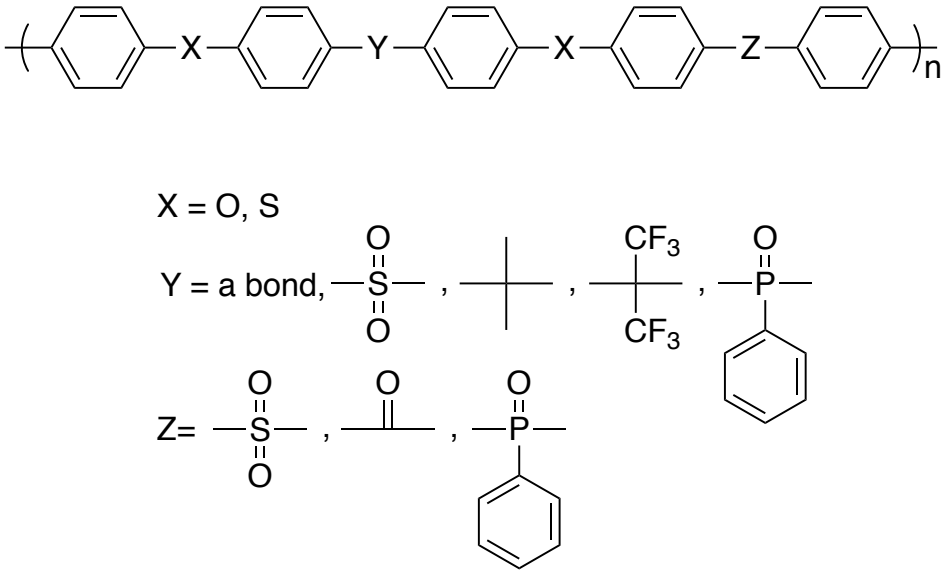

Figure 1.6. Potential poly(arylene ether) chemical structures.[10]

1.6.2 Post-Polymerization Sulfonation of Existing Aromatic Polymers

The sulfonation of previously prepared polymers is a facile route to create proton-conducting polymers from commercially available materials. Sulfonation reactions employ an electrophilic aromatic substitution reaction using reagents such as concentrated sulfuric acid, sulfur trioxide, and chlorosulfonic acid.[27-29] Due to the electrophilic nature of the reaction, the sulfonation of polymers with electron-rich rings (e.g. those with electron-donating substituents) proceeds efficiently. While sulfonation can be achieved for polymers with deactivated rings, for example poly(ether ketone) (PEK), these require much longer reaction times, higher temperatures and stronger sulfonating reagents, which may lead to polymer degradation.[30]

The post-polymerization sulfonation technique is common because it is inexpensive relative to synthesizing a sulfonated monomer and then reacting to form the polymer, and it can

be performed using commercially derived polymers such as poly(ether ether ketone) (Victrex, Gatone, Solvay)[31], poly(phenyl sulfone) (Solvay)[32-33], poly(ether sulfone) (Victrex)[34], and poly(aryl ether sulfone) (UDEL)[34]. Using this sulfonation method, the degree of sulfonation is readily controlled by the reaction time and temperature, with high degrees of sulfonation achieved at long reaction times and high temperature. The resultant membrane properties are primarily dictated by the degree of sulfonation (i.e. IEC), and water uptake and proton conductivity are shown to increase with increasing degree of sulfonation. To achieve proton conductivities similar to Nafion®, high degrees of sulfonation (usually >50 mol%) are necessary.

One of the most extensively studied post-sulfonated systems is sulfonated poly(ether ether ketone) (SPEEK). PEEK itself is a high performance, semicrystalline polymer with high temperature thermal transitions, great mechanical properties, and excellent chemical stability.[35-37] The high crystallinity of PEEK (30-50 wt%)[38] prohibits its dissolution in organic solvents, and thus sulfonation was originally explored as a means to characterize the PEEK by decreasing crystallinity and improving solubility. Due to the limited solubility of PEEK, SPEEK is primarily prepared by simultaneous dissolution and sulfonation in concentrated sulfuric acid, as shown in **Figure 1.7**.[31, 39-40] Sulfonation occurs exclusively on the electron-dense hydroquinone ring and is prohibited on the benzophenone rings due to the electron-withdrawing effect of the adjacent carbonyl. Furthermore, sulfonation is restricted to one event per repeat unit due to the electron-withdrawing effect of the sulfonic acid group, which deactivates the ring towards further substitution.[41] The sulfonation of PEEK has also been reported using sulfonating reagents such as chlorosulfonic acid, fuming sulfuric acid, and sulfur trixode/triethyl phosphate complexes, however, these reagents demonstrate polymer degradation in addition to sulfonation.[42-43] Because sulfonation proceeds effectively in concentrated sulfuric acid with limited evidence of degradation, sulfuric acid is considered the sulfonating reagent of choice for PEEK.

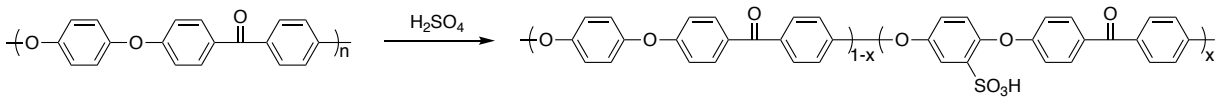

Figure 1.7. Sulfonation of poly(ether ether ketone) using sulfuric acid.

It is important to note that truly random copolymers of PEEK cannot be prepared at low degrees of sulfonation (i.e. ≤ 30 mol%) using only H_2SO_4 due to the simultaneous dissolution and sulfonation of PEEK.[42] In fact, when targeting these low degrees of sulfonation, this heterogeneous reaction process leads to a large gradient in the degree of sulfonation of each polymer chain. For example, when PEEK pellets are placed in sulfuric acid, the surface of the pellet begins to dissolve. Once dissolved, the PEEK polymer chains are much more accessible to sulfonation at any site along the repeat unit. As the PEEK pellet slowly dissolves, more and more polymer chains become accessible to sulfonation until the PEEK pellet is fully solvated. Upon reaction termination by precipitation into water, polymer chains that were initially dissolved (i.e. spent more time in full contact with sulfuric acid) will be highly sulfonated, while polymer chains from the core of the PEEK pellet, which were not in contact with sulfuric acid for long, will be lightly sulfonated. Thus, a large distribution in functionality among polymer chains is expected. With the discovery of novel solvents that do not functionalize PEEK, including methanesulfonic acid and dichloroacetic acid, PEEK chains may be completely dissolved prior to the addition of sulfonating reagent, and truly random copolymers of SPEEK can be prepared even at low ion content.[42, 44]

An alternative route for the sulfonation of rings deactivated towards EAS (i.e. rings with electron-withdrawing substituents) is the metalation route.[45] This route was developed to improve the stability of the sulfonic acid group and prevent the *ipso* substitution of SO_3H with H^+ in strong acids.[46] To prepare poly(phenylenesulfone) (PSU) sulfonated on the electron-deficient rings, the site *ortho* to the sulfone is first deprotonated using an organometallic reagent (e.g. *n*-butyllithium) and then sulfinated using SO_2 gas. The sulfinate derivative is easily oxidized to its sulfonate form and converted to the sulfonic acid form using aqueous HCl or cation exchange resins. An example

of this process is shown in **Figure 1.8**. This process is advantageous for all polymers which may be lithiated and provides a useful method to introduce the sulfonic acid functionality without the use of chlorinated solvents. With the careful choice of oxidant species, sulfonation is achieved without polymer degradation or crosslinking. Controlled crosslinking to decrease excessive swelling and increase mechanical stability is also permitted using this synthetic process by s-alkylation of sulfinate groups.[47-48] The metalation process of sulfonation, however, is more expensive and time consuming than conventional sulfonation routes and thus has not been widely adapted for commercial PEMs.

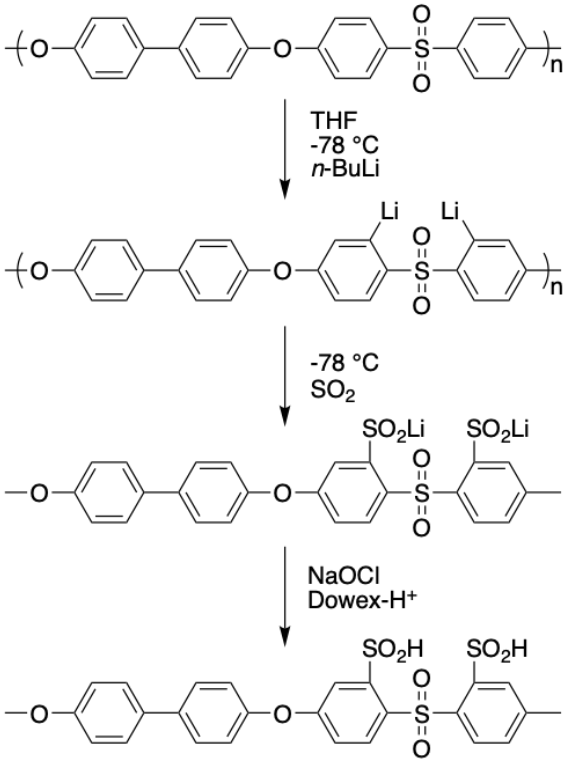

Figure 1.8. Metalation route to prepare *ortho*-sulfone sulfonated poly(phenylenesulfone).[45]

While post-polymerization sulfonation reactions are versatile, inexpensive, and easy to perform, several limitations exist. First, it is difficult to have precise control over the degree of sulfonation; rather, the degree of sulfonation is simply varied with reaction time and temperature. Furthermore, it is impossible to precisely control the location of sulfonation along the polymer

backbone. Finally, the use of strong sulfonating agents may lead to undesirable side reactions, such as crosslinking and polymer chain degradation.

1.6.3 Direct Polymerization of Sulfonated Monomers

The direct polymerization of sulfonated monomers is used to prepare sulfonated polyaromatic polymers with more precise control over the degree of sulfonation and the location of sulfonation. Poly(arylene ether)s are typically prepared by nucleophilic aromatic substitution reactions of bisphenols with activated dihalides, as shown in **Figure 1.9**. Thus, the introduction of sulfonated moieties to the polymer backbone is accomplished using sulfonated dihalides or sulfonated dialcohols. While polymers prepared using sulfonated dialcohols closely resemble those prepared by post-polymerization sulfonation (as described above), sulfonated aromatic dihalides provide a unique sulfonation site within the electron-poor rings, which increases the acidity and thermal stability of the sulfonic acid groups.

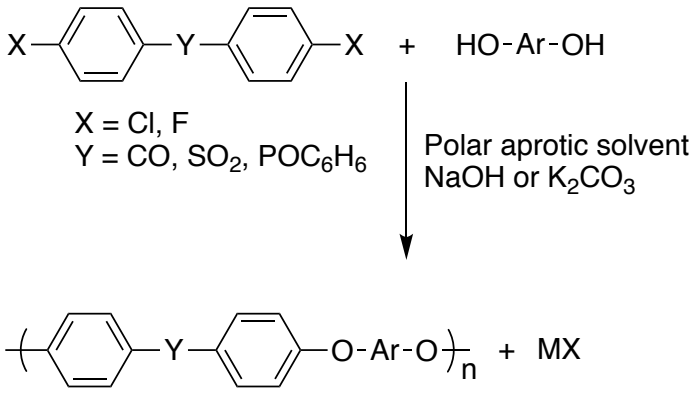

Figure 1.9. Synthesis of poly(arylene ether)s via nucleophilic aromatic substitution.

A commonly used sulfonated monomer for the synthesis of sulfonated poly(arylene ether sulfones)s is 3,3'-disulfonated-4,4'-dichlorodiphenyl sulfone (SDCDPS), whose synthesis and use in polycondensation reactions were described by Ueda and McGrath.[49-52] This monomer bears sulfonate groups at positions within the electron deficient rings, which increases both the acidity and thermal stability of the sulfonic acid sites in the resultant polymer. The polymerization of the

SDCDPS monomer proceeds effectively at similar reactions conditions to those employed with the unsulfonated 4,4-dichlorophenyl sulfone (DPS) monomer, although moderately higher temperatures and longer reaction times are required to achieve high molecular weight due to steric effects of SDCDPS. A typical polymerization of SDCDPS with biphenol is shown in **Figure 1.10**. Exact control over the degree of sulfonation is afforded by varying the ratio of the sulfonated to unsulfonated monomers used during the reaction. These sulfonated poly(arylene ether sulfones) displayed increasing water uptake and conductivity with increasing incorporation of the disulfonated monomer, however, for use as PEMs, the degree of disulfonation was limited to 50 mol% as excessive swelling occurred at sulfonation levels above this.

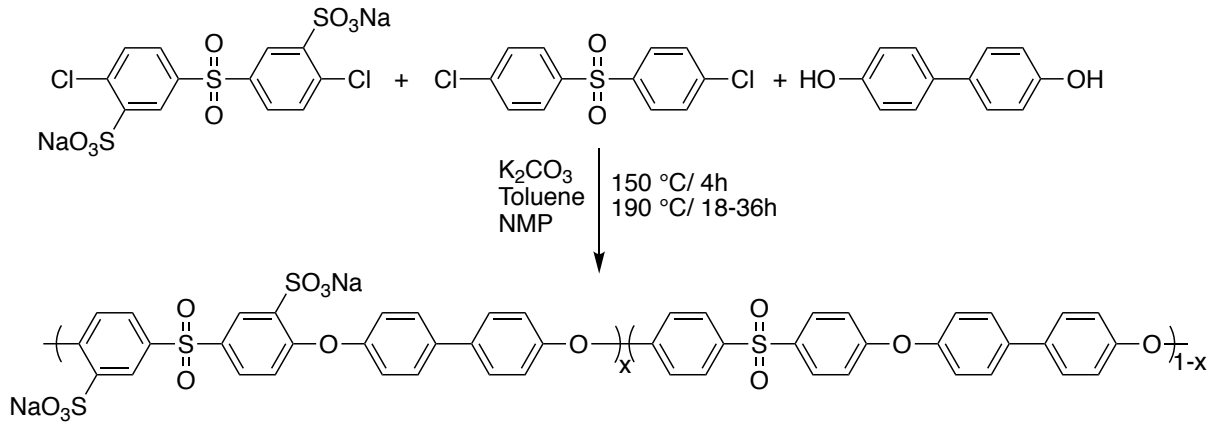

Figure 1.10. Synthesis of sulfonated poly(arylene ether sulfone) using SDCDPS.[51]

The polymerization of sulfonated poly(arylene ether ketone)s is performed in a manner similar to poly(arylene ether sulfone)s using sodium 5,5'-carbonylbis(2-fluorobenzene sulfonate), as shown in **Figure 1.11**.[53-54] The more reactive fluorinated derivative is used for these reactions in place of a chlorinated derivative due to the lower reactivity of an aromatic ketone dihalide relative to the aromatic sulfone halide. Again, the location of the sulfonic acid sites within the ketone-coupled aromatic domains resulted in increased acidity of the sulfonic acid sites and increased stability of the sulfonic acid groups upon contact with strong acid. The sulfonated aromatic poly(ether ether ketones) prepared in **Figure 1.11**[53] and those prepared by Li[55]

demonstrated comparable swelling and proton conductivity to Nafion® while significantly reducing methanol diffusion coefficients. Other poly(arylene ether ketone)s prepared by Oroujzadeh revealed proton conductivities of 80 mS/cm (similar to Nafion®) at only 45 mol% sulfonation.[56]

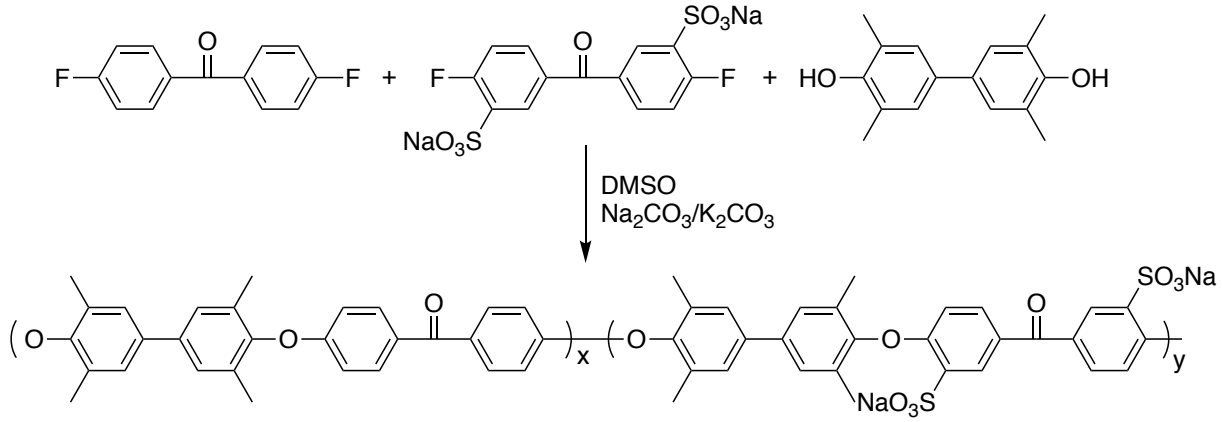

Figure 1.11. Synthesis of sulfonated poly(arylene ether ether ketone) using sodium 5,5'-carbonylbis(2-fluorobenzene sulfonate).[53]

Of particular utility in the direct polymerization of sulfonated polymers is the wide variety of bisphenol and hydroquinone derivatives available for copolymerization. The subtle differences in di-alcohol composition can dramatically alter the resultant physical properties and thereby enhance membrane performance.[57] For example, the use of 3,4-difluorophenyl hydroquinone resulted in improved oxidative stability, enhanced hydrophobic-hydrophilic phase separation, and better proton transport relative to similar poly(arylene ether sulfone)s lacking a bulky, hydrophobic side chain.[58] Likewise, the incorporation of bulky fluorenyl groups into the backbone of a poly(ether ether ketone ketone) lead to flexible membranes with good dimensional stability in water, high proton conductivities, and a considerable reduction in methanol diffusion compared to Nafion®.[59] Sulfonated aromatic di-alcohols are also useful for the direct polymerization of sulfonated poly(arylene ether)s with sulfonation sites similar to those of post-sulfonated polymers, as shown by Krishnan who demonstrated the successful polymerization of hydroquinone 2-potassium sulfonate (HPS) with bisphenol A and 4-fluorophenyl sulfone.[60]

While the direct polymerization of sulfonated poly(arylene ether)s provides accurate control over the degree of sulfonation and the location of sulfonation, the process is more expensive and labor intensive than the post-sulfonation of commercially available materials. Furthermore, the process is limited by the number of commercially available sulfonated monomers.

1.6.4 Methods to Improve the Properties of Hydrocarbon PEMS

The sulfonation architecture afforded by both post-polymerization sulfonation and direct polymerization using sulfonated monomers results in copolymers that are randomly sulfonated along the polymer backbone. Thus, the membrane properties are primarily dictated by the degree of sulfonation. In general, as the degree of sulfonation increases, water uptake and proton conductivity increase due to the increased number of hydrophilic acidic sites along the polymer backbone. Proton conductivities that rival the benchmark Nafion® are achieved at high degrees of sulfonation and high water content, however, a loss in mechanical properties and dimensional stability upon swelling is observed with increasing degree of sulfonation, thereby limiting the utility of these materials in the harsh environments of the fuel cell. Furthermore, randomly sulfonated membranes generally exhibit lower proton conductivity than Nafion® at low humidity, despite having a higher water absorption.[61] Because proton conductivity is closely coupled to water content, this suggests a difference in the phase-separated microstructure of the randomly sulfonated membranes. Unlike Nafion®, which readily phase-separates to form wide, interconnected hydrophilic channels, sulfonated poly(arylene ether)s form ambiguously phase-separated structures with more tortuous and narrow hydrophilic domains due to their rigid backbones and weak hydrophilic/hydrophobic character.[20, 62] A comparison of the microstructures of Nafion® and a sulfonated poly(ether ketone) derivative is shown in **Figure 1.12**.

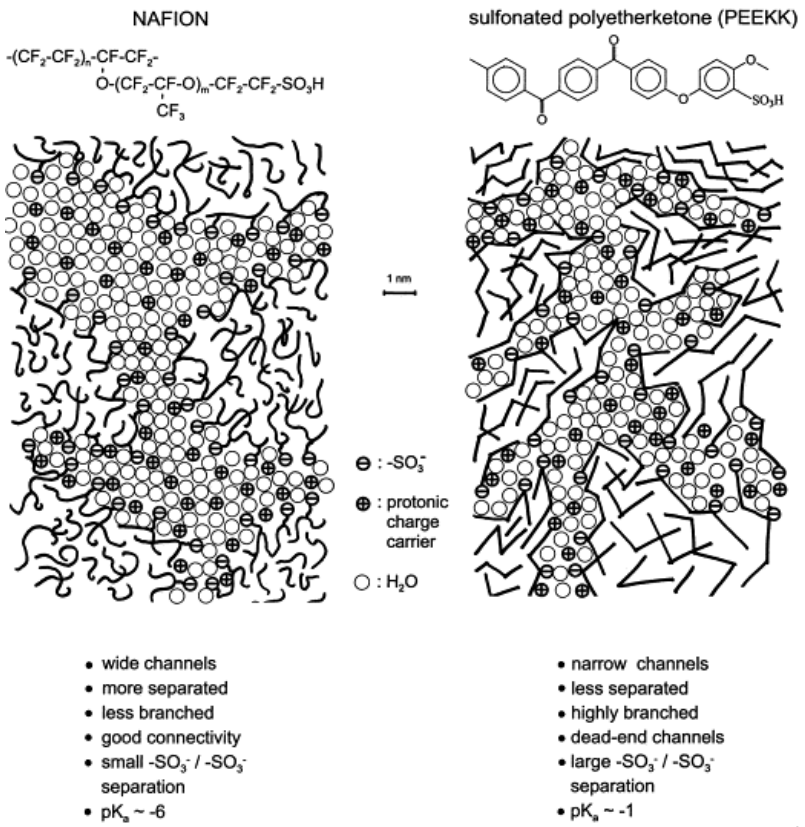

Figure 1.12. Comparison of the phase-separated microstructures of Nafion® and sulfonated poly(etherketone) (PEEKK) determined from the interpretation of SAXS profiles.[20] Reprinted from Journal of Membrane Science, Volume 185, Kreuer, K.D., On the development of proton conducting polymer membranes for hydrogen and methanol fuel cells, 29-39, Copyright (2001), with permission from Elsevier.

To improve the properties of sulfonated hydrocarbon PEMs, several methods have been employed. First, the chemical crosslinking of the membranes has been widely explored as a means to reduce swelling and increase mechanical stability at high degrees of sulfonation. For example, the crosslinking of SPEEK using a Friedel-Crafts reaction with 1,6-dibromohexane was shown to improve dimensional stability, increase thermal stability, and significantly decrease methanol permeability, with only a slight decrease in proton conductivity from that of uncrosslinked SPEEK.[63] Similar results were observed for photo-crosslinked SPEEK whose degree of crosslinking was controlled by irradiation time.[64-65] Furthermore, SPEEK membranes may be crosslinked to reduce swelling through thermally-activated reactions with the sulfonic acid group,[66-67] however, this method also reduces the IEC of SPEEK and thereby decreases proton

conductivity. Thus, crosslinking is a useful method to control water uptake and membrane mechanical properties, however, it limits proton transport within the membranes.

Composite membranes have also been explored to improve the properties of sulfonated hydrocarbon membranes. Primarily, efforts have focused on the incorporation of inorganic nanofillers such as silica, zirconium phosphosphates, and nanoclay into the sulfonated membranes.[68-70] These nanofillers act as physical crosslinks in the system, thereby improving the swelling properties and mechanical stability of the membranes and reducing fuel crossover. The incorporation of proton-conducting fillers, such as boron orthophosphate and sulfonated silica, demonstrated proton conductivities that largely exceeded the unmodified sulfonated membrane.[71-72] Overall, the preparation of composite membranes is a useful technique to control mechanical properties, water retention at high temperatures, and proton conductivity.

Additionally, synthetic strategies have been employed to introduce densely sulfonated domains onto the polymer backbone. This enables high IEC at relatively low concentrations of sulfonated monomer and promotes hydrophilic-hydrophobic phase separation by localizing the sulfonic acid domains.[73] Poly(arylene ether)s with 2 or more sulfonic acid units on each sulfonated repeat unit have been prepared by first polymerizing bisphenols with several electron-rich phenyl domains.[74-76] The phenyl domains are then sulfonated using conventional post-polymerization sulfonation techniques, as demonstrated in **Figure 1.13**. Because these polymers have a higher concentration of hydrophobic segments than singly-sulfonated polymers at similar IEC, they exhibit improved dimensional stability, moderate water swelling, and excellent mechanical properties. Furthermore, proton conductivities on par with Nafion® were observed, even at relatively low humidity.[77] The high contrast in polarity between the densely sulfonated hydrophilic domains and the hydrophobic domains resulted in clear phase-separated microstructures with continuous hydrophilic domains, which yielded the observed proton transport. Although these

novel materials demonstrate suitable membrane properties, the incorporation of monomers bearing high densities of phenyl groups is difficult during copolymerization due to its steric bulk and lower molecular weight is anticipated as the amount of this monomer increases.

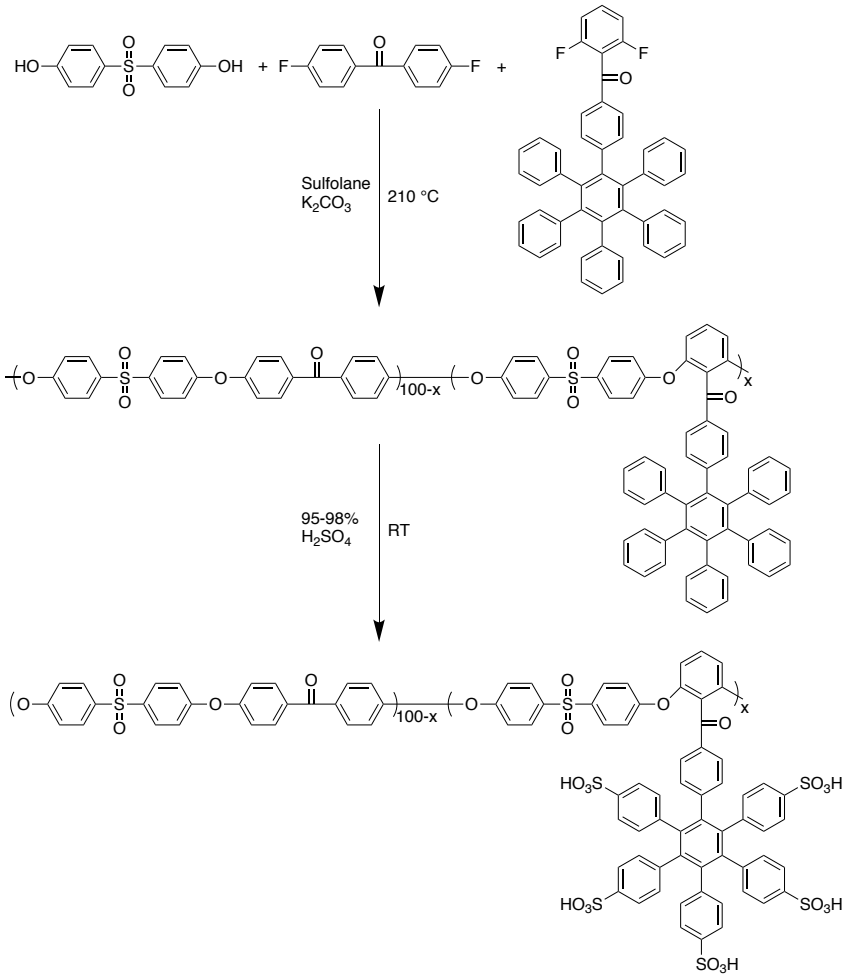

Figure 1.13. Synthesis of densely sulfonated poly(arylene ether) bearing a penta-sulfonated pendent group.[76]

Finally, multiblock copolymers comprised of hydrophilic and hydrophobic blocks are considered one of the most promising candidates to improve the properties of hydrocarbon materials for proton exchange membranes. Phase separation of the hydrophilic and hydrophobic blocks into well-defined domains creates continuous ionic channels for efficient proton transport through the hydrophilic domains. Furthermore, the hydrophobic blocks provide mechanical integrity and dimensional stability upon swelling of the membranes in water.[78] Einsla compared

the membrane properties of multiblock copolymer composed of a hydrophobic polyimide block and a sulfonated, hydrophilic poly(arylene ether sulfone) block to a randomly sulfonated poly(arylene ether sulfone) copolymer and an alternating sulfonated poly(arylene ether ketone) copolymer at similar IECs.[79] While these membranes exhibited similar water uptake, the differences in sulfonated architecture lead to distinct differences in membrane morphology and proton conductivity. As shown in **Figure 1.12**, the multiblock copolymers exhibited large, interconnected phase-separated domains. The alternating copolymers also displayed large phase-separated domains, however, these showed poor interconnectivity between the hydrophilic domains. The random copolymers displayed a relatively disordered morphology with some connectivity of the hydrophilic domains. Due to these large differences in membrane microstructure, significant differences in proton conductivity were observed with varying sulfonation architecture. The alternating copolymer displayed the lowest proton conductivity, the random copolymer displayed an intermediate proton conductivity, and the multiblock copolymer displayed the highest proton conductivity, with values comparable to Nafion®. Thus, proton transport was found to increase with increasing connectivity and decreasing tortuosity of the hydrophilic domains. Clearly, controlled multiblock sulfonation architectures are desirable for enhanced hydrophilic-hydrophobic phase separation and excellent proton transport. The preparation and use of multiblock copolymers for PEMs is discussed in detail in the following section.

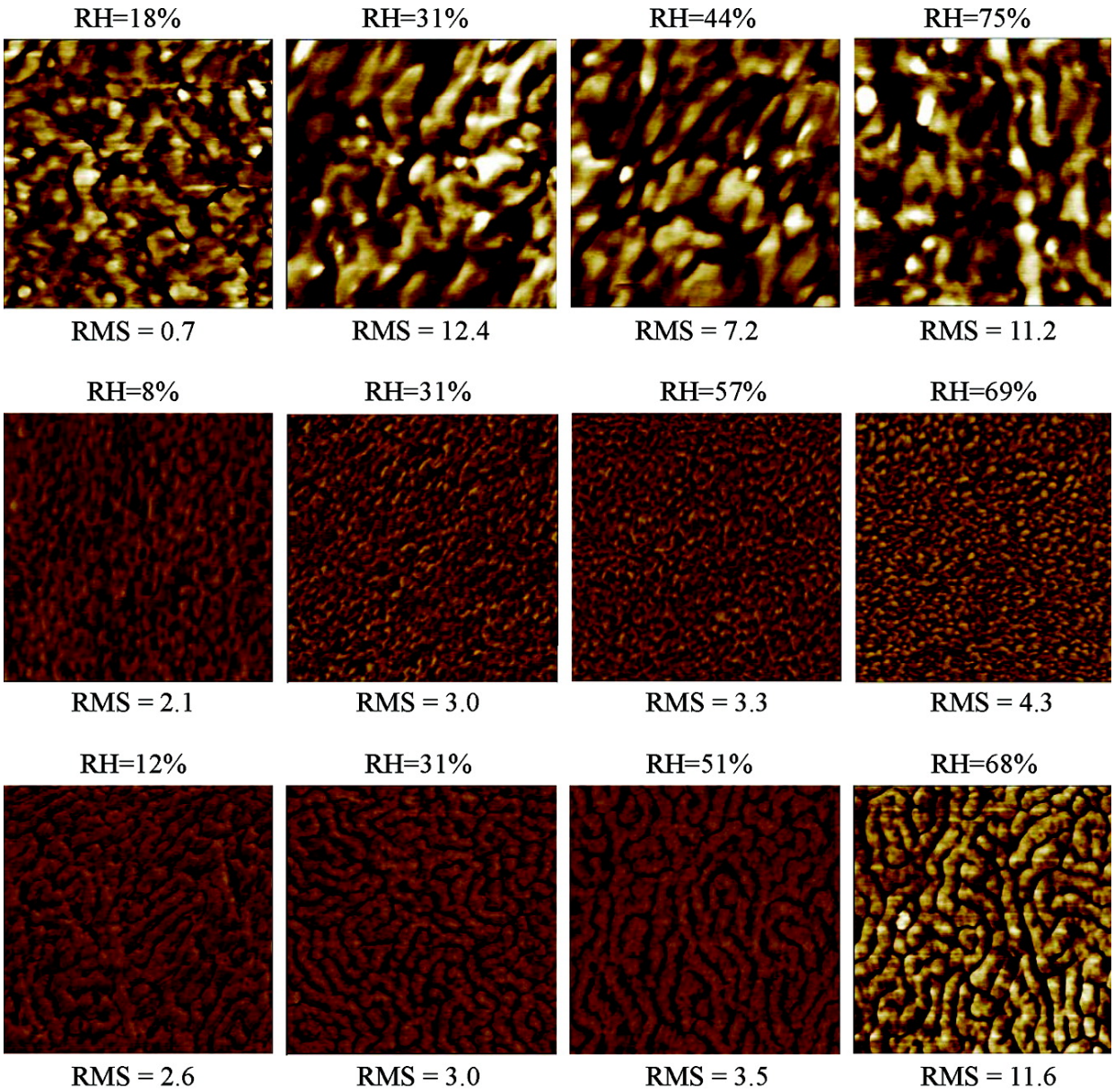

Figure 1.14. Scanning Force Microscopy (SFM) images of alternating (top), random (middle), and multiblock (bottom) PEMs as a function of relative humidity. Reprinted with permission from (Einsla, M. L.; Kim, Y. S.; Hawley, M.; Lee, H.-S.; McGrath, J. E.; Liu, B.; Guiver, M. D.; Pivovar, B. S., Toward Improved Conductivity of Sulfonated Aromatic Proton Exchange Membranes at Low Relative Humidity. *Chemistry of Materials* **2008**, *20* (17), 5636-5642.). Copyright (2008) American Chemical Society.

1.7 Multiblock Copolymers as PEMs

1.7.1 Polymerization of Multiblock Copolymers from Oligomers

Significant interest has been garnered towards the synthesis of novel block copolymers with sulfonated hydrophilic blocks and hydrophobic blocks due to the well-ordered phase-separated morphologies associated with block copolymers. At similar hydrophilic and hydrophobic block lengths, phase separation results lamellar morphologies with highly interconnected hydrophilic domains. Because these domains persist at all humidity values, it is anticipated that proton transport will be less dependent on water content than in random copolymers and high proton conductivity may be achieved at low water content. Most commonly, these block copolymers are prepared by two-step step growth polymerization, in which oligomers of the respective blocks are first prepared and then reacted with one another. The first report of fully aromatic sulfonated block copolymers were sulfonated block copolyimides prepared by Genies et al.[80] These block copolyimides were synthesized by a two-step, one-pot procedure in which oligomers of the sulfonated block are first prepared by condensation of 1,4,5,8-napthalene tetracarboxylic dianhydride (NTDA) and sulfonated 2,2'-diamino-4,4'-biphenyl disulfonic acid (BDSA) followed by addition of non-sulfonated diamine and NTDA. The sulfonated block length was controlled by the ratio of NTDA to BDSA in the first step, and IEC was controlled by the amount of non-sulfonated diamine added in the second step. Compared to random copolyimides at similar IEC values, the block copolyimides displayed higher water uptake and superior proton conductivity. SANS analysis revealed a well-defined ionomer peak for the block copolyimide and a broad, poorly defined ionomer peak for a random copolyimide analogue and thus, the superior proton conductivity was attributed to the improved order in the block copolymers.

McGrath has investigated numerous sulfonated multiblock copolymers based on fully disulfonated poly(arylene ether sulfone) hydrophilic blocks. In each case, the block copolymer was prepared by the coupling of hydrophilic oligomers synthesized from disulfonated SDCDPS to hydrophobic oligomers prepared from non-sulfonated aromatic monomers. Examples of

various disulfonated block copolymers prepared by McGrath are shown in **Figure 1.15**. Multiblock sulfonated poly(arylene ether sulfone) (**Figure 1.15A**) demonstrated superior proton conductivity and water uptake than random poly(arylene ether sulfone) at similar IEC and greater proton conductivity than Nafion®, most notably at low humidity values.[81] To further enhance phase separation between the hydrophilic and hydrophobic domains, McGrath also prepared multiblock copolymers with fluorinated hydrophobic blocks. Partially fluorinated poly(arylene ether ketone sulfone) multiblock copolymers (**Figure 1.15B**) and highly fluorinated poly(arylene ether sulfone) multiblock copolymers (**Figure 1.15C** and **D**) demonstrated superior phase separation and decreased water uptake (relative to non-fluorinated monomers) due to the increased hydrophobicity of the fluorinated domains.[82-84] The well-defined lamellar morphologies of the multiblock copolymers contributed to their excellent proton transport, especially at low humidity.

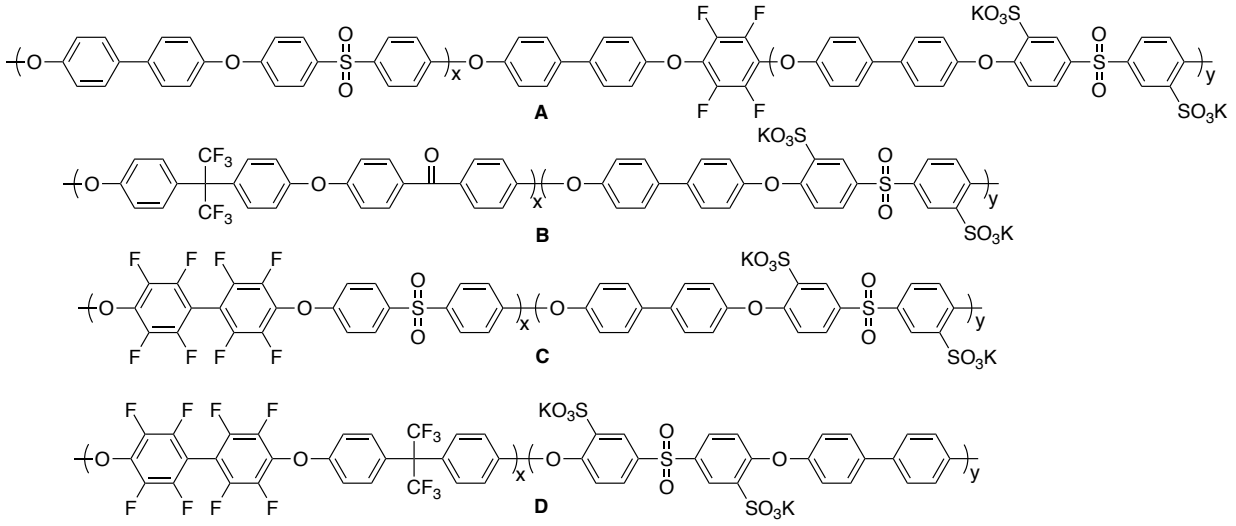

Figure 1.15. Examples of prepared multiblock sulfonated poly(arylene ether) copolymers.[82-85]

Multiblock copolymer membrane properties are dependent on the block length of the hydrophilic and hydrophobic blocks, and at similar IEC, water uptake and proton conductivity increase with increasing block length. As shown in **Figure 1.16**, multiblock copolymers displayed more phase-separated domains, better phase continuity, and increasing domain size with increasing

block length.[86] In comparison, a random analogue showed a relatively featureless morphology, suggesting hydrophilic ionic domains were homogeneously distributed throughout the polymer matrix. Thus, the increased water uptake and proton conductivity was attributed to the wider and more continuous hydrophilic channels formed with increasing block length. The phase-separation phenomenon was also investigated using SAXS, as shown in **Figure 1.17**. As with TEM, the random copolymer was featureless due to the homogeneous distribution of ionic domains within the membrane. In contrast, a well-defined peak appeared for the multiblock copolymers due to phase separation of the electron-dense ionic domains. With increasing block length, this peak shifted to lower q, suggesting larger inter-domain spacings that are consistent with the TEM results. Furthermore, the 10k-10k and 15k-15k copolymers display 2nd order scattering peaks at $2q_{max}$, thereby confirming the presence of a lamellar morphology, which becomes more defined with increasing block length.

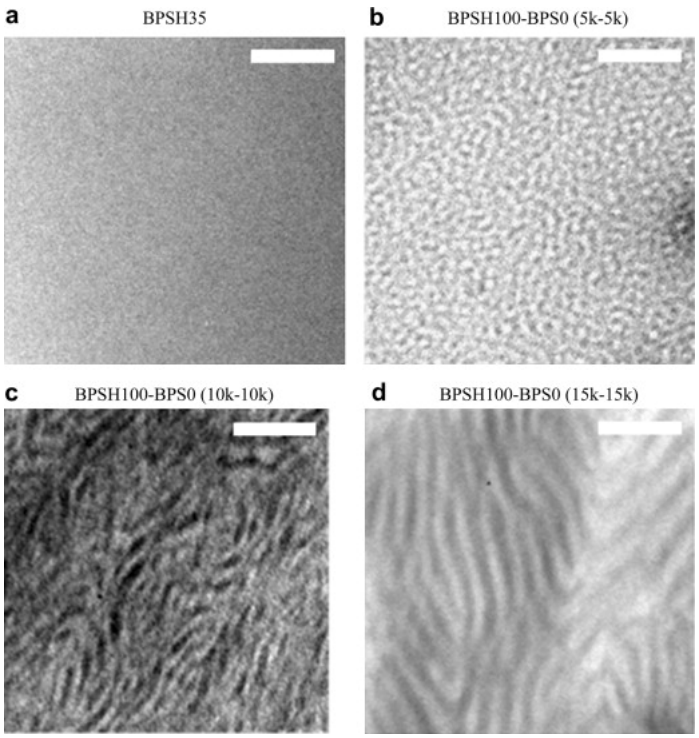

Figure 1.16. TEM micrographs of random sulfonated poly(arylene ether sulfone) (A), and multiblock sulfonated poly(arylene ether sulfone) with hydrophilic-hydrophobic block lengths of 5k-5k (B), 10k-10k (C), and 15k-15k (D). All samples have an IEC of ~1.4 meq/g. The scale bar has a length of 100 nm.[86] Reprinted from Polymer, Volume 50, Lee, M.; Park, J.K.; Lee, H.S.; Lane, O.; Moore, R.B.; McGrath, J.E., Baird, D.G., 6129-6138, Copyright (2009), with permission from Elsevier.

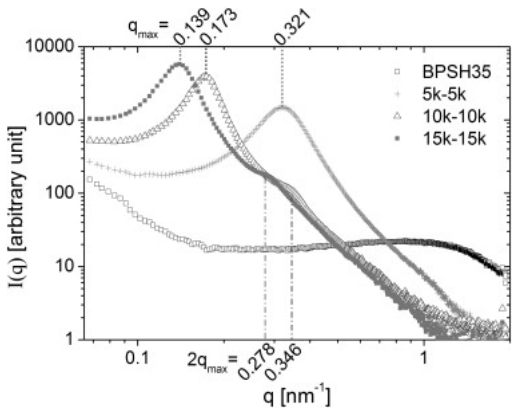

Figure 1.17. SAXS profiles of random sulfonated poly(arylene ether sulfone) (BPSH35), and multiblock sulfonated poly(arylene ether sulfone) with hydrophilic-hydrophobic block lengths of 5k-5k, 10k-10k, and 15k-15k.[86] Reprinted from Polymer, Volume 50, Lee, M.; Park, J.K.; Lee, H.S.; Lane, O.; Moore, R.B.; McGrath, J.E., Baird, D.G., 6129-6138, Copyright (2009), with permission from Elsevier.

The morphology and properties of multiblock membranes is also dependent on the casting solvent and drying conditions. Enhanced phase separation was observed using a selective solvent (DMAc) that was a good solvent for the hydrophilic blocks but a poor solvent for the hydrophobic blocks.[86] This resulted in higher water uptake and superior proton conductivity than membranes cast from a good solvent for both blocks (NMP). Furthermore, water uptake was dependent on the drying temperatures used during film casting. As the drying temperature was increased from 20 ºC to 80 ºC, water uptake of the resultant block membranes decreased, and this effect was most pronounced for the longest block lengths. Despite this drastic change in water uptake, no change in proton conductivity was observed due to the anisotropic nature of the swelling in the through-plane direction. Another factor influencing membrane performance is thermal annealing. Annealing of the membranes above the T_g of the hydrophobic block resulted in significantly decreased water uptake compared to the as-cast membranes, and water uptake became independent of block length following annealing.[87] Annealing also significantly improved the mechanical properties of the multiblock membranes in the swollen state. These effects were due to thermal rearrangement to a more well-defined lamellar morphology.

It is important to note that multiblock PEMs are not limited to those containing the hydrophilic block comprised of disulfonated dichlorodiphenyl sulfone and 4,4'-biphenol. Watanabe developed poly(arylene ether sulfone) membranes with fluorenyl groups in the hydrophilic block.[88] The fluorenyl-containing block was sulfonated by post-polymerization sulfonation, and the resulting block copolymers displayed much greater proton conductivity than random copolymer analogues, especially at low humidity. Shanmugam synthesized multiblock sulfonated poly(arylene ether ketones) that demonstrated well-ordered, phase-separated domains by transmission electron microscopy and improved proton transport relative to Nafion®.[89] Likewise, Zhao prepared SPEEK-based block copolymers with superior proton conductivity and better phase separation than random SPEEK copolymers.[90-91] Jannasch prepared highly sulfonated multiblock poly(arylene ether sulfones) with tetrasulfonated diarylsulfone blocks and demonstrated nanophase morphologies whose size increased with block length, superior proton transport to Nafion® at low temperatures, and dimensional stability in water up to 100 ºC.[92] Overall, it is evident that block copolymers (regardless of backbone composition) improve membrane performance due to the advantageous hydrophilic-hydrophobic phase separation between the blocks that provide well-defined, continuous domains for proton transport.

Thus far, amorphous multiblock copolymers for PEMs have been discussed, however, it is also useful to consider the impact of crystallinity on membrane performance. Semicrystalline morphologies in PEMs are shown to improve mechanical strength, increase phase separation, and reduce excessive swelling at high IEC relative to amorphous membranes.[10, 93-95] Because aromatic semicrystalline polymers (such as PEEK) are insoluble in most organic solvents, direct coupling between hydrophilic oligomers and semicrystalline hydrophobic oligomers is not possible. Thus, synthetic strategies employ a soluble, amorphous ketimine precursor oligomer for the hydrophobic blocks which may be coupled to the hydrophilic oligomers to produce the block

copolymer precursors.[96-97] Hydrolysis of the ketimine to a ketone affords the desired semi-crystalline hydrophobic blocks. An example of this procedure to prepare semicrystalline hydrophobic poly(ether ether ketone)-hydrophilic disulfonated poly(arylene ether sulfone) block copolymers is shown in **Figure 1.18**.[98] Differential scanning calorimetry confirmed the semicrystalline nature of the block copolymers, and proton transport of the block copolymer membranes was found to be comparable to or higher than Nafion® and significantly improved from an amorphous, random membrane. Feng also prepared sulfonated semicrystalline poly(ether ketone)-based membranes with densely sulfonated hydrophilic blocks using a similar method and showed that greatly improved dimensional stability and suppressed water uptake at high IEC compared to an amorphous membrane.[99] Thus, the incorporation of crystallizable blocks into PEMs offers a further method to improve the transport properties, dimensional stability, mechanical and thermal stability, and resistance to excess swelling at high IEC.

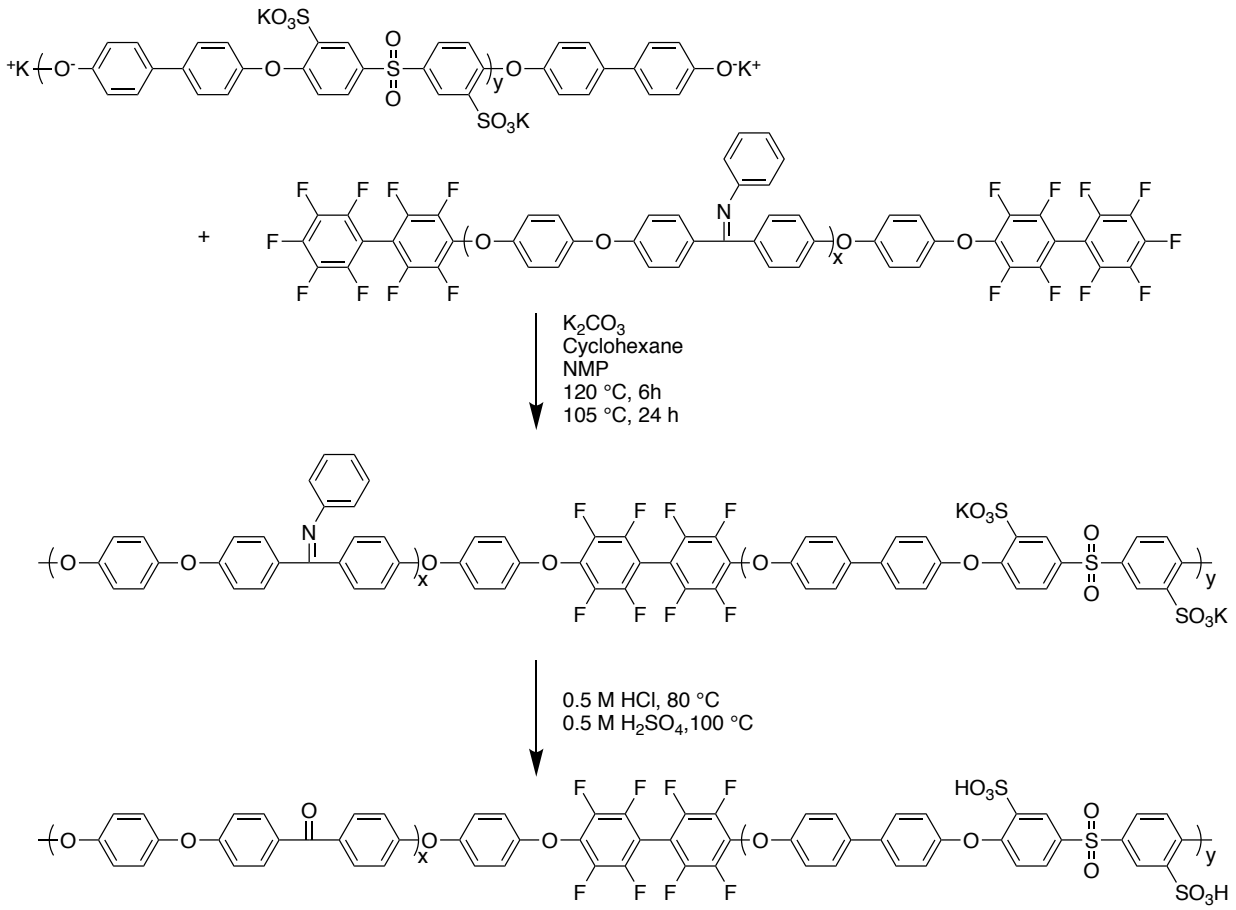

Figure 1.18. Synthetic scheme for the preparation of multiblock semicrystalline poly(ether ether ketone)-disulfonated poly(arylene ether sulfone) copolymers.[98]

While the synthesis of sulfonated multiblock copolymers is useful to prepare membranes suitable for PEM applications, the process is limited by a variety of factors. First, the procedure itself is time consuming and requires multiple steps to prepare the hydrophobic oligomer, to prepare the hydrophilic oligomer, and to couple the two together. Even still, further reactions may be required to sulfonate the hydrophilic block or to impart crystallizability to the hydrophobic block. Furthermore, the block lengths of the sulfonated domains are limited by the reactivity and the steric limitation of the sulfonated monomer, and the incorporation of highly fluorinated monomers into the hydrophobic block is expensive. Thus, despite the success of multiblock copolymer membranes, there is a need for simpler, cost-effective methods to prepare well-defined phase-separated materials with controlled water uptake, excellent proton transport, and mechanical

stability. Ideally, a novel post-polymerization sulfonation method using existing commercial polymers is desirable to prepare multiblock copolymer membranes due to its inexpensive nature and ease of availability of the starting materials.

1.7.2 Blocky Copolymers via Gel-State Sulfonation

Although post-polymerization functionalization is used extensively for the synthesis of randomly sulfonated polymers, it is not as easily applied for the preparation of sulfonated blocky copolymers. Rather, block copolymer architectures with one block reactive towards sulfonation must first be synthesized and subsequently sulfonated. Recently, a novel post-polymerization sulfonation technique utilizing semicrystalline gels was introduced to produce a 'blocky' functionalization architecture.[100] The semicrystalline gels are comprised of tightly packed crystalline domains (which act as physical crosslinks) joined together in the physical gel network by solvent-swollen amorphous chains. With the introduction of a functionalization reagent, the reactant is sterically excluded from the crystalline domains, resulting in selective sulfonation of the solvent-swollen amorphous fraction. This process produces non-random, blocky copolymers with sulfonated segments separated by unfunctionalized (and thus crystallizable) chain segments. A schematic representation comparing gel state functionalization to homogeneous functionalization in solution (i.e. conventional sulfonation) is shown in **Figure 1.19**.

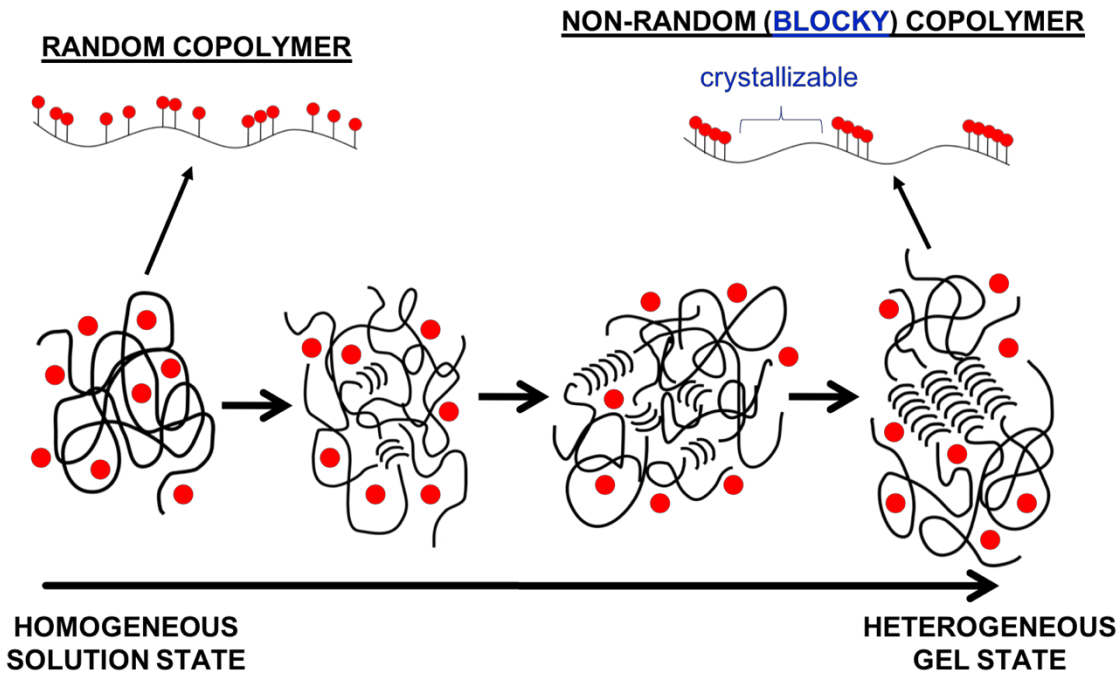

Figure 1.19. Schematic representation of functionalization in the solution state and in the gel state to produce random and blocky copolymers, respectively.

The gel state functionalization process is unique because it not only provides a simple method to prepare blocky copolymers but also preserves the crystallizability of the native homopolymer. For example, the blocky sulfonation of syndiotactic polystyrene (sPS) gels resulted in blocky SsPS copolymers with a degree of crystallinity (X_c) of 23% at 10.5 mol% sulfonation, a value fairly close to that of the sPS homopolymer (X_c = 35%). In comparison, a random SsPS copolymer at 9.2 mol% sulfonation was not capable of crystallizing under similar conditions.[100] The gel-state functionalization process also resulted in more rapid crystallization kinetics for blocky copolymers compared to random copolymers, and SAXS analysis confirmed the distribution of the polar sulfonate groups within the amorphous, interlamellar domains of the blocky SsPS.

It is also important to note that this gel-state functionalization process is not limited to sulfonation. In fact, the halogenation of sPS in the semicrystalline gel state was recently demonstrated to prepare blocky brominated copolymers.[101] NMR spectroscopy provided evidence

of long domains of unfunctionalized styrene 'blocks' as well as randomly brominated 'blocks' for blocky BrsPS prepared in the gel state. The blocky architecture afforded by the gel state bromination was further confirmed using simulations, as shown in **Figure 1.20**. As with the blocky SsPS, blocky BrsPS displayed higher crystallizability and faster crystallization kinetics than random analogues at similar degrees of functionality. USAXS/SAXS analysis of quenched, amorphous films also demonstrated a micro-phase separated morphology for the blocky BrsPS that was not apparent in the random BrsPS. Thus, blocky copolymers of polystyrene are readily obtained using this simple heterogeneous post-polymerization technique.

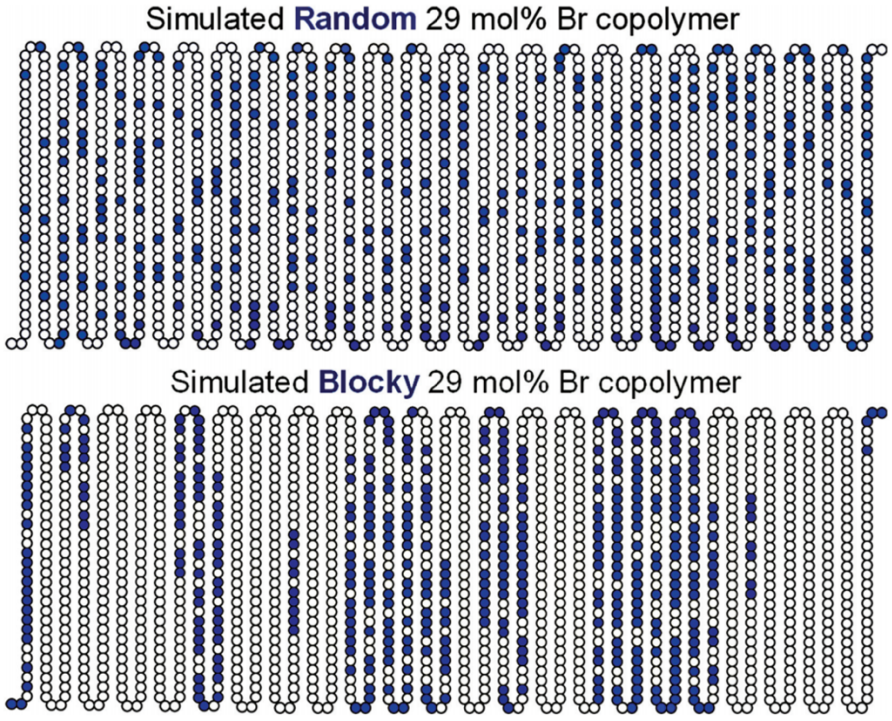

Figure 1.20. Representative random and blocky brominated sPS chains at 29 mol% bromination determined using simulations.[101] Polymer chemistry by Royal Society of Chemistry (Great Britain) Reproduced with permission of Royal Society of Chemistry in the format Thesis/Dissertation via Copyright Clearance Center.

Using this gel state procedure, it is now possible to prepare crystallizable, blocky ionomers directly without relying on lengthy polymerization processes. Given the utility of crystalline lamella for improving mechanical properties and decreasing undesirable swelling in PEM

applications, the gel state functionalization method will be extremely useful for the preparation of blocky sulfonated materials for proton transport. Not only will the crystalline domains improve the physical properties of the membranes, but also phase-separation afforded by the blocky architecture should provide continuous hydrophilic domains suitable for excellent proton transport. Because this process relies on the semicrystalline nature of polymers, gel state functionalization will be useful for crystallizable aromatic polymers such as poly(arylene ether ketone)s, poly(phenylene sulfide), poly(phenylene oxide), etc. The functionalized blocky architecture may be controlled via the semicrystalline gel morphology, and factors such as concentration, solvent, gelation temperature, degree of crystallinity, and lamellar thickness may be varied to investigate their impact on blocky copolymer properties.

While sulfonation provides a direct route to materials suitable for proton transport, it is also advantageous to investigate the blocky halogenation of polymers as a platform for secondary reactions. Given the wealth of aryl-bromide substitution chemistries available, it is possible to impart novel functionalities to the polymer backbone using a brominated intermediate. For example, Ullmann coupling may be used to attach superacid perfluorosulfonate side chains[102-105] to brominated polyaromatics, and brominated derivates may be readily phosphonated.[106-107] By establishing the blocky architecture during the gel-state functionalization process, these secondary reactions can be performed in the homogeneous solution state while preserving the blocky architecture. It is assumed that the gel-state process will produce membranes with phase-separated microstructures similar to those of polymerization hydrophilic-hydrophobic block copolymers, thus enhancing the proton transport properties for use in PEMFCs.

1.8 Ionic Aggregation in PEM Materials

The phase separation of sulfonated copolymers into hydrophilic domains and hydrophobic domains is aided by aggregation of the ionic sulfonate groups. Ionic aggregation in ion-containing

polymers dictates many material properties, including the proton transport properties, the glass transition temperature, and mechanical properties. Ionic aggregation into multiplets (i.e. groups of ion pairs) is frequently analyzed using small-angle x-ray scattering (SAXS), where a distinct 'ionomer' peak appears due to contrast between the electron-dense aggregates and surrounding polymer matrix. Several models have been developed to describe this ionic aggregation phenomenon including the core-shell model, the hard sphere model, and the Eisenberg-Hird-Moore (EHM) multiplet cluster model, as will be discussed below.

1.8.1 Core-Shell Model

The core-shell model proposes that ionomer scattering arises due to the distance between two ion-rich domains (i.e. *intra*particle scattering). In this model, a central ionic core is surrounded by a shell of associated ions at low concentration, separated by a distance of R_2-R_1 as shown in **Figure 1.21**.[108] Because this model failed to justify the driving force behind the enhanced electron density of the shell compared to the bulk polymer, the model was modified to consider a zone of depleted ionic content surrounding the central ion core.[109] Thus, contrast between the ionic core and the depleted zone as well as between the depleted zone and the bulk polymer was proposed to lead to the ionic peak observed in SAXS. Water-swelling experiments in Nafion® experimentally supported this model, however, failed to recognize aggregate rearrangement upon swelling. Furthermore, Yarusso and Cooper demonstrated poor fits of the core-shell model when quantitatively the SAXS curves of sulfonated polystyrene ionomers, instead proposing an *inter*particle origin to the scattering feature (as will be discussed in the following section).[110] Thus, this model is not frequently employed to analyze current ionomers.

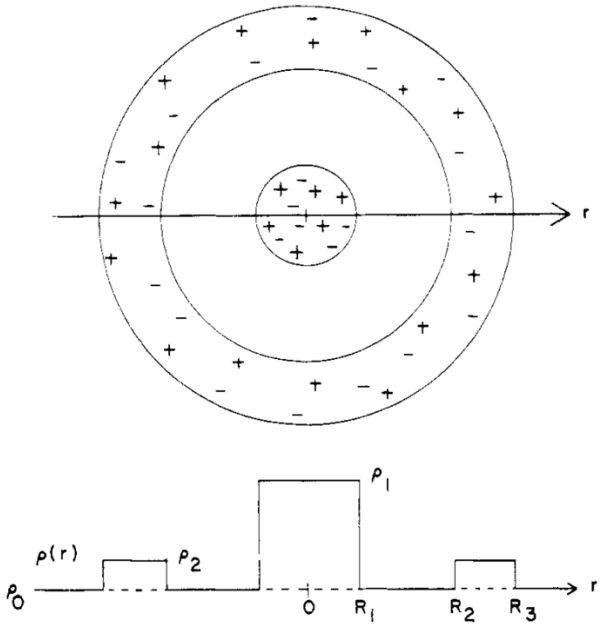

Figure 1.21. Core-shell model of ionic aggregation and the related electron density profile.[111] Reprinted with permission from (Yarusso, D. J.; Cooper, S. L., Microstructure of ionomers: interpretation of small-angle x-ray scattering data. *Macromolecules* **1983**, *16* (12), 1871-1880). Copyright (1983) American Chemical Society.

1.8.2 Hard Sphere Model

One of the most widely accepted models of ionic aggregation is the hard sphere model, which describes the origin of the ionomer peak as *inter*-aggregate scattering, whereby contrast is observed due to differences in electron density between the ion-rich aggregates and the polymer matrix. The aggregates are represented as monodisperse hard spheres, defined by an ion-rich core with radius R and a rigid shell of polymer chains surrounding the core that limits the spatial correlation between aggregates, resulting in a radius of closest approach (R_{ca}), as shown in **Figure 1.22**. Yarusso and Cooper modified the hard sphere model to allow for liquid-like order in the arrangement of ionic aggregates within the polymer matrix.[111] The Yarusso-Cooper model utilizes a Fournet three-body interference function, which accounts for the correlation between neighboring hard spheres by modeling the interference of three hard spheres.[110] Kinning and

Thomas further modified the hard sphere model by incorporating a Percus-Yevick correlation function[112] into the Yarusso-Cooper model, which accounts for interference of all hard spheres within the system.[113] Because the Kinning-Thomas model accounts for all spheres, it is more accurate than the Yarusso-Cooper model at high ionic aggregate density.[114]

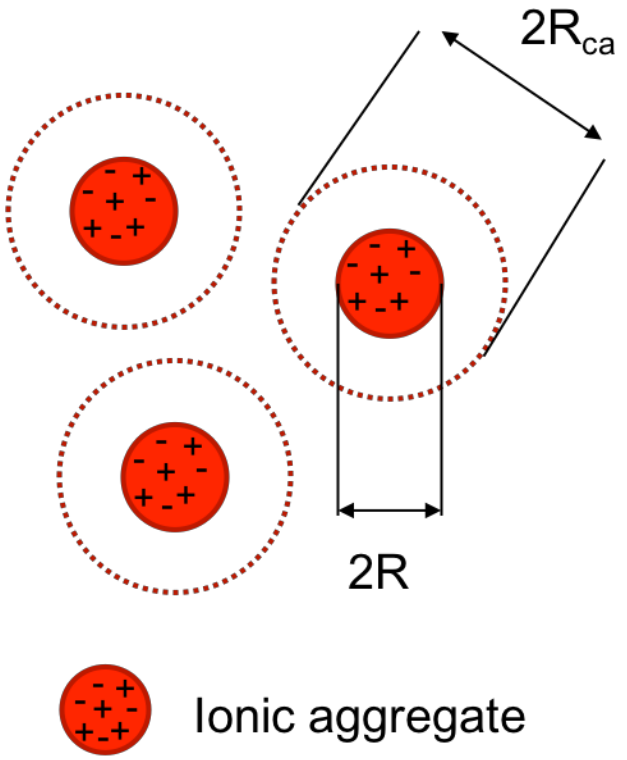

Figure 1.22. Hard-sphere model of ionic aggregation, defined by an ionic radius of R and a radius of closest approach of R_{ca}.

The Yarusso-Cooper and Kinning-Thomas models define the scattering intensity $I(q)$ as:

$$I(q) = A * f(R) * g(R_{ca}, V_p) \quad \textbf{(1.4)}$$

where A is the amplitude, $f(R)$ is the form factor term, and $g(R_{ca}, V_p)$ is the interparticle interference function.[115] Thus, the form factor is dependent on the ionic radius R, and the interparticle interference is dependent on the radius of closest approach R_{ca} and the volume per aggregate V_p.

Because the ionic aggregates are represented as hard spheres, a spherical form factor ($\Phi(x)$) is used, as shown in **Eqn 1.5**, where $x = qR$.

$$\Phi(x) = \frac{3}{x^2}(\sin x - x\cos x) \tag{1.5}$$

Thus, **Eqn 1.4** may be represented as:

$$I(q) = A * \Phi^2(x) * g(R_{ca}, V_p) \tag{1.6}$$

For the Yarusso-Cooper model, a Fournet three-body interference function is used to model the interparticle interference, and **Eqn 1.6** becomes:

$$I(q) = A * \Phi^2(x) * \frac{1}{1 + \left(\frac{8V_{ca}}{V_p}\right)\varepsilon\Phi(2qR_{ca})} \tag{1.7}$$

where V_{ca} is the volume of a sphere with radius R_{ca} and ε is a constant with a value close to 1.

For the Kinning-Thomas model, the Percus-Yevick correlation function is used to model the interparticle interference between all hard spheres, and **Eqn 1.6** becomes:

$$I(q) = A * \Phi^2(x) * \frac{1}{1 + 24\eta\left(\frac{G(B)}{B}\right)} \tag{1.8}$$

where

$$\eta = \frac{4}{3}\pi {R_{ca}}^3 \frac{1}{V_p} \tag{1.9}$$

$$B = 2qR_{ca} \tag{1.10}$$

$$G(B) = \frac{(1+2\eta)^2}{B^2(1-\eta)^4}(\sin B - B\cos B) \quad \textbf{(1.11)}$$

$$- \frac{6\eta\left(1+\frac{\eta}{2}\right)^2}{B^3(1-\eta)^4}[2B\sin B + (2-B^2)\cos B - 2]$$

$$+ \frac{\eta(1+2\eta)^2}{2B^5(1-\eta)^4}[-B^4\cos B$$

$$+ 4[(3B^2-6)\cos B + (B^3-6B)\sin B + 6]]$$

The interparticle radius (R_{ip}) (i.e. distance between aggregates) may also be extracted from the Yarusso-Cooper and Kinning-Thomas models using the following relation:

$$V_p = \frac{4}{3}\pi {R_{ip}}^3 \quad \textbf{(1.12)}$$

The utility of the modified hard-sphere models described in this section has been verified using scanning transmission electron microscopy (STEM), and ionic aggregate dimensions determined using the both STEM and the liquid-like hard sphere model were in close agreement.[116-117] In this dissertation, the Kinning-Thomas model will be used to investigate ionic aggregate morphology within prepared PEMs.

1.8.3 EHM Model

While the core-shell and hard sphere ionomer models focus solely on the morphology of the ionic aggregates, the Eisenberg-Hird-Moore (EHM) multiplet cluster model also considers the effects of ionic aggregation on physical properties.[118] The EHM model assumes an *interparticle* origin of the SAXS ionomer scattering, similar to the hard sphere model. In the EHM model, multiplets (i.e. ionic aggregates consisting of several ion pairs) act as physical crosslinks, leading to a region of restricted mobility surrounding the multiplet for polymer chains covalently bound to the ionic domains, as shown in **Figure 1.23**. As the ion content increases, the EHM model

assumes an increase in the number of multiplets and a decrease in the distance between aggregates, ultimately leading to overlapping, continuous regions of restricted mobility. When these overlapping regions become sufficiently large, they exhibit phase-separated behavior into what is defined as the 'cluster' phase and result in a distinct glass transition temperature (T_g) that is significantly higher than the T_g of the un-clustered domains. The characteristic spacing of the multiplets within this cluster phase gives rise to the ionomer peak observed in SAXS.

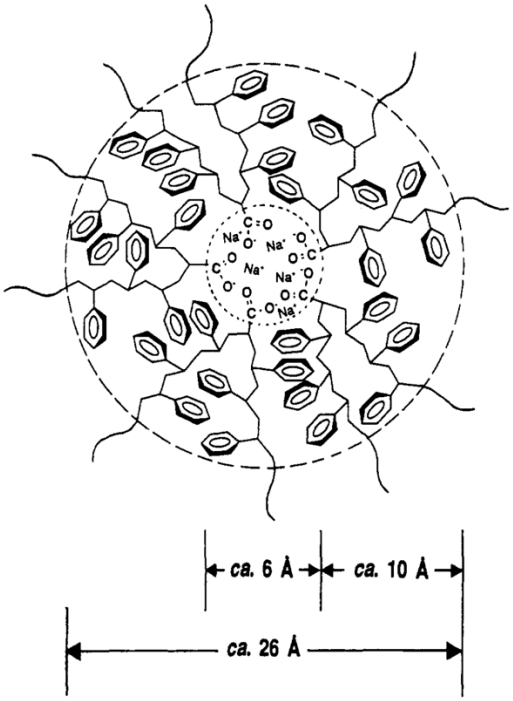

Figure 1.23. EHM multiplet cluster model of ionic aggregation demonstrating the region of restricted mobility surrounding a poly(styrene-*co*-methacrylate) ionomer multiplet.[118] Reprinted (adapted) with permission from (Eisenberg, A.; Hird, B.; Moore, R. B., A new multiplet-cluster model for the morphology of random ionomers. *Macromolecules* **1990**, *23* (18), 4098-4107). Copyright (1990) American Chemical Society.

1.9 Conclusions and Scope of Thesis

Of the sulfonated hydrocarbon materials prepared for use in PEMFCs, hydrophilic-hydrophobic multiblock copolymers have emerged as one of the most promising candidates to replace Nafion® due to their well-defined phase separation and excellent proton conductivity. Despite the exceptional transport properties of the sulfonated multiblock copolymers, their

widespread use is limited by the lengthy polymerization processes necessary for their synthesis. In this dissertation, a novel post-polymerization functionalization technique is utilized to prepare blocky copolymers from commercially-derived poly(ether ether ketone) (PEEK). By reacting in the semicrystalline gel state, functionalization is sterically restricted to the solvent-swollen amorphous fraction, yielding a blocky functionalization architecture with long segments of unfunctionalized (and thereby crystallizable) homopolymer. It is anticipated that the blocky architecture established using this method will promote phase separation between the functionalized and unfunctionalized blocks, resulting in continuous domains suitable for proton transport and excellent mechanical and dimensional stability due to preserved crystallizability.

In this work, the gel state sulfonation of PEEK is first investigated at low ion contents (Chapter 2) to determine the influence of ionic architecture (i.e. random vs. blocky) on crystallizability, crystallization kinetics, and membrane properties. This work is further extended to high degrees of sulfonation (Chapter 3), where more industrially relevant degrees of sulfonation are obtained. Additionally, the blocky bromination of PEEK is investigated and compared to random bromination (Chapter 4) to prepare reactive blocky templates for secondary substitutions. Using blocky brominated PEEK, hydrophilic-hydrophobic sulfonated-brominated PEEK copolymers are prepared and examined for use in PEMs (Chapter 5). Furthermore, the Ullmann coupling of perfluorosulfonate side chains to brominated PEEK copolymers is investigated to prepare PEMs with superacid functionalities (Chapter 6). Overall, this work elucidates a simple post-polymerization technique to prepare blocky copolymers and analyzes the resultant physical properties, crystallizability, membrane properties, and membrane morphology to determine their use as alternative hydrocarbon membranes in PEMFCs.

1.10 References

1. Annual Energy Outlook 2018. www.eia.gov/aeo (accessed June 2018).
2. UNFCC Adoption of the Paris Agreement. http://unfcc.int/resource/docs/2015/cop21/eng/l09r01.pdf (accessed June 2018).
3. June 2018 - BP Statistical Review of World Energy. https://www.bp.com/content/dam/bp/en/corporate/pdf/energy-economics/statistical-review/bp-stats-review-2018-primary-energy.pdf (accessed June 2018).
4. Scipioni, A.; Manzardo, A.; Ren, J., *Hydrogen Economy: Supply Chain, Life Cycle Analysis and Energy Transition for Sustainability*. Academic Press: 2017.
5. Mazloomi, K.; Gomes, C., Hydrogen as an energy carrier: Prospects and challenges. *Renewable and Sustainable Energy Reviews* **2012,** *16* (5), 3024-3033.
6. Alrweq, A. A. M., *Proton Exchange Membrane Fuel Cells*. Spring International Publishing AG: 2018.
7. Kraytsberg, A.; Ein-Eli, Y., Review of Advanced Materials for Proton Exchange Membrane Fuel Cells. *Energy & Fuels* **2014,** *28* (12), 7303-7330.
8. Wang, Y.; Chen, K. S.; Mishler, J.; Cho, S. C.; Adroher, X. C., A review of polymer electrolyte membrane fuel cells: Technology, applications, and needs on fundamental research. *Applied Energy* **2011,** *88* (4), 981-1007.
9. Sopian, K.; Wan Daud, W. R., Challenges and future developments in proton exchange membrane fuel cells. *Renewable Energy* **2006,** *31* (5), 719-727.
10. Hickner, M. A.; Ghassemi, H.; Kim, Y. S.; Einsla, B. R.; McGrath, J. E., Alternative Polymer Systems for Proton Exchange Membranes (PEMs). *Chemical Reviews* **2004,** *104* (10), 4587-4612.
11. Rajendran, R. G., Polymer Electrolyte Membrane Technology for Fuel Cells. *MRS Bulletin* **2005,** *30* (8), 587-590.
12. Robertson, M. A. F.; Yeager, H. L., Structure and properties of perfluorinated ionomers. In *Ionomers: Synthesis, structure, properties and applications*, Tant, M. R.; Mauritz, K. A.; Wilkes, G. L., Eds. Springer Netherlands: Dordrecht, 1997; pp 290-330.
13. Kusoglu, A.; Savagatrup, S.; Clark, K. T.; Weber, A. Z., Role of Mechanical Factors in Controlling the Structure–Function Relationship of PFSA Ionomers. *Macromolecules* **2012,** *45* (18), 7467-7476.
14. Mauritz, K. A.; Moore, R. B., State of Understanding of Nafion. *Chemical Reviews* **2004,** *104* (10), 4535-4586.
15. Hsu, W. Y.; Gierke, T. D., Ion transport and clustering in nafion perfluorinated membranes. *Journal of Membrane Science* **1983,** *13* (3), 307-326.
16. Gierke, T. D.; Munn, G. E.; Wilson, F. C., The morphology in nafion perfluorinated membrane products, as determined by wide- and small-angle x-ray studies. *Journal of Polymer Science: Polymer Physics Edition* **1981,** *19* (11), 1687-1704.
17. Moore, R.; E. Wilkerson, J.; R. Martin, C., *High-performance liquid chromatographic studies of the ion-exchange selectivity of Nafion*. 1984; Vol. 56.
18. Redepenning, J.; Anson, F. C., Permselectivities of polyelectrolyte electrode coatings as inferred from measurements with incorporated redox probes or concentration cells. *The Journal of Physical Chemistry* **1987,** *91* (17), 4549-4553.
19. Kusoglu, A.; Weber, A. Z., New Insights into Perfluorinated Sulfonic-Acid Ionomers. *Chemical Reviews* **2017,** *117* (3), 987-1104.
20. Kreuer, K. D., On the development of proton conducting polymer membranes for hydrogen and methanol fuel cells. *Journal of Membrane Science* **2001,** *185* (1), 29-39.

21. Smitha, B.; Sridhar, S.; Khan, A. A., Solid polymer electrolyte membranes for fuel cell applications—a review. *Journal of Membrane Science* **2005,** *259* (1), 10-26.
22. Subianto, S.; Cavaliere, S.; Jones, D. J.; Rozière, J., Effect of side-chain length on the electrospinning of perfluorosulfonic acid ionomers. *Journal of Polymer Science Part A: Polymer Chemistry* **2013,** *51* (1), 118-128.
23. Rozière, J.; Jones, D. J., Non-Fluorinated Polymer Materials for Proton Exchange Membrane Fuel Cells. *Annual Review of Materials Research* **2003,** *33* (1), 503-555.
24. Jalili, J.; Borsacchi, S.; Tricoli, V., Proton conducting membranes in fully anhydrous conditions at elevated temperature: Effect of Nitrilotris(methylenephosphonic acid) incorporation into Nafion- and poly(styrenesulfonic acid). *Journal of Membrane Science* **2014,** *469*, 162-173.
25. Pu, H.; Wang, D., Studies on proton conductivity of polyimide/H3PO4/imidazole blends. *Electrochimica Acta* **2006,** *51* (26), 5612-5617.
26. Kerres, J. A., Development of ionomer membranes for fuel cells. *Journal of Membrane Science* **2001,** *185* (1), 3-27.
27. Kučera, F.; Jančář, J., Homogeneous and heterogeneous sulfonation of polymers: A review. *Polymer Engineering & Science* **1998,** *38* (5), 783-792.
28. Jin, X.; Bishop, M. T.; Ellis, T. S.; Karasz, F. E., A sulphonated poly(aryl ether ketone). *British Polymer Journal* **1985,** *17* (1), 4-10.
29. Lee, J.; Marvel, C. S., Polyaromatic ether-ketone sulfonamides prepared from polydiphenyl ether-ketones by chlorosulfonation and treatment with secondary amines. *Journal of Polymer Science: Polymer Chemistry Edition* **1984,** *22* (2), 295-301.
30. Trotta, F.; Drioli, E.; Moraglio, G.; Poma, E. B., Sulfonation of polyetheretherketone by chlorosulfuric acid. *Journal of Applied Polymer Science* **1998,** *70* (3), 477-482.
31. Xing, P.; Robertson, G. P.; Guiver, M. D.; Mikhailenko, S. D.; Wang, K.; Kaliaguine, S., Synthesis and characterization of sulfonated poly(ether ether ketone) for proton exchange membranes. *Journal of Membrane Science* **2004,** *229* (1–2), 95-106.
32. Vona, M. L. D.; Sgreccia, E.; Licoccia, S.; Khadhraoui, M.; Denoyel, R.; Knauth, P., Composite Proton-Conducting Hybrid Polymers: Water Sorption Isotherms and Mechanical Properties of Blends of Sulfonated PEEK and Substituted PPSU. *Chemistry of Materials* **2008,** *20* (13), 4327-4334.
33. Di Vona, M. L.; Luchetti, L.; Spera, G. P.; Sgreccia, E.; Knauth, P., Synthetic strategies for the preparation of proton-conducting hybrid polymers based on PEEK and PPSU for PEM fuel cells. *Comptes Rendus Chimie* **2008,** *11* (9), 1074-1081.
34. Nolte, R.; Ledjeff, K.; Bauer, M.; Mülhaupt, R., Partially sulfonated poly(arylene ether sulfone) - A versatile proton conducting membrane material for modern energy conversion technologies. *Journal of Membrane Science* **1993,** *83* (2), 211-220.
35. Cebe, P.; Hong, S.-D., Crystallization behaviour of poly(ether-ether-ketone). *Polymer* **1986,** *27* (8), 1183-1192.
36. Jones, D. P.; Leach, D. C.; Moore, D. R., Mechanical properties of poly(ether-ether-ketone) for engineering applications. *Polymer* **1985,** *26* (9), 1385-1393.
37. Wang, F.; Roovers, J., Functionalization of poly(aryl ether ether ketone) (PEEK): synthesis and properties of aldehyde and carboxylic acid substituted PEEK. *Macromolecules* **1993,** *26* (20), 5295-5302.
38. Blundell, D. J.; Osborn, B. N., The morphology of poly(aryl-ether-ether-ketone). *Polymer* **1983,** *24* (8), 953-958.
39. Lee, J. K.; Li, W.; Manthiram, A., Sulfonated poly(ether ether ketone) as an ionomer for direct methanol fuel cell electrodes. *Journal of Power Sources* **2008,** *180* (1), 56-62.

40. Kaliaguine, S.; Mikhailenko, S.; Wang, K.; Xing, P.; Robertson, G.; Guiver, M., Properties of SPEEK based PEMs for fuel cell application. *Catalysis Today* **2003,** *82* (1), 213-222.
41. Huang, R. Y. M.; Shao, P.; Burns, C. M.; Feng, X., Sulfonation of poly(ether ether ketone)(PEEK): Kinetic study and characterization. *Journal of Applied Polymer Science* **2001,** *82* (11), 2651-2660.
42. Bailly, C.; Williams, D. J.; Karasz, F. E.; MacKnight, W. J., The sodium salts of sulphonated poly(aryl-ether-ether-ketone) (PEEK): Preparation and characterization. *Polymer* **1987,** *28* (6), 1009-1016.
43. Bishop, M. T.; Karasz, F. E.; Russo, P. S.; Langley, K. H., Solubility and properties of a poly(aryl ether ketone) in strong acids. *Macromolecules* **1985,** *18* (1), 86-93.
44. Anderson, L. J.; Yuan, X.; Fahs, G. B.; Moore, R. B., Blocky Ionomers via Sulfonation of Poly(ether ether ketone) in the Semicrystalline Gel State. *Macromolecules* **2018,** *51* (16), 6226-6237.
45. Xing, D.; Kerres, J., Improved performance of sulfonated polyarylene ethers for proton exchange membrane fuel cells. *Polymers for Advanced Technologies* **2006,** *17* (7-8), 591-597.
46. Kerres, J.; Cui, W.; Reichle, S., New sulfonated engineering polymers via the metalation route. I. Sulfonated poly(ethersulfone) PSU Udel® via metalation-sulfination-oxidation. *Journal of Polymer Science Part A: Polymer Chemistry* **1996,** *34* (12), 2421-2438.
47. Kerres, J.; Cui, W.; Junginger, M., Development and characterization of crosslinked ionomer membranes based upon sulfinated and sulfonated PSU crosslinked PSU blend membranes by alkylation of sulfinate groups with dihalogenoalkanes. *Journal of Membrane Science* **1998,** *139* (2), 227-241.
48. Kerres, J.; Zhang, W.; Cui, W., New sulfonated engineering polymers via the metalation route. II. Sulfinated/sulfonated poly(ether sulfone) PSU Udel and its crosslinking. *Journal of Polymer Science Part A: Polymer Chemistry* **1998,** *36* (9), 1441-1448.
49. Ueda, M.; Toyota, H.; Ouchi, T.; Sugiyama, J.-I.; Yonetake, K.; Masuko, T.; Teramoto, T., Synthesis and characterization of aromatic poly(ether sulfone)s containing pendant sodium sulfonate groups. *Journal of Polymer Science Part A: Polymer Chemistry* **1993,** *31* (4), 853-858.
50. Wang, F.; Hickner, M.; Kim, Y. S.; Zawodzinski, T. A.; McGrath, J. E., Direct polymerization of sulfonated poly(arylene ether sulfone) random (statistical) copolymers: candidates for new proton exchange membranes. *Journal of Membrane Science* **2002,** *197* (1), 231-242.
51. Wang, F.; Hickner, M.; Ji, Q.; Harrison, W.; Mecham, J.; Zawodzinski, T. A.; McGrath, J. E., Synthesis of highly sulfonated poly(arylene ether sulfone) random (statistical) copolymers via direct polymerization. *Macromolecular Symposia* **2001,** *175* (1), 387-396.
52. Sankir, M.; Bhanu, V. A.; Harrison, W. L.; Ghassemi, H.; Wiles, K. B.; Glass, T. E.; Brink, A. E.; Brink, M. H.; McGrath, J. E., Synthesis and characterization of 3,3′-disulfonated-4,4′-dichlorodiphenyl sulfone (SDCDPS) monomer for proton exchange membranes (PEM) in fuel cell applications. *Journal of Applied Polymer Science* **2006,** *100* (6), 4595-4602.
53. Gil, M.; Ji, X.; Li, X.; Na, H.; Eric Hampsey, J.; Lu, Y., Direct synthesis of sulfonated aromatic poly(ether ether ketone) proton exchange membranes for fuel cell applications. *Journal of Membrane Science* **2004,** *234* (1), 75-81.
54. Gao, Y.; Robertson, G. P.; Guiver, M. D.; Mikhailenko, S. D.; Li, X.; Kaliaguine, S., Synthesis of Poly(arylene ether ether ketone ketone) Copolymers Containing Pendant Sulfonic Acid Groups Bonded to Naphthalene as Proton Exchange Membrane Materials. *Macromolecules* **2004,** *37* (18), 6748-6754.

55. Li, X.; Liu, C.; Lu, H.; Zhao, C.; Wang, Z.; Xing, W.; Na, H., Preparation and characterization of sulfonated poly(ether ether ketone ketone) proton exchange membranes for fuel cell application. *Journal of Membrane Science* **2005,** *255* (1), 149-155.
56. Xu, J.; Ni, H.; Wang, S.; Wang, Z.; Zhang, H., Direct polymerization of a novel sulfonated poly(arylene ether ketone sulfone)/sulfonated poly(vinylalcohol) crosslinked membrane for direct methanol fuel cell applications. *Journal of Membrane Science* **2015,** *492*, 505-517.
57. Harrison, W. L.; Wang, F.; Mecham, J. B.; Bhanu, V. A.; Hill, M.; Kim, Y. S.; McGrath, J. E., Influence of the bisphenol structure on the direct synthesis of sulfonated poly(arylene ether) copolymers. I. *Journal of Polymer Science Part A: Polymer Chemistry* **2003,** *41* (14), 2264-2276.
58. Chen, R.; Li, G.; Yang, S.; Xiong, M.; Jin, J., Sulfonated poly(arylene ether sulfone) polymers containing 3,4-difluoro-phenyl moiety as proton exchange membranes. *Solid State Ionics* **2017,** *300*, 157-164.
59. Liu, B.; Kim, D.-S.; Murphy, J.; Robertson, G. P.; Guiver, M. D.; Mikhailenko, S.; Kaliaguine, S.; Sun, Y.-M.; Liu, Y.-L.; Lai, J.-Y., Fluorenyl-containing sulfonated poly(aryl ether ether ketone ketone)s (SPFEEKK) for fuel cell applications. *Journal of Membrane Science* **2006,** *280* (1), 54-64.
60. Krishnan, N. N.; Kim, H. J.; Prasanna, M.; Cho, E.; Shin, E. M.; Lee, S. Y.; Oh, I. H.; Hong, S. A.; Lim, T. H., Synthesis and characterization of sulfonated poly(ether sulfone) copolymer membranes for fuel cell applications. *Journal of Power Sources* **2006,** *158* (2), 1246-1250.
61. Kim, Y. S.; Wang, F.; Hickner, M.; Mccartney, S.; Hong, Y. T.; Harrison, W.; Zawodzinski, T. A.; Mcgrath, J. E., Effect of acidification treatment and morphological stability of sulfonated poly(arylene ether sulfone) copolymer proton-exchange membranes for fuel-cell use above 100 °C. *Journal of Polymer Science Part B: Polymer Physics* **2003,** *41* (22), 2816-2828.
62. Hickner, M. A.; Pivovar, B. S., The Chemical and Structural Nature of Proton Exchange Membrane Fuel Cell Properties. *Fuel Cells* **2005,** *5* (2), 213-229.
63. Han, S.; Zhang, M.-S.; Shin, J.; Lee, Y.-S., A convenient crosslinking method for sulfonated poly(ether ether ketone) membranes via friedel–crafts reaction using 1,6-dibromohexane and aluminum trichloride. *Journal of Applied Polymer Science* **2014,** *131* (17).
64. Zhong, S.; Cui, X.; Cai, H.; Fu, T.; Zhao, C.; Na, H., Crosslinked sulfonated poly(ether ether ketone) proton exchange membranes for direct methanol fuel cell applications. *Journal of Power Sources* **2007,** *164* (1), 65-72.
65. Zhong, S.; Liu, C.; Na, H., Preparation and properties of UV irradiation-induced crosslinked sulfonated poly(ether ether ketone) proton exchange membranes. *Journal of Membrane Science* **2009,** *326* (2), 400-407.
66. Hande, V. R.; Rao, S.; Rath, S. K.; Thakur, A.; Patri, M., Crosslinking of sulphonated poly (ether ether ketone) using aromatic bis(hydroxymethyl) compound. *Journal of Membrane Science* **2008,** *322* (1), 67-73.
67. Mikhailenko, S. D.; Wang, K.; Kaliaguine, S.; Xing, P.; Robertson, G. P.; Guiver, M. D., Proton conducting membranes based on cross-linked sulfonated poly(ether ether ketone) (SPEEK). *Journal of Membrane Science* **2004,** *233* (1), 93-99.
68. Kim, D. S.; Liu, B.; Guiver, M. D., Influence of silica content in sulfonated poly(arylene ether ether ketone ketone) (SPAEEKK) hybrid membranes on properties for fuel cell application. *Polymer* **2006,** *47* (23), 7871-7880.
69. Tripathi, B. P.; Shahi, V. K., SPEEK–zirconium hydrogen phosphate composite membranes with low methanol permeability prepared by electro-migration and in situ precipitation. *Journal of Colloid and Interface Science* **2007,** *316* (2), 612-621.

70. Jaafar, J.; Ismail, A. F.; Matsuura, T.; Nagai, K., Performance of SPEEK based polymer–nanoclay inorganic membrane for DMFC. *Journal of Membrane Science* **2011,** *382* (1), 202-211.
71. Mikhailenko, S. D.; Zaidi, S. M. J.; Kaliaguine, S., Sulfonated polyether ether ketone based composite polymer electrolyte membranes. *Catalysis Today* **2001,** *67* (1), 225-236.
72. Su, Y.-H.; Liu, Y.-L.; Sun, Y.-M.; Lai, J.-Y.; Wang, D.-M.; Gao, Y.; Liu, B.; Guiver, M. D., Proton exchange membranes modified with sulfonated silica nanoparticles for direct methanol fuel cells. *Journal of Membrane Science* **2007,** *296* (1), 21-28.
73. Liu, Y.-L., Developments of highly proton-conductive sulfonated polymers for proton exchange membrane fuel cells. *Polymer Chemistry* **2012,** *3* (6), 1373-1383.
74. Feng, S.; Wang, G.; Zhang, H.; Pang, J., Graft octa-sulfonated poly(arylene ether) for high performance proton exchange membrane. *Journal of Materials Chemistry A* **2015,** *3* (24), 12698-12708.
75. Feng, S.; Shen, K.; Wang, Y.; Pang, J.; Jiang, Z., Concentrated sulfonated poly (ether sulfone)s as proton exchange membranes. *Journal of Power Sources* **2013,** *224*, 42-49.
76. Pang, J.; Shen, K.; Ren, D.; Feng, S.; Wang, Y.; Jiang, Z., Polymer electrolyte membranes based on poly(arylene ether)s with penta-sulfonated pendent groups. *Journal of Materials Chemistry A* **2013,** *1* (4), 1465-1474.
77. Matsumoto, K.; Higashihara, T.; Ueda, M., Locally and Densely Sulfonated Poly(ether sulfone)s as Proton Exchange Membrane. *Macromolecules* **2009,** *42* (4), 1161-1166.
78. Taeger, A.; Vogel, C.; Lehmann, D.; Lenk, W.; Schlenstedt, K.; Meier-Haack, J., Sulfonated multiblock copoly(ether sulfone)s as membrane materials for fuel cell applications. *Macromolecular Symposia* **2004,** *210* (1), 175-184.
79. Einsla, M. L.; Kim, Y. S.; Hawley, M.; Lee, H.-S.; McGrath, J. E.; Liu, B.; Guiver, M. D.; Pivovar, B. S., Toward Improved Conductivity of Sulfonated Aromatic Proton Exchange Membranes at Low Relative Humidity. *Chemistry of Materials* **2008,** *20* (17), 5636-5642.
80. Genies, C.; Mercier, R.; Sillion, B.; Cornet, N.; Gebel, G.; Pineri, M., Soluble sulfonated naphthalenic polyimides as materials for proton exchange membranes. *Polymer* **2001,** *42* (2), 359-373.
81. Lee, H.-S.; Roy, A.; Lane, O.; Dunn, S.; McGrath, J. E., Hydrophilic–hydrophobic multiblock copolymers based on poly(arylene ether sulfone) via low-temperature coupling reactions for proton exchange membrane fuel cells. *Polymer* **2008,** *49* (3), 715-723.
82. Ghassemi, H.; McGrath, J. E.; Zawodzinski, T. A., Multiblock sulfonated–fluorinated poly(arylene ether)s for a proton exchange membrane fuel cell. *Polymer* **2006,** *47* (11), 4132-4139.
83. Yu, X.; Roy, A.; Dunn, S.; Yang, J.; McGrath, J. E., Synthesis and Characterization of Sulfonated- Fluorinated, Hydrophilic-Hydrophobic Multiblock Copolymers for Proton Exchange Membranes. *Macromolecular Symposia* **2006,** *245-246* (1), 439-449.
84. Yu, X.; Roy, A.; Dunn, S.; Badami, A. S.; Yang, J.; Good, A. S.; McGrath, J. E., Synthesis and characterization of sulfonated-fluorinated, hydrophilic-hydrophobic multiblock copolymers for proton exchange membranes. *Journal of Polymer Science Part A: Polymer Chemistry* **2009,** *47* (4), 1038-1051.
85. Chen, Y.; Guo, R.; Lee, C. H.; Lee, M.; McGrath, J. E., Partly fluorinated poly(arylene ether ketone sulfone) hydrophilic–hydrophobic multiblock copolymers for fuel cell membranes. *International Journal of Hydrogen Energy* **2012,** *37* (7), 6132-6139.
86. Lee, M.; Park, J. K.; Lee, H.-S.; Lane, O.; Moore, R. B.; McGrath, J. E.; Baird, D. G., Effects of block length and solution-casting conditions on the final morphology and properties of disulfonated poly(arylene ether sulfone) multiblock copolymer films for proton exchange membranes. *Polymer* **2009,** *50* (25), 6129-6138.

87. Chen, Y.; Rowlett, J. R.; Lee, C. H.; Lane, O. R.; VanHouten, D. J.; Zhang, M.; Moore, R. B.; McGrath, J. E., Synthesis and characterization of multiblock partially fluorinated hydrophobic poly(arylene ether sulfone)-hydrophilic disulfonated poly(arylene ether sulfone) copolymers for proton exchange membranes. *Journal of Polymer Science Part A: Polymer Chemistry* **2013,** *51* (10), 2301-2310.
88. Bae, B.; Miyatake, K.; Watanabe, M., Synthesis and Properties of Sulfonated Block Copolymers Having Fluorenyl Groups for Fuel-Cell Applications. *ACS Applied Materials & Interfaces* **2009,** *1* (6), 1279-1286.
89. Oh, K.; Ketpang, K.; Kim, H.; Shanmugam, S., Synthesis of sulfonated poly(arylene ether ketone) block copolymers for proton exchange membrane fuel cells. *Journal of Membrane Science* **2016,** *507*, 135-142.
90. Zhao, C.; Li, X.; Wang, Z.; Dou, Z.; Zhong, S.; Na, H., Synthesis of the block sulfonated poly(ether ether ketone)s (S-PEEKs) materials for proton exchange membrane. *Journal of Membrane Science* **2006,** *280* (1), 643-650.
91. Zhao, C.; Lin, H.; Shao, K.; Li, X.; Ni, H.; Wang, Z.; Na, H., Block sulfonated poly(ether ether ketone)s (SPEEK) ionomers with high ion-exchange capacities for proton exchange membranes. *Journal of Power Sources* **2006,** *162* (2), 1003-1009.
92. Takamuku, S.; Jannasch, P., Multiblock Copolymers with Highly Sulfonated Blocks Containing Di- and Tetrasulfonated Arylene Sulfone Segments for Proton Exchange Membrane Fuel Cell Applications. *Advanced Energy Materials* **2012,** *2* (1), 129-140.
93. Yang, A. C. C.; Narimani, R.; Frisken, B. J.; Holdcroft, S., Investigations of crystallinity and chain entanglement on sorption and conductivity of proton exchange membranes. *Journal of Membrane Science* **2014,** *469*, 251-261.
94. Hamada, T.; Hasegawa, S.; Fukasawa, H.; Sawada, S.-i.; Koshikawa, H.; Miyashita, A.; Maekawa, Y., Poly(ether ether ketone) (PEEK)-based graft-type polymer electrolyte membranes having high crystallinity for high conducting and mechanical properties under various humidified conditions. *Journal of Materials Chemistry A* **2015,** *3* (42), 20983-20991.
95. Wang, R.; Yan, X.; Wu, X.; He, G.; Du, L.; Hu, Z.; Tan, M., Modification of hydrophilic channels in Nafion membranes by DMBA: Mechanism and effects on proton conductivity. *Journal of Polymer Science Part B: Polymer Physics* **2014,** *52* (16), 1107-1117.
96. Lindfors, B. E.; Mani, R. S.; McGrath, J. E.; Mohanty, D. K., Heterogeneous hydrolysis of poly(aryl ether ketimine)s — an alternative synthetic route to semicrystalline poly(aryl ether ketone)s. *Die Makromolekulare Chemie, Rapid Communications* **1991,** *12* (6), 337-345.
97. Brink, A. E.; Gutzeit, S.; Lin, T.; Marand, H.; Lyon, K.; Hua, T.; Davis, R.; Riffle, J. S., Fine polymeric powders from poly(aryleneether ketone)s. *Polymer* **1993,** *34* (4), 825-829.
98. Chen, Y.; Lee, C. H.; Rowlett, J. R.; McGrath, J. E., Synthesis and characterization of multiblock semi-crystalline hydrophobic poly(ether ether ketone)–hydrophilic disulfonated poly(arylene ether sulfone) copolymers for proton exchange membranes. *Polymer* **2012,** *53* (15), 3143-3153.
99. Feng, S.; Pang, J.; Yu, X.; Wang, G.; Manthiram, A., High-Performance Semicrystalline Poly(ether ketone)-Based Proton Exchange Membrane. *ACS Applied Materials & Interfaces* **2017,** *9* (29), 24527-24537.
100. Fahs, G. B.; Benson, S. D.; Moore, R. B., Blocky Sulfonation of Syndiotactic Polystyrene: A Facile Route toward Tailored Ionomer Architecture via Postpolymerization Functionalization in the Gel State. *Macromolecules* **2017,** *50* (6), 2387-2396.
101. Noble, K. F.; Noble, A. M.; Talley, S. J.; Moore, R. B., Blocky bromination of syndiotactic polystyrene via post-polymerization functionalization in the heterogeneous gel state. *Polymer Chemistry* **2018,** *9* (41), 5095-5106.

102. Assumma, L.; Iojoiu, C.; Mercier, R.; Lyonnard, S.; Nguyen, H. D.; Planes, E., Synthesis of partially fluorinated poly(arylene ether sulfone) multiblock copolymers bearing perfluorosulfonic functions. *Journal of Polymer Science Part A: Polymer Chemistry* **2015,** *53* (16), 1941-1956.
103. Mikami, T.; Miyatake, K.; Watanabe, M., Poly(arylene ether)s Containing Superacid Groups as Proton Exchange Membranes. *ACS Applied Materials & Interfaces* **2010,** *2* (6), 1714-1721.
104. Xu, K.; Oh, H.; Hickner, M. A.; Wang, Q., Highly Conductive Aromatic Ionomers with Perfluorosulfonic Acid Side Chains for Elevated Temperature Fuel Cells. *Macromolecules* **2011,** *44* (12), 4605-4609.
105. Yoshimura, K.; Iwasaki, K., Aromatic Polymer with Pendant Perfluoroalkyl Sulfonic Acid for Fuel Cell Applications. *Macromolecules* **2009,** *42* (23), 9302-9306.
106. Liu, B.; Robertson, G. P.; Guiver, M. D.; Shi, Z.; Navessin, T.; Holdcroft, S., Fluorinated Poly(aryl ether) Containing a 4-Bromophenyl Pendant Group and its Phosphonated Derivative. *Macromolecular Rapid Communications* **2006,** *27* (17), 1411-1417.
107. Miyatake, K.; Hay, A. S., New poly(arylene ether)s with pendant phosphonic acid groups. *Journal of Polymer Science Part A: Polymer Chemistry* **2001,** *39* (21), 3770-3779.
108. Macknight, W. J.; Taggart, W. P.; Stein, R. S., A model for the structure of ionomers. *Journal of Polymer Science: Polymer Symposia* **1974,** *45* (1), 113-128.
109. Fujimura, M.; Hashimoto, T.; Kawai, H., Small-angle x-ray scattering study of perfluorinated ionomer membranes. 2. Models for ionic scattering maximum. *Macromolecules* **1982,** *15* (1), 136-144.
110. Fournet, G., Diffusion des rayons X par les fluides. *Acta Crystallographica* **1951,** *4* (4), 293-301.
111. Yarusso, D. J.; Cooper, S. L., Microstructure of ionomers: interpretation of small-angle x-ray scattering data. *Macromolecules* **1983,** *16* (12), 1871-1880.
112. Percus, J. K.; Yevick, G. J., Analysis of Classical Statistical Mechanics by Means of Collective Coordinates. *Physical Review* **1958,** *110* (1), 1-13.
113. Kinning, D. J.; Thomas, E. L., Hard-sphere interactions between spherical domains in diblock copolymers. *Macromolecules* **1984,** *17* (9), 1712-1718.
114. Seitz, M. E.; Chan, C. D.; Opper, K. L.; Baughman, T. W.; Wagener, K. B.; Winey, K. I., Nanoscale Morphology in Precisely Sequenced Poly(ethylene-co-acrylic acid) Zinc Ionomers. *Journal of the American Chemical Society* **2010,** *132* (23), 8165-8174.
115. Zhou, N. C.; Chan, C. D.; Winey, K. I., Reconciling STEM and X-ray Scattering Data To Determine the Nanoscale Ionic Aggregate Morphology in Sulfonated Polystyrene Ionomers. *Macromolecules* **2008,** *41* (16), 6134-6140.
116. Benetatos, N. M.; Smith, B. W.; Heiney, P. A.; Winey, K. I., Toward Reconciling STEM and SAXS Data from Ionomers by Investigating Gold Nanoparticles. *Macromolecules* **2005,** *38* (22), 9251-9257.
117. Benetatos, N. M.; Heiney, P. A.; Winey, K. I., Reconciling STEM and X-ray Scattering Data from a Poly(styrene-ran-methacrylic acid) Ionomer: Ionic Aggregate Size. *Macromolecules* **2006,** *39* (16), 5174-5176.
118. Eisenberg, A.; Hird, B.; Moore, R. B., A new multiplet-cluster model for the morphology of random ionomers. *Macromolecules* **1990,** *23* (18), 4098-4107.

Chapter 2

Blocky Ionomers via Sulfonation of Poly(ether ether ketone) in the Semicrystalline Gel State

(*Published in Macromolecules)*

Lindsey J. Anderson, Xijing Yuan, Gregory B. Fahs, Robert B. Moore*

Department of Chemistry, Macromolecules Innovation Institute, Virginia Polytechnic Institute and State University, Blacksburg, Virginia 24061, United States

*To whom correspondence should be addressed: rbmoore3@vt.edu

2.1 Abstract

Blocky sulfonated poly(ether ether ketone) (SPEEK) ionomers were synthesized by postpolymerization functionalization in the gel state. Matched sets of blocky and random SPEEK with ion contents between 3 and 11 mol % were prepared, and the thermal transitions and crystallization kinetics were examined using differential scanning calorimetry (DSC). At similar ion contents, the blocky SPEEK exhibited higher crystallizability and faster crystallization kinetics than random SPEEK. Reduced scattering contrast in the USAXS/SAXS/WAXD analysis of the blocky SPEEK copolymer membranes, relative to the random analogues, suggested that the ionic aggregates in blocky SPEEK were distributed in close proximity to the crystalline domains. Despite similar water uptake values for the low ion content random and blocky SPEEK membranes, the blocky SPEEK exhibited higher proton conductivities than their random analogues. At significantly higher ion contents (45 mol %), the blocky SPEEK membranes remained semicrystalline, showed controlled water uptake, and exhibited a 2.5 times higher conductivity over that of the amorphous, random analogues. Moreover, these new blocky, semicrystalline SPEEK membranes were found to exhibit a proton conductivity that was comparable to that of the benchmark 1100 EW Nafion®.

2.2 Introduction

Fuel cells have emerged as a promising alternative energy candidate due to their high efficiency, renewable nature, and innocuous byproducts. A key component of fuel cells is the proton exchange membrane (PEM), which acts as both the proton conductor as well as the gas separator.[1] To function in the harsh environment of a fuel cell, PEMs must exhibit chemical and electrochemical stability, mechanical strength and integrity, and high proton conductivity.[2-4] The most widely studied PEM is Nafion®, a perfluorinated ionomer that exhibits excellent thermal and mechanical stability in addition to exceptional transport properties.[5-9] The properties of Nafion® arise from the phase separation of the hydrophobic poly(tetrafluoroethylene) (PTFE) backbone from the hydrophilic sulfonic acid groups, which generates a well-defined nano-separated morphology with a continuous hydrophilic domain. Despite its success as a benchmark PEM, Nafion® has several drawbacks including high cost, difficult synthesis, and limited performance at high temperature and low humidity.[10-11] Thus, the search for novel low-cost, high-performance PEMs to replace Nafion® has gained significant attention in recent years.[12-13]

Sulfonated aromatic hydrocarbon polymers such as poly(ether ether ketone)s, poly(ether sulfone)s, polyimides, and polybenzimidazoles have been explored as viable alternative PEMs due to their excellent mechanical properties, easy processability, and high hydrolytic, oxidative, and thermal stability.[14-16] These materials are prepared by either post-polymerization sulfonation of the aromatic backbone or by direct synthesis using sulfonated monomers. The degree of sulfonation dictates the ion exchange capacity of these membranes and high degrees of sulfonation are necessary to achieve high proton conductivity.[10]

Among the widely explored hydrocarbon membranes, sulfonated poly(ether ether ketone) (SPEEK) is popular due to its low cost, ease of production, good proton conductivity, and high thermal and chemical stability.[17-20] Conventionally, SPEEK is prepared by post-polymerization

functionalization using concentrated sulfuric acid.[1, 21-22] Due to the limited solubility of PEEK, the sulfuric acid acts as both the solvent and the sulfonating reagent, resulting in heterogeneous sulfonation with a large distribution of sulfonic acid functionalities along the polymer chain. Using this method, the degree of sulfonation may be varied by sulfonation time and temperature; however, little control is granted over the ionic group distribution along the chains. In addition, the conventional method prohibits sulfonation below 20-30 mol% due to the concurrent dissolution and sulfonation of PEEK.[23]

To obtain better control over the ionic distribution along the polymer chains and enhance the properties of hydrocarbon membranes, amorphous block copolymers have been explored, wherein the hydrophilic sulfonic acid functionalities are concentrated into blocks along the polymer chain.[24-25] McGrath and coworkers synthesized block copolymers based on poly(arylene ether sulfone)s consisting of partially fluorinated ether sulfone blocks (hydrophobic block) and disulfonated ether sulfone blocks (hydrophilic block). These studies demonstrated that block copolymers have higher proton conductivity than random copolymers at similar ion contents due to improved hydrophobic/hydrophilic phase separation.[26] This enhanced performance was attributed to the fact that the multiblock architecture resulted in well-ordered lamellar morphologies with long range periodicity. In contrast, the random architecture did not demonstrate any significant long-range order, and the ionic aggregates were poorly interconnected and homogeneously distributed throughout the amorphous polymer matrix.[27] McGrath also showed that block copolymers displayed enhanced proton conductivity at low hydration levels compared to random copolymers. Thus, it was postulated that a more interconnected network of hydrophilic domains is present in block copolymers as compared to random copolymers.[28] Other work has been performed to directly synthesize SPEEK block copolymers by controlled coupling of hydrophobic and hydrophilic oligomers.[29-30] Compared to random SPEEK, the synthetically-

tailored block copolymers of SPEEK exhibited increased proton conductivity and increased water uptake due to more well-defined phase separation.

Additional studies of directly-synthesized poly(ether ether ketone)-disulfonated poly(arylene ether sulfone) block copolymers demonstrated that it is possible to preserve the semicrystalline nature of PEEK by separating the hydrophobic and hydrophilic domains into distinct blocks.[31] Again, the distinct nanophase morphology that arises in these block copolymers resulted in proton conductivities that were higher than Nafion® 212 and the random copolymer analogs, even at low humidities. The incorporation of crystallinity into PEMs has also been shown to improve mechanical and thermal stability and decrease excessive swelling in water.[13, 32-34] This is particularly important at the high degrees of sulfonation necessary to achieve good proton conductivity, where amorphous hydrocarbon membranes often swell or even dissolve in water.[35] Achieving a high degree of sulfonation with high crystallizability is advantageous to enable the production of membranes with good proton conductivity, mechanical durability, and resistance to undesirable swelling during PEM fuel cell operation.

Recently, we introduced a facile method of post-polymerization functionalization to produce 'blocky' architectures.[36-37] This method consists of sulfonating semicrystalline, aromatic polymers in the semicrystalline gel-state, as demonstrated using syndiotactic polystyrene (sPS). During sulfonation, the sulfonating reagent is sterically excluded from the tightly-packed crystalline domains present in the gels, and is only capable of reacting with the solvent-swollen amorphous chains within the physical network. Thus, selective sulfonation of the amorphous chain segments occurs and long runs of unsulfonated, crystallizable sPS homopolymer are preserved. This method not only enables the synthesis of blocky copolymers using a simple experimental procedure, but also conserves the crystallizability necessary for improved phase separation and enhanced mechanical properties once the blocky materials are cast into membranes.

With our discovery of thermoreversible, semicrystalline gels of poly(ether ether ketone) (PEEK) in dichloroacetic acid (DCA),[38] it is now possible to extend the facile gel-state functionalization method developed for sPS to other crystallizable polymers that are more suitable for PEM fuel cell applications. In this work, the sulfonation of PEEK gels was carried out to produce SPEEK with a blocky architecture. The blocky SPEEK ionomers are compared to random SPEEK ionomers at similar degrees of sulfonation to determine the influence of ionic architectures on the resultant membrane properties. Relatively low degrees of sulfonation were examined in this initial report to highlight the effect of architecture on crystallizability, crystallization kinetics, and membrane properties.

2.3 Experimental

2.3.1 Materials

Poly(ether ether ketone) (PEEK) pellets (Victrex 150G) were obtained from Victrex. Dichloroacetic acid (DCA) was purchased from Sigma-Aldrich and was dried over magnesium sulfate (Fisher Scientific), then filtered through a 0.45 μm PTFE syringe filter prior to use. Trifluoroacetic anhydride was purchased from Sigma-Aldrich. Concentrated sulfuric acid (98%), 1,2-dichloroethane (DCE), sodium chloride, and cesium chloride were purchased from Fisher Scientific.

2.3.2 Preparation of Sulfonating Reagent

Trifluoroacetyl sulfate was prepared according to previously published procedures.[39-40] Trifluoroacetic anhydride (3.8 mL; 0.027 mol) was added to a nitrogen-purged round bottom flask. The flask was cooled in an ice bath for 15 minutes and then concentrated sulfuric acid (1 mL; 0.018 mol) was added. The solution was stirred vigorously for approximately 3 hours to obtain a clear, light brown liquid.

2.3.3 Random Sulfonation of Poly(ether ether ketone)

In contrast to the conventional method to sulfonate PEEK (i.e., heterogeneous dissolution and sulfonation in concentrated sulfuric acid), we have developed a procedure to first dissolve PEEK in a non-sulfonating solvent followed by a homogeneous sulfonation to obtain a truly random functionalization. PEEK (5.0 g) was dissolved in dichloroacetic acid at 185 °C to a final concentration of 10% w/v. Once dissolved, the temperature was lowered to 80 °C and the solution as allowed to equilibrate at this temperature under nitrogen for 1 hour. Next, 0.5-1 equivalents of trifluoroacetyl sulfate was added dropwise to the PEEK solution, and the reaction was allowed to proceed for 1-4 hours. For reactions targeting degrees of sulfonation of 15 mol% and above, reactions were run for up to 24 hours. The reaction was terminated by precipitation into cold deionized water. The product was filtered, washed with deionized water, and then washed by soxhlet extraction over methanol for 24 hours. The resulting polymers were dried at 100 °C for 12 hours. Prior to any analysis, samples were ground under liquid nitrogen to form a fine powder.

2.3.4 Blocky Sulfonation of Poly(ether ether ketone)

PEEK (5.0 g) was dissolved in dichloroacetic acid at 185 °C to a final concentration of 20% w/v. Once dissolved, the solution was removed from heat and allowed to remain at room temperature for at least 24 hours. During this time, the PEEK crystallizes from solution to form a thermoreversible gel network.[38] The gel was manually broken into small particles using a spatula and diluted to a 10 w/v% suspension with additional dichloroacetic acid. For reactions targeting degrees of sulfonation higher than 15 mol%, the gel particles were diluted to a 10 w/v% suspension in 1,2-dichloroethane (DCE). These reactions were performed for up to 48 hours. The gel suspension was equilibrated at 80 °C under nitrogen for 1 hour. Once equilibrated, 0.5-1 equivalents of trifluoroacetyl sulfate was added dropwise to the PEEK solution, and the reaction was allowed to proceed for 1-4 hours. The reaction was terminated by precipitation into cold

deionized water. The product was filtered, washed with deionized water, and then washed by soxhlet extraction over methanol for 24 hours. The resulting polymers were dried at 100 °C for 12 hours. Prior to any analysis, samples were ground under liquid nitrogen to form a fine powder.

2.3.5 Membrane Preparation

SPEEK membranes were prepared by dissolving the random or blocky SPEEK (in the H^+-form) in DCA at 185 °C to a concentration of 15% w/v. Once dissolved, the solution was allowed to cool to room temperature and then filtered through a 0.45 μm PTFE syringe filter. These solutions were cast onto a glass substrate that was preheated to 100 °C using a doctor blade set to 7.5 mils. The wet films were allowed to dry on the heated substrate for 30 minutes, resulting in a final dry thickness of 25 μm. Membranes were washed with deionized water to remove residual DCA and then dried at 100 °C for 12 hours.

2.3.6 Ion Exchange

The H^+-form SPEEK samples were converted to the sodium-form (Na^+-form) by stirring the powders in 2M NaCl (aq) for 24 hours. To convert to the cesium-form (Cs^+-form), SPEEK samples (ground powders and/or cast membranes) were stirred in 1M CsCl (aq) for 24 hours. Samples in either salt form were then filtered, washed with deionized water to remove residual salt, and dried at 100 °C for 12 hours. Complete ion exchange was confirmed by thermogravimetric analysis.

2.3.7 ^{1}H NMR Spectroscopy

^{1}H NMR spectra were measured using a Bruker Avance III 600 MHz. Due to the low degree of sulfonation targeted for this study, conventional deuterated solvents were not able to dissolve the SPEEK samples, and thus a solvent suppression method was employed. SPEEK samples were dissolved in DCA at 185 °C to a concentration of 10% w/v. Once dissolved, the samples were cooled to room temperature and diluted by a factor of 5 using deuterated chloroform

($CDCl_3$) with 0.05% v/v TMS. Presaturation of the intense DCA resonance at 6 ppm was performed during acquisition to obtain a suitable spectrum, free of a solvent contribution. The degree of sulfonation was calculated from the integration of the 10' peak relative to the combined area of the 1,3,6,8 peaks.[1]

2.3.8 Thermogravimetric Analysis (TGA)

A TA Instruments TGA Q500 thermogravimetric analyzer was used to determine the thermal stability of SPEEK. Samples were heated from room temperature to 800 ºC at 10 ºC/min under an air atmosphere.

2.3.9 Differential Scanning Calorimetry (DSC)

A TA Instruments Q2000 DSC was used to determine the thermal transitions and crystallization behavior of the SPEEK samples. Na^+-form and Cs^+-form SPEEK powders were used for this analysis, as acid-form SPEEK is not thermally stable at elevated temperatures.[17, 41] Samples were pre-dried at 150 °C for 5 minutes before several heating and cooling sequences. Under a nitrogen atmosphere, the dried samples (~5-8 mg) were heated from 0 °C to 380 °C at 20 °C/min, quench cooled to 0 °C and then reheated from 0 °C to 380 °C at 20 °C/min. Furthermore, the isothermal crystallization was carried out by heating SPEEK samples from 25 ºC to 380 ºC at 20 ºC/min, isothermally holding at 380 ºC for 3 minutes, quench cooling to the desired crystallization temperature (T_c), isothermally holding at this T_c for 2 hours, quench cooling to 100 ºC, and finally heating from 100 ºC to 380 ºC at 10 ºC/min. Isothermal crystallization was carried out at 10 ºC increments from 220 ºC to 290 ºC. The glass transition temperature (T_g), enthalpy of crystallization (ΔH_c), melting temperature (T_m), and enthalpy of melting (ΔH_m) were determined from each heat scan using the TA Instruments Universal Analysis software.

To evaluate the kinetics of crystallization, isothermal crystallization experiments were carried out on the low degree of sulfonation Cs^+-form SPEEK samples at various crystallization

temperatures. Samples were ramped at 20 ºC/min to 380 ºC and were held at 380 ºC for 3 minutes to completely melt the samples and eliminate thermal history. Samples were then cooled at 60 ºC/min to the desired crystallization temperature and held at that temperature while measuring the exothermic heat of crystallization until no change in heat flow was observed. The crystallization half-time ($t_{1/2}$) was determined at each isothermal crystallization temperature and was used as a measure of the rate of bulk crystallization for each sample.

2.3.10 Water Uptake and Areal Swelling Ratio

The water uptake and swelling ratios of the SPEEK (H^+-form) membranes were determined by first drying membranes in a vacuum oven at 120 °C for 3 hours. The mass (W_{dry}) and dimensions ($L_{x,\,dry}$ x $L_{y,\,dry}$) of the dry membranes were recorded. Then, the samples were treated in boiling deionized water for 1 hour followed by equilibration in room temperature deionized water for 12 hours. Membranes were blotted to remove excess surface water and the mass (W_{wet}) and dimensions ($L_{x,\,wet}$ x $L_{y,\,wet}$) of the wet membranes were recorded. The water uptake and areal swelling ratio were calculated as:

$$\text{Water uptake} = \frac{(W_{\text{wet}} - W_{\text{dry}})}{W_{\text{dry}}} \times\ 100\% \qquad \textbf{(2.1)}$$

$$\text{Areal Swelling ratio} = \frac{\left(L_{\text{x,wet}} \times L_{\text{y,wet}}\right) - (L_{\text{x,dry}} \times L_{\text{y,dry}})}{(L_{\text{x,dry}} \times L_{\text{y,dry}})} \times\ 100\% \qquad \textbf{(2.2)}$$

The reported values are the average of four samples.

2.3.11 Proton Conductivity

Prior to analysis, SPEEK membranes were boiled in deionized water for one hour and then soaked in room temperature deionized water for 12 hours. In-plane proton conductivity was conducted using a 4-point conductivity cell from Bekktech, which was immersed in deionized water at room temperature. Measurements were taken from 1 Hz to 1.5 MHz at a voltage amplitude of 50 mV using a 1255 HF frequency analyzer coupled to a 1286 electrochemical interface, both

from Solartron Analytical. Data analysis was performed using the Zplot® and Zview® software from Scribner and Associates, Inc. The proton conductivity was calculated as:

$$\sigma = \frac{1}{\rho} = \frac{l}{R \times A} \quad \textbf{(2.3)}$$

where σ (Scm^{-1}) is the conductivity, ρ (Ωcm) is the resistivity, l (cm) is the distance between the contacting electrodes, R (Ω) is the resistance determined from the real value of the complex impedance plot that corresponds to the minimum imaginary response, and A is the cross-sectional area of the membrane calculated from the width and thickness of the membrane. Measurements were performed on three separate membranes for each sample to ensure the reproducibility of results.

2.3.12 USAXS/SAXS/WAXD Analysis

Ultra-small angle x-ray scattering (USAXS), small angle x-ray scattering (SAXS), and wide angle x-ray diffraction data (WAXD) were collected at Argonne National Laboratory beamline 9ID-C, using a photon energy of 24 keV.[42] Scattering profiles are plotted as absolute intensity versus q, where $q = \left(\frac{4\pi}{\lambda}\right) sin(\theta)$, θ is one half of the scattering angle, and λ is the X-ray wavelength. USAXS measurements were performed using a Bonse-Hart camera. SAXS measurements were taken using the Pilatus 100k camera and WAXD was collected using the Pilatus 100k-w camera. Data reduction was performed using the Irena[43] and Nika[44] data reduction software provided by Argonne. Scattering data was processed and corrected (1-dimensional data reduction, background subtraction, transmittance and thickness correction) using standard methods in the Nika software package.

For fitting of the ionomer peaks, the 'Modeling' feature of the Irena software package was utilized.[3] For as-cast membranes, the crystalline peak at 0.05 Å^{-1} was fit as the first population

with a size distribution model with a spheroid form factor (aspect ratio = 1) and a LogNormal distribution. A dilute system was used as the structure factor. The fraction, mean size, and standard deviation (of the size) was varied for the best fit. The ionomer peak was fit as a second population using a size distribution model with a spheroid form factor (aspect ratio = 1), a Gaussian distribution, and a hard sphere structure factor. The fraction, mean size, standard deviation of size, radius of the hard sphere, and volume fraction were varied for the best fit. The multiplet radius was determined as the mean size of this fit. The radius was determined to be the radius of closest approach of the multiplet. For quenched SPEEK samples, identical analysis was performed on only the ionomer peak (using procedure for second population described above).

2.4 Results and Discussion

2.4.1 Synthesis of Random and Blocky SPEEK

The sulfonation scheme of PEEK in both the homogeneous (solution-state) and heterogeneous (gel-state), using trifluoroacetyl sulfate, is shown in **Figure 2.1**. In the homogeneous solution-state, all PEEK chains are completely solvated, making each repeat unit equally likely to be functionalized with the addition of sulfonating reagent. This results in a random or statistical SPEEK copolymer. In comparison, in the heterogeneous gel-state, a physical network with two distinct domains exist – the solvent-swollen amorphous fraction and the PEEK crystallites. During functionalization, the sulfonating reagent is sterically excluded from the tightly-packed crystalline domains and thus is only capable of penetrating and functionalizing the solvent-swollen amorphous chains. This heterogeneous, gel-state reaction process results in a blocky copolymer with pendent sulfonate units that are significantly concentrated into groups along the chains separated by relatively long runs of unfunctionalized, and thus crystallizable, PEEK segments.

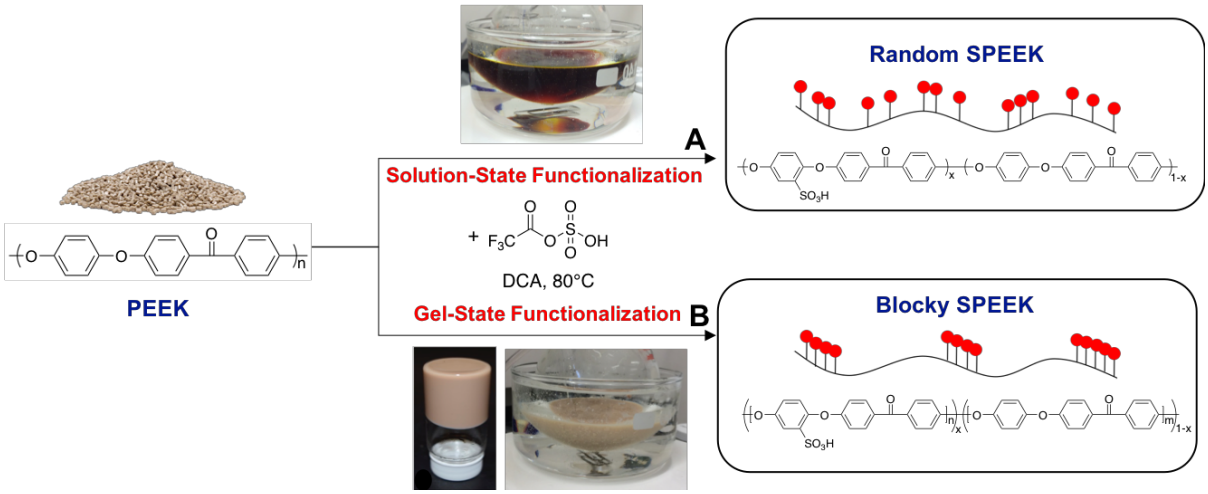

Figure 2.1. General synthesis of sulfonated poly(ether ether ketone). When performed in solution (A), a random or "statistical" copolymer is synthesized. When performed in the gel-state (B), a blocky copolymer is synthesized due to the semicrystalline nature of the gel.

To determine the effect of ionomer architecture (random versus blocky) on physical properties, a series of low degree of sulfonation SPEEK materials were prepared for each sulfonation method. A low degree of sulfonation was targeted to maintain a relatively high crystallizability for the SPEEK samples. Thereby, crystallizability may be used to probe the differences between blocky and random behavior in a manner similar to our low degree of sulfonation studies with syndiotactic polystyrene.[36] The ^{1}H NMR spectra of the random and blocky functionalized SPEEK series are shown in **Figure 2.2**. Conventionally, the ^{1}H NMR of SPEEK is performed in deuterated DMSO.[22, 45-46] However, at the low degrees of sulfonation targeted in this work, SPEEK is not soluble in any polar aprotic solvents. Thus, a solvent suppression method using DCA and $CDCl_3$ was developed (as described in the section below) to obtain well-resolved spectra suitable for integration.

As shown in **Figure 2.2**, degrees of sulfonation at 3.6, 6.0, 7.6, 8.8, and 10.9 mol% were obtained for the random SPEEK samples. The 10' and 12' peaks increase in intensity with increasing degree of sulfonation, thereby confirming that the regulation of time and reagent

concentration is sufficient to yield control over low degrees of sulfonation using trifluoroacetyl sulfate.[1] In comparison, it is essentially impossible to achieve these low degrees of sulfonation using conventional sulfonation techniques, i.e. using sulfuric acid as both the solvent and sulfonation reagent, because a significant fraction of the PEEK chains are already highly sulfonated by the time the sample fully dissolves in sulfuric acid. A matched set of blocky SPEEK at 3.7, 5.9, 7.6, 8.7, and 10.9 mol% was also obtained for direct comparison to the random analogs. The ^{1}H NMR spectra of the blocky samples displayed no significant differences from the random samples. This is understandable because sulfonation occurs exclusively at one of the four sites on the electron-dense hydroquinone ring, regardless of architecture.[47] The naming of random and blocky ionomers will herein be represented by xSPEEKz, where x signifies the architecture (R for random, B for blocky) and z is the molar degree of sulfonation.

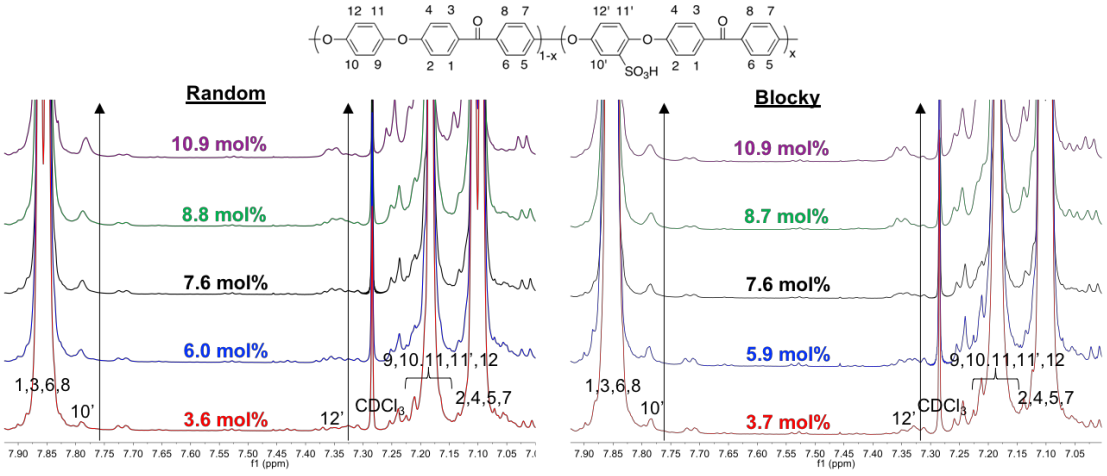

Figure 2.2. Solvent-suppressed ^{1}H NMR of random and blocky SPEEK at various degrees of sulfonation.

2.4.2 Validation of Solvent Suppression ^{1}H NMR Method

For the ^{1}H NMR analysis, a solvent suppression method using a mixed solvent system of DCA and $CDCl_3$ was established due to limited solubility of the SPEEK ionomers in typical NMR solvents. At the low degrees of sulfonation investigated in this work, both the random and blocky

SPEEK were insoluble in DMSO-d6, which is conventionally used to analyze SPEEK. At lower degrees of sulfonation, sulfuric acid may be used as the ^{1}H NMR solvent, however, this does not provide a deuterated solvent to perform the NMR locking and shimming and further sulfonates the materials throughout the measurement.[2] At approximately 30 mol% sulfonation and above, the random SPEEK samples become soluble in DMSO-d6; however, the blocky SPEEK samples up to 45 mol% sulfonation are not soluble in DMSO-d6 likely due to the maintained crystallizability. Thus, DCA was used as the primary solvent for NMR, resulting in chemical shifts similar to those observed using sulfuric acid as the solvent.[2]

To verify the validity of the DCA/$CDCl_3$ solvent system, several techniques were employed. First, the NMR spectra of random SPEEK at approximately 45 mol% sulfonation were obtained in both DMSO-d6 and DCA/$CDCl_3$. The spectra are compared in **Figure 2.3.**

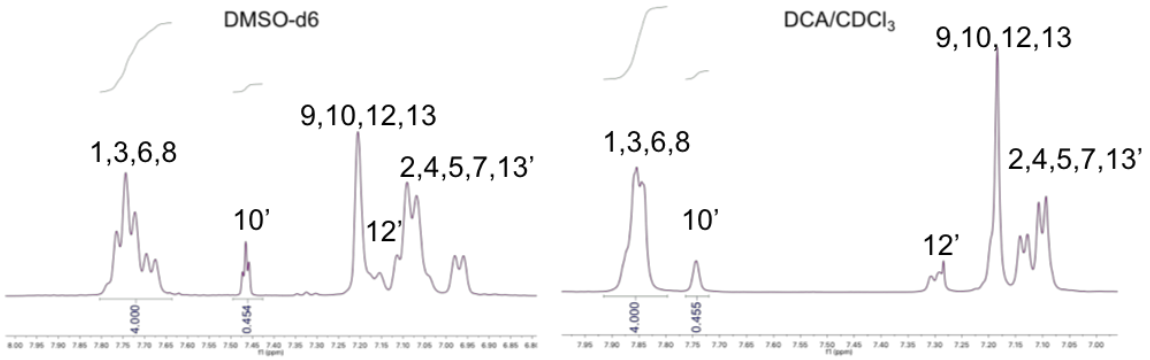

Figure 2.3. ^{1}H NMR analysis of random SPEEK at 45 mol% sulfonation using DMSO-d6 as the solvent (left) and using DCA/$CDCl_3$ (right) as the solvent.

As shown in **Figure 2.3**, the chemical shifts of the assigned protons are different for the same sample in the two different solvent systems. Integration of the assigned 10' peaks, as described in the manuscript, shows that the degree of sulfonation obtained by each solvent system is nearly identical – 45.4 mol% using DMSO-d6 and 45.5 mol% using DCA/$CDCl_3$. Thus, despite the difference in chemical shifts due to the solvent, the same degree of sulfonation is obtained.

Furthermore, a mixed solvent system of DCA/DMSO-d6 (1:5 ratio of DCA:DMSO-d6) was used on the same random SPEEK sample at 45 mol% sulfonation, as shown in **Figure 2.4.** From this figure, it is evident that the 10' peak shifts downfield with the addition of DCA to the DMSO-d6, consistent with what was observed in the DCA/$CDCl_3$ solvent mixture.

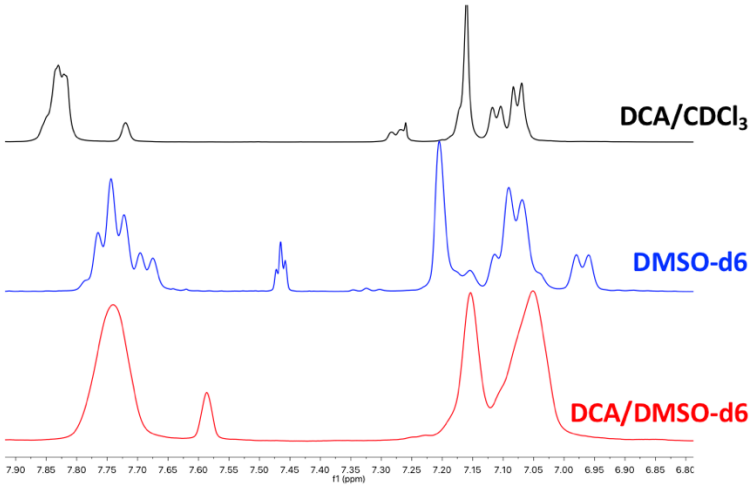

Figure 2.4. Comparison of ^1H NMR spectra of random SPEEK at 45 mol% sulfonation using various NMR solvents.

Finally, elemental analysis was utilized to further verify the DCA/$CDCl_3$ NMR method. Random SPEEK at approximately 6, 22, and 44 mol% sulfonation were analyzed to determine the sulfur content in the samples, and the results were compared to the degree of sulfonation obtained by the DCA/$CDCl_3$ NMR method. As shown in **Table 2.1**, the degree of sulfonation obtained by elemental analysis and by the NMR method are very close, signifying that the NMR method is an effective method to determine degree of sulfonation.

Table 2.1. Comparison of degree of sulfonation (DS) obtained by elemental analysis and by ^{1}H NMR.

Sulfur % (wt%)	DS by Elemental Analysis (mol%)	DS by Solvent Suppression ^{1}H NMR (mol%)
0.616	5.63	5.78
2.38	22.8	22.5
4.36	44.0	44.2

2.4.3 Thermal Analysis of Random and Blocky SPEEK

Thermogravimetric analysis (TGA) was performed on SPEEK to determine the thermal stability of SPEEK neutralized with acid, sodium, and cesium. The TGA thermograms of the PEEK homopolymer and RSPEEK10.9 in acid-form, sodium-form, and cesium-form is shown in **Figure 2.5**. The PEEK homopolymer exhibits high thermal stability, and no change in weight is observed until approximately 600 ºC. Upon sulfonation, H^{+}-form SPEEK demonstrates a two-step weight loss at 350 ºC and 550 ºC which may be attributed to proto-desulfonation and main chain degradation, respectively.[41] Once converted into a salt form (i.e. Na^{+}-form and Cs^{+}-form), SPEEK remains stable up to 550 ºC and shows one-step weight loss at this temperature. Thus, ion exchange into the salt forms prevents proto-desulfonation and allows thermal processing up to much higher temperatures. Crystallization experiments of SPEEK will be performed in Cs^{+}-form to ensure this thermal stability throughout the crystallization process.

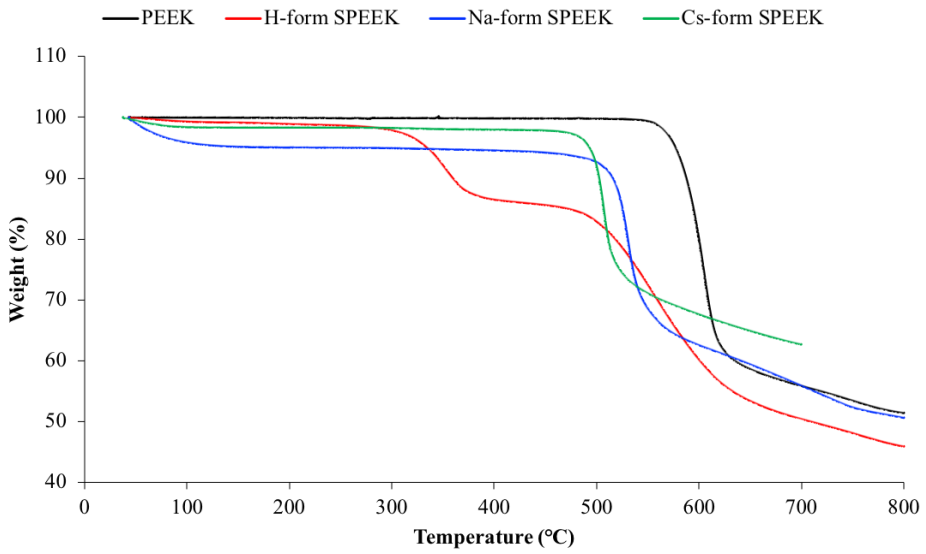

Figure 2.5. Thermogravimentric analysis of PEEK, H^+-SPEEK, Na^+-SPEEK, and Cs^+-SPEEK. The SPEEK samples shown were randomly sulfonated to a degree of sulfonation 10.9 mol%.

DSC was performed on the precipitated SPEEK samples to determine the influence of architecture on thermal transitions. As observed with sulfonated atactic polystyrene and sulfonated syndiotactic polystyrene, random architectures display a linear increase in T_g with increasing sulfonation while the T_g in blocky systems becomes independent of sulfonate content at high degrees of sulfonation.[36, 48-49] Thus, analysis of the T_g versus degree of sulfonation provides indirect evidence of architecture in the SPEEK systems. The T_g's as a function of degree of sulfonation for both the random and blocky SPEEK (in Cs^+-form) are shown in **Figure 2.6**. As expected, sulfonation of PEEK leads to a higher T_g in the SPEEK samples due to a reduction in chain mobility from the physical crosslinks formed by aggregation of the polar sulfonate groups. For degrees of sulfonation up to 7.6%, the random and blocky samples display similar T_g's that increase with increasing degree of sulfonation. Above 7.6% sulfonation, the T_g of the random samples continues to increase up to 174 ºC for RSPEEK10.9 while the T_g's of the blocky samples remain constant at about 162 ºC. The difference in T_g at higher degrees of sulfonation suggests that the gel-state sulfonation process of PEEK leads to a blocky distribution of sulfonate groups.

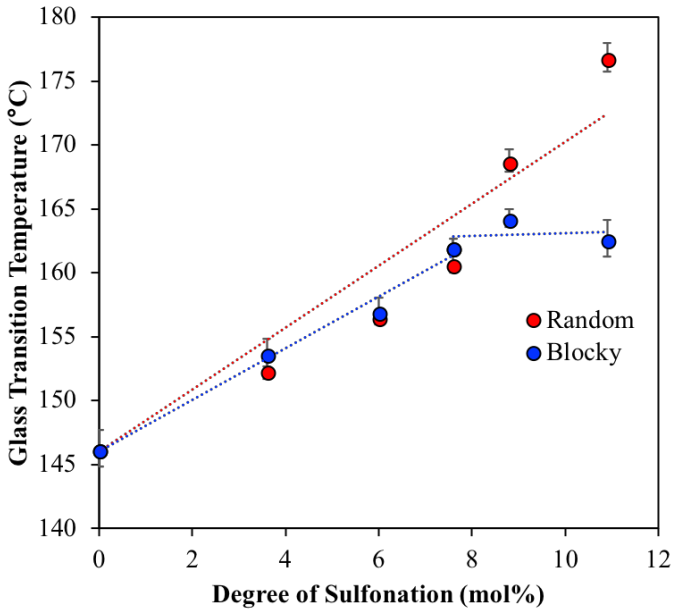

Figure 2.6. Glass transition temperature versus degree of sulfonation of random and blocky SPEEK copolymers in Cs^+-form. Linear fits are provided as a visual guide.

DSC was also utilized to determine the effect of architecture on the crystallizability of SPEEK copolymers. SPEEK samples in Cs^+-form were isothermally crystallized from the melt for two hours at 250 ºC. The DSC thermograms of PEEK, BSPEEK5.9, RSPEEK6.0, BSPEEK10.9, and RSPEEK10.9 and their respective degrees of crystallinity following isothermal crystallization at 250 ºC are displayed in **Figure 2.7.** The degree of crystallinity, X_c, was determined using the following relationship:

$$X_c = \frac{\Delta H_f}{\Delta H_f^\circ} \tag{2.4}$$

where ΔH_f is the enthalpy of fusion determined from integration of the melting endotherm and ΔH_f° is the theoretical enthalpy of fusion of 100% crystalline PEEK (130 J/g).[50] Following isothermal crystallization, the PEEK homopolymer exhibits a double melting endotherm with a low melting temperature (T_{m1}) of 265 ºC and an upper melting temperature (T_{m2}) of 342 ºC. The double melting endotherm arises from two separate crystal populations that form during isothermal

crystallization. The lower melting transition, T_{m1}, is attributed to thinner lamella formed during secondary crystallization while the upper melting transition, T_{m2}, is attributed to the main crystalline lamella formed during primary crystallization.[51-53] The T_{m1} is dependent on the crystallization temperature and generally lies 5-30 ºC above T_c.[52] Because all SPEEK copolymers shown in **Figure 2.7** were isothermally crystallized at 250 ºC, the T_{m1} for all degrees of sulfonation and both architectures is approximately 268 ºC, consistent with that of the PEEK homopolymer. The upper melting transition, however, is highly dependent on degree of sulfonation as well as architecture. At 6 mol% sulfonated, the BSPEEK5.9 ionomer exhibits a T_{m2} of 335 ºC while RSPEEK6.0 exhibits a depressed T_{m2} of 322 ºC. As expected, the T_{m2} values of both BSPEEK5.9 and RSPEEK6.0 both lie below that of the PEEK homopolymer due to melting point depression from the presence of non-crystallizable defects (i.e., sulfonated monomer units) in the copolymers. The melting point depression of RSPEEK6.0, however, is much more significant than that of BSPEEK5.9, suggesting that the blocky copolymer forms thicker primary crystalline lamella than its random analog. Upon integration of the melting endotherm, it was also determined that the degree of crystallinity of BSPEEK5.9 (X_c = 23.6%) is significantly greater than that of RSPEEK6.0 (X_c = 15.9%).

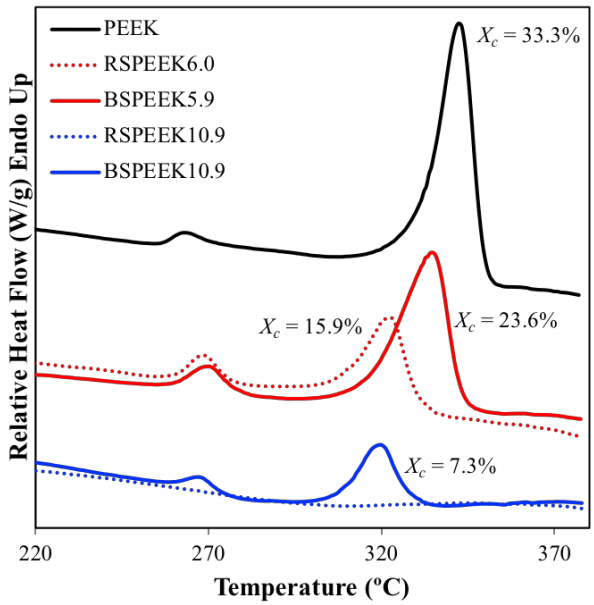

Figure 2.7. DSC thermograms of PEEK, RSPEEK6.0, BSPEEK5.9, RSPEEK10.9, and BSPEEK10.9 after isothermal crystallization for 2 hours at 250 ºC. All samples are in Cs^+-form. The crystallinity of each sample is shown at their respective melting peak.

The effect of defect sequencing along the SPEEK chain is amplified at higher degrees of sulfonation, where the random incorporation of non-crystallizable, interactive defects decreases the fraction of crystallizable runs and significantly lowers the equilibrium melting point of the copolymer, thus lowering the crystallizability at low supercoolings.[54-57] At high degrees of sulfonation, it is observed that RSPEEK10.9 is completely amorphous following isothermal crystallization at 250 ºC while BSPEEK10.9 displays the typical double melting endotherm of PEEK with an upper melting temperature of 320 ºC and a crystallinity of 7.3%. Thus, the long runs of unfunctionalized, crystallizable homopolymer preserved by gel-state sulfonation allows for the formation of thicker crystals during isothermal crystallization and a reduced effect of melting point depression consistent with non-random, "blocky" copolymers. The stark contrast in crystallizability between the random and blocky SPEEK is observed at a wide variety of crystallization temperatures, as shown in **Figure 2.8**.

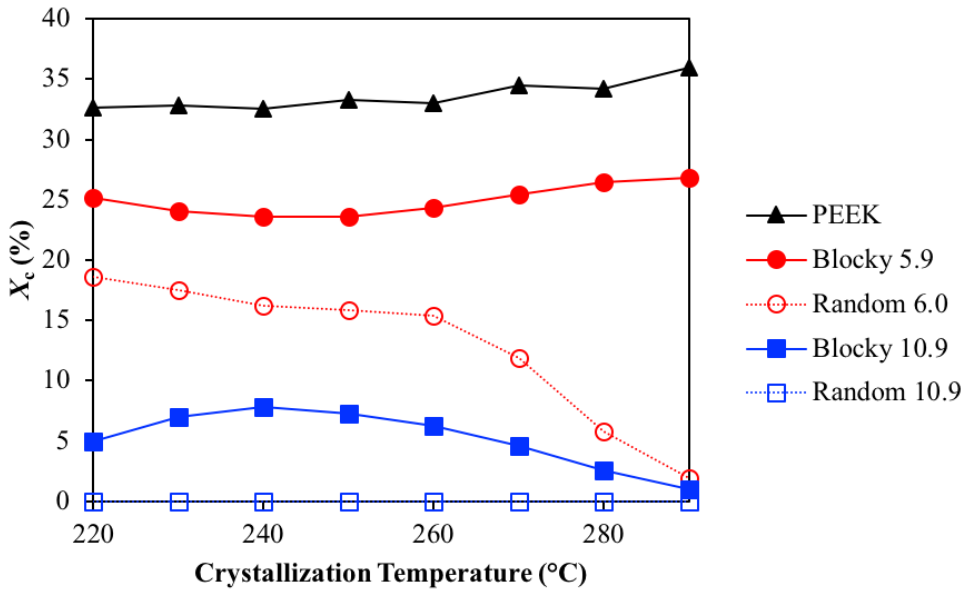

Figure 2.8. Two-hour isothermal crystallization from the melt of PEEK, BSPEEK5.9, RSPEEK6.0, BSPEEK10.9, and RSPEEK10.9 at a variety of crystallization temperatures. All samples are in Cs^+-form.

While these investigations have focused on crystallization from the melt, it is important to note that the as-precipitated SPEEK products (**Table 2.2**) exhibit much greater crystallinity due to solvation of the interactive ionic groups (and thus increased molecular mobility) in the presence of the polar solvent. Thus, a greater crystallizability is recognized for the as-cast membranes, which are prepared from a similar solution state.

Table 2.2. Full DSC analysis of random and blocky SPEEK samples. All samples are in Cs^+-form. The T_g is taken from the heat following the quench cool.

Sample	T_g (°C)	$T_{m,\ first}$ (°C)	$X_{c,\ first}$ (wt%)	$T_{m,\ quench}$ (°C)	$X_{c,\ quench}$ (wt%)
PEEK	147	345	43	343	36
RSPEEK3.6	153	333	33	331	16
BSPEEK3.7	155	335	36	332	24
RSPEEK6.0	157	324	28	327	8
BSPEEK5.9	157	331	32	330	23
RSPEEK7.6	162	319	25	323	0.2
BSPEEK7.6	162	320	30	324	2
RSPEEK8.8	168	313	21	-	-
BSPEEK8.7	163	317	26	-	-
RSPEEK10.9	174	228, 308	19	-	-
BSPEEK10.9	160	314	25	-	-

2.4.4 Isothermal Crystallization Kinetics

To further elucidate the effect of ionomer architecture on the crystallization behavior of SPEEK, DSC isothermal crystallization experiments were performed. The kinetics of bulk crystallization of the matched sets of RSPEEK3.6 and BSPEEK3.7 and RSPEEK6.0 and BSPEEK5.9 in Cs^+-form were analyzed using the following approach:

$$F_c(t) = \frac{\int_0^t \frac{dH}{dt}\,\mathrm{d}t}{\int_0^\infty \frac{dH}{dt}\,\mathrm{d}t} \tag{2.5}$$

where $F_c(t)$ is the bulk fractional crystallinity of the functionalized copolymer systems that is equal to the heat evolved during isotherm crystallization at a specific time t divided by the total heat evolved during the entire isothermal crystallization process. For 3.7 mol% sulfonation, the samples were isothermally crystallized at 260, 270, 275, 280, and 290 ºC. For 6.0 mol% sulfonation, the samples were isothermally crystallized at 220, 230, 240, 250, 260, and 270 ºC. The plots of $F_c(t)$ versus ln(t) when crystallized at 260 ºC are displayed in **Figure 2.9.** The crystallization isotherms

for both architectures and degrees of sulfonation display a sigmoidal shape, which is characteristic of a nucleation and growth crystallization process. The shapes of the isotherms are superimposable, suggesting no change in crystallization mechanism as an effect of degree of sulfonation or architecture. The rate of crystallization, however, is highly dependent on degree of sulfonation and architecture. As the degree of sulfonation increased from 3.7% to 6.0 mol%, both the random and blocky SPEEK displayed an increase in crystallization time (i.e., slower crystallization rate). However, at identical ion contents, the random samples displayed significantly longer crystallization time scales (i.e., over two orders of magnitude) than their blocky analogs. This effect was observed at all T_c's, as shown in **Figure 2.10**.

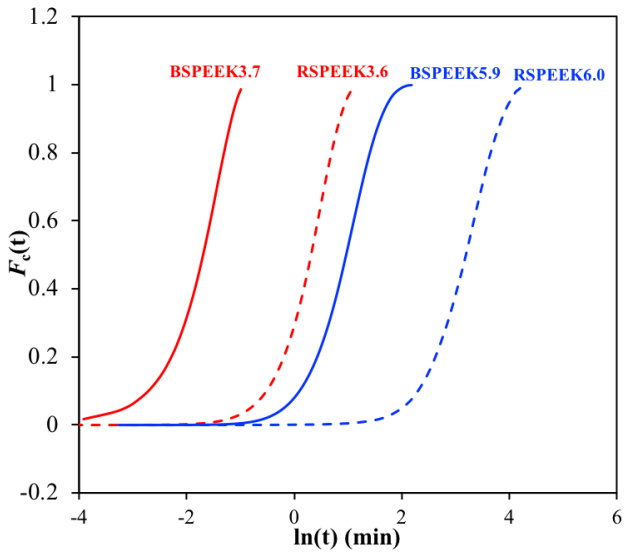

Figure 2.9. Bulk crystallization isotherms as fractional crystallinity versus ln(t) for BSPEEK3.7, RSPEEK3.6, BSPEEK5.9, and RSPEEK6.0 crystallized at 260 ºC.

The differences in crystallization kinetics between random and blocky ionomer architectures were further quantified by extracting the crystallization half-time, $t_{1/2}$, from the crystallization isotherms of **Figure 2.9** and **Figure 2.10**. The analysis was also performed using the PEEK homopolymer for comparison, as shown in **Figure 2.11**. In addition, a full Avrami analysis of the results is shown in **Table 2.3**. At 3.7 mol% sulfonation, both the random and blocky

SPEEK copolymers display higher crystallization half-times than pure PEEK. However, the BSPEEK3.7 has a smaller $t_{1/2}$, and thereby faster crystallization, than RSPEEK3.6 at all crystallization temperatures. The difference becomes even more distinct at high temperatures. For example, at 290 ºC, the $t_{1/2}$ for BSPEEK3.7 is more than three times shorter than the $t_{1/2}$ for RSPEEK3.6 (i.e., 6 minutes versus 19 minutes). As the degree of sulfonation is increased to 6 mol%, the differences between the random and blocky architectures are even more pronounced. While BSPEEK5.9 is capable of crystallizing rapidly even at elevated temperatures, higher degrees of supercooling are necessary for RSPEEK6.0 to crystallize in under an hour ($t_{1/2}$ < 30 minutes). In fact, RSPEEK6.0 displays a minimum $t_{1/2}$ value of 13 minutes at 230 ºC while BSPEEK5.9 has a $t_{1/2}$ value of 0.5 minutes at the same temperature.

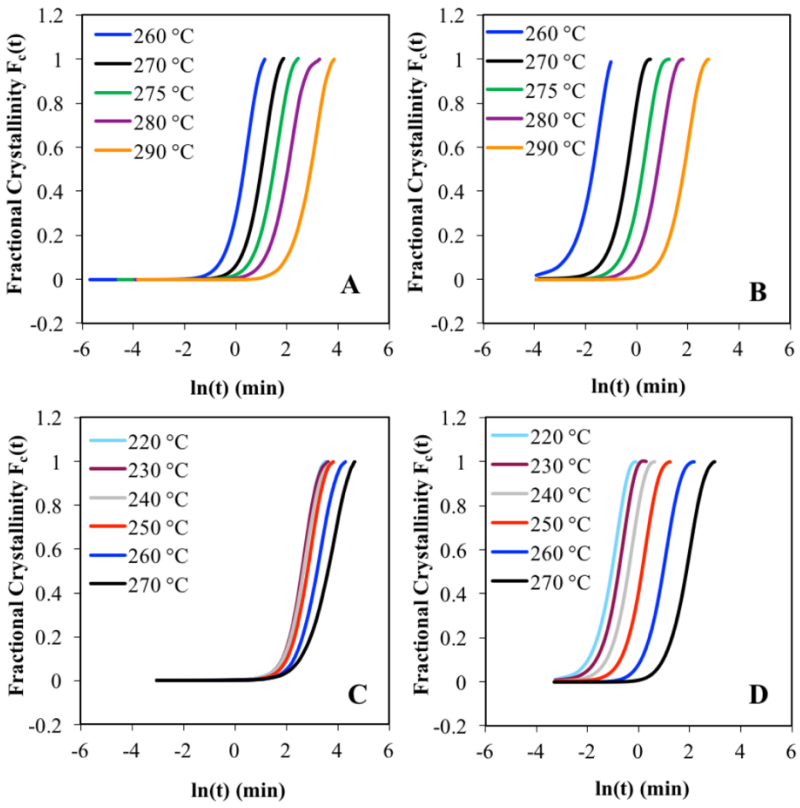

Figure 2.10. $F_c(t)$ versus ln t for various crystallization temperatures. (A) and (B) display the crystallization kinetics of ^{RSPEEK}3.6 and BSPEEK3.7, respectively. (C) and (D) display the crystallization kinetics of RSPEEK6.0 and BSPEEK5.9, respectively. All samples are in Cs^+-form. For each degree of sulfonation, longer induction periods and overall time for crystallization is greater for the random samples as compared to their blocky analogues.

At the temperatures investigated in **Figure 2.11**, the crystallization rates of PEEK, BSPEEK, and RSPEEK all decrease with increasing T_c, as expected. This is indicative of a nucleation-controlled crystallization regime, thereby suggesting that the growth of crystallites is dependent on the ability of the crystallizable chain segments to establish and grow upon a crystal surface. It is important to note, especially for ionomers, that diffusion of chains segments within the melt also plays a significant role at these temperatures due to the presence of electrostatic interactions between the interactive (SPEEK) defects that restrict polymer chain mobility through ionic aggregation.[57] Consequently, the crystallization kinetics of these ionomers are slowed by

both the rejection of defective stems (containing at least one sulfonated unit) from the growing crystal interface and by slower diffusion of the ionomer chain segments in the melt.

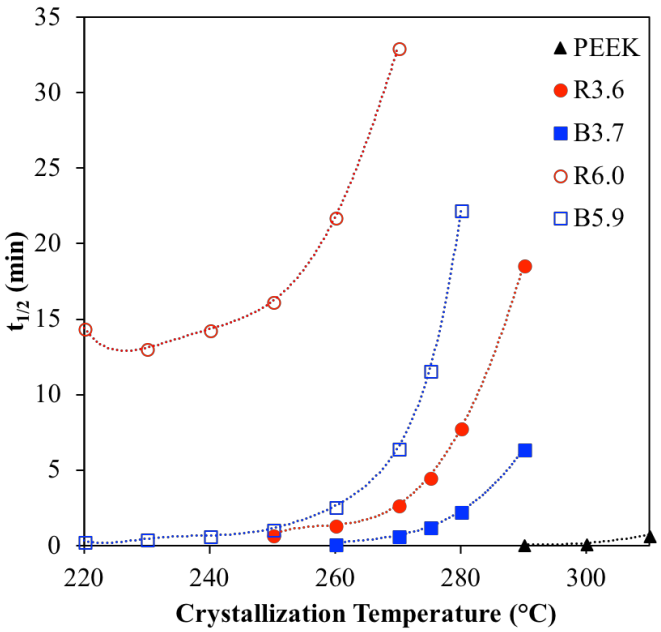

Figure 2.11. Crystallization half-time as a function of crystallization temperature for pure PEEK, RSPEEK3.6, BSPEEK3.7, RSPEEK6.0, and BSPEEK5.9. All SPEEK samples were in Cs^+-form.

For the random SPEEK ionomers, the more homogeneous distribution of sulfonate groups along the polymer chain makes it more likely to encounter a sulfonated unit at the growing crystal surface (i.e., fewer runs of pure PEEK units of sufficient length to crystallize compared to the blocky analog). This results in rejection of that defective chain segment from the crystal and thus a longer time period for bulk crystallization. For each ionic content, the prevalence of encountering a defective stem is greater for the random systems in comparison to the blocky analog, where long runs of unfunctionalized homopolymer are maintained. Thus, blocky SPEEK ionomers are able to crystallize significantly faster than their random ionomer analogs due to a reduced prevalence of encountering a defective stem at the growing crystal interface.

Table 2.3. Kinetic parameters determined from the Avrami Analysis of PEEK, RSPEEK3.6, BSPEEK3.7, RSPEEK6.0, and BSPEEK5.9.

	220 °C	230 °C	240 °C	250 °C	260 °C	270 °C	275 °C	280 °C	290 °C	300 °C	310 °C
PEEK											
$t_{1/2}$ (min)	-	-	-	-	-	-	-	-	0.10	0.18	0.72
n	-	-	-	-	-	-	-	-	2.16	2.47	3.27
K (min^{-1})	-	-	-	-	-	-	-	-	94.13	49.38	1.97
R3.6											
$t_{1/2}$ (min)	-	-	-	-	0.76	1.37	2.75	4.57	7.82	18.65	-
n	-	-	-	-	2.39	2.32	2.29	2.18	2.02	1.98	-
K (min^{-1})	-	-	-	-	1.343	0.333	0.069	0.025	0.011	0.002	-
B3.7											
$t_{1/2}$ (min)	-	-	-	-	-	0.18	0.69	1.26	2.30	6.42	-
n	-	-	-	-	-	2.02	2.23	2.19	2.16	2.18	-
K (min^{-1})	-	-	-	-	-	20.955	1.605	0.417	0.115	0.012	-
R6.0											
$t_{1/2}$ (min)	14.42	13.11	14.35	16.20	21.78	33.01	-	-	-	-	-
n	2.38	2.61	2.42	2.50	2.43	2.00	-	-	-	-	-
K (min^{-1})	$1.2x10^{-3}$	$8.5x10^{-4}$	$1.1x10^{-3}$	$6.5x10^{-4}$	$3.9x10^{-4}$	$6.4x10^{-4}$	-	-	-	-	-
B5.9											
$t_{1/2}$ (min)	0.34	0.46	0.68	1.14	2.65	6.51	11.64	22.27	-	-	-
n	2.08	2.12	2.10	1.99	1.90	1.89	1.88	1.97	-	-	-
K (min^{-1})	6.392	3.572	1.581	0.536	0.109	0.020	0.007	0.002	-	-	-

2.4.5 USAXS/SAXS/WAXD Analysis

The morphological characterization of solution-cast membranes over a wide range of length scales was carried out using USAXS/SAXS/WAXD at Argonne National Labs. The USAXS/SAXS/WAXD profiles of as-cast membranes of random and blocky SPEEK at all degrees of sulfonation as well as pure PEEK membranes are shown in **Figure 2.12**. All measurements were conducted on dry Cs^+-form membranes to achieve enhanced contrast of the ionic domains. In the WAXD region (i.e., $q > 0.6$ Å^{-1}), all samples show diffraction peaks attributed to the characteristic interplanar reflections of the PEEK crystal structure. For both the random and blocky specimens, the intensity of the crystalline peaks is observed to decrease with increasing ion content (in agreement with the decreasing crystallizability with ion content trend observed by DSC, above). While the RSPEEK10.6 was observed to be amorphous following isothermal crystallization from the melt (**Figure 2.7**), these WAXD data for solution-cast samples confirm that a significant degree of crystallinity can be developed in these low ion content SPEEK membranes during the solvent-borne casting process. The degree of crystallinity of the as-cast membranes was determined using DSC and by integration of the WAXD spectrum, as shown in **Table 2.4**. Even the RSPEEK10.6 sample yields a degree of crystallinity of 18% when cast from DCA at 100 ˚C.

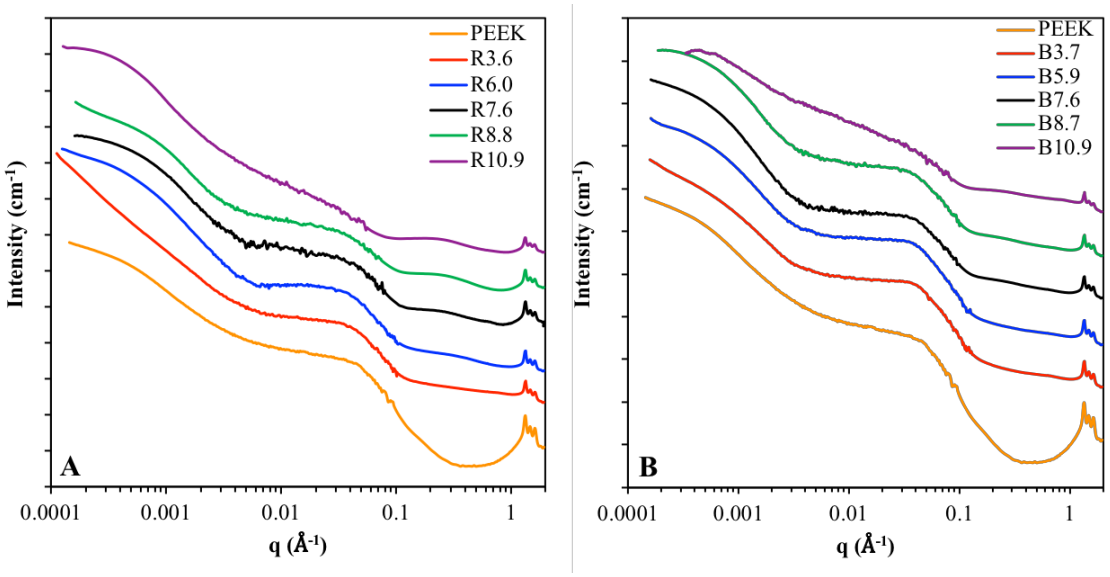

Figure 2.12. USAXS/SAXS/WAXD of Random (A) and Blocky (B) SPEEK membranes in Cs^+-form. Scattering profiles have been vertically shifted for ease of viewing. For the random SPEEK membranes, peaks at 0.05 $Å^{-1}$ and 0.2 $Å^{-1}$ are clearly visible and are attributed to the semicrystalline structure and ionomer peak, respectively. For the blocky SPEEK membranes, only the semicrystalline peak at 0.05 $Å^{-1}$ is visible.

Table 2.4. Crystallinity of as-cast SPEEK membranes (Cs^+-form) determined by DSC and XRD.

Sample	**Film $X_{c,\,DSC}$** (wt%)	**Film $X_{c,\,XRD}$** (wt%)
R3.6	36	30
B3.7	36	32
R6.0	34	27
B5.9	35	30
R7.6	27	26
B7.6	29	29
R8.8	21	23
B8.7	24	28
R10.9	17	18
B10.9	22	24

In the USAXS region (i.e., $q < 0.006$ $Å^{-1}$), the SPEEK samples generally exhibit a broad exponential "knee" similar to that observed for the pure PEEK sample. The precise origin of this scattering feature requires further investigation (beyond the scope of this study); however, given

that this knee is observed in pure PEEK, it is likely attributed to long-range heterogeneities in the spatial distribution of the PEEK crystalline domains.

In the SAXS region (i.e., 0.006 $Å^{-1}$ < q < 0.6 $Å^{-1}$), all of the samples show a distinct matrix knee at q ≈ 0.05 $Å^{-1}$ attributed to interlamellar scattering from the semicrystalline matrix.[58] To obtain an estimate of the lamellar dimensions from the interlamellar SAXS feature, the peak position of the scattering maximum for each sample was extracted from the Lorentz-corrected SAXS curve and was used to estimate the center-to-center inter-crystalline domain spacing (i.e., Long Period) from Bragg's law ($d_{Bragg} = 2\pi/q$).[59-60] Note that the excess scattering contribution from the ion-rich domains (at q values larger than ca. 0.05 $Å^{-1}$, see below) precludes the use of a more accurate analysis of lamellar dimensions using a 1-D correlation function analysis.[61] By definition, the Long Period, L_p, is considered as the sum of the crystal lamellar thickness, l_c, combined with the thickness of the interlamellar amorphous region, l_a. Assuming a linear two-phase model, the l_c dimensions may be estimated for comparison by multiplying L_p by the volume fraction of crystallinity (ϕ_c) determined by XRD of the as-cast membranes, and the l_a dimensions may be determined by subtraction of l_c from L_p.[50] As shown in **Table 2.5**, the Long Periods for the ionomers are all greater than that of pure PEEK. This behavior is expected due to statistically shorter runs of crystallizable polymer chains for the SPEEK samples that tends to limit the lamellar thickness and increase l_a. Interestingly, L_p increases systematically with ion content for the random SPEEK samples. In contrast, however, L_p remains constant at 150 Å for the blocky SPEEK samples having ion contents of 6 mol% and greater. By accounting for the differences in crystallinity between the blocky and random SPEEK samples, the linear two-phase approximation yields thicker l_c values and thinner l_a values, across the board, for the blocky SPEEK samples compared to the random SPEEK samples. Therefore, this comparative analysis further supports a blocky architecture, and suggests that the crystalline dimensions attainable with the blocky SPEEK

samples originate from a "memory" of the crystalline dimensions within the physical network during the gel-state functionalization.

Table 2.5. SAXS Analysis of SPEEK Membranes.

Sample	q_{max} (Å^{-1})	L_p (Å)	ϕ_c	l_c (Å)	l_a (Å)
PEEK	0.046	137	0.40	55	82
RSPEEK3.6	0.044	143	0.28	40	103
BSPEEK3.7	0.044	143	0.30	43	100
RSPEEK6.0	0.041	153	0.25	38	115
BSPEEK5.9	0.042	150	0.27	41	109
RSPEEK7.6	0.040	157	0.24	37	120
BSPEEK7.6	0.042	150	0.26	40	110
RSPEEK8.8	0.040	157	0.21	33	124
BSPEEK8.7	0.042	150	0.26	39	111
RSPEEK10.9	0.031	203	0.16	32	171
BSPEEK10.9	0.042	150	0.22	33	117

The SAXS region of the scattering profiles of **Figure 2.12** also contains morphological information regarding contributions from the ionic component of these ionomers. At q values greater than 0.1 Å^{-1}, it is clear that the SAXS scattering profiles of the SPEEK samples differ significantly from the featureless profile of the parent PEEK polymer. In agreement with previous SAXS studies of dry Cs^+-form SPEEK,[58] the excess SAXS scattering for these ionomers (over that of PEEK) is reasonably attributed to the ion-rich domains, which have a broad distribution of dimensions and relatively poor contrast with the semicrystalline matrix. With increasing ion content, the random SPEEK samples develop a distinct maximum, centered at q ≈ 0.25 Å^{-1}, attributed to a feature characteristic of ionomers, known as the ionomer peak. For a broad class of ionomers, the ionomer peak has been attributed to the presence of nano-phase separated ionic aggregates (i.e., mutiplets of ion-pairs) that produce interparticle interferences that yield the characteristic scattering maximum.[6] For the random SPEEK samples, the ionomer peak increases

in intensity with increasing degree of sulfonation and displays q values decreasing from 0.33 $Å^{-1}$ to 0.22 $Å^{-1}$ as the degree of sulfonation increases from 6.0 mol% to 10.9 mol%. Using a Bragg estimate from the q_{max} values (i.e., $d_{Bragg} = 2\pi/q_{max}$), this yields an inter-multiplet domain distance of 19-29 Å, which is consistent with previous studies of conventionally sulfonated SPEEK membranes in the literature.[59, 62-63] Fitting of the ionomer peaks using a size distribution model with a spheroid form factor and hard sphere structure factor shows that the multiplet radii of the random SPEEK membranes increase from 5.0 Å to 5.9 Å as the degree of sulfonation increases from 6.0 mol% to 10.9 mol% (**Table 2.6**). Gebel and Gomes have similarly reported small ionic domains with radii of 4-6 Å for SPEEK membranes using various fitting procedures.[58, 64] Based on this analysis, it is evident that the random SPEEK ionomers are behaving as typical ionomers,[6] whereby both the size of the multiplets and the center-to-center distance between multiplets increase with degree of sulfonation.

Table 2.6. Multiplet radii of as-cast random SPEEK membranes fit using a size distribution model with a spheroid form factor and hard sphere structure factor.

Sample	Multiplet Radius (Å)
RSPEEK6.0	5.0
RSPEEK7.6	5.4
RSPEEK8.8	5.6
RSPEEK10.9	5.9

In distinct contrast to the behavior of the random SPEEK samples, it is surprising to observe that a distinct ionomer peak is not present for the as-cast blocky SPEEK samples. The unexpected absence of an ionomer peak in the as-cast blocky SPEEK samples is further explored by comparing the scattering features of quenched samples of random and blocky SPEEK at 8.8 mol% sulfonation, as shown in **Figure 8**. For the quenched samples, both the random and blocky SPEEK demonstrate one primary scattering feature – the ionomer peak at ~0.25 $Å^{-1}$. Fitting of

these ionomer peaks using the method described above shows similar multiplet radii of the two architectures (6.7 Å for RSPEEK8.8 and 6.6 Å for BSPEEK8.7). Despite similar peak positions, the ionomer peak appears more prominent in the RSPEEK8.8 than in BSPEEK8.7. With the introduction of crystallinity (as shown by the as-cast membranes), the large crystalline shoulder at 0.05 $Å^{-1}$ appears and the ionomer peaks for both the random and blocky samples appear to decrease in intensity while shifting to higher q. By comparison, it is clear that the ionomer peak is essentially absent for the semicrystalline blocky SPEEK. In agreement with the work of Gebel,[58] the data in **Figure 8** confirm that the intensity of the ionomer peak is diminished due to scattering contrast in the semicrystalline state (i.e., the electron density of the semicrystalline matrix is similar to the electron density of the ionic aggregates).

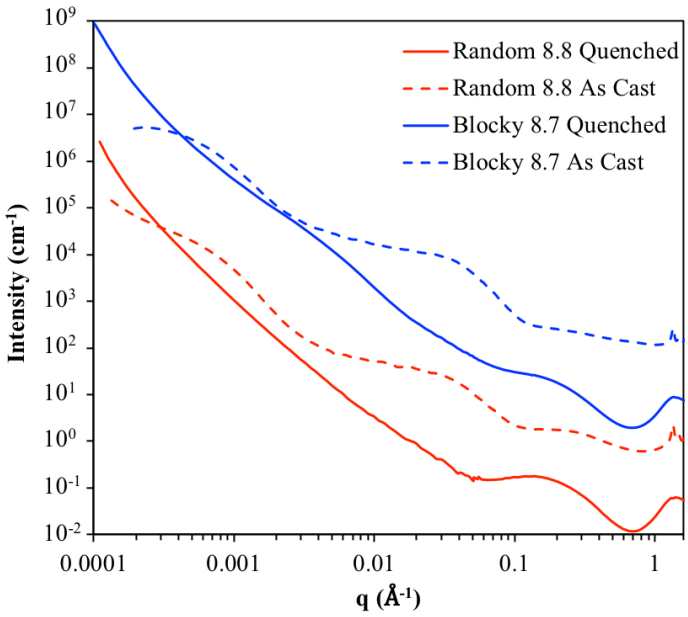

Figure 2.13. USAXS/SAXS/WAXS profiles of quenched RSPEEK8.8 (solid red), as-cast RSPEEK8.8 (dashed red), quenched BSPEEK8.7 (solid blue), and as-cast BSPEEK8.7 (dashed blue). Profiles have been shifted for ease of comparison.

While the intensity of the ionomer peak in SPEEK is clearly affected by the limited contrast with the semicrystalline matrix, the apparent greater sensitivity to this scattering contrast for the

blocky SPEEK may suggest that the ionic aggregates are more uniformly distributed in near proximity to the PEEK crystallites relative to the spatial distribution of aggregates and crystallites in the random analog. While it is beyond the scope of this initial investigation into the gel-state sulfonation of PEEK, it is of interest to note that this phenomenon is not unique to this blocky SPEEK. Our model blocky sulfonated syndiotactic polystyrene system[36] shows the same absence of an ionomer peak compared to the random analog (**Figure 2.14**). Of course, further analysis will be required to determine the origin of this unanticipated scattering behavior. Nevertheless, it is intriguing to consider how this potentially altered distribution of ionic domains could affect the transport properties in membrane applications.

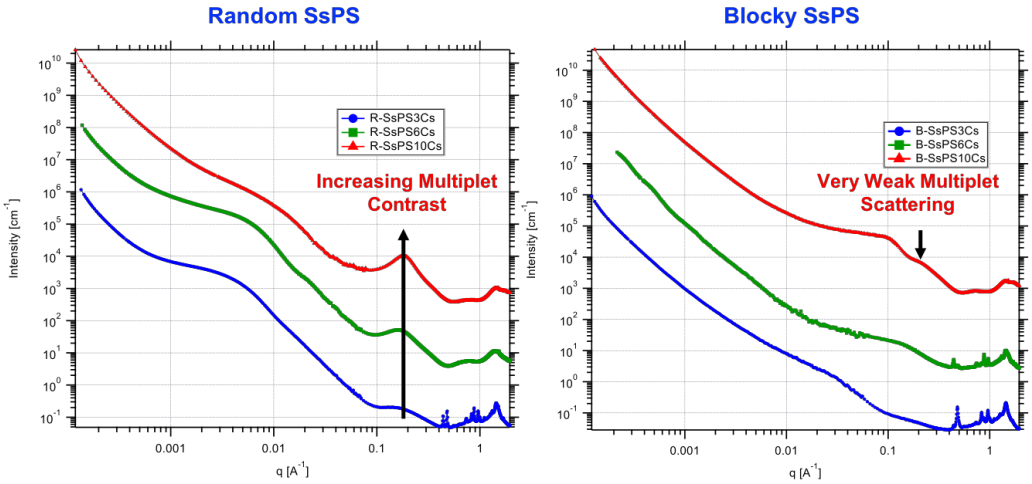

Figure 2.14. USAXS/SAXS/WAXS of random (left) and blocky (right) sulfonated syndiotactic polystyrene (SsPS) at 3 mol% (blue), 6 mol% (green), and 10 mol% (red) sulfonation in Cs^+-form.

2.4.6 Membrane Properties

SPEEK is commonly employed as an alternative hydrocarbon proton exchange membrane for fuel cell applications.[65-67] While these applications require the use of materials with significantly higher degrees of sulfonation than that of the ionomer samples studied here, this initial comparison of membrane properties is used to represent the benefit of a blocky architecture

in creating efficient conduction pathways and the impetus for expanding this facile, gel-state synthetic scheme to higher degrees of functionalization. As shown in **Figure 2.15**, the water uptake of SPEEK membranes (H^+-form) increases as the degree of sulfonation increases. Likewise, the areal swelling increases with increasing degree of sulfonation. This effect is expected as increasing sulfonation increases the number of hydrophilic ionic groups along the backbone. No difference is observed between the random and blocky SPEEK membranes at any degree of sulfonation, signifying that water uptake is independent of architecture at these low degrees of functionalization.

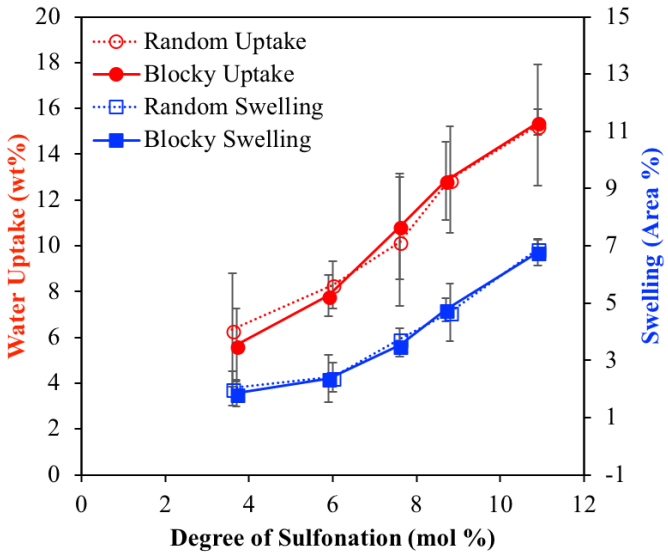

Figure 2.15. Water uptake and swelling of random and blocky SPEEK at various degrees of sulfonation.

The proton conductivity of the SPEEK (H^+-form) membranes immersed in water was also examined, as shown in **Figure 2.16**. For the low degrees of sulfonation (**Figure 2.16A**), the blocky SPEEK membranes exhibit higher proton conductivities, across all degrees of sulfonation, relative to their random membrane analogs. Since proton conductivity is often observed to be directly correlated to the water content,[68-69] it is of interest to note that the blocky ionomers have higher

conductivity than the random analogs despite having similar water uptake values. The degree of crystallinity for each of the membranes is also included for comparison next to each data point (the crystallinity values obtained by DSC and XRD are also listed in **Table 2.4**). By inspection, both the proton conductivity and the degree of crystallinity tend to diverge with increasing ion content. Given the similar water contents for the blocky and random analogs, this behavior may be attributed to the impact of crystallinity on the spatial distribution of the functional ionic groups within the amorphous phase of these membranes. As crystallinity develops during the casting process, this phase-separation phenomenon consequently increases the local concentration of ionic groups within the remaining amorphous phase. Because the blocky samples exhibit higher crystallinity than their random analogs, the local ion concentration in the amorphous phase is somewhat greater for the blocky SPEEK at similar ion contents.[36] Moreover, with a constant number of water molecules per sulfonate group, the consequence of a higher ion concentration for the blocky membranes implies that the blocky and random analogous have different local distributions of water within the ionic domains. Coupled with the SAXS analysis above, it may be reasonable to conclude that the hydrated ionic domains in the blocky membranes are more interconnected, providing for more efficient percolation pathways for proton and water transport. Future studies will focus on a systematic study of morphology-conductivity relationships over a range of water contents to probe this potential link between ionomer architecture and ionic domain connectivity.

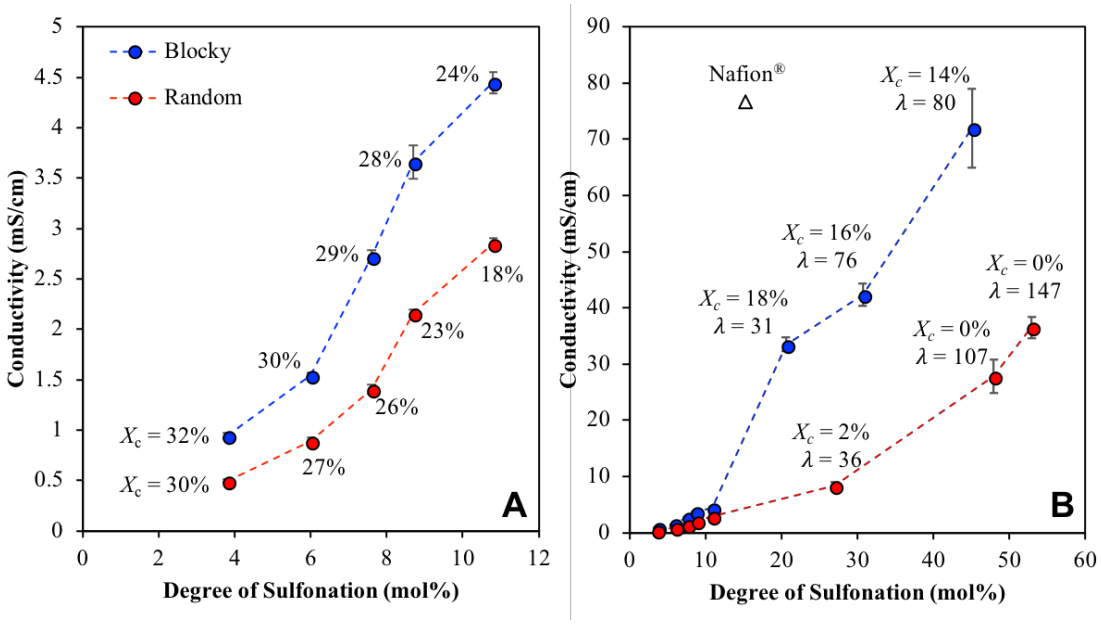

Figure 2.16. Proton conductivity of random and blocky SPEEK at various degrees of sulfonation. The X_c values displayed were determined using DSC, and λ (mol sulfonate/mol water) was determined using the water uptake. The open triangle represents the proton conductivity of the benchmark 1100 EW Nafion® evaluated under identical conditions.

To demonstrate the impact of a blocky ionomer architecture on SPEEK membranes containing ion contents relevant to PEMFC applications, the data in **Figure 2.16B** shows conductivity results for SPEEK membranes having degrees of sulfonation exceeding 10 mol%. For comparison, the degrees of crystallinity (X_c) and water content (λ) values are listed next to each data point. As expected, the conductivities for all membranes continue to increase with degree of sulfonation. In addition, for these higher degrees of sulfonation, the water uptake is observed to increase as expected with ion content, and the values significantly diverge with the random SPEEK swelling much more than the blocky SPEEK. For a given degree of sulfonation, it is clear that the blocky architecture yields a profound increase in conductivity over that of a random analog. This behavior is consistent with the results of other block ionomer membrane systems, and further demonstrates the profound importance of "blocking-up" the ions to achieve improved membrane performance.[27, 70] Moreover, it is important to note that the blocky

BSPEEK45 membrane has a room temperature conductivity value (σ = 72 mS/cm) that is quite comparable to the conductivity of Nafion® under the same conditions (σ = 77 mS/cm). Furthermore, it is evident that by sulfonating in the semicrystalline gel-state, a significant degree of crystallinity is retained that is unachievable in the random, solution-state synthesis. The crystallinity of the blocky SPEEK not only imparts mechanical integrity to the membranes but also prevents excessive swelling at high degrees of functionality. For example, the RSPEEK53 membrane swells extensively (λ = 147), near the point of dissolving, and begins to breaks apart upon exposure to water. In contrast, the semicrystalline BSPEEK45 membrane (X_c = 14.4%) is mechanically stable with a more controlled water uptake at almost half the water content of the random analog.

2.5 Conclusions

In this work, a simple post-polymerization technique to create blocky SPEEK ionomers has been demonstrated. By sulfonating in the heterogeneous gel-state, sulfonation is restricted to the solvent swollen amorphous fraction, which preserves long 'blocks' of crystallizable pure PEEK chain segments in the resulting blocky ionomer. Evidence of the blocky architecture was provided by analysis of the SPEEK T_g's. While random SPEEK displayed a T_g that increased with increasing degree of sulfonation, blocky SPEEK exhibited a T_g that was independent of degree of sulfonation above 7.6% sulfonated, consistent with the blocky architecture. Further analysis of the thermal transitions demonstrated that the blocky architecture leads to enhanced crystallizability and less significant melting point depression as compared to random copolymers. Even at ion contents as low as 3.6%, the blocky SPEEK demonstrated higher crystallizability and significantly faster crystallization kinetics than random SPEEK. Additionally, membranes cast from the low ion-content blocky and random SPEEK displayed similar water uptake and swelling that was dependent on degree of sulfonation. Despite the similar water content, blocky SPEEK membranes

exhibited higher proton conductivity than random SPEEK membranes attributed to a somewhat higher ion content in the amorphous phase (due to increased crystallinity) and perhaps a more interconnected network of ionic aggregates. For SPEEK membranes of significantly higher ionic content, the conductivity of the blocky membranes was significantly greater than the random analogs, and even rivaled that of the benchmark Nafion®. Overall, this study demonstrated that sulfonation of PEEK in the gel-state provides a facile method to produce blocky functional copolymers with high ion content, high crystallizability, and profoundly higher conductivity than that of conventionally sulfonated PEEK.

2.6 References

1. Xing, P.; Robertson, G. P.; Guiver, M. D.; Mikhailenko, S. D.; Wang, K.; Kaliaguine, S., Synthesis and characterization of sulfonated poly(ether ether ketone) for proton exchange membranes. *Journal of Membrane Science* **2004,** *229* (1–2), 95-106.
2. Shi, Z.; Holdcroft, S., Synthesis and Proton Conductivity of Partially Sulfonated Poly([vinylidene difluoride-co-hexafluoropropylene]-b-styrene) Block Copolymers. *Macromolecules* **2005,** *38* (10), 4193-4201.
3. Drioli, E.; Regina, A.; Casciola, M.; Oliveti, A.; Trotta, F.; Massari, T., Sulfonated PEEK-WC membranes for possible fuel cell applications. *Journal of Membrane Science* **2004,** *228* (2), 139-148.
4. Chen, Y.; Guo, R.; Lee, C. H.; Lee, M.; McGrath, J. E., Partly fluorinated poly(arylene ether ketone sulfone) hydrophilic–hydrophobic multiblock copolymers for fuel cell membranes. *International Journal of Hydrogen Energy* **2012,** *37* (7), 6132-6139.
5. Mauritz, K. A.; Moore, R. B., State of Understanding of Nafion. *Chemical Reviews* **2004,** *104* (10), 4535-4586.
6. Eisenberg, A.; Hird, B.; Moore, R. B., A new multiplet-cluster model for the morphology of random ionomers. *Macromolecules* **1990,** *23* (18), 4098-4107.
7. Hsu, W. Y.; Gierke, T. D., Ion transport and clustering in nafion perfluorinated membranes. *Journal of Membrane Science* **1983,** *13* (3), 307-326.
8. Gierke, T. D.; Munn, G. E.; Wilson, F. C., The morphology in nafion perfluorinated membrane products, as determined by wide- and small-angle x-ray studies. *Journal of Polymer Science: Polymer Physics Edition* **1981,** *19* (11), 1687-1704.
9. Kusoglu, A.; Weber, A. Z., New Insights into Perfluorinated Sulfonic-Acid Ionomers. *Chemical Reviews* **2017,** *117* (3), 987-1104.
10. Chang, Y.; Lee, Y.-B.; Bae, C., Partially fluorinated sulfonated poly (ether amide) fuel cell membranes: influence of chemical structure on membrane properties. *Polymers* **2011,** *3* (1), 222-235.
11. Swier, S.; Chun, Y. S.; Gasa, J.; Shaw, M. T.; Weiss, R. A., Sulfonated poly(ether ketone ketone) ionomers as proton exchange membranes. *Polymer Engineering & Science* **2005,** *45* (8), 1081-1091.
12. Osborn, A. M. Investigation of Phase Morphology and Blend Stability in Ionomeric Perfluorocyclobutane (PFCB)/Poly(vinylidene difluoride) (PVDF) Copolymer Blend Membranes. Virginia Tech, Blacksburg, VA, 2010.
13. Hickner, M. A.; Ghassemi, H.; Kim, Y. S.; Einsla, B. R.; McGrath, J. E., Alternative Polymer Systems for Proton Exchange Membranes (PEMs). *Chemical Reviews* **2004,** *104* (10), 4587-4612.
14. Knauth, P.; Di Vona, M. L., Sulfonated aromatic ionomers: Analysis of proton conductivity and proton mobility. *Solid State Ionics* **2012,** *225*, 255-259.
15. Di Vona, M. L.; Sgreccia, E.; Licoccia, S.; Alberti, G.; Tortet, L.; Knauth, P., Analysis of Temperature-Promoted and Solvent-Assisted Cross-Linking in Sulfonated Poly(ether ether ketone) (SPEEK) Proton-Conducting Membranes. *The Journal of Physical Chemistry B* **2009,** *113* (21), 7505-7512.
16. Zhang, G.; Fu, T.; Wu, J.; Li, X.; Na, H., Synthesis and characterization of a new type of sulfonated poly(ether ether ketone ketone)s for proton exchange membranes. *Journal of Applied Polymer Science* **2010,** *116* (3), 1515-1523.

17. Knauth, P.; Hou, H.; Bloch, E.; Sgreccia, E.; Di Vona, M. L., Thermogravimetric analysis of SPEEK membranes: Thermal stability, degree of sulfonation and cross-linking reaction. *Journal of Analytical and Applied Pyrolysis* **2011,** *92* (2), 361-365.
18. Rikukawa, M.; Sanui, K., Proton-conducting polymer electrolyte membranes based on hydrocarbon polymers. *Progress in Polymer Science* **2000,** *25* (10), 1463-1502.
19. Higashihara, T.; Matsumoto, K.; Ueda, M., Sulfonated aromatic hydrocarbon polymers as proton exchange membranes for fuel cells. *Polymer* **2009,** *50* (23), 5341-5357.
20. Reyes-Rodriguez, J. L.; Solorza-Feria, O.; Garcia-Bernabe, A.; Gimenez, E.; Sahuquillo, O.; Compan, V., Conductivity of composite membrane-based poly(ether-ether-ketone) sulfonated (SPEEK) nanofiber mats of varying thickness. *RSC Advances* **2016,** *6* (62), 56986-56999.
21. Lee, J. K.; Li, W.; Manthiram, A., Sulfonated poly(ether ether ketone) as an ionomer for direct methanol fuel cell electrodes. *Journal of Power Sources* **2008,** *180* (1), 56-62.
22. Kaliaguine, S.; Mikhailenko, S.; Wang, K.; Xing, P.; Robertson, G.; Guiver, M., Properties of SPEEK based PEMs for fuel cell application. *Catalysis Today* **2003,** *82* (1), 213-222.
23. Bailly, C.; Williams, D. J.; Karasz, F. E.; MacKnight, W. J., The sodium salts of sulphonated poly(aryl-ether-ether-ketone) (PEEK): Preparation and characterization. *Polymer* **1987,** *28* (6), 1009-1016.
24. Seo, D. W.; Lim, Y. D.; Lee, S. H.; Hossain, M. A.; Islam, M. M.; Lee, H. C.; Jang, H. H.; Kim, W. G., Preparation and characterization of block copolymers containing multi-sulfonated unit for proton exchange membrane fuel cell. *Electrochimica Acta* **2012,** *86*, 352-359.
25. Meier-Haack, J.; Taeger, A.; Vogel, C.; Schlenstedt, K.; Lenk, W.; Lehmann, D., Membranes from sulfonated block copolymers for use in fuel cells. *Separation and Purification Technology* **2005,** *41* (3), 207-220.
26. Yu, X.; Roy, A.; Dunn, S.; Badami, A. S.; Yang, J.; Good, A. S.; McGrath, J. E., Synthesis and characterization of sulfonated-fluorinated, hydrophilic-hydrophobic multiblock copolymers for proton exchange membranes. *Journal of Polymer Science Part A: Polymer Chemistry* **2009,** *47* (4), 1038-1051.
27. Lee, M.; Park, J. K.; Lee, H.-S.; Lane, O.; Moore, R. B.; McGrath, J. E.; Baird, D. G., Effects of block length and solution-casting conditions on the final morphology and properties of disulfonated poly(arylene ether sulfone) multiblock copolymer films for proton exchange membranes. *Polymer* **2009,** *50* (25), 6129-6138.
28. Roy, A.; Hickner, M. A.; Yu, X.; Li, Y.; Glass, T. E.; McGrath, J. E., Influence of chemical composition and sequence length on the transport properties of proton exchange membranes. *Journal of Polymer Science Part B: Polymer Physics* **2006,** *44* (16), 2226-2239.
29. Zhao, C.; Li, X.; Wang, Z.; Dou, Z.; Zhong, S.; Na, H., Synthesis of the block sulfonated poly(ether ether ketone)s (S-PEEKs) materials for proton exchange membrane. *Journal of Membrane Science* **2006,** *280* (1–2), 643-650.
30. Zhao, C.; Lin, H.; Shao, K.; Li, X.; Ni, H.; Wang, Z.; Na, H., Block sulfonated poly(ether ether ketone)s (SPEEK) ionomers with high ion-exchange capacities for proton exchange membranes. *Journal of Power Sources* **2006,** *162* (2), 1003-1009.
31. Chen, Y.; Lee, C. H.; Rowlett, J. R.; McGrath, J. E., Synthesis and characterization of multiblock semi-crystalline hydrophobic poly(ether ether ketone)–hydrophilic disulfonated poly(arylene ether sulfone) copolymers for proton exchange membranes. *Polymer* **2012,** *53* (15), 3143-3153.
32. Yang, A. C. C.; Narimani, R.; Frisken, B. J.; Holdcroft, S., Investigations of crystallinity and chain entanglement on sorption and conductivity of proton exchange membranes. *Journal of Membrane Science* **2014,** *469*, 251-261.

33. Hamada, T.; Hasegawa, S.; Fukasawa, H.; Sawada, S.-i.; Koshikawa, H.; Miyashita, A.; Maekawa, Y., Poly(ether ether ketone) (PEEK)-based graft-type polymer electrolyte membranes having high crystallinity for high conducting and mechanical properties under various humidified conditions. *Journal of Materials Chemistry A* **2015,** *3* (42), 20983-20991.
34. Wang, R.; Yan, X.; Wu, X.; He, G.; Du, L.; Hu, Z.; Tan, M., Modification of hydrophilic channels in Nafion membranes by DMBA: Mechanism and effects on proton conductivity. *Journal of Polymer Science Part B: Polymer Physics* **2014,** *52* (16), 1107-1117.
35. Gao, X.; Liu, Y.; Li, J., Review on Modification of Sulfonated Poly (-ether-ether-ketone) Membranes Used as Proton Exchange Membranes. *Materials Science* **2015,** *21* (4), 574-582.
36. Fahs, G. B.; Benson, S. D.; Moore, R. B., Blocky Sulfonation of Syndiotactic Polystyrene: A Facile Route toward Tailored Ionomer Architecture via Postpolymerization Functionalization in the Gel State. *Macromolecules* **2017,** *50* (6), 2387-2396.
37. Benson, S. D. The Effect of Nanoscale Particles and Ionomer Architecture on the Crystallization Behavior of Sulfonated Syndiotactic Polystyrene. Ph.D. Dissertation, Virginia Polytechnic Institute and State University, Blacksburg, VA, 2010.
38. Talley, S. J.; Yuan, X.; Moore, R. B., Thermoreversible Gelation of Poly(ether ether ketone). *ACS Macro Letters* **2017,** *6* (3), 262-266.
39. Corby, B. W.; Gray, A. D.; Meaney, P. J.; Falvey, M. J.; Lawrence, G. P.; Smyth, T. P., Clean-chemistry sulfonation of aromatics. *Journal of Chemical Research* **2002,** *2002* (7), 326-327.
40. Bakker, B. H.; Cerfontain, H., Sulfonation of Alkenes by Chlorosulfuric Acid, Acetyl Sulfate, and Trifluoroacetyl Sulfate. *European Journal of Organic Chemistry* **1999,** *1999* (1), 91-96.
41. Koziara, B. T.; Kappert, E. J.; Ogieglo, W.; Nijmeijer, K.; Hempenius, M. A.; Benes, N. E., Thermal Stability of Sulfonated Poly(Ether Ether Ketone) Films: on the Role of Protodesulfonation. *Macromolecular Materials and Engineering* **2016,** *301* (1), 71-80.
42. Ilavsky, J., P. R. Jemian, , Ultra-small-angle X-ray scattering at the Advanced Photon Source. *J. Appl. Crystallogr.* **2009,** *42* (3), 469-479.
43. Ilavsky, J. J., P. R. , Irena: tool suite for modeling and analysis of small-angle scattering. *J. Appl. Crystallogr.* **2009,** *42*, 347-353.
44. Ilavsky, J., Nika: software for two-dimensional data reduction. *J. Appl. Crystallogr.* **2012,** *45* (2), 324-328.
45. Banerjee, S.; Kar, K. K., Impact of degree of sulfonation on microstructure, thermal, thermomechanical and physicochemical properties of sulfonated poly ether ether ketone. *Polymer* **2017,** *109*, 176-186.
46. Iulianelli, A.; Basile, A., Sulfonated PEEK-based polymers in PEMFC and DMFC applications: a review. *International Journal of Hydrogen Energy* **2012,** *37* (20), 15241-15255.
47. Huang, R. Y. M.; Shao, P.; Burns, C. M.; Feng, X., Sulfonation of poly(ether ether ketone)(PEEK): Kinetic study and characterization. *Journal of Applied Polymer Science* **2001,** *82* (11), 2651-2660.
48. Weiss, R. A.; Turner, S. R.; Lundberg, R. D., Sulfonated polystyrene ionomers prepared by emulsion copolymerization of styrene and sodium styrene sulfonate. *Journal of Polymer Science: Polymer Chemistry Edition* **1985,** *23* (2), 525-533.
49. Weiss, R. A.; Lundberg, R. D.; Turner, S. R., Comparisons of styrene ionomers prepared by sulfonating polystyrene and copolymerizing styrene with styrene sulfonate. *Journal of Polymer Science: Polymer Chemistry Edition* **1985,** *23* (2), 549-568.
50. Blundell, D. J.; Osborn, B. N., The morphology of poly(aryl-ether-ether-ketone). *Polymer* **1983,** *24* (8), 953-958.

51. Tan, S.; Su, A.; Luo, J.; Zhou, E., Crystallization kinetics of poly(ether ether ketone) (PEEK) from its metastable melt. *Polymer* **1999,** *40* (5), 1223-1231.
52. Verma, R. K.; Velikov, V.; Kander, R. G.; Marand, H.; Chu, B.; Hsiao, B. S., SAXS studies of lamellar level morphological changes during crystallization and melting in PEEK. *Polymer* **1996,** *37* (24), 5357-5365.
53. Chen, H.-L.; Porter, R. S., Melting behavior of poly(ether ether ketone) in its blends with poly(ether imide). *Journal of Polymer Science Part B: Polymer Physics* **1993,** *31* (12), 1845-1850.
54. Flory, P. J., Theory of crystallization in copolymers. *Transactions of the Faraday Society* **1955,** *51* (0), 848-857.
55. Flory, P. J., Thermodynamics of Crystallization in High Polymers II. Simplified Derivation of Melting-Point Relationships. *The Journal of Chemical Physics* **1947,** *15* (9), 684-684.
56. Orler, E. B.; Moore, R. B., Influence of Ionic Interactions on the Crystallization of Lightly Sulfonated Syndiotactic Polystyrene Ionomers. *Macromolecules* **1994,** *27* (17), 4774-4780.
57. Orler, E. B.; Calhoun, B. H.; Moore, R. B., Crystallization Kinetics as a Probe of the Dynamic Network in Lightly Sulfonated Syndiotactic Polystyrene Ionomers. *Macromolecules* **1996,** *29* (18), 5965-5971.
58. Gebel, G., Structure of Membranes for Fuel Cells: SANS and SAXS Analyses of Sulfonated PEEK Membranes and Solutions. *Macromolecules* **2013,** *46* (15), 6057-6066.
59. Song, J.-M.; Shin, J.; Sohn, J.-Y.; Nho, Y. C., Ionic aggregation characterization of sulfonated PEEK ionomers using by X-ray and DMA techniques. *Macromolecular Research* **2012,** *20* (5), 477-483.
60. Crevecoeur, G.; Groeninckx, G., Binary blends of poly (ether ether ketone) and poly (ether imide): miscibility, crystallization behavior and semicrystalline morphology. *Macromolecules* **1991,** *24* (5), 1190-1195.
61. Verma, R.; Marand, H.; Hsiao, B., Morphological Changes during Secondary Crystallization and Subsequent Melting in Poly(ether ether ketone) as Studied by Real Time Small Angle X-ray Scattering. *Macromolecules* **1996,** *29* (24), 7767-7775.
62. Yang, B.; Manthiram, A., Comparison of the small angle X-ray scattering study of sulfonated poly(etheretherketone) and Nafion membranes for direct methanol fuel cells. *Journal of Power Sources* **2006,** *153* (1), 29-35.
63. Luu, D. X.; Cho, E.-B.; Han, O. H.; Kim, D., SAXS and NMR Analysis for the Cast Solvent Effect on sPEEK Membrane Properties. *The Journal of Physical Chemistry B* **2009,** *113* (30), 10072-10076.
64. Kawaguti, C. A.; Dahmouche, K.; Gomes, A. d. S., Nanostructure and properties of proton-conducting sulfonated poly(ether ether ketone) (SPEEK) and zirconia–SPEEK hybrid membranes for direct alcohol fuel cells: effect of the nature of swelling solvent and incorporation of heteropolyacid. *Polymer International* **2012,** *61* (1), 82-92.
65. Smitha, B.; Sridhar, S.; Khan, A. A., Solid polymer electrolyte membranes for fuel cell applications—a review. *Journal of Membrane Science* **2005,** *259* (1), 10-26.
66. Li, Q.; He, R.; Jensen, J. O.; Bjerrum, N. J., Approaches and Recent Development of Polymer Electrolyte Membranes for Fuel Cells Operating above 100 °C. *Chemistry of Materials* **2003,** *15* (26), 4896-4915.
67. Peighambardoust, S. J.; Rowshanzamir, S.; Amjadi, M., Review of the proton exchange membranes for fuel cell applications. *International Journal of Hydrogen Energy* **2010,** *35* (17), 9349-9384.
68. Hickner, M. A.; Pivovar, B. S., The Chemical and Structural Nature of Proton Exchange Membrane Fuel Cell Properties. *Fuel Cells* **2005,** *5* (2), 213-229.

69. Peckham, T. J.; Schmeisser, J.; Rodgers, M.; Holdcroft, S., Main-chain, statistically sulfonated proton exchange membranes: the relationships of acid concentration and proton mobility to water content and their effect upon proton conductivity. *Journal of Materials Chemistry* **2007,** *17* (30), 3255-3268.
70. Elabd, Y. A.; Hickner, M. A., Block Copolymers for Fuel Cells. *Macromolecules* **2011,** *44* (1), 1-11.

Chapter 3

Blocky Sulfonation of Poly(ether ether ketone) in a Non-Solvent

3.1 Introduction

Sulfonated poly(ether ether ketone) (SPEEK) is an attractive candidate for proton exchange membranes (PEMs) due to its high thermal stability, excellent mechanical properties, good proton conductivity, and low cost.[1-4] Conventionally, randomly sulfonated SPEEK is prepared by post-polymerization sulfonation of PEEK in sulfuric acid, and the degree of sulfonation is controlled by reaction time and temperature.[5-7] High proton transport is achieved at high ion content, however, the performance of these membranes is limited due to over-swelling of membranes in hydrated conditions and weak hydrophilic-hydrophobic phase separation, which restricts proton transport due to poorly connected hydrophilic domains.[8]

To improve the membrane properties of SPEEK, block copolymer systems have been investigated. Multiblock SPEEK copolymers consisting of methylated hydrophobic blocks and disulfonated hydrophilic blocks displayed improved proton transport and water uptake compared to random SPEEK analogues due to enhanced hydrophilic-hydrophobic phase separation.[9-10] Likewise, sulfonated poly(arylene ether ketone) multiblock copolymers prepared by Lee demonstrated excellent proton transport (similar to Nafion®) and phase-morphologies dependent on the length of the hydrophobic block.[11] Again, hydrophilic-hydrophobic phase separation between the blocks established a higher local ion concentration within the hydrophilic domains, contributing to enhanced proton transport and greater dimensional stability upon swelling.

Further efforts have focused not only on blocking up the sulfonate functionality of SPEEK, but also maintaining crystallizability within the hydrophobic block. Crystallinity imparts mechanical integrity to the membrane and increases solvent resistance, thereby decreasing swelling in water.[12-16] Multiblock, semi-crystalline poly(ether ketone)-based proton exchange

membranes were prepared by the simultaneous sulfonation and hydrolysis of distinct poly(ether ketimine) blocks, resulting in crystallizable poly(ether ketone) (PEK) blocks and densely sulfonated poly(ether ether ketone) blocks.[17] This process afforded semicrystalline membranes with decreased water uptake, decreased dimensional swelling, and improved proton transport compared to random, amorphous copolymer analogues.

Recently, a novel post-polymerization sulfonation method was introduced to prepare blocky sulfonated copolymers with maintained crystallizability.[18-19] Sulfonation was carried out in the semicrystalline gel state, whereby the sulfonating reagent is sterically excluded from the densely-packed crystalline domains and exclusively reacts with the solvent-swollen amorphous domains, yielding a 'blocky' architecture. Blocky SPEEK and blocky sulfonated syndiotactic polystyrene (SsPS) demonstrated enhanced crystallizability and faster crystallization kinetics when compared to random copolymers at similar ion contents, suggesting long segments of unfunctionalized homopolymer were preserved during the gel-state sulfonation process. Furthermore, blocky SPEEK membranes displayed enhanced proton transport compared to random SPEEK due to an increased ion content within the amorphous domains (an effect of increased crystallinity) and likely more interconnected hydrophilic domains. Although this method provided a simple post-polymerization process to prepare blocky SPEEK copolymers, it is limited to low ion contents (i.e. <15 mol%) due to dissolution of the semicrystalline gel over time during sulfonation. In this work, methods to push towards high degrees of sulfonation while maintaining the semicrystalline gel-state will be investigated. In particular, the use of chlorinated non-solvents to suspend the semicrystalline gel will be examined to preserve the gel architecture during sulfonation, thereby enabling longer reaction times and high concentrations of sulfonating reagent without the concern of gel dissolution. The effect of the non-solvent gel-state functionalization process on the resultant blocky SPEEK membrane properties is investigated and compared to

random SPEEK copolymers prepared in the homogeneous solution state and blocky SPEEK copolymers prepared in dichloroacetic acid (DCA).

3.2 Experimental

3.2.1 Materials

Poly(ether ether ketone) (PEEK) pellets (Victrex 150G) were obtained from Victrex. Dichloroacetic acid (DCA) was purchased from Sigma-Aldrich and was dried over magnesium sulfate (Fisher Scientific), then filtered through a 0.45 μm PTFE syringe filter prior to use. Trifluoroacetic anhydride, chlorosulfonic acid, and dimethylacetamide (DMAc) was purchased from Sigma-Aldrich. Concentrated sulfuric acid (98%), 1,2-dichloroethane (DCE), sodium chloride, and cesium chloride were purchased from Fisher Scientific.

3.2.2 Synthesis of trifluoroacetyl sulfate

Trifluoroacetyl sulfate (TFAS) was prepared according to previously published procedures.[20-21] Trifluoroacetic anhydride (3.8 mL; 0.027 mol) was added to a nitrogen-purged round bottom flask. The flask was cooled in an ice bath for 15 minutes and then concentrated sulfuric acid (1 mL; 0.018 mol) was added. The solution was stirred vigorously for approximately 3 hours to obtain a clear, light brown liquid.

3.2.3 Random Sulfonation of PEEK

PEEK (5.0 g) was dissolved in dichloroacetic acid at 185 °C to a final concentration of 10% w/v. Once dissolved, the temperature was lowered to 80 °C and the solution as allowed to equilibrate at this temperature under nitrogen for 1 hour. Next, 0.5-2 equivalents of trifluoroacetyl sulfate was added dropwise to the PEEK solution, and the reaction was allowed to proceed for 1-24 hours. The reaction was terminated by precipitation into ice-cold deionized water or cold 1M NaOH (aq) for reactions over 10 hours. The product was filtered, washed with deionized water, and then washed by soxhlet extraction over methanol for 24 hours. The resulting polymers were

dried at 100 °C for 12 hours. Prior to any analysis, samples were ground under liquid nitrogen to form a fine powder.

3.2.4 Blocky Sulfonation of PEEK in Non-Solvent

PEEK (5.0 g) was dissolved in dichloroacetic acid at 185 °C to a final concentration of 20% w/v. Once dissolved, the solution was removed from heat and allowed to remain at room temperature for at least 24 hours to form a thermoreversible, semicrystalline gel network.[22] The gel was manually broken into small pieces using a metal spatula and diluted to a 4 w/v% suspension in 1,2-dichloroethane (DCE). The gel suspension was equilibrated at 80 °C under nitrogen for 1 hour. Once equilibrated, 0.5-2 equivalents of the desired sulfonating reagent (trifluoroacetyle sulfate or chlorosulfonic acid) were added to the PEEK solution as a 2 v/v% solution in 1,2-dichloroethane using a syringe pump at a rate of 75 mL/hr, and the reaction was allowed to proceed for up to 7 days. TFAS was used as the sulfonating reagent for degrees of sulfonation targeting 30 mol% and below, and chlorosulfonic acid was used as the sulfonating reagent for reactions targeting degrees of sulfonation above 30 mol%. The reaction was terminated by precipitation into cold 1M NaOH (aq). The product was filtered, washed with deionized water, and then washed by soxhlet extraction over methanol for 24 hours. The resulting polymers were dried at 100 °C for 12 hours. Prior to any analysis, samples were ground under liquid nitrogen to form a fine powder.

3.2.5 Membrane Preparation

Random SPEEK casting solutions were prepared by dissolving the SPEEK (in H^+-form) in dimethylacetamide (DMAc) at 150 ºC to a final concentration of 10 w/v%. Due to solubility limitations of blocky SPEEK in polar aprotic solvents, blocky SPEEK casting solutions were prepared by dissolving SPEEK (in Na^+-form) in dichloroacetic acid (DCA) at 150 ºC to a final concentration of 10 w/v%. Na^+-form blocky SPEEK was used because H^+-form SPEEK was not

fully soluble in DCA at high degrees of sulfonation (>25 mol%). Once dissolved, the casting solutions were cooled to room temperature and then filtered through a 0.45 μm PTFE syringe filter. The solutions were cast onto glass at 100 ºC using a doctor blade set to 7.5 mils and allowed to dry on the heated substrate for 30 minutes, resulting in a final thickness of approximately 25 μm. Membranes were washed with deionized water to remove residual solvent and then dried at 100 ºC for 12 hours.

3.2.6 Ion Exchange

H^+-form SPEEK samples were converted to the cesium form (Cs^+-form) by stirring powders or membranes in 1M CsCl (aq) for 24 hours. H^+-SPEEK samples were similarly converted to the Na^+-form by stirring in 2M NaCl (aq) for 24 hours. SPEEK samples in a salt form (i.e. Cs^+ or Na^+) were converted to acid form (H^+) by stirring in 1M HCl (aq) for 24 hours. Following ion exchange, samples were washed with deionized water and dried at 100 ºC for 12 hours.

3.2.7 ^{1}H NMR of Spectroscopy

^{1}H NMR spectra were measured using a Bruker Avance III 600 MHz. At all degrees of sulfonation explored in this work, blocky SPEEK samples were insoluble in conventional deuterated solvents, and thus a solvent suppression method was employed for ^{1}H NMR analysis. SPEEK samples were dissolved in DCA at 185 °C to a concentration of 10% w/v. Once dissolved, the samples were cooled to room temperature and diluted by a factor of 5 using deuterated chloroform ($CDCl_3$) with 0.05% v/v TMS. Presaturation of the intense DCA resonance at 6 ppm was performed during acquisition to obtain a suitable spectrum, free of a solvent contribution. This method was also employed for random SPEEK below 30 mol% sulfonation due to solubility limitations in conventional deuterated solvents. For random SPEEK at 30 mol% sulfonation and above, ^{1}H NMR spectra were acquired in DMSO-d6. For more information regarding the validity

of the solvent-suppression method, please see **Chapter 2**. The degree of sulfonation for all SPEEK samples was calculated from the integration of the 10' peak relative to the combined area of the 1,3,6,8 peaks.[6]

3.2.8 FTIR Spectroscopy

FTIR was performed using a Varian 670-IR spectrometer with a DTGS detector using the Pike Technologies GladiATR^{TM} attachment (diamond crystal). Spectra were collected as the average of 32 scans at 4 cm^{-1} resolution.

3.2.9 Differential Scanning Calorimetry (DSC)

A TA Instruments Q2000 DSC was used to determine the thermal transitions and crystallization behavior of the SPEEK samples. Na^+-form and Cs^+-form SPEEK samples were used for this analysis because acid-form SPEEK is not thermally stable at elevated temperatures.[1, 23] Samples were pre-dried at 150 °C for 5 minutes before a heat-cool-heat sequence. Under a nitrogen atmosphere, the dried samples (~5-8 mg) were heated from 50 °C to 380 °C at 20 °C/min, quench cooled to 50 °C, and then reheated from 0 °C to 380 °C at 20 °C/min. The glass transition temperature (T_g), melting temperature (T_m), and enthalpy of melting (ΔH_m) were determined from the heating scans using the TA Instruments Universal Analysis software.

3.2.10 Tensile Properties

The tensile properties of SPEEK membranes (H^+-form) were examined using an Instron 5867. Samples were cut into dogbones (ASTM 638 – Type IV dimensions) and extended at a rate of 5 mm/min. 5 dogbones were run for each SPEEK membrane sample. All membranes were dried at 100 ºC for 12 hours prior to analysis.

3.2.11 Water Uptake and Areal Swelling Ratio

The water uptake and swelling ratios of the SPEEK (H^+-form) membranes were determined by first drying membranes in a vacuum oven at 120 °C for 3 hours. The mass (W_{dry}) and dimensions

($L_{x,\,dry}$ x $L_{y,\,dry}$) of the dry membranes were recorded. Then, the samples were treated in boiling deionized water for 1 hour followed by equilibration in room temperature deionized water for 12 hours or by only equilibrating in room temperature deionized water for 12 hours. Membranes were blotted to remove excess surface water and the mass (W_{wet}) and dimensions ($L_{x,\,wet}$ x $L_{y,\,wet}$) of the wet membranes were recorded. The water uptake and areal swelling ratio were calculated as:

$$\text{Water uptake} = \frac{(W_{\text{wet}} - W_{\text{dry}})}{W_{\text{dry}}} \times\ 100\% \tag{3.1}$$

$$\text{Areal Swelling ratio} = \frac{\left(L_{\text{x,wet}} \times L_{\text{y,wet}}\right) - (L_{\text{x,dry}} \times L_{\text{y,dry}})}{(L_{\text{x,dry}} \times L_{\text{y,dry}})} \times\ 100\% \tag{3.2}$$

The reported values are the average of four samples.

3.2.12 Proton Conductivity

Prior to analysis, SPEEK membranes were boiled in deionized water for one hour and then soaked in room temperature deionized water for 12 hours. In-plane proton conductivity was conducted using a 4-point conductivity cell from Bekktech, which was immersed in deionized water at room temperature. Measurements were taken from 1 Hz to 1.5 MHz at a voltage amplitude of 50 mV using a 1255 HF frequency analyzer coupled to a 1286 electrochemical interface, both from Solartron Analytical. Data analysis was performed using the Zplot® and Zview® software from Scribner and Associates, Inc. The proton conductivity was calculated as:

$$\sigma = \frac{1}{\rho} = \frac{l}{R \times A} \tag{3.3}$$

where σ (Scm^{-1}) is the conductivity, ρ (Ωcm) is the resistivity, l (cm) is the distance between the contacting electrodes, R (Ω) is the resistance determined from the real value of the complex impedance plot that corresponds to the minimum imaginary response, and A is the cross-sectional

area of the membrane calculated from the width and thickness of the membrane. Measurements were performed on three separate membranes for each sample to ensure the reproducibility of results.

3.2.13 Morphological Analysis using USAXS/SAXS/WAXD

Ultra-small angle x-ray scattering (USAXS), small angle x-ray scattering (SAXS), and wide angle x-ray diffraction (WAXD) data were collected at Argonne National Laboratory beamline 9ID-C using a photon energy of 24 keV.[24] Scattering profiles are plotted as absolute intensity vs. q, where $q = \left(\frac{4\pi}{\lambda}\right)\sin(\theta)$, θ is one half of the scattering angle, and λ is the X-ray wavelength. USAXS measurements were collected using a Bonse-Hart camera as the detector. SAXS measurements utilized the Pilatus 100k camera, and WAXD utilized the Pilatus 100k-w camera. Data reduction was performed using the Irena[25] and Nika[26] software packages provided by Argonne.

3.3 Results and Discussion

3.3.1 Random and Blocky Sulfonation of PEEK

In this work, the sulfonation of PEEK in the heterogeneous gel state is explored to synthesize blocky SPEEK copolymers with high degrees of functionalization. The blocky ionomer architecture is compared to random SPEEK prepared by sulfonation in the homogeneous solution state. The successful gel-state sulfonation of PEEK was carried out previously with 20 w/v% PEEK gels using dichloroacetic acid (DCA) as both the gelation solvent and sulfonation solvent.[19] This gel-state approach successfully produced SPEEK with a blocky functionalization architecture, and these blocky SPEEK copolymers demonstrated high crystallizability and improved proton transport relative to random SPEEK at similar degrees of functionalization. The degree of sulfonation in this gel-state process, however, was limited to approximately 15 mol% due to dissolution of the gel at time scales necessary to achieve higher degrees of functionality. In

this section, methods to stabilize the gel-state during sulfonation will be explored to achieve blocky SPEEK with high degrees of sulfonation.

3.3.1.1 Gel-State Sulfonation in Mixed Solvents

To better stabilize the gel state over time, mixed solvent systems were explored. Solvent mixtures containing 90:10 (v:v) ratios of DCA:nonsolvent were prepared and used as the suspending/reaction solvent for the PEEK gel. It is anticipated that by adding a small amount of a nonsolvent, the PEEK gel will become less soluble in the suspending solvent, thereby increasing the stability of the gel. The non-solvents used for this analysis included 1,2-dichloroethane (DCE), chloroform ($CHCl_3$), hexanes, and *n*-pentane. Each of these solvents is miscible with DCA and does not dissolve PEEK on its own. For these reactions, the typical sulfonation procedure described above was performed using the solvent mixture as both the suspending solvent and solvent for diluting the sulfonating reagent (TFAS). A 1:1 molar ratio of TFAS:PEEK repeat unit (100% TFAS) was used.

For the reaction using pure DCA as the solvent, the gel suspension immediately changed color from tan to yellow following the addition of TFAS. As the reaction proceeded, the suspension became a cloudy orange-brown color, and then the gel pieces began to wear away and dissolve. The gel pieces remained present for up to 3 hours before dissolving completely into a transparent, dark brown solution. For the solvent systems containing DCE, $CHCl_3$, hexanes, and *n*-pentane, the reaction proceeded effectively and color changes similar to the reaction in DCA were observed. For these reactions, however, the gel stability significantly decreased and the gel only remained for 60-75 minutes, less than half the time of reactions in pure DCA. It is important to note that each reaction was terminated immediately following complete gel dissolution. Due to the short time-scales of these reactions, limited sulfonation was achieved.

Following results using 90:10 (v:v) DCA:nonsolvent mixtures using DCA as the primary solvent, it was hypothesized that adding a larger ratio of nonsolvent into the solvent system may help prevent gel dissolution over time. To examine this, the blocky sulfonation procedure was performed using 50:50 (v:v) DCA:$CHCl_3$ as the solvent system and a 1:1 molar ratio of TFAS:PEEK repeat unit. A visual representation of this reaction over time is shown in **Figure 3.1**. In the early stages of the reaction, when the suspension appears cloudy, many gel pieces of all sizes are present. As the suspension turns to a dark brown color, however, it is evident that the smaller gel pieces have dissolved and only large gel pieces remain. With longer reaction times, the gel pieces become thinner and thinner before eventually dissolving completely. In this system, the gel remained viable for up to 90 minutes before complete dissolution. Although the gel does not remain for long enough time periods to provide blocky-type sulfonation, the gel state was stable for a longer time period than any of the 90:10 (v:v) DCA:nonsolvent solvent systems. Thus, further increasing the amount of nonsolvent in the reaction system should enable longer periods of gel stability.

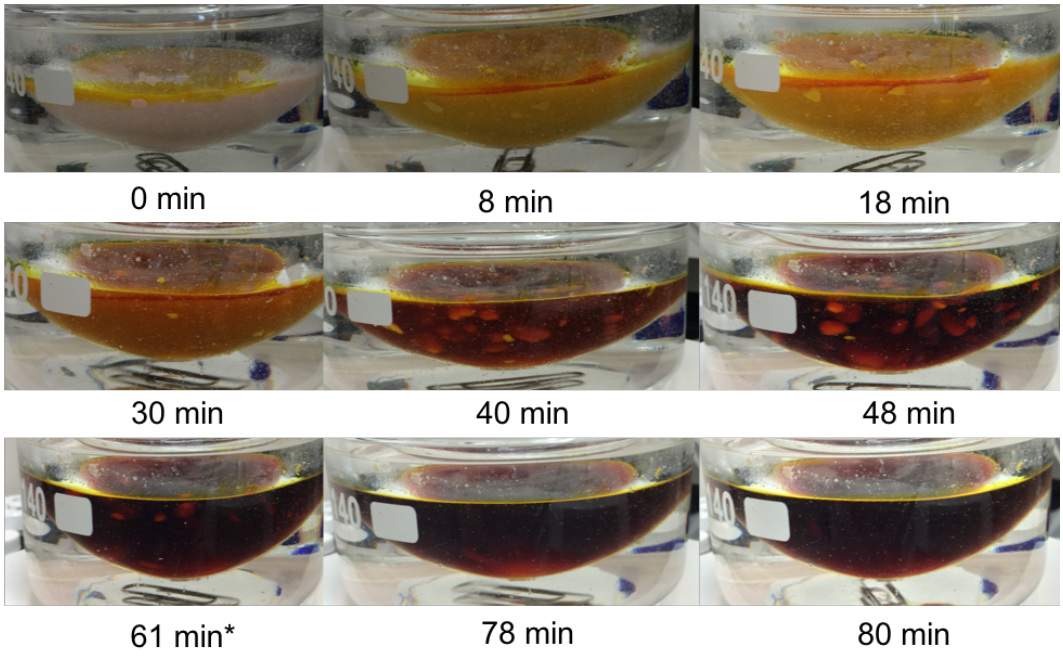

Figure 3.1. Gel-state sulfonation of PEEK using 50:50 (v:v) DCA:$CHCl_3$ as the reaction solvent. The * denotes the time at which all sulfonating reagent has been added.

3.3.1.2 Gel-State Sulfonation in Chlorinated Solvents

To further combat gel dissolution, chlorinated non-solvents for PEEK were investigated as gel-suspension solvents. Chlorinated solvents have been used extensively in sulfonation reactions[27-28] and by using a non-solvent for PEEK as the suspending solvent, the gel structure may be less likely to dissolve with the addition of sulfonating reagent. The first solvent investigated was chloroform. As with the DCA reactions, 100% TFAS was added as a 2 v/v% solution in chloroform and a 20 w/v% PEEK gel was used. Reactions were performed at 60 ºC due to the boiling point of chloroform (61.2 ºC). During this reaction, the gel suspension changed from a cloudy tan to a cloudy yellow color several minutes after the initial addition of TFAS. As the reaction proceeded, the gel suspension turned to a cloudy orange color and then finally to a seemingly clear yellow, transparent solution with orange-brown gel pieces throughout. Upon completion of the addition of TFAS, it appeared that the brown gel pieces were aggregating, however, after stirring for another hour the gel pieces were well dispersed again. Images of the gel

suspensions throughout the reaction are displayed in **Figure 3.2**. The gel pieces are clearly visible throughout the entire reaction and do not dissolve like the reactions in DCA or DCA/nonsolvent mixed solvents.

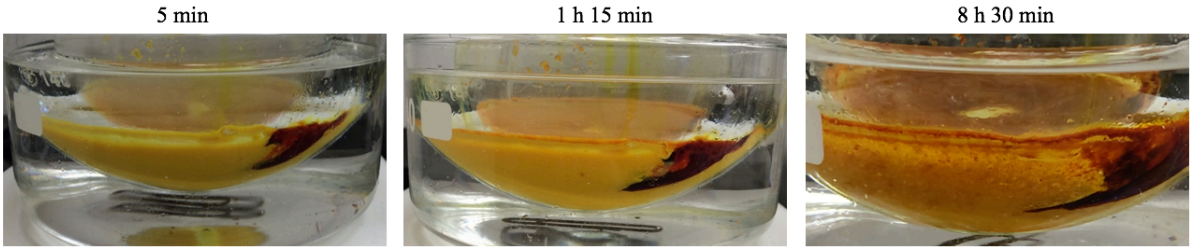

Figure 3.2. Gel-state sulfonation of PEEK in $CHCl_3$ at 60 ºC. The gel structure is stable with the addition of 100% TFAS for many hours.

Due to limited gel dissolution at long reaction times when performing the gel-state reaction in $CHCl_3$, this non-solvent method was adapted for further gel-state reactions targeting high degrees of sulfonation. Subsequent reactions were performed in 1,2-dichloroethane (1,2-DCE) to enable reaction temperatures of 80 ºC, which speeds up the sulfonation reaction.[29] Degrees of sulfonation of between 20 and 50 mol% were targeted for blocky and random SPEEK by varying the concentration of sulfonating reagent used and reaction time. The reaction conditions and the resultant degrees of sulfonation are shown in **Table 3.1**. For random SPEEK, regulation of the degree of sulfonation is easily controlled with reaction time. To get to high degrees of sulfonation for blocky SPEEK, however, it is clear that the concentration of sulfonating reagent is a key factor. With increasing sulfonating reagent concentration, an increase in the degree of sulfonation is observed. Little difference is observed with increasing reaction time at similar sulfonating reagent concentrations. It is important to note that long reaction times are necessary to achieve high degrees of sulfonation for the blocky SPEEK compared to random SPEEK. This may be due to dilution of the sulfonating reagent in DCE and/or diffusion of the reagent into the amorphous domains of the gel, which slows the reaction.

Table 3.1. Reaction conditions of random and blocky reactions and resultant degrees of sulfonation for the sulfonation of PEEK at 80 ºC.

Reaction Type	Degree of Sulfonation (mol%)	Sulfonating Reagent Concentration (mol%)	Reaction Time (h)
Blocky*	8	100	8
Blocky	21	80	24
Blocky	27	100	24
Blocky	25	100	48
Blocky	28	110	96
Blocky	30	120	68
Blocky	31	120	96
Blocky	41	130	96
Blocky	45	140	96
Random	8	100	2
Random	20	100	4
Random	27	100	8
Random	31	100	10
Random	38	100	12
Random	48	100	16
Random	52	100	18

*Indicates a reaction performed at 60 ºC.

The ^{1}H NMR spectra of random and blocky SPEEK at 20 mol% sulfonation is shown in **Figure 3.3**. The degree of sulfonation was determined by integration of the 10' peak with respect to the 1, 3, 6, 8 proton peaks. Little difference is observed in the ^{1}H NMR spectra between the blocky and random samples due to the electrophilic nature of the sulfonation reaction. Sulfonation occurs exclusively at one of the four chemically equivalent positions on the hydroquinone ring of the PEEK repeat unit, and once sulfonated this ring becomes deactivated towards further substitution due to the electron-withdrawing effect of the sulfonate group. Furthermore, the two phenyl rings of the benzophenone segment of the PEEK repeat unit are deactivated towards sulfonation due to the electron-withdrawing effect of the adjacent carbonyl group. Thus, sulfonation proceeds at a similar position on the PEEK repeat unit, independent of architecture. SPEEK samples will be represented by xSPEEKz, where x defines the architecture (R for random, B for blocky) and z is the molar degree of sulfonation.

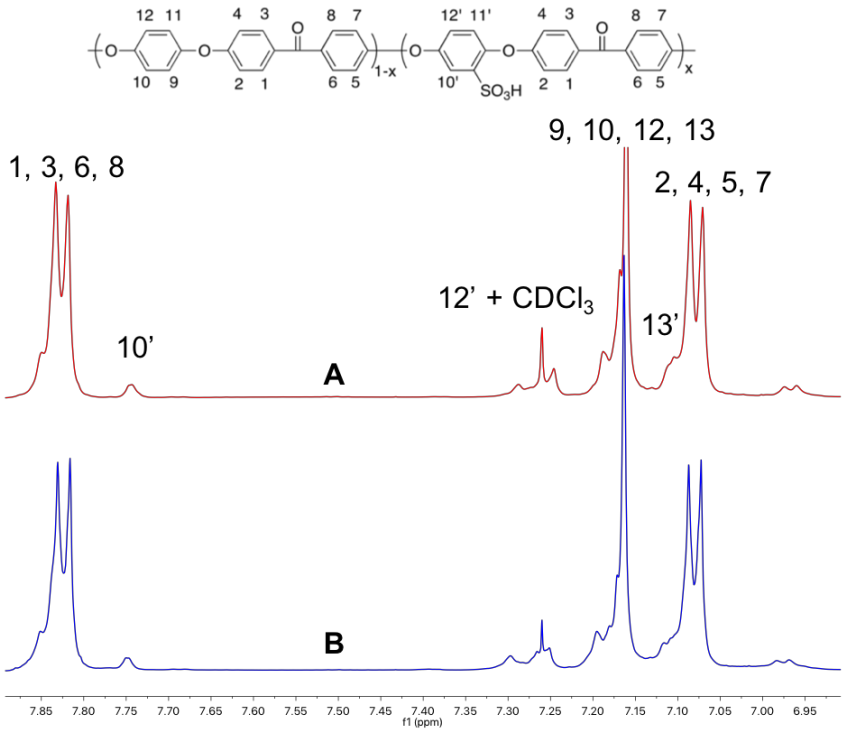

Figure 3.3. ^{1}H NMR spectra of RSPEEK20 (A) and BSPEEK21 (B). Solvent suppression ^{1}H NMR was performed in DCA/$CDCl_3$ mixed solvents.

3.3.2 FTIR Spectroscopy

FTIR spectroscopy was performed to identify changes in structure with increasing degrees of sulfonation. The FTIR spectra of PEEK, random SPEEK, and blocky SPEEK with different degrees of sulfonation is shown in **Figure 3.4**. Upon sulfonation, several new peaks appear at 1020, 1075, and 1250 cm^{-1} that may be attributed to the sulfonic acid group.[30] The peak at 1020 cm^{-1} is due to stretching of the S=O group, and the peaks at 1075 cm^{-1} and 1250 cm^{-1} are attributed to the symmetric and asymmetric stretching of the sulfone group (O=S=O), respectively. These bands increase in intensity with increasing degree of sulfonation, as expected, when compared to the backbone carbonyl peak at 1650 cm^{-1}. When comparing BSPEEK and RSPEEK at similar degrees of sulfonation, little difference is observed in the FTIR spectra suggesting that sulfonation occurs by similar electrophilic aromatic substitution mechanisms in both the solution state and in the gel state.

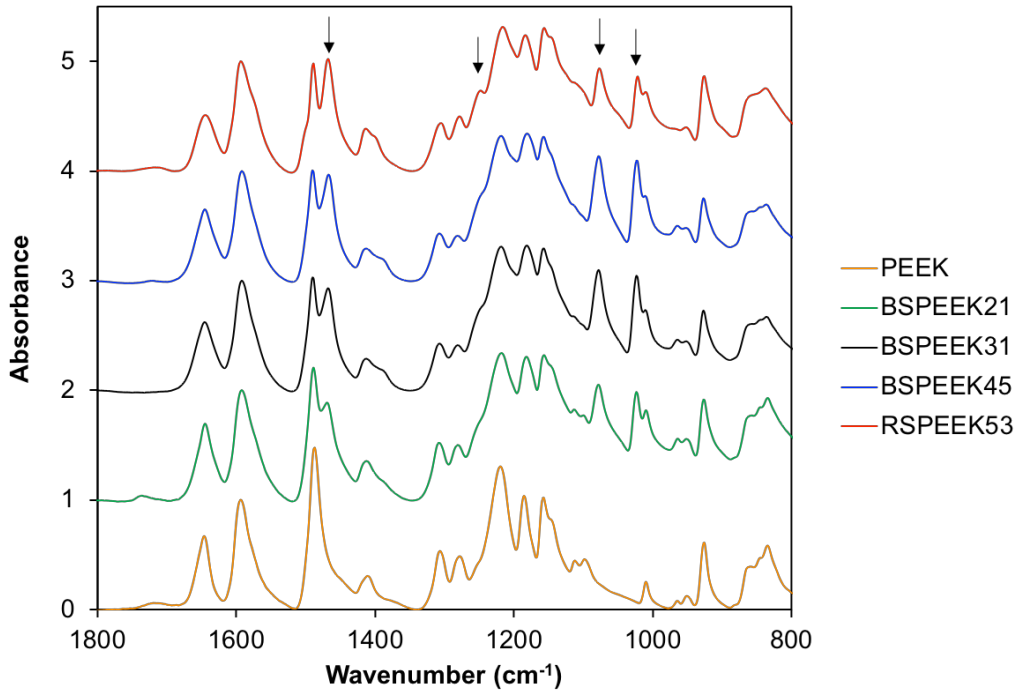

Figure 3.4. FTIR spectra of PEEK, blocky SPEEK at 21, 31, and 45 mol% sulfonation, and random sPEEK at 53 mol% sulfonation.

Furthermore, the aromatic C-C band at 1490 cm^{-1} splits and forms a new peak at 1470 cm^{-1}.[31] The peak at 1490 cm^{-1} may be attributed to the skeletal ring vibrations of 1,4-disubstituted rings, while the new peak at 1470 cm^{-1} is attributed to skeletal ring vibrations of a 1,2,4-trisubstituted rings.[32] Thus, increasing the degree of sulfonation simultaneously decreases the intensity of the peak at 1490 cm^{-1} and increases the intensity of the peak at 1470 cm^{-1}. The ratio of these two peaks (A_{1470}/A_{1490}) was compared to molar degree of sulfonation determined by ^{1}H NMR, as shown in **Figure 3.5**. For this analysis, random SPEEK from 30-60 mol% sulfonation was used because of its high solubility in DMSO-d6 and easy integration of the NMR spectra using conventional methods, thereby ensuring accurate degrees of sulfonation.[33] A linear relationship is observed in A_{1470}/A_{1490} with degree of sulfonation, characterized by an R^2 value of 0.99. The great correlation between A_{1470}/A_{1490} and the degree of sulfonation permits the use of the A_{1470}/A_{1490} value to estimate the degree of sulfonation for SPEEK samples that will not dissolve in

conventional deuterated solvents, such as blocky SPEEK. At high degrees of sulfonation (above 30 mol%), blocky SPEEK was only partially soluble in the DCA/$CDCl_3$ mixed solvent and thus, the calibration curve of **Figure 3.5** was used to confirm the degree of sulfonation.

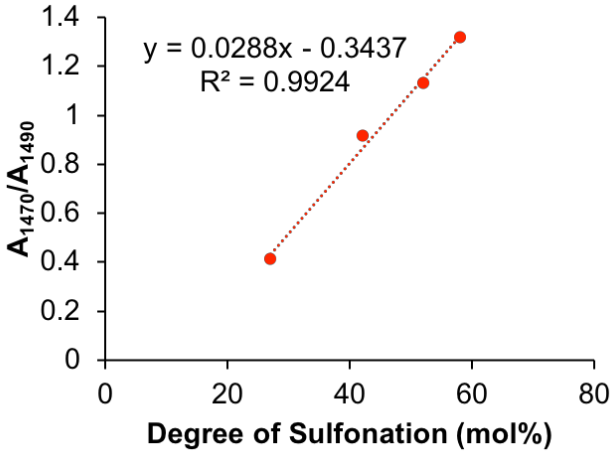

Figure 3.5. Calibration curve relating the ratio of the absorbance at 1470 cm^{-1} and the absorbance at 1490 cm^{-1} (A_{1470}/A_{1490}) to the degree of sulfonation determined by ^1H NMR.

3.3.3 Differential Scanning Calorimetry (DSC)

DSC was performed to investigate the influence of sulfonation method (i.e. gel state vs. solution state) on the crystallizability of the resultant SPEEK. First, low degrees of sulfonation were investigated to compare the gel state methods in DCA to gel state methods in the nonsolvent (DCE). DSC thermograms of the first heats of as-precipitated PEEK, RSPEEK8, BSPEEK8 (DCA), and BSPEEK8 (DCE) are shown in **Figure 3.6**. The as-precipitated SPEEK products were ground and neutralized to Cs^+-form prior to analysis. The PEEK homopolymer exhibits a large, sharp endotherm at 347 ºC that is attributed to the melting of the PEEK crystals.[34] Upon sulfonation, the melting endotherm shifts to lower temperatures due to the introduction of interactive 'defects' onto the polymer chain, which decrease crystal size. For RSPEEK8 and BSPEEK8(DCA) the melting endotherms shift to 319 ºC and 320 ºC, respectively, and broaden compared to PEEK, suggesting a larger distribution in crystal sizes upon sulfonation. In contrast, BSPEEK8(DCE) shows a smaller decrease in T_m to 338 ºC, and the melting endotherm remains

narrow, similar to PEEK. Integration of the melting endotherms enabled the determination of the degree of crystallinity, X_c, for each sample using the following equation:

$$X_{\mathrm{c}} = \frac{\Delta H_{\mathrm{f}}}{\Delta H_f^{\circ}}$$

where ΔH_{f} is the enthalpy of fusion determined by integration of the melting endotherm and $\Delta H_{\mathrm{f}}^{o}$ is the enthalpy of fusion of 100% crystalline PEEK determined theoretically (130 J/g).[35] The PEEK homopolymer is highly crystalline following precipitation from DCA (X_c = 54%). Random sulfonation leads to a significant loss in crystallinity (X_c = 25%), and blocky sulfonation in DCA somewhat improves this loss (X_c = 30%). Blocky sulfonation in non-solvent substantially improves the maintained crystallinity from blocky sulfonation in DCA to X_c = 45%. Thus, by performing gel-state sulfonations in non-solvent, the PEEK crystalline network is less perturbed during sulfonation and blocky SPEEK with high crystallizability and low melting point depression may be synthesized.

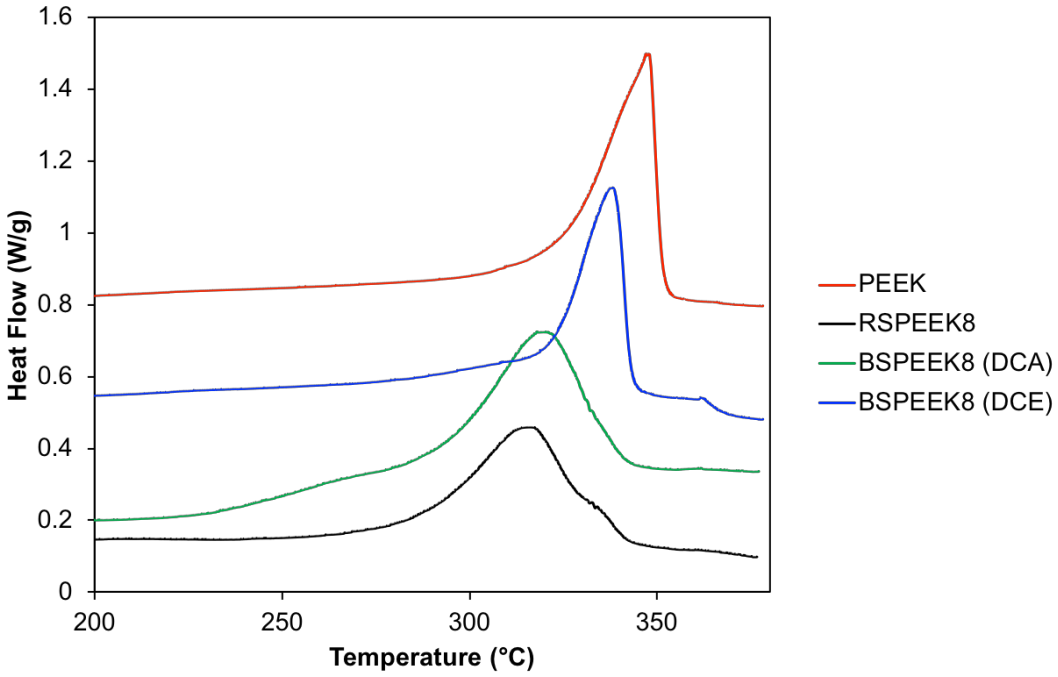

Figure 3.6. DSC thermograms of the first heat of as-precipitated SPEEK products compared to PEEK. The PEEK thermogram shows the first heat of a 20 w/v% PEEK gel that was suspended in DCA and subsequently precipitated into water. Random SPEEK, blocky SPEEK prepared in DCA, and blocky SPEEK prepared in a nonsolvent (DCE) are also shown. All SPEEK samples are 8 mol% sulfonated and have been neutralized to the Cs^+-form prior to analysis. Thermograms are shifted for ease of viewing.

DSC was also performed on the as-precipitated random and blocky SPEEK samples at high degrees of sulfonation (≥20 mol%). The degree of crystallinity for each sample was determined from the first heat using the equation above, and the results are displayed in **Figure 3.7**. The first heat was used for this analysis to obtain an estimate of the maximum crystallinity. At these high degrees of sulfonation, the interactive nature of the ionic groups limits crystallization from the melt, and thus subsequent heats cannot be used to determine crystallizability. Precipitation from the solution state or gel state, however, yields a high degree of chain mobility due to solvation of the interactive ionic groups, thereby resulting in a high degree of crystallinity upon precipitation. As shown in **Figure 3.7**, blocky sulfonation in DCE results in a much higher X_c than blocky sulfonation in DCA and random sulfonation. X_c decreases rapidly for random SPEEK as the degree of sulfonation increases, and no crystallinity is observed above 27 mol%

sulfonation. In contrast, blocky SPEEK prepared using the non-solvent method shows a much more gradual loss in crystallinity with increasing degree of sulfonation. When compared to RSPEEK27 (X_c = 2%), BSPEEK31 exhibits a substantially higher degree of crystallinity (X_c = 16.5%), and 14% crystallinity is preserved for blocky SPEEK at even higher degrees of sulfonation (i.e. 45 mol%). The differences in crystallinity observed for random SPEEK and blocky SPEEK is a clear effect of the reaction conditions and the resultant copolymer architecture. When sulfonating in the homogeneous solution state, sulfonation is possible at any monomer along the polymer chain and thus, the number of chain segments of sufficient length to crystallize decreases rapidly as the degree of sulfonation increases. When sulfonating in the gel state, however, sulfonation is restricted to the amorphous domains of the semicrystalline network, preserving long runs of unfunctionalized, crystallizable chain segments. Gel state sulfonation in the non-solvent is able to preserve a larger portion of these crystallizable chain segments (i.e. higher X_c) than gel state reactions in DCA due to the inability of the non-solvent to dissolve the crystalline network over time. In summary, it is apparent that gel state sulfonation in a non-solvent (DCE) preserves high levels of crystallizability while sulfonating to high degrees of functionalization.

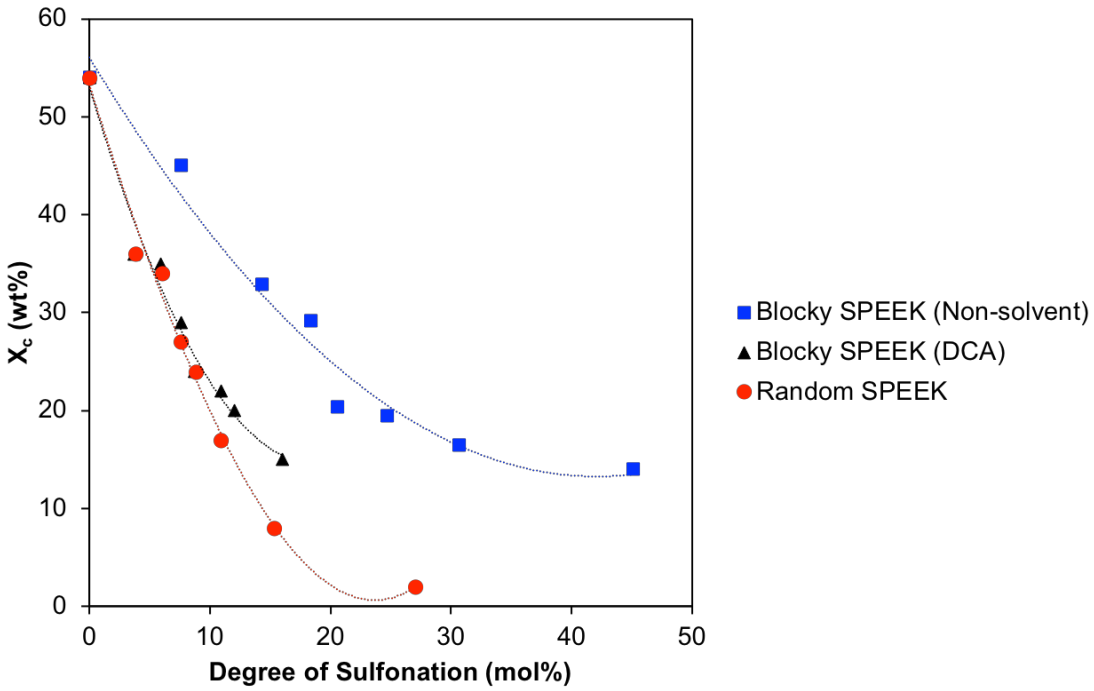

Figure 3.7. Degree of crystallinity determined from the first heat of blocky SPEEK prepared in a non-solvent, blocky SPEEK prepared in DCA, and random SPEEK. All samples were neutralized to Cs^+-form prior to analysis.

Because the SPEEK products will be used as membranes, it is also of interest to compare the DSC thermograms of as-cast random SPEEK and blocky SPEEK, as shown in **Figure 3.8**. Membranes were converted into Cs^+-form prior to DSC analysis to ensure thermal stability at elevated temperatures.[19, 23] Random SPEEK is amorphous above 20 mol% sulfonation and displays an increase in T_g with increasing degree of sulfonation. A small, broad melting endotherm around 240 ºC is present for as-cast RSPEEK20, signifying the presence of a small amount of crystals (X_c = 6%). On the other hand, the first heats of blocky SPEEK up to 45 mol% bromination each show a melting endotherm at approximately 340 ºC. The melting of the blocky SPEEK membranes occurs at much higher temperatures than that of RSPEEK20, and thus, polymer crystals with longer lamella are anticipated for blocky SPEEK than random SPEEK due to the gel-state process preserving long, unfunctionalized chain segments. The degree of crystallinity of as-cast blocky SPEEK decreases with increasing degree of sulfonation, as observed with the as-precipitated

products. BSPEEK21 has a degree of crystallinity of 16.6%, and this value decreases to 7.7% for BSPEEK 31 and to 1.6% for BSPEEK45.

The blocky SPEEK membranes also exhibit a broad transition at ~160-200 ºC. It is uncertain if these are associated with the T_g of the blocky SPEEK, the evaporation of residual casting solvent, and/or the melting of small crystals. Thus, the blocky SPEEK membranes were heated into the melt, quench cooled, and subsequently reheated. The DSC thermograms of the second heat of the blocky SPEEK membranes is shown in **Figure 3.8C**. After cooling from the melt, no crystallinity is observed in any of the blocky SPEEK membranes. This is due to the electrostatic network formed at the high ion content, which greatly restricts the mobility of polymer chains and limits crystallizability from the melt. Blocky SPEEK samples each display a T_g at approximately 160 ºC, just above the T_g of pure PEEK (145 ºC).[36] In addition, upon closer inspection there appears to be broad step-wise transitions at temperatures around 200 ºC and above. While these transitions are difficult to completely discern in the DSC, they suggest potential high temperature T_g's that may be attributed to the sulfonated blocks of blocky SPEEK. Because there is a distribution in sulfonated block length and density of sulfonation within the blocks, these transitions are broad and do not exhibit a single, clearly discernable transition in the DSC. The observed T_g's of RSPEEK and BSPEEK at various degrees of sulfonation are plotted in **Figure 3.9**. With increasing degree of sulfonation, the T_g increases fairly linearly from 181 ºC for RSPEEK20 to 250 ºC for RSPEEK53. This dramatic increase in T_g is due to the increased strength of the electrostatic network with increasing degree of sulfonation.[37] For blocky SPEEK, only a low temperature T_g is clearly observed and this T_g increases slightly from 160 ºC for BSPEEK21 to 165 ºC for BSPEEK45. The presence of this lower temperature T_g, that is close in value to the T_g of PEEK and is significantly lower than RSPEEK at similar degrees of sulfonation suggests a phase-separated system for the blocky SPEEK.[18, 38] The T_g at ~160 ºC is the T_g of the

unfunctionalized blocks, and a high temperature transition is expected for the sulfonated blocks, although this transition is difficult to distinguish due to the reasons described above.

To further elucidate the broad transitions of blocky BrPEEK as-cast membranes at 160-200 ºC, WAXD was performed on BSPEEK21. The amorphous halo and crystalline peaks were fit, and the degree of crystallinity (X_c) was determined by dividing the area under the crystalline peaks by the total area under the WAXD spectrum. According to WAXD, BSPEEK21 had a X_c value of 19.1 % - higher than the X_c value determined by DSC (16.6%). In fact, WAXD analysis revealed a X_c value several percent higher for all blocky SPEEK membranes compared to integration of the high temperature melting endotherm in DSC. Thus, the broad transitions around 160-200 ºC likely include the melting of small crystallites in addition to the glass transitions of the unfunctionalized and sulfonated blocks.

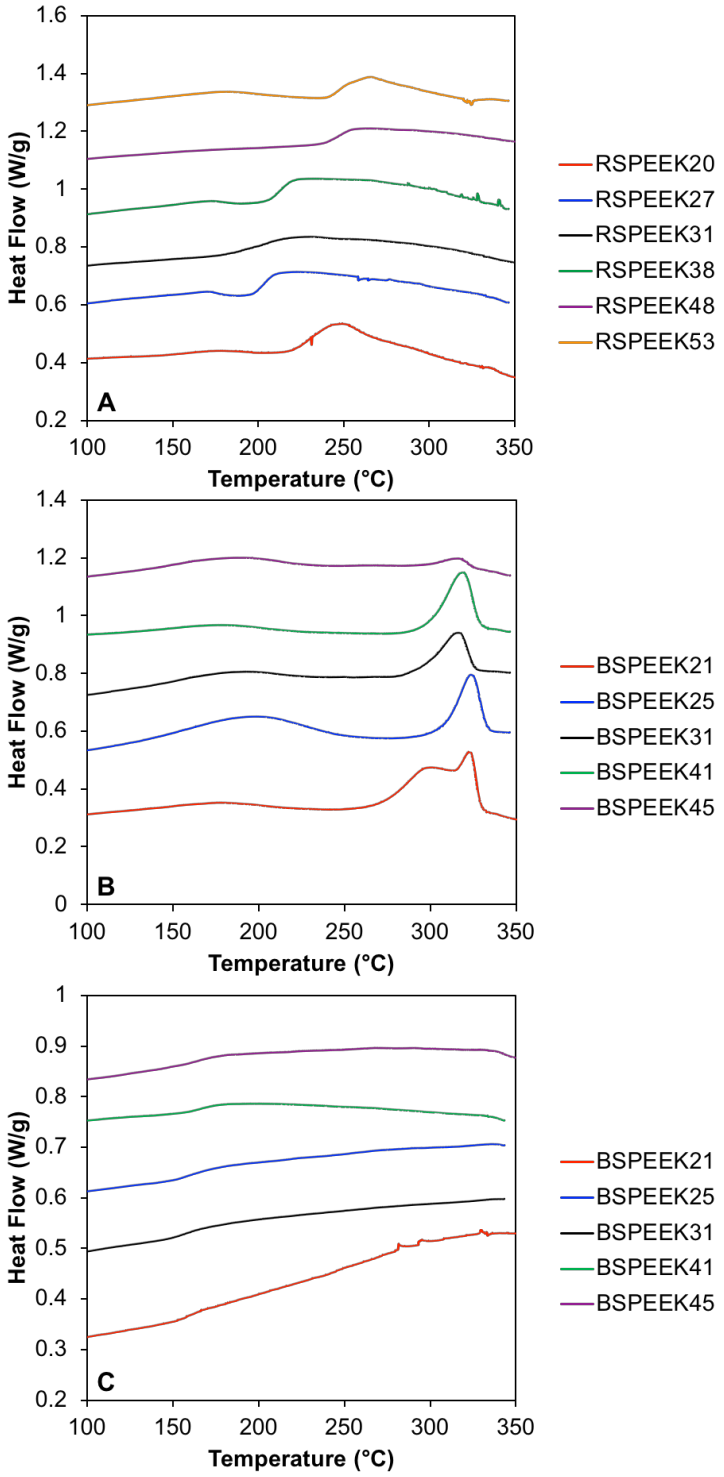

Figure 3.8. DSC thermograms of the first heat of as-cast random SPEEK (A) and as-cast blocky SPEEK (B). The second heat of blocky SPEEK (C) following a slow cool is also shown. All samples are in Cs^+-form.

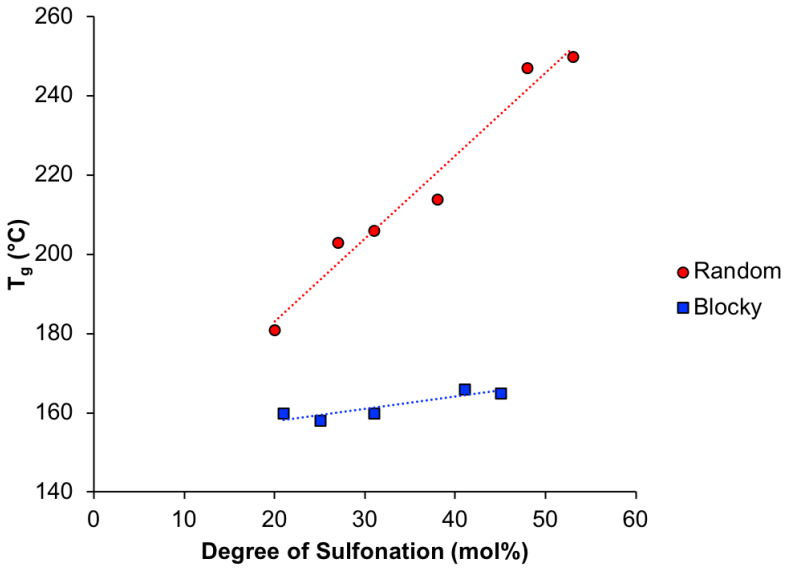

Figure 3.9. Glass transition temperature (T_g) of random SPEEK (red circles) and blocky SPEEK (blue squares) as a function of degree of sulfonation.

3.3.4 Tensile Properties

PEEK is known for its excellent mechanical properties, with a modulus around 3 GPa and a tensile strength of 100 MPa.[39] The mechanical properties of unfunctionalized PEEK are a function of both the degree of crystallinity and the thermal history of the polymer, and generally a low elongation at break is observed due to the high crystallinity of PEEK.[40] Sulfonation has been found to decrease the mechanical performance of PEEK, especially at high degrees of sulfonation, leading to a decrease in modulus and tensile strength at break.[41] The mechanical properties of the as-cast random and blocky SPEEK membranes were determined by tensile testing. The representative stress vs. strain profiles of BSPEEK21, BSPEEK41, BSPEEK45, RSPEEK15, RSPEEK27, and Nafion® 211CS are displayed in **Figure 3.10**, and the extracted tensile properties (i.e. modulus, tensile strength, and strain at break) are shown in **Table 3.2**. RSPEEK20 and RSPEEK27 both have a modulus around 2 GPa. A slight decrease in ultimate tensile strength is observed with increasing degree of sulfonation, and the strain at break increases by 50% for RSPEEK27 compared to RSPEEK20. The differences in RSPEEK20 and RSPEEK27 are most

likely an effect of crystallinity. While RSPEEK20 exhibits a small amount of crystallinity following casting (6%), RSPEEK27 is completely amorphous. The crystalline domains act as physical crosslinks within the membranes, restricting the mobility of the chains and thereby leading to increased strength and a more brittle nature (i.e. decrease strain at break). The effect of crystallinity is even more pronounced with BSPEEK. With increasing degree of sulfonation and decreasing crystallinity, the modulus decreases, the ultimate tensile strength decreases, and the elongation at break increases. It is important to note that at similar degree of sulfonation, BSPEEK exhibits a greater ultimate tensile strength and significantly decreased strain at break than RSPEEK due to the increased crystallinity preserved by reacting in the gel-state. Compared to Nafion®, the benchmark proton exchange membrane material, both random and blocky SPEEK membranes exhibit much higher moduli (4-5 times higher), increased strength at break, and decreased elongation at break. Overall, tensile analysis demonstrated that blocky and random SPEEK display suitable high moduli and tensile strengths for use as proton exchange membranes.

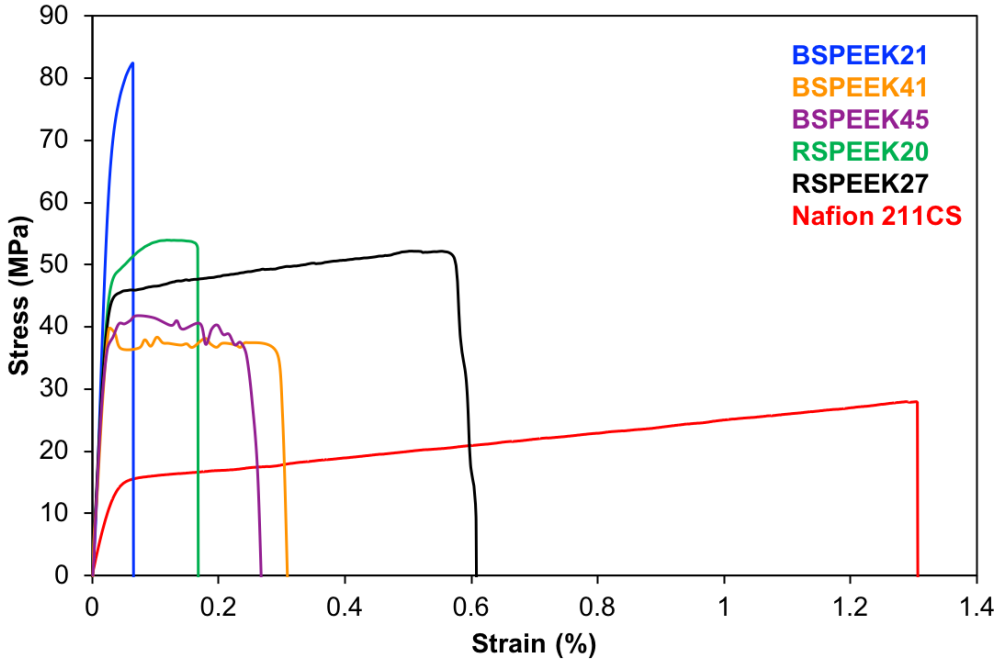

Figure 3.10. Stress vs. strain curves of blocky SPEEK and random SPEEK compared to Nafion® 211 CS. All samples are in H^+-form.

Table 3.2. Tensile properties of blocky SPEEK and random SPEEK compared to Nafion® 211CS.

Sample	Sulfonation Degree	Young's Modulus	Ultimate Tensile Strength	Strain at Break
Blocky H^+-SPEEK	20.6 mol%	2550 ± 200 MPa	71 ± 9 MPa	5 ± 2 %
Blocky H^+-SPEEK	40.6 mol%	1870 ± 40 MPa	42 ± 1 MPa	30 ± 9%
Blocky H^+-SPEEK	45.1 mol%	1650 ± 200 MPa	42 ± 6 MPa	21 ± 7%
Random H^+-SPEEK	15.3 mol%	1950 ± 180 MPa	53 ± 12 MPa	17 ± 6%
Random H^+-SPEEK	27.0 mol%	1950 ± 160 MPa	50 ± 7 MPa	70 ± 35%
Nafion® 211CS	-	450 ± 10 MPa	28 ± 1 MPa	120 ± 10 %

3.3.5 Morphological Analysis of Random and Blocky SPEEK

The morphological characterization of random and blocky SPEEK membranes was carried out at Argonne National Laboratory. The USAXS/SAXS/WAXD scattering profiles of random and blocky SPEEK from 20-50 mol% sulfonation are shown in **Figure 3.11**. All membranes were converted into Cs^+-form for scattering analysis to provide suitable contrast for the ionic domains.

In the USAXS region (i.e. $q < 0.006$ Å^{-1}), random SPEEK membranes are relatively featureless, however, blocky SPEEK membranes display a matrix knee at low q. Because this feature is only observed for crystalline blocky SPEEK, it is reasonably assumed that this feature is due to long-range heterogeneities in the crystalline domain spatial organization, however, further analysis is necessary to determine its precise origin.[19]

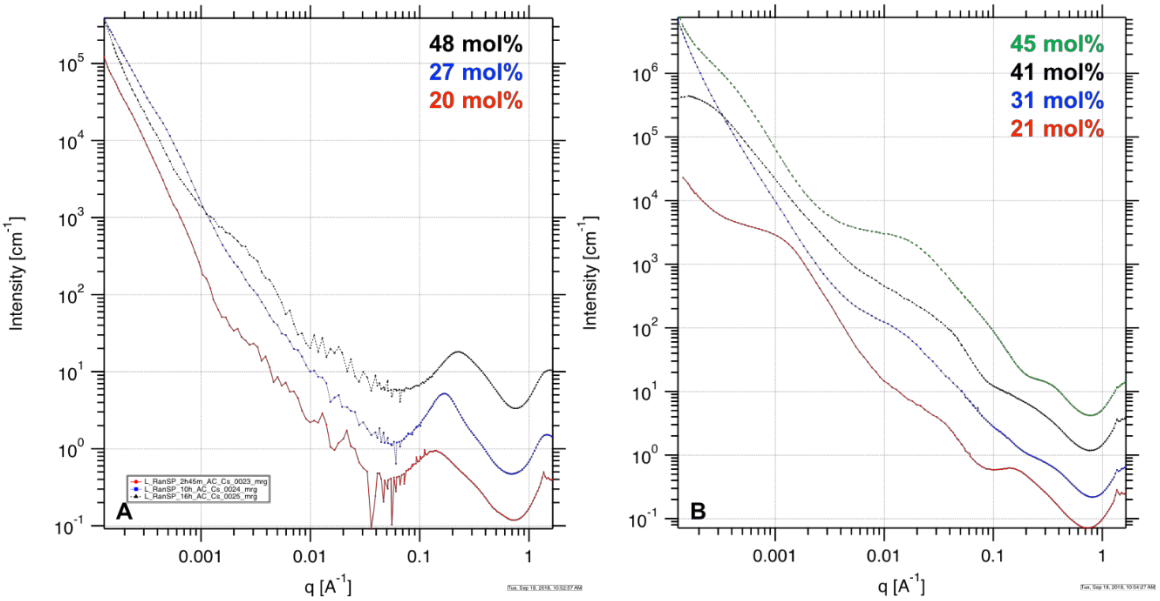

Figure 3.11. USAXS/SAXS/WAXD scattering profiles of as-cast random (A) and blocky (B) SPEEK copolymers in Cs^+-form.

In the SAXS region (i.e., 0.006 Å^{-1} < q < 0.6 Å^{-1}), as shown in **Figure 3.12**, a clear peak is observed for the random SPEEK membranes between 0.1 and 0.3 Å^{-1}. This peak is defined as the ionomer peak that arises due to phase separation and aggregation of the ionic domains into distinct clusters.[42] The center-to-center distance between these scattering objects may be estimated by determining the Bragg spacing ($d_{Bragg} = 2\pi/q_{max}$) from the peak maximum (q_{max}), as shown in **Table 3.3**.[43] With increasing degree of sulfonation, the ionomer peak of RSPEEK shifts to higher q, and thus, the distance between the ionic aggregates decreases with increasing degree of sulfonation. Similar results were observed for SPEEK prepared by conventional sulfonation in

sulfuric acid, where an increase in the number of ionic clusters and thereby smaller distance between clusters was observed with increasing degree of sulfonation (44-58 mol%).[44]

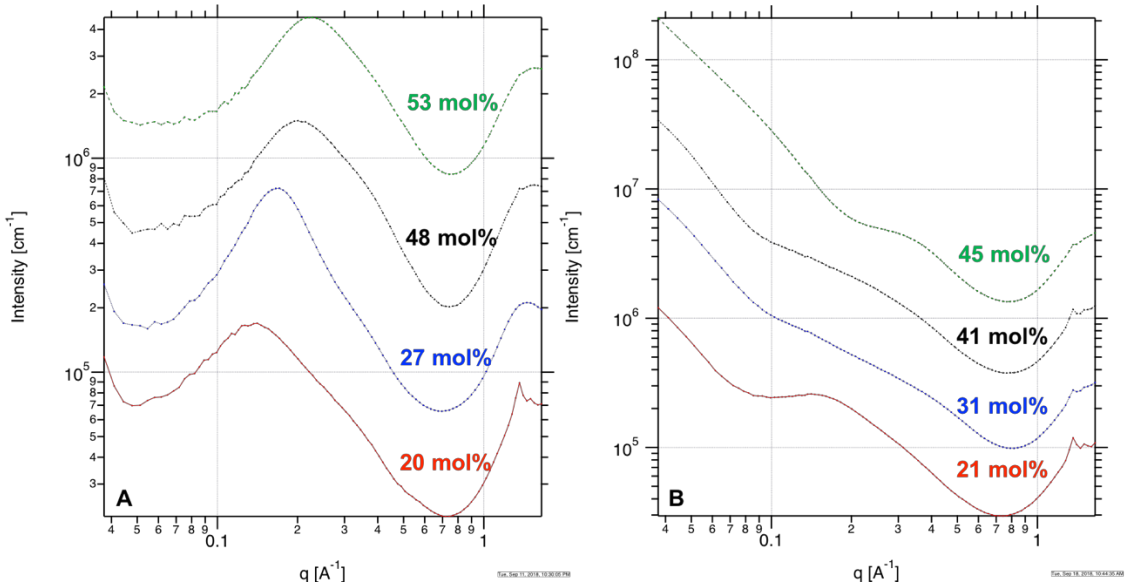

Figure 3.12. SAXS of as-cast random (A) and blocky (B) SPEEK copolymers in Cs^+-form.

The morphology of the random SPEEK ionic aggregates was further investigated by fitting of the ionomer peaks using the Kinning-Thomas (KT) modified hard sphere model. Using this model, it is assumed that the ionic sulfonate group aggregate into liquid-like hard spheres that are defined by a core ionomer radius (R), a radius of closest approach (R_{ca}), and by an inter-particle radius (R_{ip}).[45-46] The R_{ca} is larger than R itself due to steric hindrance from the polymer chains associated with the ionic aggregate surrounding the ion dense core. The results of the KT model fitting for RSPEEK are shown in **Table 3.3**. With increasing degree of sulfonation, the ionic aggregates become smaller and more densely populated, noted by the decrease in R and R_{ca} and simultaneous increase in R_{ip}. Likely, there are a larger number of smaller ionic aggregates throughout the membrane RSPEEK membranes as the degree of sulfonation increases.

Table 3.3. Morphological parameters of random SPEEK determined from analysis of the ionomer peak position (q_{max}, d_{Bragg}) and fitting of the Kinning-Thomas function (R, R_{ca}, R_{ip}).

DS (mol%)	q_{max} (Å^{-1})	d_{Bragg} (Å)	R (Å)	R_{ca} (Å)	R_{ip} (Å)
20	0.14	45	8.3	19.2	37.2
27	0.17	37	7.6	16.7	28.9
48	0.20	31	4.9	12.2	22.8
53	0.23	27	3.1	13.0	23.2

For blocky SPEEK, an ionomer peak appears in the SAXS profile between 0.1 and 0.5 Å^{-1}, however, it is much less intense than that of random SPEEK at similar ion contents. Similar to RSPEEK, the q_{max} shifts to higher q with increasing degree of sulfonation, suggesting a decrease in the distance between ionic aggregates. It is interesting to note that the ionomer peaks of BSPEEK are shifted to higher q than RSPEEK at similar degrees of sulfonation. In fact, the ionomer peak of BSPEEK45 exhibits a Bragg spacing of 17.0 Å (q_{max} = 0.37 Å^{-1}), almost half that of RSPEEK48 (d_{Bragg} = 31.4 Å). The closer spacing of the ionic domains indicates that a more continuous ionic pathway for proton transport may be achieved by blocking up the ions, thereby contributing to improved proton transport.

It is also important to note that all of the BSPEEK membranes are crystalline, and a broad matrix knee is observed for blocky samples between 0.02 and 0.06 Å^{-1} that may be attributed to inter-lamellar scattering of the crystalline domains.[42] While this knee is present in all blocky SPEEK membranes, it is interesting to note that the inter-lamellar knee is difficult to discern in RPSEEK20, despite containing 6% crystallinity. Typically, conversion of the membranes to Cs^+-form increases contrast for the ionomer domains and matches the electron density of the crystalline domains, making the crystalline domains indiscernible to X-rays.[42] Thus, it is reasonable to assume that the crystalline domains of RSPEEK20 are adequately contrast-matched by the Cs^+ ions. The

persistence of the semicrystalline matrix knee in the Cs^+-form blocky SPEEK membranes suggests different spatial ordering of the ionic aggregates with respect to the crystalline lamella for blocky SPEEK. It is hypothesized that the ionic aggregates of blocky SPEEK are more closely associated with the crystalline domains, resulting in similar electron densities of the semicrystalline matrix and ionic aggregates and a lower scattering intensity of the ionomer peak. During membrane casting, crystallization may aide in ionic aggregation, yielding small ionic aggregates that are closely spaced. It is of interest to determine how the different ionic domain distributions of random and blocky SPEEK contribute to membrane transport properties.

3.3.6 Water Uptake and Conductivity

Proton transport in sulfonated proton exchange membranes depends on the degree of sulfonation, hydration level, temperature, and ionomer morphology.[8, 47-48] Water content plays a critical role in proton transport by solvating the sulfonic acid sites and leading to dissociation of the protons.[6] Proton transport proceeds through hydrated, hydrophilic channels and is mediated by the amount of acidic sites and water, which may either be directly associated with the protons of free within the channels.[49] At excessively high water content, however, the mechanical integrity of the membranes may be compromised due to large dimensional changes and decreased mechanical strength.

The water uptake of the as-cast random and blocky SPEEK membranes (H^+-form) was determined by boiling the membranes for 1 hour in deionized water and then equilibrating the membranes in room temperature water for 12 hours. **Figure 3.13** displays the water uptake of the SPEEK membranes in terms of wt% as well as the number of moles of water per sulfonic acid site (λ). Water uptake increases with increasing degree of sulfonation for both blocky SPEEK and random SPEEK due to an increased number of hydrophilic sulfonic acid sites on the polymer

chain. At all degrees of sulfonation, as-cast blocky SPEEK membranes demonstrated increased water uptake compared to random SPEEK. This is consistent with several studies on directly polymerized multiblock poly(arylene ether sulfones), whereby blocking up the sulfonate functionalities into distinct blocks lead to enhanced water uptake compared to random analogues.[50-52] Water uptake of the multiblock copolymers was dependent on the sulfonated block length and the extent of phase separation between the hydrophilic and hydrophobic blocks, and it was determined that the well-connected hydrophilic domains of the multiblock ionomers lead to the increase in water uptake compared to random copolymers at similar ion exchange capacities.[53] Thus, the enhanced water uptake of blocky SPEEK suggests a more phase-separated microstructure with better connected hydrophilic domains compared to random SPEEK.

At ion contents above 40 mol%, considerably high water uptake is observed for both blocky SPEEK and random SPEEK membranes. RSPEEK48 and RSPEEK53 appear highly swollen and close to the point of dissolution after boiling in water. Likewise, BSPEEK45 exhibits significant dimensional swelling upon boiling in water, however, the membrane maintains better maintains its integrity compared to the RSPEEK membranes. To better control the water uptake, blocky SPEEK membranes (in Cs^+-form) were annealed at 280 ºC for 20 hours. Annealing the membranes drastically decreased the water uptake of blocky SPEEK due to further crystallization of the unfunctionalized blocks, resulting in more controlled water uptake at high degrees of functionality. Similar results were not observed for annealing of the RSPEEK samples, suggesting that the crystallizability of blocky SPEEK may be utilized to tune water content. Further analysis of the effect of membrane annealing will be discussed in **Section 3.3.7**.

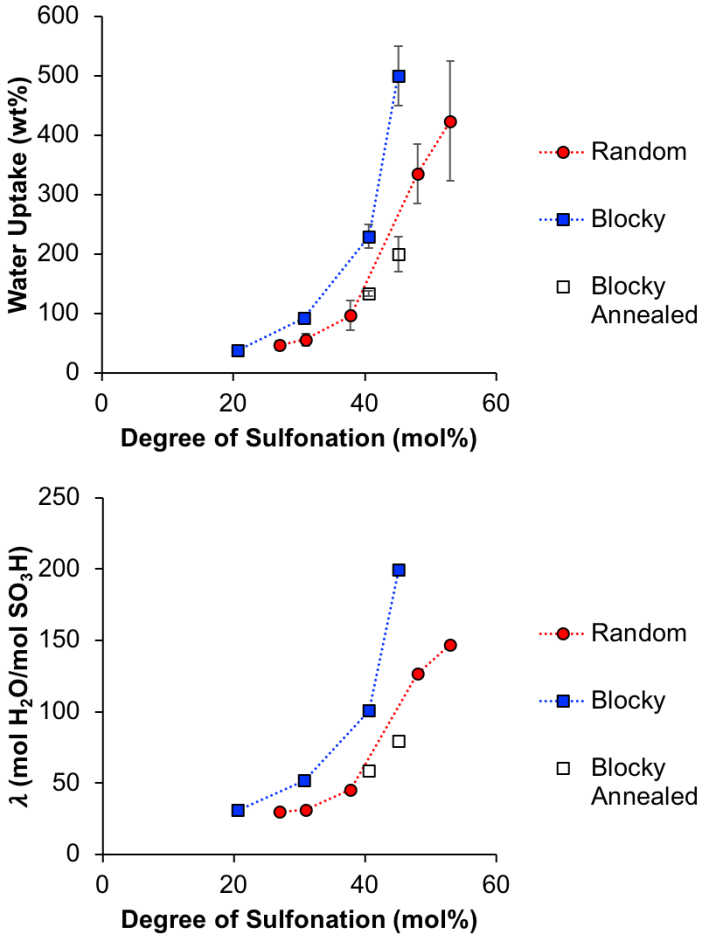

Figure 3.13. Water uptake and λ of as-cast random and blocky SPEEK (H^+-form) with increasing degrees of sulfonation. Blocky samples annealed at 280 ºC for 20 hours is also shown for comparison.

The proton conductivity of fully-hydrated SPEEK membranes was measured while immersing the membranes in water at room temperature, as shown in **Figure 3.14**. Across all degrees of sulfonation, the blocky SPEEK membranes exhibit significantly higher proton conductivities than random SPEEK. In fact, the conductivity of BSPEEK is over twice that of RSPEEK at all degrees of sulfonation examined. Because proton conductivity is directly correlated to water content,[49, 54] the increased water content of blocky SPEEK likely contributed to its enhanced proton transport. Furthermore, when considering the SAXS analysis above, it is reasonable to assume that the blocky SPEEK membranes form more interconnected hydrophilic domains that provide more efficient pathways for proton and water transport through the

membranes. These results are consistent with hydrophilic-hydrophobic multiblock hydrocarbon membranes prepared by step-growth polymerization,[55-56] further confirming the efficacy of gel-state post-polymerization sulfonation for preparing blocky copolymers with enhanced membrane performance. It is also significant to note that the conductivity of BSPEEK45 (72 mS/cm) approaches the conductivity of Nafion® (77 mS/cm) under similar hydrated conditions.

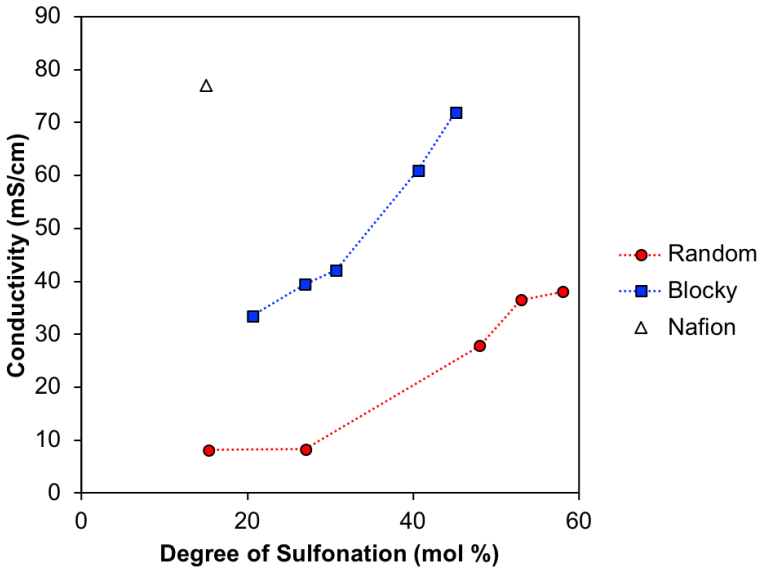

Figure 3.14. Proton conductivity of random and blocky SPEEK at high degrees of sulfonation. Measurements were conducted in water at 25 ºC.

The proton conductivity of random and blocky SPEEK membranes and Nafion® as a function of relative humidity (RH) at 80 ºC is shown in **Figure 3.15**. At all RH values, the proton conductivity of BSPEEK41 is several orders of magnitude greater than the conductivity of its random analogue RSPEEK42. Furthermore, the conductivity of BSPEEK41 is much greater than random SPEEK at even higher degrees of sulfonation (RSPEEK53, RSPEEK58) and reaches the conductivity of Nafion® at high humidity, further confirming the improved proton transport generated by blocking up the sulfonic acid groups. At partially hydrated states, the connectivity between hydrophilic domains is one of the key factors dictating proton conductivity.[53] Thus, in agreement with SAXS analysis and water uptake results, the blocky SPEEK membranes are

capable of forming phase-separated morphologies with better connectivity between the hydrophilic ionic domains than random SPEEK membranes.

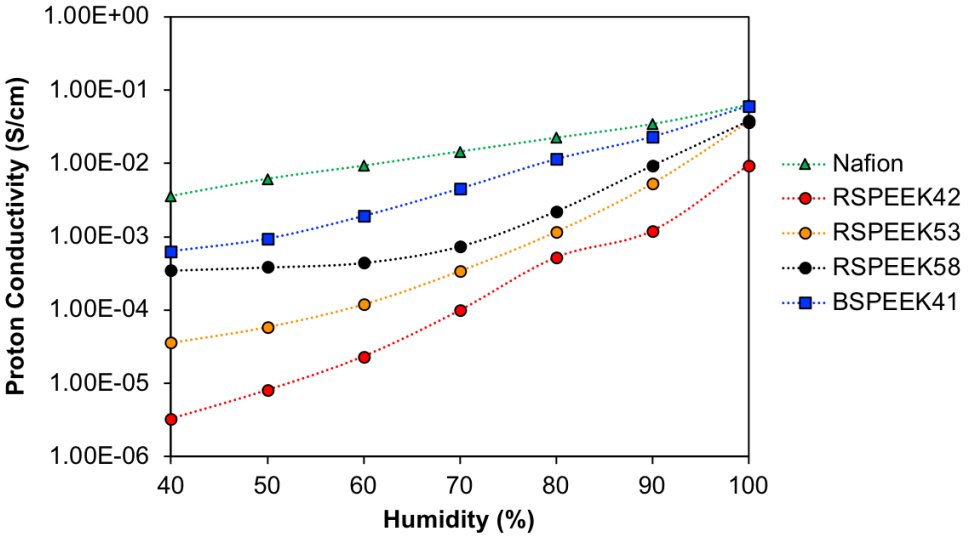

Figure 3.15. Proton conductivity at 80 ºC as a function of humidity.

3.3.7 Effect of Annealing on Membrane Properties

At high ion contents, high water uptake may lead to loss of mechanical integrity, dilution of the charge carriers, and less than ideal proton conductivity. Thus, careful consideration must be paid to optimize water content at high degrees of sulfonation. The effect of annealing on the membrane properties of blocky SPEEK was investigated as a means to control the water uptake of the membranes. Random and blocky SPEEK membranes were converted to Cs^+-form and annealed at 250 ºC for 2 hours. The ionomer morphology of the annealed membranes was investigated using SAXS analysis, as shown in **Figure 3.16**. Similar to the SAXS of as-cast SPEEK (**Figure 3.12**), random SPEEK displays a prominent ionomer peak at ~0.2 $Å^{-1}$ while blocky SPEEK displays a more suppressed ionomer peak at slightly higher q (~0.3 $Å^{-1}$). The ionomer peaks shift towards higher q with increasing degree of sulfonation, suggesting a smaller distance between ionic aggregates at high functionality. Quantification of the q_{max} values and the resultant Bragg spacings for the random and blocky SPEEK ionomer peaks are shown in **Table 3.4**. As the degree of

sulfonation increases from 20 mol% to 53 mol%, the inter-aggregate distance of random SPEEK decreases from 39 Å to 23 Å. These values are slightly lower than the as-cast samples (**Table 3.3**) and indicate that annealing leads to ionic aggregates that are more closely spaced than in the as-cast state. At similar degrees of sulfonation, shorter inter-aggregate distances are observed for blocky SPEEK than random SPEEK. The blocky ionomer peak positions do not appear to shift significantly from the as-cast state, and the intensity of the ionomer peak remains suppressed, implying that no large change in ionomer morphology arises from annealing.

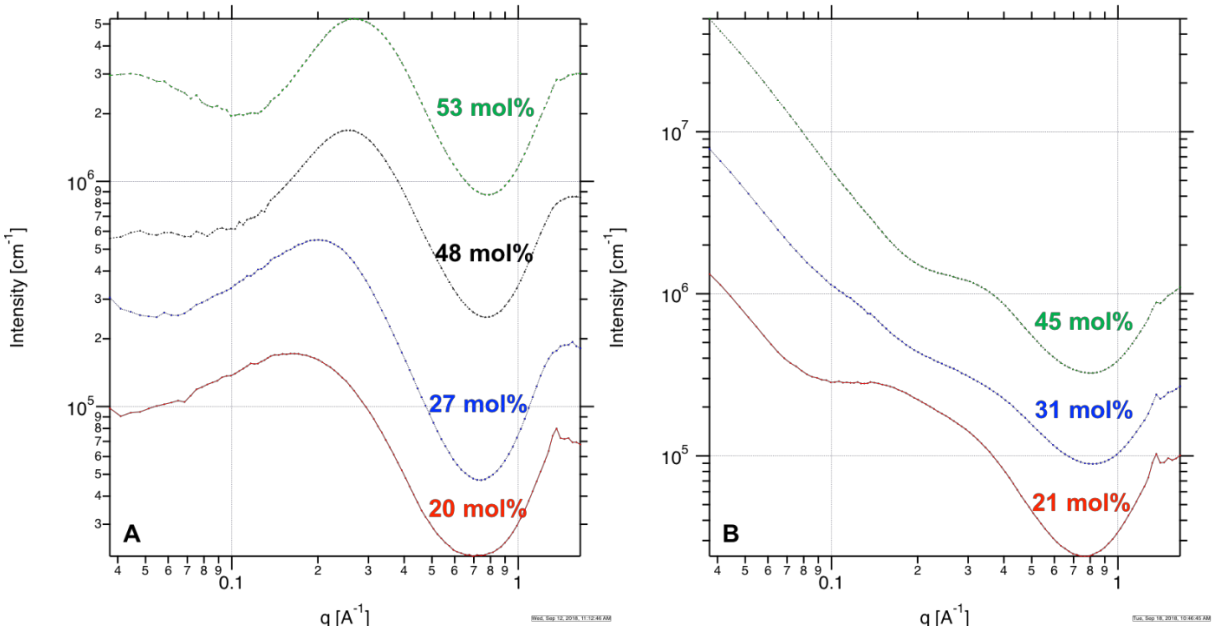

Figure 3.16. SAXS profiles of random (A) and blocky (B) SPEEK following annealing at 250 ºC for 2 hours. All samples are in Cs^+-form.

Table 3.4. Scattering maxima and Bragg spacing of random and blocky SPEEK ionomer peaks.

Sample	q_{max} (Å^{-1})	d_{Bragg} (Å)
RSPEEK20	0.16	39
RSPEEK27	0.20	31
RSPEEK48	0.26	24
RSPEEK53	0.27	23
BSPEEK21	0.24	26
BSPEEK31	0.38	17
BSPEEK45	0.35	18

Fitting of the random ionomer peaks using the Kinning-Thomas model, as shown in **Table 3.5**, further verified the decrease in inter-aggregate spacing (R_{ip}) after annealing RSPEEK at 250 ºC for 2 hours (compare to **Table 3.3**). Likewise, a decrease in R and R_{ca} is observed following annealing, suggesting that the thermal energy provided during annealing organizes the ionic aggregates of the RSPEEK membranes into smaller domains that are closer together.

Table 3.5. Morphological parameters of random SPEEK annealed at 250 ºC for 2 hours determined from fitting of the Kinning-Thomas model (R, R_{ca}, R_{ip}).

DS (mol%)	R (Å)	R_{ca} (Å)	R_{ip} (Å)
20	7.1	13.8	30.0
27	6.8	12.6	23.7
48	3.7	10.4	19.1
53	2.8	9.8	18.1

The effect of annealing on membrane properties was also investigated. BSPEEK41 and BSPEEK45 membranes were converted into Cs^+-form and annealed at 250 ºC for 2 hours or for 280 ºC for 20 hours. Water uptake and dimensional swelling were determined following annealing, as shown in **Table 3.6**. Annealing effectively decreased both the water uptake and dimensional swelling of the membranes. Increasing annealing time and temperature further amplified this decrease in swelling. For example, while BSPEEK45 exhibited 500 wt% water uptake and 220% areal swelling following annealing at 250 ºC for 2 hours, these values decreased to 200 wt% and 80%, respectively, following annealing at 280 ºC for 20 hours. The decrease in water content for blocky samples is likely an effect of increased crystallinity and/or lamellar thickening that occurs during annealing. This was confirmed by DSC analysis which showed an increase in crystallinity from 4.2% to 6.4% and an increase in T_m from 311 ºC to 319 ºC following annealing of the as-cast BSPEEK41 membrane at 280 ºC for 20 hours. Thus, annealing may be used to tune the degree of swelling of the blocky SPEEK membranes and prevent excessive swelling at high ion content

(which can dilute charge carries and result in lower proton conductivity). Annealing further enables membranes to better maintain their shape, as shown in **Figure 3.17**, and helps limit areal swelling.

Table 3.6. Water uptake and areal swelling of blocky SPEEK (H^+-form) following annealing. Samples were annealed in Cs^+-form and then converted to H^+-form prior to analysis. Water uptake was determined gravimetrically after boiling membranes in water for 1 hour.

DS (mol %)	Treatment	Water Uptake (wt%)	Δ_x (%)	Δ_y (%)	Δ_{area} (%)
41	As-cast	230 ± 20	36 ± 6	37 ± 5	86 ± 13
41	Annealed 250 °C, 2 hr	170 ± 10	39 ± 6	37 ± 1	91 ± 9
41	Annealed 280 °C, 20 hr	134 ± 3	28 ± 5	26 ± 7	60 ± 10
45	Annealed 250 °C, 2 hr	500 ± 50	76 ± 7	83 ± 12	220 ± 20
45	Annealed 280 °C, 20 hr	200 ± 30	35 ± 6	32 ± 6	80 ± 10

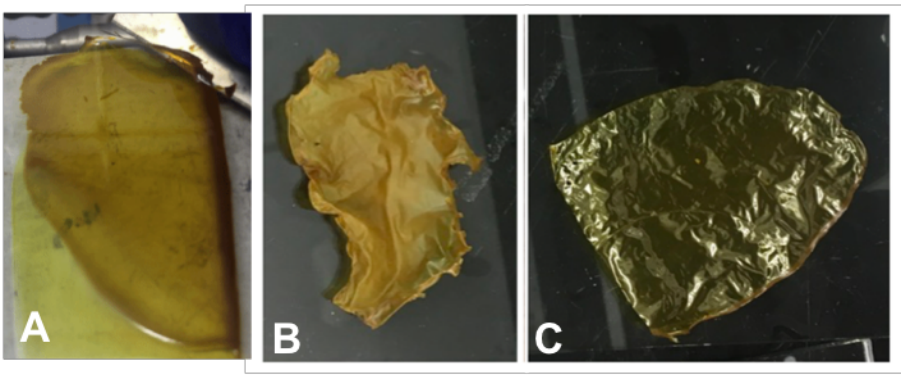

Figure 3.17. Images of BPSEEK41 as-cast (A), as-cast after swelling in water and drying (B), and annealed at 250 ºC for 2 hours after swelling in water and drying (C). Annealing enables membranes to better maintain their as-cast dimensions and shape following hydration and dehydration.

Because annealing has significant implications on the water content of the blocky SPEEK membranes, the proton conductivity is anticipated to change upon annealing. The proton conductivity of blocky SPEEK in water at 25 ºC is shown in **Table 3.7** after equilibrating the membranes in room temperature water for 12 hours and after boiling the membranes in water for

1 hour. Little difference is observed in the proton conductivity of the annealed membranes and as-cast membranes following equilibration in room temperature water. Following treatment in boiling water, however, the conductivities were found to increase with increasing annealing time and temperature. It is important to note, however, that these conductivities are generally lower than those of membranes equilibrated in room temperature water. Boiling the membranes in water leads to an increase in the total water content of the membranes. Because water uptake at these degrees of sulfonation is considerably high (i.e. >200 wt%), further increasing the water content by boiling results in significant dilution of the protons within the hydrophilic domains, and thus a decrease in proton conductivity. Increasing annealing time and temperature decreases the total water uptake resulting from boiling of the membranes (**Table 3.6**) and results in increased proton conductivity for the blocky SPEEK membranes. Therefore, the membrane properties of blocky SPEEK are easily controlled with annealing temperature and time, and annealing is useful for improving the proton conductivity of fully-hydrated membranes. It is also important to note that similar to the proton conductivity observed with membranes equilibrated in room temperature water, the proton conductivity of blocky SPEEK in the partially hydrated state (i.e. at various RH) does not change upon annealing. Thus, annealing most significantly impacts membranes subjected to boiling conditions in water.

Table 3.7. Conductivity of blocky and random SPEEK before and after annealing.

Sample	DS (mol %)	Treatment	Conductivity RT (mS/cm)	Conductivity Boiled (mS/cm)
Nafion® 211	-	-	63	77
Blocky H^+-SPEEK	41	As-Cast	61	43 ± 9
Blocky H^+-SPEEK	41	Annealed 250 °C, 2 hr	62	55 ± 5
Blocky H^+-SPEEK	41	Annealed 280 °C, 20 hr	67	72 ± 10
Blocky H^+-SPEEK	45	Annealed 250 °C, 2 hr	72	34 ± 2
Blocky H^+-SPEEK	45	Annealed 280 °C, 20 hr	73	60 ± 7
Random H^+-SPEEK	48	As-Cast	28	-
Random H^+-SPEEK	53	As-Cast	37	-
Random H^+-SPEEK	58	As-Cast	38	-

3.3.8 Additional Factors Controlling Blocky SPEEK Properties

3.3.8.1 Controlled Addition Rate of Sulfonating Reagent

The rate of sulfonating reagent addition was investigated to determine its effect on degree of sulfonation. A syringe pump was used in place of a dropping flask to enable the controlled addition of sulfonating reagent. Reactions were performed in 1,2-DCE at 80 ºC for 24 hours using the experimental procedures outlined in **Section 3.2.4**. The 2 v/v% TFAS solution (1:1 molar ratio of TFAS:PEEK) was added at rates of 45 mL/hr, 60 mL/hr, and 75 mL/hr until all solution was added. ^{1}H NMR analysis revealed that faster rates of TFAS addition resulted in higher degrees of sulfonation. The 45 mL/hr reaction resulted in 19.5 mol% sulfonated PEEK, the 60 mL/hr reaction resulted in 26.3 mol% sulfonated PEEK, and the 75 mL/hr reaction resulted in 26.9 mol% sulfonated PEEK. DSC was performed on the Na^+-form of the as-precipitated products, as shown in **Figure 3.18.** The DSC thermograms all exhibit a large high temperature endotherm associated with the melting of polymer crystals, thereby confirming the preservation of crystallinity with increasing addition rate of sulfonating reagent. As expected, a smaller degree of crystallinity is

observed with increasing degree of sulfonation. Using these results, the addition rate of 75 mL/hr was chosen for gel state reactions to target high degrees of sulfonation.

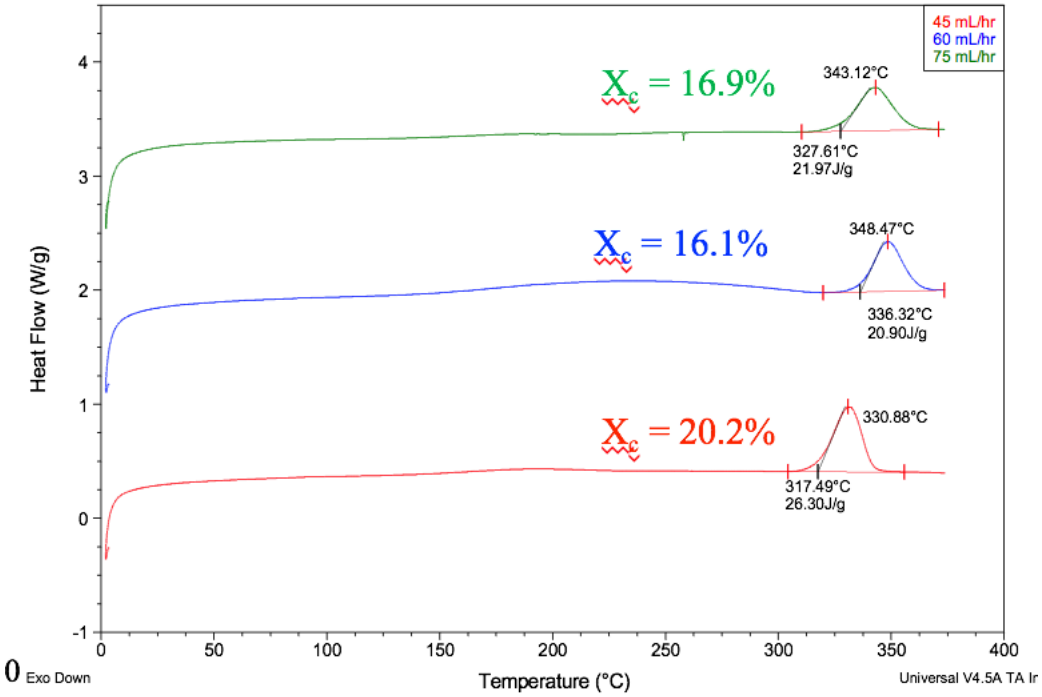

Figure 3.18. DSC of Na^+-SPEEK precipitated products formed from syringe-pump reactions with varying addition rates of sulfonating reagent. The 45 mL/hr reaction is shown in red, the 60 mL/hr reaction is shown in blue, and the 75 mL reaction is shown in green. The degree of crystallinity determined by integration of the melting endotherms is also shown.

3.3.8.2 Influence of Casting Conditions on Membrane Properties

To investigate the effect of casting conditions on membrane properties, BSPEEK27 was used. Solutions of BSPEEK27 (H^+-form) were prepared to a final concentration of 10 w/v% in 4-chlorophenol by dissolving at 185 ºC. Once cooled to room temperature, the solution was filtered and membranes were cast onto glass at the following temperatures: 100 ºC, 125 ºC, 150 ºC, and 175 ºC. High casting temperatures were investigated to determine if the increased mobility at high temperatures would enable better phase separation and ordering in the membranes. Membranes cast from 100 to 175 ºC were a similar yellow-brown color, and the membranes became darker brown as the casting temperature increased. The BSPEEK27 membranes were converted to Na^+-

form by stirring in 2M NaCl (aq) overnight and DSC was performed, as shown in **Figure 3.19.** The DSCs of each membrane displayed almost identical thermal transitions, with T_g's around 190 ºC and melting endotherms around 300 ºC. Integration of the melting endotherms demonstrated that the enthalpy of melting decreased with increasing casting temperature, and thus crystallinity decreased with increasing casting temperature. While 11.7% crystallinity was obtained by casting at 100 ºC, only 8.2% crystallinity was obtained by casting at 175 ºC. This difference in crystallinity is likely attributed to time required for solvent evaporation during casting. At 100 ºC, it takes over 10 minutes for the 4-chlorophenol to fully evaporate from the cast solution. At 175 ºC, however, it takes less than a minute for the 4-chlorophenol to fully evaporate. Thus, at elevated temperatures above 100 ºC, there is not enough time for the SPEEK solution to crystallize before the solvent has evaporated, resulting in decreased membrane crystallinity.

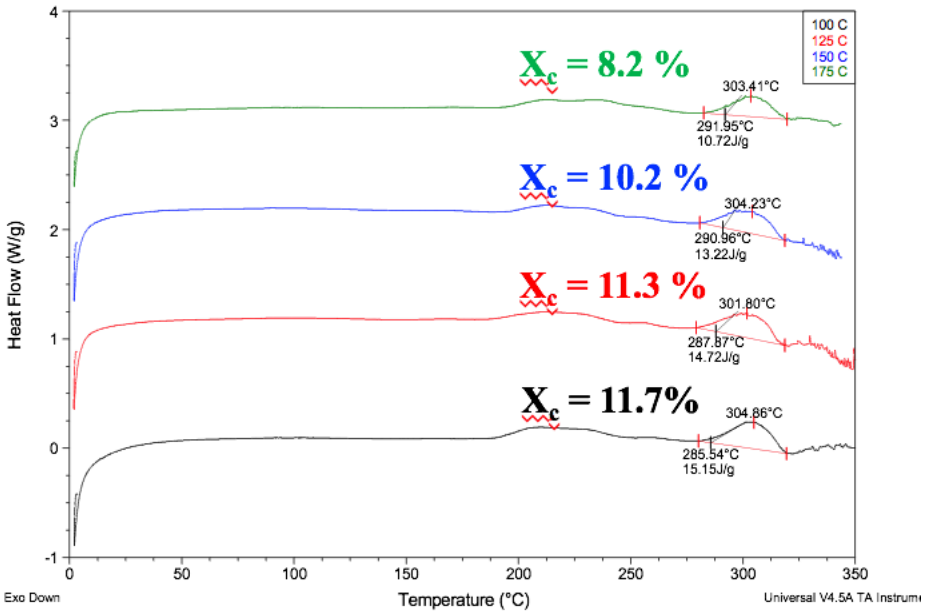

Figure 3.19. DSC of Na^+-SPEEK membranes (DS=26.9%) cast from H^+-SPEEK solutions onto glass at 100 ºC (black), 125 ºC (red), 150 ºC (blue), and 175 ºC (green). Crystallinity decreases with increasing casting temperature.

Water uptake and proton conductivity of H^+-SPEEK membranes cast at temperatures ranging from 100 ºC to 175 ºC were also determined. With increasing casting temperature, the water uptake and the proton conductivity decrease, as shown in **Figure 3.20.** For membranes cast at 100 ºC, the water uptake is 70% and the conductivity is 40 mS/cm. These values decrease to 55% water uptake and 27 mS/cm conductivity as the casting temperature was increased to 175 ºC. Despite these values decreasing, all casting temperatures demonstrate superior water uptake and conductivity than a homogeneous random SPEEK membrane at 27.0% sulfonation (8.3 mS/cm). When compared to the DSC results from **Figure 3.19**, it is shown that as the crystallinity decreases, the water uptake and proton conductivity decrease. Thus, there is likely an interplay between crystallization and ionic aggregate organization, and achieving high degrees of crystallinity with this blocky architecture is advantageous for blocky SPEEK products and membranes.

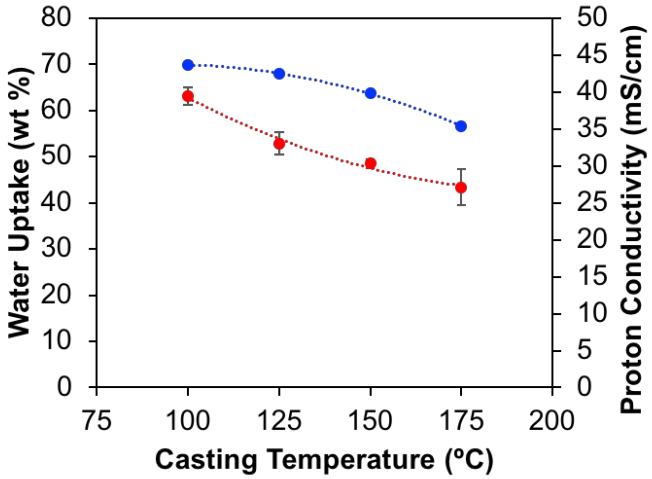

Figure 3.20. Water uptake (blue) and proton conductivity (red) of H^+-SPEEK (DS=26.9%) membranes cast at various temperatures.

3.4 Conclusions and Future Work

In this work, a novel gel-state sulfonation procedure using a non-solvent was developed to synthesize blocky SPEEK with high crystallizability at high degrees of sulfonation. Gel-state sulfonation in 1,2-dichloroethane (non-solvent) was found to increase gel stability during

sulfonation compared to gel-state sulfonation in dichloroacetic acid (DCA). The increased gel stability enabled the synthesis of blocky SPEEK with up to 45 mol% sulfonation in DCE, whereas gel-state sulfonation was limited to approximately 15 mol% in DCA.

Blocky SPEEK prepared in DCE showed much greater crystallizability and higher melting temperatures than random SPEEK and blocky SPEEK prepared in DCA. DSC of as-cast membranes demonstrated that random SPEEK is amorphous above 20 mol% sulfonation, and only a small amount of crystallinity (X_c=6%) is observed for RSPEEK20. Blocky SPEEK membranes, however, exhibit considerable levels of crystallinity at all degrees of sulfonation investigated and the melting of these crystals occurs at high temperatures, suggesting larger crystalline lamella than RSPEEK20. Furthermore, the T_g of random SPEEK was found to increase linearly from 181 ºC to 250 ºC as the degree of sulfonation increased from 20 to 53 mol% due to decreased chain mobility from increased electrostatic interactions. In contrast, blocky SPEEK exhibited a clear T_g at approximately 160 ºC for degrees of sulfonation between 21 and 45 mol%. This T_g is close to the T_g of pure PEEK, and thus phase separation of the unfunctionalized blocks and sulfonation blocks is likely for blocky SPEEK.

Tensile testing demonstrated the high modulus and ultimate tensile strength of both blocky and random SPEEK, and at similar ion contents blocky SPEEK exhibited higher tensile strength and decreased strain at break than random SPEEK due to the increased crystallinity of the blocky SPEEK. Morphological analysis revealed that ionic aggregates are more closely spaced in blocky SPEEK than random SPEEK analogues, and the ionic domains are likely closely associated with crystalline domains for blocky SPEEK. Furthermore, blocky SPEEK membranes had higher water uptake and proton conductivity than random SPEEK membranes at similar or higher degrees of sulfonation, likely due to improved phase separation and better connectivity of the hydrophilic domains in the blocky SPEEK.

Continuing work on the gel-state reactions using will push towards 50% sulfonation and higher in the hopes of achieving superior performance than Nafion®, especially at low humidity. Targeting 50% sulfonation and above may also enable easier processing of the blocky SPEEK into strong membranes using more conventional solvents, such as polar aprotic solvents.

3.5 References

1. Knauth, P.; Hou, H.; Bloch, E.; Sgreccia, E.; Di Vona, M. L., Thermogravimetric analysis of SPEEK membranes: Thermal stability, degree of sulfonation and cross-linking reaction. *Journal of Analytical and Applied Pyrolysis* **2011,** *92* (2), 361-365.
2. Rikukawa, M.; Sanui, K., Proton-conducting polymer electrolyte membranes based on hydrocarbon polymers. *Progress in Polymer Science* **2000,** *25* (10), 1463-1502.
3. Higashihara, T.; Matsumoto, K.; Ueda, M., Sulfonated aromatic hydrocarbon polymers as proton exchange membranes for fuel cells. *Polymer* **2009,** *50* (23), 5341-5357.
4. Reyes-Rodriguez, J. L.; Solorza-Feria, O.; Garcia-Bernabe, A.; Gimenez, E.; Sahuquillo, O.; Compan, V., Conductivity of composite membrane-based poly(ether-ether-ketone) sulfonated (SPEEK) nanofiber mats of varying thickness. *RSC Advances* **2016,** *6* (62), 56986-56999.
5. Lee, J. K.; Li, W.; Manthiram, A., Sulfonated poly(ether ether ketone) as an ionomer for direct methanol fuel cell electrodes. *Journal of Power Sources* **2008,** *180* (1), 56-62.
6. Xing, P.; Robertson, G. P.; Guiver, M. D.; Mikhailenko, S. D.; Wang, K.; Kaliaguine, S., Synthesis and characterization of sulfonated poly(ether ether ketone) for proton exchange membranes. *Journal of Membrane Science* **2004,** *229* (1–2), 95-106.
7. Kaliaguine, S.; Mikhailenko, S.; Wang, K.; Xing, P.; Robertson, G.; Guiver, M., Properties of SPEEK based PEMs for fuel cell application. *Catalysis Today* **2003,** *82* (1), 213-222.
8. Kreuer, K. D., On the development of proton conducting polymer membranes for hydrogen and methanol fuel cells. *Journal of Membrane Science* **2001,** *185* (1), 29-39.
9. Zhao, C.; Li, X.; Wang, Z.; Dou, Z.; Zhong, S.; Na, H., Synthesis of the block sulfonated poly(ether ether ketone)s (S-PEEKs) materials for proton exchange membrane. *Journal of Membrane Science* **2006,** *280* (1–2), 643-650.
10. Zhao, C.; Lin, H.; Shao, K.; Li, X.; Ni, H.; Wang, Z.; Na, H., Block sulfonated poly(ether ether ketone)s (SPEEK) ionomers with high ion-exchange capacities for proton exchange membranes. *Journal of Power Sources* **2006,** *162* (2), 1003-1009.
11. Lee, K. H.; Chu, J. Y.; Kim, A. R.; Yoo, D. J., Enhanced Performance of a Sulfonated Poly(arylene ether ketone) Block Copolymer Bearing Pendant Sulfonic Acid Groups for Polymer Electrolyte Membrane Fuel Cells Operating at 80% Relative Humidity. *ACS Applied Materials & Interfaces* **2018,** *10* (24), 20835-20844.
12. Yang, A. C. C.; Narimani, R.; Frisken, B. J.; Holdcroft, S., Investigations of crystallinity and chain entanglement on sorption and conductivity of proton exchange membranes. *Journal of Membrane Science* **2014,** *469*, 251-261.
13. Hamada, T.; Hasegawa, S.; Fukasawa, H.; Sawada, S.-i.; Koshikawa, H.; Miyashita, A.; Maekawa, Y., Poly(ether ether ketone) (PEEK)-based graft-type polymer electrolyte membranes having high crystallinity for high conducting and mechanical properties under various humidified conditions. *Journal of Materials Chemistry A* **2015,** *3* (42), 20983-20991.
14. Wang, R.; Yan, X.; Wu, X.; He, G.; Du, L.; Hu, Z.; Tan, M., Modification of hydrophilic channels in Nafion membranes by DMBA: Mechanism and effects on proton conductivity. *Journal of Polymer Science Part B: Polymer Physics* **2014,** *52* (16), 1107-1117.
15. Hickner, M. A.; Ghassemi, H.; Kim, Y. S.; Einsla, B. R.; McGrath, J. E., Alternative Polymer Systems for Proton Exchange Membranes (PEMs). *Chemical Reviews* **2004,** *104* (10), 4587-4612.
16. Chen, Y.; Lee, C. H.; Rowlett, J. R.; McGrath, J. E., Synthesis and characterization of multiblock semi-crystalline hydrophobic poly(ether ether ketone)–hydrophilic disulfonated poly(arylene ether sulfone) copolymers for proton exchange membranes. *Polymer* **2012,** *53* (15), 3143-3153.

17. Feng, S.; Pang, J.; Yu, X.; Wang, G.; Manthiram, A., High-Performance Semicrystalline Poly(ether ketone)-Based Proton Exchange Membrane. *ACS Applied Materials & Interfaces* **2017,** *9* (29), 24527-24537.
18. Fahs, G. B.; Benson, S. D.; Moore, R. B., Blocky Sulfonation of Syndiotactic Polystyrene: A Facile Route toward Tailored Ionomer Architecture via Postpolymerization Functionalization in the Gel State. *Macromolecules* **2017,** *50* (6), 2387-2396.
19. Anderson, L. J.; Yuan, X.; Fahs, G. B.; Moore, R. B., Blocky Ionomers via Sulfonation of Poly(ether ether ketone) in the Semicrystalline Gel State. *Macromolecules* **2018,** *51* (16), 6226-6237.
20. Corby, B. W.; Gray, A. D.; Meaney, P. J.; Falvey, M. J.; Lawrence, G. P.; Smyth, T. P., Clean-chemistry sulfonation of aromatics. *Journal of Chemical Research* **2002,** *2002* (7), 326-327.
21. Bakker, B. H.; Cerfontain, H., Sulfonation of Alkenes by Chlorosulfuric Acid, Acetyl Sulfate, and Trifluoroacetyl Sulfate. *European Journal of Organic Chemistry* **1999,** *1999* (1), 91-96.
22. Talley, S. J.; Yuan, X.; Moore, R. B., Thermoreversible Gelation of Poly(ether ether ketone). *ACS Macro Letters* **2017,** *6* (3), 262-266.
23. Koziara, B. T.; Kappert, E. J.; Ogieglo, W.; Nijmeijer, K.; Hempenius, M. A.; Benes, N. E., Thermal Stability of Sulfonated Poly(Ether Ether Ketone) Films: on the Role of Protodesulfonation. *Macromolecular Materials and Engineering* **2016,** *301* (1), 71-80.
24. Ilavsky, J.; Zhang, F.; Allen, A. J.; Levine, L. E.; Jemian, P. R.; Long, G. G., Ultra-Small-Angle X-ray Scattering Instrument at the Advanced Photon Source: History, Recent Development, and Current Status. *Metallurgical and Materials Transactions A* **2013,** *44* (1), 68-76.
25. Ilavsky, J.; R. Jemian, P., *Irena: Tool Suite for Modeling and Analysis of Small Angle Scattering*. 2009; Vol. 42, p 347-353.
26. Ilavsky, J., Nika: software for two-dimensional data reduction. *Journal of Applied Crystallography* **2012,** *45* (2), 324-328.
27. Miron, S.; Richter, G. H., Sulfonation of 2-pentene by chlorosulfonic acid. *Journal of the American Chemical Society* **1949,** *71* (2), 453-455.
28. Kučera, F.; Jančář, J., Preliminary study of sulfonation of polystyrene by homogeneous and heterogeneous reaction. *Chemical Papers* **1996,** *50* (4), 224-227.
29. Zaidi, S. M. J.; Mikhailenko, S. D.; Robertson, G. P.; Guiver, M. D.; Kaliaguine, S., Proton conducting composite membranes from polyether ether ketone and heteropolyacids for fuel cell applications. *Journal of Membrane Science* **2000,** *173* (1), 17-34.
30. Devaux, J.; Delimoy, D.; Daoust, D.; Legras, R.; Mercier, J. P.; Strazielle, C.; Nield, E., On the molecular weight determination of a poly(aryl-ether-ether-ketone) (PEEK). *Polymer* **1985,** *26* (13), 1994-2000.
31. Xing, P.; Robertson, G. P.; Guiver, M. D.; Mikhailenko, S. D.; Kaliaguine, S., Synthesis and characterization of poly(aryl ether ketone) copolymers containing (hexafluoroisopropylidene)-diphenol moiety as proton exchange membrane materials. *Polymer* **2005,** *46* (10), 3257-3263.
32. Al Lafi, A. G., The sulfonation of poly(ether ether ketone) as investigated by two-dimensional FTIR correlation spectroscopy. *Journal of Applied Polymer Science* **2015,** *132* (2), n/a-n/a.
33. Huang, R. Y. M.; Shao, P.; Burns, C. M.; Feng, X., Sulfonation of poly(ether ether ketone)(PEEK): Kinetic study and characterization. *Journal of Applied Polymer Science* **2001,** *82* (11), 2651-2660.
34. Cheng, S. Z.; Cao, M.; Wunderlich, B., Glass transition and melting behavior of poly (oxy-1, 4-phenyleneoxy-1, 4-phenylenecarbonyl-1, 4-phenylene)(PEEK). *Macromolecules* **1986,** *19* (7), 1868-1876.

35. Blundell, D. J.; Osborn, B. N., The morphology of poly(aryl-ether-ether-ketone). *Polymer* **1983,** *24* (8), 953-958.
36. Cebe, P.; Hong, S.-D., Crystallization behaviour of poly(ether-ether-ketone). *Polymer* **1986,** *27* (8), 1183-1192.
37. Bailly, C.; Williams, D. J.; Karasz, F. E.; MacKnight, W. J., The sodium salts of sulphonated poly(aryl-ether-ether-ketone) (PEEK): Preparation and characterization. *Polymer* **1987,** *28* (6), 1009-1016.
38. Weiss, R. A.; Turner, S. R.; Lundberg, R. D., Sulfonated polystyrene ionomers prepared by emulsion copolymerization of styrene and sodium styrene sulfonate. *Journal of Polymer Science: Polymer Chemistry Edition* **1985,** *23* (2), 525-533.
39. Jones, D. P.; Leach, D. C.; Moore, D. R., Mechanical properties of poly(ether-ether-ketone) for engineering applications. *Polymer* **1985,** *26* (9), 1385-1393.
40. Cebe, P.; Chung, S. Y.; Hong, S.-D., Effect of thermal history on mechanical properties of polyetheretherketone below the glass transition temperature. *Journal of Applied Polymer Science* **1987,** *33* (2), 487-503.
41. Reyna-Valencia, A.; Kaliaguine, S.; Bousmina, M., Tensile mechanical properties of sulfonated poly(ether ether ketone) (SPEEK) and BPO4/SPEEK membranes. *Journal of Applied Polymer Science* **2005,** *98* (6), 2380-2393.
42. Gebel, G., Structure of Membranes for Fuel Cells: SANS and SAXS Analyses of Sulfonated PEEK Membranes and Solutions. *Macromolecules* **2013,** *46* (15), 6057-6066.
43. Li, X.; Zhang, G.; Xu, D.; Zhao, C.; Na, H., Morphology study of sulfonated poly(ether ether ketone ketone)s (SPEEKK) membranes: The relationship between morphology and transport properties of SPEEKK membranes. *Journal of Power Sources* **2007,** *165* (2), 701-707.
44. Yang, B.; Manthiram, A., Comparison of the small angle X-ray scattering study of sulfonated poly(etheretherketone) and Nafion membranes for direct methanol fuel cells. *Journal of Power Sources* **2006,** *153* (1), 29-35.
45. Hall, L. M.; Seitz, M. E.; Winey, K. I.; Opper, K. L.; Wagener, K. B.; Stevens, M. J.; Frischknecht, A. L., Ionic Aggregate Structure in Ionomer Melts: Effect of Molecular Architecture on Aggregates and the Ionomer Peak. *Journal of the American Chemical Society* **2012,** *134* (1), 574-587.
46. Kinning, D. J.; Thomas, E. L., Hard-sphere interactions between spherical domains in diblock copolymers. *Macromolecules* **1984,** *17* (9), 1712-1718.
47. Brunello, G.; Mateker, W.; Lee, S. G.; Il Choi, J.; Soon Jang, S., *Effect of temperature on structure and water transport of hydrated sulfonated poly(ether ether ketone): A molecular dynamics simulation approach*. 2011; Vol. 3.
48. Liu, S.; Savage, J.; Voth, G. A., Mesoscale Study of Proton Transport in Proton Exchange Membranes: Role of Morphology. *The Journal of Physical Chemistry C* **2015,** *119* (4), 1753-1762.
49. Peckham, T. J.; Schmeisser, J.; Rodgers, M.; Holdcroft, S., Main-chain, statistically sulfonated proton exchange membranes: the relationships of acid concentration and proton mobility to water content and their effect upon proton conductivity. *Journal of Materials Chemistry* **2007,** *17* (30), 3255-3268.
50. Liang, C.; Maruyama, T.; Ohmukai, Y.; Sotani, T.; Matsuyama, H., Characterization of random and multiblock copolymers of highly sulfonated poly(arylene ether sulfone) for a proton-exchange membrane. *Journal of Applied Polymer Science* **2009,** *114* (3), 1793-1802.
51. Liang, C.; Maruyama, T.; Ohmukai, Y.; Sotani, T.; Matsuyama, H., Characterization of random and multiblock copolymers of highly sulfonated poly (arylene ether sulfone) for a proton-exchange membrane. *Journal of applied polymer science* **2009,** *114* (3), 1793-1802.

52. Lee, H.-S.; Roy, A.; Lane, O.; Dunn, S.; McGrath, J. E., Hydrophilic–hydrophobic multiblock copolymers based on poly(arylene ether sulfone) via low-temperature coupling reactions for proton exchange membrane fuel cells. *Polymer* **2008,** *49* (3), 715-723.
53. Roy, A.; Yu, X.; Dunn, S.; McGrath, J. E., Influence of microstructure and chemical composition on proton exchange membrane properties of sulfonated–fluorinated, hydrophilic–hydrophobic multiblock copolymers. *Journal of Membrane Science* **2009,** *327* (1), 118-124.
54. Hickner, M. A.; Pivovar, B. S., The Chemical and Structural Nature of Proton Exchange Membrane Fuel Cell Properties. *Fuel Cells* **2005,** *5* (2), 213-229.
55. Lee, M.; Park, J. K.; Lee, H.-S.; Lane, O.; Moore, R. B.; McGrath, J. E.; Baird, D. G., Effects of block length and solution-casting conditions on the final morphology and properties of disulfonated poly(arylene ether sulfone) multiblock copolymer films for proton exchange membranes. *Polymer* **2009,** *50* (25), 6129-6138.
56. Elabd, Y. A.; Hickner, M. A., Block Copolymers for Fuel Cells. *Macromolecules* **2011,** *44* (1), 1-11.

Chapter 4

Blocky Bromination of Poly(ether ether ketone)

(*Manuscript in preparation for publication*)

Lindsey J. Anderson, Robert B. Moore*

Department of Chemistry, Macromolecules Innovation Institute, Virginia Polytechnic Institute and State University, Blacksburg, Virginia 24061, United States

*To whom correspondence should be addressed: rbmoore3@vt.edu

4.1 Abstract

In this report, the bromination of poly(ether ether ketone) (PEEK) using the mild reagent *N*-bromosuccinimide (NBS) is explored to generate controlled random and blocky microstructures. Bromination proceeded quantitatively in both the solution state and semicrystalline gel state, and degrees of bromination between 25 and 175 mol% were obtained for both random and blocky BrPEEK. Spectroscopic evidence revealed a higher prevalence of unfunctionalized repeat units for blocky BrPEEK than random BrPEEK at similar degrees of functionality. Furthermore, at similar degrees of bromination blocky BrPEEK exhibited greater crystallizability, higher melting temperatures, and faster crystallization kinetics than random BrPEEK, suggesting longer segments of unfunctionalized PEEK in blocky BrPEEK. Morphological analysis using USAXS/SAXS/WAXS revealed excess scattering at low q for blocky BrPEEK, which was attributed to phase contrast between the electron-dense brominated 'blocks' and the electron poor (relatively) unfunctionalized blocks. Overall, this work demonstrates that bromination of PEEK in the semicrystalline gel state proceeds quantitatively while preserving crystallizability and effectively blocking up the functionality.

4.2 Introduction

Poly(ether ether ketone) (PEEK) is an aromatic high-performance polymer with excellent mechanical properties, high-temperature thermal transitions, and great chemical resistance.[1-3] PEEK is also semicrystalline with a high degree of crystallinity between 30 and 50 wt%.[4] Often, PEEK is chemically modified to impart novel physical-chemical properties for applications such as ion exchange and advanced composites.[5-6] For example, the post-polymerization sulfonation of PEEK has been extensively explored in the preparation of novel materials for proton exchange membranes.[7-11] The nitration[5, 12], hydroxylation[13], and amination[14-15] have also been investigated to improve the physical properties of PEEK.

Another useful functionalization procedure is the bromination of aromatic polymers, which provides a synthetic intermediate towards further functionalization. The bromine functionality is highly reactive towards a wide variety of nucleophiles including amines, phenols, alcohols, carbanions, nitriles, carboxylates, and thiol groups.[16-17] Furthermore, the bromines may be useful as reactive sites for crosslinking or grafting sites, and aryl bromides can be utilized for Ullmann coupling.[18-19] The post-polymerization bromination of high performance aromatic polymers has been demonstrated extensively with polyphenylsulfones[20-22], polyimides[23-24], and poly(phenylene oxide)[25-27]. Current literature, however, demonstrates limited precedence for the direct post-polymerization bromination of PEEK. While several reports describe the bromination of methylated-PEEK[28-31], only two known reports describe the bromination of commercially-derived (un-methylated) PEEK. Kumar et al. brominated PEEK with elemental bromine in concentrated sulfuric acid, however, failed to describe the impact of potential sulfonation from the solvent employed.[32] Furthermore, Bock utilized *N*-bromosuccinimide (NBS) in methanesulfonic acid to synthesize brominated PEEK (BrPEEK) and demonstrated reaction success up to high degrees of

functionality (e.g. 240 mol%).[33] In both reports of PEEK bromination, BrPEEK was employed as a precursor for the subsequent phosphonation of PEEK.

Most post-polymerization bromination reactions occur in the homogeneous solution state, thus yielding a random distribution of bromine groups along the polymer backbone until sufficiently high degrees of bromination are achieved (i.e. each repeat unit is fully brominated). In order to synthesize controlled brominated architectures using (such as multiblock copolymers) using post-polymerization functionalization, a polymer template must be used with the previously established architecture. For example, multiblock copolymers with only one block that is reactive towards bromination could be utilized for selective bromination.[34-35] Recently, a novel post-polymerization technique utilizing semicrystalline thermoreversible gels was introduced for the blocky sulfonation of polystyrene[36] and PEEK[36-37] and for the blocky bromination of polystyrene.[38] Within the heterogeneous gel state, a network of two distinct domains exists: tightly packed lamellar crystallites and solvent-swollen amorphous domains. With the addition of a functionalization reagent, the desired chemistry is sterically restricted to reaction upon the solvent-swollen amorphous chains, resulting in non-random (blocky) functionalization. This process also maintains 'blocks' of unfunctionalized, and thus potentially crystallizable, chain segments that were organized in the polymer crystallites during the reaction. Therefore, this facile procedure not only provides a means of controlling architecture during post-polymerization functionalization, but also preserves the crystallizability of the polymer.

In this work, the bromination of semicrystalline gels of PEEK in dichloroacetic acid is explored to synthesize blocky BrPEEK copolymers.[39-40] The blocky BrPEEK is compared to random BrPEEK at similar degrees of functionalization to determine the influence of architecture on the physical properties of BrPEEK, including thermal transitions, crystallizability, crystallization kinetics, and morphology.

4.3 Experimental

4.3.1 Materials

Poly(ether ether ketone) (PEEK) pellets (Victrex 150G) were acquired from Victrex. Dichloroacetic acid (DCA) was purchased from Sigma-Aldrich and was dried using magnesium sulfate (Fisher Scientific) then filtered through a 0.45 μm PTFE syringe filter prior to use. *N*-bromosuccinimide (NBS) was purchased from Sigma-Aldrich and was purified by recrystallization from water using the procedure outlined previously.[36]

4.3.2 Random Bromination of Poly(ether ether ketone)

To synthesize randomly brominated PEEK, reactions were performed in the homogeneous solution state. First, PEEK (5.0 g) was dissolved in dichloroacetic acid (DCA) at 185 ^{O}C to a final concentration of 10 w/v%. Once dissolved, the temperature was lowered to 80 ^{O}C, and the PEEK solution was equilibrated at this temperature under an argon purge for 1 hour. Meanwhile, a solution of *N*-bromosuccinimide (NBS) was prepared by dissolving the desired mass of NBS in 20 mL of DCA. Reactions were performed using the following molar ratios of NBS to PEEK repeat unit: 0.25:1, 0.5:1, 0.75:1, 1:1, 1.5:1, 1.75:1. Next, the NBS solution was added dropwise to the stirring PEEK solution. The reaction was allowed to proceed at 80 ^{O}C for 24 hours and was then terminated by precipitation into DI H_2O. The product was filtered, washed with DI H_2O, and then washed by soxhlet extraction over methanol for 24 hours. The resulting polymer was dried at 100 ^{O}C for 12 hours to produce a white product. Prior to any analysis, the product was ground using liquid nitrogen to form a fine powder.

4.3.3 Blocky Bromination of Poly(ether ether ketone)

To synthesize blocky brominated PEEK, reactions were performed in the heterogeneous gel state. PEEK gels were prepared by dissolving PEEK (5.0 g) in DCA at 185 ^{O}C to a final

concentration of 20 w/v%. Upon dissolution, the PEEK solution was removed from heat and left at room temperature for at least 24 hours. During this time, the PEEK crystallizes from solution to form a thermoreversible gel network.[39] Prior to reaction, the gel was manually broken into small pieces using a metal spatula and was suspended in DCA to a final concentration of 10 w/v%. The gel suspension was equilibrated at 80 ^{O}C under argon for 1 hour. Meanwhile, a solution of *N*-bromosuccinimide (NBS) was prepared by dissolving the desired mass of NBS in 20 mL of DCA. Reactions were performed using the following molar ratios of NBS to PEEK repeat unit: 0.25:1, 0.5:1, 0.75:1, 1:1, 1.5:1, 1.75:1. Next, the NBS solution was added dropwise to the stirring PEEK suspension. The reaction was allowed to proceed at 80 ^{O}C for 24 hours and was then terminated by precipitation into DI H_2O. The product was filtered, washed with DI H_2O, and then washed by soxhlet extraction over methanol for 24 hours. The resulting polymer was dried at 100 ^{O}C for 12 hours to produce a white product. Prior to any analysis, the product was ground using liquid nitrogen to form a fine powder.

4.3.4 ^{1}H NMR Spectroscopy

^{1}H. NMR spectra were measured using a Bruker Avance III 600 MHz. Due to the limited solubility of the brominated PEEK (BrPEEK), conventional deuterated solvents were not able to be used for analysis. Instead, a solvent suppression method using DCA and deuterated chloroform ($CDCl_3$) was utilized, as described previously.[37] In summary, BrPEEK samples were dissolved in DCA at 185 ^{O}C to a final concentration of 10 w/v%. Once dissolved, solutions were cooled to room temperature and diluted by a factor of 5 using $CDCl_3$ with 0.05% v/v TMS. Presaturation of the intense DCA resonance at 6 ppm was performed during acquisition to obtain a suitable spectrum, free of a solvent contribution.

4.3.5 FTIR Spectroscopy

FTIR was performed using a Varian 670-IR spectrometer with a DTGS detector using the Pike Technologies GladiATR^{TM} attachment (diamond crystal). Spectra were collected as the average of 32 scans at 4 cm^{-1} resolution.

4.3.6 Thermal Properties

A TA Instruments TGA Q500 thermogravimetric analyzer was used to determine the thermal stability of the BrPEEK copolymers for further analysis using DMA and DSC. Samples were heated from 25 °C to 700 °C at a rate of 10 °C/min. A TA Instruments Q800 DMA in oscillatory tension mode was used to determine the mechanical properties of quenched BrPEEK samples as a function of temperature. Samples were ramped at 2 ºC/min to 400 ºC at a frequency of 1 Hz, an oscillatory amplitude of 10 μm, and a static force of 0.01 N to determine the effect of modulus versus temperature. The glass transition temperature was determined from the peak in tanδ vs. temperature. A TA Instruments Q2000 DSC was used to determine the thermal properties and crystallization kinetics of the BrPEEK samples. Samples were pre-dried at 150 ^{O}C for 5 minutes before several heating and cooling cycles. Dried samples (~5-8 mg) were heated from room temperature to 380 °C at 20 °C/min, quench cooled to 0 °C, and then heated to 380 °C at a rate of 20 °C/min. Isothermal crystallization was performed by heating BrPEEK samples at 20 °C/min to 380 °C, isothermally holding at 380 °C for 3 minutes, quench cooling (60 °C/min) to the desired crystallization temperature (T_c), isothermally holding at this T_c until the DSC trace returned to the baseline, quench cooling (60 °C/min) to 100 °C, and then heating at 10 °C/min to 380 °C. Isothermal crystallization was carried out at T_c's between 230 °C and 320 °C. The crystallization half time ($t_{1/2}$) was determined at each isothermal crystallization temperature and was used as a measure of the bulk crystallization rate for each BrPEEK sample. DSC thermograms were analyzed and the glass transition temperature (T_g), enthalpy of crystallization (ΔH_c), melting

temperature (T_m), and enthalpy of melting (ΔH_m) were determined using the TA Instruments Universal Analysis software.

4.3.7 USAXS/SAXS/WAXD Analysis

Ultra-small angle x-ray scattering (USAXS), small angle x-ray scattering (SAXS), and wide angle x-ray diffraction (WAXD) data were collected at Argonne National Laboratory beamline 9ID-C using a photon energy of 24 keV.[41] Scattering profiles are plotted as absolute intensity vs. q, where $q = \left(\frac{4\pi}{\lambda}\right)\sin(\theta)$, θ is one half of the scattering angle, and λ is the X-ray wavelength. USAXS measurements were collected using a Bonse-Hart camera as the detector. SAXS measurements utilized the Pilatus 100k camera, and WAXD utilized the Pilatus 100k-w camera. Data reduction was performed using the Irena[42] and Nika[43] software packages provided by Argonne.

4.3.8 Thermal Treatment of BrPEEK

To prepare quenched films of BrPEEK, the polymers were melt pressed between two aluminum plates layered with Kapton films. Steel shims were utilized to control the film thickness to approximately 100 μm. Samples were heated for 5 minutes at 380 ºC, and then the top aluminum plate was added. Next, the melted samples were subjected to several press-release-press cycles in which the press cycles afforded 10 tons of force onto the samples. The aluminum plates and sandwiched polymer film were immediately placed into an ice-bath to yield amorphous, ductile films. Samples were subsequently dried at 100 ºC in a vacuum over overnight. Annealing of quenched films was performed by placing the quenched films in an oven at 250 ºC for 1 hour.

4.4 Results and Discussion

4.4.1 Synthesis and Characterization of Random and Blocky BrPEEK

The bromination of PEEK using *N*-bromosuccinimide (NBS) was performed in the solution state and in the gel state to produce random BrPEEK and blocky BrPEEK, respectively.

The reaction schemes and resultant polymer architectures of these synthetic routes are shown in **Figure 4.1**. When reacting in the solution state, each PEEK repeat unit is fully solvated. Thus, each repeat unit is equally as likely to react with the brominating reagent and a random (statistical) architecture is obtained for the BrPEEK product. In contrast, when reacting in the semicrystalline gel state, PEEK chains are organized into a network consisting of tightly-packed polymer crystallites and solvent-swollen amorphous domains. When the brominating reagent is added, it is sterically excluded from the tightly-packed crystalline domains and is thereby only capable of penetrating and functionalizing the solvent-swollen amorphous domains. This results in selective bromination of the amorphous domains and produces a blocky architecture with preserved crystallizability.

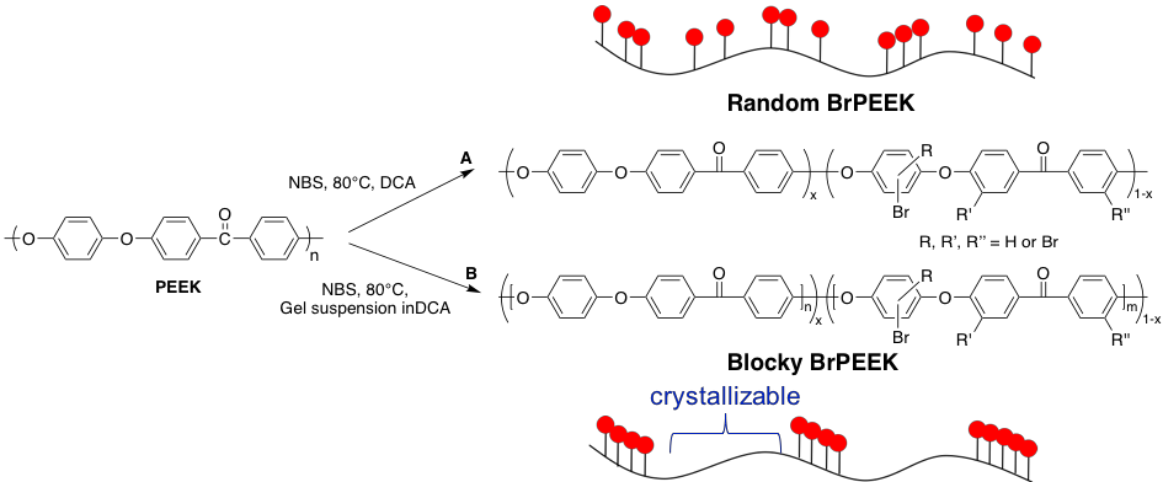

Figure 4.1. Reaction schemes for the random (A) and blocky (B) bromination of PEEK. In the solution state (A), all chains are equally accessible to bromination and result in a random architecture. In the gel state (B), bromination occurs solely in the amorphous domains, resulting in blocks of BrPEEK and blocks of unfunctionalized PEEK. Bromination may occur at one or more of the bromination sites indicated per repeat unit.

In this work, NBS was utilized as the brominating reagent. Although NBS is generally considered a mild brominating reagent, when it is dissolved in a strong acid, such as sulfuric acid (H_2SO_4) or methanesulfonic acid, it is capable of brominating even highly deactivated aromatic rings.[33, 44-45] In the strong acid, NBS becomes protonated and liberates a bromonium ion (Br^+). The

bromonium ion is highly electrophilic and may undergo electrophilic aromatic substitution (EAS) with each of the aromatic rings of the PEEK repeat unit, resulting in multiple sites for functionalization on a single repeat unit (as shown in **Figure 4.1**). Because the hydroquinone segment is surrounded by electron-donating ether linkages, bromination of this ring occurs readily by EAS at any position. Multiple brominations of this ring are also possible at high degrees of functionalization. Furthermore, the benzophenone segment of the PEEK repeat unit may be functionalized at positions ortho to the ether linkages due to similar electron-donating effects. The electron-withdrawing effect of the carbonyl group, however, deactivates positions ortho to it and prevents bromination at these sites. Because several reaction sites are present per repeat unit, high degrees of bromination (above 100 mol%) are readily synthesized. This is particularly useful for targeting high degrees of bromination with blocky BrPEEK, where high degrees of functionality are achievable while maintaining a significant fraction of unfunctionalized repeat units.

Utilizing the high electrophilicity of NBS in acid, the bromination of PEEK from 25 – 175 mol% in the solution state and in the gel state was explored to determine the influence of copolymer architecture (random vs. blocky) on polymer properties. The ^{1}H NMR spectra and peak assignments of the PEEK homopolymer, blocky BrPEEK targeting 150 mol% bromination (blocky BrPEEK150), and random BrPEEK150 are shown in **Figure 4.2**. PEEK itself displays 3 distinct chemical shifts: a doublet around 7.85 ppm (c protons), a singlet at 7.15 ppm (a protons), and a doublet around 7.10 ppm (b protons). Upon bromination, several new peaks appear at approximately 8.10 ppm, 7.75 ppm, 7.45 ppm, 7.03 ppm and 6.75 ppm, indicating shifts in aromatic signals due to the addition of the electrophilic bromine on the aromatic groups. The degree of bromination was determined by integrating the a and b protons with respect to the c protons. Because the c protons are not capable of being functionalized due to their proximity to the electron-withdrawing carbonyl, the total integration of c and c’ is set to 4 protons. The

remaining a, a', b, and b' peaks were integrated and the degree of bromination was determined using the following relation:

$$\mathbf{DS_{Br}} = \mathbf{8} - \int \mathbf{H_a}\,, \mathbf{H_{a\prime}}\,, \mathbf{H_b}\,, \mathbf{H_{b\prime}}$$

The degrees of bromination determined by ^{1}H NMR are displayed in **Table 4.1**. From this analysis, it is evident that the resultant degree of bromination for both blocky and random BrPEEK copolymers is close (within a few mol%) to the target degree of bromination (as controlled by NBS amount). Thus, the bromination of PEEK in DCA proceeds quantitatively using NBS, in agreement with the literature precedence in methanesulfonic acid.[33]

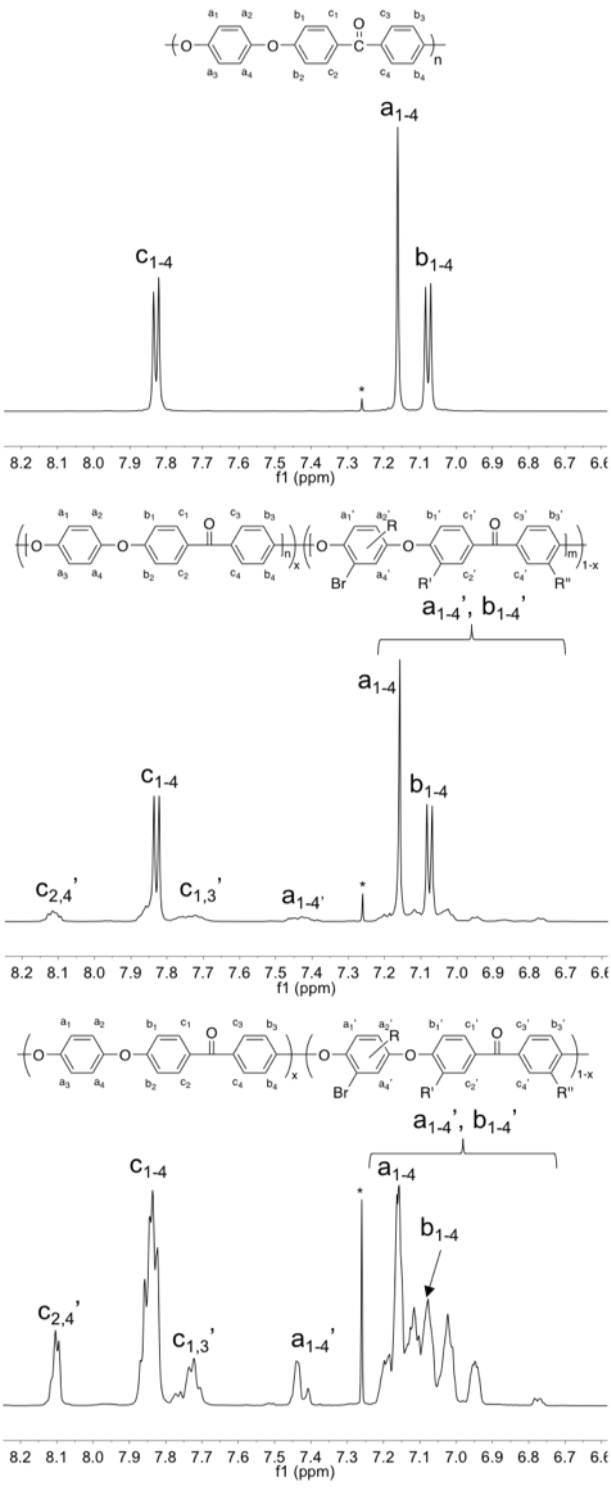

Figure 4.2. [1]H NMR of PEEK, Blocky BrPEEK150, and Random BrPEEK150.

Table 4.1. Degrees of bromination as determined by integration of the ^{1}H NMR spectra.

Target DS_{Br} (mol%)	DS_{Br} by ^{1}H NMR (mol%)	
	Random	Blocky
25	22	25
50	51	49
75	74	75
100	99	98
150	151	144
175	175	176

Despite the similarities in the obtained degrees of bromination and peak positions, the ^{1}H NMR spectra exhibit significant differences in peak shape between blocky and random samples, especially at high degrees of bromination. The ^{1}H NMR spectra of the random and blocky BrPEEK samples at increasing degrees of bromination are displayed in **Figure 4.3**. Initially for both copolymer architectures, the signature PEEK doublets at 7.85 ppm and 7.10 ppm and singlet at 7.15 ppm are clearly observed in the BrPEEK spectrum. This is unsurprising, as at low degrees of bromination a large fraction of unbrominated PEEK is present in each sample. As the degree of bromination increases, however, the random BrPEEK displays a decrease in intensity and broadening of the PEEK homopolymer peaks. Above 100% bromination, these characteristic peaks are no longer distinctly observed in the random samples, indicating that all repeat units have likely been functionalized. In contrast, the blocky BrPEEK samples display clear, unperturbed PEEK homopolymer peaks even at high degrees of bromination (up to 175 mol%). This confirms the efficacy of the gel-state reaction in preserving long blocks of unfunctionalized PEEK.

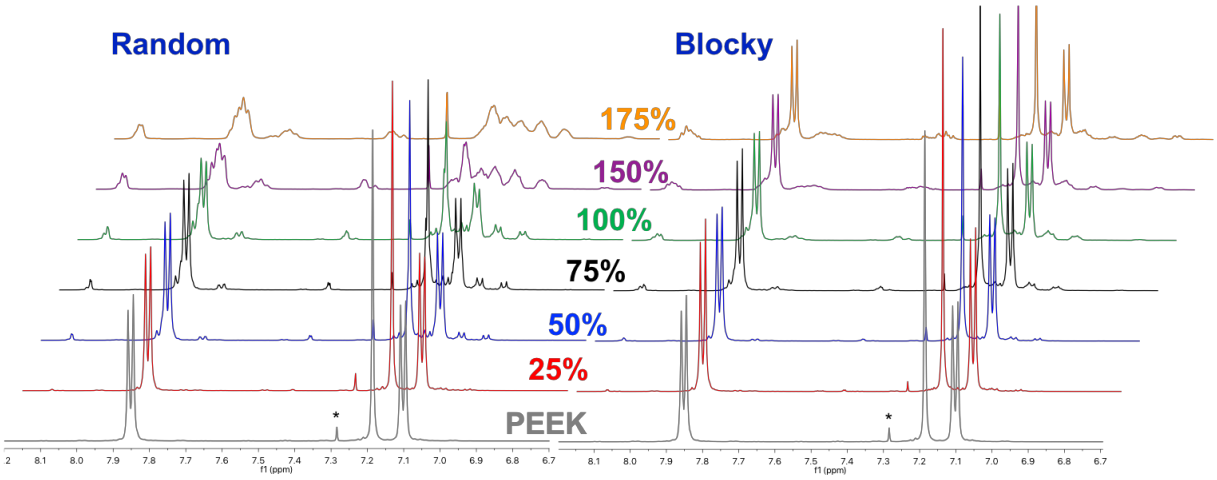

Figure 4.3. ^{1}H NMR of random (left) and blocky (right) BrPEEK with increasing degree of bromination. The solvent ($CDCl_3$) peak is indicated with an asterisk.

The ^{13}C NMR spectra of PEEK, random BrPEEK150, and blocky BrPEEK150 were also investigated in DCA/$CDCl_3$, as shown in **Figure 4.4**. Samples were run on a Varian Inova 400 MHz NMR and 2000 scans were performed. For ease of comparison, the assignments of the PEEK carbons are labelled. Similar to ^{1}H NMR results, the signals of pure PEEK are dominant within the ^{13}C NMR spectra of blocky BrPEEK150, indicating that a large fraction of unfunctionalized homopolymer remains in the blocky brominated copolymer. The random BrPEEK150, however, does not display a substantial prevalence of the homopolymer PEEK signals. In fact, the only peak of the homopolymer that remains noticeably prevalent is that of the e carbon (i.e. the position of the aromatic ring that is incapable of being brominated).

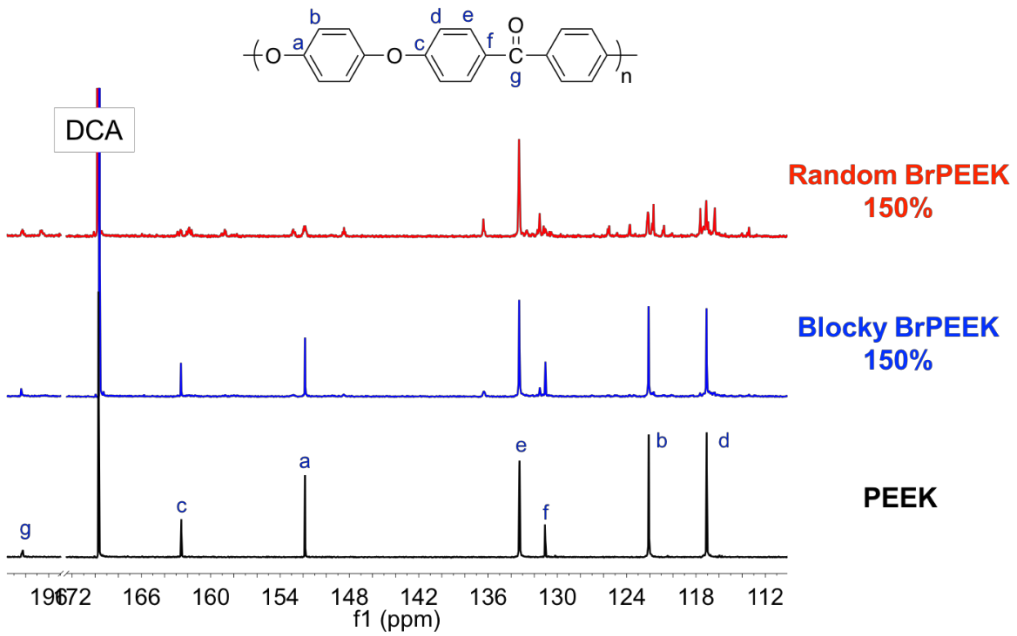

Figure 4.4. ^{13}C NMR of PEEK, Blocky BrPEEK150, and Random BrPEEK150 in DCA/$CDCl_3$.

To further confirm the differences in architecture FTIR was performed, as shown in **Figure 4.5**. For both blocky and random BrPEEK, a new peak arises at 1040 cm^{-1} and grows with increasing degree of bromination. This peak is attributed to aryl C-Br stretching, thereby confirming reaction success.[32, 46] Furthermore, a peak at 1470 cm^{-1} appears and grows in intensity for both architectures with increasing degree of bromination. This is coupled with a concurrent decrease in intensity of the peak at 1490 cm^{-1}. The 1470 cm^{-1} peak is attributed to the skeletal ring vibrations of 1,2,4-trisubstituted rings while the 1490 cm^{-1} peak is attributed to the skeletal ring vibrations of a 1,4-disubstituted ring.[47] Thus, as the PEEK is brominated, we would expect to see this simultaneous rise and fall of the 1470 cm^{-1} and 1490 cm^{-1} peaks, respectively, with increasing degrees of bromination. At high degrees of bromination (ca. 100-175 mol%), the 1470 cm^{-1} peak is much more intense for random BrPEEK than for blocky BrPEEK. This demonstrates that in the solution-state, where the length of all chains is capable of being functionalized, mono-bromination of the aromatic rings is dominant. In contrast, in the gel-state multiple substitutions per ring are

occurring in order to preserve the long stretches of unbrominated PEEK. This is further confirmed by the additional C-Br peak at 1065 cm^{-1} that arises for the blocky samples at high degrees of bromination.

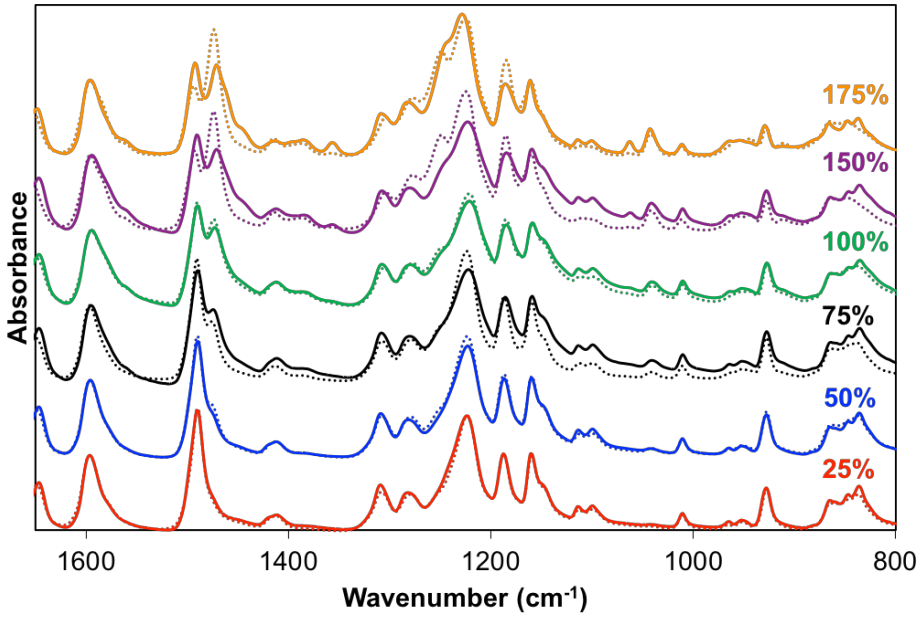

Figure 4.5. FTIR of random (dashed lines) and blocky (solid lines) BrPEEK at increasing degrees of bromination.

4.4.2 Thermal Properties of BrPEEK

Thermogravimetric analysis (TGA) was performed to determine the stability of PEEK, random BrPEEK, and blocky BrPEEK, as shown in **Figure 4.6**. PEEK itself displays a degradation temperature (noted by the temperature at which 5 wt% mass loss is observed, $T_{d,5\%}$) of 577 ºC. As the degree of bromination increases, the $T_{d,5\%}$ of both blocky and random BrPEEK decreases to around 440 ºC at 150 mol% bromination. Little difference is observed between the blocky and random BrPEEK, indicating that the degree of bromination is the main factor in $T_{d,5\%}$. Due to the high thermal stability of these copolymers, DSC and DMA experiments up to 400 ºC (as performed in this work) will not cause thermal degradation of the BrPEEK.

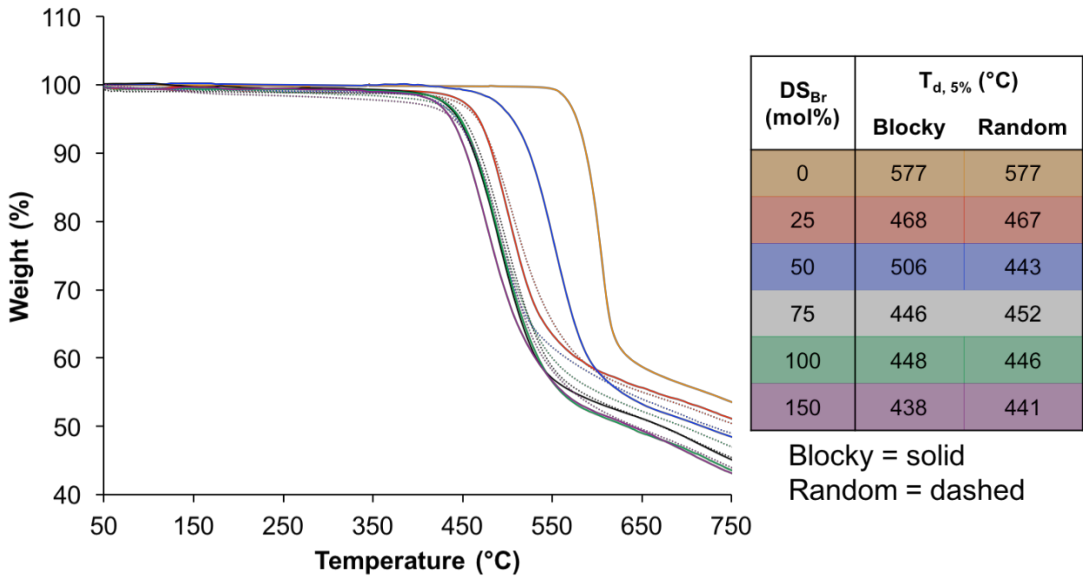

DS_{Br} (mol%)	$T_{d,\ 5\%}$ (°C)	
	Blocky	Random
0	577	577
25	468	467
50	506	443
75	446	452
100	448	446
150	438	441

Figure 4.6. TGA thermograms of PEEK, random BrPEEK and blocky BrPEEK. Blocky BrPEEK is shown as solid lines and random BrPEEK is shown as dashed lines with identical colors at analogous degrees of bromination.

DSC and DMA of quenched BrPEEK samples were utilized to determine the influence of copolymer architecture on the glass transition temperature (T_g). As shown in **Figure 4.7**, a linear increase in T_g is observed with increasing degree of bromination for both random and blocky BrPEEK. The increase in T_g is associated with the steric hindrance of torsional rotations about the phenyl rings upon bromination.[48] The bulky bromine groups thereby limit chain mobility, leading to an increase in T_g.[49] Additionally, there surprisingly appears to be no difference between the T_g of random and blocky BrPEEK at similar degrees of bromination. Typically, conventional block copolymers display two separate T_g's associated with each component, while random copolymers display a single T_g intermediate of the two monomers. For the blocky BrPEEK copolymers synthesized in this work, the lengths of each brominated block are not uniform – rather there exists both a gradient of block lengths and degrees of bromination within each 'block'. Furthermore, there may be some phase mixing between the densely brominated blocks and the unfunctionalized

blocks. One or both of these factors may contribute to an intermediate T_g that is observed, similar to the T_g of the random BrPEEK copolymer.

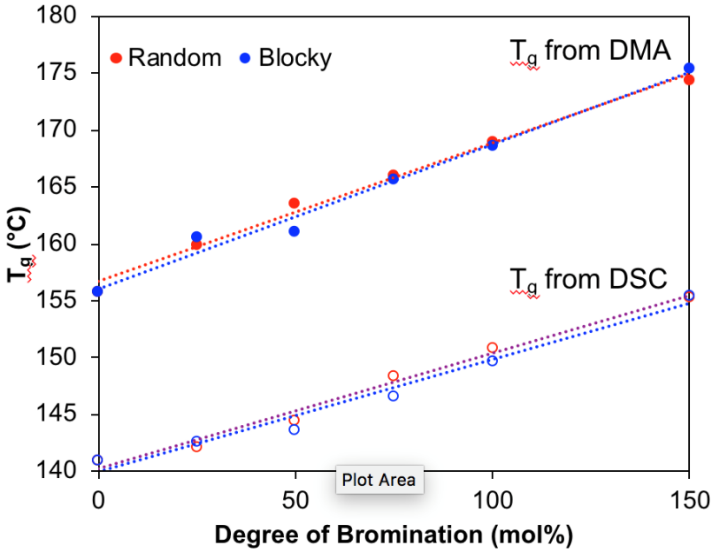

Figure 4.7. Glass transition temperature (T_g) of quenched random (red) and blocky (blue) BrPEEK from dynamic mechanical analysis (DMA) and differential scanning calorimetry (DSC). The T_g was determined from the peak maximum of tanδ for DMA and by the inflection point in DSC.

The DMA thermograms of random and blocky BrPEEK were used to determine their mechanical properties and glass transition temperature (T_g), as shown in **Figure 4.8**. Based on the graph of storage modulus vs. temperature it is evident that random and blocky BrPEEK copolymers flow at approximately 150 ºC, indicating a transition from the glassy state to flowing. Random and blocky BrPEEK at 25 and 50 mol% bromination display a subsequent increase in storage modulus following this transition, related to the crystallization of these copolymers during the analysis. Analysis of tanδ vs. temperature enables the quantification of the T_g, taken as the temperature value at the tanδ peak. No difference in full-width half-max (FWHM) was observed in the tanδ peak between random and blocky architectures, and T_g displays a linear increase with increasing degree of bromination for both architectures, as described above.

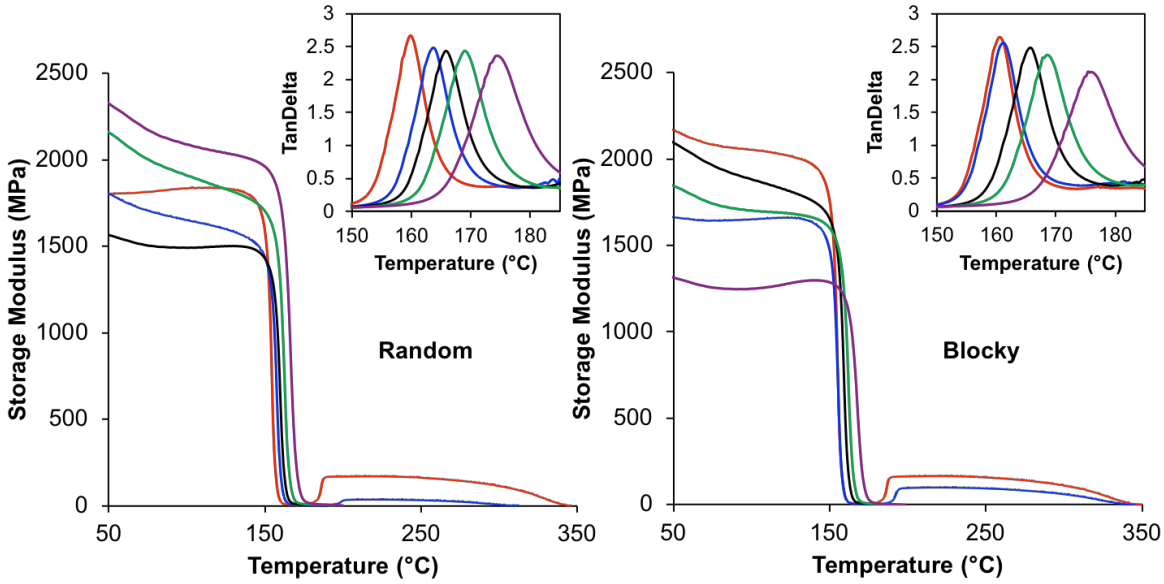

Figure 4.8. DMA thermograms of random BrPEEK (left) and blocky BrPEEK (right) at various degrees of bromination: 25 mol% (red), 50 mol% (blue), 75 mol% (black), 100 mol% (green), and 150 mol% (purple). The graphs of tanδ vs. temperature is also shown as an insert to each graph.

The influence of copolymer architecture on the crystallization behavior of BrPEEK was investigated using DSC. BrPEEK samples were heated into the melt, quench cooled, and then subsequently heated to determine the crystallizability of random and blocky BrPEEK. The DSC thermograms of the quench cool and the subsequent heat following the quench cool for random and blocky BrPEEK at increasing degrees of bromination are shown in **Figure 4.9**. Both random and blocky BrPEEK display a decrease in crystallization temperature (T_c) and melting temperature (T_m) with increasing degree of bromination, as expected. Furthermore, the magnitude of the crystallization exotherms and melting endotherms decreases with increasing degree of bromination. The bromine groups introduced to the polymer backbone act as chain defects that disrupt and limit the fraction of crystallizable polymer, leading to smaller lamellar crystals, a lower T_c and T_m, and less crystallinity. Bromination architecture plays a key role in the magnitude of these effects, and random BrPEEK displays significantly greater T_c and T_m depression and a larger

loss of crystallinity than blocky BrPEEK when referenced to the PEEK homopolymer. For example, the T_c of random BrPEEK50 is dramatically depressed from 294 ºC (PEEK) to 242 ºC at relatively low degrees of bromination, while blocky BrPEEK50 is only depressed to 278 ºC. Above 50 mol% bromination, random BrPEEK is not capable of crystallizing during the rapid quench cool. In contrast, blocky BrPEEK completely crystallizes during the quench cool at all degrees of functionalization explored and displays only a slight, linear decrease in T_c to 243 ºC at high degrees of bromination (blocky BrPEEK175).

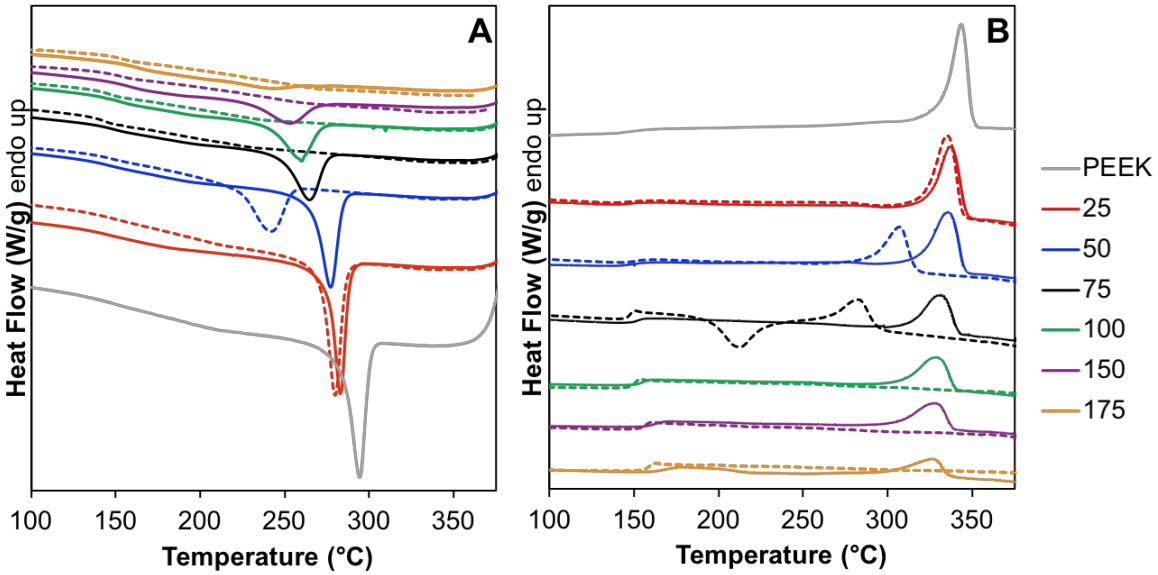

Figure 4.9. DSC thermograms of a quench cool (A) and subsequent heat following the quench cool (B) of PEEK and BrPEEK at various degrees of bromination. Blocky BrPEEK samples are displayed as solid lines and Random BrPEEK samples are displayed as dashed lines.

Similarly, the melting endotherm exhibits more substantial T_m depression for random BrPEEK than for blocky BrPEEK. The T_m of random BrPEEK falls rapidly from 345 ºC (PEEK) to 283 ºC for random BrPEEK75, and no melting endotherm is observed above 75 mol% bromination. In contrast, the T_m of blocky BrPEEK displays a nominal decrease in T_m from 345 ºC to 327 ºC for blocky BrPEEK175. For comparison to random BrPEEK75 (T_m = 283 ºC), blocky BrPEEK75 displays a T_m of 331 ºC. Furthermore, as the degree of bromination increases, the size

of the melting endotherms decreases more rapidly for random BrPEEK than blocky BrPEEK, signifying a greater loss in crystallinity. The degree of crystallinity, X_c, for each sample was determined using the following equation:

$$X_c = \frac{\Delta H_f}{\Delta H_f^\circ}$$

where ΔH_f is the enthalpy of fusion determined by integration of the melting endotherm and ΔH_f^o is the enthalpy of fusion of 100% crystalline PEEK determined theoretically (130 J/g).[4] Pure PEEK is highly crystalline (X_c = 36 wt%) following a quench cool, and blocky BrPEEK displays similarly high levels of crystallinity, maintaining X_c = 17 wt% at 75 mol% bromination and X_c = 9 wt% at 175 mol% bromination. Random BrPEEK, however, exhibits only 12 wt% crystallinity at 75 mol% bromination and no crystallinity above this level of functionality. Thus, it is evident that by blocking up the bromine functionalities into the amorphous domains, the blocky BrPEEK remains crystallizable up to higher degrees of functionalization and produces larger crystals than random analogs. This is easily attributed to the difference in bromine distribution along the polymer backbones. For random copolymers in which a statistical distribution of bromines is expected, it is more likely to encounter a bromine defect at the growing polymer crystal. This results in a smaller fraction (and length) of crystallizable runs, leading to a lower equilibrium melting temperature and lower crystallizability.[50-51] For blocky copolymers, however, long crystalline runs are preserved during the bromination process via the semicrystalline gel network. This maintains a high level of crystallizability and a higher equilibrium melting temperature more similar to the PEEK homopolymer itself.

Although this analysis has focused on crystallization and crystallizability from the melt, it is also useful to observe trends in the first heat of the BrPEEK copolymers as an estimation of the maximum crystallinity of each sample. Similar trends are observed in the first heat as with the heat following a quench cool in terms of melting point depression and decrease in crystallinity;

however, it is important to note that random BrPEEK100 displays a melting endotherm in the first heat (T_m =237 ºC, X_c = 7 wt%) that is not observed in subsequent heats. This suggests that crystallization from solution may enable higher degrees of crystallinity. This is further supported by higher degrees of crystallinity calculated for both blocky and random BrPEEK at all degrees of bromination compared to quench crystallization from the melt. The complete analysis (T_c, T_m, X_c) of the first heat, quench cool, and heat following a quench cool for random and blocky BrPEEK at all degrees of bromination is shown in **Table 4.2**. The DSC thermograms of the first heat of random and blocky BrPEEK is shown in **Figure 4.10**.

Table 4.2. Thermal properties of random and blocky BrPEEK.

Sample	$T_{m, first}$ (ºC)	$X_{c, first}$ (wt%)	$T_{c, quench}$ (ºC)	$T_{m, quench}$ (ºC)	$X_{c, quench}$ (wt%)
PEEK	345	43	294	343	36
RBrPEEK25	342	39	280	336	28
BBrPEEK25	340	42	283	338	26
RBrPEEK50	312	26	242	308	18
BBrPEEK50	339	37	277	336	25
RBrPEEK75	286	20	-	283	12
BBrPEEK75	336	24	265	331	17
RBrPEEK100	237	7	-	-	-
BBrPEEK100	334	23	260	329	16
RBrPEEK150	-	-	-	-	-
BBrPEEK150	331	18	253	329	13
RBrPEEK175	-	-	-	-	-
BBrPEEK175	330	11	243	326	9

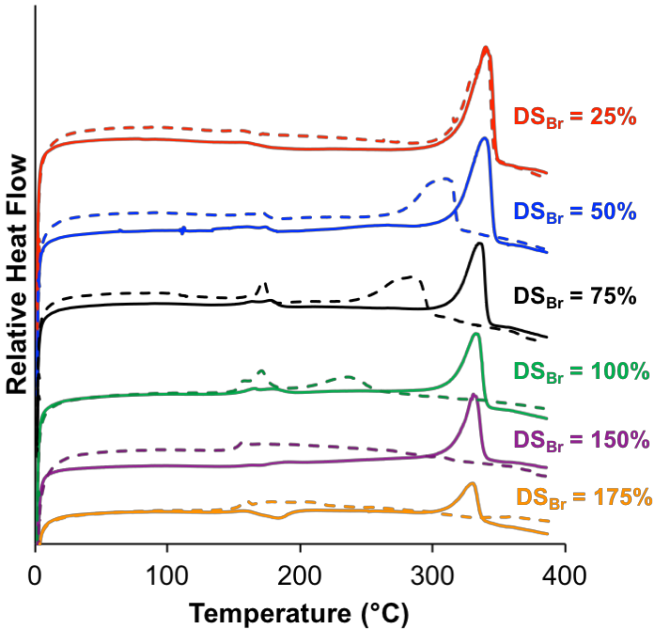

Figure 4.10. DSC thermograms of the first heats of random (dashed lines) and blocky (solid lines) at various degrees of bromination.

To further elucidate the effect of architecture on thermal transitions, it is useful to compare the melting point depression to Flory's theory of crystallization in copolymers. Using Flory's theory, the T_m of a random copolymer may be determined using the following relation:

$$\frac{1}{T_m} - \frac{1}{T_m^\circ} = -\left(\frac{R}{\Delta H_u}\right)\ln(X_A)$$

where T_m is the melting temperature of the random copolymer, T_m° is the melting temperature of 100% crystalline PEEK, R is the gas constant, ΔH_u is the enthalpy of fusion per unit (37,400 J/mol)[4], and X_A is the mol fraction of A (crystallizable) units.[50] Because bromination of PEEK is possible at multiple sites per repeat unit, X_A is not simply (1- degree of bromination); rather it must be calculated based on the average number of repeat units that remain unfunctionalized following bromination. To determine X_A, the ^{1}H NMR spectra were integrated peak by peak. An example demonstrating this integration process is shown in **Figure 4.11** using Random BrPEEK 75. Prior to integration, ^{1}H NMR spectra were phase-corrected, baseline corrected, and referenced to the

$CDCl_3$ peak at 7.26 ppm. Peaks were then integrated automatically using the MestReNova software. The area under the PEEK homopolymer peaks at 7.86 ppm, 7.85 ppm, 7.15 ppm, 7.11 ppm, and 7.09 ppm were added together and compared to the total area under the ^{1}H NMR spectrum (i.e. the area under all integrated peaks) to yield X_A.

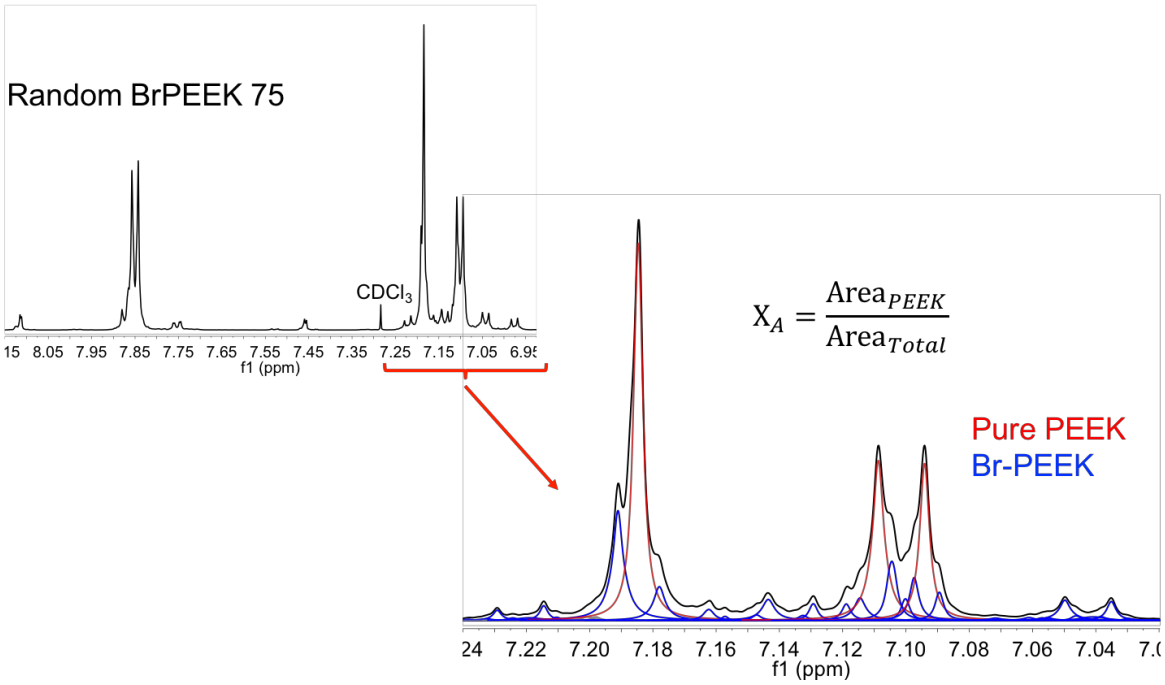

Figure 4.11. Integration of ^{1}H NMR spectrum of Random BrPEEK75 to determine $\boldsymbol{X_A}$.

A plot of the calculated X_A as a function of degree of bromination is shown in **Figure 4.12**. For both random and blocky BrPEEK, the X_A values lie above what would be expected for a single bromination event per repeat unit, confirming that multiple bromination events are occurring per repeat unit, even at low degrees of bromination. As the degree of bromination increases, the X_A value decreases rapidly for random BrPEEK until above 100 mol% bromination where there is no evidence of any unfunctionalized repeat units. Blocky BrPEEK, however, exhibits a milder reduction in X_A with increasing degree of bromination. In fact, blocky BrPEEK150 has a calculated X_A of 64 mol%, which corresponds to an average of 4 bromines per repeat unit within

the brominated blocks. This further exemplifies the fact that blocky BrPEEK is more likely to have more bromination events per repeat unit and a greater occurrence of multiple substitutions per aromatic ring than random BrPEEK, as evidenced earlier with the FTIR results.

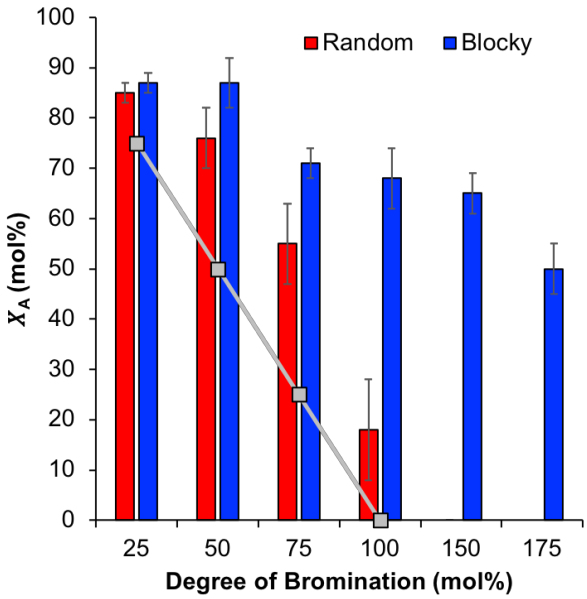

Figure 4.12. X_A as determined by integration of ^{1}H NMR. Random BrPEEK is represented in red and blocky BrPEEK is represented in Blue. A gray line is added for reference of a ratio of 1 bromination event per 1 PEEK repeat unit.

Using the X_A values determined from the ^{1}H NMR spectra, the theoretical melting point can be calculated using Flory's equation above. For simplicity and ease of comparison to the experimental data, the T_m of the unfunctionalized PEEK homopolymer (345 ºC) was used in place of T_m° in the equation. The theoretical T_m values for random and blocky BrPEEK copolymers and their comparison to experimental results are displayed in **Figure 4.13**. The melting point depression of random BrPEEK closely follows the theoretical melting point depression calculated using Flory's theory, confirming that bromination in the solution state yield statistical copolymers with predictable physical properties. Furthermore, Flory's theory predicts a much more gradual decline in T_m for blocky BrPEEK, however, it consistently overestimates the melting point

depression with increasing degree of bromination. This is likely due to the fact that the theory assumes a random distribution of functionality along the polymer backbone. Although an accurate X_A is incorporated into the equation, no consideration is given to the lengths of the unfunctionalized blocks. Thus, the experimental T_m observed is larger than the calculated T_m.

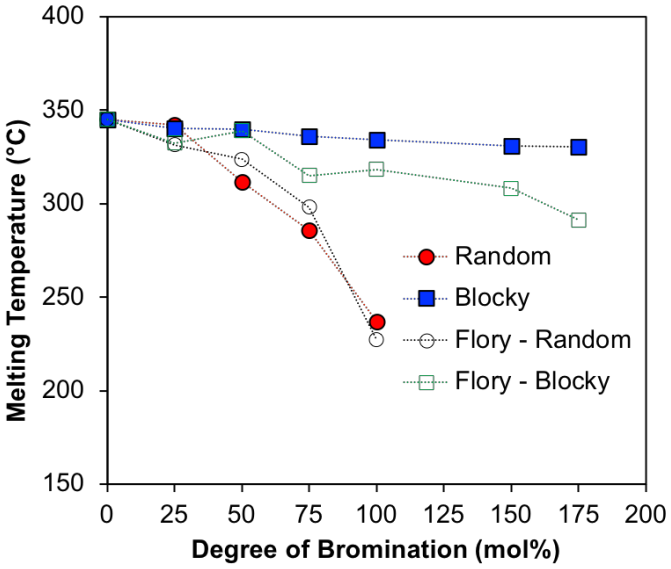

Figure 4.13. Experimental melting temperature of random (red circles) and blocky (blue circles) BrPEEK as a function of degree of bromination. Melting temperatures were derived from the peak of the melting endotherm of the first heat of the as-precipitated product. Theoretical melting temperatures calculated using Flory's theory of copolymer melting for random BrPEEK (unfilled black circules) and blocky BrPEEK (unfilled green squares) are also shown.

4.4.3 Isothermal Crystallization Kinetics

The effect of architecture on the time-scale of BrPEEK crystallization was investigated using DSC isothermal crystallization experiments. The crystallization kinetics of random and blocky BrPEEK at degrees of bromination up to 150 mol% were examined using the following approach:

$$F_c(t) = \frac{\int_0^t \frac{dH}{dt} dt}{\int_0^\infty \frac{dH}{dt} dt}$$

where $F_c(t)$ is the bulk fractional crystallinity of the brominated copolymer that is equal to the heat evolved during isothermal crystallization at a specific time t divided by the total heat evolved throughout the entire isothermal crystallization procedure. Isothermal crystallization was performed at temperatures between 230 and 320 ºC for random BrPEEK and between 270 and 320 ºC for blocky BrPEEK. The half times of crystallization, $t_{1/2}$, at each crystallization temperature were extracted from the crystallization isotherms ($F_c(t)$ vs. t) and compared to the PEEK homopolymer, as shown in **Figure 4.14**. At all analogous degrees of bromination, the $t_{1/2}$ values at a specific temperature are considerably shorter for blocky BrPEEK than for random BrPEEK. For example, at T_c = 290 ºC, PEEK and blocky BrPEEK50 crystallize in under a minute while random BrPEEK crystallizes takes 48 minutes ($t_{1/2}$ = 24 min) to crystallize. Overall, blocky BrPEEK samples exhibit rapid crystallization kinetics at time-scales similar to the PEEK homopolymer at high temperatures as well as high degrees of bromination (i.e. 150 mol%). Random BrPEEK, however, requires high degrees of supercooling to achieve rapid crystallization at fairly moderate degrees of bromination. The temperature must be lowered to 280 ºC to allow the complete crystallization of random BrPEEK50 in under ten minutes ($t_{1/2}$ < 5 min) and further lowered to 240 ºC for the same result with random BrPEEK75. The differences in crystallization kinetics are highly suggestive of the differences in architectures. The long uninterrupted segments of PEEK in the blocky BrPEEK readily associate into crystalline domains and thus facilitate rapid crystallization. For random BrPEEK, there is a much smaller population of uninterrupted PEEK segments of sufficient length of crystallize. Bromine defects are more likely to be encountered at the crystallization growth front in the random BrPEEK, resulting in rejection of the chain from the crystal and a prolonged crystallization time.

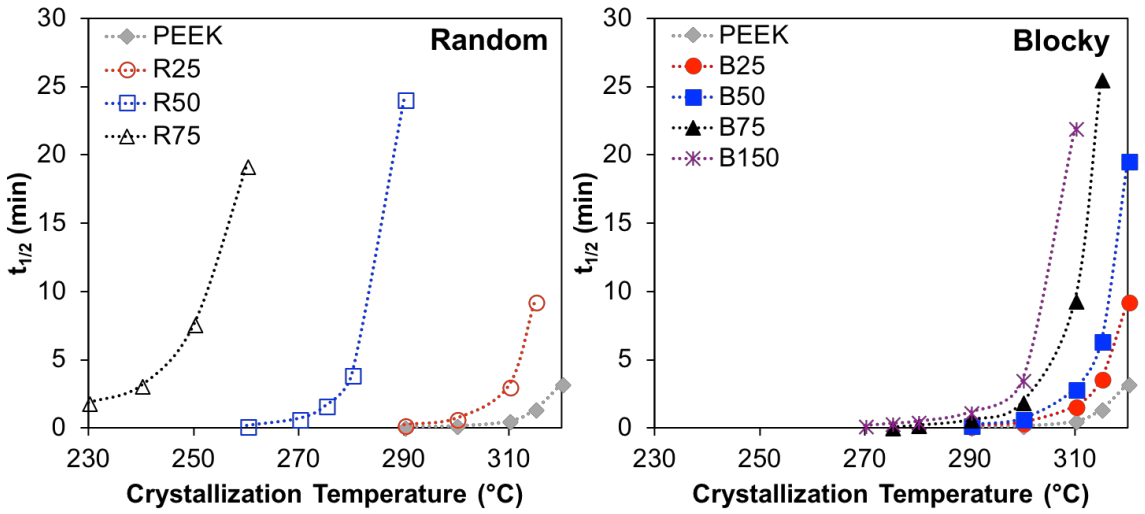

Figure 4.14. Half time of crystallization as determined by isothermal crystallization at various temperatures.

4.4.4 Morphological Analysis using USAXS/SAXS/WAXS

The crystalline morphology of isothermally crystallized BrPEEK was investigated using USAXS/SAXS/WAXD at Argonne National Labs. To prepare samples for scattering analysis, quenched films were annealed for 1 hour at 250 ºC. At this temperature and time-scale, complete crystallization is expected based on the crystallization kinetics described in the previous section. The WAXD regions (i.e., $q < 0.6$ Å^{-1}) of random and blocky BrPEEK are shown in **Figure 4.15**. The four distinct PEEK crystalline reflections indexed as (110), (111), (200), and (211) are apparent for random BrPEEK up to 75 mol% bromination and for blocky BrPEEK up to 175 mol%.[52-53] Thus, similar to the DSC results, blocky BrPEEK is crystallizable across all degrees of functionality while random BrPEEK is amorphous above 75 mol% bromination. For blocky BrPEEK at high degrees of functionality, it also interesting to note that the intensity of the WAXD spectra is attenuated due to the high concentration of bromines. Despite this, the crystalline reflections of PEEK are clearly observed.

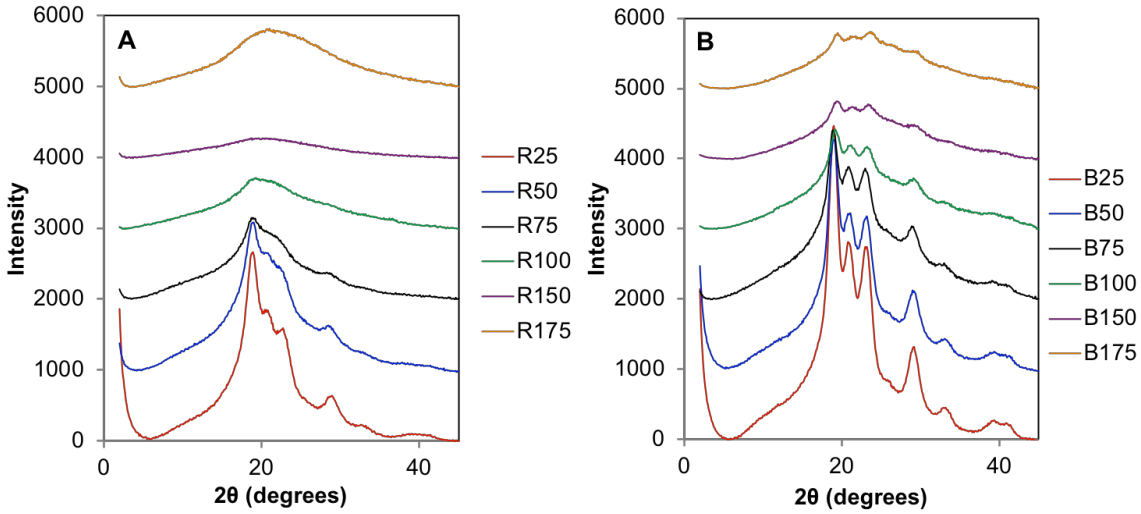

Figure 4.15. WAXD profiles of random BrPEEK (A) and blocky BrPEEK (B) at varying degrees of bromination.

The USAXS/SAXS scattering profiles of random and blocky BrPEEK at various degrees of bromination is displayed in **Figure 4.16**. In the SAXS region (i.e., 0.006 $Å^{-1} < q < 0.6$ $Å^{-1}$), a matrix knee appears for the semicrystalline BrPEEK at approximately 0.05 $Å^{-1}$ that may be attributed to the interlamellar scattering of the crystalline matrix.[54] For random BrPEEK, the interlamellar peak shifts to lower q with increasing degree of bromination, signifying an increase in the interlamellar spacing. In direct contrast, the blocky BrPEEK displays a shift in the semicrystalline peak towards larger q (i.e. smaller interlamellar dimension) with increasing degrees of bromination.

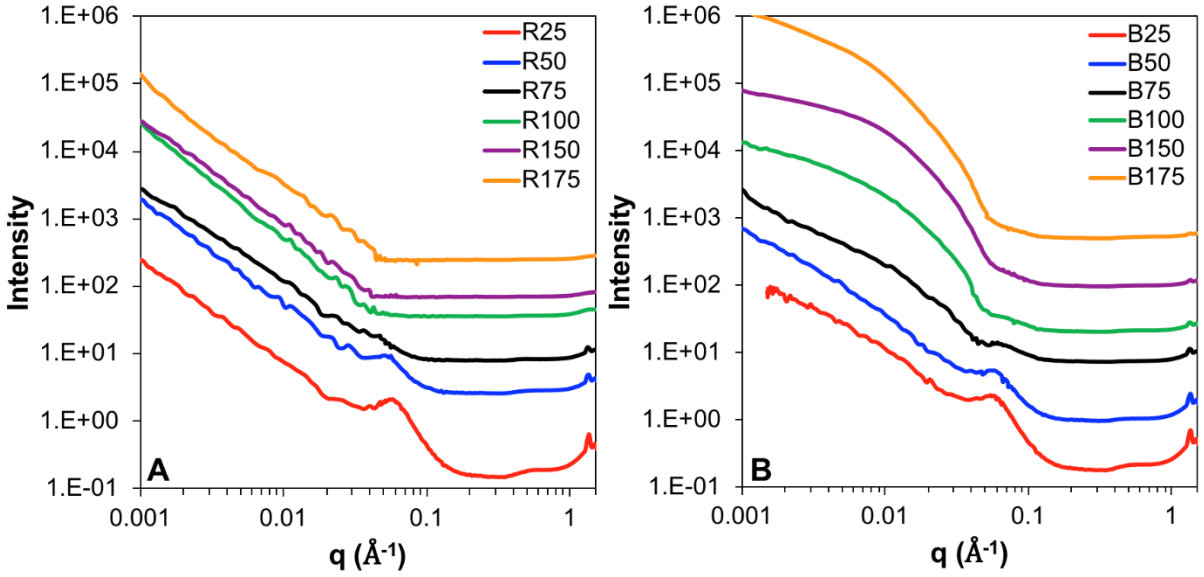

Figure 4.16. USAXS/SAXS/WAXS of random (A) and blocky (B) BrPEEK with increasing degrees of bromination.

To quantify the lamellar dimensions of the crystalline domains, the peak position of the interlamellar scattering feature was extracted from the Lorentz-corrected SAXS curve and was used to estimate the center-to-center crystalline domain spacing (i.e., long period) using Bragg's law ($d_{Bragg} = 2\pi/q$).[55] The long period, L_p, is defined as the sum of the lamellar thickness of the polymer crystal, l_c, and the thickness of the interlamellar amorphous region, l_a. Assuming a linear two-phase model, the l_c dimension is estimated by multiplying the volume fraction of crystallinity (ϕ_c) (determined using XRD) by the L_p. Thus, l_a is calculated by subtraction of l_c from L_p. As shown in **Table 4.3**, L_p increases from 11.5 nm to 16.2 nm for random BrPEEK as the degree of bromination increases from 25 to 75 mol%. L_p decreases from 11.7 nm to 8.2 nm for blocky BrPEEK as the degree of bromination increases from 25 to 150 mol%. Comparison of the crystalline thickness shows that l_c decreases with increasing degree of bromination for both random and blocky BrPEEK and little difference is observed in the l_c of the two architectures. Smaller crystals are expected due to the decrease in T_m observed with DSC, however, it is surprising that

the random and blocky BrPEEK display similar l_c dimensions despite the greater melting point depression of random BrPEEK. This unexpected result may stem from the simplification of the semicrystalline nature into a linear 2-phase approximation. The l_a dimensions mirror the changes observed for L_p, with random BrPEEK displaying an increase in l_a with increasing degree of bromination and blocky BrPEEK displaying a decrease in l_a. Thus, as the degree of bromination increases for blocky BrPEEK, the polymer crystals become smaller and more closely spaced whereas for random BrPEEK the polymer crystals become smaller and are spaced further apart.

Table 4.3. SAXS analysis of BrPEEK crystalline domains.

Sample	q (nm^{-1})	L_p (nm)	ϕ_c (vol%)	l_c (nm)	l_a (nm)
RBrPEEK25	0.55	11.5	0.36	4.1	7.4
BBrPEEK25	0.54	11.7	0.34	4.0	7.7
RBrPEEK50	0.46	13.6	0.24	3.3	10.3
BBrPEEK50	0.56	11.2	0.31	3.5	7.7
RBrPEEK75	0.39	16.2	0.15	2.4	13.8
BBrPEEK75	0.59	10.6	0.21	2.2	8.4
RBrPEEK100	-	-	-	-	-
BBrPEEK100	0.69	9.2	0.19	1.7	7.4
RBrPEEK150	-	-	-	-	-
BBrPEEK150	0.76	8.2	0.16	1.3	6.9

The quantitative changes in L_p were also confirmed using a 1-D correlation analysis (see **Table 4.4**), however, excess scattering at low q prevented this analysis in blocky BrPEEK samples above 75 mol% bromination. Similar to the results obtained using the two-phase analysis, the L_p of blocky BrPEEK decreases with increasing degree of bromination and the L_p of random BrPEEK increases with increasing degree of bromination.

Table 4.4. Interlamellar spacing of random and blocky BrPEEK using 1-D correlation analysis.

Sample	L_p (nm)
RBrPEEK25	9.7
BBrPEEK25	9.8
RBrPEEK50	10.6
BBrPEEK50	9.5
RBrPEEK75	11.6
BBrPEEK75	8.0

The USAXS region ($q < 0.006$ Å^{-1}) also demonstrates significant differences in the random and blocky BrPEEK copolymers. For the random BrPEEK, a power-law slope is observed at low *q*. This does not appear to change as the degree of bromination is increased from 25 to 175 mol%. In comparison, the blocky BrPEEK samples display a broad exponential knee at low *q*. This knee increases in intensity as the degree of bromination increases up to 175 mol%. A likely origin of this excess scattering at low *q* for the blocky BrPEEK samples is phase contrast between the densely brominated amorphous domains and the unbrominated polymer matrix. The peak increases in intensity with increasing degree of bromination because the concentration of the bromine group increases in the blocks, thereby improving contrast. Fitting of the knee using the Unified Fit Model provided by the Irena software shows an increasing domain size with increasing degree of bromination: 155 Å for blocky BrPEEK75, 168 Å for blocky BrPEEK100, 224 Å for blocky BrPEEK150, and 311 Å for blocky BrPEEK 175. It is useful to note that these domain sizes are similar to those of phase-separated block copolymers prepared by conventional synthetic methods.[56] This suggests that the gel state method is capable of producing blocky copolymers that perform like conventional block copolymers. No excess scattering at low *q* is observed for random BrPEEK because of the homogeneous distribution of the bromine groups within the polymer matrix which does not provide suitable phase contrast.

The morphology of quenched films of BrPEEK was also investigated using SAXS. For random BrPEEK, no noticeable difference is observed as the degree of bromination increases; samples from 25 – 150 mol% bromination exhibit similar SAXS profiles. For blocky BrPEEK, however, the intensity at $q \approx 0.2$ nm^{-1} increases with increasing degree of bromination. This is likely due to phase contrast between the brominated and unbrominated blocks, as described with respect to the crystallized BrPEEK samples. Thus, phase contrast is evident between the densely brominated blocks and the unfunctionalized blocks in the amorphous state as well as the semicrystalline state.

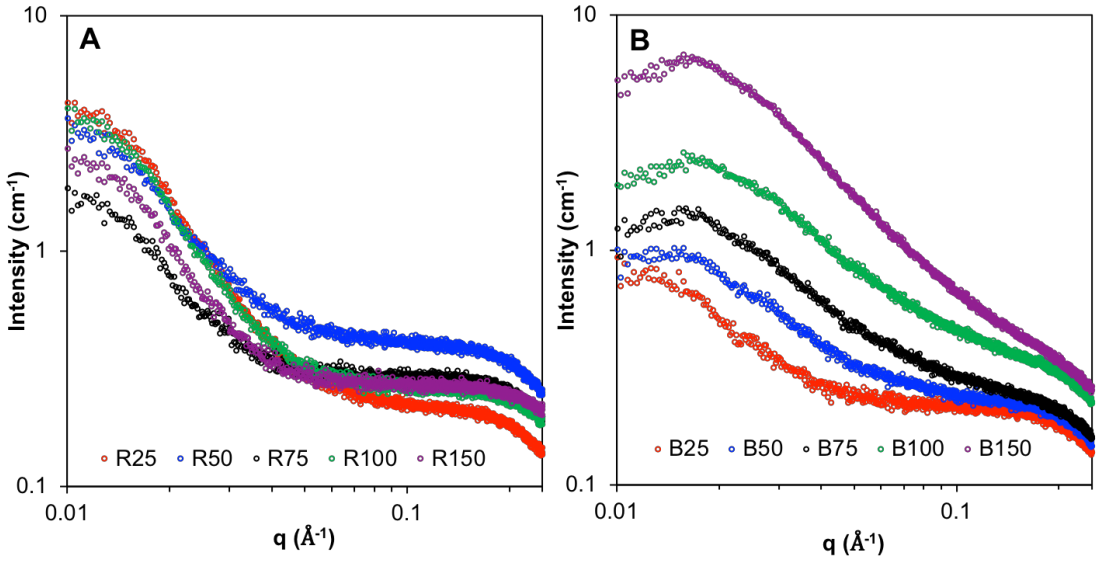

Figure 4.17. SAXS scattering profiles of random BrPEEK (A) and blocky BrPEEK (B) at varying degrees of bromination.

4.5 Influence of Gel Concentration on Blocky BrPEEK

The influence of gel concentration on the properties of blocky BrPEEK was also investigated. PEEK gels were prepared by dissolving PEEK in DCA at 185 ºC to final concentrations of 12.5 w/v%, 15.0 w/v%, 17.5 w/v%, 20.0 w/v%, and 22.5 w/v%. Once dissolved, the solutions were cooled to room temperature and allowed to gel at room temperature for several

days. Gels were then suspended to a final concentration of 10 w/v% in DCA and bromination targeting 100 mol% functionalization was carried out according to the procedure outlined in **Section 4.3.3**. The ^{1}H NMR spectra of the resultant products is shown in **Figure 4.18**. The degrees of bromination determined from integration of the ^{1}H NMR spectra were 101, 95, 96, 95, and 99 mol% for the 12.5, 15.0, 17.5, 20.0, and 22.5 w/v% PEEK gels, respectively. The ^{1}H NMR spectra display no significant differences among the samples, suggesting similar bromination architectures at this degree of bromination.

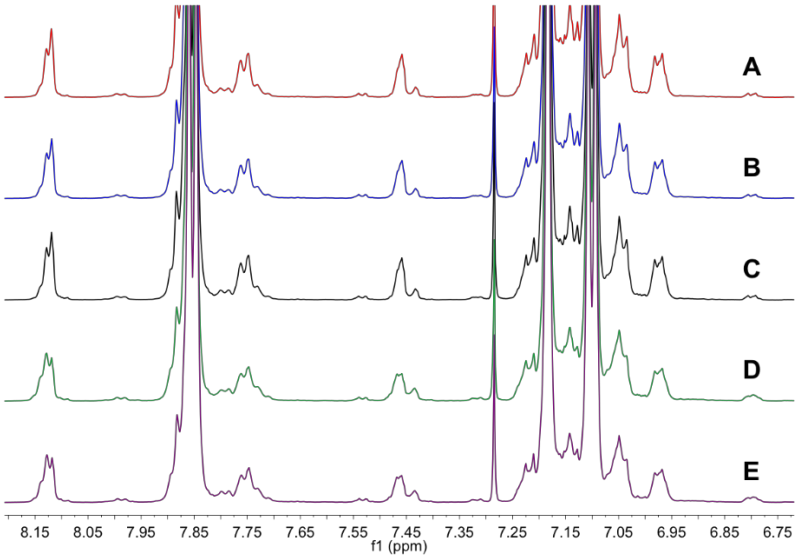

Figure 4.18. ^{1}H NMR spectra of blocky BrPEEK100 prepared from 12.5 w/v% (A), 15.0 w/v% (B), 17.5 w/v% (C), 20.0 w/v% (D), and 22.5 w/v% (E) PEEK gels. Solvent suppression ^{1}H NMR was performed using DCA/$CDCl_3$ as the solvent.

DSC was performed to determine the influence of the initial gel concentration on the crystallizability of the blocky BrPEEK100 samples. Samples were heated into the melt and then isothermally crystallized at 250 ºC for 1 hour. The subsequent heats, as shown in **Figure 4.19**, following isothermal crystallization were analyzed to determine T_g, T_m, and the degree of crystallinity. The T_g did not change as a result of the initial gel concentration and all blocky BrPEEK100 samples exhibited a T_g of approximately 175 ºC. Furthermore, a large double melting

endotherm was observed for all blocky BrPEEK100 samples at elevated temperatures. The double melting endotherm arises due to the isothermal nature of the crystallization, whereby primary and secondary crystallization occur. The lower melting temperature generally lies 5-30 ºC above the crystallization temperature and is associated with the melting of crystals formed during secondary crystallization while the upper melting temperature is associated with the melting of primary crystalline lamella.[57-59] It is apparent from **Figure 4.19** that the magnitude of the upper melting endotherm increases with increasing gel concentration. Furthermore, the upper melting endotherm appears to shift to slightly higher melting temperatures as the gel concentration is increased.

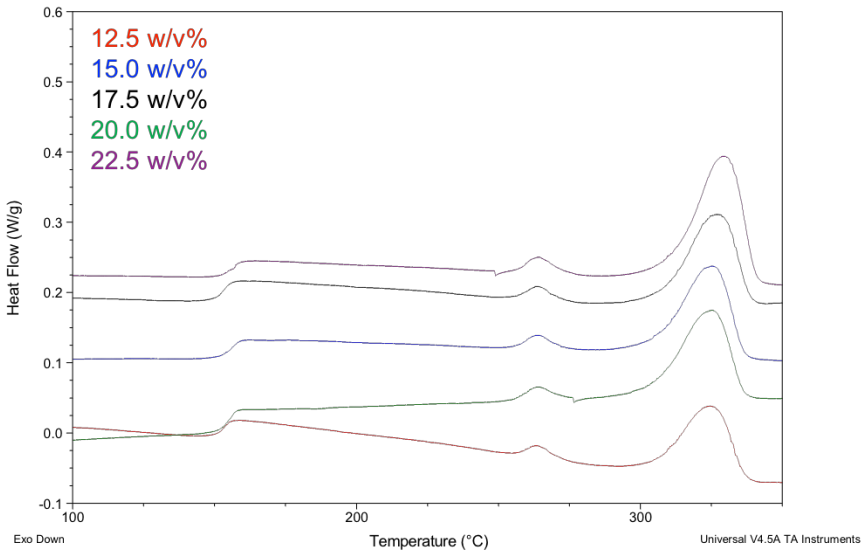

Figure 4.19. DSC thermograms of the heat following isothermal crystallization at 250 ºC for 1 hour for blocky BrPEEK100 prepared using various initial concentrations of PEEK gels.

To better quantify the change in thermal properties, the T_m of the upper melting endotherm and the degree of crystallinity obtained from integrating the melting endotherm are plotted as a function of initial gel concentration in **Figure 4.20**. These results are compared to the crystallization behavior of the as-precipitated BrPEEK100 samples determined from the first heat.

Following precipitation, blocky BrPEEK100 samples exhibit a melting temperature of approximately 332 ºC, independent of gel concentration. Upon isothermal crystallization from the melt, however, the melting temperature appears to increase linearly from 322 ºC for blocky BrPEEK100 prepared from a 12.5 w/v% gel to 329 ºC for blocky BrPEEK100 prepared from a 22.5 w/v% gel. Furthermore, the degree of crystallinity increases for blocky BrPEEK100 with increasing gel concentration. This effect is observed in both the first heat as well as the heat following isothermal crystallization. For both thermal histories, the X_c value of blocky BrPEEK prepared from a 22.5 w/v% gel is nearly twice that of blocky BrPEEK100 prepared from a 12.5 w/v% gel. Thus, regulation of the initial PEEK gel concentration may be utilized to tune the degree of crystallinity at a targeted degree of bromination.

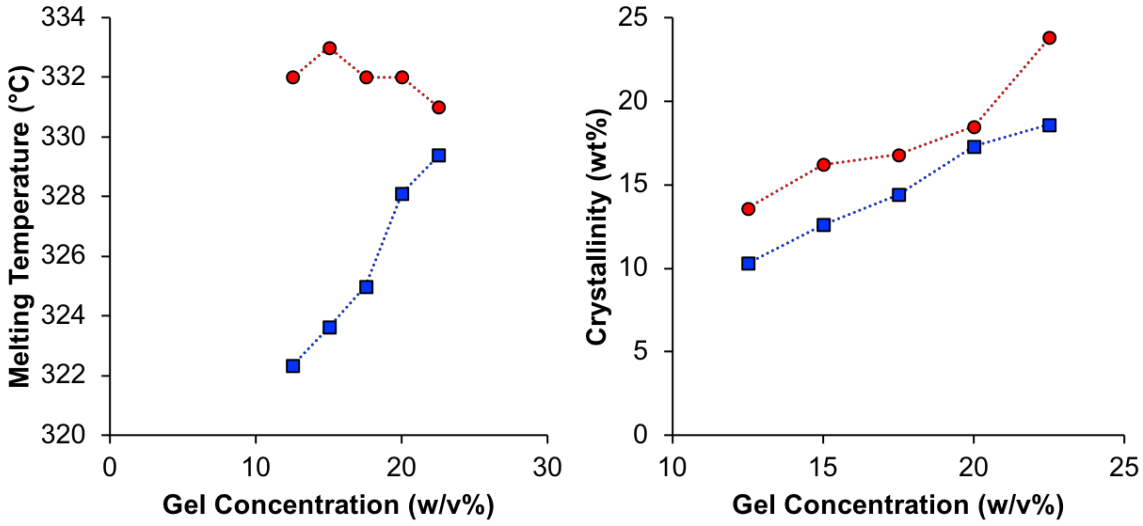

Figure 4.20. Melting temperature and percent crystallinity of blocky BrPEEK100 made from various initial concentrations of PEEK gels. Values were determined from the DSC thermograms of the first heat (red circles) and the heat following isothermal crystallization from the melt at 250 ºC for 1 hour (blue squares).

The crystallization kinetics of the blocky BrPEEK100 samples was also investigated using the analysis described in **Section 4.4.3**. Samples were isothermally crystallized at temperatures from 270 ºC to 310 ºC, and the resultant crystallization half-times ($t_{1/2}$) values were determined as

shown in **Figure 4.21**. Blocky BrPEEK100 prepared from all gel concentrations crystallizes rapidly (i.e. under 5 minutes) at temperatures of 290 ºC and above. Above 290 ºC, the $t_{1/2}$ values for blocky BrPEEK100 appear to decrease with increasing initial gel concentration. In fact, at 310 ºC, blocky BrPEEK100 from a 22.5 wt% gel completely crystallizes in 16 minutes whereas blocky BrPEEK100 from a 12.5 wt% gel takes 42 minutes at the same temperature. Thus, increasing the concentration of the PEEK gel used for bromination not only increases the crystallizability of the resultant blocky BrPEEK, but also results in faster crystallization kinetics.

It is important to note that no difference in crystallizability or crystallinity is observed for unfunctionalized PEEK precipitated from gels of concentrations between 12.5 w/v% and 22.5 w/v%. Thus, differences in the crystallizability and crystallization kinetics of blocky BrPEEK100 prepared from various concentration PEEK gels arises from subtle differences in the gel state during bromination. At 12.5 w/v%, the PEEK gels are very soft and disperse into small pieces readily when suspending in solvent and stirring. As the concentration of PEEK increases, the gel becomes more and more firm, and at 22.5 w/v%, the PEEK gels require significantly more work to break up and disperse the gels in solvent. While the 12.5 w/v% gels form a cloudy suspension with difficult to discern gel pieces, the 22.5 w/v% gels pieces appear more particulate in solution. The increased firmness and density of the gel pieces at high concentration may lead to a greater functionality at the surface of the gel, thus maintaining higher degrees of crystallinity overall upon functionalization.

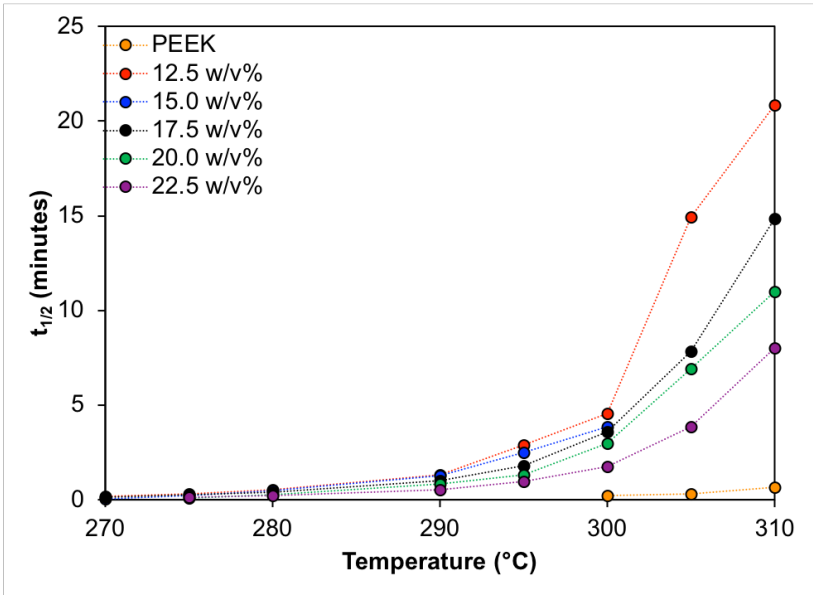

Figure 4.21. Half time of crystallization ($t_{1/2}$) of blocky BrPEEK100 prepared from PEEK gels of differing concentration.

The morphology of blocky BrPEEK100 prepared from various concentration PEEK gels was also investigated using USAXS/SAXS/WAXD analysis at Argonne national labs, as shown in **Figure 4.22**. Prior to analysis, quenched films were annealed at 250 ºC for 1 hour to crystallize the samples. In the WAXD region (i.e., $q < 0.6$ Å^{-1}), crystalline reflections are observed for all samples at positions similar to crystallized PEEK, demonstrating that the crystalline lattice structure does not change upon bromination. In the SAXS regions (i.e., 0.006 Å$^{-1} < q < 0.6$ Å^{-1}), a small peak at approximately $q = 0.06$ Å^{-1} is observed for all samples. This peak is attributed to the inter-lamellar scattering of the samples, and thus similar long periods are expected for blocky BrPEEK100 prepared from all concentrations of gels when the samples are crystallized from the melt. Using the two-phase approximation described in **Section 4.4.4** and the degree of crystallinity of the blocky BrPEEK100 samples, it is reasonable to assume that with increasing initial gel concentrations, a larger lamellar thickness and shorter amorphous thickness are expected. Finally,

in the USAXS region, (i.e., $q < 0.006$ Å^{-1}), excess scattering is observed due to the phase contrast between the densely brominated blocks and the unfunctionalized blocks, as described above.

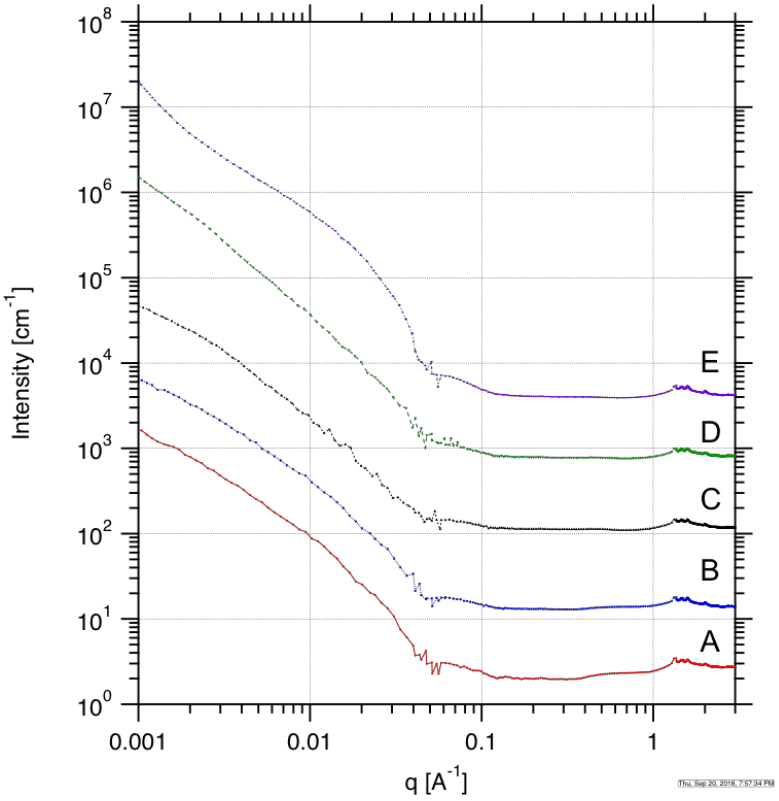

Figure 4.22. USAXS/SAXS/WAXD of blocky BrPEEK100 made from 12.5 w/v% (A), 15.0 w/v% (B), 17.5 w/v% (C), 20.0 w/v% (D), and 22.5 w/v% (E) PEEK gels in DCA.

Overall, bromination proceeds quantitatively using NBS in DCA using PEEK gels with concentrations ranging from 12.5 w/v% to 22.5 w/v%. No apparent difference is observed in the ^{1}H NMR spectra, suggesting similar bromination architectures for all blocky BrPEEK100 samples. The initial gel concentration was found to alter crystallization behavior, and blocky BrPEEK100 prepared from high concentration (22.5 w/v%) PEEK gels crystallized more rapidly and to a higher degree of crystallinity compared to gels of lower concentration (12.5 w/v%). Thus, the crystallizability of blocky BrPEEK may be altered not only by the degree of bromination, but also by the concentration of PEEK in the initial gel state. Further analysis on the morphology and

behavior of the PEEK gels during bromination is necessary to accurately determine the origin of this change in crystallizability with gel concentration.

4.6 Gelation of Blocky BrPEEK

Due to the high crystallizability of the blocky BrPEEK copolymers, as shown in **Table 4.2**, the ability of the BrPEEK samples to gel in DCA was investigated. This process yields insight into the functionalization architecture arising from the initial gel state of PEEK, and gelation of the BrPEEK would enable the production of functionalized aerogels with reactive moieties. Random and blocky BrPEEK samples at degrees of bromination from 25 – 150 mol% were dissolved in DCA at 185 ºC to a final concentration of 20 w/v%. For comparison, a PEEK sample was prepared in a similar manner. Once dissolved, samples were removed from heat and allowed to remain at room temperature. Gelation was defined by the passing of the 'tip test' in which the solution vial was inverted and the absence of flow noted gelation.

Within a two-week time frame, gelation was observed for PEEK, random BrPEEK25, and blocky BrPEEK at all degrees of bromination. The gelation time was found to increase with increasing degree of bromination; while PEEK itself gels in a matter of hours, random and blocky BrPEEK25 took 12 hours to gel and this gelation time increased to 2 weeks for blocky BrPEEK150. It is notable that no random BrPEEK sample above 25 mol% bromination is capable of gelling within 2 weeks. At low degrees of functionality (i.e. 25 mol%), random BrPEEK25 exhibits similar degrees of crystallinity, melting temperatures, and ratios of unfunctionalized homopolymer (X_A) (see **Table 4.2** and **Figure 4.12**) to blocky BrPEEK25. Thus, both random and blocky BrPEEK25 are capable of crystallizing and thereby gelling at similar time scales. At degrees of bromination of 50 mol% and above, however, random BrPEEK is not capable of gelling within two weeks. This is likely due to both the decrease in crystallinity and random distribution of functionality associated with homogeneous bromination. Because blocky BrPEEK150 is able

to gel within two weeks with less crystallinity than random BrPEEK50 (26% vs. 18%), it is evident that long domains of unfunctionalized homopolymer are necessary to enable gelation into a physical, crystalline network.

To investigate the morphology of the random and blocky BrPEEK gels, USAXS/SAXS analysis was performed at Argonne National Laboratory. The resultant scattering profiles are displayed in **Figure 4.23**. PEEK itself displays two prominent scattering features at q = 0.0006 Å^{-1} and at q = 0.04 Å^{-1}. All blocky BrPEEK gels similarly display two scattering features at q = 0.001 Å^{-1} and at q = 0.04 Å^{-1}, however, random BrPEEK25 displays only one feature at q = 0.04 Å^{-1}. The Unified Fit Model was applied to extract the radius of gyration (R_g) of the structural features using the Irena tool provided by Argonne.[60] The Unified Fit Model is a multi-level Beaucage model that fits structural levels comprised of a Guinier region and a power law tail.[61-62] The radii of gyration determined using this analysis are shown in **Table 4.5**. The feature observed at q = 0.04 Å^{-1} (R_{g2}) for all samples may be attributed the inter-lamellar scattering of the semicrystalline gels, and thus extraction of R_{g2} yields the lamellar thickness.[52] A R_{g2} value of approximately 5 nm was determined for PEEK and all blocky BrPEEK, and R_{g2} increased to 6.5 nm for random BrPEEK25. Clearly, the blocky BrPEEK prepared from the gel-state is able to crystallize to form similar crystalline lamella to the PEEK homopolymer. This further reiterates that the PEEK gel state is not perturbed throughout the blocky bromination process, and the original gel architecture controls the semicrystalline architecture of the resultant blocky BrPEEK. It is also important to note that as the degree of bromination increases, the peak position of the inter-lamellar scattering shifts to slightly lower q. The Bragg spacing ($d_{Bragg} = 2\pi/q$) is a measure of the long period of the polymer crystals, and this shift to lower q signifies an increase in the long period of the blocky BrPEEK crystals. Because the lamellar thickness does not change, this indicates that blocky BrPEEK gels have longer amorphous domains in between crystalline lamella than unfunctionalized PEEK gels.

At low q, R_{g1} was determined to be 311 nm for the PEEK gel and from 203-226 nm for blocky BrPEEK gels. No trend in R_{g1} was observed with increasing degrees of bromination. The peak associated with R_{g1} is likely due to aggregates of the crystalline lamellar stacks. Bromination thereby decreases the size of these aggregates from those of pure PEEK. The random bromination architecture, however, does not allow for the aggregation of the lamellar stacks as evidenced by a lack of scattering at low q. Further analysis is necessary to determine the precise origin of the aggregates and factors that dictate aggregate size.

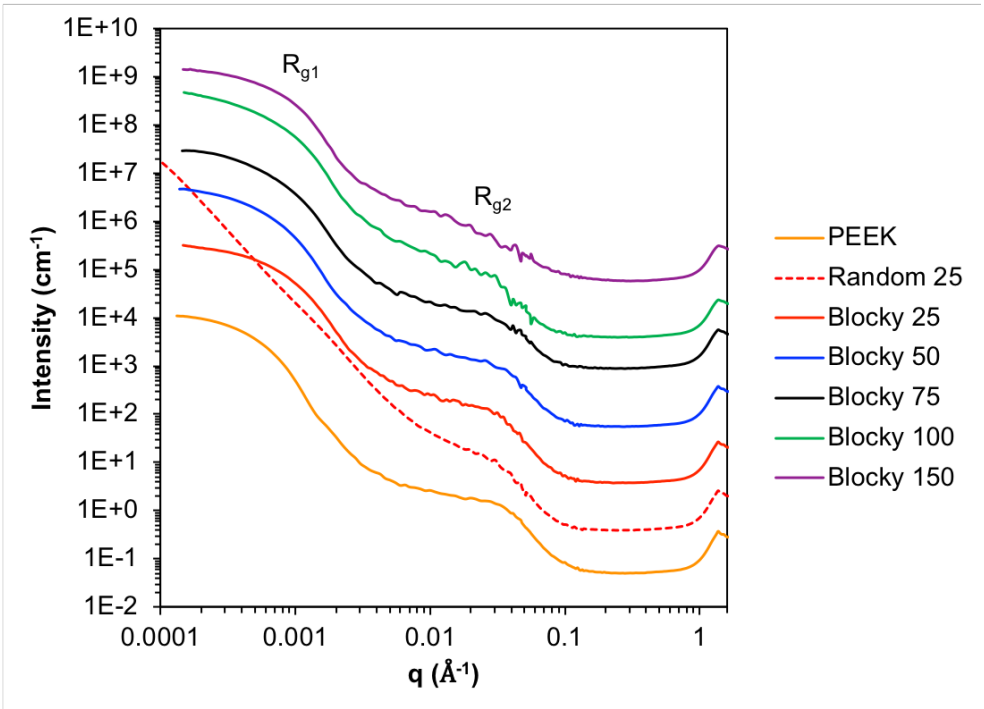

Figure 4.23. USAXS/SAXS scattering profiles of 20 w/v% PEEK and BrPEEK gels in DCA.

Table 4.5. Radii of gyration of 20 w/v% PEEK, random BrPEEK25, and blocky BrPEEK gels determined using the Unified Fit Model.

Sample	R_{g1} (nm)	R_{g2} (nm)
PEEK	311	5.0
R25	-	6.5
B25	203	5.3
B50	226	4.9
B75	215	5.1
B100	204	5.0
B150	212	5.0

To determine morphological differences in the random and blocky BrPEEK gels, gels were solvent-exchanged from DCA to water and freeze-dried to create aerogels. The aerogels were sputter-coated with iridium (5 nm thickness) in a Cressington 208HR high-resolution sputter coater and analyzed using field-emission scanning electron micrsocopy (FE-SEM) using a LEO (Zeiss) 1550 FE-SEM with in-lens detection. FE-SEM images of blocky BrPEEK25 and random BrPEEK25 are displayed in **Figure 4.24**. Both random and blocky BrPEEK25 gels consist of interconnected globular features. For blocky BrPEEK25, the aerogel morphology is similar to that of PEEK gels in DCA,[39, 63] where globular features are uniform in size (~200 nm) and display thin-layered assemblies that are reasonably attributed to the edges of stacked lamella. The random BrPEEK25 aerogel, however, has globular features that are not uniform in size and display more jagged features compared to blocky BrPEEK25. The lack of complete uniformity of the globular aggregate sizes may lead to the loss of the low *q* peak observed above in the random BrPEEK25 gels.

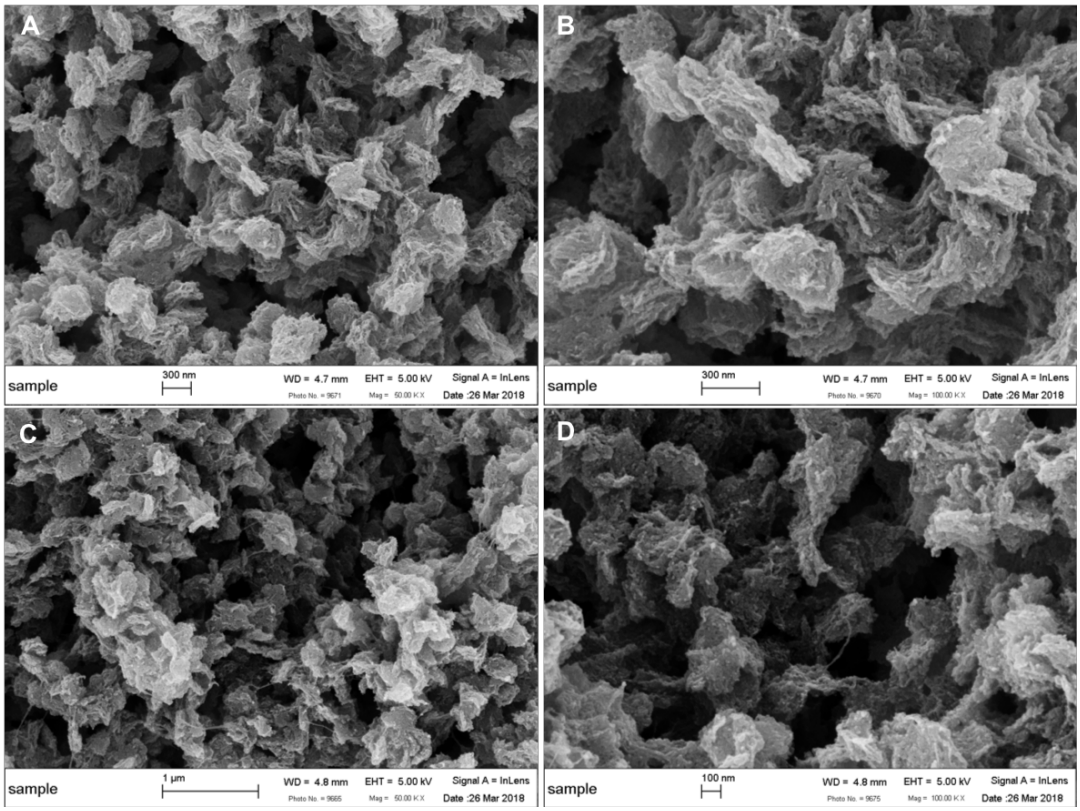

Figure 4.24. FE-SEM images of aerogels made from blocky BrPEEK25 (A, B) and random BrPEEK25 (C, D).

Overall, it is evident that the bromination conditions drastically influence the crystallizability and gelation of BrPEEK. When brominated in the gel-state, blocky BrPEEK up to 150 mol% brominated maintains a large fraction of unfunctionalized chain segments of sufficient length to crystallize and thereby is highly crystallizable. This enables the blocky BrPEEK samples to gel in DCA and form semicrystalline, thermoreversible gels with similar morphologies to pure PEEK gels. Random BrPEEK synthesized by solution-state bromination, however, is not capable of gelling above 25 mol% bromination because of the random distribution of functionality, which leads to statistically shorter domains of unfunctionalized homopolymer and less crystallizability.

4.7 Conclusions

In this chapter, the random and blocky bromination of poly(ether ether ketone) in dichloroacetic acid was investigated. Bromination with NBS in DCA was found to proceed

quantitatively in both the solution-state and in the gel-state to produce random and blocky BrPEEK, respectively. ^{1}H NMR and ^{13}C NMR spectroscopy demonstrated a higher ratio of unfunctionalized repeat units (X_A) in the blocky BrPEEK samples than random BrPEEK at similar degrees of functionalization. FTIR spectroscopy revealed that mono-bromination of aromatic rings dominates during random bromination, however, multiple bromination events per aromatic ring are prevalent for blocky bromination.

Thermal analysis of random and blocky BrPEEK revealed a linear increase in T_g with increasing degree of bromination, and similar T_g's were observed for random and blocky BrPEEK at similar degrees of bromination. Crystallization experiments demonstrated significant melting point depression and loss of crystallinity for random BrPEEK with increasing degree of bromination. In fact, no crystallinity was observed for random BrPEEK above 75 mol% bromination. Blocky BrPEEK, however, exhibited high crystallizability at all degrees of bromination. While the degree of crystallinity decreased slightly, little evidence of melting point depression was observed for blocky BrPEEK with increasing degree of bromination. The melting point depression was modeled using X_A and Flory's theory of crystallization in copolymers and the T_m's of random BrPEEK determined experimentally were found to be in good agreement with Flory's theory. Flory's theory, however, overestimated the melting point depression of blocky BrPEEK, providing further evidence that gel-state bromination leads to a blocky architecture with long chain segments of unfuntionalized homopolymer that is crystallizable. Finally, blocky BrPEEK was found to crystallize rapidly at all degrees of bromination, while random BrPEEK exhibited slower and slower crystallization kinetics with increasing degree of bromination.

The semicrystalline morphology of random and blocky BrPEEK was also examined using USAXS/SAXS/WAXD analysis. The long period was found to increase for random BrPEEK and decrease for blocky BrPEEK with increasing degree of bromination. Using the linear two-phase

model and the crystallinity values of the BrPEEK films, it was found that both random and blocky BrPEEK displayed similar decreases in lamellar thickness with increasing degree of bromination. The amorphous domain thickness, however, was found to increase for random BrPEEK and remained fairly unchanged for blocky BrPEEK. Thus, random BrPEEK formed crystals that were further spaced apart than for blocky BrPEEK. Furthermore, excess scattering was observed for blocky BrPEEK at low q due to phase contrast between the unfunctionalized blocks and densely brominated blocks. Fitting of the low q peak using the Unified Fit Model revealed increasing domain sizes with increasing degree of bromination, and these domains were similar in size to conventional block copolymers.

Initial gel concentration was also found to influence the crystallizability and crystallization kinetics of blocky BrPEEK. With increasing PEEK concentration in the initial gel used during the gel-state bromination, blocky BrPEEK was found to have higher crystallinity and more rapid crystallization kinetics. Thus, further control over crystallizability and bromination may be achieved by varying the PEEK gel concentration.

Finally, the gelation of BrPEEK was investigated. Blocky BrPEEK at up to 150 mol% bromination was found to gel at 20.0 w/v% in DCA within two weeks. In contrast, random BrPEEK25 was the only random sample capable of gelling during this time frame. USAXS/SAXS analysis demonstrated that blocky BrPEEK gels have multi-level ordering with semicrystalline morphologies and lamellar thicknesses similar to the pure PEEK gel. Random BrPEEK, however, displayed only an inter-lamellar scattering feature with larger crystalline lamella than blocky BrPEEK and PEEK. FE-SEM of BrPEEK aerogels revealed a globular structure for both blocky and random BrPEEK25, however, the size of the features was more uniform and the shape was less jagged in blocky BrPEEK25 than random BrPEEK25.

4.8 References

1. Cebe, P.; Hong, S.-D., Crystallization behaviour of poly(ether-ether-ketone). *Polymer* **1986,** *27* (8), 1183-1192.
2. Jones, D. P.; Leach, D. C.; Moore, D. R., Mechanical properties of poly(ether-ether-ketone) for engineering applications. *Polymer* **1985,** *26* (9), 1385-1393.
3. Wang, F.; Roovers, J., Functionalization of poly(aryl ether ether ketone) (PEEK): synthesis and properties of aldehyde and carboxylic acid substituted PEEK. *Macromolecules* **1993,** *26* (20), 5295-5302.
4. Blundell, D. J.; Osborn, B. N., The morphology of poly(aryl-ether-ether-ketone). *Polymer* **1983,** *24* (8), 953-958.
5. Conceição, T. F.; Bertolino, J. R.; Barra, G. M. O.; Pires, A. T. N., Poly (ether ether ketone) derivatives: Synthetic route and characterization of nitrated and sulfonated polymers. *Materials Science and Engineering: C* **2009,** *29* (2), 575-582.
6. Conceição, T. F.; Bertolino, J. R.; Barra, G. M. O.; Mireski, S. L.; Joussef, A. C.; Pires, A. T. N., Preparation and characterization of poly(ether ether ketone) derivatives. *Journal of the Brazilian Chemical Society* **2008,** *19*, 111-116.
7. Banerjee, S.; Kar, K. K., Impact of degree of sulfonation on microstructure, thermal, thermomechanical and physicochemical properties of sulfonated poly ether ether ketone. *Polymer* **2017,** *109*, 176-186.
8. Kaliaguine, S.; Mikhailenko, S.; Wang, K.; Xing, P.; Robertson, G.; Guiver, M., Properties of SPEEK based PEMs for fuel cell application. *Catalysis Today* **2003,** *82* (1), 213-222.
9. Lee, J. K.; Li, W.; Manthiram, A., Sulfonated poly(ether ether ketone) as an ionomer for direct methanol fuel cell electrodes. *Journal of Power Sources* **2008,** *180* (1), 56-62.
10. Xing, P.; Robertson, G. P.; Guiver, M. D.; Mikhailenko, S. D.; Wang, K.; Kaliaguine, S., Synthesis and characterization of sulfonated poly(ether ether ketone) for proton exchange membranes. *Journal of Membrane Science* **2004,** *229* (1–2), 95-106.
11. Huang, R. Y. M.; Shao, P.; Burns, C. M.; Feng, X., Sulfonation of poly(ether ether ketone)(PEEK): Kinetic study and characterization. *Journal of Applied Polymer Science* **2001,** *82* (11), 2651-2660.
12. Shukla, D.; Negi, Y. S.; Sen Uppadhyaya, J.; Kumar, V., *Synthesis and Modification of Poly(ether ether ketone) and their Properties: A Review*. 2012; Vol. 52, p 189-228.
13. Díez-Pascual, A. M.; Martínez, G.; Gómez, M. A., Synthesis and Characterization of Poly(ether ether ketone) Derivatives Obtained by Carbonyl Reduction. *Macromolecules* **2009,** *42* (18), 6885-6892.
14. Jasti, A.; Prakash, S.; Shahi, V. K., Stable and hydroxide ion conductive membranes for fuel cell applications: Chloromethyaltion and amination of poly(ether ether ketone). *Journal of Membrane Science* **2013,** *428*, 470-479.
15. Henneuse-Boxus, C.; Boxus, T.; Dulière, E.; Catherine, P.; Tesolin, L.; Adriaensen, Y.; Marchand-Brynaert, J., Surface amination of PEEK film by selective wet-chemistry. *Polymer* **1998,** *39* (22), 5359-5369.
16. Ummadisetty, S.; Kennedy, J. P., Quantitative syntheses of novel polyisobutylenes fitted with terminal primary □Br, □OH, □NH2, and methacrylate termini. *Journal of Polymer Science Part A: Polymer Chemistry* **2008,** *46* (12), 4236-4242.
17. Zheng, J.; Liu, F.; Lin, Y.; Zhang, Z.; Zhang, G.; Wang, L.; Liu, Y.; Tang, T., Synthesis of Diverse Well-Defined Functional Polymers Based on Hydrozirconation and Subsequent Anti-Markovnikov Halogenation of 1,2-Polybutadiene. *Macromolecules* **2012,** *45* (3), 1190-1197.

18. Guiver, M. D.; Kutowy, O., Method of manufacturing halogenated aromatic polysulfone compounds and the compounds so produced. Google Patents: 1991.
19. Shimura, T.; Watanabe, M.; Miyatake, K., Synthesis of superacid-modified poly(arylene ether sulfone)s via post-bromination. *RSC Advances* **2012,** *2* (12), 5199-5204.
20. Botvay, A.; Máthé, Á.; Pöppl, L.; Rohonczy, J.; Kubatovics, F., Preparation and characterization of brominated polyethersulfones. *Journal of Applied Polymer Science* **1999,** *74* (1), 1-13.
21. Weiber, E. A.; Jannasch, P., Polysulfones with highly localized imidazolium groups for anion exchange membranes. *Journal of Membrane Science* **2015,** *481*, 164-171.
22. Kim, H.-J.; Hong, S.-I., The transport properties of CO2 and CH4 for brominated polysulfone membrane. *Korean Journal of Chemical Engineering* **1999,** *16* (3), 343-350.
23. Xiao, Y.; Dai, Y.; Chung, T.-S.; Guiver, M. D., Effects of Brominating Matrimid Polyimide on the Physical and Gas Transport Properties of Derived Carbon Membranes. *Macromolecules* **2005,** *38* (24), 10042-10049.
24. Guiver, M. D.; Robertson, G. P.; Dai, Y.; Bilodeau, F.; Kang, Y. S.; Lee, K. J.; Jho, J. Y.; Won, J., Structural characterization and gas-transport properties of brominated matrimid polyimide. *Journal of Polymer Science Part A: Polymer Chemistry* **2002,** *40* (23), 4193-4204.
25. Hamad, F.; Khulbe, K. C.; Matsuura, T., Characterization of gas separation membranes prepared from brominated poly (phenylene oxide) by infrared spectroscopy. *Desalination* **2002,** *148* (1), 369-375.
26. White, D. M.; Orlando, C. M., Brominated Poly(Phenylene Oxide)s. II. Bromination of Poly(2,6-Dimethyl-1,4-Phenylene Oxide). In *Polyethers*, AMERICAN CHEMICAL SOCIETY: 1975; Vol. 6, pp 178-184.
27. Bonfanti, C.; Lanzini, L.; Roggero, A.; Sisto, R., Chemical modification of poly(2,6-dimethyl-1,4-phenylene oxide) by bromination-alkynylation. *Journal of Polymer Science Part A: Polymer Chemistry* **1994,** *32* (7), 1361-1369.
28. Wang, F.; Roovers, J., Functionalization of poly (aryl ether ether ketone): Synthesis of bromomethylated PEEK and its functionalization. *Journal of Polymer Science Part A: Polymer Chemistry* **1994,** *32* (13), 2413-2424.
29. Li, H.; Zhang, G.; Ma, W.; Zhao, C.; Zhang, Y.; Han, M.; Zhu, J.; Liu, Z.; Wu, J.; Na, H., Composite membranes based on a novel benzimidazole grafted PEEK and SPEEK for fuel cells. *International Journal of Hydrogen Energy* **2010,** *35* (20), 11172-11179.
30. Beasy, M.; Wang, F.; Roovers, J., Synthesis and bromination of di-, tri-and tetra-methyl substituted poly (aryl ether ether ketone) s. *Polymer Bulletin* **1994,** *32* (3), 281-287.
31. Si, J.; Lu, S.; Xu, X.; Peng, S.; Xiu, R.; Xiang, Y., A Gemini Quaternary Ammonium Poly (ether ether ketone) Anion-Exchange Membrane for Alkaline Fuel Cell: Design, Synthesis, and Properties. *ChemSusChem* **2014,** *7* (12), 3389-3395.
32. Shukla, D.; Negi, Y. S.; Kumar, V., Modification of Poly(ether ether ketone) Polymer for Fuel Cell Application. *Journal of Applied Chemistry* **2013,** *2013*, 7.
33. Bock, T. R. Catalytic phosphonation of high performance polymers and POSS - Novel components for polymer blend and nanocomposite fuel cell membranes. Ph.D. Dissertation, Albert-Ludwig University, Freidburg, Germany, 2006.
34. Rao, A. H. N.; Thankamony, R. L.; Kim, H.-J.; Nam, S.; Kim, T.-H., Imidazolium-functionalized poly(arylene ether sulfone) block copolymer as an anion exchange membrane for alkaline fuel cell. *Polymer* **2013,** *54* (1), 111-119.
35. Zhao, Z.; Wang, J.; Li, S.; Zhang, S., Synthesis of multi-block poly(arylene ether sulfone) copolymer membrane with pendant quaternary ammonium groups for alkaline fuel cell. *Journal of Power Sources* **2011,** *196* (10), 4445-4450.

36. Fahs, G. B.; Benson, S. D.; Moore, R. B., Blocky Sulfonation of Syndiotactic Polystyrene: A Facile Route toward Tailored Ionomer Architecture via Postpolymerization Functionalization in the Gel State. *Macromolecules* **2017,** *50* (6), 2387-2396.
37. Anderson, L. J.; Yuan, X.; Fahs, G. B.; Moore, R. B., Blocky Ionomers via Sulfonation of Poly(ether ether ketone) in the Semicrystalline Gel State. *Macromolecules* **2018**.
38. Noble, K. F.; Noble, A. M.; Talley, S. J.; Moore, R. B., Blocky bromination of syndiotactic polystyrene via post-polymerization functionalization in the heterogeneous gel state. *Polymer Chemistry* **2018**.
39. Talley, S. J.; Yuan, X.; Moore, R. B., Thermoreversible Gelation of Poly(ether ether ketone). *ACS Macro Letters* **2017,** *6* (3), 262-266.
40. J. Talley, S.; L. AndersonSchoepe, C.; J. Berger, C.; A. Leary, K.; A. Snyder, S.; Moore, R., *Mechanically robust and superhydrophobic aerogels of poly(ether ether ketone)*. 2017; Vol. 126.
41. Ilavsky, J.; Zhang, F.; Allen, A. J.; Levine, L. E.; Jemian, P. R.; Long, G. G., Ultra-Small-Angle X-ray Scattering Instrument at the Advanced Photon Source: History, Recent Development, and Current Status. *Metallurgical and Materials Transactions A* **2013,** *44* (1), 68-76.
42. Ilavsky, J.; R. Jemian, P., *Irena: Tool Suite for Modeling and Analysis of Small Angle Scattering*. 2009; Vol. 42, p 347-353.
43. Ilavsky, J., Nika: software for two-dimensional data reduction. *Journal of Applied Crystallography* **2012,** *45* (2), 324-328.
44. Rajesh, K.; Somasundaram, M.; Saiganesh, R.; Balasubramanian, K. K., Bromination of Deactivated Aromatics: A Simple and Efficient Method. *The Journal of Organic Chemistry* **2007,** *72* (15), 5867-5869.
45. Duan, J. X.; Zhang, L. H.; Dolbier, W. R., *A convenient new method for the bromination of deactivated aromatic compounds*. 1999; p 1245-1246.
46. Perrot, C.; Gonon, L.; Marestin, C.; Morin, A.; Gebel, G., Aging mechanism of Sulfonated poly(aryl ether ketone) (sPAEK) in an hydroperoxide solution and in fuel cell. *Journal of Power Sources* **2010,** *195* (2), 493-502.
47. Al Lafi, A. G., The sulfonation of poly(ether ether ketone) as investigated by two-dimensional FTIR correlation spectroscopy. *Journal of Applied Polymer Science* **2015,** *132* (2), n/a-n/a.
48. McCaig, S.; Seo, E. D.; Paul, D. R., *Effects of bromine substitution on the physical and gas transport properties of five series of glassy polymers*. 1999; Vol. 40, p 3367-3382.
49. Mukherjee, A. K.; Mohan, A., Thermal studies on brominated atactic polypropylene. *Journal of Applied Polymer Science* **1992,** *44* (5), 773-779.
50. Flory, P. J., Theory of crystallization in copolymers. *Transactions of the Faraday Society* **1955,** *51* (0), 848-857.
51. Flory, P. J., Thermodynamics of Crystallization in High Polymers II. Simplified Derivation of Melting‐Point Relationships. *The Journal of Chemical Physics* **1947,** *15* (9), 684-684.
52. Hsiao, B. S.; Gardner, K. H.; Wu, D. Q.; Chu, B., Time-resolved X-ray study of poly(aryl ether ether ketone) crystallization and melting behaviour: 1. Crystallization. *Polymer* **1993,** *34* (19), 3986-3995.
53. Fougnies, C.; Damman, P.; Dosière, M.; Koch, M. H. J., Time-Resolved SAXS, WAXS, and DSC Study of Melting of Poly(aryl ether ether ketone) (PEEK) Annealed from the Amorphous State. *Macromolecules* **1997,** *30* (5), 1392-1399.
54. Gebel, G., Structure of Membranes for Fuel Cells: SANS and SAXS Analyses of Sulfonated PEEK Membranes and Solutions. *Macromolecules* **2013,** *46* (15), 6057-6066.

55. Crevecoeur, G.; Groeninckx, G., Binary blends of poly (ether ether ketone) and poly (ether imide): miscibility, crystallization behavior and semicrystalline morphology. *Macromolecules* **1991,** *24* (5), 1190-1195.
56. Lohse, D. J.; Hadjichristidis, N., Microphase separation in block copolymers. *Current Opinion in Colloid & Interface Science* **1997,** *2* (2), 171-176.
57. Tan, S.; Su, A.; Luo, J.; Zhou, E., Crystallization kinetics of poly(ether ether ketone) (PEEK) from its metastable melt. *Polymer* **1999,** *40* (5), 1223-1231.
58. Verma, R. K.; Velikov, V.; Kander, R. G.; Marand, H.; Chu, B.; Hsiao, B. S., SAXS studies of lamellar level morphological changes during crystallization and melting in PEEK. *Polymer* **1996,** *37* (24), 5357-5365.
59. Chen, H.-L.; Porter, R. S., Melting behavior of poly(ether ether ketone) in its blends with poly(ether imide). *Journal of Polymer Science Part B: Polymer Physics* **1993,** *31* (12), 1845-1850.
60. Ilavsky, J.; Jemian, P. R., Irena: tool suite for modeling and analysis of small-angle scattering. *Journal of Applied Crystallography* **2009,** *42* (2), 347-353.
61. Beaucage, G., Approximations leading to a unified exponential/power‐law approach to small‐angle scattering. *Journal of Applied Crystallography* **1995,** *28* (6), 717-728.
62. Beaucage, G., Small‐angle scattering from polymeric mass fractals of arbitrary mass‐fractal dimension. *Journal of Applied Crystallography* **1996,** *29* (2), 134-146.
63. Talley, S. J.; AndersonSchoepe, C. L.; Berger, C. J.; Leary, K. A.; Snyder, S. A.; Moore, R. B., Mechanically robust and superhydrophobic aerogels of poly(ether ether ketone). *Polymer* **2017,** *126* (Supplement C), 437-445.

Chapter 5

Sulfonation of Blocky Brominated PEEK to Prepare Hydrophilic-Hydrophobic Blocky Copolymers for Efficient Proton Conduction

(*Manuscript Submitted for Publication to Solid State Ionics*)

Lindsey J. Anderson, Robert B. Moore*

Department of Chemistry, Macromolecules Innovation Institute, Virginia Polytechnic Institute and State University, Blacksburg, Virginia 24061, United States

*To whom correspondence should be addressed: rbmoore3@vt.edu

5.1 Abstract

Hydrophilic-hydrophobic blocky copolymers of poly(ether ether ketone) (PEEK) were prepared using a two-step post-polymerization technique. First, PEEK was brominated in the semicrystalline gel state to create a blocky BrPEEK template, which was subsequently functionalized by sulfonating the remaining runs of unfunctionalized PEEK units. The resultant degree of sulfonation of the blocky brominated, sulfonated PEEK (BrSPEEK) copolymers was inversely related to the degree of bromination, and degrees of sulfonation ranging from 26 to 71 mol% were obtained for degrees of bromination between 27 and 144 mol%. Thermal analysis using DSC and DMA revealed distinct multi-phase behavior for blocky BrSPEEK copolymers at degrees of sulfonation up to 40 mol%, suggesting phase separation between the densely brominated blocks and the sulfonated blocks into hydrophobic and hydrophilic domains, respectively. This phase separation contributed to improved dimensional stability upon swelling and enhanced proton transport at lower water content for blocky BrSPEEK membranes compared to random SPEEK membranes. Finally, morphological analysis using SAXS demonstrated that ionic aggregate size remained relatively unchanged for blocky BrSPEEK at all degrees of

sulfonation, and the ionic aggregates became more closely spaced with increasing degree of sulfonation. Overall, this work demonstrates a facile, post-polymerization technique to prepare hydrophilic, hydrophobic blocky copolymers with excellent dimensional swelling and transport properties that rival those of directly polymerized block copolymers.

5.2 Introduction

Aromatic hydrocarbon-based polymers have been widely explored as potential proton exchange (PEM) membranes due to their low cost, great mechanical properties, and high thermal and chemical stability.[1-2] Primarily, these membranes are prepared by post-polymerization sulfonation of high performance aromatic polymers such as poly(arylene ether ketones)[3-6], poly(sulfones)[7-9], and poly(ether sulfones)[10-12] or by direct polymerization using sulfonated monomers.[1, 13-15] Membrane performance is dictated by the degree of sulfonation, and high proton conductivity is achieved at high ion exchange capacities (IEC).[16] At high degrees of functionalization, however, excessive swelling in hydrated conditions is commonly observed in the randomly sulfonated membranes, leading to dilution of the charge carriers (i.e. a reduction in proton conductivity) and a loss of mechanical strength.[17] The incorporation of hydrophobic domains, such as halogenated repeat units, into these random copolymer systems has been found to enhance membrane mechanical properties, improve dimensional stability during swelling and deswelling, and provide suitable proton conductivity.[18-21]

Further efforts to improve hydrocarbon membrane properties and to develop proton exchange membranes with controlled water uptake, mechanical stability, and excellent proton transport at high IEC have focused on the synthesis of multiblock copolymers comprised of hydrophobic blocks and hydrophilic blocks.[19, 22-27] Most commonly, these block copolymers are prepared by step-growth polymerization from oligomers of each desired block, utilizing a densely

sulfonated block to provide acidic sites for proton transport and a hydrophobic block to impart mechanical integrity. Enhanced phase-separation between the hydrophilic and hydrophobic domains results in continuous hydrophilic domains, leading to improved proton transport relative to random analogs. The water uptake, proton conductivity, and mechanical properties of multiblock copolymer membranes is readily tuned by varying the lengths of the hydrophilic and hydrophobic components.[28] The wide-spread application of these multiblock systems is limited, however, due to the generally arduous synthetic procedures, limited commercial availability of sulfonated monomers, and decreasing reactivity of the sulfonated oligomers at mild reaction conditions, which limits the resultant molecular weight of the copolymers.[20, 29]

Our recent results show that is now possible to synthesize blocky copolymers by functionalizing in the semicrystalline gel state.[30-32] During this gel-state process, the functionalization reagent is sterically excluded from the tightly-packed crystalline domains, and thus, functionalization is restricted to the solvent-swollen amorphous segments within the semicrystalline network. This results in a blocky copolymer with highly functionalized 'blocks' and unfunctionalized, crystallizable 'blocks'. Blocky copolymers of sulfonated poly(ether ether ketone) (SPEEK) prepared in this manner exhibited enhanced crystallizability and more rapid crystallization kinetics than random copolymers at similar degrees of sulfonation, suggesting long 'blocks' of unfunctionalized PEEK remained due to the gel-state functionalization process. The blocky architecture also facilitated enhanced proton transport for blocky SPEEK compared to random SPEEK at similar degrees of sulfonation.[31] By establishing a blocky architecture during the gel-state functionalization process, it is now possible to perform secondary reactions in the homogeneous solution state while preserving the blocky architecture. For example, hydrophilic-hydrophobic block copolymers may be prepared by first brominating in the gel-state to establish the blocky architecture and then sulfonating the remaining unfunctionalized blocks. In this work,

the secondary sulfonation of blocky BrPEEK prepared by gel-state bromination is examined. Blocky BrPEEK was chosen as the starting material because high functionality is achievable (over 150 mol%)[33] with high degrees of crystallinity (i.e., attributed to long runs of unfunctionalized repeat units), thereby providing densely brominated hydrophobic "blocks" and polar functional "blocks." It is anticipated that the sulfonation of blocky BrPEEK will yield copolymers capable of undergoing hydrophilic-hydrophobic phase separation,[34] and the effect of this phase behavior will be investigated with respect to membrane properties such as water uptake, dimensional stability upon swelling, and proton conductivity.

5.3 Experimental

5.3.1 Materials

Poly(ether ether ketone) (PEEK) pellets (Victrex 150G) were acquired from Victrex. Dichloroacetic acid (DCA) was purchased from Sigma-Aldrich and was dried using magnesium sulfate (Fisher Scientific) then filtered through a 0.45 μm PTFE syringe filter prior to use. *N*-bromosuccinimide (NBS) was purchased from Sigma-Aldrich and was purified by recrystallization from water. Concentrated sulfuric acid (98%), sodium chloride, and cesium chloride were purchased from Fisher Scientific and used as received. Dimethylacetamide (DMAc) was purchased from Sigma-Aldrich and used as received.

5.3.2 Sulfonation of Blocky BrPEEK

Blocky BrPEEK was first prepared by brominating PEEK in the semicrystalline gel state. PEEK gels were prepared by dissolving PEEK (5 g) in dichloroacetic acid (DCA) to a final concentration of 20 w/v% at 185 ºC. Once dissolved, the PEEK solution was removed from heat and left at room temperature for at least 24 hours, during which PEEK crystallizes from solution to form a thermoreversible gel network.[35-36] The gel was then broken up into small pieces and dispersed in DCA to a final concentration of 10 w/v%. The gel suspension was equilibrated at 80

ºC under argon for 1 hour, and then a solution of *N*-bromosuccinimide (NBS) in DCA (20 mL) was added dropwise. Degrees of bromination of 25, 50, 75, 100, and 150 mol% were targeted by varying the molar ratio of NBS to PEEK repeat units used. The reaction proceeded at 80 ºC for 24 hours and was terminated by precipitation into DI H_2O. The product was filtered, washed with H_2O, and then washed by Soxhlet extraction over methanol for 24 hours. The resulting blocky BrPEEK polymer was dried at 100 ºC for 12 hours to produce a white product that was used for subsequent sulfonation. The degree of bromination was determined using ^{1}H NMR.[33]

For the secondary sulfonation, blocky BrPEEK (5.0 g) was dissolved in dichloroacetic acid (DCA) at 150 ºC to a final concentration of 10 w/v%. Once fully dissolved, the solution temperature was lowered to 80 ºC and 140 mL of concentrated sulfuric acid (excess) was added to the reaction flask. The reaction was allowed to stir at 80 ºC under argon for 24 hours, and then the reaction was terminated by precipitation into cold DI H_2O. The product was filtered, washed with DI H_2O, and then washed by Soxhlet extraction over water for 24 hours. The resulting polymer was dried at 100 ºC for 12 hours.

5.3.3 Membrane Preparation

BrSPEEK samples (H^+-form) were dissolved in dimethylacetamide (DMAc) at 100 ºC to a final concentration of 12 w/v%. Once dissolved, the casting solution was cooled to room temperature and was filtered through a 0.45 μm PTFE syringe filter. The solutions were cast onto glass at 80 ºC using a doctor blade set to 7.5 mils. The films were left at 80 ºC for 30 minutes to dry, resulting in a membrane thickness of 25 μm. Membranes were removed from the glass by swelling in water and were subsequently dried at 100 ºC for 12 hours. To convert BrSPEEK membranes to the sodium form (Na^+-form), membranes were stirred in 2M NaCl (aq) for 24 hours. To convert to the cesium form (Cs^+-form) , BrSPEEK membranes were stirred in 1M CsCl (aq) for 24 hours. Following ion exchange, samples were removed from the salt solution, washed with

DI H_2O to remove residual salt, and dried at 100 ºC for 12 hours. Annealing of BrSPEEK membranes was carried out by first converting to Cs^+-form, and then putting membranes into an oven at 250 ºC for 2 hours.

5.3.4 ^{1}H NMR Spectroscopy

^{1}H NMR spectra of the blocky BrPEEK were measured using a Bruker Avance III 600 MHz. BrPEEK samples were dissolved in DCA/$CDCl_3$ solvent mixture and a solvent suppression method was utilized to resolve the spectra, as described previously.[33] ^{1}H NMR spectra of blocky BrSPEEK were measured using an Agilent U4-DD2 400 MHz NMR. BrSPEEK samples were dissolved in DMSO-d6 for analysis.

5.3.5 FTIR Spectroscopy

FTIR was performed using a Varian 670-IR spectrometer with a deuterated triglycine sulfate (DTGS) detector using the Pike Technologies GladiATR™ attachment (diamond crystal). Spectra were collected as the average of 32 scans at 4 cm^{-1} resolution. FTIR spectra were ATR corrected, baseline corrected, and normalized to the peak at 1590 cm^{-1} (C=C skeletal ring vibration)[38] prior to analysis.

5.3.6 Thermal Analysis

A TA Instruments Q2000 DSC was used to determine the thermal properties of blocky BrPEEK and BrSPEEK. BrSPEEK was ion-exchanged to Na^+-form or Cs^+-form prior to DSC measurements. Samples were pre-dried at 150 ºC for 5 minutes before several heating and cooling cycles. Dried samples (~5-8 mg) were heated from room temperature to 380 °C at 20 °C/min, quench cooled to 0 °C, and then heated to 380 °C at a rate of 20 °C/min. A TA Instruments Q800 DMA in oscillatory tension mode was used to determine the thermo-mechanical properties of quenched BrPEEK samples as a function of temperature. Samples were ramped at 2 ºC/min to 400

ºC at a frequency of 1 Hz, an oscillatory amplitude of 10 μm, and a static force of 0.01 N. DMA was performed on Na^+-form samples.

5.3.7 SAXS Analysis

Small angle x-ray scattering (SAXS) data were collected at Argonne National Laboratory beamline 9ID-C using a photon energy of 24 keV.[41] Scattering profiles are plotted as absolute intensity vs. q, where $q = \left(\frac{4\pi}{\lambda}\right)\sin(\theta)$, θ is one half of the scattering angle, and λ is the X-ray wavelength (0.5895 Å). SAXS measurements utilized the Pilatus 100k camera, and data reduction was performed using the Irena[42] and Nika[43] software packages provided by Argonne.

5.3.8 Water Uptake and Dimensional Swelling

The water uptake and swelling ratios of the BrSPEEK (H^+-form) membranes were determined by first drying membranes in a vacuum oven at 120 °C for 3 hours. The mass (W_{dry}) and dimensions ($L_{x,\,dry}$ x $L_{y,\,dry}$) of the dry membranes were recorded. Then, the samples were equilibrated in room temperature deionized water for 12 hours. Membranes were blotted to remove excess surface water and the mass (W_{wet}) and dimensions ($L_{x,\,wet}$ x $L_{y,\,wet}$) of the wet membranes were recorded. The water uptake and areal swelling ratio were calculated as:

$$\text{Water uptake} = \frac{(W_{\text{wet}} - W_{\text{dry}})}{W_{\text{dry}}} \times\ 100\% \qquad \textbf{(5.1)}$$

$$\text{Areal Swelling ratio} = \frac{\left(L_{\text{x,wet}} \times L_{\text{y,wet}}\right) - (L_{\text{x,dry}} \times L_{\text{y,dry}})}{(L_{\text{x,dry}} \times L_{\text{y,dry}})} \times\ 100\% \qquad \textbf{(5.2)}$$

The reported values are the average of four samples.

5.3.9 Proton Conductivity

Prior to analysis, BrSPEEK membranes were equilibrated in DI H_2O at room temperature for at least 12 hours. In-plane proton conductivity was conducted using a 4-point conductivity cell from Bekktech, which was immersed in DI H_2O at room temperature. Measurements were taken

from 1 Hz to 1.5 MHz at a voltage amplitude of 50 mV using a 1255 HF frequency analyzer coupled to a 1286 electrochemical interface, both from Solartron Analytical. Data analysis was performed using the Zplot® and Zview® software from Scribner and Associates, Inc. The proton conductivity was calculated as:

$$\sigma = \frac{1}{\rho} = \frac{l}{R \times A} \tag{5.3}$$

where σ (Scm^{-1}) is the conductivity, ρ (Ωcm) is the resistivity, l (cm) is the distance between the contacting electrodes, R (Ω) is the resistance determined from the real value of the complex impedance plot that corresponds to the minimum imaginary response, and A is the cross-sectional area of the membrane calculated from the width and thickness of the membrane. Measurements were performed on three separate membranes for each sample to ensure the reproducibility of results.

5.4 Results and Discussion

5.4.1 Synthesis of Blocky BrSPEEK

To synthesize blocky brominated-sulfonated PEEK (BrSPEEK), blocky BrPEEK was first prepared by brominating PEEK in the semicrystalline gel state using *N*-bromosuccinimide (NBS) in dichloroacetic acid (DCA). Blocky BrPEEK was chosen as a template for further sulfonation due to the high stability of the semicrystalline gel-state during bromination, which yields blocky copolymers with a wide range of functionality, a high degree of crystallizability, and thereby a large content of unfunctionalized chain segments of sufficient length of crystallize. The unfunctionalized, crystallizable 'blocks' are readily sulfonated using conventional procedures, and thus blocky BrPEEK provides a suitable template for hydrophobic-hydrophilic blocky copolymers consisting of densely brominated and sulfonated segments along a given chain. It is also important to note that the initial gel-state reactions generate the blocky template, and this allows for

secondary reactions in a homogeneous solution state while preserving the blocky architecture. Overall, this process allows for the development of hydrophilic-hydrophobic blocky copolymers using a simple post-polymerization functionalization procedure.

Blocky BrPEEK was prepared with target degrees of bromination at 25, 50, 75, 100, and 150 mol%, and the resultant degree of bromination for each sample was found to be 27, 56, 78, 101, and 144 mol%. Thus, near quantitative bromination was achieved due to the highly electrophilic character of NBS in strong acid, consistent with literature precedence for small molecules and for PEEK brominated in methanesulfonic acid.[33, 44-45] It is important to note that these high degrees of bromination (>100 mol%) are achievable because multiple sites on a single PEEK repeat unit are capable of being functionalized. A complete analysis of the spectroscopic, thermal, and morphological characteristics of blocky BrPEEK compared to random BrPEEK will be described in a subsequent publication.

Following the gel-state bromination, secondary sulfonation of the blocky BrPEEK was performed by dissolving the BrPEEK in DCA and then adding concentrated sulfuric acid (H_2SO_4), as shown in **Figure 5.1**. Sulfonation using H_2SO_4 proceeds via an electrophilic aromatic substitution reaction and occurs exclusively within the hydroquinone ring of the PEEK repeat unit due to the increased electron density from the electron-donating ether linkages.[6] The previously brominated rings are deactivated towards sulfonation due to the electron-withdrawing effect of the halogen. Likewise, only one sulfonation event per repeat unit is expected due to the electron-withdrawing effect of the sulfonic acid group. Thus, sulfonation occurs exclusively on the unfunctionalized repeat units of the blocky BrPEEK copolymers, and although this procedure is identical to that typically used to prepared random SPEEK from PEEK, the previously established blocky brominated architecture templates the sulfonation into distinct “blocks.”

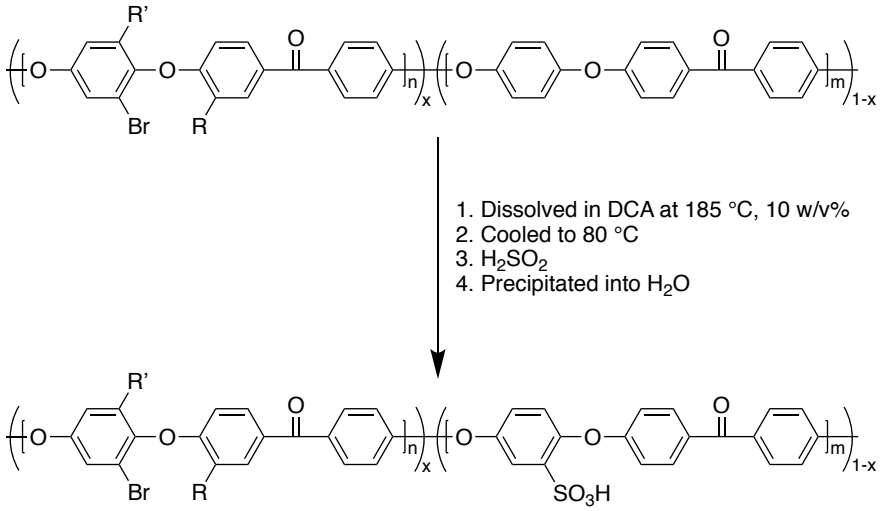

Figure 5.1. Reaction scheme for the sulfonation of blocky BrSPEEK from blocky BrPEEK.

The ^{1}H NMR spectra of blocky BrPEEK and the resultant blocky BrSPEEK is shown in **Figure 5.2**. Prior to sulfonation, blocky BrPEEK shows distinct doublets at 7.85 ppm and 7.10 ppm and a singlet at 7.15 ppm that are attributed to unfuntionalized PEEK repeat units within the blocky copolymers,[31] and peaks at 8.10 ppm, 7.75 ppm, 7.45 ppm, 7.03 ppm, and 6.75 ppm are attributed to the brominated repeat units.[33] Due to the large number of unfunctionalized repeat units, blocky BrPEEK is highly crystallizable and its solubility is limited to known solvents for PEEK, such as DCA. Upon sulfonation, the blocky BrSPEEK copolymers are no longer crystallizable and become readily soluble in polar aprotic solvents such as dimethyl sulfoxide (DMSO), dimethylacetamide (DMAc), and *N*-methyl-2-pyrrolidone (NMP). The ^{1}H NMR spectra of blocky BrSPEEK in DMSO-d6 reveals new peaks that arise at 7.47 ppm, 7.23 ppm, and 7.07 ppm. These peak positions are in close agreement with those of sulfonated PEEK (SPEEK) and arise due to shifts in the protons of the hydroquinone ring upon sulfonation, as assigned in **Figure 5.2**.[4, 6, 40] With decreasing degree of bromination, the peaks at 7.47 ppm, 7.23 ppm, and 7.07 ppm increase in intensity, suggesting an increase in the degree of sulfonation. The actual degree of sulfonation was quantified by integration of the peak at 7.47 ppm (a_3*), and the results are displayed in **Table 5.1**.

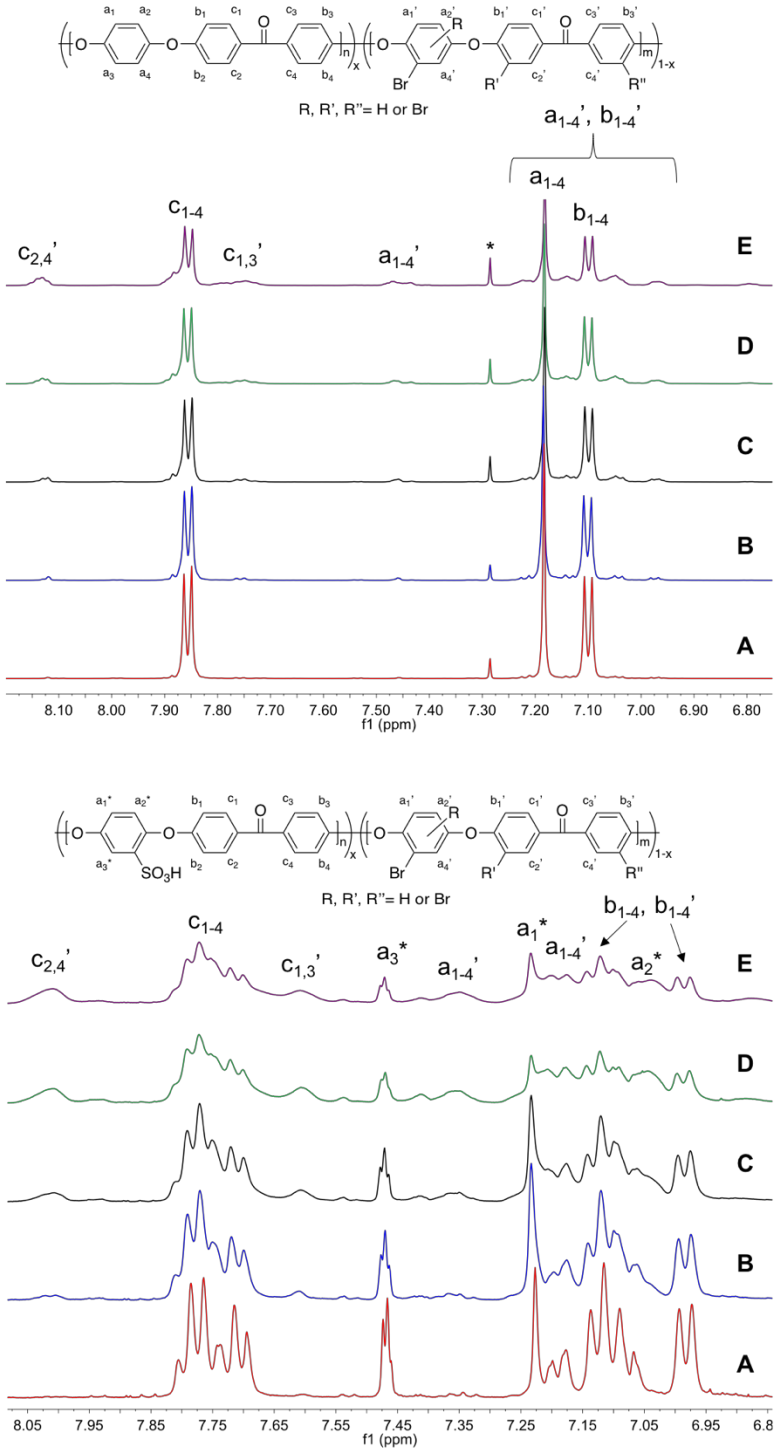

Figure 5.2. ^{1}H NMR spectra of blocky BrPEEK (top) at 25 (A), 50 (B), 75 (C), 100 (D), and 150 (E) mol% bromination and the ^{1}H NMR spectra of the resultant blocky BrSPEEK (bottom) following sulfonation. Blocky BrPEEK samples were analyzed using solvent suppression ^{1}H NMR using DCA/$CDCl_3$ mixed solvent. $CDCl_3$ is represented by an asterisk. BrSPEEK samples were run in DMSO-d6.

Integration of the BrSPEEK ^{1}H NMR spectra revealed degrees of sulfonation ranging between 26 mol% and 71 mol%, for BrPEEK templates containing degrees of bromination ranging from 144 mol% to 27 mol%, respectively. The degree of sulfonation was clearly limited by the degree of bromination, and as expected, the resultant degree of sulfonation decreased with increasing degree of bromination due to deactivation of brominated hydroquinone rings towards sulfonation. Because these reactions were run for long periods of time, it is likely that the BrSPEEK products are sulfonated to near their maximum extent, and this further confirms that the previously established brominated architecture not only templates the distribution of repeat units available for sulfonation, but also dictates the quantity of reactive units. Henceforth, the blocky BrSPEEK samples will be named as BrSPEEK*x*-*y* where *x* is the degree of bromination and *y* is the degree of sulfonation. It should be noted that $x + y \neq 100$ because it is possible to brominate multiple sites on a single PEEK repeat unit.

Table 5.1. Degree of bromination and degree of sulfonation determined by ^{1}H NMR.

Sample	Degree of Bromination (mol%)	Degree of Sulfonation (mol%)
BrSPEEK27-71	27	71
BrSPEEK56-52	56	52
BrSPEEK78-40	78	40
BrSPEEK101-30	101	30
BrSPEEK144-26	144	26

For comparison, random BrPEEK150 was also sulfonated according the procedure in **Section 5.3.2**. Random BrPEEK150 itself is completely amorphous due to the random distribution of bromines and high degree of bromination, and it is assumed that at least one bromine is present per repeat unit. The ^{1}H NMR spectra before and after sulfonation are shown in **Figure 5.3**. Following sulfonation, several new peaks appear between 7.4 ppm and 7.6 ppm associated with the protons adjacent to the sulfonic acid group. Because sulfonation is an electrophilic reaction, sulfonation is restricted to unfunctionalized hydroquinone domains, and several distinct chemical

environments arise due to different degrees of bromination of the adjacent benzophenone domain. This is noticeably different than the blocky BrSPEEK copolymers which display a single peak associated with the a_3^* proton at a chemical shift identical to that of pure SPEEK. This further exemplifies that the blocky architecture successfully templates the sulfonation reaction to completely unfunctionalized repeat units due to the relatively high degree of bromination within the densely brominated blocks (where little unfunctionalized hydroquinone domains exist for reactions).

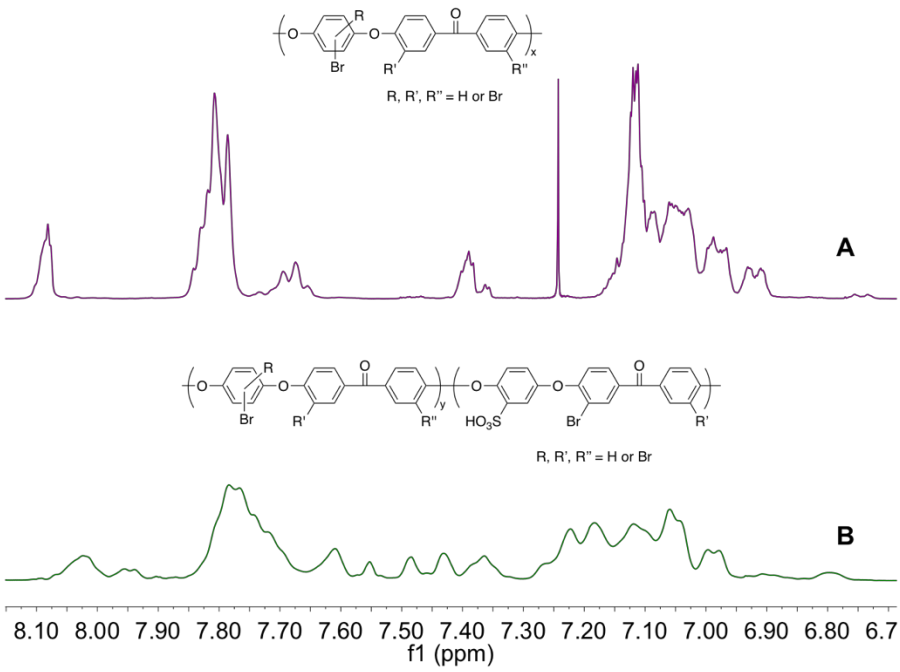

Figure 5.3. ^{1}H NMR spectra of random BrPEEK150 in $CDCl_3$ (A) and random BrSPEEK150 following sulfonation in DMSO-d6 (B).

The blocky BrSPEEK copolymers were also analyzed using FTIR spectroscopy, as shown in **Figure 5.4**. Prior to sulfonation, blocky BrPEEK copolymers exhibited several defining peaks. Peaks at 1490 cm^{-1} and 1470 cm^{-1} were assigned to the skeletal ring vibrations of 1,4-disubstituted aromatic rings and 1,2,4-trisubstituted aromatic rings, respectively.[47] The peak at 1470 cm^{-1} was larger for blocky BrPEEK150 than blocky BrPEEK25 due to the increased functionality of

BrPEEK150 yielding an increased number of trisubstituted aromatic rings. Furthermore, a peak is present at 1040 cm^{-1} that is attributed to aryl C-Br stretching.[48-49] Upon sulfonation of both BrPEEK27 and BrPEEK150, the peak at 1490 cm^{-1} drastically decreases in intensity and the peak at 1470 cm^{-1} increases in intensity, signifying the sulfonation of previously unfunctionalized hydroquinone rings of blocky BrPEEK copolymer. Little difference is observed between the normalized intensities of the BrSPEEK27-71 and BrSPEEK144-26 at 1490 cm^{-1} and 1470 cm^{-1}, suggesting that nearly all available reactive sites (on the hydroquinone ring) have been brominated or sulfonated in the resultant blocky BrSPEEK copolymers. Furthermore, new peaks arise at 705 cm^{-1} (S-O stretching), 1020 cm^{-1} (S=O stretching), 1075 cm^{-1} (O=S=O symmetric stretching), and 1250 cm^{-1} (O=S=O asymmetric stretching) due to introduction of the sulfonic acid sites to the polymer backbone.[47] These peaks are more intense for BrSPEEK27-71 than BrSPEEK144-26 because of its higher degree of sulfonation.[50]

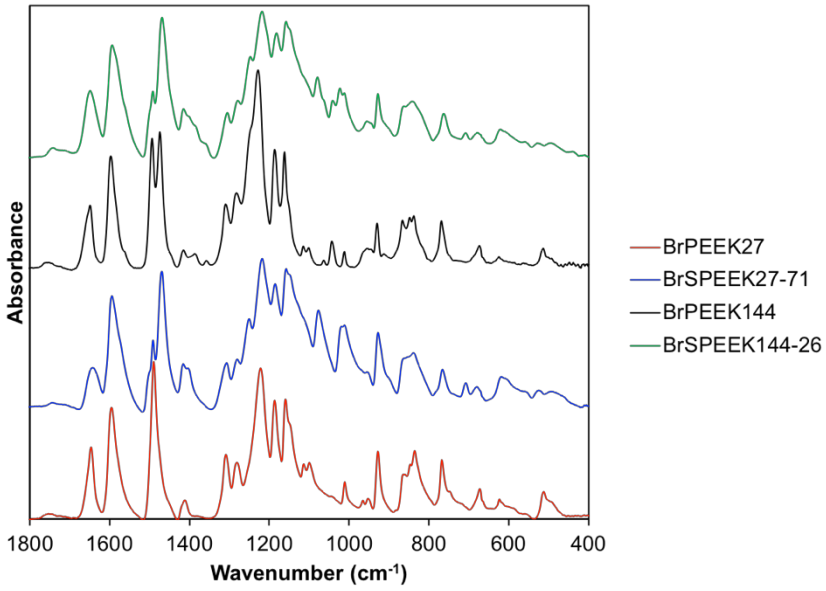

Figure 5.4. FTIR spectroscopy of BrPEEK27, BrSPEEK27-71, BrPEEK144, and BrSPEEK144-26.

5.4.2 Thermal Properties of Blocky BrSPEEK Membranes

Due to the high solubility of BrSPEEK in polar aprotic solvents, BrSPEEK solutions were readily cast from DMAc to form tough, crease-able membranes. The thermal properties of the resultant membranes were analyzed using DSC, as shown in **Figure 5.5**. All blocky BrSPEEK membranes are completely amorphous, indicating that all (or most) of the crystalline domains within the initial blocky BrPEEK have been functionalized. At high degrees of bromination, the BrSPEEK78-40, BrSPEEK101-30, and BrSPEEK144-26 samples all show two distinct glass transitions in the DSC thermograms. This dual T_g behavior, commonly observed in conventional block copolymers, is clear evidence that the gel-state functionalization process creates a well-defined blocky microstructure such that bromine-dense "blocks" phase separate from the ion-dense "blocks", resulting in a low T_g and a high T_g for the brominated and sulfonated "blocks," respectively. The T_g's determined from the DSC thermograms are shown in **Table 5.2**. As the degree of bromination decreases (and degree of sulfonation increases), the low temperature glass transition decreases in magnitude and the high temperature glass transition increases in magnitude, consistent with the change in functionalization. At high degrees of sulfonation (i.e. BrSPEEK56-52, BrSPEEK27-71), only one glass transition temperature is observed at high temperatures, associated with the T_g of the sulfonated blocks. It is likely that at these lower degrees of bromination, the electrostatic network dominates the mobility of the polymer chains, and thus it is difficult to observe a T_g from the brominated blocks.[51] Overall, the DSC results suggest that the blocky BrSPEEK copolymers are forming phase-separated microstructures, attributed to a distinct blocky character, that results in multiple glass transitions.

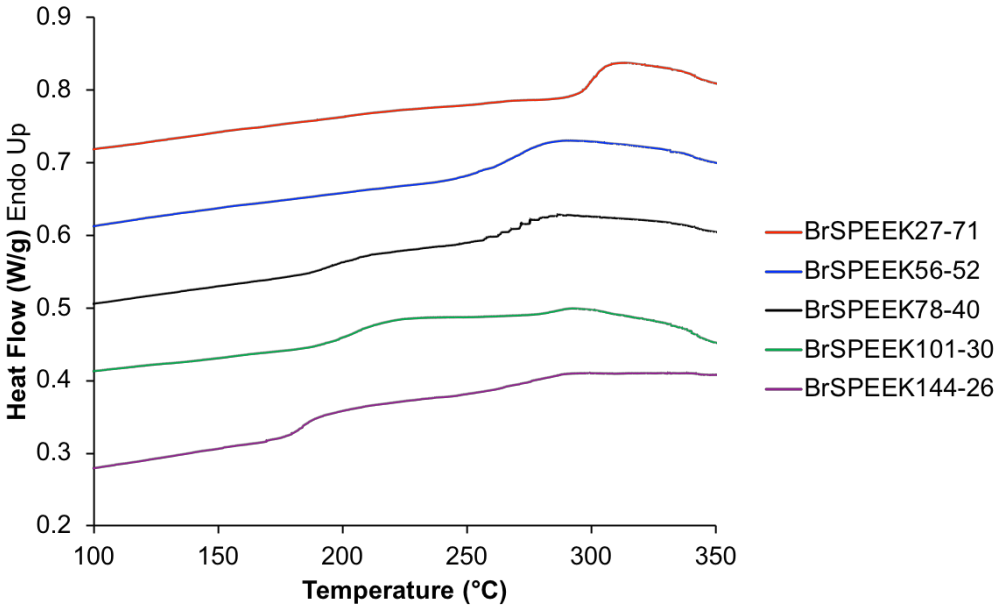

Figure 5.5. DSC thermograms of BrSPEEK membranes in Cs^+-form. The heat following a quench cool from the melt is shown.

Table 5.2. Glass transition temperature(s) of blocky BrSPEEK samples.

Sample	T_{g1} (°C)	T_{g2} (°C)
BrSPEEK27-71	-	302
BrSPEEK56-52	-	272
BrSPEEK78-40	198	280
BrSPEEK101-30	201	293
BrSPEEK144-26	184	275

To further elucidate the multi-phase behavior of the blocky BrSPEEK copolymers, dynamic mechanical analysis (DMA) was performed. **Figure 5.6** compares the tanδ profiles of blocky BrSPEEK27-71, BrSPEEK78-40, and BrSPEEK144-26. Similar to the DSC results, two transitions are observed for BrSPEEK78-40 and BrSPEEK144-26, and one transition is observed for BrSPEEK27-71. Again, the lower temperature transition is attributed to the glass transition of the brominated blocks while the upper temperature is attributed to the SPEEK blocks and is due to the onset of long-range mobility upon destabilization of the electrostatic network.[52] Comparison of the T_g's from tanδ to the starting blocky BrPEEK copolymers demonstrates that the T_g

associated with the brominated blocks is higher for the BrSPEEK copolymers. This difference in T_g is likely due to restriction of mobility in the brominated blocks by the electrostatic network or by a small degree of phase-mixing between the brominated and sulfonated blocks. Because the length of the blocks is controlled by the semicrystalline microstructure of the PEEK gel (during bromination), it is likely that the blocks in these copolymers are relatively short compared to conventionally synthesized multiblock copolymers.[32] Thus, brominated blocks will likely be in close proximity to the ionic aggregates, thereby restricting their mobility and leading to a higher T_g than in the unsulfonated blocky BrPEEK copolymers. It is also of interest to note that the magnitude of tanδ peak for the sulfonated blocks is much higher than the magnitude of the tanδ peak for the brominated blocks. This is due to a much greater change in the loss modulus as the ionic phase transitions into a dynamic network. Thus, in agreement with our DSC results, it is clear that the electrostatic network is dominating the mobility of the polymer chains.

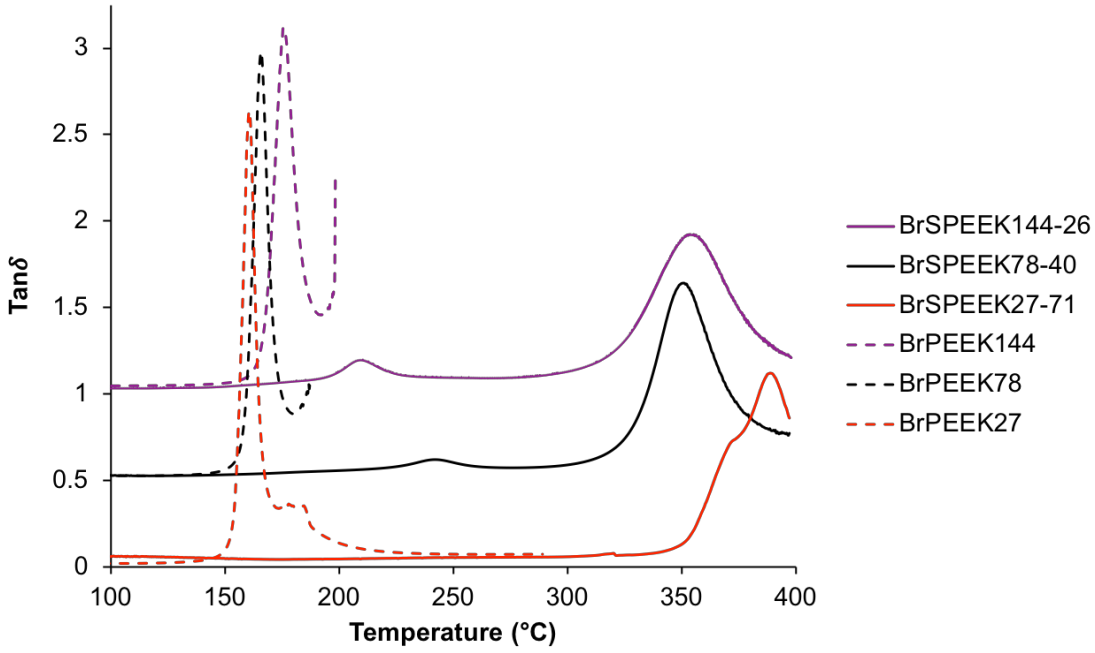

Figure 5.6. Tanδ of blocky BrSPEEK27-71, BrSPEEK78-40, and BrSPEEK144-26 and native BrPEEK27, BrPEEK78, and BrPEEK144. All BrSPEEK samples are in Na^+-form.

The location of the glass transition temperatures observed in tanδ is dependent on the sulfonate counterion, as shown in **Figure 5.7**. Blocky BrSPEEK144-26 shows similar tanδ peaks in Na^+-form and Cs^+-form, however the peak locations are at higher temperatures for Na^+-form than Cs^+-form. As the size of the counterion increases, the charge becomes more delocalized and the electrostatic attractive forces are weaker between ion pairs within the ionic aggregate.[53-54] Thus, changing the counterion from Na^+ to Cs^+ weakens the electrostatic network and decreases the T_g of the sulfonated blocks significantly. It is also important to note that the peak attributed to the BrPEEK blocks shifts to lower temperatures when changing from Na^+ to Cs^+ counterions, further confirming that the brominated blocks are influenced by the strength of the electrostatic network due to their close proximity to sulfonated blocks.

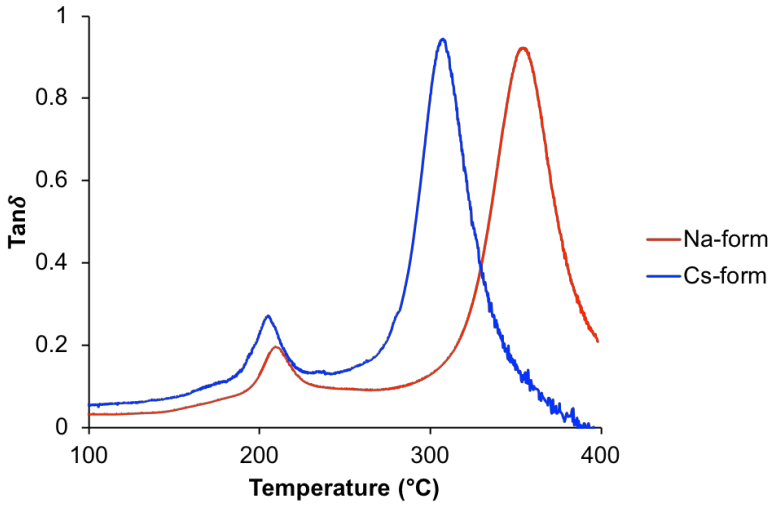

Figure 5.7. Tanδ of blocky BrSPEEK144-26 in Na^+-form and Cs^+-form.

To confirm that the multiple transitions observed for the blocky BrSPEEK copolymers using DSC and DMA are accurately attributed to phase-separation of the brominated and sulfonated blocks, a simple blend of sulfonated PEEK and brominated PEEK was prepared. Random SPEEK52 and random BrPEEK150 were dissolved at a 1:1 (w:w) ratio in DMAc and

were cast onto glass at 80 ºC. Blend membranes were converted into Na^+-form and were analyzed using DSC and DMA. As shown in **Figure 5.8**, the blend of SPEEK and BrPEEK shows two distinct glass transitions that are readily attributed to the glass transitions of the two components. The T_g's do not change upon blending, and there is no evidence of miscibility and phase mixing between the SPEEK and BrPEEK. The multi-phase behavior of the SPEEK/BrPEEK blend closely resembles that of the blocky BrSPEEK copolymers, suggesting that the blocky BrSPEEK undergo phase separation between the brominated and sulfonated blocks.

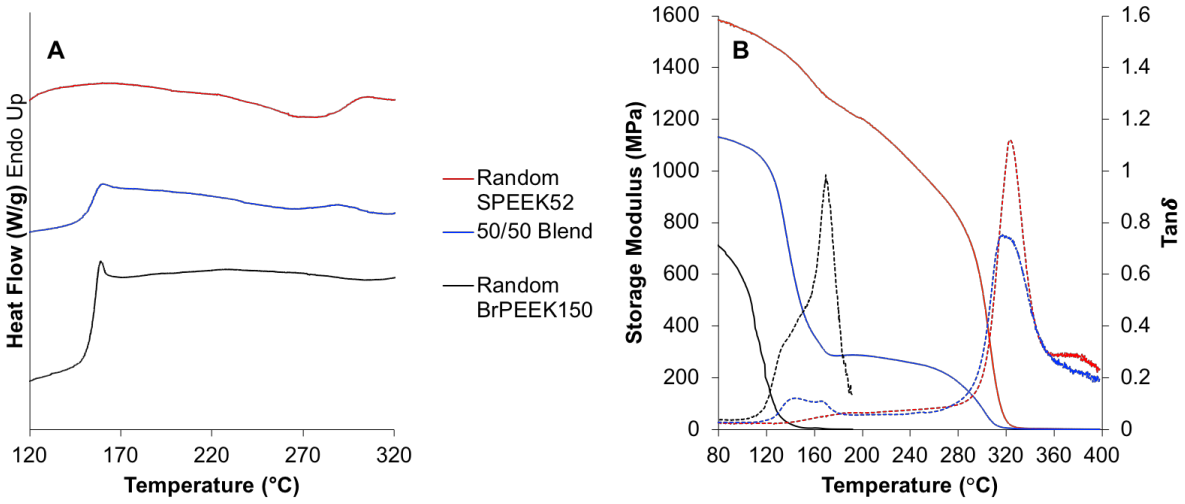

Figure 5.8. DSC (A) and DMA (B) of random SPEEK52, random BrPEEK150, and a 50/50 blend of the two.

5.4.3 Blocky BrSPEEK Membrane Properties

Water uptake is an important parameter dictating not only the proton conductivity but also the mechanical stability of proton exchange membranes.[55] The gravimetric water uptake, λ, and areal swelling of the as-cast blocky BrSPEEK membranes (H^+-form) is shown in **Figure 5.9**. The results are compared to random SPEEK prepared by sulfonation in DCA. As expected, water uptake and areal swelling increases with increasing degree of sulfonation for all samples due to the introduction of more hydrophilic acid sites. Overall, on a per mol% sulfonation basis, blocky

BrSPEEK membranes exhibit considerably less water uptake and areal swelling than random SPEEK membranes. This effect is magnified at high degrees of sulfonation (i.e. >40 mol%), where random SPEEK membranes tend to over-swell in water as noted by the sharp climb in water uptake, λ, and areal swelling with increasing degree of sulfonation. In contrast, blocky BrSPEEK membranes exhibit a more gradual rise in water uptake and dimensional swelling with increasing degree of sulfonation. It is evident that the hydrophobic bromine blocks limit the total water uptake and enable control over swelling, especially at high degrees of sulfonation. Annealing of the BrSPEEK membranes decreases the water uptake moderately and contributes to a reduction in areal swelling at high degrees of sulfonation (BrSPEEK27-71).

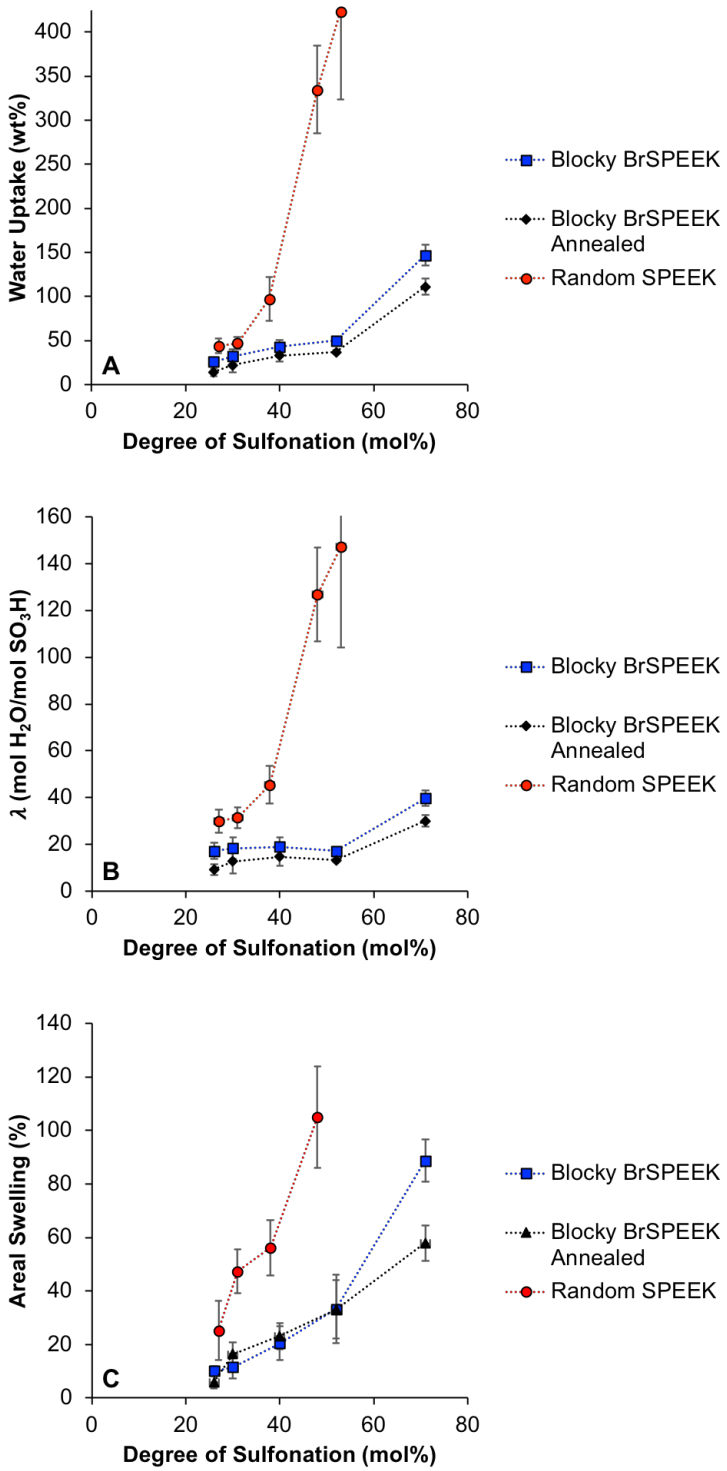

Figure 5.9. Gravimetric water uptake (A), λ (B), and areal swelling (C) as a function of degree of sulfonation for blocky BrSPEEK, blocky BrSPEEK annealed at 250 ºC for 2 hours, and random SPEEK.

The conductivity of fully-hydrated BrSPEEK membranes in water at room temperature is shown in **Figure 5.10**. Conductivity increases with increasing degree of sulfonation, and little difference is observed between the conductivity of BrSPEEK and random SPEEK at similar degrees of sulfonation. When compared to SPEEK prepared by conventional means[56-58] (i.e. sulfonation in H_2SO_4), however, BrSPEEK membranes exhibit profoundly improved proton conductivity, likely due to the more controlled sulfonation microstructure. It is also important to note that at high degrees of sulfonation BrSPEEK27-71 approaches the conductivity of Nafion® (77 mS/cm). Surprisingly, the random SPEEK also produces comparably high conductivity on a per mol% sulfonate group basis, relative to the conventional SPEEK. This is also likely a result of an improved distribution of functional groups along the chains attributed to our "dissolution first, then sulfonate" process using the non-sulfonating solvent DCA. In contrast, the conventional sulfonation process, using concentrated H_2SO_4, involves simultaneous dissolution and sulfonation, which likely leads to a very heterogeneous degree of sulfonation from chain to chain (i.e., the first chains to dissolve are in contact with the sulfonating reagent for a much longer time, leading to higher degrees of sulfonation, compared to the lightly sulfonated chains that were last to dissolve. Thus, the polar domains in the conventional SPEEK are presumably less ordered with more heterogeneous percolation pathways for the transport of protons and water – leading to lower conductivity.

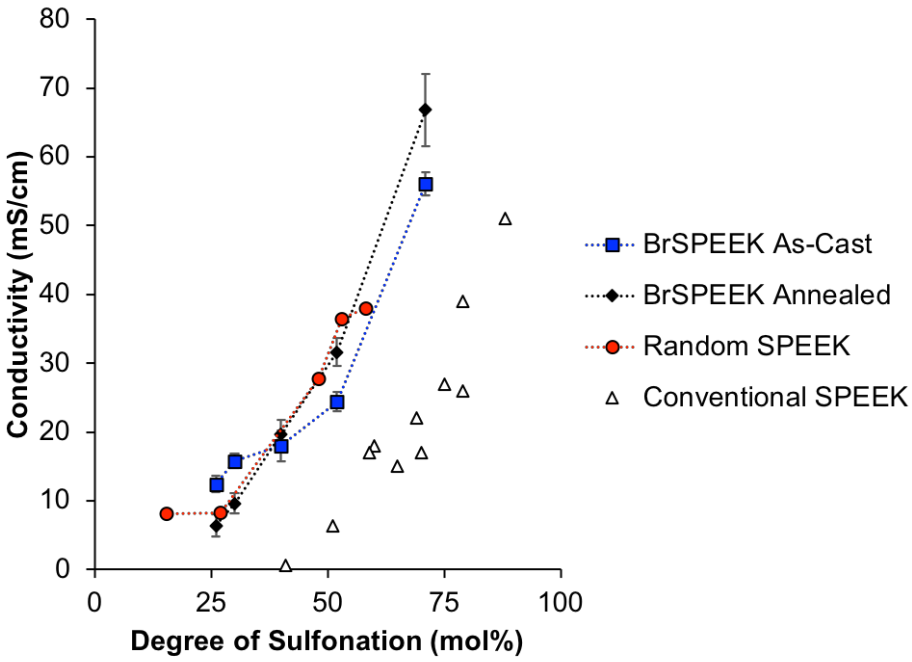

Figure 5.10. Conductivity of as-cast blocky BrSPEEK, annealed blocky BrSPEEK, random SPEEK, and conventional SPEEK from literature[49-51] in water at room temperature.

Despite the similar proton conductivities for as-cast BrSPEEK and random SPEEK as a function of degree of sulfonation, it is important to consider the differences in water uptake among these samples. The conductivity as a function of λ is shown in **Figure 5.11**. Clearly, the blocky BrSPEEK membranes exhibit improved proton transport at much lower λ than random SPEEK. The blocky BrSPEEK membranes are capable of undergoing hydrophilic-hydrophobic phase separation, as shown by the multi-phase behavior in DSC and DMA. This phase separation creates continuous hydrophilic domains that enable efficient proton transport at lower water contents compared to the random system. In contrast, the sulfonic acid groups on the random SPEEK likely form discrete polar aggregates that are not well inter-connected. Thus, to successfully connect the polar domains and achieve adequate proton transport, high water contents are necessary for random SPEEK.

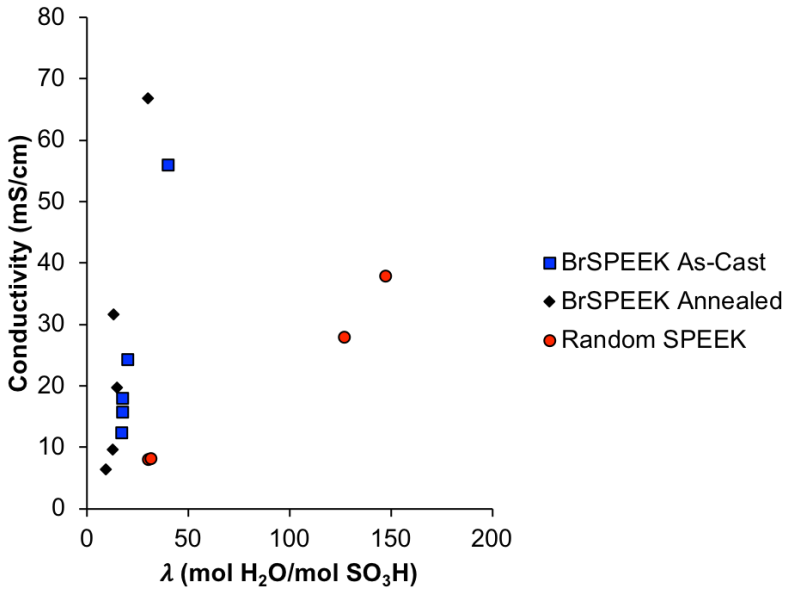

Figure 5.11. Conductivity of as-cast BrSPEEK, annealed BrSPEEK, and random SPEEK as a function of λ.

The conductivity of as-cast BrSPEEK78-40 as a function of humidity at 80 ºC is shown in **Figure 5.12**, as compared to the benchmark Nafion®, random SPEEK42, and blocky SPEEK41. The blocky SPEEK41 sample was prepared by gel-state sulfonation in 1,2-dichloroethane, as described in our previous work.[31] Blocky BrSPEEK78-40 exhibited improved proton transport compared to random SPEEK42 at all humidity values examined. Furthermore, the conductivity of blocky BrSPEEK78-40 approaches that of blocky SPEEK41 and Nafion® at high humidity. These results further reiterate the improved hydrophilic-hydrophobic phase separation of blocky BrSPEEK copolymers compared to random SPEEK copolymers. Continuous hydrophilic domains are created even at low water contents (i.e. low humidity), creating less tortuous paths for proton transport. The difference in proton conductivity between blocky BrSPEEK78-40 and blocky SPEEK41 at low humidity likely stems from semicrystalline nature of blocky SPEEK41, which helps drive ionic aggregation into small, closely-spaced domains.[31] Regardless, it is evident that

the blocky architecture of the BrSPEEK copolymers contributes significantly to improved proton transport and more controlled water uptake due to hydrophilic-hydrophobic phase separation.

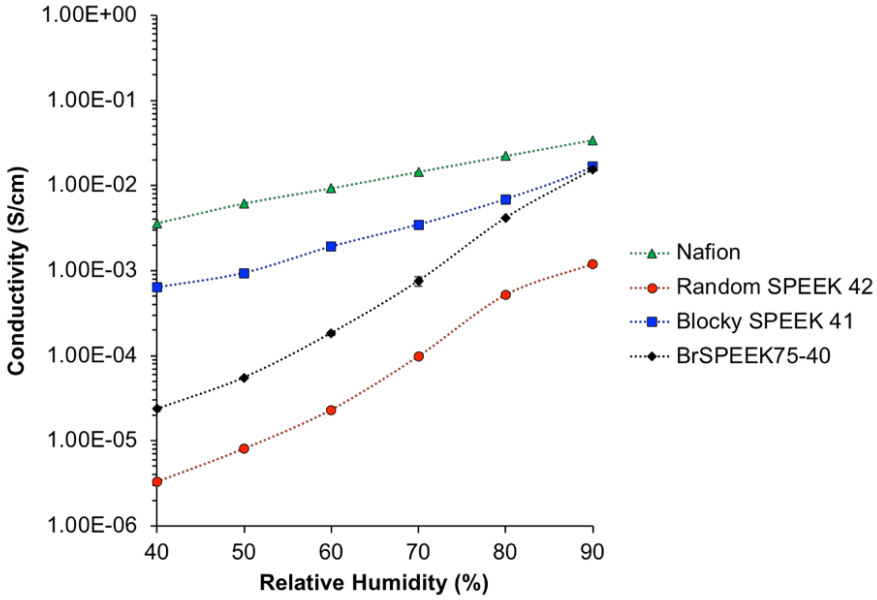

Figure 5.12. Conductivity of Nafion®, random SPEEK at 42 mol% sulfonation, blocky SPEEK at 41 mol% sulfonation, and blocky BrSPEEK78-40 as a function of relative humidity. Measurements were conducted at 80 ºC.

5.4.4 Ionomer Morphology

The ionic aggregate morphology of the BrSPEEK membranes was investigated using small-angle x-ray scattering (SAXS) at Argonne National Laboratory. The SAXS scattering profiles of the as-cast blocky BrSPEEK membranes in Cs^+-form are shown in **Figure 5.13A**. A clear ionomer peak at approximately q = 0.25 $Å^{-1}$ is observed, and this peak increases in intensity with increasing degree of sulfonation.[59] Furthermore, the ionomer peak shifts slightly to higher q with increasing degree of sulfonation, suggesting a decrease in the inter-aggregate distance. The center-to-center distance between ionic aggregates was quantified by determining the Bragg spacing of the ionomer peak ($d_{Bragg} = 2\pi/q$)[60] (see Supplementary Material **Table 5S.1**), and the Bragg spacing decreased nominally from 26 Å to 22 Å with increasing degree of sulfonation.

For comparison, the SAXS profiles of random SPEEK with degrees of sulfonation from 20-53 mol% are shown in **Figure 5.13B**. A pronounced ionomer peak is present that shifts from $q \approx 0.1$ Å^{-1} to $q \approx 0.3$ Å^{-1} as the degree of sulfonation increases from 20 to 53 mol%. Thus, the distance between ionic aggregates decreases from 45 Å to 27 Å with increasing degree of sulfonation. Based on these results, it is apparent that the ionomer morphology and inter-aggregate distance is much more dependent on the degree of sulfonation for random SPEEK than for blocky BrSPEEK. Furthermore, blocky BrSPEEK membranes exhibit smaller inter-aggregate spacings than random SPEEK at similar degrees of sulfonation; which, in correlation with the improved proton conductivity, suggests a more closely-packed, interconnected ionomer morphology due to the hydrophobic-hydrophilic phase separation of blocky BrSPEEK.

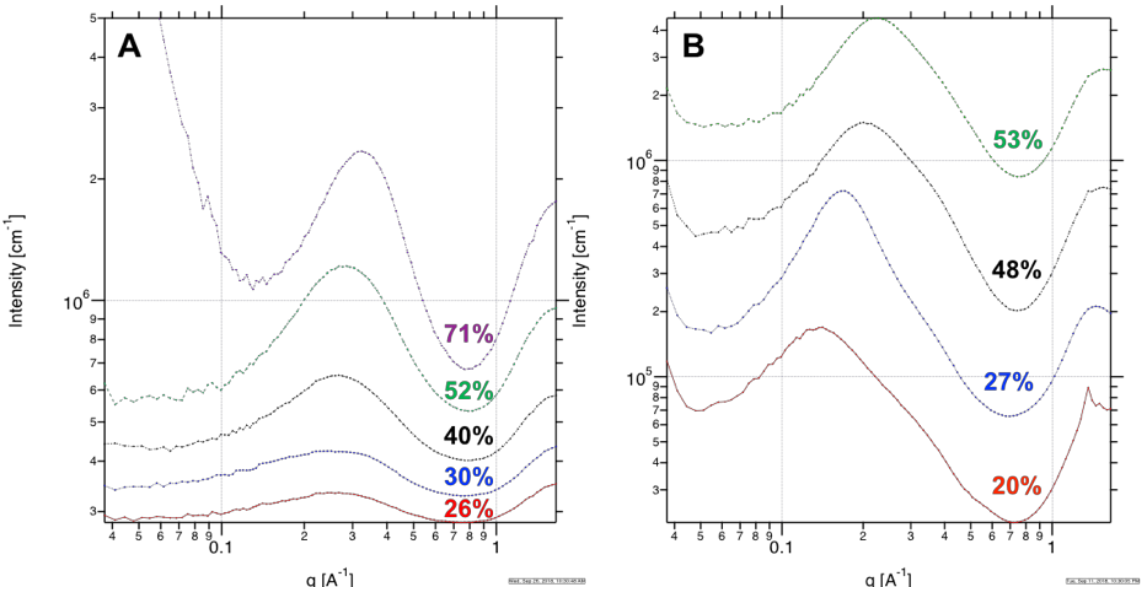

Figure 5.13. SAXS profiles of as-cast blocky BrSPEEK (A) and as-cast random SPEEK (B) at various degrees of sulfonation. All samples are in Cs^+-form.

The ionomer peaks of blocky BrSPEEK and random SPEEK were further analyzed using the Kinning-Thomas modified hard sphere model.[61] The core ionic radius (R), the radius of closest approach (R_{ca}), and the inter-particle radius (R_{ip}) determined using this method are shown in **Table**

5.3. Ionomer radii around 3-5 Å and R_{ca} around 8.5-10.5 Å were determined for as-cast BrSPEEK membranes using this analysis. No specific trend in R or R_{ca} is observed with increasing degree of sulfonation, suggesting that blocky BrSPEEK forms similar sized ionic aggregates independent of ion content. This result is consistent with the work of Weiss, who demonstrated that ionic aggregate size in a sulfonated poly(styrene-*b*-(ethylene-*co*-butylene)-*b*-styrene) block copolymer was insensitive to the degree of sulfonation.[62] In contrast, the R of random SPEEK decreases systematically from 8.3 to 3.1 Å and R_{ca} decreases from 19.2 to 13.0 Å as the degree of sulfonation increases. Thus, by blocking up the ionic aggregates in BrSPEEK, more consistent ionic aggregate morphologies are obtained due facile hydrophobilic-hydrophilic phase separation and the close proximity of sulfonate groups along the polymer chain within the sulfonated "blocks." Moreover, for both blocky BrSPEEK and random SPEEK, R_{ip} decreases with increasing degree of sulfonation, suggesting more closely spaced ionic aggregates as was observed with the Bragg spacing analysis.

Table 5.3. Ionomer radius (R), radius of closest approach (R_{ca}), and inter-particle radius (R_{ip}) of BrSPEEK membranes determined by fitting to the Kinning-Thomas model.

Sample	DS (mol%)	R (Å)	R_{ca} (Å)	R_{ip}(Å)
Blocky BrSPEEK27-71	71	3.0	9.7	17.8
Blocky BrSPEEK56-52	52	5.0	10.1	19.8
Blocky BrSPEEK78-40	40	4.4	9.8	22.8
Blocky BrSPEEK101-30	30	3.9	8.5	29.6
Blocky BrSPEEK144-26	26	3.7	10.5	36.8
Random SPEEK53	53	3.1	13.0	23.2
Random SPEEK48	48	4.9	12.2	22.8
Random SPEEK27	27	7.6	16.7	28.9
Random SPEEK20	20	8.3	19.2	37.2

5.5 Conclusions

In this work, blocky BrSPEEK copolymers were prepared by sulfonation of blocky BrPEEK using H_2SO_4. The resultant degree of sulfonation depended on the initial blocky BrPEEK templating, and increasing degree of sulfonation was observed with decreasing bromine content in

the initial blocky BrPEEK. Distinct multi-phase behavior was observed using DSC and DMA for blocky BrSPEEK membranes at degrees of sulfonation up to 40 mol%, suggesting phase-separation between the brominated blocks and sulfonated blocks into hydrophobic and hydrophilic domains, respectively. SAXS analysis revealed similar ionic-aggregate sizes for blocky BrSPEEK membranes at all degrees of functionality, and ionic aggregates became more closely spaced with increasing degree of sulfonation. Improved dimensional stability upon swelling and enhanced proton transport at lower water content were observed for blocky BrSPEEK membranes compared to random SPEEK ionomers due to the hydrophilic-hydrophobic phase separation and a closer packing of ionic aggregates, resulting in improved order within the blocky hydrophilic domains.

5.6 Supporting Information

The SAXS scattering profiles of the as-cast and annealed blocky BrSPEEK membranes in Cs^+-form are shown in **Figure 5S.1**. For both samples, an ionomer peak around q = 0.25 $Å^{-1}$ is observed, and this peak increases in intensity with increasing degree of sulfonation. Furthermore, the peak maximum shifts to higher q with increasing degree of sulfonation, implying a decrease in inter-aggregate spacing. This shift to higher q appears more prevalent for the annealed blocky BrSPEEK membranes compared to the as-cast membranes.

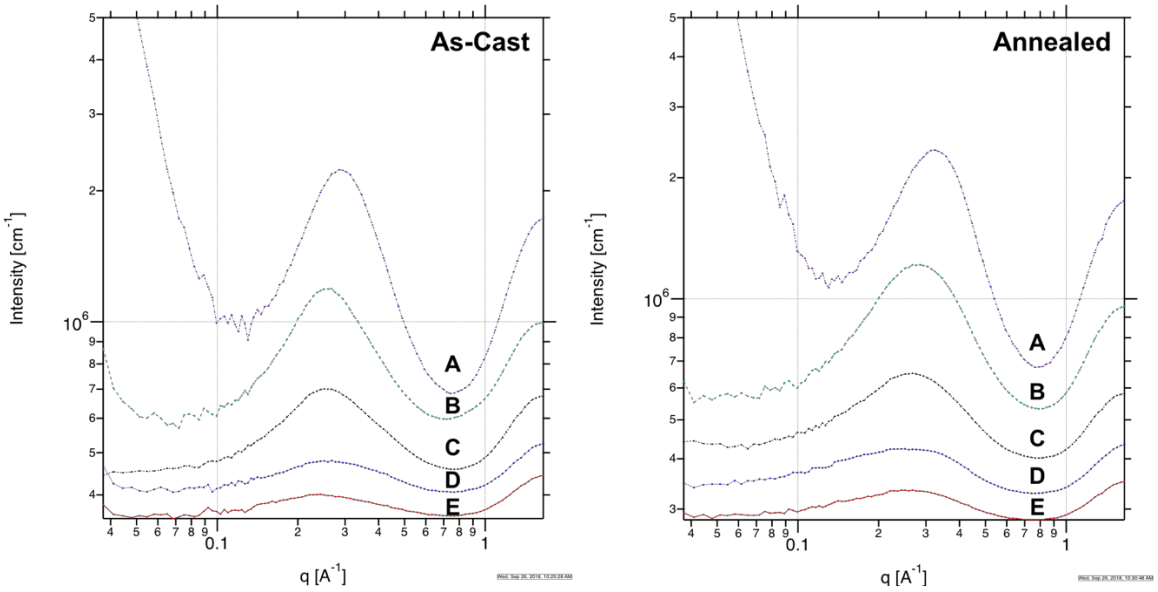

Figure 5S.14. SAXS profiles of as-cast and annealed blocky BrSPEEK27-71 (A), BrSPEEK56-52 (B), BrSPEEK78-40 (C), BrSPEEK101-30 (D), and BrSPEEK144-26 (E) in Cs^+-form.

The Bragg spacing of the ionomer peaks was determined to estimate the inter-aggregate distance of the as-cast and annealed BrSPEEK membranes and the results are shown in **Table 5S.1**. At degrees of sulfonation of 40 mol% and below, similar center-to-center distances (25 Å) are observed for as-cast BrSPEEK membranes. This value decreases slightly to 22 Å for blocky BrSPEEK27-71, and it is apparent that as-cast BrSPEEK membranes exhibit similar spacing between the ionic aggregates. Annealing of the blocky BrSPEEK membranes leads to a slight shift in the ionomer peak to higher *q* at degrees of sulfonation above 40 mol%, resulting in a shorter inter-aggregate distance as compared to as-cast BrSPEEK membranes. The Bragg spacing of the annealed BrSPEEK membranes steadily decreases from 27.5 Å to 19.4 Å for BrSPEEK144-26 and BrSPEEK27-71, respectively.

Table 5S.4. Bragg Spacing of BrSPEEK membranes determined from the ionomer peak in SAXS.

Sample	As -Cast d_{Bragg} (Å)	Annealed d_{Bragg} (Å)
BrSPEEK27-71	22.0	19.4
BrSPEEK56-52	23.5	22.0
BrSPEEK78-40	25.0	23.5
BrSPEEK101-30	25.0	25.0
BrSPEEK144-26	25.8	27.5

The ionomer peaks were also analyzed using the Kinning-Thomas modified hard sphere model, and the extracted core ionic radius (R), the radius of closest approach (R_{ca}), and inter-particle radius (R_{ip}) are shown in **Table 5S.2**. Ionomer radii around 3-5 Å and R_{ca} around 8.5-10.5 Å were determined for both as-cast and annealed BrSPEEK membranes using this analysis. No trend in R or R_{ca} is observed with increasing degree of sulfonation, suggesting that blocky BrSPEEK forms similar sized ionic aggregates independent of ion content. Similar to the Bragg spacing analysis, the R_{ip} decreases with increasing degree of sulfonation, and slightly lower R_{ip} values are determined for annealed samples compared to as-cast samples. The closer spacing of the ionic domains likely contributes to the slightly improved proton transport of annealed BrSPEEK compared to as-cast BrSPEEK at high ion contents.

Table 5S.5. Ionomer radius (R), radius of closest approach (R_{ca}), and inter-particle radius (R_{ip}) of BrSPEEK membranes determined by fitting to the Kinning-Thomas model.

Sample	Treatment	R (Å)	R_{ca} (Å)	R_{ip}(Å)
BrSPEEK27-71	As-Cast	3.0	9.7	17.8
BrSPEEK56-52	As-Cast	5.0	10.1	19.8
BrSPEEK78-40	As-Cast	4.4	9.8	22.8
BrSPEEK101-30	As-Cast	3.9	8.5	29.6
BrSPEEK144-26	As-Cast	3.7	10.5	36.8
BrSPEEK27-71	Annealed	4.2	8.6	15.3
BrSPEEK56-52	Annealed	4.8	8.8	17.2
BrSPEEK78-40	Annealed	4.6	9.0	21.0
BrSPEEK101-30	Annealed	4.3	8.8	27.2
BrSPEEK144-26	Annealed	4.1	9.5	34.4

5.7 References

1. Park, C. H.; Lee, C. H.; Guiver, M. D.; Lee, Y. M., Sulfonated hydrocarbon membranes for medium-temperature and low-humidity proton exchange membrane fuel cells (PEMFCs). *Progress in Polymer Science* **2011,** *36* (11), 1443-1498.
2. Peighambardoust, S. J.; Rowshanzamir, S.; Amjadi, M., Review of the proton exchange membranes for fuel cell applications. *International Journal of Hydrogen Energy* **2010,** *35* (17), 9349-9384.
3. Robertson, G. P.; Mikhailenko, S. D.; Wang, K.; Xing, P.; Guiver, M. D.; Kaliaguine, S., Casting solvent interactions with sulfonated poly(ether ether ketone) during proton exchange membrane fabrication. *Journal of Membrane Science* **2003,** *219* (1), 113-121.
4. Xing, P.; Robertson, G. P.; Guiver, M. D.; Mikhailenko, S. D.; Wang, K.; Kaliaguine, S., Synthesis and characterization of sulfonated poly(ether ether ketone) for proton exchange membranes. *Journal of Membrane Science* **2004,** *229* (1–2), 95-106.
5. Li, L.; Zhang, J.; Wang, Y., Sulfonated poly(ether ether ketone) membranes for direct methanol fuel cell. *Journal of Membrane Science* **2003,** *226* (1), 159-167.
6. Huang, R. Y. M.; Shao, P.; Burns, C. M.; Feng, X., Sulfonation of poly(ether ether ketone)(PEEK): Kinetic study and characterization. *Journal of Applied Polymer Science* **2001,** *82* (11), 2651-2660.
7. Fu, Y. Z.; Manthiram, A., Synthesis and characterization of sulfonated polysulfone membranes for direct methanol fuel cells. *Journal of Power Sources* **2006,** *157* (1), 222-225.
8. Lufrano, F.; Gatto, I.; Staiti, P.; Antonucci, V.; Passalacqua, E., Sulfonated polysulfone ionomer membranes for fuel cells. *Solid State Ionics* **2001,** *145* (1), 47-51.
9. Noshay, A.; Robeson, L. M., Sulfonated polysulfone. *Journal of Applied Polymer Science* **1976,** *20* (7), 1885-1903.
10. Guan, R.; Zou, H.; Lu, D.; Gong, C.; Liu, Y., Polyethersulfone sulfonated by chlorosulfonic acid and its membrane characteristics. *European Polymer Journal* **2005,** *41* (7), 1554-1560.
11. Nolte, R.; Ledjeff, K.; Bauer, M.; Mülhaupt, R., Partially sulfonated poly(arylene ether sulfone) - A versatile proton conducting membrane material for modern energy conversion technologies. *Journal of Membrane Science* **1993,** *83* (2), 211-220.
12. Matsumoto, K.; Higashihara, T.; Ueda, M., Locally and Densely Sulfonated Poly(ether sulfone)s as Proton Exchange Membrane. *Macromolecules* **2009,** *42* (4), 1161-1166.
13. Wang, F.; Hickner, M.; Ji, Q.; Harrison, W.; Mecham, J.; Zawodzinski, T. A.; McGrath, J. E., Synthesis of highly sulfonated poly(arylene ether sulfone) random (statistical) copolymers via direct polymerization. *Macromolecular Symposia* **2001,** *175* (1), 387-396.
14. Andrew, M.; Mukundan, T.; McGrath, J. E., Sulfonated Poly(Arylene Ether Sulfone) Copolymers - Acid and Salt Form: Potential Biofunctional Polymers. *Journal of Bioactive and Compatible Polymers* **2004,** *19* (4), 315-329.
15. Wang, F.; Hickner, M.; Kim, Y. S.; Zawodzinski, T. A.; McGrath, J. E., Direct polymerization of sulfonated poly(arylene ether sulfone) random (statistical) copolymers: candidates for new proton exchange membranes. *Journal of Membrane Science* **2002,** *197* (1), 231-242.
16. Chang, Y.; Lee, Y.-B.; Bae, C., Partially fluorinated sulfonated poly (ether amide) fuel cell membranes: influence of chemical structure on membrane properties. *Polymers* **2011,** *3* (1), 222-235.
17. Kreuer, K. D., On the development of proton conducting polymer membranes for hydrogen and methanol fuel cells. *Journal of Membrane Science* **2001,** *185* (1), 29-39.

18. Jeong, Y.-G.; Seo, D.-W.; Lim, Y.-D.; Jin, H.-M.; Islam Mollah, M. S.; Ur, S.-C.; Pyun, S.-Y.; Kim, W.-G., Synthesis and characterization of sulfonated bromo-poly(2,6-dimethyl-1,4-phenylene oxide)-co-(2,6-diphenyl-1,4-phenylene oxide) copolymer as proton exchange membrane. *Electrochimica Acta* **2010,** *55* (4), 1425-1430.
19. Ghassemi, H.; McGrath, J. E.; Zawodzinski Jr, T. A., Multiblock sulfonated–fluorinated poly(arylene ether)s for a proton exchange membrane fuel cell. *Polymer* **2006,** *47* (11), 4132-4139.
20. Yu, X.; Roy, A.; Dunn, S.; Badami, A. S.; Yang, J.; Good, A. S.; McGrath, J. E., Synthesis and characterization of sulfonated-fluorinated, hydrophilic-hydrophobic multiblock copolymers for proton exchange membranes. *Journal of Polymer Science Part A: Polymer Chemistry* **2009,** *47* (4), 1038-1051.
21. Wiles, K. B.; de Diego, C. M.; de Abajo, J.; McGrath, J. E., Directly copolymerized partially fluorinated disulfonated poly(arylene ether sulfone) random copolymers for PEM fuel cell systems: Synthesis, fabrication and characterization of membranes and membrane–electrode assemblies for fuel cell applications. *Journal of Membrane Science* **2007,** *294* (1), 22-29.
22. Abhishek, R.; A., H. M.; Xiang, Y.; Yanxiang, L.; E., G. T.; E., M. J., Influence of chemical composition and sequence length on the transport properties of proton exchange membranes. *Journal of Polymer Science Part B: Polymer Physics* **2006,** *44* (16), 2226-2239.
23. Assumma, L.; Iojoiu, C.; Mercier, R.; Lyonnard, S.; Nguyen, H. D.; Planes, E., Synthesis of partially fluorinated poly(arylene ether sulfone) multiblock copolymers bearing perfluorosulfonic functions. *Journal of Polymer Science Part A: Polymer Chemistry* **2015,** *53* (16), 1941-1956.
24. Bae, B.; Miyatake, K.; Uchida, M.; Uchida, H.; Sakiyama, Y.; Okanishi, T.; Watanabe, M., Sulfonated Poly(arylene ether sulfone ketone) Multiblock Copolymers with Highly Sulfonated Blocks. Long-Term Fuel Cell Operation and Post-Test Analyses. *ACS Applied Materials & Interfaces* **2011,** *3* (7), 2786-2793.
25. Chen, Y.; Guo, R.; Lee, C. H.; Lee, M.; McGrath, J. E., Partly fluorinated poly(arylene ether ketone sulfone) hydrophilic–hydrophobic multiblock copolymers for fuel cell membranes. *International Journal of Hydrogen Energy* **2012,** *37* (7), 6132-6139.
26. Elabd, Y. A.; Hickner, M. A., Block Copolymers for Fuel Cells. *Macromolecules* **2011,** *44* (1), 1-11.
27. Jung, M. S.; Kim, T.-H.; Yoon, Y. J.; Kang, C. G.; Yu, D. M.; Lee, J. Y.; Kim, H.-J.; Hong, Y. T., Sulfonated poly(arylene sulfone) multiblock copolymers for proton exchange membrane fuel cells. *Journal of Membrane Science* **2014,** *459*, 72-85.
28. Roy, A.; Hickner, M. A.; Yu, X.; Li, Y.; Glass, T. E.; McGrath, J. E., Influence of chemical composition and sequence length on the transport properties of proton exchange membranes. *Journal of Polymer Science Part B: Polymer Physics* **2006,** *44* (16), 2226-2239.
29. Sulfonated Poly(aryl ether)-Type Polymers as Proton Exchange Membranes: Synthesis and Performance. In *Membranes for Energy Conversion*.
30. Fahs, G. B.; Benson, S. D.; Moore, R. B., Blocky Sulfonation of Syndiotactic Polystyrene: A Facile Route toward Tailored Ionomer Architecture via Postpolymerization Functionalization in the Gel State. *Macromolecules* **2017,** *50* (6), 2387-2396.
31. Anderson, L. J.; Yuan, X.; Fahs, G. B.; Moore, R. B., Blocky Ionomers via Sulfonation of Poly(ether ether ketone) in the Semicrystalline Gel State. *Macromolecules* **2018,** *51* (16), 6226-6237.
32. Ferrell, W. H.; Kushner, D. I.; Hickner, M. A., Investigation of Polymer–Solvent Interactions in Poly(styrene sulfonate) Thin Films. *Journal of Polymer Science, Part B: Polymer Physics* **2017,** *55*, 1365-1372.

33. Anderson, L. J.; Yuan, X.; Fahs, G. B.; Moore, R. B., Blocky Ionomers via Sulfonation of Poly(ether ether ketone) in the Semicrystalline Gel State. *Macromolecules* **2018**.
34. Ilavsky, J.; Zhang, F.; Allen, A. J.; Levine, L. E.; Jemian, P. R.; Long, G. G., Ultra-Small-Angle X-ray Scattering Instrument at the Advanced Photon Source: History, Recent Development, and Current Status. *Metallurgical and Materials Transactions A* **2013,** *44* (1), 68-76.
35. Ilavsky, J.; R. Jemian, P., *Irena: Tool Suite for Modeling and Analysis of Small Angle Scattering*. 2009; Vol. 42, p 347-353.
36. Ilavsky, J., Nika: software for two-dimensional data reduction. *Journal of Applied Crystallography* **2012,** *45* (2), 324-328.
37. Rajesh, K.; Somasundaram, M.; Saiganesh, R.; Balasubramanian, K. K., Bromination of Deactivated Aromatics: A Simple and Efficient Method. *The Journal of Organic Chemistry* **2007,** *72* (15), 5867-5869.
38. Duan, J. X.; Zhang, L. H.; Dolbier, W. R., *A convenient new method for the bromination of deactivated aromatic compounds*. 1999; p 1245-1246.
39. Bock, T. R. Catalytic phosphonation of high performance polymers and POSS - Novel components for polymer blend and nanocomposite fuel cell membranes. Ph.D. Dissertation, Albert-Ludwig University, Freidburg, Germany, 2006.
40. Zaidi, S. M. J.; Mikhailenko, S. D.; Robertson, G. P.; Guiver, M. D.; Kaliaguine, S., Proton conducting composite membranes from polyether ether ketone and heteropolyacids for fuel cell applications. *Journal of Membrane Science* **2000,** *173* (1), 17-34.
41. Al Lafi, A. G., The sulfonation of poly(ether ether ketone) as investigated by two-dimensional FTIR correlation spectroscopy. *Journal of Applied Polymer Science* **2015,** *132* (2), n/a-n/a.
42. Shukla, D.; Negi, Y. S.; Kumar, V., Modification of Poly(ether ether ketone) Polymer for Fuel Cell Application. *Journal of Applied Chemistry* **2013,** *2013*, 7.
43. Perrot, C.; Gonon, L.; Marestin, C.; Morin, A.; Gebel, G., Aging mechanism of Sulfonated poly(aryl ether ketone) (sPAEK) in an hydroperoxide solution and in fuel cell. *Journal of Power Sources* **2010,** *195* (2), 493-502.
44. Devaux, J.; Delimoy, D.; Daoust, D.; Legras, R.; Mercier, J. P.; Strazielle, C.; Nield, E., On the molecular weight determination of a poly(aryl-ether-ether-ketone) (PEEK). *Polymer* **1985,** *26* (13), 1994-2000.
45. Song, J.-M.; Shin, J.; Sohn, J.-Y.; Nho, Y. C., Ionic aggregation characterization of sulfonated PEEK ionomers using by X-ray and DMA techniques. *Macromolecular Research* **2012,** *20* (5), 477-483.
46. Orler, E. B.; Calhoun, B. H.; Moore, R. B., Crystallization Kinetics as a Probe of the Dynamic Network in Lightly Sulfonated Syndiotactic Polystyrene Ionomers. *Macromolecules* **1996,** *29* (18), 5965-5971.
47. Orler, E. B.; Moore, R. B., Influence of Ionic Interactions on the Crystallization of Lightly Sulfonated Syndiotactic Polystyrene Ionomers. *Macromolecules* **1994,** *27* (17), 4774-4780.
48. Alipour Moghaddam, J.; Parnian, M. J.; Rowshanzamir, S., Preparation, characterization, and electrochemical properties investigation of recycled proton exchange membrane for fuel cell applications. *Energy* **2018,** *161*, 699-709.
49. Jiang, R.; Kunz, H. R.; Fenton, J. M., Investigation of membrane property and fuel cell behavior with sulfonated poly(ether ether ketone) electrolyte: Temperature and relative humidity effects. *Journal of Power Sources* **2005,** *150*, 120-128.
50. Kaliaguine, S.; Mikhailenko, S.; Wang, K.; Xing, P.; Robertson, G.; Guiver, M., Properties of SPEEK based PEMs for fuel cell application. *Catalysis Today* **2003,** *82* (1), 213-222.

51. Luu, D. X.; Cho, E.-B.; Han, O. H.; Kim, D., SAXS and NMR Analysis for the Cast Solvent Effect on sPEEK Membrane Properties. *The Journal of Physical Chemistry B* **2009,** *113* (30), 10072-10076.
52. Gebel, G., Structure of Membranes for Fuel Cells: SANS and SAXS Analyses of Sulfonated PEEK Membranes and Solutions. *Macromolecules* **2013,** *46* (15), 6057-6066.
53. Li, X.; Zhang, G.; Xu, D.; Zhao, C.; Na, H., Morphology study of sulfonated poly(ether ether ketone ketone)s (SPEEKK) membranes: The relationship between morphology and transport properties of SPEEKK membranes. *Journal of Power Sources* **2007,** *165* (2), 701-707.

Chapter 6

Poly(ether ether ketone) Bearing Perfluorosulfonic Acid Side Chains

6.1 Introduction

Proton exchange membrane (PEM) fuel cells have attracted significant interest in recent years as a potential clean energy source. The key component of these fuel cells, the proton exchange membrane, requires materials with high proton conductivity, excellent thermal and chemical stabilities, and good mechanical properties in both the dry and hydrated states to perform effectively in the harsh operating conditions of the fuel cell.[1-3] Nafion®, a perfluroinated ionomer bearing perfluoroether-sulfonic acid side chains, is the most widely used and studied PEM due to its exceptional proton conductivity and excellent thermal and mechanical stability.[4-8] The excellent proton transport of Nafion® and other Nafion®-like perfluorinated ionomers is due in part to the superacid nature of the perfluorosulfonic acid side chains and also to hydrophilic-hydrophobic phase separation between the PFTE backbone and hydrophilic side chains which results in continuous hydrophilic domains for proton transport. Despite its commercial success, Nafion® membranes have several shortcomings including their difficult synthesis, high cost, and limited operation temperature.[9-10] To overcome these disadvantages, sulfonated aromatic hydrocarbon polymers have been investigated as potential PEMs due to their high thermal stability, low cost, and ease of synthesis into a wide variety of polymeric backbones and architectures.[11-12]

For typical sulfonated hydrocarbon membranes, the sulfonate group is directly attached to the polymer backbone, making it much less acidic ($pK_a \sim -1$), and thereby less conductive, than the perfluorosulfonic acid side-chain of Nafion® ($pK_a \sim -6$).[13] Several methods have been applied to improve the conductivity of these sulfonated membranes including crosslinking[14-16], blending of polymers[17-19], composite membranes[20-21], and synthesizing multiblock copolymers to prepare

phase-separated, continuous hydrophilic domains.[3, 22-27] Recent efforts have investigated the use of pendant superacid side chains (similar to those of Nafion®) to enhance proton transport in random aromatic copolymers as an alternative to the aforementioned methods.

To synthesize aromatic membranes bearing superacid Nafion®-like side chains, several methods are employed. Perfluorosulfonic acid side chains are coupled to aromatic polymers using Ullmann coupling,[28] lithiation followed by nucleophilic substitution,[29] and using Suzuki cross-coupling reactions.[30-31] Of these methods, Ullmann coupling is most extensively explored in the literature to prepare perfluorosulfonated (PFS) aromatic copolymers. Ullmann coupling proceeds via the coupling of aryl halides to perfluoroalkyl halides using a copper catalyst in polar aprotic solvents.[32] The introduction of the reactive aryl-halide groups to the polymer backbone is achieved by direct polymerization of halogenated monomers[33-36] or by post-polymerization halogenation of the polymer.[23, 37-39] Furthermore, monomers bearing PFS side chains may be synthesized and utilized during polymerization to prepare functionalized aromatic polymers.[40-41] PFS-bearing hydrocarbon membranes have been prepared with poly(arylene ether ketone), poly(arylene ether sulfone), poly(arylene ether), and poly(phenylene) backbones, suggesting a wide range of copolymers compositions and architectures can be prepared. Introduction of the PFS side chain was found to enhance hydrophobic-hydrophilic phase separation compared to directly-attached sulfonic acid groups, and resulted in enhanced proton transport, specifically at high temperature and low humidity conditions.

In this work, poly(ether ether ketone) (PEEK) bearing pendant PFS side chains (PFS-PEEK) is synthesized by post-polymerization bromination of PEEK and subsequent Ullmann coupling with iodinated PFS. PFS-PEEK membranes are prepared and analyzed to determine the influence of the superacid side chain on thermal properties, morphology, water uptake, and proton

conductivity. To our knowledge, this is the first report of PFS-PEEK prepared using commercially-derived PEEK.

6.2 Experimental

6.2.1 Materials

Poly(ether ether ketone) (PEEK) pellets (Victrex 150G) were acquired from Victrex. Random BrPEEK at 125 mol% bromination was prepared using methods described in **Chapter 4**. 1,1,2,2-tetrafluoro-2-(1,1,2,2-tetrafluoro-2-iododethoxy)ethanesulfonyl fluoride (PFS-F) and 1 M tetra-*n*-butylammonium fluoride in THF were obtained from Acros Organics. 2,6-lutidine was obtained from Alfa Alesar. Nano-copper (60-80 nm particle size) and dimethylacetamide (DMAc) were obtained from Sigma-Aldrich. Dichloromethane (DCM), tetrahydrofuran (THF), and potassium carbonate were obtained from Fisher Scientific. All chemicals were used as received.

6.2.2 Synthesis of potassium 1,1,2,2-tetrafluoro-2-(1,1,2,2-tetrafluoro-2-iodoethoxy) ethanesulfonate (PFS-K)

Potassium 1,1,2,2-tetrafluoro-2-(1,1,2,2-tetrafluoro-2-iodoethoxy)ethanesulfonate (PFS-K) was prepared using the method described previously.[37] A solution of PFS-F (5.0 g, 11.7 mmol) in 1.7 mL of dichloromethane was prepared. Water (1.7 mL), 2,6-lutidine (1.73 mL, 14.9 mmol), and 30 μL of 1 M tetra-*n*-butylammonium fluoride in THF were added to the PFS-F solution, and the reaction mixture was stirred for 4 days at room temperature. The product was extracted with dichloromethane, and the solvent was removed by rotary evaporation. The residue was diluted in THF (5 mL) and potassium carbonate (0.94 g, 6.8 mmol) was added. This was stirred at room temperature for 10 hours, filtered to remove any remaining solid, and the filtrate was rotary evaporated to yield a solid product. The product was purified by recrystallization from 1:1 (v:v) THF:toluene to yield potassium 1,1,2,2-tetrafluoro-2-(1,1,2,2,-tetrafluoro-2-iodoethoxy)

ethanesulfonate (PFS-K). ^{19}F NMR in DMSO-d6 confirmed reaction success showing peaks at: -72.66 ppm, -82.21 ppm, -85.78 ppm, and -117.83 ppm (**Figure 6.3**).

6.2.3 Ullmann Coupling of Brominated PEEK and PFS-K

Random BrPEEK (2.0 g, 5.2 mmol) and nanocopper powder (2.5 g, 39.7 mmol) were placed in a round bottom flask equipped with an argon inlet and a magnetic stir bar. The reaction flask was subjected to 3 cycles of pulling vacuum and refilling with argon to remove any moisture from the flask. 25 mL of DMAc was added to the flask and the reaction was stirred at 120 ºC for 4 hours. Next, PFS-K (of variable concentration) was dissolved in 20 mL of DMAc and was slowly added to the reaction flask. The reaction temperature was increased to 160 ºC and the reaction was allowed to stir for at least 72 hours. The reaction mixture was cooled to room temperature and filtered to remove copper. The filtrate was precipitated into 2 M HNO_3, filtered, and washed with water. The solid product (PFS-PEEK) was dried at 60 ºC under vacuum to yield a yellow-brown powder.

6.2.4 Membrane Preparation

PFS-PEEK membranes were prepared by dissolving PFS-PEEK in DMSO to a final concentration of 10 w/v%. Solutions were cast onto glass at 80 ºC using a doctor blade set to 7.5 mils. The films were left at 80 ºC for 30 minutes to dry and were subsequently removed from the glass and dried at 100 ºC for 12 hours. To convert the PFS-PEEK membranes to Cs^+-form, membranes were boiled in 1 M CsCl (aq) for 3 hours. To acidify the PFS-PEEK membranes, membranes were boiled in 1 M HCl (aq) for 3 hours. Following ion exchange or acidification, membranes were washed with water and dried at 100 ºC for 12 hours.

6.2.5 Spectroscopic Methods

^{1}H NMR and ^{19}F NMR spectra of PFS-PEEK samples were measured in DMSO-d6 using an Agilent U4-DD2 400 MHz NMR. Hexafluorobenzene was used as an internal standard for ^{19}F NMR to determine the equivalent weight of the PFS-PEEK samples.

FTIR was performed using a Varian 670-IR spectrometer with a DTGS detector using the Pike Technologies GladiATR™ attachment (diamond crystal). Spectra were collected as the average of 32 scans at 4 cm^{-1} resolution. FTIR spectra were ATR corrected, baseline corrected, and normalized to the peak at 1590 cm^{-1} prior to analysis.

6.2.6 Determination of Equivalent Weight

The equivalent weight (EW) and ion exchange capacity (IEC) were determined by integration of the ^{19}F NMR spectra using hexafluorobenzene (HFB) as an internal standard. Because a known mass (~50 mg) and a known concentration of HFB were analyzed, the equivalent weight was readily determined using the following relations:

$$r_{PFS/HFB} = \frac{n_{PFS}}{n_{HFB}} = \frac{\left(\frac{integral_{PFS}}{N_{PFS}}\right)}{\left(\frac{integral_{HFB}}{N_{HFB}}\right)} \quad \textbf{(6.1)}$$

$$\mathrm{EW} = \frac{mass_{PFS}}{n_{PFS}} \quad \textbf{(6.2)}$$

where $r_{PFS/HFB}$ is the molar ratio of PFS-PEEK to HFB, n_{PFS} and n_{HFB} are the number of moles of PFS-PEEK and HFB, $integral_{PFS}$ and $integral_{HFB}$ are the values determined by integration of the c' peak of PFS-PEEK and the peak of HFB, N_{PFS} and N_{HFB} are the number of fluorines assigned to each peak that is integrated, EW is equivalent weight, and $mass_{PFS}$ is the initial mass of PFS-PEEK placed in the NMR tube. Ion exchange capacity (IEC) was determined as 1/EW.

Ion exchange capacity was also determined by back-titration. Titrations performed by equilibrating a known weight of acidified PFS-PEEK in 25 mL 1M NaCl. 5 mL aliquots were then

titrated with 0.01 M NaOH (standardized with KHP) to determine IEC. The IEC shown in the average of 3 titrations.

6.2.7 Thermal Characterization

Differential scanning calorimetry (DSC) was performed using a TA Instruments Q2000 DSC. Samples were subjected to a heat-cool-heat cycle at a heating rate of 10 ºC/min, a cooling rate of 60 ºC/min, and a temperature range of 40 ºC to 380 ºC. A TA Instruments Q800 DMA in oscillatory tension mode was used to determine the mechanical properties of quenched BrPEEK samples as a function of temperature. Samples were ramped at 2 ºC/min to 400 ºC at a frequency of 1 Hz, an oscillatory amplitude of 10 μm, and a static force of 0.01 N. Samples were converted to Cs^+-form before all DSC and DMA measurements to ensure thermal stability.

6.2.8 Water Uptake and Proton Conductivity

The water uptake of the of the acidified PFS-PEEK membranes was determined gravimetrically. Membranes were dried in a vacuum oven at 100 ºC for 3 hours and the dry weights (W_{dry}) were recorded. Samples were boiled in water for 1 hour and then equilibrated in room temperature water for 12 hours. Membranes were blotted with a Kimwipe to remove excess surface water and the mass (W_{wet}) of the wet membranes was recorded. The water uptake was calculated using the following:

$$\text{Water uptake} = \frac{(W_{wet} - W_{dry})}{W_{dry}} \times 100\% \quad \textbf{(6.3)}$$

Prior to proton conductivity measurements, acidified PFS-PEEK membranes were boiled in water for 1 hour and then equilibrated in room temperature water for 12 hours. In-plane proton conductivity was conducted using a 4-point conductivity cell from Bekktech, which was immersed in DI H_2O at room temperature. Measurements were taken from 1 Hz to 1.5 MHz at a voltage amplitude of 50 mV using a 1255 HF frequency analyzer coupled to a 1286 electrochemical

interface, both from Solartron Analytical. Data analysis was performed using the Zplot® and Zview® software from Scribner and Associates, Inc. The proton conductivity was calculated as:

$$\sigma = \frac{1}{\rho} = \frac{l}{R \times A} \tag{6.4}$$

where σ (Scm^{-1}) is the conductivity, ρ (Ωcm) is the resistivity, l (cm) is the distance between the contacting electrodes, R (Ω) is the resistance determined from the real value of the complex impedance plot that corresponds to the minimum imaginary response, and A is the cross-sectional area of the membrane calculated from the width and thickness of the membrane. Measurements were performed on three separate membranes for each sample to ensure the reproducibility of results.

6.2.9 SAXS Analysis

Ultra-small angle x-ray scattering (USAXS), small angle x-ray scattering (SAXS), and wide angle x-ray diffraction (WAXD) data were collected at Argonne National Laboratory beamline 9ID-C using a photon energy of 24 keV.[42] Scattering profiles are plotted as absolute intensity vs. q, where $q = \left(\frac{4\pi}{\lambda}\right)\sin(\theta)$, θ is one half of the scattering angle, and λ is the X-ray wavelength. SAXS measurements utilized the Pilatus 100k camera, and WAXD utilized the Pilatus 100k-w camera. Data reduction was performed using the Irena[43] and Nika[44] software packages provided by Argonne.

6.3 Results and Discussion

6.3.1 Synthesis of PFS-PEEK

To prepare perfluorosulfonated PEEK (PFS-PEEK), Ullmann coupling was utilized, as shown in **Figure 6.1**. Randomly brominated PEEK at high degrees of functionality (125 mol%) was chosen as the precursor polymer due to its high number of reactive sites and its high solubility in DMAc at reaction conditions. Although iodinated aryl groups are typically preferred for rapid

Ullmann coupling, the coupling of aryl-bromides with numerous types of substituents to iodinated perfluoroalkyl chains proceeds efficiently, especially for aryl-bromides with electron-withdrawing groups at the *meta* position.[35, 45-46] Thus, coupling of PFS-K to BrPEEK is expected to proceed effectively using a copper catalyst.

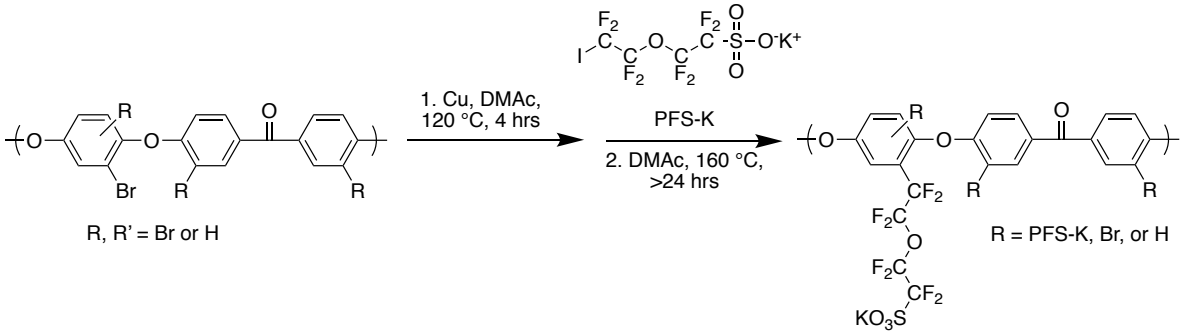

Figure 6.1. Reaction scheme for the Ullmann coupling of random BrPEEK with I-PFS-K.

In this work, the degree of perfluorosulfonation was controlled by varying the amount of PFS-K added to the reaction flask. Initially, the random BrPEEK is pale yellow-white in color, and following perfluorosulfonation the PFS-PEEK product is yellow-brown in color, consistent with sulfonated polymers. The structure of the resultant PFS-PEEK was determined using ^{1}H and ^{19}F NMR, as shown in **Figure 6.2** and **Figure 6.3**. The ^{1}H NMR spectra in DMSO revealed new peaks at 7.93 ppm, 7.45 ppm, and 7.08 ppm (a*, b*, and c*) that may be attributed to the protons adjacent to the perfluorosulfonate side chain. These peaks increase in intensity with increasing PFS-K concentration, and the peak positions confirm the successful coupling of PFS-K onto both the hydroquinone domains and the benzophenone domains of the BrPEEK. Furthermore, a decrease in the intensity of the of the c' and a' protons (protons adjacent to bromine) is observed, indicating a loss in bromine upon perfluorosulfonation and signifying reaction success. **Figure 6.3** shows the ^{19}F NMR spectra of the iodinated PFS-K side chain and the side chain following coupling to the PEEK backbone. The I-CF_2 signal at -72.66 ppm disappears following the Ullmann

coupling reaction, and a new signal at -111 ppm appears that is attributed to the fluorine of an aryl-CF_2- bond. Thus, successful coupling of PFS-K to the BrPEEK backbone was achieved.

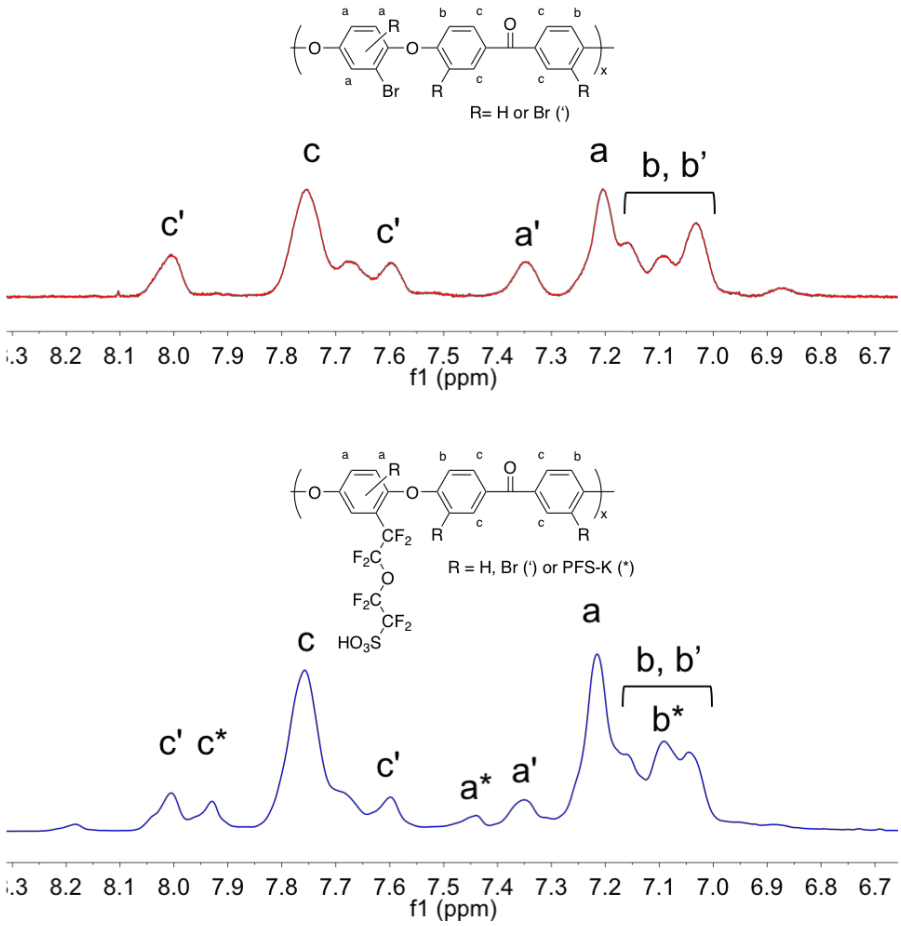

Figure 6.2. ^{1}H NMR spectra of random BrPEEK (top) and PFS-PEEK at 1,532 EW (bottom).

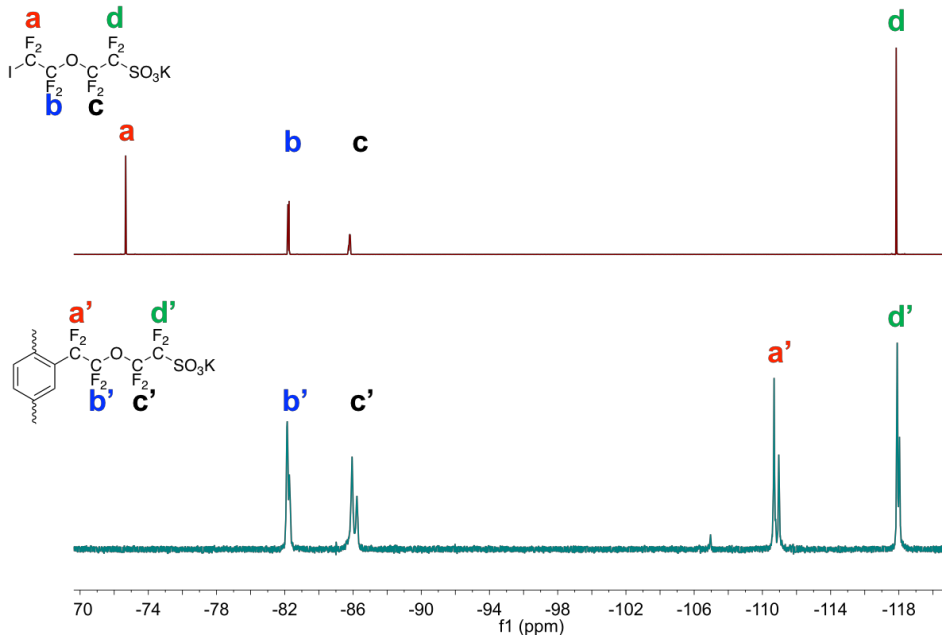

Figure 6.3. ^{19}F NMR spectra of I-PFS (top) and PFS-PEEK (bottom) obtained in DMSO-d6.

A control reaction was also performed to validate that no cross-coupling is observed between BrPEEK chains. Reactions were performed as described in **Section 6.2.3**, however no PFS-K was added to the reaction flask. No change in the ^{1}H NMR spectra of the BrPEEK before and after this control was observed, as shown in **Figure 6.4**. Thus, it is likely that no cross-coupling is occurring between the brominated PEEK chains. Integration of the spectra, however, indicates that the degree of bromination decreases from 125 mol% initially to 80 mol% following the control reaction. This suggests that the organo-copper intermediate (Ar-Cu) described in the mechanism of the Ullmann reaction was formed, and although it was unreactive towards other BrPEEK aryl bromides, it reacted with H^+ in the 2 M HNO_3 (aq) used to terminate/precipitate the reaction, resulting in reductive debromination.[35, 47] Because full debromination was not observed in this control reaction (not all Ar-Br groups became activated), it is likely that PFS-Cu intermediates also play a key role in the perfluorosulfonation of BrPEEK.

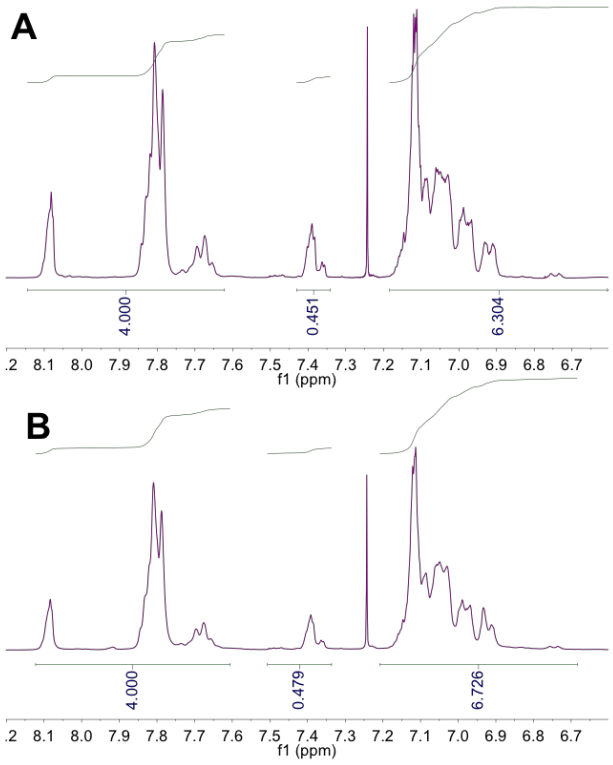

Figure 6.4. ^{1}H NMR spectra of random BrPEEK at 125 mol% bromination before (A) and after (B) the control Ullmann reaction. ^{1}H NMR was conducted in $CDCl_3$.

The equivalent weight (EW) and thereby the ion exchange capacity (IEC) of the PFS-PEEK samples was determined using ^{19}F NMR and a known amount of hexafluorobenzene as an internal standard, as shown **Table 6.1**. The target equivalent weights were determined using the following relation:

$$\mathrm{EW} = \left(\frac{100}{DS} - 1\right) \times MW_{nonionic} + MW_{ionic} \qquad \textbf{(6.5)}$$

where DS is the degree of perfluorosulfonation in mol%, $MW_{nonionic}$ is the molecular weight of the nonionic (i.e. BrPEEK) repeat unit, and MW_{ionic} is the molecular weight of the perfluorosulfonated repeat unit. It is important to note that this target value was calculated assuming no loss of bromine other than those lost during the coupling procedure. Assuming some unreacted, activated bromine is cleaved during precipitation in 2 M HNO_3, the actual target EW should likely be a lower value.

Elemental analysis will be helpful to completely elucidate the bromine content following the coupling reactions. As shown in **Table 6.1**, the actual degree of perfluorosulfonation is less than the targeted degree, and thus the EW is higher than the calculated target EW (and IEC is lower than targeted). The obtained degree of perfluorosulfonation increased with increasing amount of PFS added during the reaction (i.e. target DS), and at least 2/3 of the added PFS reacted with BrPEEK, suggesting a fairly good reaction yield. Differences in the yield between reactions is potentially the result of differences in PFS addition rate. More rapid addition could lead to cross-coupling of the more reactive iodinated PFS chains to one another instead of to the less reactive aryl bromide. Slow addition is desired to effectively dilute unreacted PFS and promote coupling to BrPEEK.

Table 6.1. Equivalent weight (EW) and ion exchange capacity (IEC) of PFS-PEEK determined by ^{19}F NMR. The target values

Target DS (mol%)	Target EW (g/mol)	Target IEC (mmol/g)	DS by NMR (mol%)	EW by NMR (g/mol)	IEC by NMR (mmol/g)
25	1,606	0.62	16	2,687	0.37
35	1,184	0.84	30	1,532	0.65
52	859	1.16	34	1,360	0.74
60	777	1.29	41	1,175	0.85
68	718	1.39	65	813	1.23

The perfluorosulfonation of BrPEEK was also investigated using FTIR, as shown in **Figure 6.5**. Perfluorosulfonation lead to the appearance of several new characteristic peaks when compared to BrPEEK. Peaks appear at 960 cm^{-1} and 990 cm^{-1} that are attributed to the symmetric and asymmetric stretching of (-CF_2-O-CF_2-), and a peak appears at 1140 cm^{-1} that is attributed to the symmetric stretching of (-CF_2-).[35] Furthermore, peaks appear at 1060 cm^{-1} and 1105 cm^{-1} that are assigned to stretching vibrations of the sulfonic acid group (-SO_3H).[33] It is also interesting to note that the large peak at 1470 cm^{-1} decreases in intensity following perfluorosulfonation, and

this is coupled with an increase in the intensity of the peak at 1490 cm^{-1}. These peaks are attributed to the skeletal ring vibrations of 1,2,4-trisubstituted aromatic rings and 1,4-disubstituted aromatic rings, respectively, and thus, debromination is confirmed in addition to perfluorosulfonation.[48]

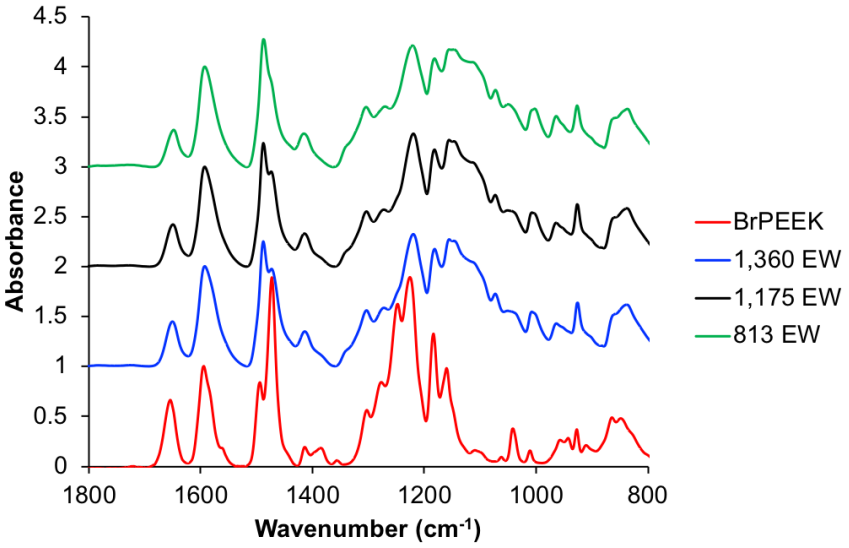

Figure 6.5. FTIR of initial BrPEEK and PFS-PEEK at various EW.

It should be noted that perflurosulfonation of BrPEEK results in significant changes to the polymer solubility. The original BrPEEK was highly soluble in $CHCl_3$ at room temperature, and only swelled in polar solvents such as DMSO and DMAc at room temperature. Elevated temperatures are necessary for dissolution of BrPEEK in DMSO and DMAc. Upon perfluorosulfonation, PFS-PEEK is insoluble in $CHCl_3$ and readily soluble in solvents such as DMSO, DMAc, and NMP at room temperature. These changes in solubility are consistent those observed by Liu upon the perfluorosulfonation of an iodinated PEEK derivative and demonstrate that the perfluorosulfonic acid side chain increases the polymer solubility in polar solvents.[33]

6.3.2 Thermal Properties of PFS-PEEK

The thermal properties of the PFS-PEEK membranes were investigated using DSC, as shown in **Figure 6.6**. The unreacted BrPEEK is completely amorphous and displays a pronounced

glass transition temperature (T_g) at 155 ºC. The T_g increases upon perfluorosulfonation, and the glass transition also becomes less pronounced. The increase in T_g is due to the aggregation of the ionic domains, which restricts the mobility of attached backbone chains. Consequently, an increase in T_g is observed with increasing degree of perfluorosulfonation (i.e. as EW decreases), and the T_g increases from 179 ºC to 210 ºC as the EW decreases from 1,350 g/mol to 813 g/mol. These T_g's are similar to those of sulfonated PEEK (SPEEK) at similar EW (T_g = 203 ºC at 1,150 g/mol EW).

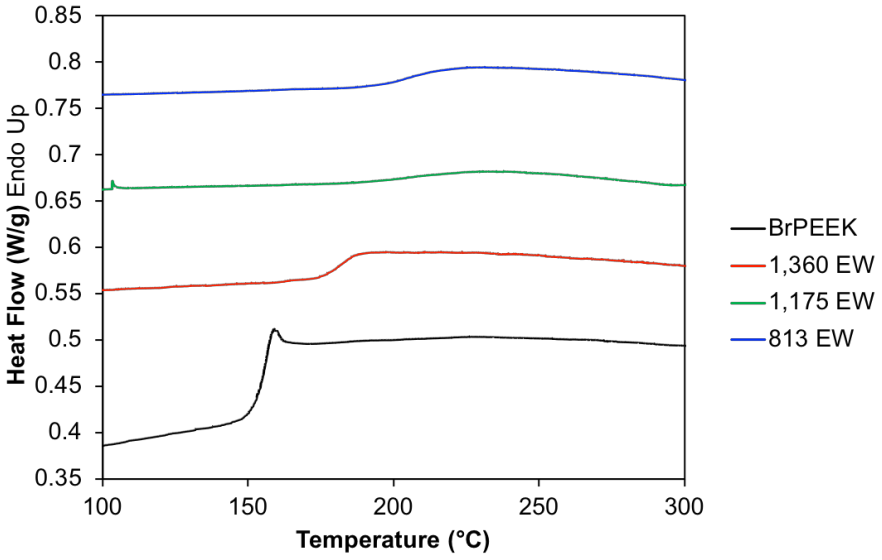

Figure 6.6. DSC thermograms of BrPEEK and PFS-PEEK (Cs^+-form) at various EW. The second heat is shown.

The thermal transitions of PFS-PEEK were further investigated using dynamic mechanical analysis (DMA), and tanδ as a function of temperature is displayed in **Figure 6.7**. BrPEEK displays a single transition at 170 ºC that is attributed to the glass transition of the polymer. Likewise, a single transition is observed for PFS-PEEK at temperatures higher than BrPEEK (T_g between 190 ºC and 205 ºC) that is attributed to destabilization of the ionic network (i.e. the T_g of the PFS domains). These transitions correlate well with those observed in DSC and again

demonstrate that the thermal transitions are dependent on the degree of perfluorosulfonation and thus the strength of the ionic network.

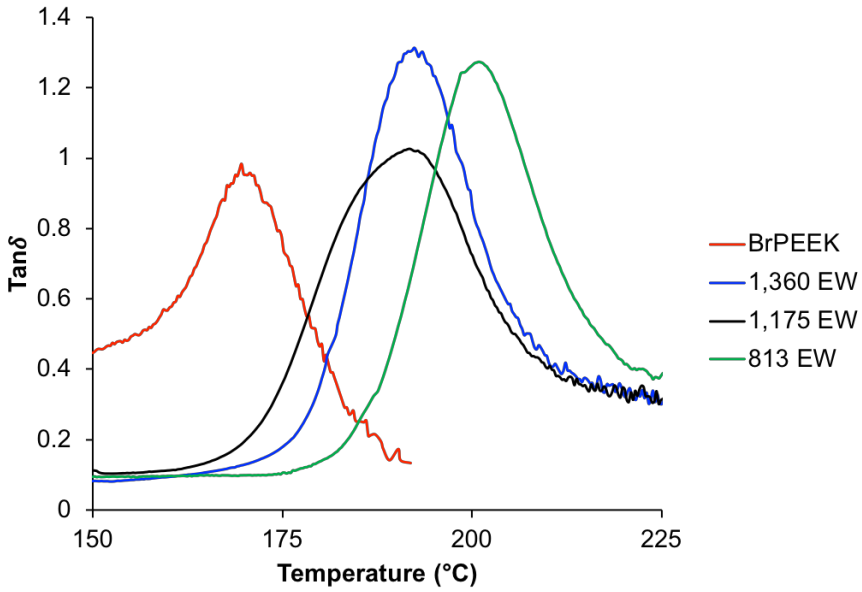

Figure 6.7. Tanδ of as-cast PFS-PEEK membranes in Cs^+-form.

6.3.3 Water Uptake and Conductivity of PFS-PEEK Membranes

For proton exchange membranes, water uptake is a key membrane characteristic that is closely related to proton conductivity. Water uptake aides in proton transport through the membranes, and thus conductivity generally increases with water uptake. Over-swelling of the membrane in water, however, leads to dilution of charge carriers and a loss in mechanical integrity, thereby hindering membrane performance. The water uptake of acidified PFS-PEEK was determined following boiling in water for 1 hour and then equilibrating in room temperature water for 12 hours. As shown in **Figure 6.8**, the water uptake of PFS-PEEK increases with decreasing EW due to a larger number of hydrophilic sulfonic acid sites. When compared to random SPEEK (prepared by homogeneous sulfonation in DCA[49]), PFS-PEEK exhibits less water uptake. For example, at 1,175 g/mol EW, PFS-PEEK exhibits a water uptake of 23 wt% while random SPEEK

exhibits a water uptake of 56 wt% at 1,148 g/mol EW. This is potentially attributed to the presence of unreacted, hydrophobic bromines remaining along the backbone of PFS-PEEK that limit the water uptake. It is important to note that at this EW, SPEEK begins to exhibit considerable dimensional swelling after boiling water, while the dimensions of PFS-PEEK remain relatively stable.

Furthermore, when compared to conventional SPEEK from the literature[50-52] (prepared by dissolution and sulfonation in H_2SO_4), PFS-PEEK membranes display higher water uptake at higher EW. The heterogeneous nature of the concurrent dissolution and sulfonation of PEEK using the conventional method leads to a large distribution in functionality along the polymer chain and overall less water uptake due to the resultant membrane morphology. Because of the more controlled, random architecture of the PFS-PEEK, improved water uptake is achieved.

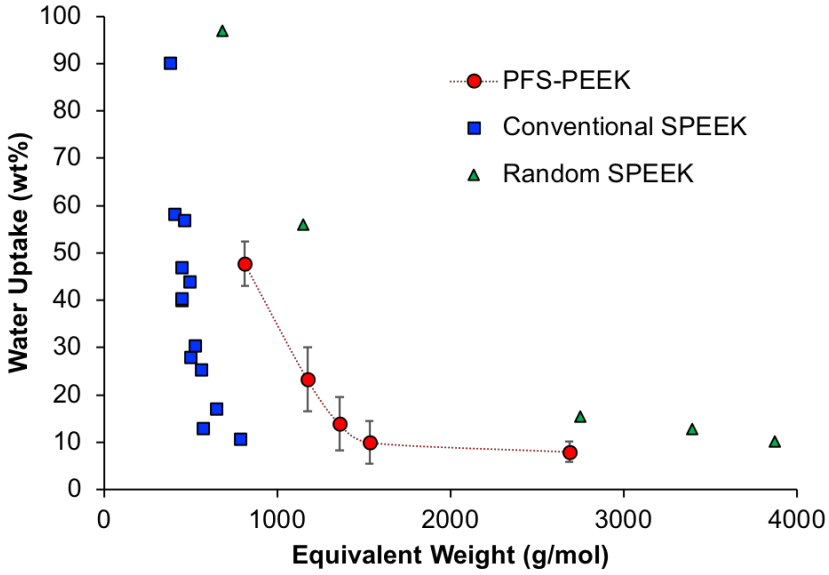

Figure 6.8. Water uptake of PFS-PEEK membranes (red circles) as compared to conventionally prepared SPEEK (blue squares)[50-52] and random SPEEK (green triangles).

The proton conductivity of PFS-PEEK membranes immersed in room temperature water is shown in **Figure 6.9**. When compared to random SPEEK and conventional SPEEK, PFS-PEEK

exhibits superior proton conductivity at similar EW. Considering the lower water uptake of PFS-PEEK compared to random SPEEK, this difference in proton conductivity is profound because increased water uptake is generally associated with higher conductivity. It is interesting to compare the EW required to reach a similar proton conductivity for the PFS-PEEK, random SPEEK, and conventional SPEEK membranes. For example, to achieve a proton conductivity of ~40 mS/cm, EWs of 813 g/mol, 624 g/mol, and 445 g/mol are required for PFS-PEEK, random SPEEK, and conventional SPEEK, respectively. This corresponds to degrees of sulfonation of 41 mol% for PFS-PEEK, 53 mol% for random SPEEK, and 79 mol% conventional SPEEK. Thus, less functionality is required for PFS-PEEK than directly sulfonated PEEK to achieve similar proton conductivity values. This is easily ascribed to the superacidic nature of the PFS side chain, which leads to greater proton dissociation and more loosely bound waters of hydration around the perfluorosulfonate group than the aryl sulfonate group, which facilitate proton transport.[53-54]

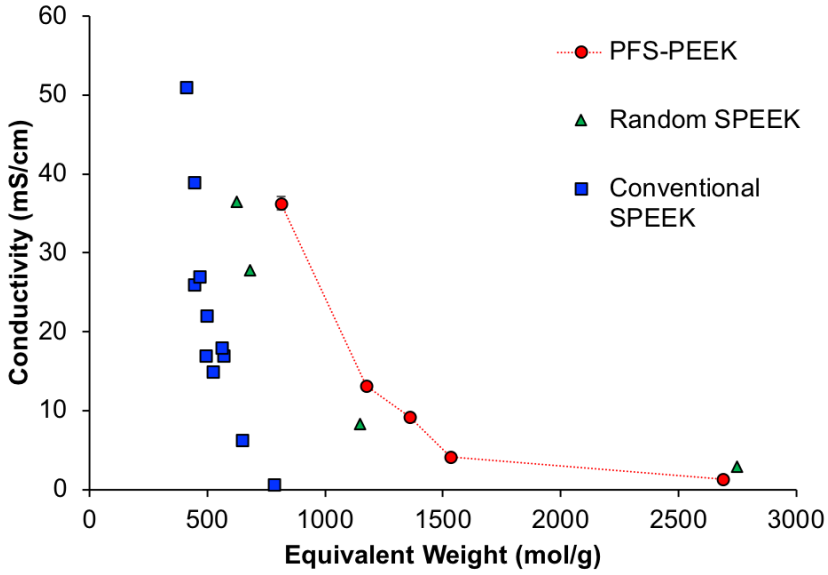

Figure 6.9. Conductivity of PFS-PEEK membranes (red circles) as compared to conventionally prepared SPEEK (blue squares)[50-52] and random SPEEK (green triangles).

The proton conductivity of PFS-PEEK was also compared to similar perfluorinated aromatic polymers, as shown in **Figure 6.10**. At comparable IEC values, PFS-PEEK demonstrates superior proton conductivity than perfluorinated poly(arylene ether ketone) (PFS-PAEK)[33], perfluorinated poly(arylene ether sulfone) (PFS-PAES)[23], and perfluorinated poly(arylene ether sulfone) multiblock copolymers[37] bearing identical PFS side chains. For example, at IEC ~ 0.9 meq/g, PFS-PEEK exhibits a conductivity of 36 mS/cm, while PFS-PAEK exhibits a conductivity of 24 mS/cm and PFS-PAES exhibits a conductivity of 15 mS/cm. Based on these results, it is expected that further increasing the IEC of PFS-PEEK will yield membranes with proton conductivities that rival or exceed the conductivity of Nafion® (77 mS/cm).

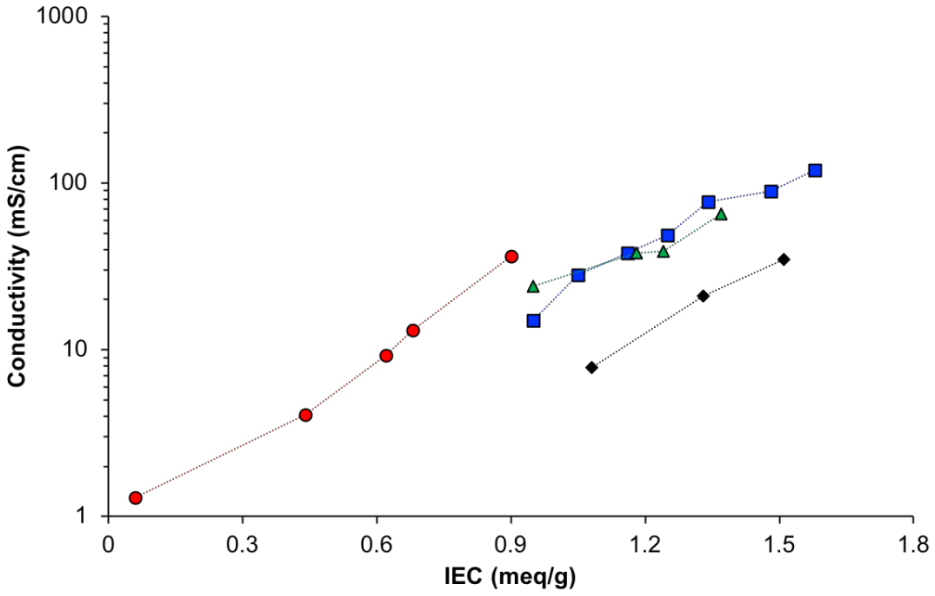

Figure 6.10. Proton conductivity as a function of IEC for PFS-PEEK (red circles), PFS-poly(arylene ether ketone)[33] (green triangles), PFS-poly(arylene ether sulfone)[23] (blue squares), and partially fluorinated PFS-poly(arylene ether sulfone) multiblock copolymers[37] (black diamonds).

6.3.4 Morphology of PFS-PEEK Membranes

Small-angle X-ray scattering (SAXS) was utilized to examine the ionomer morphology of PFS-PEEK, as shown in **Figure 6.11A**. SAXS was performed on membranes in Cs^+-form to

provide suitable contrast to examine the ionomer peak.[55] The SAXS profile of PFS-PEEK displays a clear ionomer peak at q ≈ 0.2 Å^{-1} that grows in intensity with decreasing EW (increasing IEC). Using Bragg's law (d = 2π/*q*), this peak position correlates to an inter-aggregate distance of 31 Å. In comparison, random SPEEK (as shown in **Figure 6.11B**) displays a prominent ionomer peak between 0.1 and 0.3 Å^{-1}. The ionomer peak shifts to higher *q* with increasing degree of sulfonation, and the center-to-center distance between ionic aggregates decreases from 45 Å to 27 Å as the EW decreases from 1,522 g/mol to 824 g/mol.

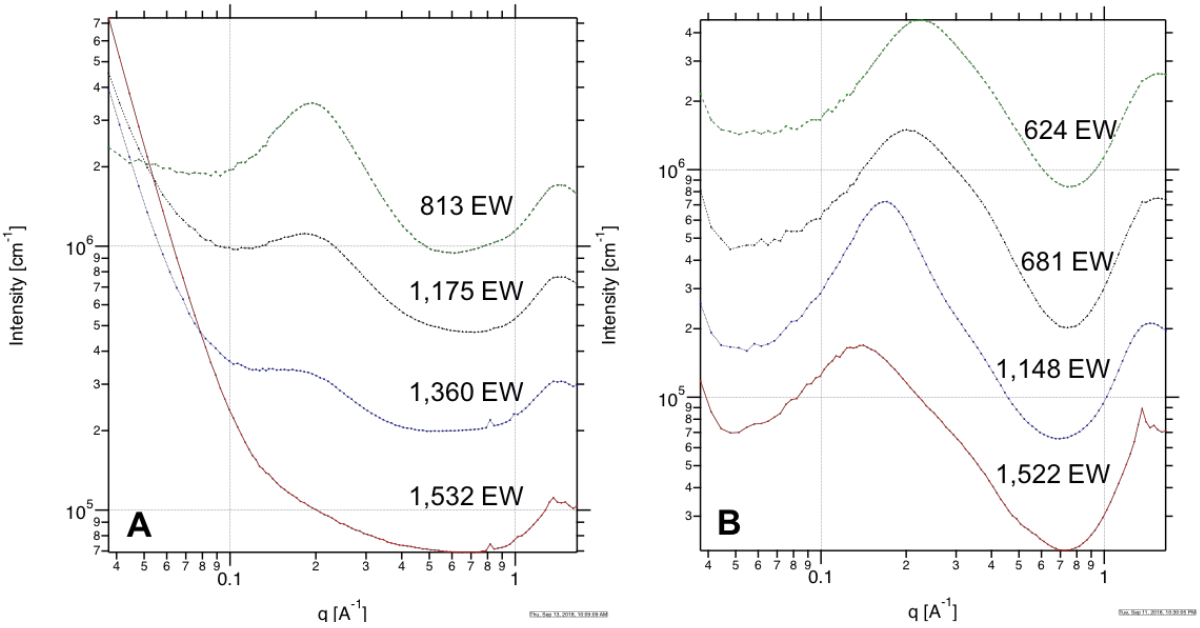

Figure 6.11. SAXS profiles of PFS-PEEK (A) and random SPEEK (B).

To further elucidate the differences in ionomer morphology, the ionomer peaks of PFS-PEEK and SPEEK were fit using the Kinning-Thomas modified hard sphere model. Using this model, the characteristic radius of ionic aggregates (*R*), the radius of closest approach (R_{ca}), and the inter-particle radius (R_{ip}) were determined, as shown in **Table 6.2**. With decreasing EW, PFS-PEEK displays an increase in *R* from 4.1 Å to 7.1 Å and a decrease in R_{ip} from 48 Å to 27 Å. SPEEK also displays a decrease in R_{ip} with decreasing EW, consistent with the center-to-center domain

distance determined from the Bragg spacing, however *R* decreases from 8.3 Å to 3.1 Å with decreasing EW. Thus, for both PFS-PEEK and random SPEEK, the ionic domains are become more closely spaced as the ion content increases. The ionic aggregate radius, however, increases with ion content with PFS-PEEK and decreases with ionic content for random SPEEK. The small cluster sizes and close domain spacing of random SPEEK implies that only narrow hydrophilic channels are generated in the membranes, while the larger domain spacing of PFS-PEEK implies wider hydrophilic channels. This likely leads to a less tortuous pathway for proton transport within the PFS-PEEK hydrophilic domains and combined with the superacidic nature of the PFS side chain, results in superior proton conductivity than SPEEK at similar EW.[13, 56]

Table 6.2. Ionomer peak fits of PFS-PEEK membranes.

Sample	EW (g/mol)	R (Å)	R_{ca} (Å)	R_{ip} (Å)
PFS-PEEK	1532	4.1	13.7	48.1
	1360	6.6	13.9	28.7
	1175	6.9	13.5	28.1
	813	7.1	13.4	26.5
SPEEK	1522	8.3	19.2	37.2
	1148	7.6	16.7	38.9
	681	4.9	12.2	22.8
	624	3.1	13.0	23.2

6.4 Blocky PFS-PEEK

Multiblock copolymers bearing PFS side chains have recently attracted significant interest due to their excellent hydrophilic-hydrophobic phase separation and superior proton conductivity to random copolymer analogues at similar IEC.[23, 57-59] To this end, the perfluorination of blocky BrPEEK was explored. Blocky BrPEEK was previously prepared by bromination of PEEK in the semicrystalline gel state. Using this method, bromination is restricted to the solvent-swollen amorphous domains, yielding highly functionalized domains and long domains of unfunctionalized PEEK that were tightly packed within the crystalline domains during

bromination.[49, 60-61] This gel-state functionalization process not only imparts a blocky architecture, but also maintains a high degree of crystallizability in the resultant copolymers, even at high degrees of functionality. Thus, the perfluorosulfonation of blocky BrPEEK is expected to yield crystallizable ionomers with excellent mechanical integrity (imparted by the crystallites) and improved phase separation compared to random PFS-PEEK.

Perfluorosulfonation reactions with blocky BrPEEK (DS_{Br} = 150 mol%) were carried out using the procedure in **Section 6.2.3**. It is important to note that blocky BrPEEK does not dissolve in the reaction solvent DMAc at these conditions due to its high crystallinity. It does, however, swell in DMAc at these conditions. Thus, blocky BrPEEK was ground into a fine powder prior to perfluorosulfonation and dispersed in DMAc for Ullmann coupling. The reaction was terminated by precipitation into 2 M HNO_3 (aq) and the product was stirred in 2 M HNO_3 (aq) for at least 12 hours to oxidize residual copper to its soluble $Cu(NO_3)_2$ form. Degrees of perfluorosulfonation of 30, 45, and 60 mol% were targeted (i.e. EW = 1,440 g/mol, 1,050 g/mol, and 856 g/mol, respectively), and the blocky PFS-PEEK products were found to be an opaque brown color, similar to random PFS-PEEK. FTIR was utilized to compare the blocky PFS-PEEK to the blocky BrPEEK starting material, as shown in **Figure 6.12**. Similar to reactions with random PFS-PEEK, new peaks appear at 960 cm^{-1}, 990 cm^{-1}, and 1140 cm^{-1} that are attributed the stretching vibrations of the perfluorinated side chain,[35] and peaks appear at 1060 cm^{-1} and 1105 cm^{-1} due to stretching vibrations of the sulfonic acid group.[33] Thus, the perfluorinated side chain was successfully coupled to the blocky BrPEEK backbone, despite the heterogeneous reaction conditions.

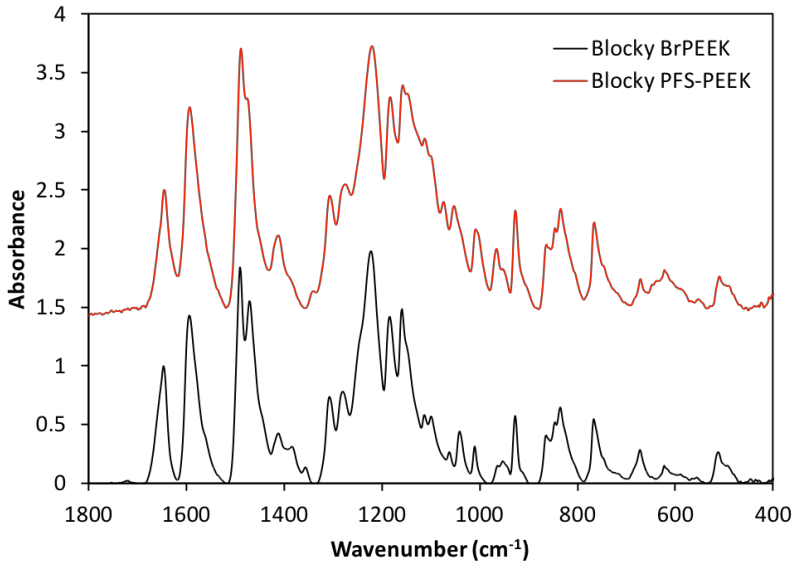

Figure 6.12. FTIR of blocky BrPEEK150 and blocky PFS-PEEK targeting 45 mol% perfluorosulfonation.

It is interesting to note that, unlike random PFS-PEEK, blocky PFS-PEEK is not fully soluble in polar aprotic solvents such as NMP or DMSO, likely due to the presence of long segments of unfunctionalized PEEK and crystallinity. In fact, blocky PFS-PEEK (at all degrees of functionality targeted) is only partially soluble in dichloroacetic acid (DCA), a good solvent for PEEK itself. Because blocky BrPEEK is soluble in DCA, this suggests that the perfluorosulfonic acid side chains are changing the solubility of blocky PFS-PEEK. To further characterize the blocky PFS-PEEK, the PFS-PEEK was dissolved in DCA at 175 ºC. At this temperature, blocky PFS-PEEK was mostly soluble. ^{19}F NMR spectra of the soluble fraction was collected in DCA, as shown in **Figure 6.13**. Clearly, similar peaks appear at similar chemical shifts to those observed in random PFS-PEEK (see **Figure 6.3**), and the location of the a' fluorines at -112 ppm confirms successful aryl-coupling of the iodinated PFS-K. The use of the internal standard HFB to determine EW was precluded due to the fact that blocky PFS-PEEK was not fully soluble in DCA, and thus no accurate EW was determined. Other solvents, such as phenol, 4-chlorophenol, and

hexafluoroisopropanol (HFIP) were attempted to dissolve blocky PFS-PEEK, however, only partial solubility was noted in each.

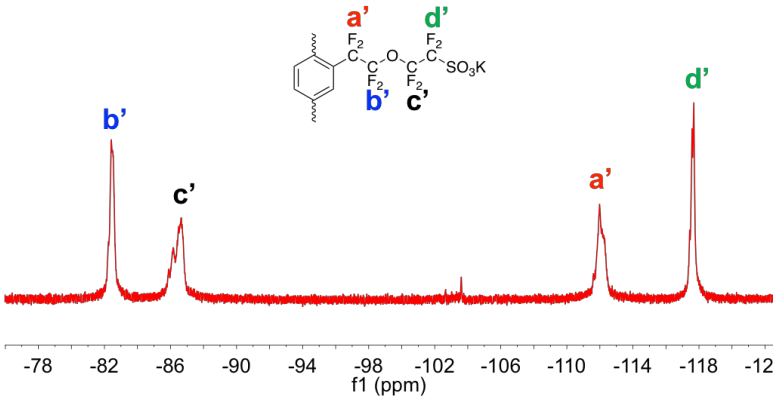

Figure 6.13. ^{19}F NMR of blocky PFS-PEEK targeting 60 mol% perfluorosulfonation.

Blocky PFS-PEEK membranes were prepared by casting from 10 w/v% solutions in DCA. Again, it is notable that the blocky PFS-PEEK is not completely soluble in this solvent, however, the insoluble fraction was removed prior to casting. The solutions were cast onto glass at 100 ºC, and resulted in brittle, opaque membranes. The ionomer morphology was investigated using USAXS/SAXS/WAXS at Argonne National Laboratory, as shown in **Figure 6.14**. The SAXS/WAXS profile of blocky PFS-PEEK targeting 60 mol% perfluorosulfonation reveals a clear ionomer peak at ~0.25 $Å^{-1}$ and WAXS peaks that are characteristic of the PEEK crystal structure. This suggests that the perfluorosulfonation of blocky BrPEEK preserves the crystallizability established during the gel-state bromination procedure. **Figure 6.14B** reveals the USAXS/SAXS profiles of blocky PFS-PEEK targeting 30 mol%, 45 mol%, and 60 mol% perfluorosulfonation. In the SAXS region (i.e. 0.006 $Å^{-1} < q < 0.6$ $Å^{-1}$), two distinct scattering features are present for the blocky PFS-PEEK membranes. A knee appears at $q \approx 0.05$ $Å^{-1}$ that is due to the interlamellar

scattering of the semicrystalline matrix, further verifying the semicrystalline nature of the blocky PFS-PEEK[58], and an ionomer peak appears at approximately 0.2 $Å^{-1}$ due to scattering of the ion-rich domains. The ionomer peak grows in intensity and shifts from 0.15 $Å^{-1}$ to 0.26 $Å^{-1}$ with increasing PFS content (i.e. a larger number of ionic groups). The center-to-center distance between the ionic aggregates, determined using Bragg's law ($d = 2\pi/q$) and the q value at the ionomer peak maximum, decreased from 43 Å to 24 Å with increasing PFS content, suggesting more closely spaced ionic domains. These spacings are similar to those observed with random PFS-PEEK (i.e. 25-47 Å).

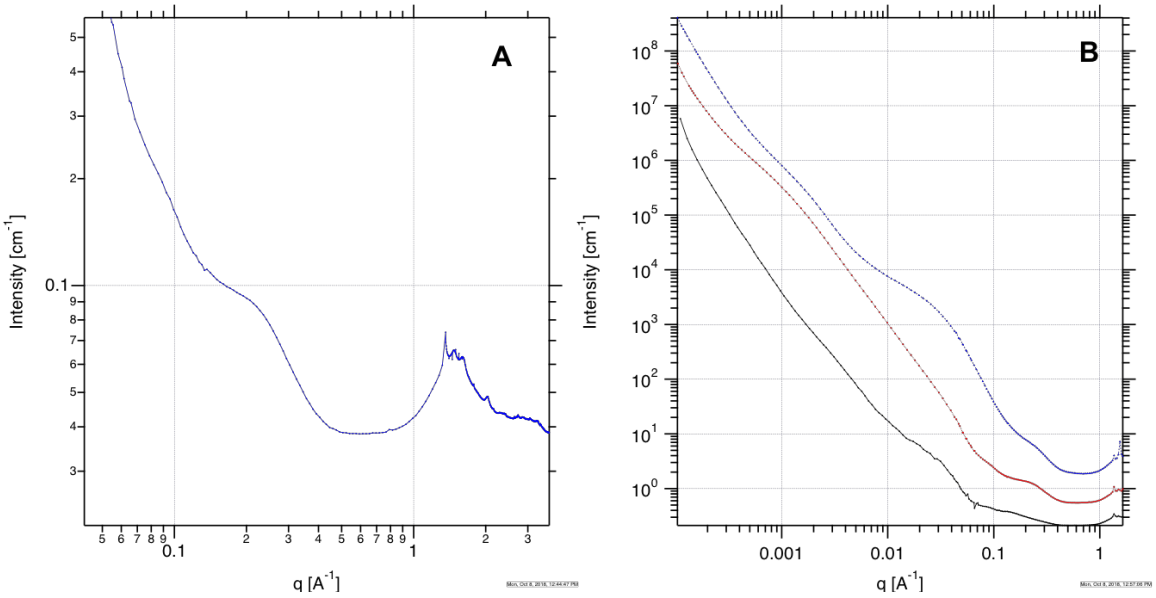

Figure 6.14. SAXS/WAXS profiles (A) of blocky PFS-PEEK (target DS = 60 mol%) and USAXS/SAXS profiles (B) of blocky PFS-PEEK with target DS = 30 mol% (black), target DS = 45 mol% (red), and target DS = 60 mol% (blue). All samples are in Cs^+-form.

The blocky PFS-PEEK membranes prepared using DCA were extremely brittle and broke into many small pieces upon swelling with water to remove them from the glass casting plate. Luckily, a membrane piece of blocky PFS-PEEK (target DS = 60 mol%) that was large enough for impedance analysis was obtained and was used to determine proton conductivity. The conductivity of blocky PFS-PEEK (60 mol%) in water at room temperature was found to be 27

mS/cm, much greater than the proton conductivity of random PFS-PEEK targeting 60 mol% functionality (13 mS/cm). This suggests that the blocky architecture is likely contributing to improved proton transport, however, the brittle membrane properties must be overcome to function in the operating environments of a fuel cell. Clearly, further work is required to determine an optimal solvent or solvent mixture for the blocky PFS-PEEK and to determine appropriate casting conditions for the blocky PFS-PEEK. The optimization of casting conditions will help elucidate the influence of both the blocky architecture and the crystalline domains on ionomer morphology and transport properties.

6.5 Conclusions

In this work, the perfluorosulfonation of brominated PEEK is examined. The successful Ullmann coupling of an iodinated perfluorosulfonate group (PFS) to random BrPEEK was demonstrated using a nano-copper catalyst, and PFS-PEEK was prepared at EW's between 800 and 2,600 g/mol by varying the PFS concentration during the coupling reaction. The PFS-PEEK membranes displayed increased glass transition temperatures with increasing degree of perfluorosulfonation due to restriction of the backbone chains by the electrostatic network. PFS-PEEK membranes displayed decreased water uptake compared to random SPEEK at similar EW. Despite the lower water content, PFS-PEEK demonstrated superior proton conductivity than random SPEEK and conventionally prepared SPEEK at similar EW, suggesting that the superacidic side chain greatly contributes to improved proton transport. Furthermore, the PFS-PEEK membranes displayed greater proton conductivity than other PFS-bearing hydrocarbon membranes at similar IEC, justifying the use of the PEEK-based hydrocarbon membrane. SAXS analysis of the ionomer domains revealed larger ionic aggregates, and thereby wider hydrophilic channels, for PFS-PEEK than random SPEEK, and thus, the enhanced proton conductivity of PFS-PEEK compared to random SPEEK is likely an effect of both the superacidic nature of the side

chains and the less tortuous hydrophilic pathways for proton transport. Perfluorosulfonation was also found to proceed effectively with blocky BrPEEK, resulting in semicrystalline membranes with superacidic side chains for proton transport. Future work will examine PFS-PEEK at higher degrees of perfluorosulfonation and investigate the effect of the blocky PFS-PEEK architecture on membrane properties.

6.6 References

1. Shi, Z.; Holdcroft, S., Synthesis and Proton Conductivity of Partially Sulfonated Poly([vinylidene difluoride-co-hexafluoropropylene]-b-styrene) Block Copolymers. *Macromolecules* **2005,** *38* (10), 4193-4201.
2. Drioli, E.; Regina, A.; Casciola, M.; Oliveti, A.; Trotta, F.; Massari, T., Sulfonated PEEK-WC membranes for possible fuel cell applications. *Journal of Membrane Science* **2004,** *228* (2), 139-148.
3. Chen, Y.; Guo, R.; Lee, C. H.; Lee, M.; McGrath, J. E., Partly fluorinated poly(arylene ether ketone sulfone) hydrophilic–hydrophobic multiblock copolymers for fuel cell membranes. *International Journal of Hydrogen Energy* **2012,** *37* (7), 6132-6139.
4. Mauritz, K. A.; Moore, R. B., State of Understanding of Nafion. *Chemical Reviews* **2004,** *104* (10), 4535-4586.
5. Eisenberg, A.; Hird, B.; Moore, R. B., A new multiplet-cluster model for the morphology of random ionomers. *Macromolecules* **1990,** *23* (18), 4098-4107.
6. Hsu, W. Y.; Gierke, T. D., Ion transport and clustering in nafion perfluorinated membranes. *Journal of Membrane Science* **1983,** *13* (3), 307-326.
7. Gierke, T. D.; Munn, G. E.; Wilson, F. C., The morphology in nafion perfluorinated membrane products, as determined by wide- and small-angle x-ray studies. *Journal of Polymer Science: Polymer Physics Edition* **1981,** *19* (11), 1687-1704.
8. Kusoglu, A.; Weber, A. Z., New Insights into Perfluorinated Sulfonic-Acid Ionomers. *Chemical Reviews* **2017,** *117* (3), 987-1104.
9. Chang, Y.; Lee, Y.-B.; Bae, C., Partially fluorinated sulfonated poly (ether amide) fuel cell membranes: influence of chemical structure on membrane properties. *Polymers* **2011,** *3* (1), 222-235.
10. Swier, S.; Chun, Y. S.; Gasa, J.; Shaw, M. T.; Weiss, R. A., Sulfonated poly(ether ketone ketone) ionomers as proton exchange membranes. *Polymer Engineering & Science* **2005,** *45* (8), 1081-1091.
11. Park, C. H.; Lee, C. H.; Guiver, M. D.; Lee, Y. M., Sulfonated hydrocarbon membranes for medium-temperature and low-humidity proton exchange membrane fuel cells (PEMFCs). *Progress in Polymer Science* **2011,** *36* (11), 1443-1498.
12. Peighambardoust, S. J.; Rowshanzamir, S.; Amjadi, M., Review of the proton exchange membranes for fuel cell applications. *International Journal of Hydrogen Energy* **2010,** *35* (17), 9349-9384.
13. Kreuer, K. D., On the development of proton conducting polymer membranes for hydrogen and methanol fuel cells. *Journal of Membrane Science* **2001,** *185* (1), 29-39.
14. Hou, H.; Di Vona, M. L.; Knauth, P., Building bridges: Crosslinking of sulfonated aromatic polymers—A review. *Journal of Membrane Science* **2012,** *423-424*, 113-127.
15. Di Vona, M. L.; Sgreccia, E.; Narducci, R.; Pasquini, L.; Hou, H.; Knauth, P., Stabilized Sulfonated Aromatic Polymers by in situ Solvothermal Cross-Linking. *Frontiers in Energy Research* **2014,** *2* (39).
16. Han, S.; Zhang, M.-S.; Shin, J.; Lee, Y.-S., A convenient crosslinking method for sulfonated poly(ether ether ketone) membranes via friedel–crafts reaction using 1,6-dibromohexane and aluminum trichloride. *Journal of Applied Polymer Science* **2014,** *131* (17).
17. Swier, S.; Ramani, V.; Fenton, J. M.; Kunz, H. R.; Shaw, M. T.; Weiss, R. A., Polymer blends based on sulfonated poly(ether ketone ketone) and poly(ether sulfone) as proton exchange membranes for fuel cells. *Journal of Membrane Science* **2005,** *256* (1), 122-133.

18. Jörissen, L.; Gogel, V.; Kerres, J.; Garche, J., New membranes for direct methanol fuel cells. *Journal of Power Sources* **2002,** *105* (2), 267-273.
19. Cui, W.; Kerres, J.; Eigenberger, G., Development and characterization of ion-exchange polymer blend membranes. *Separation and Purification Technology* **1998,** *14* (1), 145-154.
20. Erce, Ş.; Erdener, H.; Akay, R. G.; Yücel, H.; Baç, N.; Eroğlu, İ., Effects of sulfonated polyether-etherketone (SPEEK) and composite membranes on the proton exchange membrane fuel cell (PEMFC) performance. *International Journal of Hydrogen Energy* **2009,** *34* (10), 4645-4652.
21. Chang, J.-H.; Park, J. H.; Park, G.-G.; Kim, C.-S.; Park, O. O., Proton-conducting composite membranes derived from sulfonated hydrocarbon and inorganic materials. *Journal of Power Sources* **2003,** *124* (1), 18-25.
22. Abhishek, R.; A., H. M.; Xiang, Y.; Yanxiang, L.; E., G. T.; E., M. J., Influence of chemical composition and sequence length on the transport properties of proton exchange membranes. *Journal of Polymer Science Part B: Polymer Physics* **2006,** *44* (16), 2226-2239.
23. Assumma, L.; Iojoiu, C.; Mercier, R.; Lyonnard, S.; Nguyen, H. D.; Planes, E., Synthesis of partially fluorinated poly(arylene ether sulfone) multiblock copolymers bearing perfluorosulfonic functions. *Journal of Polymer Science Part A: Polymer Chemistry* **2015,** *53* (16), 1941-1956.
24. Bae, B.; Miyatake, K.; Uchida, M.; Uchida, H.; Sakiyama, Y.; Okanishi, T.; Watanabe, M., Sulfonated Poly(arylene ether sulfone ketone) Multiblock Copolymers with Highly Sulfonated Blocks. Long-Term Fuel Cell Operation and Post-Test Analyses. *ACS Applied Materials & Interfaces* **2011,** *3* (7), 2786-2793.
25. Elabd, Y. A.; Hickner, M. A., Block Copolymers for Fuel Cells. *Macromolecules* **2011,** *44* (1), 1-11.
26. Ghassemi, H.; McGrath, J. E.; Zawodzinski Jr, T. A., Multiblock sulfonated–fluorinated poly(arylene ether)s for a proton exchange membrane fuel cell. *Polymer* **2006,** *47* (11), 4132-4139.
27. Jung, M. S.; Kim, T.-H.; Yoon, Y. J.; Kang, C. G.; Yu, D. M.; Lee, J. Y.; Kim, H.-J.; Hong, Y. T., Sulfonated poly(arylene sulfone) multiblock copolymers for proton exchange membrane fuel cells. *Journal of Membrane Science* **2014,** *459*, 72-85.
28. Mikami, T.; Miyatake, K.; Watanabe, M., Poly(arylene ether)s Containing Superacid Groups as Proton Exchange Membranes. *ACS Applied Materials & Interfaces* **2010,** *2* (6), 1714-1721.
29. Ghassemi, H.; Schiraldi, D. A.; Zawodzinski, T. A.; Hamrock, S., Poly(arylene ether)s with Pendant Perfluoroalkyl Sulfonic Acid Groups as Proton-Exchange Membrane Materials. *Macromolecular Chemistry and Physics* **2011,** *212* (7), 673-678.
30. Chang, Y.; Mohanty, A. D.; Smedley, S. B.; Abu-Hakmeh, K.; Lee, Y. H.; Morgan, J. E.; Hickner, M. A.; Jang, S. S.; Ryu, C. Y.; Bae, C., Effect of Superacidic Side Chain Structures on High Conductivity Aromatic Polymer Fuel Cell Membranes. *Macromolecules* **2015,** *48* (19), 7117-7126.
31. Chang, Y.; Brunello, G. F.; Fuller, J.; Hawley, M.; Kim, Y. S.; Disabb-Miller, M.; Hickner, M. A.; Jang, S. S.; Bae, C., Aromatic Ionomers with Highly Acidic Sulfonate Groups: Acidity, Hydration, and Proton Conductivity. *Macromolecules* **2011,** *44* (21), 8458-8469.
32. Kobayashi, Y.; Kumadaki, I., Trifluoromethylation of aromatic compounds. *Tetrahedron Letters* **1969,** *10* (47), 4095-4096.
33. Liu, S.; Luo, W.; Zhang, H.; Li, X.; Hu, W.; Guiver, M. D.; Liu, B., Novel iodo-containing poly(arylene ether ketone)s as intermediates for grafting perfluoroalkyl sulfonic acid groups. *Reactive and Functional Polymers* **2017,** *111*, 7-13.

34. Nakabayashi, K.; Higashihara, T.; Ueda, M., Polymer Electrolyte Membranes Based on Poly(phenylene ether)s with Pendant Perfluoroalkyl Sulfonic Acids. *Macromolecules* **2011,** *44* (6), 1603-1609.
35. Zeng, Y.; Gu, L.; Zhang, L.; Cheng, Z.; Zhu, X., Synthesis of highly proton-conductive poly(arylene ether sulfone) bearing perfluoroalkyl sulfonic acids via polymer post-modification. *Polymer* **2017,** *123*, 345-354.
36. Takuya, S.; Kenji, M.; Masahiro, W., Synthesis, Properties, and Fuel Cell Performance of Perfluorosulfonated Poly(arylene ether)s. *Bulletin of the Chemical Society of Japan* **2010,** *83* (8), 960-968.
37. Yoshimura, K.; Iwasaki, K., Aromatic Polymer with Pendant Perfluoroalkyl Sulfonic Acid for Fuel Cell Applications. *Macromolecules* **2009,** *42* (23), 9302-9306.
38. Nakagawa, T.; Nakabayashi, K.; Higashihara, T.; Ueda, M., Polymer electrolyte membrane based on poly(ether sulfone) containing binaphthyl units with pendant perfluoroalkyl sulfonic acids. *Journal of Polymer Science Part A: Polymer Chemistry* **2011,** *49* (14), 2997-3003.
39. Shimura, T.; Watanabe, M.; Miyatake, K., Synthesis of superacid-modified poly(arylene ether sulfone)s via post-bromination. *RSC Advances* **2012,** *2* (12), 5199-5204.
40. Xu, K.; Oh, H.; Hickner, M. A.; Wang, Q., Highly Conductive Aromatic Ionomers with Perfluorosulfonic Acid Side Chains for Elevated Temperature Fuel Cells. *Macromolecules* **2011,** *44* (12), 4605-4609.
41. Oshima, T.; Yoshizawa-Fujita, M.; Takeoka, Y.; Rikukawa, M., Use of a High-Performance Poly(p-phenylene)-Based Aromatic Hydrocarbon Ionomer with Superacid Groups in Fuel Cells under Low Humidity Conditions. *ACS Omega* **2016,** *1* (5), 939-942.
42. Ilavsky, J.; Zhang, F.; Allen, A. J.; Levine, L. E.; Jemian, P. R.; Long, G. G., Ultra-Small-Angle X-ray Scattering Instrument at the Advanced Photon Source: History, Recent Development, and Current Status. *Metallurgical and Materials Transactions A* **2013,** *44* (1), 68-76.
43. Ilavsky, J.; R. Jemian, P., *Irena: Tool Suite for Modeling and Analysis of Small Angle Scattering*. 2009; Vol. 42, p 347-353.
44. Ilavsky, J., Nika: software for two-dimensional data reduction. *Journal of Applied Crystallography* **2012,** *45* (2), 324-328.
45. McLoughlin, V. C. R.; Thrower, J., A route to fluoroalkyl-substituted aromatic compounds involving fluoroalkylcopper intermediates. *Tetrahedron* **1969,** *25* (24), 5921-5940.
46. Chen, G. J.; Tamborski, C., Polyfluoroalkylation of bromoaromatic compounds via perfluoroalkylcopper intermediates. *Journal of Fluorine Chemistry* **1989,** *43* (2), 207-228.
47. Lewin, A. H.; Cohen, T., The mechanism of the Ullmann reaction. Detection of an organocopper intermediate. *Tetrahedron Letters* **1965,** *6* (50), 4531-4536.
48. Al Lafi, A. G., The sulfonation of poly(ether ether ketone) as investigated by two-dimensional FTIR correlation spectroscopy. *Journal of Applied Polymer Science* **2015,** *132* (2), n/a-n/a.
49. Anderson, L. J.; Yuan, X.; Fahs, G. B.; Moore, R. B., Blocky Ionomers via Sulfonation of Poly(ether ether ketone) in the Semicrystalline Gel State. *Macromolecules* **2018,** *51* (16), 6226-6237.
50. Jiang, R.; Kunz, H. R.; Fenton, J. M., Investigation of membrane property and fuel cell behavior with sulfonated poly(ether ether ketone) electrolyte: Temperature and relative humidity effects. *Journal of Power Sources* **2005,** *150*, 120-128.
51. Kaliaguine, S.; Mikhailenko, S.; Wang, K.; Xing, P.; Robertson, G.; Guiver, M., Properties of SPEEK based PEMs for fuel cell application. *Catalysis Today* **2003,** *82* (1), 213-222.

52. Luu, D. X.; Cho, E.-B.; Han, O. H.; Kim, D., SAXS and NMR Analysis for the Cast Solvent Effect on sPEEK Membrane Properties. *The Journal of Physical Chemistry B* **2009,** *113* (30), 10072-10076.
53. Paddison, S., *The Modeling of Molecular Structure and Ion Transport in Sulfonic Acid Based Ionomer Membranes*. 2001; Vol. 4.
54. Black, S. B.; Chang, Y.; Bae, C.; Hickner, M. A., FTIR Characterization of Water–Polymer Interactions in Superacid Polymers. *The Journal of Physical Chemistry B* **2013,** *117* (50), 16266-16274.
55. Gebel, G., Structure of Membranes for Fuel Cells: SANS and SAXS Analyses of Sulfonated PEEK Membranes and Solutions. *Macromolecules* **2013,** *46* (15), 6057-6066.
56. Yang, B.; Manthiram, A., Comparison of the small angle X-ray scattering study of sulfonated poly(etheretherketone) and Nafion membranes for direct methanol fuel cells. *Journal of Power Sources* **2006,** *153* (1), 29-35.
57. Mikami, T.; Miyatake, K.; Watanabe, M., Synthesis and properties of multiblock copoly(arylene ether)s containing superacid groups for fuel cell membranes. *Journal of Polymer Science Part A: Polymer Chemistry* **2011,** *49* (2), 452-464.
58. Nguyen, H.-D.; Assumma, L.; Judeinstein, P.; Mercier, R.; Porcar, L.; Jestin, J.; Iojoiu, C.; Lyonnard, S., Controlling Microstructure–Transport Interplay in Highly Phase-Separated Perfluorosulfonated Aromatic Multiblock Ionomers via Molecular Architecture Design. *ACS Applied Materials & Interfaces* **2017,** *9* (2), 1671-1683.
59. Assumma, L.; Nguyen, H.-D.; Iojoiu, C.; Lyonnard, S.; Mercier, R.; Espuche, E., Effects of Block Length and Membrane Processing Conditions on the Morphology and Properties of Perfluorosulfonated Poly(arylene ether sulfone) Multiblock Copolymer Membranes for PEMFC. *ACS Applied Materials & Interfaces* **2015,** *7* (25), 13808-13820.
60. Noble, K. F.; Noble, A. M.; Talley, S. J.; Moore, R. B., Blocky bromination of syndiotactic polystyrene via post-polymerization functionalization in the heterogeneous gel state. *Polymer Chemistry* **2018**.
61. Fahs, G. B.; Benson, S. D.; Moore, R. B., Blocky Sulfonation of Syndiotactic Polystyrene: A Facile Route toward Tailored Ionomer Architecture via Postpolymerization Functionalization in the Gel State. *Macromolecules* **2017,** *50* (6), 2387-2396.

Chapter 7

Conclusions and Suggested Future Work

7.1 Concluding Remarks

In this work, the functionalization of poly(ether ether ketone) (PEEK) was investigated to develop novel hydrocarbon materials for proton exchange membrane fuel cells (PEMFCs). Conventionally, PEEK is functionalized by sulfonation in concentrated sulfuric acid, which is used as both the solvent and the sulfonating reagent. Despite the fact that H_2SO_4 reacts with PEEK during dissolution, it is one of the few reported solvents for PEEK. Thus, the scope of post-polymerization functionalization reactions for PEEK has been limited to sulfonation, with little control over copolymer architecture and no prospects for other types of functionalization.

With the discovery of a novel solvent for PEEK (dichloroacetic acid – DCA) that does not functionalize the PEEK, it is now possible to perform truly homogeneous reactions with PEEK to prepare randomly functionalized PEEK. It is even more remarkable that PEEK is capable of forming semicrystalline, thermoreversible gels in DCA[1-2], and thus, an entirely new, heterogeneous reaction state is possible. Using inspiration from the sulfonation of semicrystalline gels of syndiotactic polystyrene[3], the gel-state sulfonation of PEEK in DCA was explored to prepared blocky sulfonated PEEK (SPEEK) copolymers with densely sulfonated domains and unfunctionalized, crystallizable domains. Compared to random SPEEK ionomers at similar degrees of sulfonation (DS), blocky SPEEK exhibited enhanced crystallizability, decreased melting point depression, and faster crystallization kinetics, even at ion contents at low as 3.6 mol%. Superior proton conductivity was observed for blocky SPEEK membranes compared to random SPEEK analogues, despite similar water content and swelling ratios for the blocky and random SPEEK membranes at ion contents up to 15 mol%. X-ray scattering further elucidated the semicrystalline architecture of the random and blocky SPEEK ionomers and revealed a suppressed

ionomer peak for the blocky SPEEK compared to random SPEEK, likely due to close association of the blocky ionic domains with the crystalline lamella. Thus, distinctly different ionomer morphologies were evident for random SPEEK prepared in the homogeneous solution state and blocky SPEEK prepared in the heterogeneous gel state, contributing to the improved proton transport of blocky SPEEK.

Sulfonation in the semicrystalline gel state using DCA as the reaction solvent afforded blocky copolymers with up to 15 mol% sulfonation, however, the conditions required (i.e. reaction times and sulfonation reagent concentration) to produce blocky SPEEK at higher DS resulted in dissolution of the gel. To stabilize the semicrystalline gel state during sulfonation and to progress towards more industrially relevant DS, gel state sulfonation reactions were performed using a chlorinated non-solvent (1,2-dichloroethane) as the reaction solvent. The non-solvent method afforded blocky SPEEK with both high DS and high crystallinity (e.g. 45 mol% DS with X_c = 14 wt%), and blocky SPEEK prepared in this manner exhibited considerably greater crystallizability and less significant melting point depression than random SPEEK and blocky SPEEK prepared in DCA. Furthermore, phase separation between unfunctionalized blocks and ion-rich blocks was noted for the blocky SPEEK membranes due to the presence of a low-temperature T_g on par with the T_g of PEEK. This effect was not observed for random SPEEK membranes, which exhibited a single high-temperature T_g above ~200 ºC that increased with increasing DS. This hydrophilic-hydrophobic phase separation of the blocky SPEEK contributed to enhanced water uptake and improved proton conductivity compared to random SPEEK. Morphological analysis using USAXS/SAXS further elucidated that blocky SPEEK membranes had more closely spaced ionic aggregates compared to random SPEEK and close association of the ionic domains to the crystalline lamella was noted for blocky SPEEK, even at high DS. Thus, sulfonation in the semicrystalline gel state was shown to produce SPEEK copolymers with controlled blocky

architectures, high functionality, and maintained crystallizability that resulted in membranes with superior proton transport to random SPEEK copolymers. This simple post-polymerization method thereby afforded copolymers with properties reminiscent of directly-synthesized multiblock copolymers and the benchmark ionomer, Nafion®.

The discovery of DCA as a solvent for PEEK also enabled the exploration of functionalization chemistries aside from sulfonation. The random and blocky bromination of PEEK was investigated to develop PEEK derivatives with reactive aryl-bromides, thereby broadening the scope of potential functionalities extensively. Bromination using *N*-bromosuccinimide proceeded quantitatively in both the solution-state and gel-state, producing random and blocky BrPEEK copolymers, respectively, with high degrees of bromination up to 175 mol%. Blocky BrPEEK displayed significant spectroscopic evidence of long domains of unfunctionalized homopolymer, and these translated to a higher melting temperature, increased degree of crystallinity, and more rapid crystallization kinetics when compared to random BrPEEK at similar degrees of bromination. In fact, while the melting point depression of random BrPEEK followed in close agreement to Flory's theory of crystallization in copolymers, blocky BrPEEK displayed a nominal decrease in T_m from that of PEEK itself. Furthermore, the controlled architecture and high crystallizability of blocky BrPEEK even enabled the gelation of blocky BrPEEK at all degrees of bromination up to 150 mol%. It is also remarkable that USAXS/SAXS analysis revealed excess scattering at low q for blocky BrPEEK films, suggesting phase-contrast between the densely brominated domains and the unfunctionalized domains. This not only confirms the blocky architecture, but also suggests phase-separation into domains similar in size to conventional block copolymers. Overall, blocky bromination proceeded more efficiently than blocky sulfonation, due to the inability of the brominating reagent (NBS) to dissolve the semicrystalline gels and afforded controlled architectures for subsequent reactions.

The use of the blocky BrPEEK template to prepare hydrophilic-hydrophobic multiblock copolymers was explored by sulfonating the remaining unfunctionalized domains, thereby producing blocky brominated-sulfonated PEEK (BrSPEEK). It is important to note that because the blocky architecture was previously established during the gel-state functionalization process, this sulfonation reaction may be carried out in the homogeneous solution state, while preserving the blocky architecture. The degree of sulfonation was readily controlled by the blocky brominated architecture, and the resultant DS was found to increase with decreasing bromine content and increasing crystallinity (i.e. increasing unfunctionalized PEEK content). Multi-phase behavior was observed using DSC and DMA for BrSPEEK with degrees of sulfonation up to 40 mol%, suggesting phase separation between the densely brominated blocks and the ionic blocks. This phase separation contributed to decreased water uptake and areal swelling compared to random SPEEK and resulted in considerably higher proton conductivity at much lower hydration levels (λ).

Finally, the Ullmann coupling of perfluorosulfonic acid (PFS) side chains to BrPEEK was explored to produce PFS-PEEK membranes with superacid functionalities. The coupling of PFS to BrPEEK proceeded efficiently in both the solution state (random BrPEEK) and heterogeneous state (blocky BrPEEK) using a nano-copper catalyst to produce PFS-PEEK with equivalent weights (EW) from 800 g/mol to 2,600 g/mol. Compared to random SPEEK at similar EW, PFS-PEEK membranes exhibited decreased water content, less dimensional swelling, and improved proton transport. SAXS analysis revealed that the improved proton transport properties were not only due to the superacidic nature of the pendant chain, but also due to wider hydrophilic channels within the membranes, resulting in more continuous pathways for proton transport. Furthermore, the perfluorosulfonation of blocky BrPEEK yielded blocky PFS-PEEK with maintained

crystallizability. This work provided the first report of perfluorosulfonated PEEK prepared by post-polymerization functionalization using commercially-derived PEEK.

Overall, this work provided a novel platform for the preparation of hydrocarbon proton exchange membranes using a simple post-polymerization functionalization procedure. The established methods produced blocky-type copolymers with properties reminiscent of multiblock copolymers prepared by direct polymerization from monomers/oligomers.

7.2 Future Work

7.2.1 Novel Polymers for Gel-State Functionalization

A wide variety of polymers exhibit semicrystalline morphologies, yet only a handful have been shown to produce thermoverersible, semicrystalline gels from solution. Of those shown to form thermoreversible gels are syndiontactic polystyrene, poly(ether ether ketone)[1-2], poly(phenylene oxide)[4-5], isotactic poly(propylene)[6-7], poly(ethylene)[8-9], poly(vinylidene fluoride)[10-11], poly(vinyl chloride)[2], and stereoregular poly(methyl methacrylate)[12-13], representing just a minute population of all semicrystalline polymers. Likely, many more semicrystalline polymers are capable of forming semicrystalline gels from solution given the right polymer-solvent pair, and thus, a widely unexplored void exists for both the gelation of semicrystalline polymers and the types of polymers that may be functionalized using gel-state chemistries.

A simple extension of the gel-state functionalization process is the blocky bromination of PPO, which (as stated above) has been proven to form semicrystalline, thermoreversible gels in several known solvents. PPO is a particularly useful platform, because the functionalization of PPO (e.g. sulfonation, bromination, quaternary ammonium functionalized, etc.) has been extensively explored to prepare PPO derivatives for membrane applications.[14-18] To test the potential of PPO-based gel-state chemistry, the solubility and gelation of PPO in DCA was explored. PPO readily dissolved in DCA, and formed semicrystalline, thermoreversible gels at

sufficiently high concentrations (i.e. ~30-50 wt%). Bromination was performed using *N*-bromosuccinimide (NBS) in solution and in the gel-state using the method previously developed for PEEK (**Chapter 4**), as shown in **Figure 7.1**.

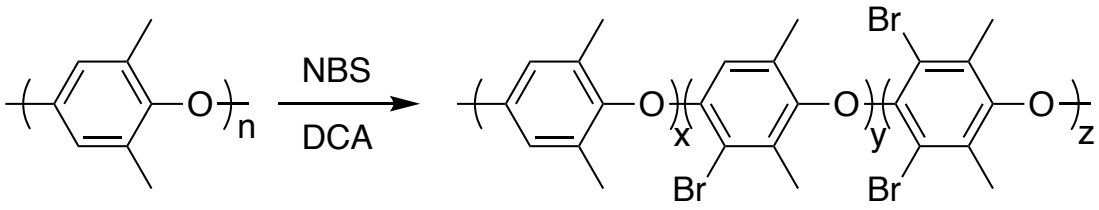

Figure 7.1. Synthetic scheme for the bromination of poly(2,6-dimethyl-1,4-phenylene oxide) (PPO).

The degree of bromination was controlled by varying the amount of NBS added to the reaction flask, and bromination to 25, 50, 75, and 100 mol% was targeted. ^{1}H NMR spectra of PPO and randomly brominated PPO at 50 mol% bromination (RBrPPO50) is shown in **Figure 7.2**. Upon bromination, new peaks appear at 6.15 ppm and 2.3 ppm due to aryl-bromination of the PPO backbone, and no evidence of methyl-bromination was observed.[19] The degree of bromination was calculated by integration of the a/a' signals relative to the b/b' signals, and the actual degree of bromination is reported in **Table 7.1**. As observed with PEEK, the random bromination of PPO proceeds quantitatively until high degrees of bromination are targeted (i.e. 100 mol%). The blocky bromination of PPO, however, is not as quantitative, resulting in degrees of bromination of 39 mol% and 56 mol% for targets of 50 mol% and 100 mol%, respectively. This difference is attributed to the high likelihood of monobromination (>93%) of the PPO repeat unit, determined by integrating the a' peak and comparing to the total degree of bromination. Because dibromination is not likely on the PPO repeat unit and bromination is the gel state is restricted to only the amorphous domains, the resultant degree of bromination is controlled by the total amorphous content within the semicrystalline gel.

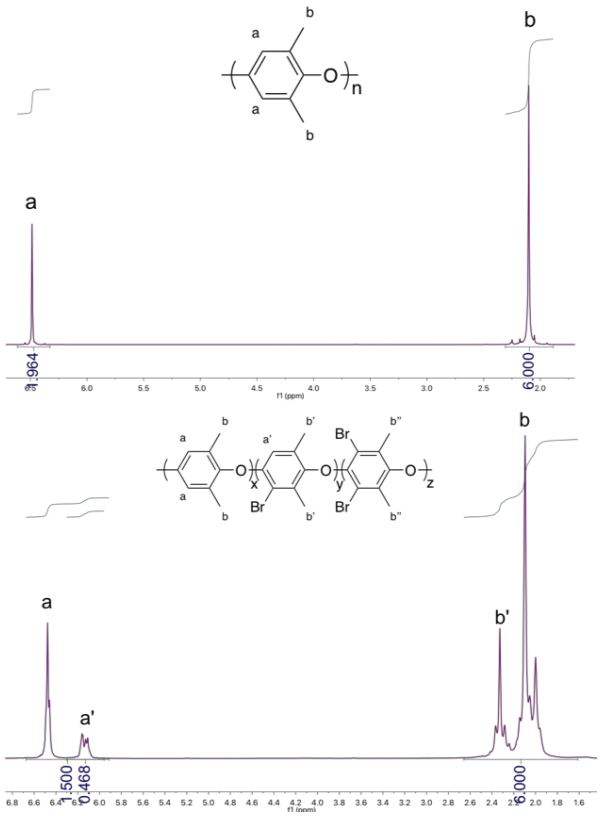

Figure 7.2. ^{1}H NMR spectra and peak assignments of PPO (top) and random BrPPO targeting 50 mol% bromination (bottom).

Table 7.1. Degree of bromination for random and blocky BrPPO determined by ^{1}H NMR.

Sample	Architecture	Target DS_{Br} (mol%)	DS_{Br} by ^{1}H NMR (mol%)	% Monobromination
RBrPPO25	Random	25	25	97
RBrPPO50	Random	50	50	94
RBrPPO75	Random	75	75	93
RBrPPO93	Random	100	93	96
BBrPPO39	Blocky	50	39	96
BBrPPO56	Blocky	100	56	99

It is useful to compare the spectra of RBrPPO from 25-100 mol% bromination to BBrPPO56, as shown in **Figure 7.3**. With increasing degree of bromination, the BrPPO shows a decrease in the intensities of the a and b peaks, coupled with an increase in intensities of the a' and b' peaks. Interestingly, although the BBrPPO56 ^{1}H NMR spectrum displays clear a and b peaks

associated with unfunctionalized repeat units of PPO, the a' and b' closely resemble the peak shapes and intensities of more highly functionalized RBrPPO (i.e. between 75 and 93 mol% bromination) than the RBrPPO50 analogue. This implies the presence of distinct blocks of highly functionalized BrPPO, where long sequences of uninterrupted BrPPO contribute to the unique chemical signature.

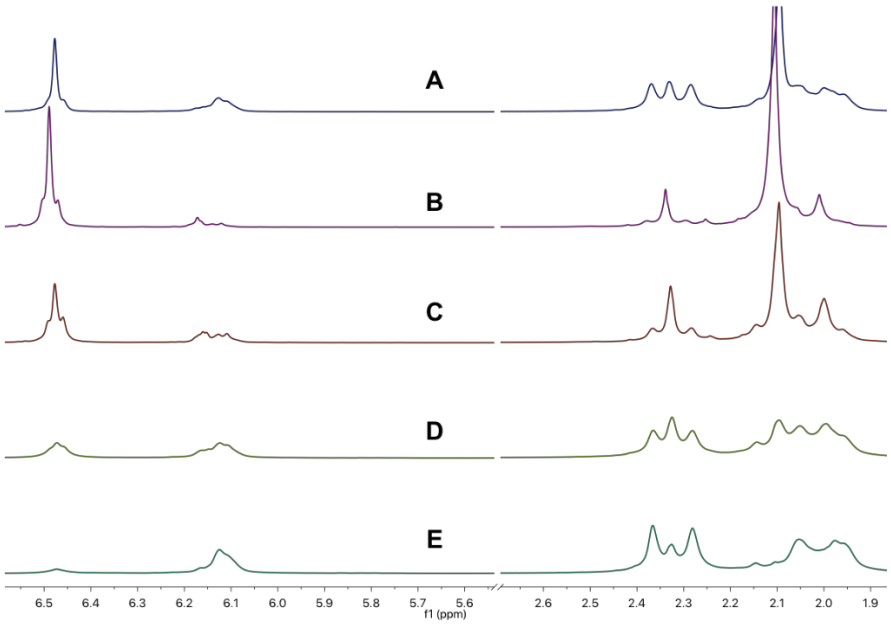

Figure 7.3. ^{1}H NMR spectra of BBrPPO56 (A), RBrPPO25 (B), RBrPPO50 (C), RBrPPO75 (D), and RBrPPO93 (E). Spectra were obtained in $CDCl_3$.

The thermal properties of the RBrPPO and BBrPPO copolymers was also investigated using DSC, as shown in **Figure 7.4**. The glass transition temperature of both RBrPPO and BBrPPO increased linearly with degree of bromination and showed no dependence on bromination architecture. It is important to note that the as-precipitated random BrPPO copolymers were completely amorphous following precipitation into water. The as-precipitated blocky BrPPO copolymers, however, displayed a distinct melting endotherm around 290 ºC, confirming the presence of crystalline domains following the solvent-borne precipitation process. Thus, the gel

state bromination of PPO not only leads to blocky functionalization, but also preserves the crystallizability of the PPO gels.

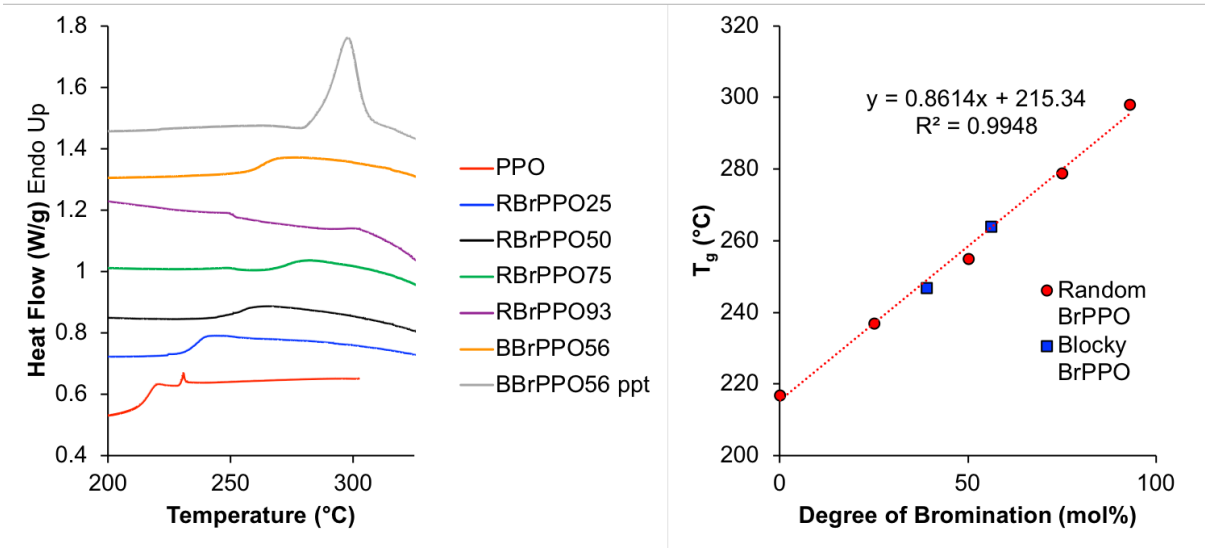

Figure 7.4. DSC thermograms of PPO and BrPPO showing the heat following a quench cool. The first heat of as-precipitated BBrPPO56 is shown for comparison. The T_g's determined from these thermograms is plotted as a function of degree of bromination.

This preliminary study on the bromination of PPO suggests that the gel-state functionalization method is readily applied to other semicrystalline polymer systems to create blocky copolymers. The investigation into novel solvents that facilitate gel formation for semicrystalline polymers will yield a multitude of new platforms upon which blocky functionalization may be applied to prepare new, crystallizable blocky copolymers. Furthermore, the manipulation of the semicrystalline gel state (i.e. solvent, concentration, etc) should be investigated to determine the influence of gel structure on the resultant block lengths and membrane properties.

7.2.2 Phase Behavior of Blocky Copolymers

The blocky bromination of PEEK established in this work provides a useful template for secondary functionalization reactions. A wide variety of PEEK substituents will be explored, as

shown in **Figure 7.5**, to develop blocky PEEK platforms with unique phase behavior. Manipulation of side-chain functionality will provide a better understanding of the sequence distribution established during the gel-state functionalization method and will enable the synthesis of novel PEEK materials for applications such a proton exchange membrane, anion exchange membranes, water purification, metal complexing, etc.

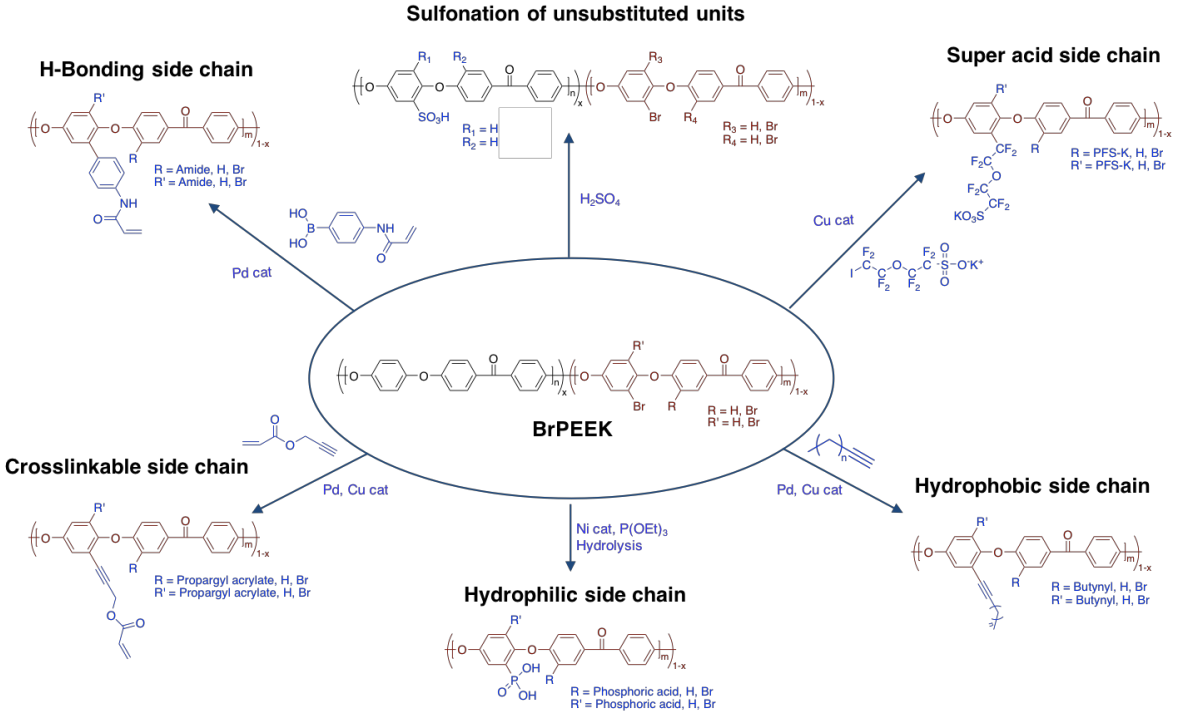

Figure 7.5. Schematic representation of possible functionalization routes utilizing brominated PEEK.

7.2.3 Novel Functionalization Chemistries in the Gel-State

While blocky bromination provides a useful platform for secondary functionalization, it is of interest to explore novel functionalization chemistries to directly functionalize the PEEK backbone. Friedel-Crafts alkylation reactions are a potential avenue of exploration, allowing for alkyl side chains of variable length.[20] The potential reaction scheme for the Frieldel-Crafts alkylation of PEEK is shown in **Figure 7.6**. The facile manipulation of the alkyl side chain length

on blocky functionalized PEEK using this method would provide a systematic study of blocky crystallization and phase behavior as a function of architecture and side chain composition. Furthermore, the use of bromoalkylated tertiary alcohols for Friedel-Crafts reactions with PEEK would provide a new platform for secondary functionalization and the simple preparation of quaternary ammonium functionalized anion exchange materials.

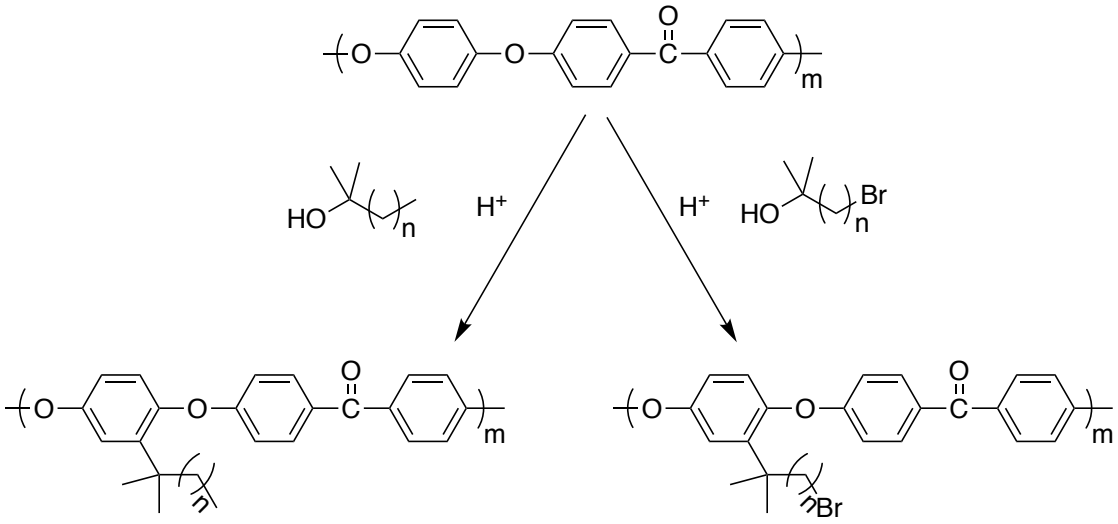

Figure 7.6. Reaction scheme for the Friedel-Crafts alkylation and bromoalkylation of PEEK.

7.3 References

1. Talley, S. J.; AndersonSchoepe, C. L.; Berger, C. J.; Leary, K. A.; Snyder, S. A.; Moore, R. B., Mechanically robust and superhydrophobic aerogels of poly(ether ether ketone). *Polymer* **2017,** *126* (Supplement C), 437-445.
2. Talley, S. J.; Yuan, X.; Moore, R. B., Thermoreversible Gelation of Poly(ether ether ketone). *ACS Macro Letters* **2017,** *6* (3), 262-266.
3. Fahs, G. B.; Benson, S. D.; Moore, R. B., Blocky Sulfonation of Syndiotactic Polystyrene: A Facile Route toward Tailored Ionomer Architecture via Postpolymerization Functionalization in the Gel State. *Macromolecules* **2017,** *50* (6), 2387-2396.
4. Daniel, C.; Zhovner, D.; Guerra, G., Thermal Stability of Nanoporous Crystalline and Amorphous Phases of Poly(2,6-dimethyl-1,4-phenylene) Oxide. *Macromolecules* **2013,** *46* (2), 449-454.
5. Daniel, C.; Longo, S.; Cardea, S.; Vitillo, J. G.; Guerra, G., Monolithic nanoporous–crystalline aerogels based on PPO. *RSC Advances* **2012,** *2* (31), 12011-12018.
6. Xiao, Z.; Sun, N., Crystallization behavior for metallocene-catalyzed isotactic polypropylene in alkane solvents of various molecular sizes. *Journal of Thermal Analysis and Calorimetry* **2016,** *124* (1), 295-303.
7. Matsuda, H.; Inoue, T.; Okabe, M.; Ukaji, T., Study of Polyolefin Gel in Organic Solvents I. Structure of Isotactic Polypropylene Gel in Organic Solvents. *Polymer Journal* **1987,** *19*, 323.
8. Domszy, R. C.; Alamo, R.; Edwards, C. O.; Mandelkern, L., Thermoreversible gelation and crystallization of homopolymers and copolymers. *Macromolecules* **1986,** *19* (2), 310-325.
9. Edwards, C. O.; Mandelkern, L., Crystallization–gelation process of homopolymers and copolymers from solution. *Journal of Polymer Science: Polymer Letters Edition* **1982,** *20* (7), 355-359.
10. Dasgupta, D.; Nandi, A. K., Multiporous Polymeric Materials from Thermoreversible Poly(vinylidene fluoride) Gels. *Macromolecules* **2005,** *38* (15), 6504-6512.
11. Yadav, P. J. P.; Patra, A. K.; Sastry, P. U.; Ghorai, B. K.; Maiti, P., Solvent Retention, Thermodynamics, Rheology and Small Angle X-ray Scattering Studies on Thermoreversible Poly(vinylidene fluoride) Gels. *The Journal of Physical Chemistry B* **2010,** *114* (35), 11420-11429.
12. Saiani, A.; Spěváček, J.; Guenet, J.-M., Phase Behavior and Polymer/Solvent Interactions in Thermoreversible Gels of Syndiotactic Poly(methyl methacrylate). *Macromolecules* **1998,** *31* (3), 703-710.
13. Ryan, C. F.; Fleischer, P. C., The Gel Melting Point as a Measure of the Tacticity of Poly(methyl methacrylate). *The Journal of Physical Chemistry* **1965,** *69* (10), 3384-3400.
14. Gopi, K. H.; Peera, S. G.; Bhat, S. D.; Sridhar, P.; Pitchumani, S., Preparation and characterization of quaternary ammonium functionalized poly(2,6-dimethyl-1,4-phenylene oxide) as anion exchange membrane for alkaline polymer electrolyte fuel cells. *International Journal of Hydrogen Energy* **2014,** *39* (6), 2659-2668.
15. Zhu, L.; Pan, J.; Christensen, C. M.; Lin, B.; Hickner, M. A., Functionalization of Poly(2,6-dimethyl-1,4-phenylene oxide)s with Hindered Fluorene Side Chains for Anion Exchange Membranes. *Macromolecules* **2016,** *49* (9), 3300-3309.
16. Yu, H.; Xu, T., Fundamental studies of homogeneous cation exchange membranes from poly(2,6-dimethyl-1,4-phenylene oxide): Membranes prepared by simultaneous aryl-sulfonation and aryl-bromination. *Journal of Applied Polymer Science* **2006,** *100* (3), 2238-2243.

17. Yu, B.; Cong, H.; Zhao, X., Hybrid brominated sulfonated poly(2,6-diphenyl-1,4-phenylene oxide) and SiO2 nanocomposite membranes for CO2/N2 separation. *Progress in Natural Science: Materials International* **2012,** *22* (6), 661-667.
18. Yang, S.; Gong, C.; Guan, R.; Zou, H.; Dai, H., Sulfonated poly(phenylene oxide) membranes as promising materials for new proton exchange membranes. *Polymers for Advanced Technologies* **2006,** *17* (5), 360-365.
19. White, D. M.; Orlando, C. M., Brominated Poly(Phenylene Oxide)s. II. Bromination of Poly(2,6-Dimethyl-1,4-Phenylene Oxide). In *Polyethers*, AMERICAN CHEMICAL SOCIETY: 1975; Vol. 6, pp 178-184.
20. Jeon, J. Y.; Umstead, Z.; Kangovi, G. N.; Lee, S.; Bae, C., Functionalization of Syndiotactic Polystyrene via Superacid-Catalyzed Friedel–Crafts Alkylation. *Topics in Catalysis* **2018**, 1-6.

Appendix A

Development and Modification of Polymers for Soft Tissue Engineering

A.1 Introduction

Tissue engineering is a multidisciplinary field that unites the fundamentals of chemistry, engineering, biology, and clinical science to develop novel materials for tissue repair and regeneration. The development of tissue engineering reveals the structure-property relationships of native tissue and provides means to generate substitutes that mimic, mend, and maintain tissue function. In recent years, the field of tissue engineering has expanded in response to a clinical demand for organ replacement. The development of substitutes for numerous organs, including kidneys, the pancreas, the liver, skin, etc., attempts to alleviate this demand, however, further progress is necessary to provide truly biomimetic and bio-enhancing materials.

Skin is one of the largest and most complex organs, and it serves as the barrier between the human body and the environment. Thus, damage to skin is unavoidable. Typically, skin repairs itself through a self-healing mechanism; however, when damage becomes too extensive or too deep, external support is necessary to restore skin function and appearance.[1] The conventional clinical approach to skin repair is skin grafting from undamaged, healthy donor sites.[2] Skin wounds caused by burns, soft tissue trauma, necrosis, and chronic ulcers pose a particular problem to clinicians. Widespread burns limit the availability of suitable donor sites and the use of non-self donors readily increases the risk of infection and rejection of the tissue.[3] Furthermore, skin grafting potentially leads to displeasing aesthetics including discoloration and scarring. The development of innovative materials and designs is thus necessary to provide appropriate graft sources with optimal healing properties.

A.2 Overview and Goals of Soft Tissue Engineering

The fundamental principle behind tissue engineering is to provide feasible and effective replacements for current clinical procedures, encompassing realms from drug therapy to the replacement of entire organs. Control over cell proliferation and growth must be achieved to facilitate and stimulate this growth and repair of tissue. Thus, a comprehensive understanding of the cellular mechanisms of healing is necessary and often develops hand-in-hand with novel engineered materials. Furthermore, tissue engineering seeks to regulate and enhance drug delivery to control inflammation, infection, etc.[1] Overall, engineered materials must provide structural and biochemical support to enable the development of normal tissue structure and facilitate cell function, as shown in **Figure A.1**.

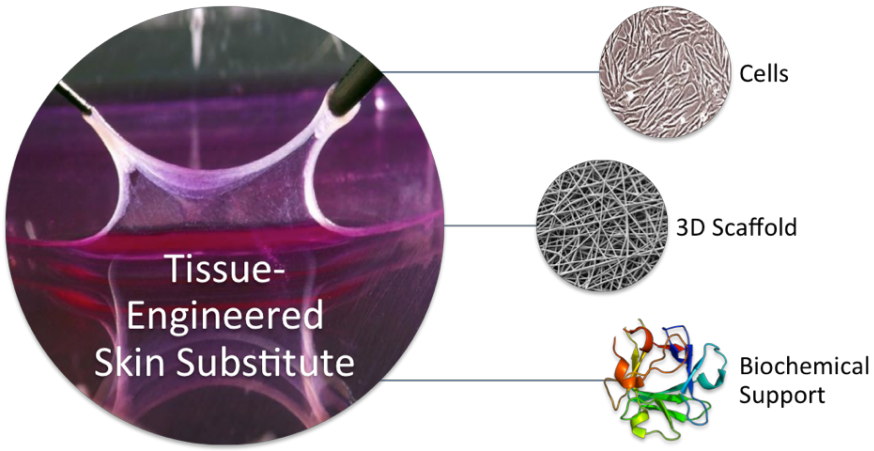

Figure A.1. Diagram demonstrating the primary tenants of generating a tissue-engineering skin equivalent. The combination of cells, 3D scaffold, and biochemical support provide an environment suitable for cell proliferation and growth.

Tissue engineered skin substitutes seek to facilitate healing and restoration of skin function through inspiration from natural, physiological design. As shown in **Figure A.2**, the skin is composed of three distinct layers, the epidermis, dermis, and the hypodermis. The epidermis is the

outermost layer, composed of keratinocytes, that provides a waterproof, protective barrier for the human body against infection, moisture loss, heat, and UV radiation.[1] The dermis lies beneath the epidermis and consists of fibroblast cells that secrete extracellular matrix (ECM) precursors, such as those that form collagen fibers. The ECM provides biochemical and structural support to the surrounding cells, and thus the dermis imparts most of the mechanical strength and elasticity of the skin.[4] Moreover, the dermis houses nerves and blood vessels that provide sensation and nutrients to the surrounding cells. Finally, the hypodermis is the innermost layer of skin. The hypodermis consists primarily of adipose cells that provide insulation, regulate body temperature, and store energy.[4]

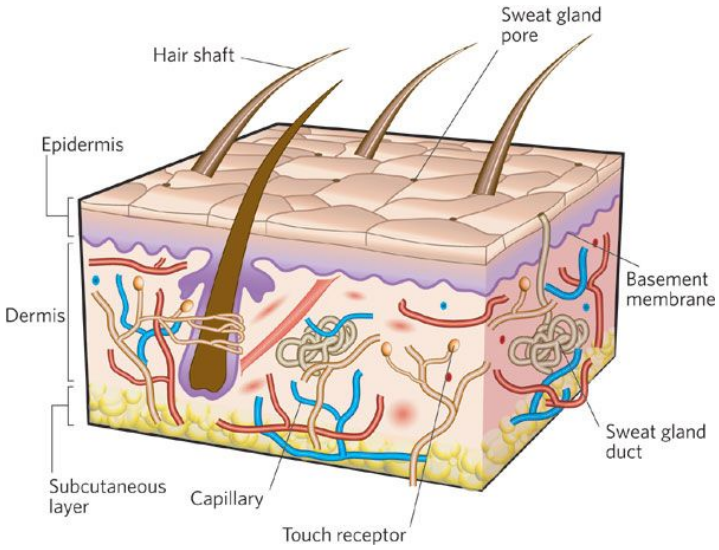

Figure A.2. Diagram displaying the anatomy of skin. The dermis provides the main structural support and houses elements such as blood vessels, nerves, hair follicles, and sweat glands.[5] Reprinted with permission from MacNeil: Springer Nature; Nature; Progress and Opportunities for tissue-engineered skin, MacNeil, S.; 2007.

Skin replacements generally seek to mimic the ECM of the dermis while providing protection equivalent to the epidermis. Tissue scaffolds for skin must minimize inflammation and protect against infections, moisture loss, and scarring. The engineered substitutes need to promote cell adhesion and mobility, in addition to encouraging vascularization and maintaining mechanical

integrity. Clinical considerations such as biocompatibility, storage conditions, and ease of use and fabrication of tissue scaffolds must also be optimized. Many current approaches attempt to address each of these tenants, however, further progress is necessary to produce replacements comparable or superior to native skin.

A.3 Current Clinical Approaches

A.3.1 Skin Grafting

The primary method for the treatments of chronic skin wounds or burns is skin grafting from another location on the same individual, also known as autografting.[6] Skin grafting is divided into two categories: split thickness and full thickness. Split thickness skin grafts (STSGs) are the most commonly used, as they are capable of covering large wound beds. STSGs consist of the complete epidermis along with part of the dermis. They are harvested from donor regions such as the buttocks, back, or thighs and subsequently meshed or "pie-crusted" to enlarge the graft up to 9 times, as shown in **Figure A.3**.[7-8] The holes produced in meshing and "pie-crusting" enable the draining of the wound and thus help promote acceptance of the graft. Because only part of the dermis is employed, little vascularization of the wound bed is required but high levels of contractions occur.[2]

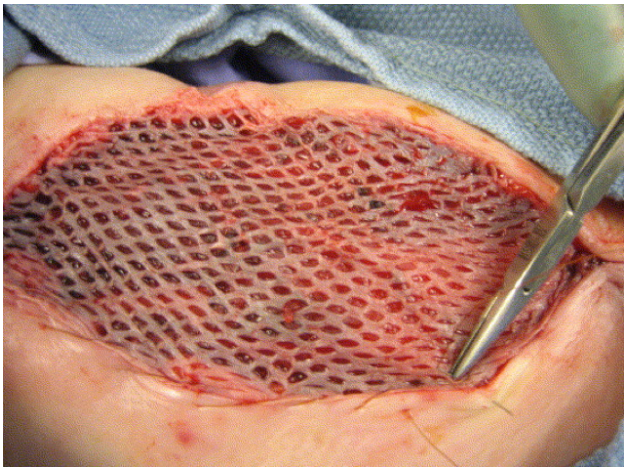

Figure A.3. The use of a meshed split-thickness skin graft to cover a wound bed.[7] Reprinted from Operative Techniques in General Surgery,Volume 8, Miraliakbari, R.; Mackay, D. R., Skin Grafts, 197-206, Copyright (2006), with permission from Elsevier.

Full thickness skin grafts (FTSGs) consist of the complete epidermis along with the complete dermis. FTSGs are typically used for smaller, more visible regions with good vascularization.[2] Because the entire dermis is transplanted, attention to hair, pigmentation, and texture of the donor site must be taken into account. FTSGs are extracted from regions such as the eyelid, face, inner arm, and groin and are subsequently "pie-crusted" to allow for drainage.[8] Overall, FTSGs exhibit better recovery than STSGs, however, their scope is much more limited and STSGs are utilized more frequently, especially for large wound coverage.

Although both split thickness and full thickness skin grafting are commonplace in clinical settings, numerous methodologies to employ the techniques exist. One such application of STSG is termed "halo" grafting, which merges the donor and recipient regions by excising a circular halo graft from around the wound. This creates only one area to be dressed and often results in a quick healing time and limited scarring.[6] Furthermore, variation in the location of donor graft for STSGs occurs. STSGs harvested from the scalp are increasing in prominence due to quick recovery, efficient re-epithelialization of the wound and minimal scarring, infection and recovery time.[2, 7]

Moreover, the timing of grafting, particularly with burns, is variable. Similar results are observed between early and late excision in terms of resulting appearance and functionality, however, early excision and grafting has shown a reduction in mortality rates and length of hospital stay, thus reducing the cost of care.[3,9]

A.3.2 Skin Substitutes

In addition to skin grafting, clinicians utilize various skin substitutes when donor graft sources are limited. The design of commercial substitutes seeks to replace the epidermis, dermis or both using cells and/or tissues from the individual themselves, from individuals of the same species, or from individuals of different species, termed autologous, allogeneic, and xenogeneic sources, respectively. Commercial epidermal constructs consist primarily of sheets of cultured autologous keratinocytes. Approximately 3 weeks are required from the time of skin biopsy to prepare these cell sheets. Therefore, appropriate wound dressings must be used in the meantime.[10] Other epidermal constructs include suspensions of keratinocytes placed on a scaffold or sprayed directly onto the wound. The suspensions are prepared and used in the operating room directly following skin biopsy. Dermal constructs consist of acellular dermis from allogenic or xenogenic sources.[10] The decellularization attempts to prevent an immunogenic response from the recipient and promote *in vivo* incorporation of cells.[11] Cell remnants are often unavoidable and thus dermal replacements are generally used as a temporary dressing rather than a permanent one.[12] Once the wound bed has been properly colonized and vascularized by cells, the dermal substitute is replaced by a STSG.[10] Finally, composite (dermo-epidermal) constructs consist of keratinocytes and fibroblasts cultured *in vitro* into a xenogeneic collagen scaffold or a synthetic polymer scaffold.[13] The cells used are from either autologous or allogeneic sources. Approximately 4 weeks are required to produce the composite from the time of skin biopsy. Thus, composite constructs are often used for chronic ulcers or burns as temporary dressings.

Numerous other skin substitutes involving synthetic and naturally derived polymeric scaffolds are under investigation, however, these are not yet commercially available. Despite the multitude of products available for commercial use, no skin substitute(s) has emerged as the superior dressing(s). Further exploration is necessary to uncover a construct that provides all of the qualities necessary to promote cell growth and repair while remaining cost effective and relatively easy to produce and store.

A.4 Polymeric Materials Used in Tissue Constructs

Novel approaches for skin equivalents often incorporate polymers into the cellular scaffold. These polymers may be either naturally derived or synthetically derived. A list of commonly used polymers is summarized in **Table A.1**.

Table A.1. Polymers frequently used in skin substitute applications.[1, 11, 13]

Synthetic Polymers	Poly(glycolic acid) (PGA) Poly(lactic acid) (PLA) Poly(lactic-*co*-glycolic acid) (PLGA) Poly(ε-caprolactone) Poly(ethylene glycol) (PEG) Poly(butylene terephthalate) (PBT) Poly(vinyl alcohol) (PVA) Silicone Nylon Polyurethanes
Naturally Derived Polymers	Collagen Chitosan Hyaluronic acid (HA) Glucosaminoglycan (GAG) Agarose Alginate Fibroin Polypeptides

In general, these include polyesters, polyurethanes, and polysaccharides, among others. The use of synthetic polymers in skin substitutes minimizes the risk of infection because pathogens are less likely to interact with a synthetic polymer than a biological scaffold.[11] Furthermore, synthetic

materials have a known composition and readily manipulated morphology, making them capable of establishing scaffolds with good mechanical properties and little if any immunogenic response or toxicity.[14] Finally, polymers are generally less expensive than biological scaffolds, making them a cost-effective alternative.

A.4.1 Properties Necessary for Polymer Scaffolds

A key necessity when using polymers in skin equivalents is biodegradability. Degradation of the scaffold into biocompatible products, by hydrolytic or enzymatic cleavage, must occur at a rate similar to integration by native cells to allow for proper tissue regeneration. Thus, control of the degradation rate is essential. A scaffold that degrades too quickly will lack the structure and mechanical properties necessary to support cell growth and migration while a scaffold that degrades too slowly will elicit a foreign body response and trigger rejection of the skin substitute.[12] The biodegradation rate of most polymers is dependent on its properties including chemical composition, hydrophilicity, molecular weight, crystallinity, etc.[15] An example of controlling the enzymatic degradation rate of a hyaluronan hydrogel by varying the concentration of enzyme is shown in **Figure A.4**.

The degradation of polymers used must be well controlled, reproducible, and tunable to generate skin scaffolds with optimal properties. The mechanism of degradation is important for maintaining the structural integrity of the scaffold. Some polymers undergo bulk degradation in which the internal structure is broken down. This results in a profound reduction in molecular weight and loss of mechanical integrity. Other polymers undergo surface degradation in which the exterior of the scaffold degrades at a constant rate. Although this results in a smaller scaffold, it has maintained its internal structure and mechanical stability.[15] Thus, polymers undergoing surface degradation are desirable for tissue-engineered constructs to provide mechanical integrity over longer periods.

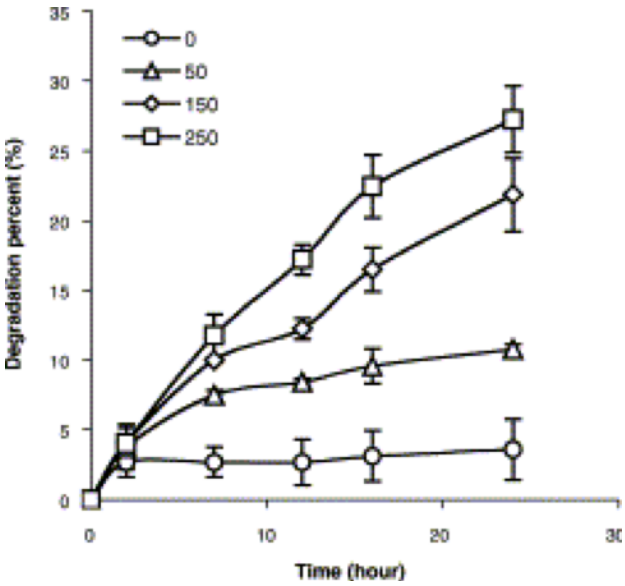

Figure A.4. Enzymatic degradation profiles of crosslinked hyaluronan hydrogels with variable concentrations of enzyme (0. 50, 150, 250 U/mL).[16] Reprinted from Biomaterials, Volume 25, Shu, X. Z.; Liu, Y.; Palumbo, F. S.; Luo, Y.; Prestwich, G. D., In situ crosslinkable hyaluronan hydrogels for tissue engineering, 1339-1348, Copyright (2004), with permission from Elsevier.

In addition to biodegradability, polymers chosen for skin tissue engineering must degrade into nontoxic byproducts. Other qualities that a polymer must possess include biocompatibility and hydrophilicity to allow for cell growth and proliferation without immunogenic rejection. Furthermore, the mechanical strength of the polymer as well as its processability dictate the ability to shape a given polymer into a scaffold with strength suitable to support cellular growth. These properties are highly dependent on the chemical composition of the polymer. Further modifications of polymers by chemical means or by processing techniques may enhance their utility as a tissue scaffold. A summary of the structures and properties of commonly used polymers is displayed in **Table A.2**.

Table A.2. Structure and properties of frequently used polymers.[17] Note: thermal and mechanical data was not readily available for the polysaccharides.

Name	Structure	T_g (°C)	T_m (°C)	Modulus (MPa)	Tensile Strength (MPa)
Poly(glycolic acid) (PGA)	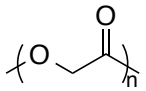	35-45	187-222	6800	375, 20% elongation
Poly(lactic acid) (PLA)	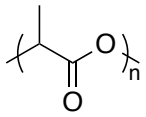	49-59	160-190	1720-1930	59.5
Poly(ε-caprolactone) (PCL)	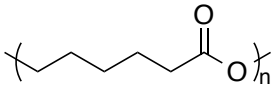	-60	58-60	90-150	30-50, 100-300% elongation
Poly(ethylene glycol) (PEG)	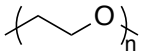	-95--15	45-65	5000-9000	16, 550% elongation
Poly(butylene terephthalate) (PBT)	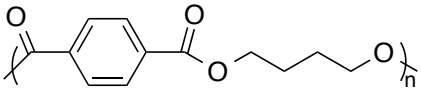	37-52	215-230	2530	40, 40% elongation
Poly(vinyl alcohol) (PVA)	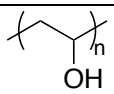	75-85	230-267	380	34, 225% elongation
Silicone (PDMS)	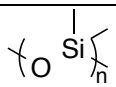	-127	-62	1	6.4, 90% elongation
Nylon	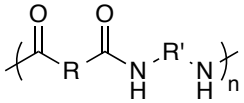 Note: Nylon 6,6 properties are shown	57-58	267-280	1500-3000	83, 60% elongation
Polyurethanes	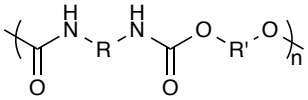 Note: no property data shown because it is dependent on R, R’	-	-	-	-
Poly(hydroxy butyrate) (PHB)	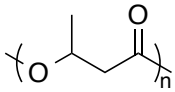	9-15	167-179	4000	28-40, 6-7% elongation
Collagen	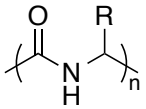 R group specifies amino acid	120	230	2600	2-7, 15% elongation
Chitosan	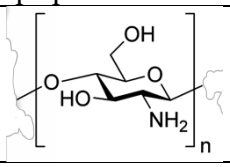	50	137	530	130, 14% elongation

Name	Structure	T_g (°C)	T_m (°C)	Modulus (MPa)	Tensile Strength (MPa)
Hyaluronic acid (HA)	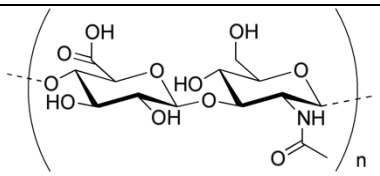 Note: This is a type of gluycosaminoglycan	-	-	-	-
Agarose	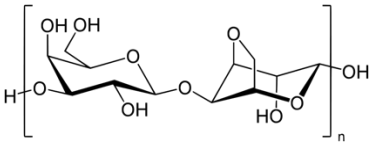	-	-	-	-
Alginate	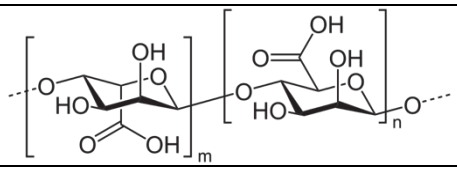	-	-	-	-
Fibroin	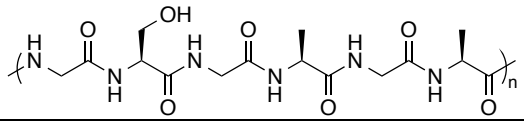	-	-	9800	18-25% elongation

A.5 Mimicking of Biological Form and Function

A.5.1 Hydrogels

Hydrogels have emerged recently as promising skin equivalents. Hydrogels are crosslinked networks formed from hydrophilic polymers and swollen with water or biological fluid. The formation of hydrogels occurs through chemical crosslinking, physical crosslinking, and/or through phase transitions. Chemical crosslinking involves the joining of polymer chains with permanent covalent bonds. This process occurs using multifunctional agents, photopolymerization, Michael addition reactions, Schiff base reactions, or Diels-Alder reactions to generate the covalent bonds necessary for network formation.[18-19] Physical crosslinking involves the joining of polymer chains through non-covalent interactions. This includes electrostatic aggregation, chain entanglements, hydrogen bonding, and phase transitions in response to temperature, pH, etc.[18] Physical crosslinking is reversible, enabling gelation to be tuned based on conditions. Hydrogels display good biocompatibility, interact well with cells, and exhibit

morphology similar to the ECM of cells, making them extremely suitable as a tissue scaffold.[20] Control of hydrogel architecture and biocompatibility is necessary to produce optimal properties for cell growth and proliferation.

A.5.1.1 Control of Hydrogel Structure for Optimal Cell Growth

The control of porosity in hydrogels is crucial to promoting substantial tissue incorporation and encouraging the return of tissue function. The pore architecture, including the pore size and interconnectivity of pores, dictates the degree of tissue assimilation, vascularization and diffusion of nutrients.[20] An increase in pore size corresponds to an increase in cell growth and ECM secretion, as shown in **Figure A.5**. Genipin-crosslinked gelatin scaffolds, whose pore size was controlled by crosslinking temperature, revealed more dedifferentiated cells and a smaller release of ECM for gels containing smaller pores than those with pores from 250 to 500 μm.[21] This trend was also observed in poly(L-lactic acid) scaffolds formed by salt leaching.[22] The trend is attributed to the difference in number of cells a small pore can take up versus a large pore. The limited number of cells in a small pore cannot secrete enough ECM to support the cells and maintain their phenotype, unlike a large pore, which can take up more cells. Pore size is also influential in the vascularization of hydrogels by similar reasoning. Peptide-conjugated poly(ethylene glycol) (PEG) hydrogels prepared by particulate leaching displayed an increased rate of vascularization with increasing pore size in both 3D cell culture and rodent models. For pores less than 50 μm, cells and blood vessels were only capable of occupying the external surface whereas pores greater than 50 μm allowed for extensive cell and vessel growth throughout the entire gel.[23] Therefore, control of pore size when generating hydrogels is necessary to provide pores large enough to enable proper cell migration and vascularization. Likely, there exists an optimal range for pore size in which the pores are large enough to allow for cellular and vascular infiltration yet small enough to provide the structure and surface area necessary to support cell growth.

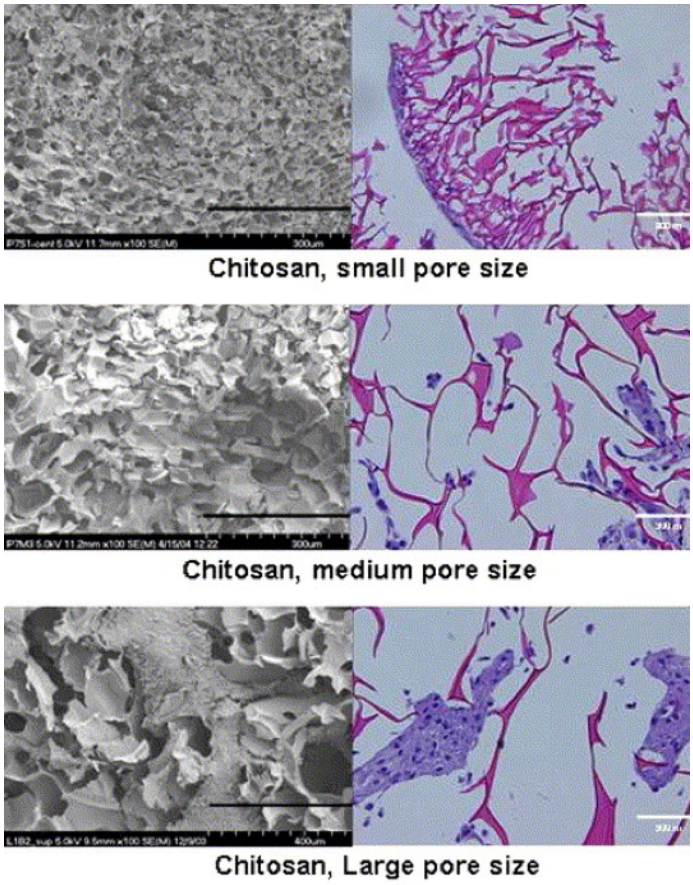

Figure A.5. Scanning electron microscopy and histology of chitosan sponges containing pore sizes ≤ 10 μm (small), 10-50 μm (medium), and 70-120 μm (large) after 4 weels of cell culture. The images reveal increasing cellular penetration and increasing ECM secretion with increasing pore size.[24] Reprinted from Acta Biomaterialia, Volume 2, Griffon, D. J.; Sedighi, M. R.; Schaeffer, D. V.; Eurell, J. A.; Johnson, A. L., Chitosan scaffolds: Interconnective pore size and cartilage engineering, 313-320, Copyright (2006), with permission from Elsevier.

Additionally, the interconnectivity of pores is crucial to promoting nutrient diffusion, waste management, and cellular ingrowth. Chitosan sponges revealed improved cell proliferation and metabolic activity with increasing interconnective pore size.[24] Comparatively, a nonwoven mesh of PGA fibers presented an increase in GAG expression, collagen secretion, and cell growth compared to chitosan scaffolds. The nonwoven mesh structure provided a better-interconnected, porous network than the sponges that prompted the greater integration and expression of ECM factors.[24] The trend of increasing GAG and DNA expression with increasing interconnected pore

size was also observed in porous scaffolds of poly(ethylene glycol)-terephthalate/poly(butylene terephthalate) (PEGT/PBT) copolymers formed by compression molding and 3D fiber deposition.[25] Many techniques have emerged to control the pore size and architecture of hydrogels include particle leaching, freeze-drying, gas foaming, and use of a degradable porogen. Other methods include phase separation, electrospinning, or combinations of the various techniques.[20, 26] Electrospinning represents a specific subset of nanofibrous preparation and will be discuss in further detail later in the review. Overall, methods to control pore size and architecture seek to direct cellular ingrowth and provide environments suitable for sustained integration of tissue.

A.5.1.2 Integration of Biological Agents into Hydrogels

Hydrogels are further enhanced for use in tissue engineering through the encapsulation of cells and growth factors, among other biological agents, as shown in **Figure A.6**. Hydrogels designed to encapsulate living cells must gel under mild conditions and provide adequate structure and chemistry to permit cell survival. Commonly used polymers for such applications include alginate, collagen, and fibrin.[27] Integration of cells into the hydrogel seeks to effectively distribute the cells throughout the network. This provides regions for cell growth throughout the scaffold without relying solely on the proper integration of cells directly seeded on its surface. A more homogeneous distribution of fibroblasts throughout the entire matrix and delayed formation of large cell aggregates were observed for fibroblast-encapsulating alginate hydrogels compared to alginate hydrogels directly seeded with fibroblasts onto the surface.[28] The delayed aggregation suggests a greater degree of vascularization and more efficient nutrient/waste diffusion of the cells. Furthermore, a higher level of ECM components was observed in the co-dispersed hydrogel compared to the directly seeded hydrogel, indicating superior cell proliferation. Similar trends were observed in fibrolast-encapsulating poly(ethylene glycol)-poly(L-alanine) (PEG-L-PA) thermoresponsive hydrogels when compared to a commercially available Matrigel system.

Fibroblast-encapsulating PEG-L-PA exhibited accelerated wound healing, enhanced epithelialization and improved the appearance of native skin compared to treatment with phosphate buffered saline treatment and cell-free PEG-L-PA thermogels.[29] These results suggest that the encapsulation of cells is a suitable method to promote rapid and uniform cell growth throughout the hydrogel scaffold.

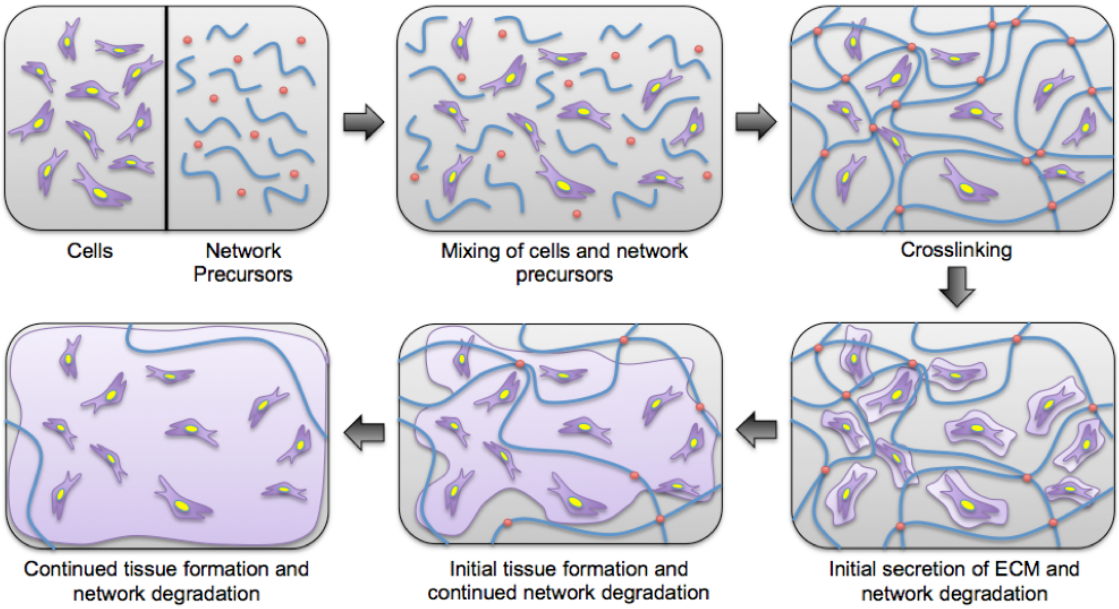

Figure A.6. Method of encapsulating cells within a polymer hydrogel. Cells and polymer network precursors are first mixed in solution. Crosslinking of the solution leads to networks with cells dispersed throughout. Subsequent secretion of ECM by the cells and degradation of the network enables the formation of viable tissue.

Encapsulation of growth factors into hydrogels is also of notable interest. Growth factors are biological molecules that regulate cellular processes by acting as signals between cells. Thus, the controlled presence of growth factors enables the stimulation and direction of cell growth. A gelatin hydrogel with epidermal growth factor (EGF)-loaded microspheres exhibited controlled release of EGF and enhanced wound healing compared to those without EGF-loaded microspheres.[30] EGF stimulates wound healing, however, it is quickly decomposed by proteases

before it can become biologically active when used in free form. By encapsulating EGF, sustained release, diminished degradation, and thus increased proliferation of epidermal cells is achieved.[30] This prolonged release is further exhibited by dextran-epichlorohydrin hydrogels encompassing EGF and/or basic fibroblasts growth factor (bFGF). The combination of these growth factors resulted in enhanced neovascularization and accelerated wound healing in rat models.[31] In brief, encapsulation of cells and growth factors within hydrogels promotes superior cellular integration and proliferation by providing an environment that allows the cells to thrive. Encapsulation of factors into hydrogels may further be extended to the release of drugs to prevent inflammation and infection or proteins to promote cellular function.

A.5.1.3 Stimuli-Responsive Materials

Stimuli responsive hydrogels, in particular temperature sensitive thermogels, are utilized for *in situ* gelation. Thermogels with sol-to-gel transitions around physiological temperature are particularly useful for injectable scaffolds. Before administration, these systems exist as a free-flowing liquid and upon injection or contact form hydrogels. Chitosan-agarose hydrogels (CAHs) form injectable thermogels with tunable mechanical properties and improved healing based on the functionalization of chitosan. The CAHs exhibited a continuous layer of cells and typical fibroblast morphology after just 72 hours in *in vitro* studies using fibroblasts. Furthermore, *in vivo* rat models demonstrated a high degree of re-epithelialization and limited inflammation using CAHs.[32] Significant wound healing and ECM secretion have been observed with numerous injectable thermogels, especially those that also incorporate encapsulation of drugs, proteins, or cells.[16, 29, 33-34] Additionally, the use of chemically crosslinkable thermogels enables the enhancement of mechanical properties and manipulation of degradation character by covalent crosslinking.[35-36] Overall, injectable thermogels are useful not only for their growth-promoting properties but also for their readily moldable shapes and tunable mechanical properties.

A.5.2 Electrospun Nanofibrous Materials

Recent trends toward nanofibrous materials for skin tissue engineering have emerged due to their high surface area to volume and readily accessible frameworks that mimic the ECM. While these materials may be encompassed by the realm of hydrogels, electrospun scaffolds for tissue engineering have become prominent due to their unique structural architecture and nanoscale dimensions. The high surface area of electrospun nanofibers provides more area for the attachment of cells than other methods of polymeric scaffold preparations.[37] Increased cell adhesion is associated with an increase in cell migration, proliferation, and differentiation, thus electrospun scaffolds should form optimal scaffolds for tissue engineering.[38] Manipulation of a wide variety of electrospinning parameters, such as voltage, solution viscosity, distance to the collector and flow rate, allows production of nanofibers of numerous diameters, porosity, and morphologies.[39] Therefore, electrospun scaffolds are easily engineered to exhibit the ideal structure and properties necessary for cell growth and return of tissue function. The electrospinning technique is applicable for a wide variety of materials including polyethers, polyesters, polyurethanes, poly(meth)acrylates, cationic polyelectrolytes, nucleobase-containing polyelectrolytes, phospholipids, and radical polymers, among others.[40-43]

A.5.2.1 Fundamentals of Electrospinning

Electrospinning is a technique, pioneered by Reneker, that utilizes a high voltage to produce nanofibers from a polymer solution or melt.[44-46] The typical electrospinning setup includes a syringe filled with the polymer solution, a syringe pump, a power supply connected to the syringe needle, and a grounded collector, as shown in **Figure A.7**. As the syringe pump pushes the polymer solution from the needle tip, a high voltage is applied which charges the polymer solution. At some critical voltage, the electrostatic repulsions of the charged polymer solution overcome the surface tension present, producing an electrified jet that emerges from what is termed the Taylor cone.[46]

The jet then undergoes bending instability and accelerates towards the grounded collector. Solvent evaporation and increasing electrostatic repulsion elongate the fibers and result in the nonwoven mats generated on the collector.[47]

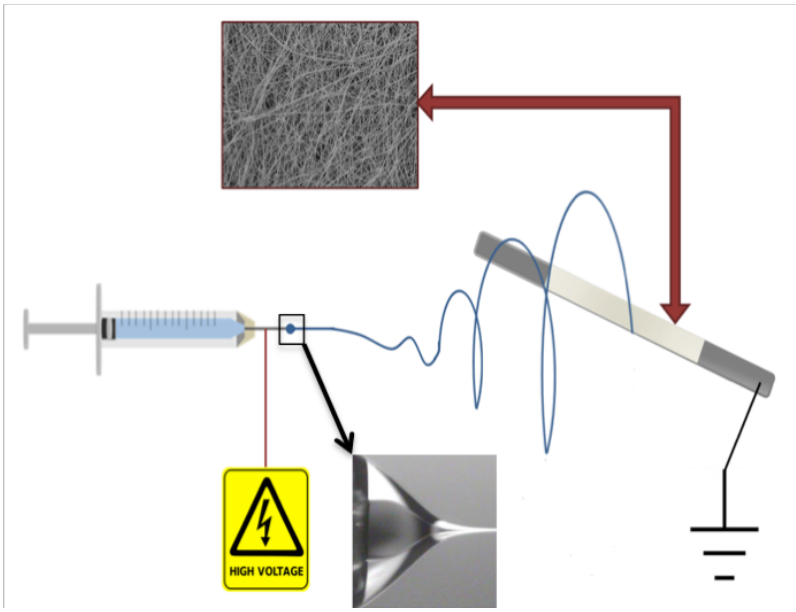

Figure A.7. Diagram of the electrospinning setup. The power source produces a Taylor cone from which a jet emerges. The jet accelerates towards the collector and forms a nanofibrous nonwoven mat.

A.5.2.2 Control of Fiber Diameter

The size of electrospun fibers is a function of flow rate, voltage, solution concentration, humidity, etc. This, in turn, influences the adhesion of cells to electrospun nanofibers as cells attach along the length of the fiber. Results with electrospun poly(lactic acid-*co*-caprolactone) (PLACL) reveal superior fibroblast adhesion to fibers with smaller diameters compared to those with larger diameters.[48] Furthermore, electrospun mats of poly(lactic acid-*co*-glycolic acid) (PLAGC) revealed an optimal fiber diameter range for cell adhesion, suggesting that scaffolds with fiber diameters from 350 to 1100 nm provide cell proliferation superior to scaffolds with fiber diameters above or below this range, as shown in **Figure A.8**.[37] The key factor promoting increased cellular

adhesion is the increased surface area associated with smaller fiber diameters. A tradeoff exists in decreasing the fiber diameter, however. In addition to cell adhesion, fiber diameter influences the wettability, porosity, and mechanical properties of scaffolds. Smaller diameter fibers yield mats with increased mechanical strength but decreased wettability and porosity.[37] By manipulating electrospinning parameters, it is possible to determine a range of fiber diameters that provide sufficient porosity and wettability while maintaining good surface area and mechanical properties, thereby enabling optimal cellular infiltration.

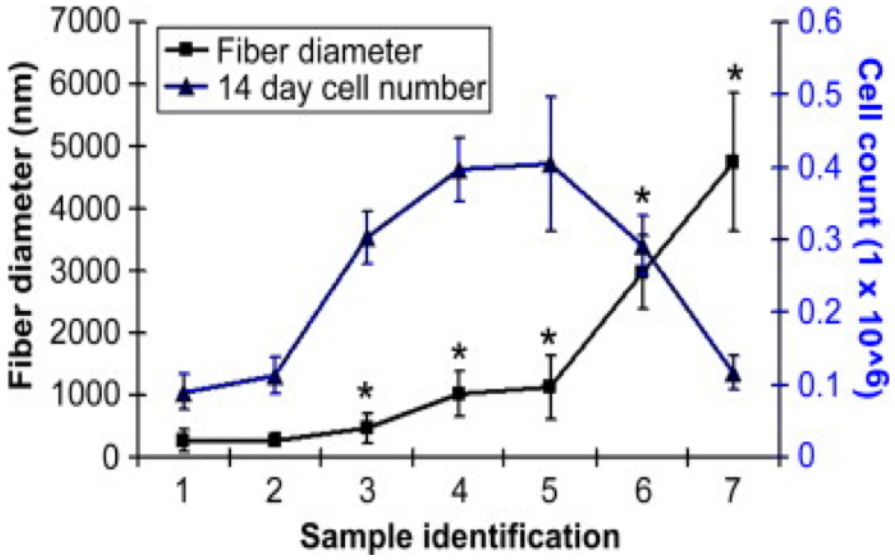

Figure A.8. Effect of fiber diameter on the proliferation of human skin fibroblasts (hSFs). Optimal cell growth was observed for fibers with diameters from 350 nm to 1000 nm.[37] Reprinted from Biomaterials, Volume 29, Kumbar, S. G.; Nukavarapu, S. P.; James, R.; Nair, L. S.; Laurencin, C. T., Electrospun poly(lactic acid-co-glycolic acid) scaffolds for skin tissue engineering, 4100-4107, Copyright (2008), with permission from Elsevier.

A.5.2.3 Control of Porosity

As stated in regard to hydrogels, control of porosity is necessary for proper cell migration and proliferation. With electrospun scaffolds, the trend of superior cellular integration with larger pores holds. However, it is much more difficult to control porosity with electrospinning. As fiber diameter decreases, pore size decreases exponentially. Thus, at smaller fiber diameters, small

nutrients are capable of diffusing through the pore but there is not enough space for cellular integration.[49] Methods to control porosity include changing the type of collector used, combining salt leaching with electrospinning, generating multiple diameter fibers concurrently, electrospinning with sacrificial material, gas foaming, cryogenic electrospinning and electrospinning combined with cell electrospraying.[50] A simplified approach includes manually introducing 171 μm pores into the fiber mat using a needle tip. Fiber mats containing these micropores exhibited faster and superior healing compared to fiber mats with no micropores introduced, thus displaying their ability to allow and promote cellular infiltration.[51] The idea of inserting micropores, also termed microchannels, into a porous scaffold has also been applied using photolithography and demonstrated enhanced cell elongation and spreading.[52] Thus, the utility of micropores for promoting cellular infiltration and growth is evident across numerous techniques. The key feature for the introduction of micropores is their size. The pores must be large enough to allow cells to enter, yet small enough to provide suitable mechanical properties and structural support for cells. Overall, the regulation of pore architecture by electrospinning methodology or manual introduction provides pores large enough to allow for nutrient and waste diffusion as well as cellular integration.

A.5.2.4 Electrospun Polymer Blends for Enhanced Properties

To improve the electrospinnability and/or wound healing ability, polymer blends are often employed. Polymer blends also seek to improve mechanical properties, hydrophilicity, and fiber morphology. Blends are particularly useful due to the tunable nature of their properties based on the relative concentrations of each component. Such concentration dependence on fiber morphology was exhibited by blends of *N*-carboxyethyl chitosan (CECS) and poly(vinyl alcohol) (PVA).[53] Blends of PVA and poly(hydroxy butyrate) (PHB) revealed disruption in crystallinity and accelerated degradation of PHB with increasing PVA fraction. Relative composition of the

blends also influenced the adhesion of fibroblasts and keratinocytes.[54] Blending poly(ε-caprolactone-*co*-lactide) with pluronic enhanced tensile strength and hydrophliicity of the electrospun scaffold.[55] Thus, blending two polymers together provides a means of tuning many properties necessary to form a suitable skin substitute, in particular mechanical integrity, degradation rate, and scaffold architecture. Moreover, polymers are blended with substances that optimize healing properties. Electrospun polyurethane (PU) blended with emu oil, shown in **Figure A.9**, displayed decreased inflammation, good antibacterial activity, and enhanced cytocompatibility and cell proliferation.[56] Similar results were obtained for blends with aloe vera.[48] Electrospinning of such blends provides a means of distributing the therapeutic agent throughout the entire scaffold and therefore optimizes healing properties.

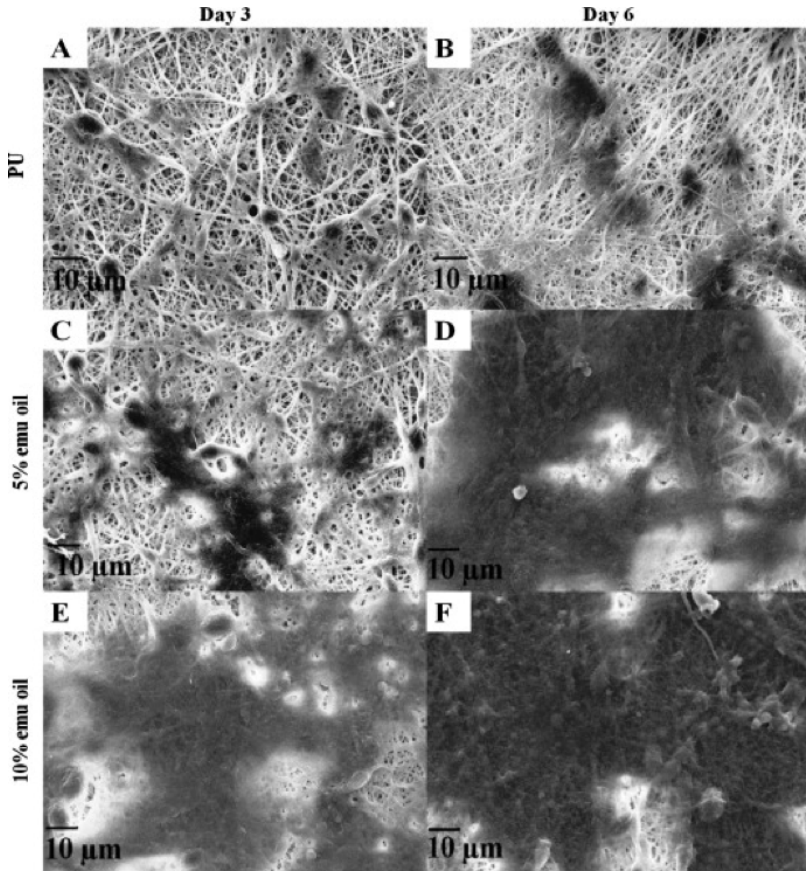

Figure A.9. SEM images displaying the fibroblast adhesion on PU (A, B), PU/5 wt% Emu oil (C, D), and PU/10 wt% Emu oil (E, F) after days 3 and 6 of culture. As the amount of emu oil increased, there was an increase in cell adhesion and growth.[56] Reprinted from Colloids and Surfaces A: Physicochemical and Engineering Aspects, Volume 415, Unnithan, A. R.; Pichiah, R.; Gnanasekaran, G.; Seenivasan, K.; Barakat, N. A. M.; Cha, Y. S.; Jung, C. H.; Shanmugam, A.; Kim, H. Y., Emu oil-based electrospun nanofibrous scaffolds for wound skin tissue engineering, 454-460, Copyright (2012), with permission from Elsevier.

A.5.2.5 Comparisons of Hydrogel and Electrospun Architectures

Comparisons of electrospun mats to other potential scaffold morphologies reveals a distinct advantage of electrospinning in terms of biocompatibility and speed of wound healing. Electrospun scaffolds of chitosan were compared to evaporated 2D and 3D films and freeze-dried sponges. *In vitro* testing displayed enhanced cellular infiltration and proliferation for electrospun scaffolds. Furthermore, *in vivo* testing in rat models demonstrated respectable vascularization and ECM secretion for electrospun scaffolds, while sponges induced a foreign body granuloma.[57]

Crosslinked electrospun scaffolds of a collagen, chitosan and PEO blend also displayed an increased rate of wound healing *in vivo* compared to gauze and a collagen sponge dressing.[58] Overall, these results indicate that the nanofibrillar structure of electrospun fibers enhances cellular integration and tissue growth compared to other scaffold architectures, making them desirable for skin substitutes.

A.5.3 Other Methods to Produce 3D Tissue Scaffolds

Numerous methods apart from those described above exist to fabricate 3D scaffolds for skin. Nanofibrillar structures with great control over 3D shape and porosity are formed using self-assembly and thermally induced phase separation.[59] Melt molding also produces porous scaffolds, however, it is difficult to control the micro-architecture. Additionally, 3D printing, micro-stereolithography, and selective laser sintering have emerged to form scaffolds with highly controlled structure and reproducibility.[60] Although these techniques offer alternative methods for scaffold fabrication, hydrogels, and more particularly electrospun scaffolds, remain prominent as engineered skin equivalents. 3D printing has begun to rival their prevalence in organ tissue scaffolds, however, it is not commonly used for skin substitutes.

A.5.4 Modifications to Improve Properties of Polymeric Scaffolds

As evidenced previously, modifications to improve cell adhesion, proliferation, vascularization, and overall wound healing include control of pore size, encapsulation of cells and/or growth factors, and control of scaffold structure. Furthermore, mechanical properties and wettability are influenced by varying components of polymer blends. Additional modifications to improve scaffold properties include the introduction of "click-able" units to conjugate bioactive peptides and/or fluorescent molecules to the scaffold.[61] This enables the delivery of drugs or other proteins from the polymer as well as aides in imaging. Inorganic/polymer composites containing hydroxyapatite, bioactive glass, or glass-ceramic fillers seek to improve the mechanical properties,

degradation rates, and bioactivity of tissue scaffolds.[62] Finally, adhesive coatings, fibrin glue, and graft copolymers are employed to improve cell adhesion and proliferation.[63-65] Combinations of these numerous approaches will enable scaffolds with highly tunable architectures, bioactivity, and strength.

A.6 Conclusions and Further Challenges

Despite the obvious advances in polymeric scaffolds for use as skin substitutes, several challenges remain to be met. Currently, methods for scaffold production are long and arduous, often involving complex fabrication and cultivation. Furthermore, the production and storage is expensive and yields scaffolds with limited shelf life.[1, 11] Thus, techniques to produce tissue scaffolds need to be standardized and optimized for large-scale production and storage. In addition, incorporation of native skin elements such as hair follicles and sweat glands and better understanding of factors that promote angiogenesis will enhance the form and function of tissue scaffolds. Finally, a standard dermal substitute must be established as a control to allow for better interpretation and comparison of results.[12] The emergence of tissue scaffolds that truly mimic the form and function of skin will completely transform clinical treatments for burns, ulcers, and other skin lesions and will provide novel, realistic models for testing that would otherwise be performed in animal studies. In this work, methods will be employed to control the morphology of crosslinked electrospun PEO and provide scaffolds suitable for soft tissue engineering. Modifications to the PEO network through the adsorption of silica is performed to enhance bioactivity and promote cellular adhesion.

A.7 References

1. Zhang, Z.; Michniak-Kohn, B. B., Tissue engineered human skin equivalents. *Pharmaceutics* **2012,** *4* (1), 26-41.
2. Shimizu, R.; Kishi, K., Skin graft. *Plastic surgery international* **2012,** *2012*, 563493.
3. Orgill, D. P., Excision and Skin Grafting of Thermal Burns. *N. Engl. J. Med.* **2009,** *360* (9), 893-901.
4. Kamel, R. A.; Ong, J. F.; Eriksson, E.; Junker, J. P. E.; Caterson, E. J., Tissue Engineering of Skin. *Journal of the American College of Surgeons* **2013,** *217* (3), 533-555.
5. MacNeil, S., Progress and opportunities for tissue-engineered skin. *Nature* **2007,** *445*, 874.
6. Paul, S. P., "Halo" Grafting—A Simple and Effective Technique of Skin Grafting. *Dermatol. Surg.* **2010,** *36* (1), 115-119.
7. Weyandt, G. H.; Bauer, B.; Berens, N.; Hamm, H.; Broecker, E.-B., Split-Skin Grafting from the Scalp: The Hidden Advantage. *Dermatol. Surg.* **2009,** *35* (12), 1873-1879.
8. Miraliakbari, R.; Mackay, D. R., Skin Grafts. *Operative Techniques in General Surgery* **2006,** *8* (4), 197-206.
9. Mohammadi, A. A.; Bakhshaeekia, A. R.; Marzban, S.; Abbasi, S.; Ashraf, A. R.; Mohammadi, M. k.; Toulide-ie, H. R.; Tavakkolian, A. R., Early excision and skin grafting versus delayed skin grafting in deep hand burns (a randomised clinical controlled trial). *Burns* **2011,** *37* (1), 36-41.
10. Böttcher-Haberzeth, S.; Biedermann, T.; Reichmann, E., Tissue engineering of skin. *Burns* **2010,** *36* (4), 450-460.
11. Catalano, E.; Cochis, A.; Varoni, E.; Rimondini, L.; Azzimonti, B., Tissue-engineered skin substitutes: an overview. *Journal of artificial organs : the official journal of the Japanese Society for Artificial Organs* **2013,** *16* (4), 397-403.
12. van der Veen, V. C.; Boekema, B. K. H. L.; Ulrich, M. M. W.; Middelkoop, E., New dermal substitutes. *Wound Repair and Regeneration* **2011,** *19*, s59-s65.
13. Shevchenko, R. V.; James, S. L.; James, S. E., A review of tissue-engineered skin bioconstructs available for skin reconstruction. *J. R. Soc., Interface* **2010,** *7* (43), 229-258.
14. Mohamed, A.; Xing, M. M., Nanomaterials and nanotechnology for skin tissue engineering. *Int. J. Burns Trauma* **2012,** *2* (1), 29.
15. Dhandayuthapani, B.; Yoshida, Y.; Maekawa, T.; Kumar, D. S., Polymeric Scaffolds in Tissue Engineering Application: A Review. *Int. J. Polym. Sci.* **2011,** *2011*.
16. Zheng Shu, X.; Liu, Y.; Palumbo, F. S.; Luo, Y.; Prestwich, G. D., In situ crosslinkable hyaluronan hydrogels for tissue engineering. *Biomaterials* **2004,** *25* (7), 1339-1348.
17. Polymer: A Properties Database. CRC Press: Boca Raton, FL, 2010.
18. Hunt, J. A.; Chen, R.; van Veen, T.; Bryan, N., Hydrogels for tissue engineering and regenerative medicine. *J. Mater. Chem. B* **2014,** *2* (33), 5319-5338.
19. Nguyen, K. T.; West, J. L., Photopolymerizable hydrogels for tissue engineering applications. *Biomaterials* **2002,** *23* (22), 4307-4314.
20. Annabi, N.; Nichol, J. W.; Zhong, X.; Ji, C.; Koshy, S.; Khademhosseini, A.; Dehghani, F., Controlling the porosity and microarchitecture of hydrogels for tissue engineering. *Tissue Eng., Part B* **2010,** *16* (4), 371-383.
21. Lien, S.-M.; Ko, L.-Y.; Huang, T.-J., Effect of pore size on ECM secretion and cell growth in gelatin scaffold for articular cartilage tissue engineering. *Acta Biomater.* **2009,** *5* (2), 670-679.

22. Zeltinger, J.; Sherwood, J. K.; Graham, D. A.; Mueller, R.; Griffith, L. G., Effect of pore size and void fraction on cellular adhesion, proliferation, and matrix deposition. *Tissue engineering* **2001,** *7* (5), 557-72.
23. Chiu, Y.-C.; Cheng, M.-H.; Engel, H.; Kao, S.-W.; Larson, J. C.; Gupta, S.; Brey, E. M., The role of pore size on vascularization and tissue remodeling in PEG hydrogels. *Biomaterials* **2011,** *32* (26), 6045-6051.
24. Griffon, D. J.; Sedighi, M. R.; Schaeffer, D. V.; Eurell, J. A.; Johnson, A. L., Chitosan scaffolds: Interconnective pore size and cartilage engineering. *Acta Biomater.* **2006,** *2* (3), 313-320.
25. Malda, J.; Woodfield, T. B. F.; van der Vloodt, F.; Wilson, C.; Martens, D. E.; Tramper, J.; van Blitterswijk, C. A.; Riesle, J., The effect of PEGT/PBT scaffold architecture on the composition of tissue engineered cartilage. *Biomaterials* **2005,** *26* (1), 63-72.
26. Hawkins, A. M.; Milbrandt, T. A.; Puleo, D. A.; Hilt, J. Z., Composite hydrogel scaffolds with controlled pore opening via biodegradable hydrogel porogen degradation. *J. Biomed. Mater. Res., Part A* **2014,** *102* (2), 400-412.
27. Nicodemus, G. D.; Bryant, S. J., Cell Encapsulation in Biodegradable Hydrogels for Tissue Engineering Applications. *Tissue Eng., Part B* **2008,** *14* (2), 149-165.
28. Lin, H.-Y.; Peng, C.-W.; Wu, W.-W., Fibrous hydrogel scaffolds with cells embedded in the fibers as a potential tissue scaffold for skin repair. *J. Mater. Sci.: Mater. Med.* **2014,** *25* (1), 259-269.
29. Yun, E. J.; Yon, B.; Joo, M. K.; Jeong, B., Cell Therapy for Skin Wound Using Fibroblast Encapsulated Poly(ethylene glycol)-poly(l-alanine) Thermogel. *Biomacromolecules* **2012,** *13* (4), 1106-1111.
30. Huang, S.; Zhang, Y.; Tang, L.; Deng, Z.; Lu, W.; Feng, F.; Xu, X.; Jin, Y., Functional Bilayered Skin Substitute Constructed by Tissue-Engineered Extracellular Matrix and Microsphere-Incorporated Gelatin Hydrogel for Wound Repair. *Tissue Eng., Part A* **2009,** *15* (9), 2617-2624.
31. Doğan, A. K.; Gümüşderelioğlu, M.; Aksöz, E., Controlled release of EGF and bFGF from dextran hydrogels in vitro and in vivo. *J. Biomed. Mater. Res., Part B* **2005,** *74B* (1), 504-510.
32. Miguel, S. P.; Ribeiro, M. P.; Brancal, H.; Coutinho, P.; Correia, I. J., Thermoresponsive chitosan–agarose hydrogel for skin regeneration. *Carbohydr. Polym.* **2014,** *111* (0), 366-373.
33. Tan, H.; Ramirez, C. M.; Miljkovic, N.; Li, H.; Rubin, J. P.; Marra, K. G., Thermosensitive injectable hyaluronic acid hydrogel for adipose tissue engineering. *Biomaterials* **2009,** *30* (36), 6844-6853.
34. Wang, F.; Li, Z.; Khan, M.; Tamama, K.; Kuppusamy, P.; Wagner, W. R.; Sen, C. K.; Guan, J., Injectable, rapid gelling and highly flexible hydrogel composites as growth factor and cell carriers. *Acta Biomater.* **2010,** *6* (6), 1978-1991.
35. Potta, T.; Chun, C.; Song, S.-C., Injectable, dual cross-linkable polyphosphazene blend hydrogels. *Biomaterials* **2010,** *31* (32), 8107-8120.
36. Potta, T.; Chun, C.; Song, S.-C., Rapid Photocrosslinkable Thermoresponsive Injectable Polyphosphazene Hydrogels. *Macromol. Rapid. Commun.* **2010,** *31* (24), 2133-2139.
37. Kumbar, S. G.; Nukavarapu, S. P.; James, R.; Nair, L. S.; Laurencin, C. T., Electrospun poly(lactic acid-co-glycolic acid) scaffolds for skin tissue engineering. *Biomaterials* **2008,** *29* (30), 4100-4107.
38. Smith, L. A.; Ma, P. X., Nano-fibrous scaffolds for tissue engineering. *Colloids, Surf., B* **2004,** *39* (3), 125-131.

39. McKee, M. G.; Wilkes, G. L.; Colby, R. H.; Long, T. E., Correlations of Solution Rheology with Electrospun Fiber Formation of Linear and Branched Polyesters. *Macromolecules* **2004,** *37* (5), 1760-1767.
40. McKee, M. G.; Hunley, M. T.; Layman, J. M.; Long, T. E., Solution Rheological Behavior and Electrospinning of Cationic Polyelectrolytes. *Macromolecules* **2005,** *39* (2), 575-583.
41. Hemp, S. T.; Hunley, M. T.; Cheng, S.; DeMella, K. C.; Long, T. E., Synthesis and solution rheology of adenine-containing polyelectrolytes for electrospinning. *Polymer* **2012,** *53* (7), 1437-1443.
42. McKee, M. G.; Layman, J. M.; Cashion, M. P.; Long, T. E., Phospholipid Nonwoven Electrospun Membranes. *Science* **2006,** *311* (5759), 353-355.
43. Suga, T.; Hunley, M. T.; Long, T. E.; Nishide, H., Electrospinning of radical polymers: redox-active fibrous membrane formation. *Polym J* **2012,** *44* (3), 264-268.
44. Li, D.; Xia, Y., Electrospinning of nanofibers: reinventing the wheel. *Adv. Mater.* **2004,** *16* (14), 1151-1170.
45. Reneker, D. H.; Yarin, A. L.; Fong, H.; Koombhongse, S., Bending instability of electrically charged liquid jets of polymer solutions in electrospinning. *Journal of Applied Physics* **2000,** *87* (9), 4531-4547.
46. Reneker, D. H.; Chun, I., Nanometre diameter fibres of polymer, produced by electrospinning. *Nanotechnology* **1996,** *7* (3), 216.
47. Dong, Z.; Kennedy, S. J.; Wu, Y., Electrospinning materials for energy-related applications and devices. *J. Power Sources* **2011,** *196* (11), 4886-4904.
48. Suganya, S.; Venugopal, J.; Ramakrishna, S.; Lakshmi, B. S.; Dev, V. R. G., Naturally derived biofunctional nanofibrous scaffold for skin tissue regeneration. *Int. J. Biol. Macromol.* **2014,** *68* (0), 135-143.
49. Cui, W.; Jin, Y.; Zhu, X.; Li, X., Electrospun Fibrous Mats with High Porosity as Potential Scaffolds for Skin Tissue Engineering. *Biomacromolecules* **2008,** *9* (7), 1795-1801.
50. Rnjak-Kovacina, J.; Weiss, A. S., Increasing the pore size of electrospun scaffolds. *Tissue Eng., Part B* **2011,** *17* (5), 365-372.
51. Bonvallet, P. P.; Culpepper, B. K.; Bain, J. L.; Schultz, M. J.; Thomas, S. J.; Bellis, S. L., Microporous Dermal-Like Electrospun Scaffolds Promote Accelerated Skin Regeneration. *Tissue Eng., Part A* **2014,** *20* (17-18), 2434-2445.
52. Bryant, S. J.; Cuy, J. L.; Hauch, K. D.; Ratner, B. D., Photo-patterning of porous hydrogels for tissue engineering. *Biomaterials* **2007,** *28* (19), 2978-2986.
53. Zhou, Y.; Yang, D.; Chen, X.; Xu, Q.; Lu, F.; Nie, J., Electrospun Water-Soluble Carboxyethyl Chitosan/Poly(vinyl alcohol) Nanofibrous Membrane as Potential Wound Dressing for Skin Regeneration. *Biomacromolecules* **2007,** *9* (1), 349-354.
54. Asran, A. S.; Razghandi, K.; Aggarwal, N.; Michler, G. H.; Groth, T., Nanofibers from Blends of Polyvinyl Alcohol and Polyhydroxy Butyrate As Potential Scaffold Material for Tissue Engineering of Skin. *Biomacromolecules* **2010,** *11* (12), 3413-3421.
55. Liu, N.-h.; Pan, J.-f.; Miao, Y.-E.; Liu, T.-x.; Xu, F.; Sun, H., Electrospinning of poly (ε-caprolactone-co-lactide)/Pluronic blended scaffolds for skin tissue engineering. *J. Mater. Sci.* **2014,** *49* (20), 7253-7262.
56. Unnithan, A. R.; Pichiah, P. B. T.; Gnanasekaran, G.; Seenivasan, K.; Barakat, N. A. M.; Cha, Y.-S.; Jung, C.-H.; Shanmugam, A.; Kim, H. Y., Emu oil-based electrospun nanofibrous scaffolds for wound skin tissue engineering. *Colloids Surf., A* **2012,** *415* (0), 454-460.
57. Tchemtchoua, V. T.; Atanasova, G.; Aqil, A.; Filee, P.; Garbacki, N.; Vanhooteghem, O.; Deroanne, C.; Noel, A.; Jerome, C.; Nusgens, B.; Poumay, Y.; Colige, A., Development of a

Chitosan Nanofibrillar Scaffold for Skin Repair and Regeneration. *Biomacromolecules* **2011,** *12* (9), 3194-3204.
58. Chen, J.-P.; Chang, G.-Y.; Chen, J.-K., Electrospun collagen/chitosan nanofibrous membrane as wound dressing. *Colloids Surf., A* **2008,** *313–314* (0), 183-188.
59. Holzwarth, J. M.; Ma, P. X., 3D nanofibrous scaffolds for tissue engineering. *J. Mater. Chem.* **2011,** *21* (28), 10243-10251.
60. Mata, A.; Fleischman, A. J.; Roy, S., Microfabricated 3D Scaffolds for Tissue Engineering Applications. *MRS Online Proc. Libr.* **2004,** *845*, null-null.
61. Lin, F.; Yu, J.; Tang, W.; Zheng, J.; Xie, S.; Becker, M. L., Postelectrospinning "Click" Modification of Degradable Amino Acid-Based Poly(ester urea) Nanofibers. *Macromolecules* **2013,** *46* (24), 9515-9525.
62. Misra, S. K.; Valappil, S. P.; Roy, I.; Boccaccini, A. R., Polyhydroxyalkanoate (PHA)/Inorganic Phase Composites for Tissue Engineering Applications. *Biomacromolecules* **2006,** *7* (8), 2249-2258.
63. Missirlis, D.; Spatz, J. P., Combined Effects of PEG Hydrogel Elasticity and Cell-Adhesive Coating on Fibroblast Adhesion and Persistent Migration. *Biomacromolecules* **2013,** *15* (1), 195-205.
64. Han, C.-m.; Zhang, L.-p.; Sun, J.-z.; Shi, H.-f.; Zhou, J.; Gao, C.-y., Application of collagen-chitosan/fibrin glue asymmetric scaffolds in skin tissue engineering. *Journal of Zhejiang University SCIENCE B* 2010, pp 524-530.
65. Chen, H.; Huang, J.; Yu, J.; Liu, S.; Gu, P., Electrospun chitosan-graft-poly (ε-caprolactone)/poly (ε-caprolactone) cationic nanofibrous mats as potential scaffolds for skin tissue engineering. *Int. J. Biol. Macromol.* **2011,** *48* (1), 13-19.

Appendix B

Preparation and Characterization of Crosslinked, Electrospun Poly(ethylene oxide)

B.1 Introduction

Electrospinning is a useful technique for the preparation of nanofibrous materials with high surface area and controlled, porous frameworks. The electrospinning process utilizes an applied electric force to charge a polymer solution as it is expelled from a syringe.[1] At sufficient charge, the electrostatic repulsions in the polymer solution are strong enough to overcome the surface tension of the solution and a jet is expelled. The jet is attracted towards a grounded collector and as it travels towards the collector undergoes elongation of the jet and evaporation of the solvent, resulting in a nonwoven nanofibrous mat.[2] Control of nanofiber architecture, such as fiber diameter, is readily achieved by changing electrospinning parameters such as solution concentration, solvent, applied voltage, and distance to collector.[3] Overall, the electrospinning process provides a simple, inexpensive means to prepare nanofibers with high surface area to volume ratios and high porosity.

Electrospun scaffolds have been prepared from a wide variety of synthetic and natural materials, enabling their widespread use in applications such as filtration[4-5], batteries[6], composites[7], biomedical devices[8], etc. In particular, electrospun scaffolds have demonstrated specific utility in tissue engineering to provide porous, mechanically stable platforms to support cell growth. The nanoscale morphology of the electrospun materials closely mimics the size-scale and structure of the native extracellular matrix of cells, providing a biomimetic architecture for tissue replacements.[9-10] The nanoscale dimensions also provide a high surface area for cell attachment and high porosity conducive to cellular infiltration and growth.[11-12]

Poly(ethylene oxide) (PEO) is a FDA approved polymer that is frequently used in tissue engineering applications due to its hydrophilicity, good biocompatibility, lack of immunogenic

response, and resistance to protein adsorption.[13] PEO has also been used in drug conjugation and sustained drug release among other applications.[14] While PEO is a useful material for biomedical applications, its high solubility in water and common organic solvents precludes its use in the solid-state. To overcome this, crosslinking reactions may be performed to produce insoluble materials that swell with water and provide mechanically robust, hydrophilic scaffolds for cell growth.[15-16]

In this work, the fabrication of crosslinked, electrospun PEO is explored to prepare insoluble, nanofibrous scaffolds for tissue engineering applications (such as skin substitutes and wound dressing). PEO is UV-crosslinked during electrospinning using pentaerythritol triacrylate (PETA), and the effect of crosslinker concentration and UV exposure time on nanofiber properties is investigated. Nanofiber morphology, gel fraction, porosity, equilibrium swelling, and mechanical properties are investigated to determine the potential utility of the crosslinked PEO scaffolds for tissue engineering applications.

B.2 Experimental

B.2.1 Materials

Poly(ethylene oxide) (PEO) with $M_v \sim 300{,}000$ g/mol was obtained from Sigma-Aldrich. Pentaerythritol triacrylate was also obtained from Sigma-Aldrich. Acetonitrile, methanol, and chloroform was obtained from Fisher Scientific. All materials were used as received.

B.2.2 Co-electrospinning of PEO and PETA

Non-woven mats were prepared by electrospinning a solution of PEO and PETA at room temperature a KDscientific 100 syringe pump and a Spellman Berton 205B high voltage source. Solutions of PEO and PETA were prepared at compositions between 5 and 8 wt% in acetonitrile, with variable concentrations of PETA. The concentration of PETA was varied from 10-30 wt% based on the weight of PEO, and the samples were named PEO*x* where *x* is the concentration of

PETA. The electrospinning solutions were extruded at a flow rate of 2 mL/hr from a 3-mL syringe through a blunt tip stainless steel needle having an internal diameter of 0.8 mL. A negative-biased voltage of 19 kV was applied to the needle tip and the resulting nanofibers were collected on a grounded aluminum rotating rod collector (1 cm diameter, 200 RPM) placed 25 cm from the needle tip.

B.2.3 Crosslinking of PEO-PETA Mats

To crosslink the PEO-PETA nanofibers, a 459-watt mercury vapor UV lamp was placed directly above the aluminum collector. During electrospinning, the UV lamp was turned on to allow crosslinking of the nanofibers as they were collected. An opaque (black) electrospinning box was used to ensure no one was exposed to harmful UV light. When investigating the influence of UV cure time on the resultant PEO-PETA nanofibers, the UV lamp was also turned off and on for various times during the electrospinning process.

B.2.4 Gel Fraction, Porosity, and Equilibrium Swelling Measurements

Gel fraction of the crosslinked PEO nanofibers was determined gravimetrically. As-spun samples were cut into discs (20 mm diameter) and dried under vacuum overnight prior to analysis. The dried discs were weighed and then placed in excess methanol and ultrasonicated for one hour to remove any unreacted PETA and linear (not crosslinked) PEO. The discs were removed from the methanol, dried under vacuum overnight, and weighed again. The gel fraction was determined as the weight following sonication divided by the original weight of the dried discs.

Porosity was determined using the *n*-butanol uptake method. Analysis was performed on the crosslinked PEO samples after the removal of the sol fraction by sonication in methanol. Dried discs (20 mm) of crosslinked PEO were weighed and then placed in excess *n*-butanol. After 1 hour, samples were removed, excess *n*-butanol was blotted from the surface, and the weight of the samples with adsorbed *n*-butanol was recorded. The porosity was determined by dividing the

volume of *n*-butanol within the nanofiber mat by the total volume of both the nanofiber mat and *n*-butanol within the mat.

Equilibrium swelling measurements in water and in chloroform were determined. Crosslinked PEO samples were cut into discs (20 mm) and dried under vacuum prior to analysis. Samples were placed in excess swelling solvent and allowed to equilibrate until no further weight change is observed. The samples were removed from solvent, blotted to remove excess solvent at the surface, and the swollen weight was recorded. Wet samples were then dried under vacuum overnight and the dry weight was recorded. The equilibrium swelling ratio was determined by subtracting the dry weight from the wet weight and then dividing by the dry weight.

B.2.5 FTIR Spectroscopy

FTIR was performed using a Varian 670-IR spectrometer with a DTGS detector using the Pike Technologies GladiATR^{TM} attachment (diamond crystal). Spectra were collected from 4000 to 400 cm^{-1} as the average of 32 scans at 4 cm^{-1} resolution. Prior to collection of spectra, an air background was taken and was automatically subtracted from each sample spectrum. Spectra were ATR corrected and baseline corrected prior to analysis.

B.2.6 Scanning Electron Microscopy

SEM images were acquired using a JEOL NesoScope JCM-5000 Benchtop SEM. SEM samples were sputter coated with gold prior to imaging. Fiber diameter histrograms were determined using the Nikon Instruments NIS-Elements Basic Research imaging software.

B.2.7 Differential Scanning Calorimetry

Differential scanning calorimetry (DSC) was performed on a TA Instruments DSC Q2000. Samples were dried overnight under vacuum prior to analysis. Under a nitrogen atmosphere, samples (5-8 mg) were equilibrated at -85 ºC. Samples were subjected to a heat-cool-heat cycle with temperature bounds of -85 ºC to 85 ºC and heating/cooling rates of 10 ºC/min. The glass

transition temperature (T_g), crystallization temperature (T_c), enthalpy of crystallization (ΔH_c), melting temperature (T_m), and enthalpy of melting (ΔH_m) was determined using the TA Instruments Universal Analysis software.

B.2.8 Dynamic Mechanical Analysis

Dynamic mechanical analysis (DMA) was performed on a TA Instruments DMA Q800 in oscillatory tension mode. Samples were equilibrated at -100 ºC and then ramped at 3 ºC/min to 100 ºC at a frequency of 10 Hz, an oscillatory amplitude of 15 μm, and a static force of 0.01 N. Stress relaxation experiments were performed at 10 % strain at 70 ºC for 10 minutes.

B.2.9 Tensile Testing

Tensile testing was performed on an Instron 5867 equipped with pneumatic grips. Samples were cut into dogbones (ASTM D638) and were tested with a strain rate of 20 mm/min and a gage length of 10 mm.

B.3 Results and Discussion

B.3.1 Co-electrospinning of PEO and PETA

Polymer concentration in solution is a key parameter in the electrospinning process for permitting fiber formation and regulating the fiber morphology and size.[17] At low concentrations, solution viscosity is low and surface tension dominates the fiber formation process, resulting in electrosprayed polymer droplets instead of nanofibers.[18-19] As the solution concentration increases, viscosity increases and the polymer chains become more entangled, resulting in a mixture of droplets and nanofibers deemed a 'beads on a string' morphology.[20-21] Finally, when the concentration has reached a critical point, smooth nanofibers will be formed and the diameter of these nanofibers will increase with increasing concentration.[22] To determine the optimal electrospinning conditions for co-electrospinning PEO and PETA, PEO10 solutions containing variable concentrations of PEO in acetonitrile were electrospun and analyzed. PEO10 solutions

were prepared at 5 wt%, 6 wt%, 7 wt% and 8 wt% PEO in acetonitrile and were electrospun at the conditions described above (i.e. 2 mL/hr flow rate, 19 kV voltage). The morphology of the resultant nanofiber mats was investigated using SEM, as shown in **Figure B.1**. At low concentrations (5 wt%, 6 wt%), PEO10 nanofibers exhibit a beaded fiber morphology. The beads are prevalent across the entirety of the nanofiber mats, indicating that electrospraying remains an issue at these concentrations. As the concentration increases to 7 wt%, PEO10 exhibits some beading, however it is minimal. Finally, at a concentration of 8 wt%, PEO10 displays smooth, fibers with a uniform size and isotropic distribution. Thus, to ensure uniform fibers, future solutions were prepared using 8 wt% PEO in acetonitrile while varying the PETA content.

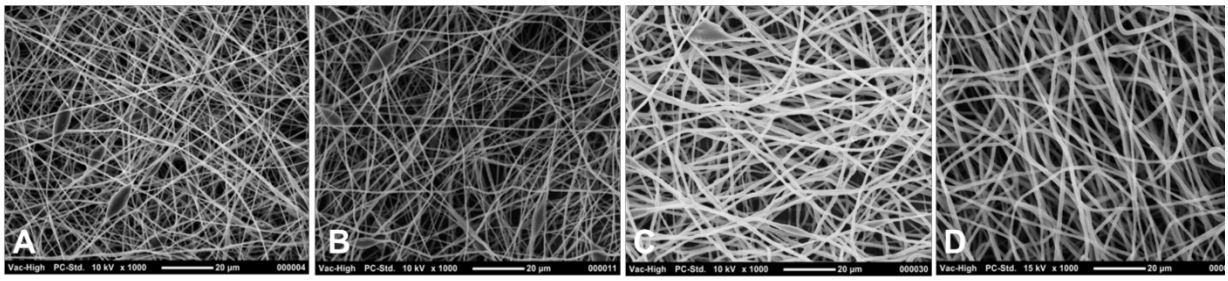

Figure B.1. SEM images of PEO10 electrospun from 5 wt% (A), 6 wt% (B), 7 wt% (C), and 8 wt% (D) solutions in acetonitrile.

B.3.2 Crosslinking Mechanism of PEO/PETA

The photo-initiated crosslinking of PEO is a simple approach to greatly reduce the solubility of PEO in polar solvents and provide stable materials that will swell, but not dissolve, in water. The co-electrospinning of PEO with pentaerythritol triacrylate (PETA) thereby allows for the UV-curing of the PEO nanofibers to synthesize crosslinked, insoluble nanofibers. PETA has been shown to act as both a photo-initiator and crosslinker for PEO films[23], and has even been used to crosslink electrospun PEO in the presence of incorporated cellulose nanocrystals.[24] The proposed crosslinking mechanism of PEO using PETA is shown in **Figure B.2**. Upon irradiation with UV light, a photon is absorbed by PETA which excites the carbonyl into an excited triplet

state. From this excited triplet state, the PETA can abstract a hydrogen from the PEO polymer chain and cleave the C=O bond, forming a PEO radical and PETA radical, respectively.[24] Once the radicals have been generated, three main crosslinking processes may occur. First, two polymeric (PEO) radicals close in space may combine to crosslink the 2 polymer chains to one another. Second, the PEO radical may combine with the radical formed on PETA and directly link the PEO to the PETA. Because PETA is trifunctional (3 C=O groups), it has the ability to produce 3 radicals which may combine with up to 3 PEO chains to crosslink it. Finally, the radicals formed on the PEO chain or on PETA may attack the unsaturated C=C bond of PETA to initiate the polymerization of PETA.[23] This polymerization may be terminated by radical-radical coupling with a PEO chain (as described above) to crosslink the material. Likely, the exact mechanism of crosslinking is a combination of these processes. Because a relatively large amount of PETA is required to form insoluble PEO films, it is likely that the free-radical polymerization of PETA plays a key role in the crosslinking of electrospun PEO.[25]

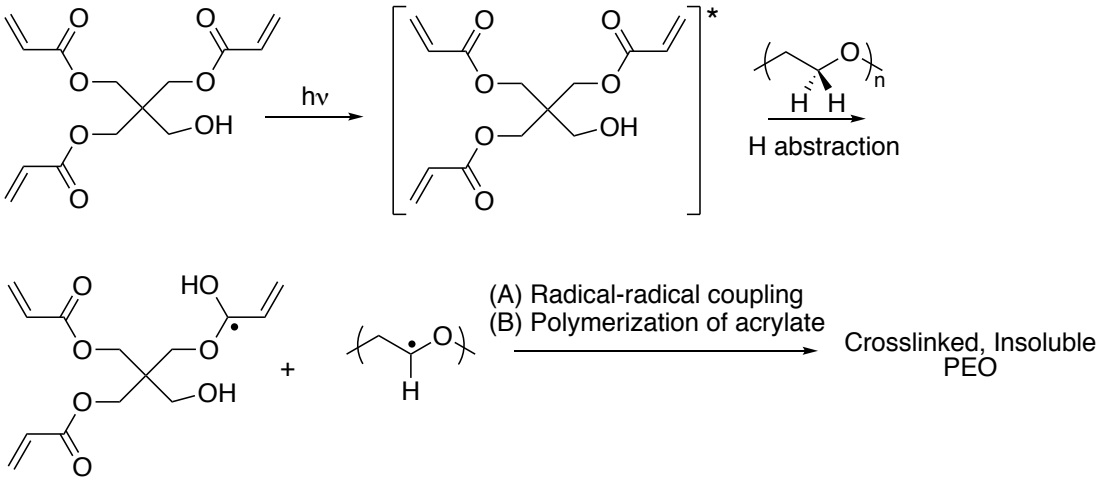

Figure B.2. Proposed mechanism for PEO crosslinking using PETA.

To investigate the PETA crosslinking mechanism with PEO, FTIR was performed first on thin films of PEO10. Films were cast from electrospinning solutions (8 wt% PEO in acetonitrile,

10 wt% PETA by weight of PEO) onto a glass substrate to a final thickness of 6 μm. Samples were then placed directly under the UV light and irradiated for 10, 20, 30, 45, and 60 minutes. FTIR spectra were collected in transmission mode and the results are shown in **Figure B.3**. PETA displays 3 primary peaks of interest throughout the crosslinking process: the C=O bond at 1730 cm^{-1}, the C=C double bond at 1625 cm^{-1}, and the C-H of the acrylic $RC=CH_2$ at 1410 cm^{-1}. With no UV irradiation, these three peaks are clearly observed for the PEO10, yielding a baseline for the unreacted PETA. Upon UV irradiation the C=O peak decreases in intensity, demonstrating the conversion of the carbonyl to a hydroxyl group due to hydrogen abstraction from the PEO backbone. At 30 minutes of irradiation and above, the C=O peak does not appear to change in intensity or shape, suggesting that all of the photoinitiated PETA has reacted with the PEO and other PETA molecules. Furthermore, during UV irradiation, the C=C peak at 1625 cm^{-1} and the C-H peak at 1410 cm^{-1} rapidly decrease in intensity to the point where no C=C bonds are observed past 30 minutes of irradiation. This is highly suggestive that the radical-induced polymerization of the PETA acylate groups is occurring during crosslinking, and the degree of this polymerization may be influenced by UV cure time.

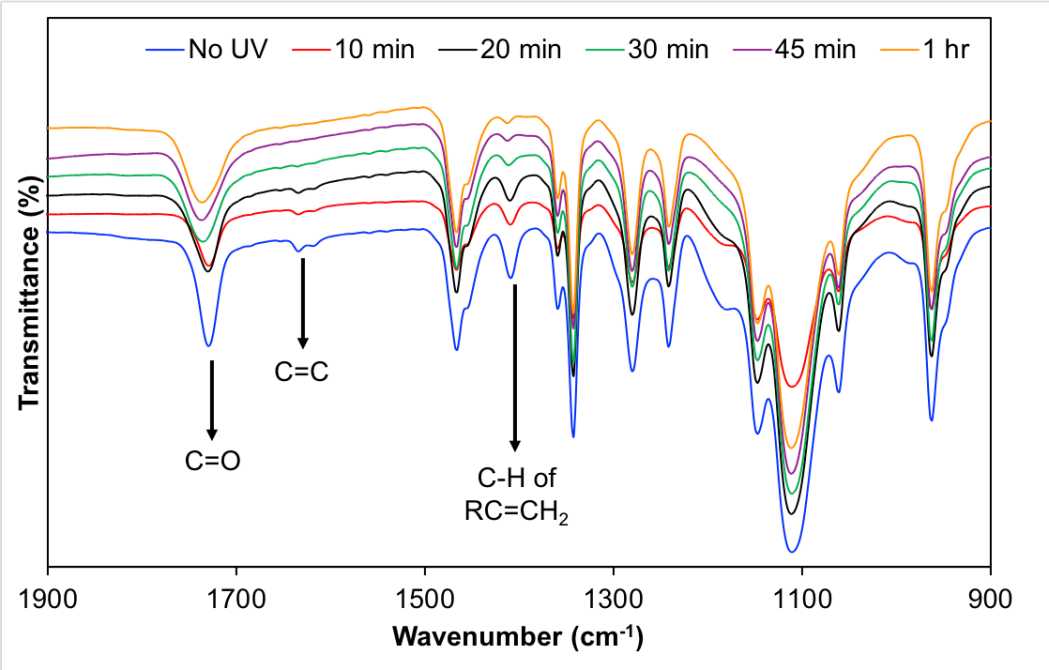

Figure B.3. FTIR of PEO10 thin films with various times of UV irradiation. The PETA bonds of interest are noted.

B.3.3 Development of *In-Situ* UV Curing

To crosslink electrospun PEO/PETA nanofiber mats, most procedures involve first co-electrospinning the PEO and PETA and then irradiating each side of the mat with UV light, similar to PEO/PETA films.[24-25] Although this process produces crosslinked PEO at the surface of the nanofiber mats, the UV light is not able to penetrate deep enough to cure the core of the mat due to the large UV absorptivity coefficient of PETA. In fact, it was determined that UV is only able to penetrate up to 35 μm into the PEO/PETA matrix, thereby limiting the total thickness able to be obtained. To get more homogeneous crosslinking throughout the entire depth of the nanofiber mats, the electrospinning setup was modified to allow for the concurrent electrospinning and UV-curing of PEO. A hole the size of the UV lamp window was cut into the top of the electrospinning box directly above the rotating rod collector, as shown in **Figure B.4**. The UV lamp was turned on throughout the entirety of the electrospinning process to generate the free radicals necessary to

crosslink the PEO within the nanofibers. By electrospinning with constant UV irradiation, the nanofiber mats display no uncrosslinked core – rather, they exhibit a uniform level of crosslinking throughout the entire depth of the mat.

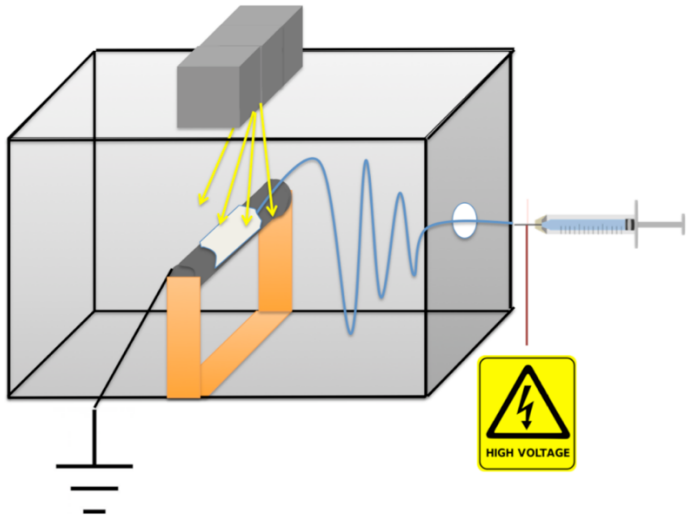

Figure B.4. Electrospinning setup for the *in-situ* crosslinking of PEO nanofibers.

B.3.4 Determination of PETA Incorporation by FTIR

To determine the actual chemical incorporation of PETA into the electrospun mats, FTIR was performed. PEO/PETA films were prepared with variable ratios of PETA:PEO (between 5 and 35 wt%) to develop a calibration curve for PETA quantification. The FTIR spectra of the as-cast films (not UV-irradiated) are shown in **Figure B.5**. FTIR spectra were normalized to the peak at 1340 cm^{-1} (C-H deformation modes of PEO)[26]. Next, the area under the C=O peak at 1730 cm^{-1} (PETA) was determined and divided by the area under the peak at 1340 cm^{-1} to yield a ratio of peak areas with amount of PETA. The calibration curve determined using this method is displayed in **Figure B.6**.

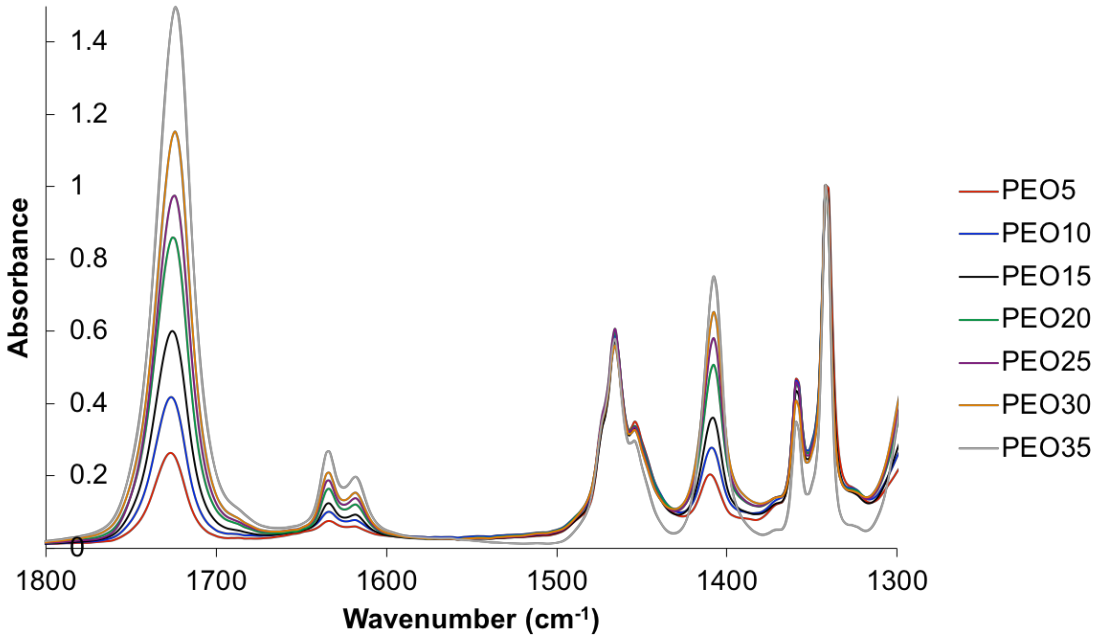

Figure B.5. FTIR of PEO/PETA films with various amounts of PETA by weight of PEO.

As the amount of PETA increases, the C=O peak intensity increases linearly with a relationship of $A_{1730}/A_{1340} = 0.1605[PETA]$ and an R^2 value of 0.99. Thus, the ratio of these peak areas may easily be utilized to estimate the amount of PETA chemically reacted with the PEO nanofibers. Although the PEO/PETA films used for this analysis were not crosslinked by UV light, the equation will translate to crosslinked mats as well due to the crosslinking mechanism of PETA described above. Upon excitation of the carbonyl, hydrogen abstraction from PEO will occur at the same time as hydroxyl generation, and thus the intensity of the C=O peak should decrease at the same rate as the intensity of the C-H peak of PEO.

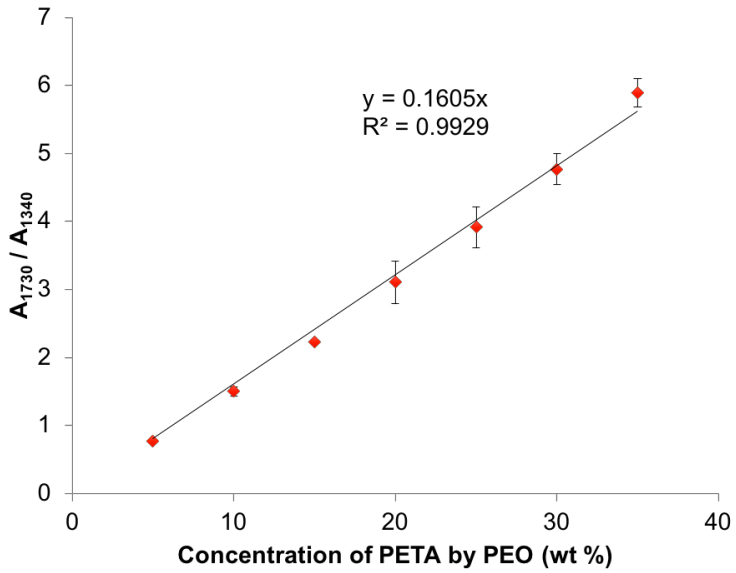

Figure B.6. Calibration curve determined by comparing the FTIR spectra of PEO/PETA films with variable PETA concentration.

FTIR analysis and the calibration curve were used to estimate the PETA incorporation of as-spun, *in-situ* crosslinked PEO10, PEO20, and PEO30. Furthermore, samples were washed by ultrasonication in excess acetonitrile for 1 hour to remove any uncrosslinked material and determine the actual degree of PETA crosslinking. As shown in **Table B.1**, the actual incorporation of PETA for both the as-spun mats and the washed mats closely matches the amount of PETA in the electrospinning solution. Thus, full incorporation of the PETA is expected with *in-situ* curing of PEO during electrospinning.

Table B.1. Determination of PETA concentration in crosslinked PEO nanofiber mats.

	Sample	A_{1730}/A_{1340}	PETA Conc. (wt %)
As-Spun	PEO10	1.5 ± 0.1	9.0 ± 0.5
	PEO20	2.6 ± 0.5	16.5 ± 3.2
	PEO30	4.6 ± 0.1	28.6 ± 0.9
Washed	PEO10	1.9 ± 0.4	11.7 ± 2.8
	PEO20	2.8 ± 0.3	17.2 ± 1.7
	PEO30	4.6 ± 0.6	28.4 ± 3.5

B.3.5 Characterization of Crosslinked, Electrospun PEO

With the successful crosslinking of PEO with PETA using *in-situ* crosslinking, the influence of PETA content on the PEO nanofiber morphology was investigated using SEM. As shown in **Figure B.7**, the PEO/PETA electrospun mats have smooth, uniform nanofibers with isotropic orientations. Little visual difference is observed with increasing PETA incorporation, suggesting that fiber morphology depends primarily on the concentration of PEO in solution. The fiber diameters and fiber diameter distributions were also determined from the SEM images. PEO10, PEO20, and PEO30 all exhibit unimodal fiber diameter distributions with diameters of 0.96 ± 0.12 μm, 0.98 ± 0.11 μm, and 1.00 ± 0.14 μm, respectively. Thus, it is evident that the fiber diameter is independent of PETA concentration. Any variation in the fiber diameters must therefore be established by the electrospinning processing conditions, including PEO concentration, applied voltage, and flow rate.

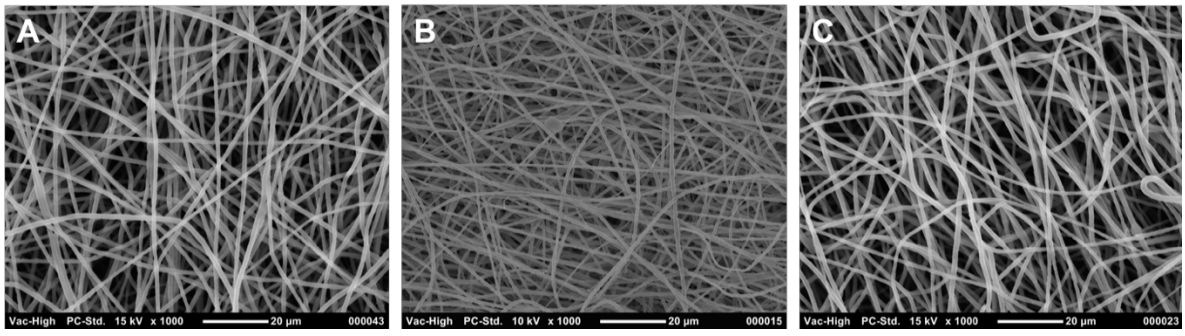

Figure B.7. SEM images of PEO10 (A), PEO20 (B), and PEO30 (C).

The gel fraction (i.e crosslinked fraction) of PEO10, PEO20, and PEO30 was determined gravimetrically after ultrasonicating the nanofiber mats in excess methanol for one hour to remove any soluble fraction. The original mass of the fiber mat was compared to the mass following sonication to calculate the insoluble (gel) fraction, and the results are displayed in **Table B.2**. The

in-situ crosslinking of PEO with PETA results in nanofibers with a high degree of retained mass (>85 wt%) following solvent exposure. Because linear (uncrosslinked) PEO is completely soluble in methanol, PETA acted effectively as both the photo-initiator and crosslinking agent to form a chemically crosslinked, insoluble PEO network. As the PETA concentration increases from 10 wt% to 20 wt%, the gel fraction increases considerable from 87 wt% to 97 wt%. Above 20 wt% PETA, no significant change in observed in gel fraction. Thus, to get almost complete crosslinking of all PEO/PETA, a PETA concentration of at least 20 wt% should be used.

The gel fractions for all PEO/PETA compositions prepared by *in-situ* UV curing are considerably higher than previous reports whereby the nanofibers were cured post-electrospinning. Zhou reported a maximum gel fraction of only 47 wt% with 10 wt% PETA loading (comparable to PEO10), and Forbey reported gel fractions of 82, 84, and 86 wt% for PEO10, 20, and 30, respectively.[24-25] Thus, the concurrent electrospinning and crosslinking process established in this work is capable of crosslinking the PEO throughout the depth of the fiber mat, resulting in a greater insoluble fraction. This high gel fraction corroborates the use of the crosslinked PEO as a bioinert, solid support for tissue engineering.

Table B.2. Gel fraction and porosity of crosslinked PEO nanofiber mats with various amounts of PETA.

Sample	Gel Fraction (wt%)	Porosity (vol%)
PEO10	87 ± 2	70 ± 2
PEO20	97 ± 1	76 ± 3
PEO30	96 ± 1	85 ± 2

For applications such as tissue engineering scaffolds, the porosity (and control of porosity) of electrospun mats is a key necessity to provide for the diffusion of nutrients and waste, space for cellular ingrowth and proliferation, and vascularization.[27-28] In general, an increase in porosity improves cellular infiltration and allows for cells to distribute and grow throughout the entire nanofiber matrix.[29-30] The porosity of *in-situ* crosslinked PEO10, PEO20, and PEO30 was

determined using the *n*-butanol uptake method.[31] Samples were submerged in excess *n*-butanol for 1 hour, and the mass was recorded before and after the absorption of *n*-butanol. The porosity is then determined using the following relation:

$$\text{Porosity} = \frac{M_{n-\text{BuOH}}/\rho_{n-\text{BuOH}}}{M_{n-\text{BuOH}}/\rho_{n-\text{BuOH}} + M_{\text{PEO}}/\rho_{\text{PEO}}} \quad \textbf{(B.1)}$$

where $M_{n\text{-BuOH}}$ is the mass of butanol absorbed into the mat, $\rho_{n\text{-BuOH}}$ is the density of *n*-butanol, M_{PEO} is the mass of the dry mat, and ρ_{PEO} is the density of PEO. The calculated porosities for crosslinked PEO are shown in **Table B.2**. As the concentration of PETA increases, the porosity also increases. For example, the porosity of PEO10 is 70 vol% and this increases to 85 vol% for PEO30. To understand the differences in these porosities, SEM images were taken of the crosslinked PEO mats after extraction of the sol fraction using methanol, as shown in **Figure B.8**. Comparison to the SEM images of as-spun crosslinked PEO (**Figure B.7**) shows that the discrete fiber morphology of the as-spun fiber mats is somewhat distorted following solvent exposure. At low PETA contents, PEO10 shows a significant degree of fiber melding, resulting in densification of the fibers and a smaller porosity of the mat. The fiber melding is likely an effect of a relatively low crosslinking density, which leaves longer runs of mobile PEO that can fuse with other neighboring chains. PEO20 also shows some evidence of fiber melding, however, PEO30 maintains most of its discrete fiber character. Thus, as the concentration of PETA increases (and the gel fraction increases), the nanofibers are more capable of maintaining their original fiber morphology upon solvent exposure, consistent with a higher observed porosity. Furthermore, this demonstrates that the UV-crosslinking process using PETA preserves the nanofibrous network of the electrospun mats even upon exposure to solvent, providing a suitable matrix for tissue scaffolding.

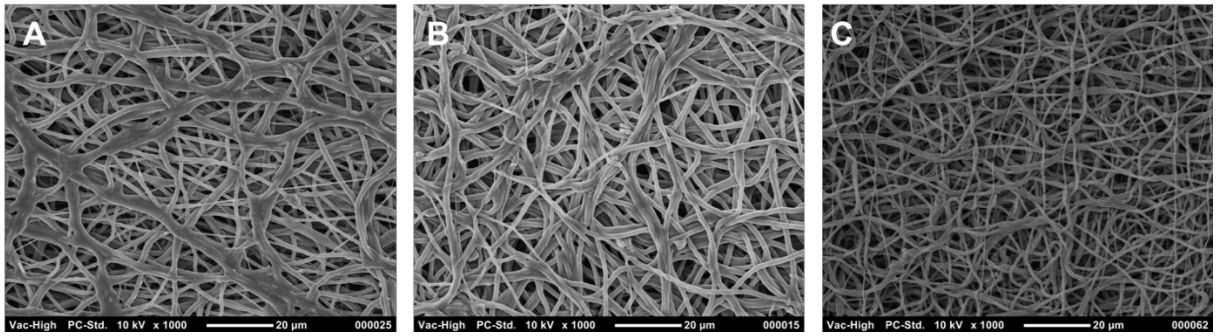

Figure B.8. SEM Images of PEO10 (A), PEO20 (B), and PEO30 (C) after extraction of the sol fraction by ultrasonication in methanol.

B.3.6 Equilibrium Swelling Behavior and Molecular Weight Between Crosslinks

The equilibrium swelling behavior of the crosslinked PEO was also determined by equilibrating the samples in room temperature water for more than 24 hours. After 24 hours, no weight change was observed with the samples over time, and the equilibrium swelling ratio was determined by weighing the wet nanofibers and comparing this to the dry weight using the following equation:

$$\text{Equilibrium Swelling Ratio} = \frac{w_{wet} - w_{dry}}{w_{dry}} \quad \textbf{(B.2)}$$

where w_{wet} is the weight of the swollen fibers and w_{dry} is the weight of the dry fibers. The equilibrium swelling ratio of the crosslinked PEO decreases with increasing amount of PETA, as shown in **Figure B.9**. This is likely due to the fact that increasing the crosslinker concentration increases the overall crosslink density and results in a greater restriction in the movement of the PEO polymer chains.[32] The amount of crystallinity may also play a role in the equilibrium swelling because crosslinked PEO swells less in water with increasing degree of crystallinity.[33] The crystallinity of the crosslinked PEO samples will be explored using differential scanning calorimetry in detail below.

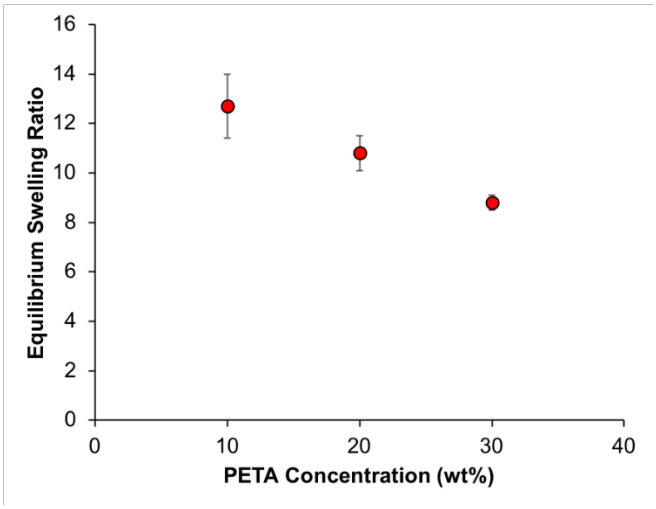

Figure B.9. Equilibrium swelling of PEO10, PEO20, and PEO30 in water.

By utilizing Flory-Rehner equilibrium swelling theory[34], the equilibrium swelling ratio may be utilized to estimate the molecular weight between crosslinks (M_c) using the following equation:

$$\frac{1}{M_c} = \frac{2}{M_n} - \frac{[\ln(1 - V_2) + V_2 + \chi {V_2}^2]}{V_1 \rho_1 ({V_2}^{\frac{1}{3}} - \frac{V_2}{2})} \quad \textbf{(B.3)}$$

where M_n is the number average molecular weight of the initial un-crosslinked polymer, V_1 is the molar volume of the solvent, ρ_1 is the initial density of the polymer, V_2 is the volume fraction of the polymer at equilibrium, and χ is the Flory-Huggins interaction parameter. Because Flory-Huggins theory assumes a random mixing of polymer and solvent, it is not appropriate to use a highly hydrogen-bonding solvent (e.g. water) for this analysis.[35] Thus, chloroform was chosen for swelling measurements to determine M_c because it is a good solvent for PEO and does not hydrogen bond.

The polymer volume fraction at equilibrium (V_2) may be determined using the following relation:

$$V_2 = \frac{\left(\frac{m_1}{\rho_1}\right)}{\left(\frac{m_1}{\rho_1}\right) + \left(\frac{m_2}{\rho_2}\right)} \quad \textbf{(B.4)}$$

where m_1 is the mass of dry polymer, m_2 is the mass of solvent in the swollen polymer, ρ_1 is the polymer density (1.21 g/cm^3), and ρ_2 is the solvent density (1.49 g/cm^3).[36] It is also important to note that the electrospun mats are highly porous, as shown in **Table B.2**. Thus, the amount of solvent swollen in the nanofibers themselves (m_2) must be determined by subtraction of the total weight of solvent with solvent within the open pores of the mats, determined using the porosity value. Furthermore, the interaction parameter (χ) must be calculated using the following equation:

$$\chi = \left(\frac{V_s}{RT}\right)\left(\delta_s - \delta_p\right)^2 + \beta \quad \textbf{(B.5)}$$

where V_s is the molar volume of the solvent, R is the universal gas constant, T is the temperature, δ_s is the solubility parameter of the solvent (9.3 cal$^{1/2}$/cm$^{3/2}$ for $CHCl_3$)[37], δ_p is the solubility parameter of the polymer (10.3 cal$^{1/2}$/cm$^{3/2}$ for PEO)[38], and β is the lattice constant (0.34). Thus, the calculated χ for the PEO-chloroform system is 0.475. Using the calculated χ and V_2, the M_c and thereby the crosslink density ($\rho_c = \rho_1/M_c$) was determined using **Equation B.3**, and the results are shown in **Table B.3**.

Table B.3. Equilibrium swelling (ES) ratio of crosslinked PEO nanofibers in chloroform and the calculated polymer volume fraction (V_2), molecular weight between crosslinks (M_c) and crosslink density (ρ_c). The ES ratio has been corrected for the porosity of the nanofiber mats.

Sample	ES Ratio	V_2	M_c (kg/mol)	ρ_c (mol/cm^3)
PEO10	4.2 ± 0.4	0.23 ± 0.02	7.6 ± 1.0	1.6 x 10^{-4}
PEO20	3.8 ± 0.2	0.25 ± 0.01	6.3 ± 0.8	2.0 x 10^{-4}
PEO30	2.6 ± 0.2	0.32 ± 0.02	2.9 ± 0.5	4.3 x 10^{-4}

Similar to the equilibrium swelling in water shown above, the ES ratio of the crosslinked PEO nanofibers shows decreased swelling in chloroform with increasing concentration of PETA. Again, this is an effect of the increase in crosslink density (ρ_c) that is associated with the increase in PETA content. As shown in **Table B.3**, the M_c value decreases slightly from 7.6 kg/mol for PEO10 to 6.3 kg/mol for PEO20 and then decreases significantly to 2.9 kg/mol for PEO30. Thereby, as expected, increasing the PETA concentration yields more dense crosslinking of the PEO nanofibers and further confirms the efficacy of PETA as both the photo-initiator and crosslinking agent for PEO. The effect of this crosslinking density on the thermal and mechanical properties of the electrospun, crosslinked PEO samples will be explored below.

B.3.7 DSC of Crosslinked PEO Nanofibers

To determine the influence of the electrospinning and crosslinking process on the thermal properties of PEO, DSC was performed. The DSC thermograms of the first heat of the as-spun nanofiber mats of PEO, PEO10, PEO20, and PEO30 are shown in **Figure B.10**. For the PEO reference, 8 wt% PEO in acetonitrile was electrospun with UV irradiation in the absence PETA, yielding an uncrosslinked comparison.

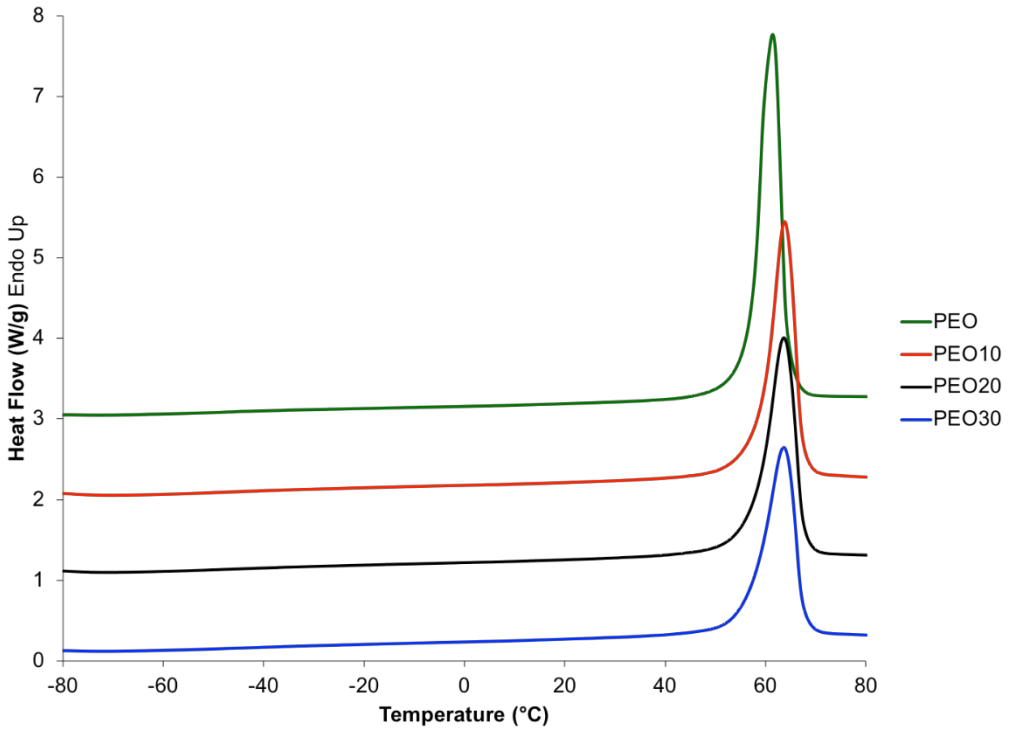

Figure B.10. DSC thermograms of the first heats of electrospun PEO, PEO10, PEO20, and PEO30.

For all samples, a broad glass transition temperature (T_g) is observed at approximately -50 ºC, and a large endotherm associated with the melting of PEO crystallites is observed at 63 ºC. These values are in agreement with the thermal properties of bulk PEO.[39-40] Little difference in the melting temperature is observed as the amount of PETA is increased, indicating that PETA incorporation has limited influence on PEO crystal size. The amplitude and area under the melting endotherm, however, decreases with increasing PETA content suggesting a loss of crystallinity. It is important to note, however, that by adding PETA to the samples, the total amount of PEO is reduced. Thus, the enthalpy of melting (ΔH_m) determined by integration of the melting endotherms must be corrected for the actual PEO content, as shown in **Table B.4**. Using these corrected ΔH_m values, the degree of crystallinity may also be calculated using $\Delta H_m/\Delta H_m^o$ where ΔH_m^o is the enthalpy of fusion of 100% crystalline PEO (197 J/g).[41-42] It is evident from **Table B.4** that

crosslinking PEO with PETA disrupts the crystallizability and reduces the crystallinity of the PEO. Crosslinking leads to a reduction in chain mobility and introduces defects into the crystallizable PEO backbone, causing this loss in crystallinity. Surprisingly, as the amount of PETA increases in the crosslinked PEO samples, the degree of crystallinity increases from 75 wt% for PEO10 to 79 wt% for PEO30. This is likely due to the crosslinking mechanism that occurs during the curing process. At low PETA incorporations (10 wt%), radical-radical couplings of PEO chains or PEO chains with PETA are the most probable crosslinking events. As the PETA content is increased, the abundance of unsaturated C=C bonds leads to a greater occurrence of PETA polymerization. This increase in the amount of PETA polymerization would lead to a smaller fraction of disrupted PEO segments, and thereby a greater fraction of crystallizable PEO.

Table B.4. DSC results of first heat of PEO, PEO10, PEO20, and PEO30 crosslinked, electrospun nanofibers.

Sample	T_{m1} (ºC)	ΔH_{m1} (J/g)	$\Delta H_{m1,\ corrected}$ (J/g)	X_c (wt%)
PEO	61	164	164	83
PEO10	64	132	147	75
PEO20	64	121	151	77
PEO30	64	109	156	79

To further elucidate the effect of crosslinking and PETA content, samples were crystallized from the melt. **Figure B.11** shows the DSC thermograms of a slow cool (10 ºC/min) of the PEO samples from the melt and the subsequent heat following this slow cool. The uncrosslinked PEO shows a large crystallization exotherm at 44 ºC during cooling and a subsequent large melting endotherm at 61 ºC during heating. Upon crosslinking with PETA, both the crystallization exotherms and melting endotherms decrease in size and become broader, indicating a loss of crystallinity and a larger range of crystal sizes. Furthermore, the melting temperatures are suppressed by a few degrees for PEO10, 20 and 30 when compared to the uncrosslinked PEO, suggesting a reduction in crystal size due to crosslinking.

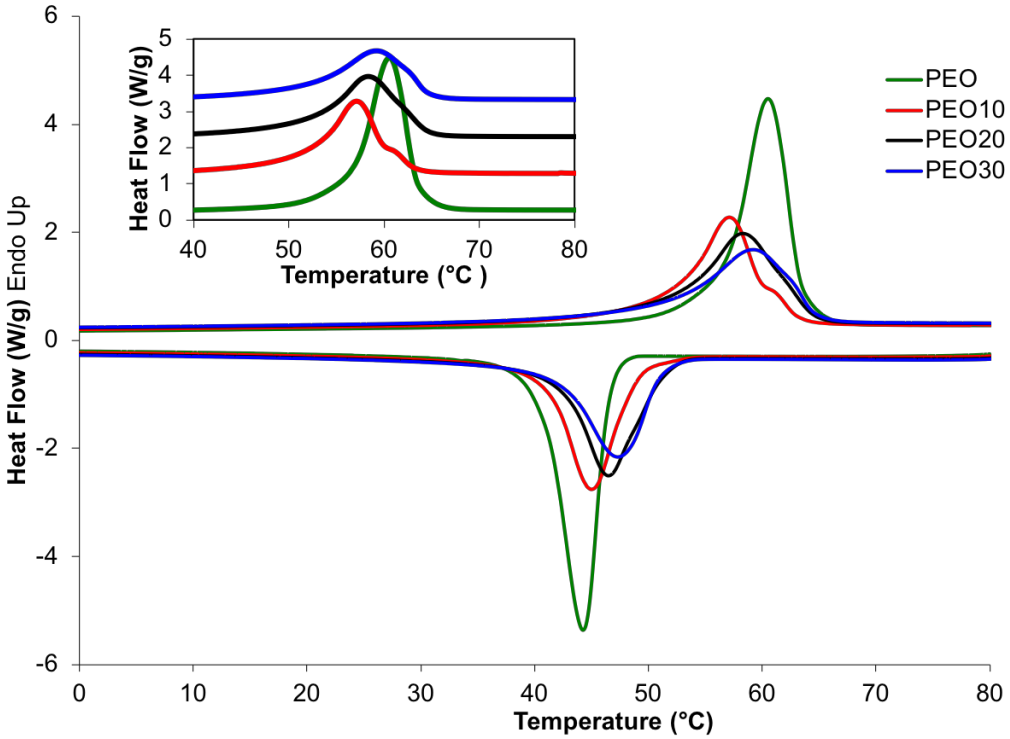

Figure B.11. Cooling of PEO, PEO10, PEO20, and PEO30 from the melt at 10 ºC/min and the subsequent heat.

It is interesting to note that, similar to the first heat, the corrected ΔH_m (and thus X_c) increases with increasing PETA content from 10 wt% to 30 wt%. Again, this is likely due to the mechanism of crosslinking permitting a greater fraction of PETA polymerization with higher concentrations of PETA, which allows for less disruption in the lengths of crystallizable PEO segments. A complete summary of the DSC results from the slow cool and the subsequent heat is shown in **Table B.5**.

Table B.5. DSC results of a slow cool from the melt and the subsequent heat PEO, PEO10, PEO20, and PEO30 crosslinked, electrospun nanofibers.

Sample	T_c (ºC)	ΔH_c	T_{m2} (ºC)	ΔH_{m2} (J/g)	$\Delta H_{m2,\ corrected}$ (J/g)	X_c (wt%)
PEO	44	136	61	143	143	73
PEO10	45	92	57	95	106	54
PEO20	47	94	58	91	114	58
PEO30	47	83	59	81	116	59

Dynamic mechanical analysis was also utilized to determine the thermal transitions of the crosslinked PEO samples. The storage modulus as a function of temperature for PEO10, PEO20, and PEO30 is shown in **Figure B.12**. Three distinct regimes appear in the DMA spectra for the crosslinked PEO. The first regime appears at low temperatures, where the PEO is in the glassy state and the storage modulus is plateaued. As the temperature is increased to approximately -30 ºC, the crosslinked PEO goes through the glass transition temperature as noted by the relaxation in the storage modulus. Finally, as the temperature increases to approximately 55 ºC, the PEO crystallites melt and yield a final plateau due to the chemically crosslinked nature of the nanofibers. These transitions are consistent with those of pure PEO itself and those observed using DSC (above).

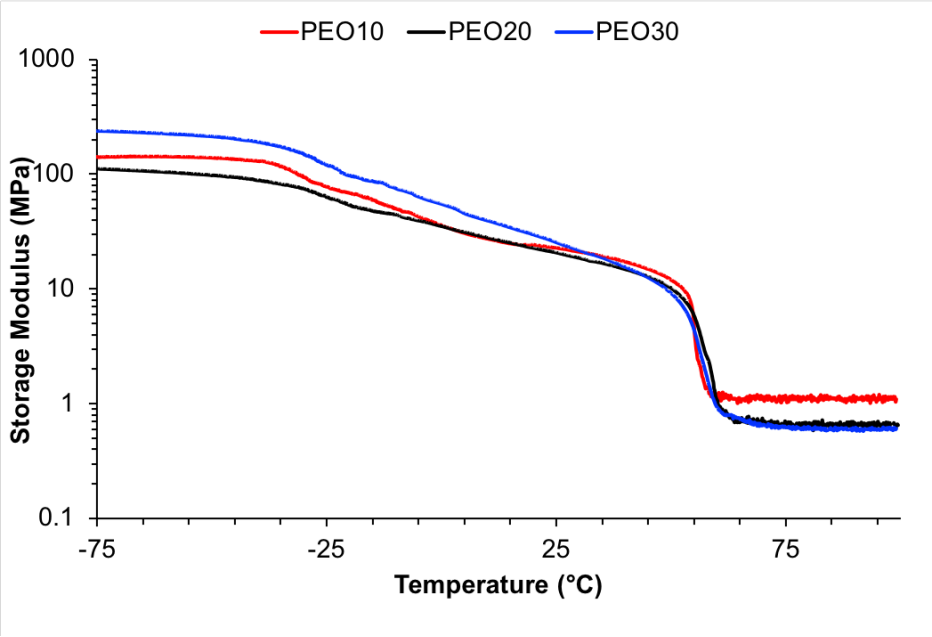

Figure B.12. DMA of PEO10, PEO20, and PEO30 crosslinked by *in-situ* UV irradiation.

B.3.8 Mechanical Properties of Crosslinked PEO Nanofibers

For use in soft tissue engineering, electrospun scaffolds must have suitable mechanical strength to support cellular growth and mimic the native tissue. Thus, the effect of PETA

concentration on the mechanical properties of the crosslinked PEO nanofibers was investigated using tensile testing. Analysis was performed on as-spun dry samples as well as wet samples that were equilibrated to their equilibrium swelling point in water, as shown in **Figure B.13**.

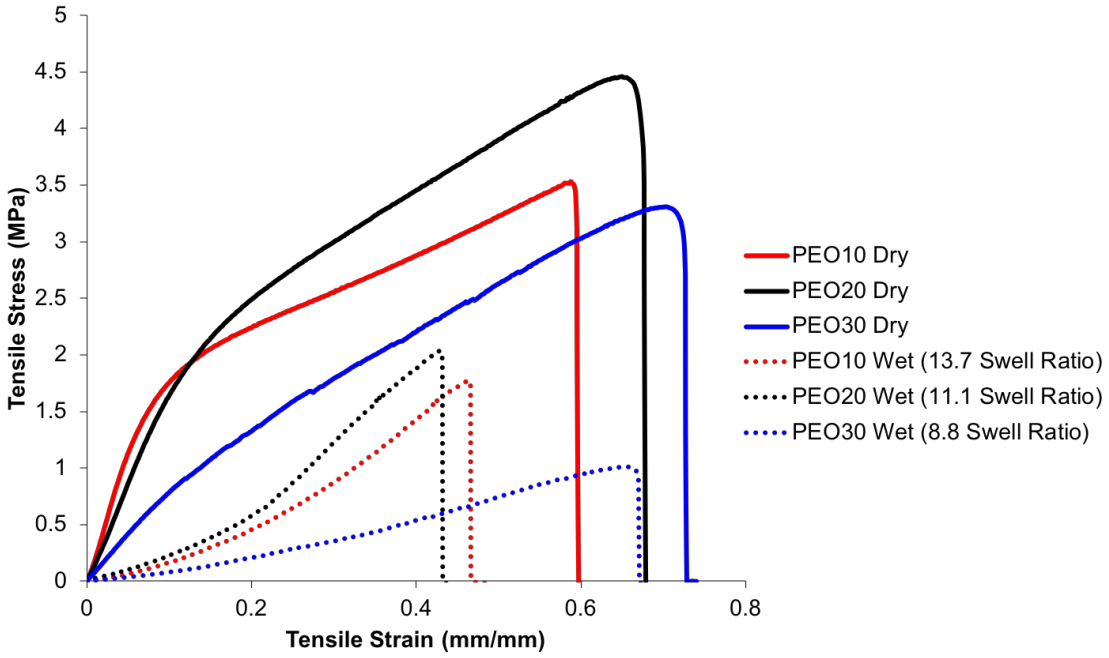

Figure B.13. Tensile stress vs. strain representative curves of PEO10 (red), PEO20 (black), and PEO30 (blue) in the dry (solid lines) and wet (dashed lines) state. The equilibrium swelling ratio is shown for the wet samples.

In general, the dry nanofiber mats displayed similar overall stress vs. strain curves, with profiles consistent with those of crosslinked polymers. Overall, there appears to be two distinct regimes: an initial region in which the nanofibers are not aligned and a region where the fibers begin to align and increase resistance (observed as a more rapid increase in stress with strain). Eventually, the fibers break at sufficient strain. Upon swelling the nanofiber mats, a significant decrease in Young's modulus and ultimate tensile strength as well as a decrease in strain at break are observed. This may be attributed to the absorbed water acting as a plasticizer for the polymer chains.[43-45] This lowers the glass transition temperature (T_g) of the polymer chains, reducing the

chain stiffness and leading to more flexible networks. A summary of the tensile properties of the dry and wet PEO10, PEO20, and PEO30 is shown in **Table B.6**.

Table B.6. Tensile properties of PEO10, PEO20, and PEO30 in the wet and dry state.

Sample	Young's Modulus (MPa)	Ultimate Tensile Strength (MPa)	Elongation at Break (%)
PEO10 dry	23 ± 2	3.9 ± 0.6	60 ± 8
PEO10 wet	1.3 ± 0.2	1.4 ± 0.4	52 ± 18
PEO20 dry	17 ± 3	3.8 ± 0.5	71 ± 22
PEO20 wet	1.6 ± 0.9	1.6 ± 0.4	50 ± 27
PEO30 dry	14 ± 5	3.1 ± 0.7	52 ± 25
PEO30 wet	0.7 ± 0.3	1.3 ± 0.2	67 ± 13

The calculated Young's modulus, ultimate tensile strength, and elongation at break are within error for the PEO10, PEO20, and PEO30. Thus, the amount of PETA does not appear to have a significant impact on the overall mechanical properties of the PEO nanofiber mats. This is likely due to the balance of the nanofiber morphology, the chemical crosslinking of the PEO by PETA, and the physical crosslinking of the PEO by polymer crystallites. The crosslinking process, however, does increase the modulus, decrease ultimate tensile strength, and decrease elongation at break from that of uncrosslinked electrospun PEO/PETA nanofibers due to restriction of the PEO polymer chains upon formation of the chemical network. It is also of use to compare the tensile properties of the crosslinked PEO nanofibers to the mechanical properties of skin to determine the efficacy of the nanofiber mats for tissue scaffolding. The ultimate tensile strength and the ultimate tensile strain of skin are in the ranges of 1-20 MPa and 30-70 %, respectively.[46] Thus, the mechanical properties of all crosslinked PEO samples fall within the range of normal skin and are comparable to other electrospun scaffolds proposed for wound dressing.[47]

It is widely recognized that the most tissues and extracellular matrix components behave as viscoelastic materials, allowing the storage and dissipation of energy and allowing for creep and stress relaxation.[48] In fact, stress relaxation has been found to play a key role in cell spreading and

proliferation, with stem cells differentiating and growing more quickly on hydrogels that relax moer quickly.[49] Thus, stress relaxation experiments were performed using the DMA to determine the relaxation behavior of the crosslinked PEO nanofibers. Stress relaxation experiments were performed at 70 ºC to melt all PEO crystallites and thereby investigate the influence of PETA concentration on the behavior of crosslinked PEO. Samples were subjected to 10% strain for a set period of time, and the stress vs. time and normalized stress vs. time graphs are shown in **Figure B.14**. When the samples are subjected to the strain, there is an instantaneous increase in stress to σ_o (initial stress). The σ_o value increases with increasing PETA concentration, suggesting that the increase in crosslink density leads to a greater restriction in polymer chain mobility and thereby a greater stress upon the introduction of strain. Over time, the polymer chains rearrange to accommodate the strain, and thus the stress decreases to a plateau due to the crosslinked nature of the PEO.

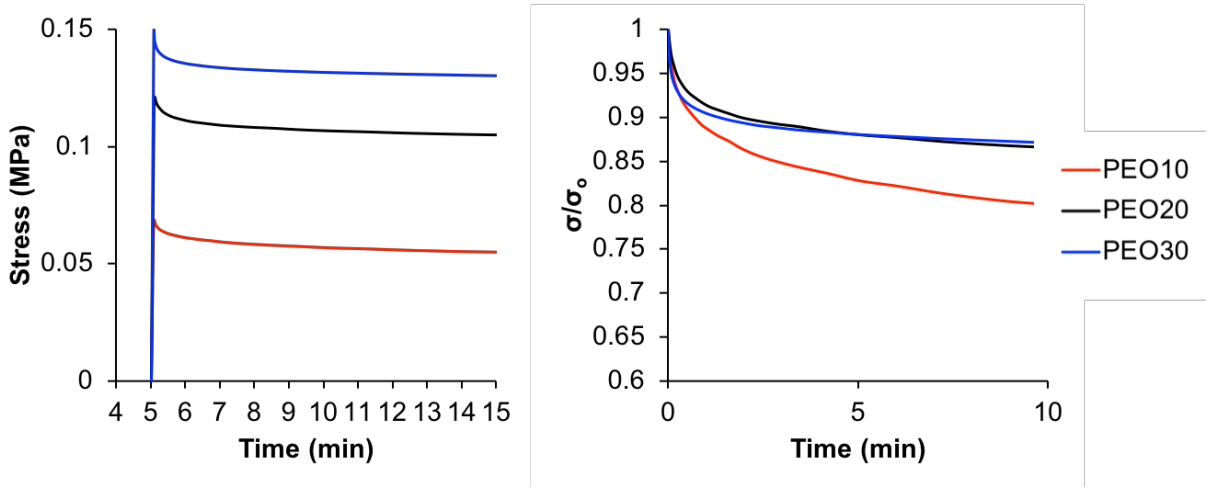

Figure B.14. Stress relaxation of PEO10, PEO20, and PEO30 nanofiber mats at 70 ºC and 10% strain. The stress as a function of time is shown on the left, and the stress normalized to the initial stress is shown on the right.

When normalized to the initial stress, PEO10 appears to relax more quickly and to a higher degree (larger decrease in stress) than PEO20 and PEO30, whose curves are nearly

superimposable. The degree of relaxation was determined as the percent change in the normalized stress from the initial onset of strain to the plateau stress at approximately 10 minutes, as shown in **Figure B.15**. For PEO10, 20 % relaxation is observed and this value increases to 23 % for PEO20 and PEO30. This is likely due to an increase in crosslinking density which restricts PEO chain mobility and limits the ability of the PEO chains to rearrange and dissipate stress.[50]

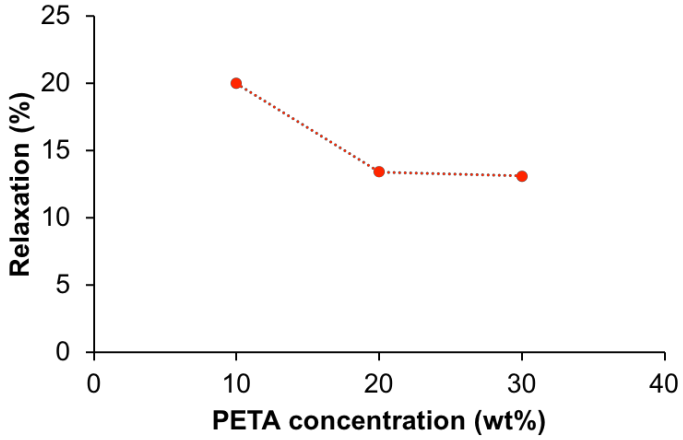

Figure B.15. Stress relaxation percentage of PEO10, PEO20, and PEO30 nanofiber mats.

B.4 Influence of UV Cure Time on Nanofiber Properties

Analysis of crosslinked electrospun PEO samples thus far has focused on the effect of PETA concentration on the properties of the nanofiber mats prepared with uninterrupted UV exposure during electrospinning. It is also important to investigate the effect of UV exposure time to determine if UV curing time can easily tune nanofiber properties. Thus, PEO20 nanofiber mats were prepared in which the UV irradiation time was varied during electrospinning by performing various off-on cycles of the UV lamp. For example, the UV lamp was turned off for a set period of time and then on for a set period of time in a cyclic manner until all of the electrospinning solution was used. The off-on cycles examined in this work (in minutes) were 10-10, 15-15, 20-20, 20-10, and 10-20.

To determine the PETA incorporation with UV cure time, FTIR analysis was performed similar to **Section B.3.4** . The ratio of the areas of the peaks at 1730 cm^{-1} and 1340 cm^{-1} was determined and used to calculate the PETA concentration with the equation A_{1730}/A_{1340} = 0.1605[PETA]. The results of this analysis are displayed in **Table B.7**. For the as-spun samples, the PETA concentration determined matched that of the electrospinning solution itself – 20 wt%, as expected. The PEO20 samples were then washed by 1-hour ultrasonication in acetonitrile to remove any uncrosslinked material. The FTIR analysis was also performed on the washed samples, and UV cure time was found to have a substantial influence on the amount of PETA covalently incorporated into the PEO nanofibers. As the UV exposure 'on' segments increased in time during the off-on cycles from 10-10 to 15-15 and then to 20-20 min, the PETA concentration determined increased from 3.6 wt% to 5.5 wt% and then to 10.7 wt%. Thus, longer uninterrupted UV exposure times were necessary to allow for considerable crosslinking of the nanofibers. Even at the off-on ratio of 20-20 min, however, only half of the available PETA has crosslinked with the PEO. To obtain a value close to the initial concentration of PETA in the electrospinning solution (and thereby full covalent incorporation of the PETA), the UV lamp must be turned on throughout the duration of electrospinning or for short 'off' times and long 'on' times during cyclic UV exposure (e.g. 10-20 min).

Table B.7. Determination of PETA content of PEO20 nanofiber mats with various timed UV cycles.

	UV Off-On (min)	A_{1730}/A_{1340}	PETA Conc. (wt %)
As-Spun	0-Always	2.6 ± 0.5	16.5 ± 3.2
	10-10	3.2 ± 0.1	20.0 ± 0.9
	20-20	3.2 ± 1.0	19.9 ± 6.6
	15-15	3.4 ± 0.9	21.3 ± 5.7
	20-10	2.7 ± 0.2	16.9 ± 1.1
	10-20	4.3 ± 0.9	26.8 ± 5.5
Washed	0-Always	2.8 ± 0.3	17.2 ± 1.7
	10-10	0.6 ± 0.3	3.6 ± 1.7
	20-20	1.7 ± 0.8	10.7 ± 5.1
	15-15	0.9 ± 0.4	5.5 ± 2.6
	20-10	1.4 ± 0.6	8.4 ± 3.4
	10-20	4.1 ± 0.3	25.7 ± 1.9

The morphology of the washed PEO20 samples with various cyclic UV times was investigated using SEM. Prior to washing, the samples exhibited a typical nanofibrous morphology similar to those observed in **Figure B.7**. The SEM images of washed PEO20 cured with nonstop UV exposure and with 10-10 min (off-on) cyclic UV exposure is shown in **Figure B.16**. With the UV lamp always turned on during electrospinning, the PEO20 nanofibers are crosslinked to a high enough degree to maintain their nanofibrous morphology after swelling with solvent. In direct contrast, the PEO20 nanofibers prepared with the UV off-on cycle of 10-10 minutes completely lost the nanofibrous architecture upon solvent exposure. Swelling in solvent lead to a significant degree of fiber melding, whereby the washed PEO20 appears more like a polymer film following solvent exposure. A similar result of fiber melding was observed in all PEO20 samples for which the UV 'on' segment was less than 20 minutes. This morphological analysis further confirmed that long, uninterrupted UV cure times are necessary to provide suitable crosslinking of the samples and to stabilize the nanofibrous morphology.

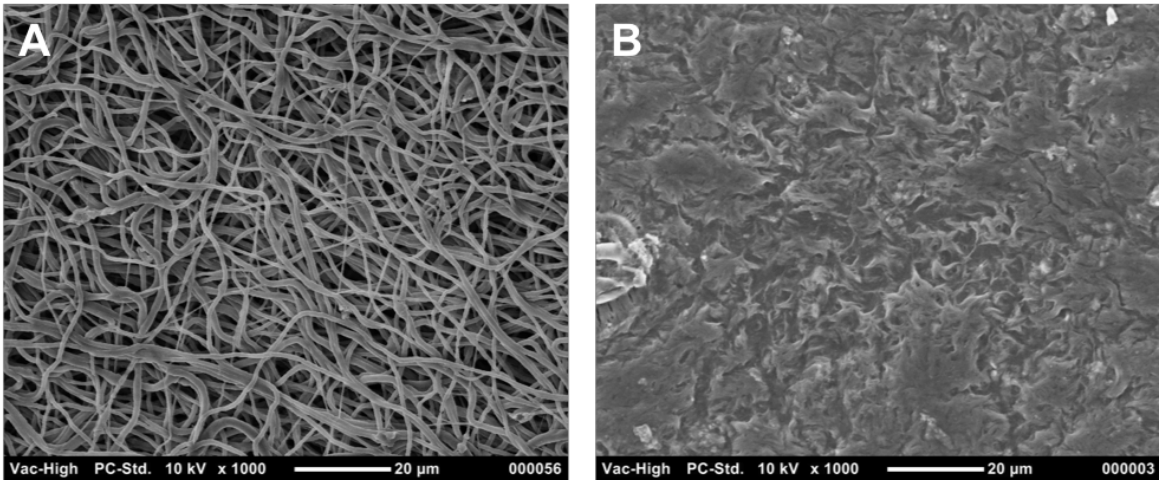

Figure B.16. SEM images of PEO20 cured with the UV lamp always on (A) and cured with the UV lamp 10 minutes on/10 minutes off (B).

To further determine the influence of UV exposure time on the crosslinked PEO20 nanofiber properties, the gel fraction and porosity values were determined using the methods described above. The results of this analysis are shown in **Figure B.17**. The UV exposure time plotted was determined as the total 'on' time of the UV lamp throughout the electrospinning process. With increasing UV cure time, the PEO 20 samples exhibited both a higher gel fraction as well as a higher porosity due to an increase in the degree of crosslinking with UV cure time. The gel fraction increased remarkably from 84 wt% at 60 minutes of UV to 96% wt% at 120 minutes of UV time. The porosity increased from 93 vol% to 97 vol% at those time points, respectively. Thus, with longer UV exposure, the PEO20 nanofibers exhibit a higher level of crosslinking and thus a more porous, stable nanofibrous structure in agreement with the above SEM analysis.

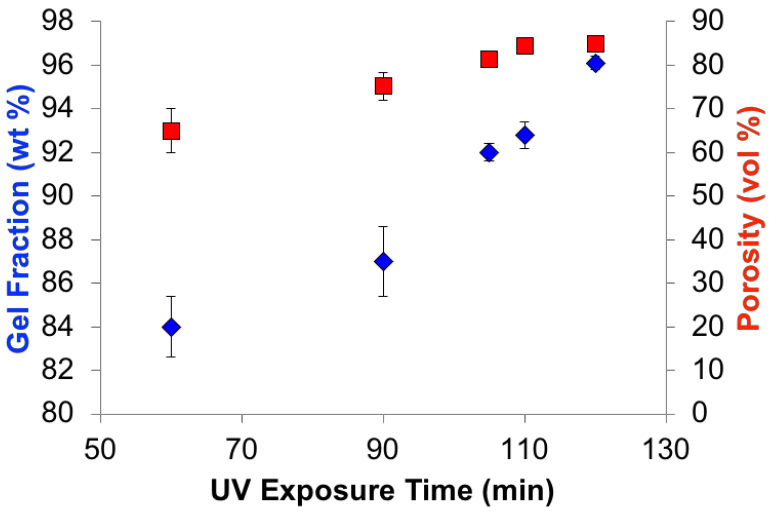

Figure B.17. Gel fraction (blue) and porosity (red) with increasing UV exposure time for PEO20.

B.4.1 Tensile Properties with Varying UV Cure Time

Clearly, the degree of crosslinking with PETA is influenced by the overall UV cure time. Thus, the UV cure time may also be used to tailor the mechanical properties of the nanofiber mats. Tensile testing of the PEO20 nanofiber mats cured for different off-on time cycles was carried out and the resultant stress vs. strain curves of the dry, as-spun mats is shown in **Figure B.18**.

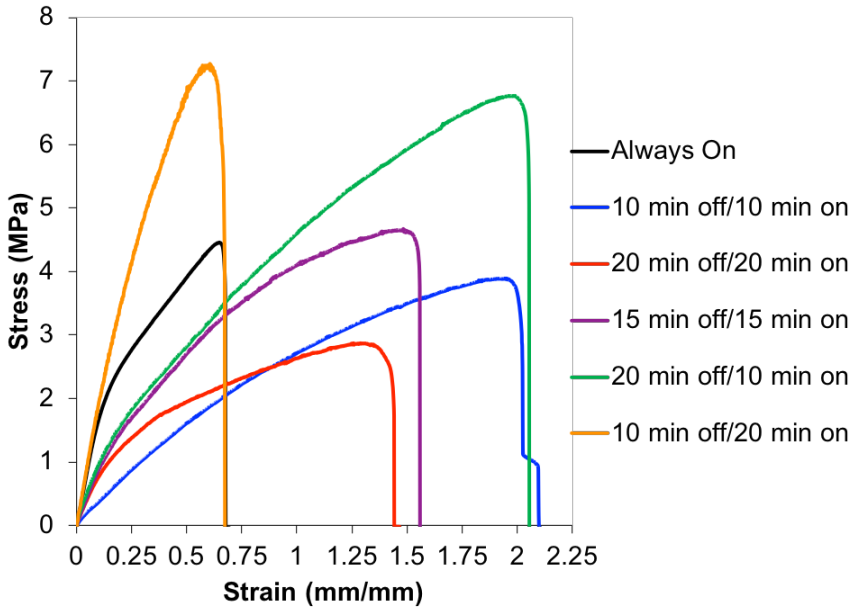

Figure B.18. Stress vs. strain representative curves of dry as-spun PEO20 with various UV cure times/cycles.

In general, with longer UV exposure time (i.e. always on or 10-20 min off-on) the representative curves appear to have a greater modulus and shorter strain at break. Samples with significant periods of UV 'off' time (≥ 1/2 of the total time) show a significantly greater strain at break, approximately twice that of the aforementioned samples. Thus, when the UV lamp is left on for at least 2/3 of the time, the high degree of crosslinking that is achieved is achieved results in a greater restriction of polymer chain mobility, increasing sample stiffness and making them more brittle (i.e. shorter elongation at break). These results were further confirmed by quantifying the modulus, tensile strength and break, and elongation at break, as shown in **Table B.8**. Comparable moduli and elongation at break were achieved for PEO20 with the UV lamp always on and on 2/3 of the time due to their similar level of PETA incorporation (see **Table B.7**). With decreasing PETA content and thereby smaller crosslink density, the modulus decreases and the elongation at break increases accordingly. Thus, the mechanical properties are readily tuned by variation in the UV cure time. Consideration of fiber morphology upon solvent exposure in

addition to the change in mechanical properties may be used to tune nanofiber properties for skin replacement scaffolds.

Table B.8. Tensile data of PEO20 samples with various UV cure times/cycles.

Sample	Modulus (MPa)	Strength at Break (MPa)	Elongation at Break (%)
Always On	17 ± 3	3.8 ± 0.5	71 ± 22
10 min off/10 min on	5 ± 2	4.0 ± 1.0	207 ± 17
20 min off/20 min on	8 ± 2	3.0 ± 0.4	146 ± 39
15 min off/15 min on	8 ± 2	4.0 ± 1.0	149 ± 11
20 min off/10 min on	10 ± 3	6.0 ± 2.0	181 ± 50
10 min off/20 min on	20 ± 3	7.0 ± 3.0	83 ± 28

It is important to note that the application of the crosslinked PEO nanofibers as porous tissue scaffolds will require the materials to be hydrated. Consequently, the mechanical properties of the nanofibers in the wet state must be examined to determine the efficacy of the scaffolds to mimic the native tissue and withstand environmental stressors. The stress vs. strain curves of PEO20 samples cured for various off-on UV exposure times determined at their equilibrium swelling state in water is displayed in **Figure B.19**. It is apparent that when the UV lamp is turned off for any time period during the electrospinning process, the wet PEO20 samples exhibit a low modulus, small stress at break, and long elongation at break when compared to PEO20 with the UV lamp always on. No noteworthy difference is observed among the PEO20 nanofibers with intermittent UV exposure. The greater swelling of these PEO20 samples in water compared to PEO20 with nonstop UV leads to a high level of plasticization among the samples. Furthermore, this analysis was performed on as-cast nanofibers without removing the sol-fraction. Thus, the uncrosslinked PETA that is present may be acting as an additional plasticizer in the system, resulting in this enhancement of polymer flexibility.[51] Coupled with the morphological analysis, it

was determined that constant UV exposure throughout electrospinning is necessary to provide a stable nanofibrous morphology, high porosity, and suitable mechanical properties.

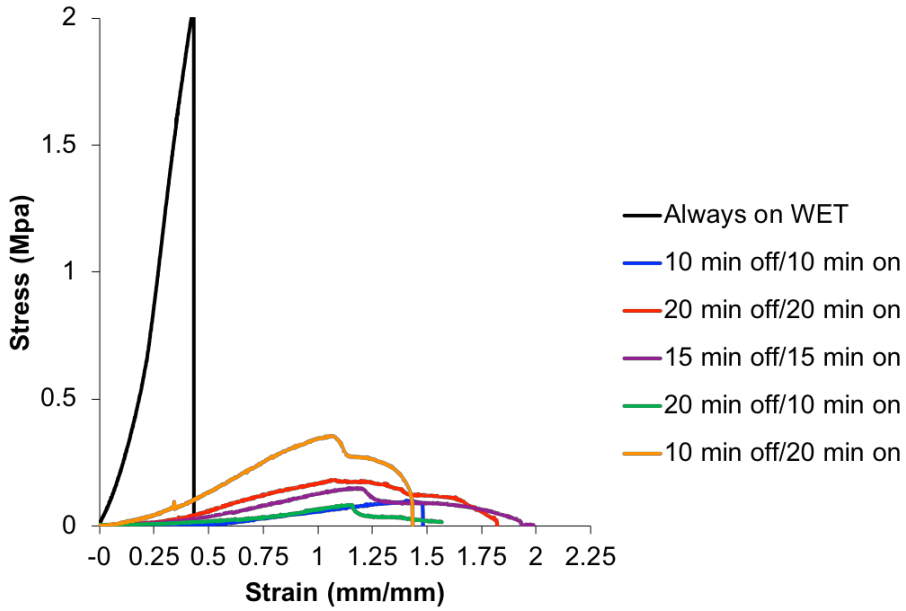

Figure B.19. Stress vs. strain representative curves of wet PEO20 with various UV cure times/cycles.

B.5 Properties of Crosslinked Electrospun PEO Over Time

Because the mechanical properties of crosslinked electrospun PEO scaffolds are tailored with PETA concentration to mimic the native tissue (e.g. skin) that it desires to replace, storage of prepared scaffolds over time must not alter the physical properties. Once implanted as a tissue scaffold, however, it is desirable for the nanofiber mat to degrade and provide space for cells to impregnate the scaffold and grow. Thus, the environment should play a key role in the mechanical integrity of the materials. To determine the influence of environmental factors on nanofiber tensile properties, electrospun crosslinked PEO20 samples were prepared with *in-situ* UV curing and stored in several locations: on the benchtop, on the benchtop in the dark, and in a desiccator under vacuum. Tensile properties of the crosslinked electrospun PEO20 were determined the day after

electrospinning and for up to 57 days after electrospinning. The representative stress vs. strain curves of the PEO20 nanofibers over time at the various storage conditions is displayed in **Figure B.20**. It is apparent that storage conditions where the nanofibers have direct contact with air (i.e. on the benchtop) leads to a loss in tensile strength at break and elongation at break for the PEO20 samples. Of the samples stored in air, the PEO20 nanofibers stored in the dark appeared to have a slower loss in mechanical properties over time than those stored on the benchtop. The PEO20 sample stored under vacuum, however, did not show any reduction in tensile properties with time. Thus, contact with oxygen from the air likely plays a key role in the degradation of PEO20 nanofibers, and exposure to any ambient UV rays accelerates this degradation. Oxygen from the air can react with radicals remaining or newly formed on the PEO20, potentially leading to degradation of the PEO polymer chains by chain scission or further crosslinking of the PEO20. With both scenarios, a decrease in mechanical properties would be expected.

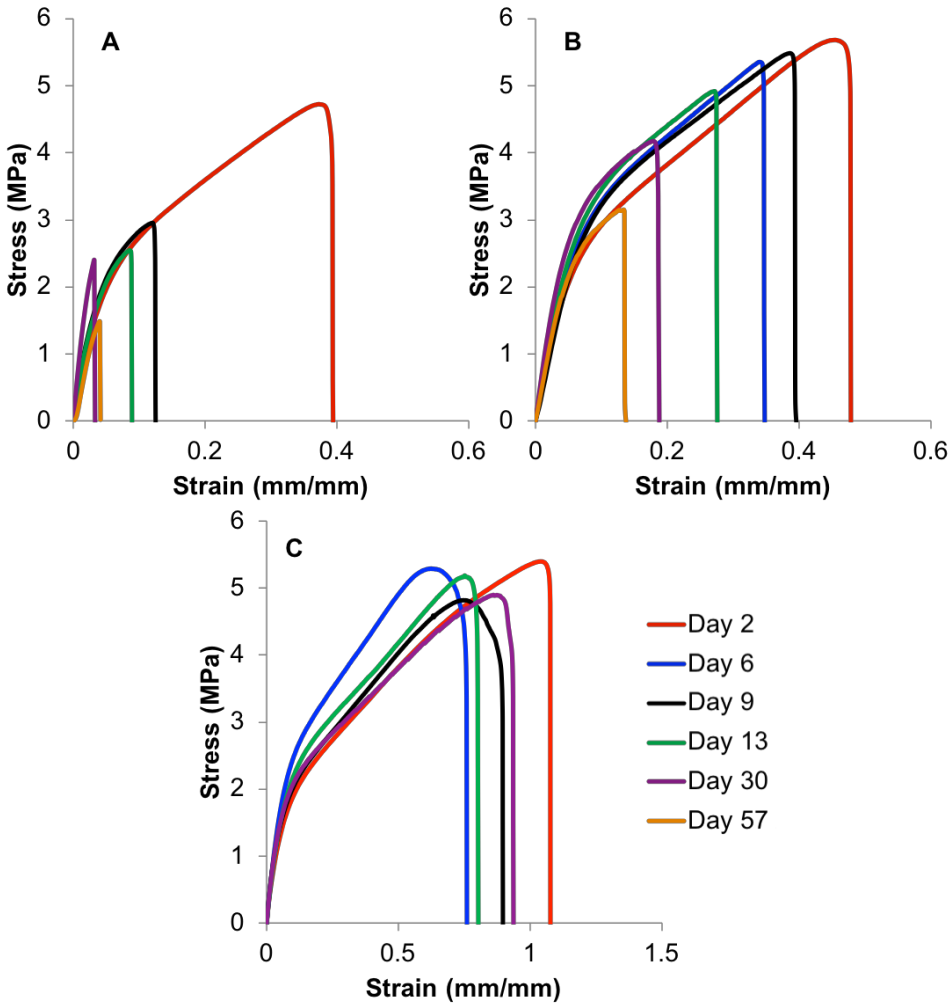

Figure B.20. Tensile properties of PEO20 mats stored over time on the benchtop (A), on the benchtop in the dark (B), and in a desiccator with vacuum (C).

To further elucidate the loss of mechanical properties of PEO20 over time, pure PEO was electrospun and stored on the bench or in a desiccator under vacuum for comparison. In these samples, reactions with PETA will have no influence on any change in mechanical properties over time. The stress vs. strain curves of electrospun PEO stored on the benchtop and in a desiccator under vacuum are shown in **Figure B.21**. Similar to the PEO20 samples, PEO exhibits a loss in tensile strength at break and strain at break over time when exposed to air and no loss of mechanical

properties when stored under vacuum. Thus, oxygen is likely facilitating the degradation of the PEO over time.

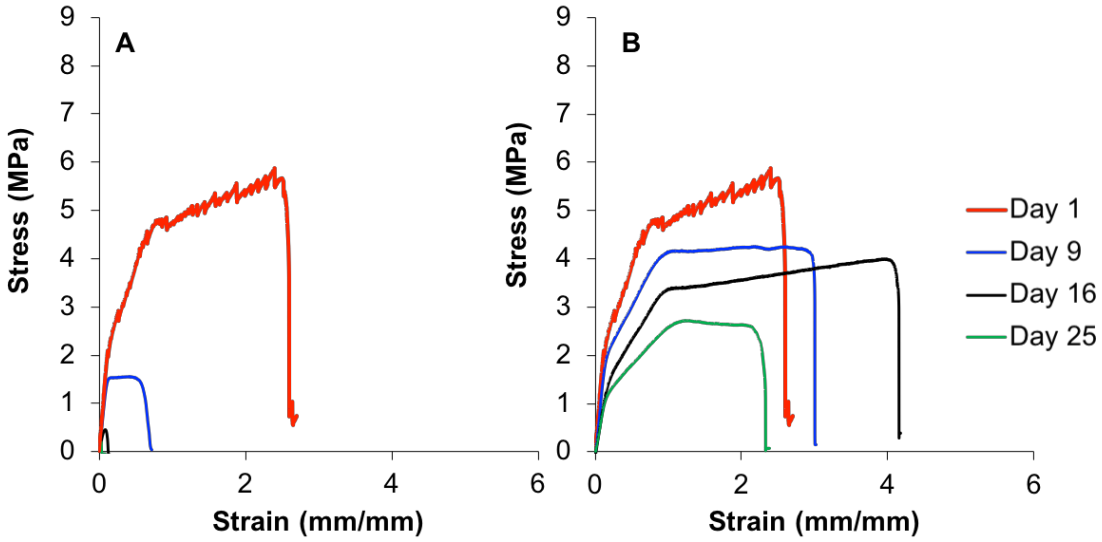

Figure B.21. Stress vs. strain curves of electrospun PEO stored on the benchtop (A) and in the desiccator under vacuum (B).

Oxidative degradation of PEO occurs by oxygen from the air reacting with radicals formed during hydrogen abstraction on the PEO backbone to form secondary hydroperoxides, ultimately leading to the formation of formates, aldehydes, and esters in addition to further radical species.[52] The formation of these species may be monitored using FTIR by examining the evolution of carbonyl bands around 1720 cm^{-1} that will appear with the formation of formates, aldehydes, and esters.[53] To determine if any oxidative degradation is occurring in the electrospun PEO and PEO20 samples, FTIR was performed at various time points for samples stored on the benchtop, as displayed in **Figure B.22**. Little difference is observed in the FTIR spectra over time for both PEO and PEO20. The carbonyl peak of the PEO20 samples becomes slightly broader with time, possibly suggesting the presence of new carbonyl species due to oxidative degradation of PEO. The PEO, however, does not show any significant carbonyl peak appear. Furthermore, the PEO20

shows a slight decrease in the peak at 1410 cm^{-1} (C-H of acrylic $RC=CH_2$) suggesting that reactions of the PETA acrylate are occurring during storage, potentially resulting in a greater crosslinking density of the PEO20.

For comparison, thin films of PEO (0.003 mm thick) were prepared and irradiated with UV light for up to 1 hour. At short irradiation times (<30 minutes) no evidence of a carbonyl peak is observed in the FTIR spectra. Above 30 minutes of UV exposure, a noticeable carbonyl peak appears at 1720 cm^{-1} that grows in intensity with increased time, providing evidence of the degradation products described above. It is important to note as well that UV exposure, even at very low times (i.e. 10-20 minutes), caused the PEO films to become much more brittle, suggesting a loss in mechanical integrity even with no observable FTIR evidence of degradation. Thus, to detect the degradation products in the FTIR spectra, a high level of degradation must occur. When compared to the films, the high surface area of the PEO and PEO20 nanofibers leads to a greater interaction with oxygen from the air, and thus oxidative degradation is likely occurring and causing the loss in mechanical properties, however, it is not to a significant enough degree to observe in the FTIR.

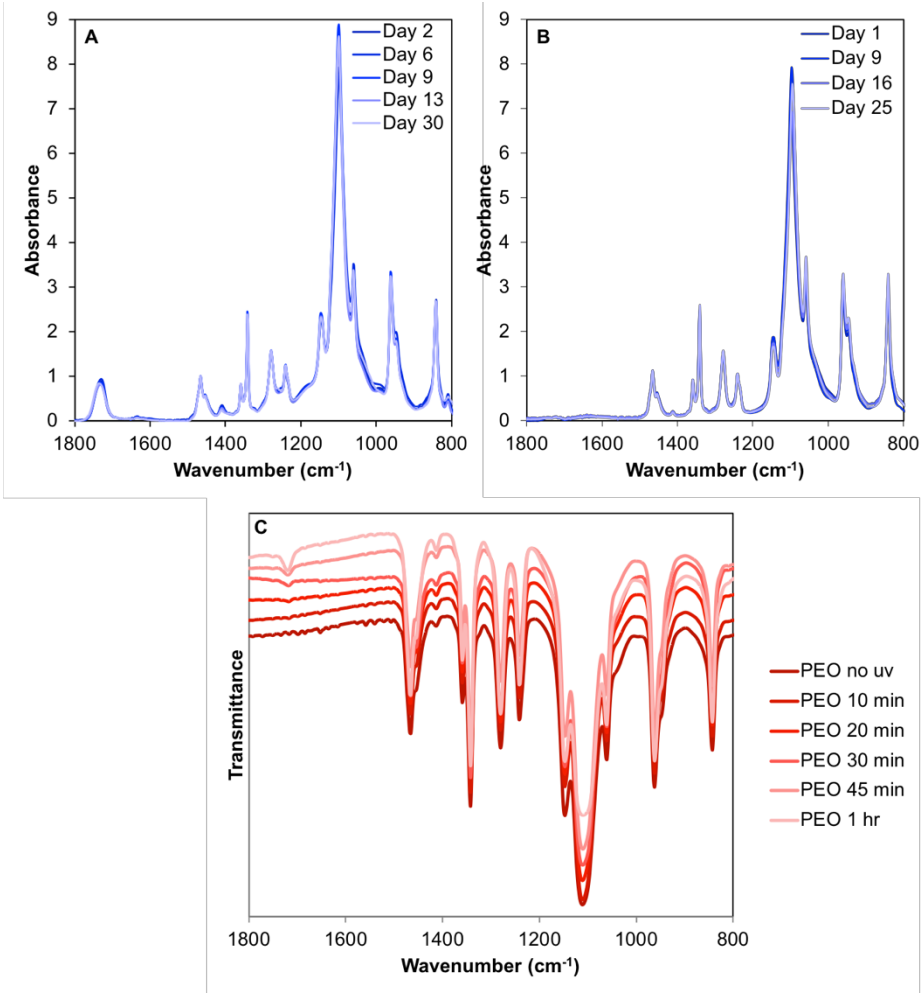

Figure B.22. FTIR spectra of electrospun PEO20 (A) and PEO (B) stored on the benchtop over time. Thin films of PEO (C) with various times of UV exposure is also shown.

Overall, from this analysis it is evident that when stored under vacuum, crosslinked PEO20 nanofibers are able to maintain their mechanical properties over time. This provides a means of storing the PEO20 nanofibers until their immediate use as a tissue scaffold. Furthermore, the loss in mechanical properties over time once exposed to air will be advantageous when the nanofiber mat is applied for use as a tissue scaffold or wound dressing. At first, the nanofibers will provide the support necessary for the initial cells to be seeded onto the surface and infiltrate through the pores of the scaffold. Then, the degradation of the nanofibers over time will allow for the further growth of the cells over time to eventually take over the entire volume covered by the scaffold.

B.6 Conclusions

In this study, a novel *in-situ* crosslinking method was developed to prepare crosslinked, electrospun PEO nanofibers with tunable properties. Curing PEO with pentaerythritol triacrylate (PETA) during electrospinning resulted in insoluble, nanofibrous scaffolds with reproducible fiber morphologies. SEM revealed that the nanofiber size was independent of PETA concentration, and may be tuned by varying the PEO concentration in solution. It was determined that constant UV exposure throughout electrospinning was necessary to fully crosslink PEO with PETA and maintain the nanofibrous architecture upon solvent exposure. With increasing PETA incorporation, a greater gel fraction, higher porosity, and decreased equilibrium swelling were observed for the nanofibers due to a greater crosslinking density.

Crosslinking of the electrospun PEO resulted in decreased crystallinity due to the disruption of crystallizable PEO segments and restriction in PEO chain mobility by the covalent crosslinks. The tensile properties demonstrated suitable tensile strength and strain at break to function as a skin replacement, and DMA experiments confirmed the efficacy of the nanofibers in dissipating stress. Tensile properties of PEO20 over time demonstrated a decrease in tensile strength and strain at break with exposure to air, suggesting oxidative degradation and further crosslinking leads to a loss in mechanical properties.

Overall, this study demonstrated a facile method of preparing crosslinked PEO scaffolds with high surface area and good mechanical strength for soft tissue engineering. Because PEO is generally considered bioinert, future work will focus on the modification of the nanofiber surfaces to promote cellular adhesion and growth.

B.7 References

1. Reneker, D. H.; Yarin, A. L.; Zussman, E.; Xu, H., Electrospinning of Nanofibers from Polymer Solutions and Melts. In *Advances in Applied Mechanics*, Aref, H.; van der Giessen, E., Eds. Elsevier: 2007; Vol. 41, pp 43-346.
2. Bhardwaj, N.; Kundu, S. C., Electrospinning: A fascinating fiber fabrication technique. *Biotechnology Advances* **2010,** *28* (3), 325-347.
3. Motamedi, A. S.; Mirzadeh, H.; Hajiesmaeilbaigi, F.; Bagheri-Khoulenjani, S.; Shokrgozar, M., Effect of electrospinning parameters on morphological properties of PVDF nanofibrous scaffolds. *Progress in Biomaterials* **2017,** *6* (3), 113-123.
4. Sundarrajan, S.; Tan, K. L.; Lim, S. H.; Ramakrishna, S., Electrospun Nanofibers for Air Filtration Applications. *Procedia Engineering* **2014,** *75*, 159-163.
5. Lackowski, M.; Krupa, A.; Jaworek, A. In *Nonwoven filtration mat production by electrospinning method*, Journal of Physics: Conference Series, IOP Publishing: 2011; p 012013.
6. Jung, J.-W.; Lee, C.-L.; Yu, S.; Kim, I.-D., Electrospun nanofibers as a platform for advanced secondary batteries: a comprehensive review. *Journal of Materials Chemistry A* **2016,** *4* (3), 703-750.
7. Jiang, S.; Chen, Y.; Duan, G.; Mei, C.; Greiner, A.; Agarwal, S., Electrospun nanofiber reinforced composites: a review. *Polymer Chemistry* **2018,** *9* (20), 2685-2720.
8. Lagaron, J. M.; Solouk, A.; Castro, S.; Echegoyen, Y., 3 - Biomedical applications of electrospinning, innovations, and products. In *Electrospun Materials for Tissue Engineering and Biomedical Applications*, Uyar, T.; Kny, E., Eds. Woodhead Publishing: 2017; pp 57-72.
9. Pham, Q. P.; Sharma, U.; Mikos, D. A. G., Electrospinning of Polymeric Nanofibers for Tissue Engineering Applications: A Review. *Tissue Engineering* **2006,** *12* (5), 1197-1211.
10. Sundararaghavan, H. G.; Metter, R. B.; Burdick, J. A., Electrospun Fibrous Scaffolds with Multi-scale and Photopatterned Porosity. *Macromolecular bioscience* **2010,** *10* (3), 265-270.
11. Wu, J.; Hong, Y., Enhancing cell infiltration of electrospun fibrous scaffolds in tissue regeneration. *Bioactive Materials* **2016,** *1* (1), 56-64.
12. Yoshimoto, H.; Shin, Y. M.; Terai, H.; Vacanti, J. P., A biodegradable nanofiber scaffold by electrospinning and its potential for bone tissue engineering. *Biomaterials* **2003,** *24* (12), 2077-2082.
13. Zhu, J., Bioactive modification of poly(ethylene glycol) hydrogels for tissue engineering. *Biomaterials* **2010,** *31* (17), 4639-4656.
14. Ma, L.; Deng, L.; Chen, J., Applications of poly(ethylene oxide) in controlled release tablet systems: a review. *Drug Development and Industrial Pharmacy* **2014,** *40* (7), 845-851.
15. Hamid, Z. A. A.; Lim, K. W., Evaluation of UV-crosslinked Poly(ethylene glycol) Diacrylate/Poly(dimethylsiloxane) Dimethacrylate Hydrogel: Properties for Tissue Engineering Application. *Procedia Chemistry* **2016,** *19*, 410-418.
16. Koupaei, N.; Karkhaneh, A.; Daliri Joupari, M., Preparation and characterization of (PCL-crosslinked-PEG)/hydroxyapatite as bone tissue engineering scaffolds. *Journal of Biomedical Materials Research Part A* **2015,** *103* (12), 3919-3926.
17. Haider, A.; Haider, S.; Kang, I.-K., A comprehensive review summarizing the effect of electrospinning parameters and potential applications of nanofibers in biomedical and biotechnology. *Arabian Journal of Chemistry* **2015**.
18. Deitzel, J. M.; Kleinmeyer, J.; Harris, D.; Beck Tan, N. C., The effect of processing variables on the morphology of electrospun nanofibers and textiles. *Polymer* **2001,** *42* (1), 261-272.

19. Pillay, V.; Dott, C.; Choonara, Y. E.; Tyagi, C.; Tomar, L.; Kumar, P.; du Toit, L. C.; Ndesendo, V. M. K., A Review of the Effect of Processing Variables on the Fabrication of Electrospun Nanofibers for Drug Delivery Applications. *Journal of Nanomaterials* **2013,** *2013*, 22.
20. Eda, G.; Shivkumar, S., Bead-to-fiber transition in electrospun polystyrene. *Journal of Applied Polymer Science* **2007,** *106* (1), 475-487.
21. Fong, H.; Chun, I.; Reneker, D. H., Beaded nanofibers formed during electrospinning. *Polymer* **1999,** *40* (16), 4585-4592.
22. Li, Z.; Wang, C., Effects of Working Parameters on Electrospinning. In *One-Dimensional nanostructures: Electrospinning Technique and Unique Nanofibers*, Springer Berlin Heidelberg: Berlin, Heidelberg, 2013; pp 15-28.
23. Doytcheva, M.; Dotcheva, D.; Stamenova, R.; Tsvetanov, C., UV-Initiated Crosslinking of Poly(ethylene oxide) with Pentaerythritol Triacrylate in Solid State. *Macromolecular Materials and Engineering* **2001,** *286* (1), 30-33.
24. Zhou, C.; Wang, Q.; Wu, Q., UV-initiated crosslinking of electrospun poly(ethylene oxide) nanofibers with pentaerythritol triacrylate: Effect of irradiation time and incorporated cellulose nanocrystals. *Carbohydrate Polymers* **2012,** *87* (2), 1779-1786.
25. Forbey, S. J. Design and Characterization of Electrospun Mats with Tailored Morphologies for Enhanced Active Layer Performance in Energy Conversion and Energy Storage Applications. Ph. D. Dissertation, Virginia Polytechnic Institute and State University, Blacksburg, VA, 2014.
26. Zhou, C.; Chu, R.; Wu, R.; Wu, Q., Electrospun Polyethylene Oxide/Cellulose Nanocrystal Composite Nanofibrous Mats with Homogeneous and Heterogeneous Microstructures. *Biomacromolecules* **2011,** *12* (7), 2617-2625.
27. Annabi, N.; Nichol, J. W.; Zhong, X.; Ji, C.; Koshy, S.; Khademhosseini, A.; Dehghani, F., Controlling the Porosity and Microarchitecture of Hydrogels for Tissue Engineering. *Tissue Engineering Part B: Reviews* **2010,** *16* (4), 371-383.
28. Soliman, S.; Sant, S.; Nichol, J. W.; Khabiry, M.; Traversa, E.; Khademhosseini, A., Controlling the porosity of fibrous scaffolds by modulating the fiber diameter and packing density. *Journal of Biomedical Materials Research Part A* **2011,** *96A* (3), 566-574.
29. Baker, B. M.; Gee, A. O.; Metter, R. B.; Nathan, A. S.; Marklein, R. L.; Burdick, J. A.; Mauck, R. L., The Potential to Improve Cell Infiltration in Composite Fiber-Aligned Electrospun Scaffolds by the Selective Removal of Sacrificial Fibers. *Biomaterials* **2008,** *29* (15), 2348-2358.
30. Zhu, X.; Cui, W.; Li, X.; Jin, Y., Electrospun Fibrous Mats with High Porosity as Potential Scaffolds for Skin Tissue Engineering. *Biomacromolecules* **2008,** *9* (7), 1795-1801.
31. Shi, Q.; Yu, M.; Zhou, X.; Yan, Y.; Wan, C., Structure and performance of porous polymer electrolytes based on P(VDF-HFP) for lithium ion batteries. *Journal of Power Sources* **2002,** *103* (2), 286-292.
32. Wong, R. S. H.; Ashton, M.; Dodou, K., Effect of Crosslinking Agent Concentration on the Properties of Unmedicated Hydrogels (). *Pharmaceutics* **2015,** *7* (3), 305-319.
33. Graham, N.; Zulfiqar, M., Interaction of poly (ethylene oxide) with solvents: 3. Synthesis and swelling in water of crosslinked poly (ethylene glycol) urethane networks. *Polymer* **1989,** *30* (11), 2130-2135.
34. Statistical Mechanics of Cross-Linked Polymer Networks II. Swelling. *The Journal of Chemical Physics* **1943,** *11* (11), 521-526.
35. Doytcheva, M.; Dotcheva, D.; Stamenova, R.; Orahovats, A.; Tsvetanov, C.; Leder, J., Ultraviolet-induced crosslinking of solid poly(ethylene oxide). *Journal of Applied Polymer Science* **1997,** *64* (12), 2299-2307.

36. Wong, R. S. H.; Ashton, M.; Dodou, K., Effect of crosslinking agent concentration on the properties of unmedicated hydrogels. *Pharmaceutics* **2015,** *7* (3), 305-319.
37. Doytcheva, M.; Dotcheva, D.; Stamenova, R.; Orahovats, A.; Tsvetanov, C.; Leder, J., Ultraviolet-induced crosslinking of solid poly (ethylene oxide). *Journal of applied polymer science* **1997,** *64* (12), 2299-2307.
38. Song, Z.; Chiang, S. W.; Chu, X.; Du, H.; Li, J.; Gan, L.; Xu, C.; Yao, Y.; He, Y.; Li, B.; Kang, F., Effects of solvent on structures and properties of electrospun poly(ethylene oxide) nanofibers. *Journal of Applied Polymer Science* **2018,** *135* (5), 45787.
39. Majumdar, R.; Alexander, K.; Riga, A., Physical characterization of polyethylene glycols by thermal analytical technique and the effect of humidity and molecular weight. *Die Pharmazie-An International Journal of Pharmaceutical Sciences* **2010,** *65* (5), 343-347.
40. Romankevich, O. V.; Frenkel, S. Y., Equilibrium melting point of polyethylene oxide. *Polymer Science U.S.S.R.* **1980,** *22* (11), 2647-2654.
41. Pfefferkorn, D.; Kyerematen, S. O.; Busse, K.; Kammer, H.-W.; Thurn-Albrecht, T.; Kressler, J., Crystallization and Melting of Poly(ethylene oxide) in Blends and Diblock Copolymers with Poly(methyl acrylate). *Macromolecules* **2011,** *44* (8), 2953-2963.
42. Buckley, C. P.; Kovacs, A. J. In *Melting behaviour of low molecular weight poly (ethylene-oxide) fractions*, Darmstadt, Steinkopff: Darmstadt, 1975; pp 44-52.
43. Deschamps, A. A.; Grijpma, D. W.; Feijen, J., Phase separation and physical properties of PEO-containing poly(ether ester amide)s. *Journal of Biomaterials Science, Polymer Edition* **2002,** *13* (12), 1337-1352.
44. Rault, J.; Le Huy, H. M., Polyamide-polyether block copolymers swollen by water. I. Properties. *Journal of Macromolecular Science, Part B* **1996,** *35* (1), 89-114.
45. Husken, D.; Gaymans, R. J., The tensile properties of poly(ethylene oxide)-based segmented block copolymers in the dry and wet state. *Journal of Materials Science* **2009,** *44* (10), 2656-2664.
46. Lemaitre, J., *Handbook of Materials Behavior Models, Three-Volume Set: Nonlinear Models and Properties*. Elsevier: 2001.
47. Ní Annaidh, A.; Bruyère, K.; Destrade, M.; Gilchrist, M. D.; Otténio, M., Characterization of the anisotropic mechanical properties of excised human skin. *Journal of the Mechanical Behavior of Biomedical Materials* **2012,** *5* (1), 139-148.
48. Mirani, R. D.; Pratt, J.; Iyer, P.; Madihally, S. V., The stress relaxation characteristics of composite matrices etched to produce nanoscale surface features. *Biomaterials* **2009,** *30* (5), 703-710.
49. Chaudhuri, O.; Gu, L.; Klumpers, D.; Darnell, M.; Bencherif, S. A.; Weaver, J. C.; Huebsch, N.; Lee, H.-p.; Lippens, E.; Duda, G. N.; Mooney, D. J., Hydrogels with tunable stress relaxation regulate stem cell fate and activity. *Nature Materials* **2015,** *15*, 326.
50. Self-replenishing and Self-healing Coatings. In *Polymer Coatings*.
51. Lim, H.; Hoag, S. W., Plasticizer Effects on Physical–Mechanical Properties of Solvent Cast Soluplus® Films. *AAPS PharmSciTech* **2013,** *14* (3), 903-910.
52. Vijayalakshmi, S. P.; Madras, G., Photocatalytic degradation of poly(ethylene oxide) and polyacrylamide. *Journal of Applied Polymer Science* **2006,** *100* (5), 3997-4003.
53. Morlat, S.; Gardette, J.-L., Phototransformation of water-soluble polymers. I: photo- and thermooxidation of poly(ethylene oxide) in solid state. *Polymer* **2001,** *42* (14), 6071-6079.

Appendix C

Modification of Crosslinked PEO Nanofibers by Adsorption of Silica Nanoparticles

C.1 Introduction

Poly(ethylene oxide) (PEO) is a non-toxic, hydrophilic polymer used extensively in biomedical applications such as drug delivery,[1-3] tissue engineering,[4-5] controlled release,[6-7] bioconjugation,[8-9] and surface functionalization.[10-12] PEO is considered bioinert and nonimmunogenic due to its ability to sterically exclude other macromolecules, including proteins.[13] The large exclusion volume of hydrated PEO and the high flexibility of PEO chains prevent the adsorption of proteins and even prevent cellular adhesion, making PEO biocompatible yet non-interacting.[14-16]

Because PEO is highly soluble in water, PEO must be crosslinked to act as non-soluble hydrogel scaffolds. Methods to synthesize crosslinked PEO include radiation crosslinking with ɣ-irradiation,[2, 17] UV-initiated crosslinking with a multifunctional acrylate,[18-20] or free radical polymerization of poly(ethylene glycol)-acrylates.[21-22] The high biocompatibility of PEO makes it an attractive material for tissue engineering scaffolds, however, low viability with PEO hydrogels is observed for anchorage-dependent cells due to the non-adhesive nature of PEO.[23] To impart cellular adhesive properties onto PEO hydrogels, specific cell-matrix interactions must be introduced to the PEO chains. One such approach includes incorporating cell-adhesive peptide sequences (e.g. RGD) found in proteins native to the extracellular matrix (ECM).[24] Other methods include the incorporation of growth factors into the scaffold by covalent attachment or by specific binding and the inclusion of enzyme-specific peptide sequences for controlled degradation and release of molecules (e.g. growth factors, drugs, etc.).[25]

An additional approach to improving the bioactivity and tailoring the mechanical properties of crosslinked PEO scaffolds involves the incorporation of silica nanoparticles into the scaffold.

Aqueous dispersions of silica nanoparticles have demonstrated efficacy in adhering gels and biological tissues through adsorption of the polymer chains in the gel to the nanoparticle surface. The adsorbed polymer chains are able to reorganize and dissipate energy under stress, thus preventing any interfacial fracture between gels or tissues.[26] *In vivo* rat studies revealed that the silica nanoparticles are capable of successfully closing deep wounds and attaching polymer membranes to tissues even in the presence of blood flow.[27] Furthermore, studies on photocrosslinked nanocomposite hydrogels prepared from poly(ethylene glycol) (PEG) and silica nanospheres demonstrated improved mechanical stiffness of the hydrogels, enhanced cell adhesion and spreading, and increased metabolic activity of the cells compared to PEG hydrogels with no silica nanospheres.[28] Because PEO readily adsorbs silica nanoparticles, incorporation of silica nanoparticles into PEO scaffolds will provide a means to not only tailor mechanical properties, but also promote cell adhesion to the scaffold through a facile means of modification.

In this work, the effect of silica adsorption on the physical properties of crosslinked, electrospun PEO is investigated. Crosslinked PEO nanofiber scaffolds were prepared by *in-situ* UV curing during electrospinning and were modified by soaking in aqueous silica dispersions of variable concentration. The effect of silica nanoparticle size and concentration on the nanofiber morphology, equilibrium swelling behavior, tensile properties, degradation rate, and cell viability was investigated to determine the potential of these modified-scaffolds for tissue engineering and wound dressing.

C.2 Experimental

C.2.1 Materials

Poly(ethylene oxide) (PEO) with $M_v \sim 300{,}000$ g/mol was obtained from Sigma-Aldrich. Pentaerythritol triacrylate (PETA) was also obtained from Sigma-Aldrich. Ludox® colloidal silica (TM-50, HS-40, and SM) was obtained from Sigma-Aldrich. The characteristic properties of the colloidal silica grades are shown in **Table C.1**. Acetonitrile, methanol, and chloroform was obtained from Fisher Scientific. All materials were used as received.

Table C.1. Characteristic properties of the Ludox® colloidal silica including the diameter and specific surface area (SSA) of the nanoparticles.

Silica	Stock Concentration (wt%)	Diameter (nm)	SSA (m^2/g SiO_2)
TM-50	50	15	110-150
HS-40	40	9	198-258
SM	30	5	320-400

C.2.2 Preparation of Crosslinked, Electrospun PEO

Following the procedure established in Appendix B, PEO20 nanofibers were prepared by the concurrent electrospinning and crosslinking of PEO with pentaerythritol triacrylate (PETA). A solution of PEO in acetonitrile was prepared to a concentration of 8 wt% and PETA was added to a concentration of 20 wt% by weight of PEO. Nonwoven mats of PEO20 were prepared by electrospinning this solution at room temperature using a KDscientific 100 syringe pump and a Spellman Berton 205B high voltage source. The electrospinning solutions were extruded at a flow rate of 2 mL/hr from a 3-mL syringe through a blunt tip stainless steel needle having an internal diameter of 0.8 mL. A negative-biased voltage of 19 kV was applied to the needle tip and the resulting nanofibers were collected on a grounded aluminum rotating rod collector (1 cm diameter, 200 RPM) placed 25 cm from the needle tip. To crosslink the PEO-PETA nanofibers, a 459-watt mercury vapor UV lamp was placed directly above the aluminum collector. During electrospinning, the UV lamp was turned on to allow crosslinking of the nanofibers as they were

collected. PEO10 and PEO30 nanofibers were also prepared using the above procedure with PETA concentrations of 10 and 30 wt%, respectively, in the electrospinning solution. Prior to use, all crosslinked PEO samples were ultrasonicated in acetonitrile for 1 hour to remove the uncrosslinked material (i.e. sol fraction).

C.2.3 Gluing of PEO20 Using Silica Dispersions

The gluing of crosslinked, electrospun PEO20 was investigated using silica dispersions with various particle sizes. The lap-shear adhesion tests were performed on an Instron 5867 with a 20 mm/min strain rate. Prior to testing, the sol fraction of PEO20 nanofibers was removed by ultrasonicating the nanofiber mat in acetonitrile for one hour and then drying the remaining gel fraction overnight under vacuum. Electrospun PEO20 was hydrated to a swelling ratio of 425 wt% and cut into ribbons with a width of 6 mm. Gluing was achieved by spreading 12 μL of the silica solution (Ludox TM-50, HS-40, or SM) across the overlap surface (6 mm x 6 mm). Water was used as a control 'glue' solution. A contact pressure of 10 kPa was applied for 30 seconds to glue the overlap surface. The total length of the glued ribbons was 20 mm. **Figure C.1** shows a schematic representation of the gluing of the PEO20 ribbons.

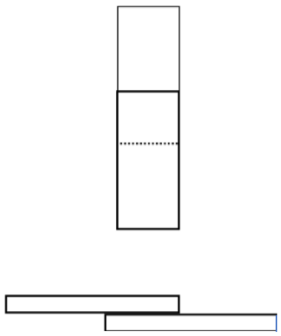

Figure C.1. Diagram identifying the gluing junction of PEO20 nanofiber scaffolds.

To determine the reparability of the gluing junctions, 12 μL of Ludox SM was used to glue a 6 mm x 6 mm junction of hydrated PEO20 ribbons, as described above. Following adhesive

failure by interfacial peeling, the gauge length was returned to its initial state, and the glued joint was repaired by placing the ribbons back in contact with one another and applying finger pressure for 15 seconds. Lap shear tests were again performed on the repaired joint.

C.2.4 Dilution of Silica Nanoparticles

Because the stock suspensions of the silica nanoparticles varied with silica size, dilutions were necessary to ensure consistent silica concentrations for comparison. The stock silica suspensions were diluted in water to final concentrations of 10 wt%, 1 wt%, 0.1 wt%, 0.01 wt% and 0.001 wt%. These dilutions were prepared for all silica sizes (TM-50, HS-40, SM).

C.2.5 Soaking of PEO20 in Silica Nanoparticle Suspensions

The adsorption of crosslinked PEO chains to the surface of silica nanoparticles was achieved by soaking PEO20 nanofiber mats in silica suspensions. PEO20 was placed in an excess volume of a silica suspension at a set concentration. The PEO20 mat was kept in solution for a set period of time. The mat was then removed from solution, washed with water to remove any non-adsorbed silica and dried under vacuum overnight. Silica-soaked PEO20 samples are referred to as PEO20-*x*-*y* where *x* is the concentration of silica nanoparticles in the soaking suspension and *y* is the type of nanoparticles (TM-50, HS-40, or SM). For example, PEO20-1-TM50 describes a PEO20 sample soaked in 1 wt% TM-50.

The amount of silica adsorbed was determined gravimetrically by weighing dry samples before and after soaking in silica suspensions. Thermogravimetric analysis (TGA) was also used to determine the silica content of silica-soaked PEO20 mats. A TA Instruments TGA Q5000 was used for analysis. Samples were heated at 10 ºC/min to 700 ºC and the residue weight was used to determine the wt% of silica in the scaffolds.

Equilibrium swelling measurements were conducted in water. PEO20 samples with adsorbed silica were cut into discs (20 mm) and dried under vacuum prior to analysis. Samples

were placed in excess water and were allowed to equilibrate until no further weight change was observed. The samples were removed from water, blotted to remove excess surface water, and the swollen weight was recorded. Wet samples were then dried under vacuum overnight and the dry weight was recorded. The equilibrium swelling ratio was determined by subtracting the dry weight from the wet weight and then dividing by the dry weight.

C.2.6 Scanning Electron Microscopy

SEM images were acquired using a JEOL NesoScope JCM-5000 Benchtop SEM. SEM samples were sputter coated with gold prior to imaging.

C.2.7 Tensile Testing

Tensile testing was performed on PEO20 and silica-adsorbed PEO20 nanofiber mats using an Instron 5867 with pneumatic grips. Samples were cut into dogbones (ASTM D638) and were tested with a strain rate of 20 mm/min and a gage length of 10 mm. Wet samples were tested by first swelling samples to equilibrium swelling in water and then cutting dogbones of the samples.

C.2.8 Stress Relaxation Experiments

Stress relaxation experiments were performed on a TA Instruments DMA Q800 in oscillatory tension mode. Nanofiber mats were cut into ribbons (6 mm diameter) for testing. A strain of 10 % was applied to samples at 37 ºC and the resultant stress was monitored for 10 minutes.

C.2.9 Differential Scanning Calorimetry

Differential scanning calorimetry (DSC) was performed on a TA Instruments DSC Q2000. Samples were dried overnight under vacuum prior to analysis. Under a nitrogen atmosphere, samples (5-8 mg) were equilibrated at -85 ºC. Samples were subjected to a heat-cool-heat cycle with temperature bounds of -85 ºC to 85 ºC and heating/cooling rates of 10 ºC/min. The glass transition temperature (T_g), crystallization temperature (T_c), enthalpy of crystallization (ΔH_c),

melting temperature (T_m), and enthalpy of melting (ΔH_m) was determined using the TA Instruments Universal Analysis software.

C.2.10 Mass Loss of Nanofibers Over Time

The degradation of PEO20 and silica-adsorbed PEO20 was investigated by monitoring weight loss over time. Samples were cut into discs (~15 mm) and dried under vacuum overnight. The dry weight was recorded and samples were placed in excess phosphate buffered saline (PBS) at 37 ºC. Samples were removed from the PBS over the course of 60 days, washed in water to remove salt from the PBS, and dried under vacuum overnight. The dry weight was then recorded. A total of 3 samples were analyzed for each time point. Mass loss was determined by subtracting the weight at time t from the initial weight of the sample and then dividing by the initial weight of the sample.

C.2.11 Cell Adhesion and Viability Studies

For use in cell studies, PEO20 and silica-adsorbed PEO20 mats were cut into 9/16" discs and were sterilized by soaking in 70:30 (v:v) ethanol: water for 1 hour. Sample discs were subsequently soaked in unsupplemented Dulbecco's Modified Eagle Medium (DMEM) for 1 hour to remove any residual ethanol. 1-hour soaks in DMEM were repeated five times, and finally an overnight soak in excess unsupplemented DMEM was performed. For adhesion tests, half of the samples were placed in excess DMEM supplemented with 10% fetal bovine serum for the overnight soak.

The adhesion of cells was investigated by transferring the samples to non-treated tissue culture well plates. Non-treated well plates were used so that the adhesion of cells occurs solely on the nanofiber scaffolds and not on the well plate itself. HeLa cells were seeded at a density of 25,000 cells/well in supplemented DMEM media. A control was performed by seeding the HeLa cells on tissue culture-treated well plates. Cells were allowed to incubate for 4 hours, and then

scaffolds were removed and washed with media to remove non-adhered cells. Cell viability was analyzed using the Cell Titer Glo® assay with n=3.

Cell viability over time was also determined. Samples were prepared using the method described above, and samples were incubated at 37 ºC. After 1, 3, and 7 days, samples were removed and washed with media to remove non-adhered cells. Each day during the study, the DMEM media was exchanged for fresh media. Again, cell viability at these time periods was analyzed using the Cell Titer Glo® assay with n=3.

For analysis of the cell morphology, cells were fixed by treating the scaffolds with 3.7% paraformaldehyde in PBS for 1 hour. The samples were subsequently dehydrated by performing washes in drying solutions containing increasing ethanol (EtOH) contents (100:0 PBS:EtOH, 80:20 PBS:EtOH, 60:40 PBS:EtOH, 40:60 PBS:EtOH, 20:80 PBS:ETOH, and 0:100 PBS:EtOH). Each wash was performed 3 times for 5 minutes each before moving on to the next washing solution. Samples were dried overnight on the benchtop and then sputter coated with gold for analysis with SEM.

C.3 Results and Discussion

C.3.1 Adhesion of PEO20 Using Silica Nanoparticles

Leibler and colleagues demonstrated the utility of silica nanoparticle solutions as hydrogel adhesives, whereby the nanoparticles adsorb onto the polymer chains and act as connectors between the chains.[29] When two hydrogels are placed in contact with one another with the nanoparticle solution spread in between the two hydrogels, a physical connection will be made through the adsorption of polymer chains from both hydrogels onto a single nanoparticle, adhering the two gels. To function properly as an adhesive, the surface of the nanoparticles must have an affinity towards the polymer chains comprising the hydrogel network resulting in a free energy gain upon monomer adsorption. Adsorption to the nanoparticle surface is anticipated to occur for

many monomers on a single network chain and for multiple network chains per nanoparticle.[30] Thus, the nanoparticles act as physical crosslinks within the gel, with the polymer chains functioning as the tie chains between the nanoparticles. When the adhesive junction is placed under strain, the reversible nature of adsorption enables the dissipation of stress through the detachment of adsorbed monomers from the nanoparticle surface. This not only relaxes the tension, but also provides space for a neighboring network chain to adsorb and replace the detached chain, thereby preventing adhesive failure.

Poly(ethylene oxide) (PEO) has been shown to readily adsorb to the surface of silica[31-33], and thus Leibler's silica adhesive may be applied to crosslinked PEO nanofibers to adhere to nanofiber mats together or to adhere the nanofibers to other surfaces, such as body tissues. To determine the adhesion of crosslinked, electrospun PEO20 nanofibers using colloidal silica solutions, lap-shear adhesion tests were performed. Ribbons of PEO20 were glued using the same volume of the silica stock solutions (see concentrations in **Table C.1**) and of silica suspensions diluted to 30 wt% in water. Water was used as a control to show the lap-shear properties with no adsorbed silica. As shown in **Figure C.2**, failure force increases as the size of the nanoparticle increases. For PEO20 glued by stock suspensions of SM (5 nm) and HS-40 (9 nm), the adhesion failed by the PEO20 ribbons slipping past one another, however, for PEO20 glued by TM-50, the ribbons tore outside the adhesive junction. When the stock silica suspensions are diluted to the same concentration (30 wt%) prior to gluing, adhesion by all nanoparticle sizes failed by slipping of the joint. It is important to note that dilution of the stock suspensions leads to a decrease in the adhesive failure force. For example, when Ludox TM-50 is diluted from 50 wt% to 30 wt%, the failure force decreases from 0.40 N to 0.34 N. Thus, the concentration as well as size of nanoparticles plays a key role in adhesive strength.

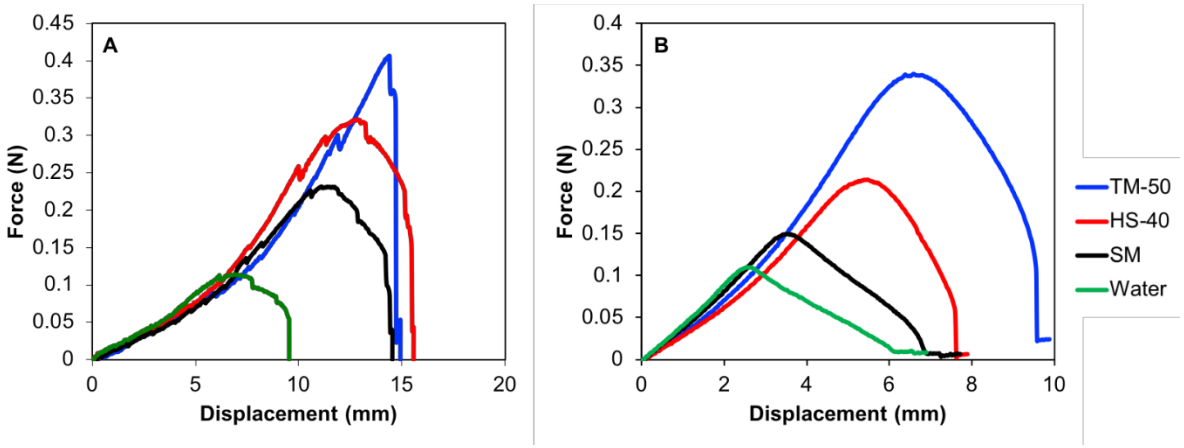

Figure C.2. Lap-shear adhesions tests for hydrated PEO20 glued using silica stock solutions (A) and 30 wt% silica solutions (B).

To better quantify the strength of adhesion, the failure force per shear area was determined, as shown in **Figure C.3**. Again, an increase in force per shear area is observed with increasing particle size. As the size of the nanoparticle increases, a greater number of PEO chains are capable of adsorbing to the surface of a single nanoparticle. This increases the density of the physical crosslinks binding the PEO20 nanofiber mats and results in strong adhesion. Increasing the concentration of the silica nanoparticles also increases the crosslinking and leads to a larger failure force per shear area.

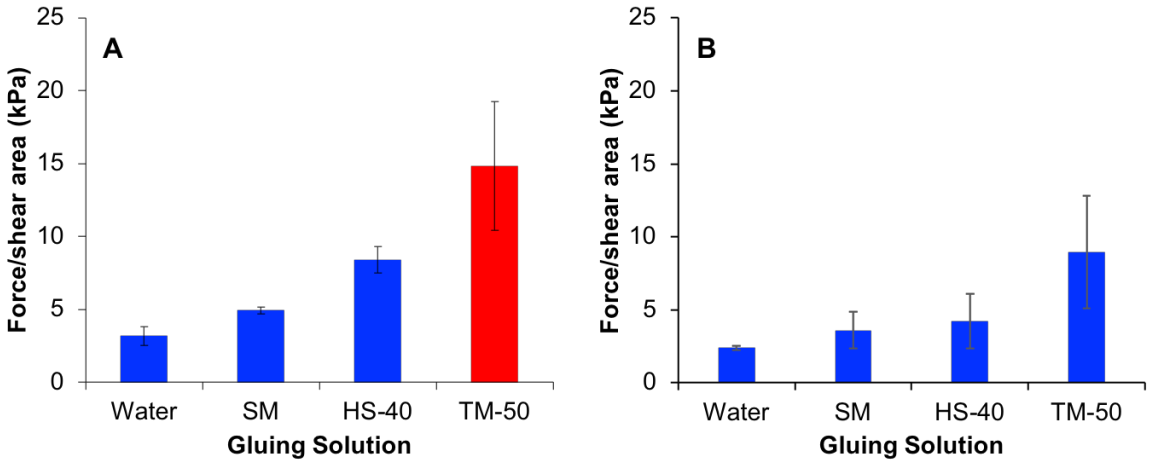

Figure C.3. Failure force per shear area for gluing solutions. A red bar indicates fracture outside of the gluing junction.

Once a PEO network chain is adsorbed to the silica nanoparticle surface, the likelihood to *total* desorption of the polymer chain from the surface is exponentially small.[30, 34] This fact coupled with the dynamic nature of polymer adsorption to the nanoparticle surface suggests that the glued interface may readily be repaired after adhesive failure. Lap shear tests were performed on hydrated PEO20 nanofibers glued with Ludox SM to test ability to repair glued interfaces. Upon failure of the adhesive junction, the two PEO20 ribbons were placed back in contact with one another with light pressure and lap shear tests were repeated. As shown in **Figure C.4**, the initial strength of the glued interface may be fully recovered with contact and light pressure on the interface. The recovery of adhesive properties is reproducible for several failure-repair cycles, demonstrating that glued interfaces may readily be repaired or repositioned without the application of additional nanoparticle solution.

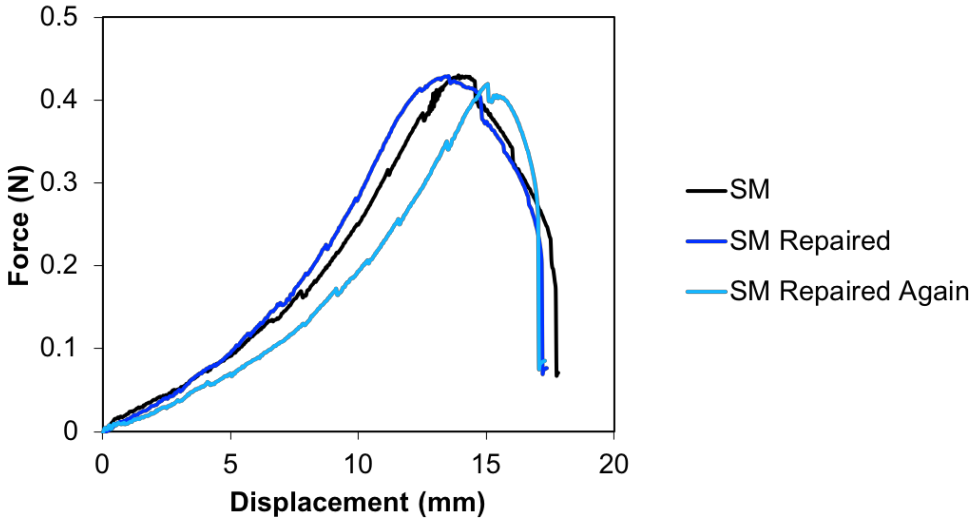

Figure C.4. Lap-shear tests following the repair of gluing junction with light finger pressure. PEO20 ribbons glued with Ludox SM nanoparticles were used.

Scanning electron micrsocopy (SEM) was utilized to investigate the gluing junction of the nanofibers. As shown in **Figure C.5**, application of Ludox TM-50 lead to the adhesion of nanofibers across the gluing junction. PEO nanofibers clearly transverse across the gluing junction, binding the nanofiber mats to one another. It is also evident that the nanofibrous morphology is not impeded with the application of silica nanoparticles. Thus, the high surface area of the PEO20 nanofibers provides a large surface for the adsorption of nanoparticles and thereby a large surface area for adhesion between the nanofiber mats. Overall, it is apparent that this facile gluing process using silica suspensions provides a useful means for adhering PEO20 nanofibers to one another and will be useful for application to tissue surfaces (e.g. for skin grafting).

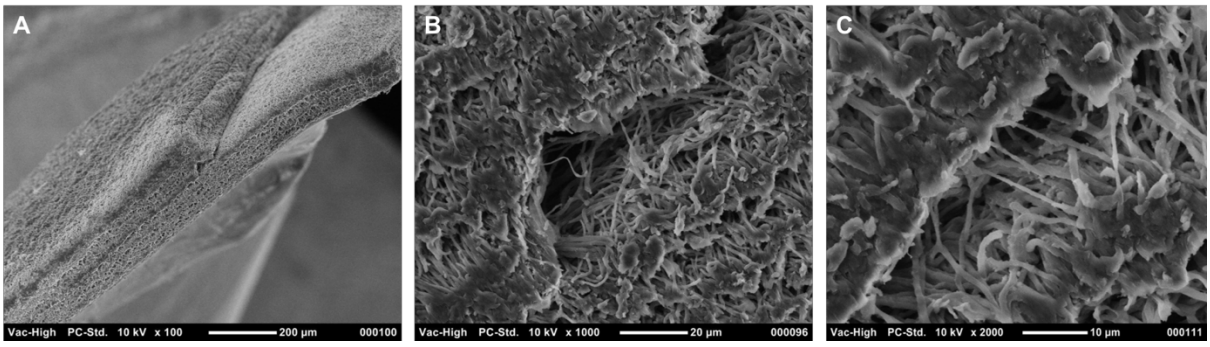

Figure C.5. SEM images of the glued interface of PEO20 nanofibers glued with Ludox TM-50 silica nanoparticles.

C.3.2 Adsorption of Crosslinked PEO Nanofibers to Silica Nanoparticles

With the successful gluing of PEO20 nanofiber mats using silica solutions, it is also of interest to determine the influence of the adsorption of silica nanoparticles to the entire surface of the PEO20 nanofibers. Adsorption of silica in this manner provides a means to immediately adhere the nanofiber scaffolds during biological implantation. Furthermore, the introduction of physical crosslinking to the PEO20 nanofibers through silica adsorption is a facile method to manipulate the mechanical properties of the nanofibers and provides a surface suitable for cellular adhesion.[28] In this section, crosslinked PEO20 nanofibers were modified through the adsorption of silica nanoparticles of various sizes. The effect of silica concentration and size on the nanofiber morphology, mechanical properties, and cellular adhesion will be investigated.

C.3.2.1 Variation in Silica Adsorption with Time

First, the effect of time on the amount of silica adsorbed to PEO20 nanofiber mats was examined. Crosslinked PEO20 nanofibers were dried and then placed in Ludox TM-50 silica suspensions diluted to various concentrations (0.01 wt%, 0.1 wt%, and 1 wt%) in water. The PEO20 nanofibers were allowed to equilibrate in the silica suspensions for set periods of time and were then removed, washed with deionized water to remove any non-adsorbed silica, and dried. As a control, PEO20 samples were also soaked in water for similar times. The weight change with

soaking time was determined using thermogravimetric analysis (TGA), as shown in **Figure C.6**. Because silica is an inorganic nanoparticle, it will not degrade at elevated temperatures. Thus, residue weight in TGA can be correlated to the amount of silica adsorbed onto the PEO20 nanofibers. For PEO20 soaked in water, a constant residue weight of approximately 1 wt% was observed at all soak times. This residue weight is attributed to the carbon ash remaining following the degradation of PEO20. With the adsorption of silica, the residue weight increases as the soak time increases, implying a greater amount of silica is adsorbed to the PEO20 network chains as the chains are allowed to equilibrate with the silica for longer.

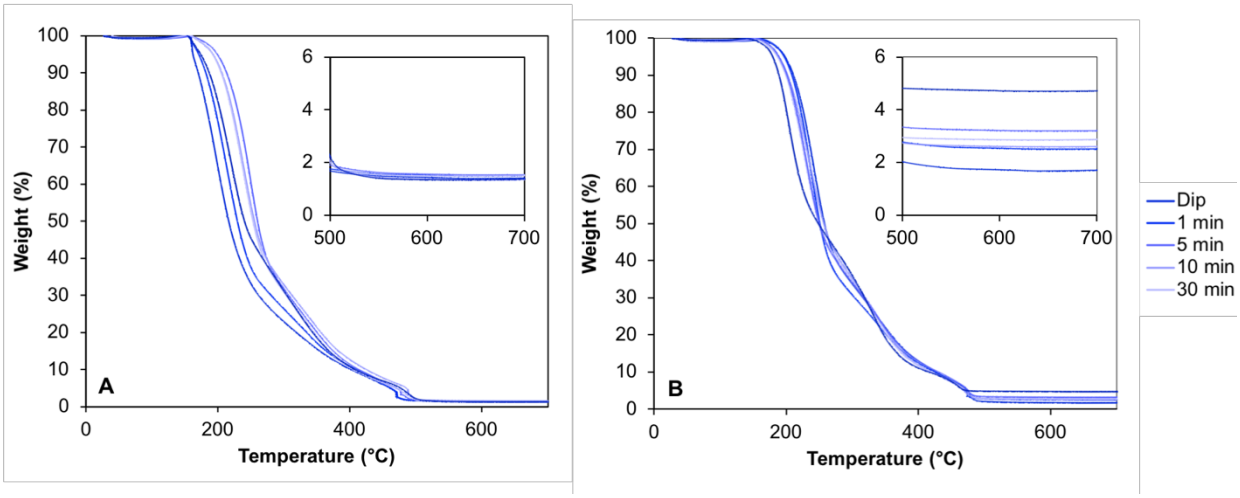

Figure C.6. TGA PEO20 soaked in water (A) and in 0.1 wt% Ludox TM-50 (B) for various time periods.

To quantify the silica adsorption over time, the residue weight determined from TGA was plotted as a function of time for PEO20 soaked in water, 0.01 wt% TM-50, 0.1 wt% TM-50, and 1 wt% TM-50, as shown in **Figure C.7**. As expected, the residue weight increases with increasing time for all concentrations. A rapid increase in weight is observed with just a dip (1 second) in the silica solutions, suggesting that adsorption occurs rapidly to the PEO network chains. The weight continues to increase until approximately 10 minutes when the residue weight appears to level off for all silica solution concentrations. Thus, the equilibrium state between adsorbed nanoparticles

with the PEO network chains and silica nanoparticles in solution is likely achieved within 30 minutes of soaking in silica solutions. Additionally, the residue weight increases as the concentration of silica increases. This is due to the fact that increasing the silica concentration increases the number or adsorption sites for the PEO nanofibers, thereby increasing the total amount of silica adsorbed with a constant PEO20 composition.

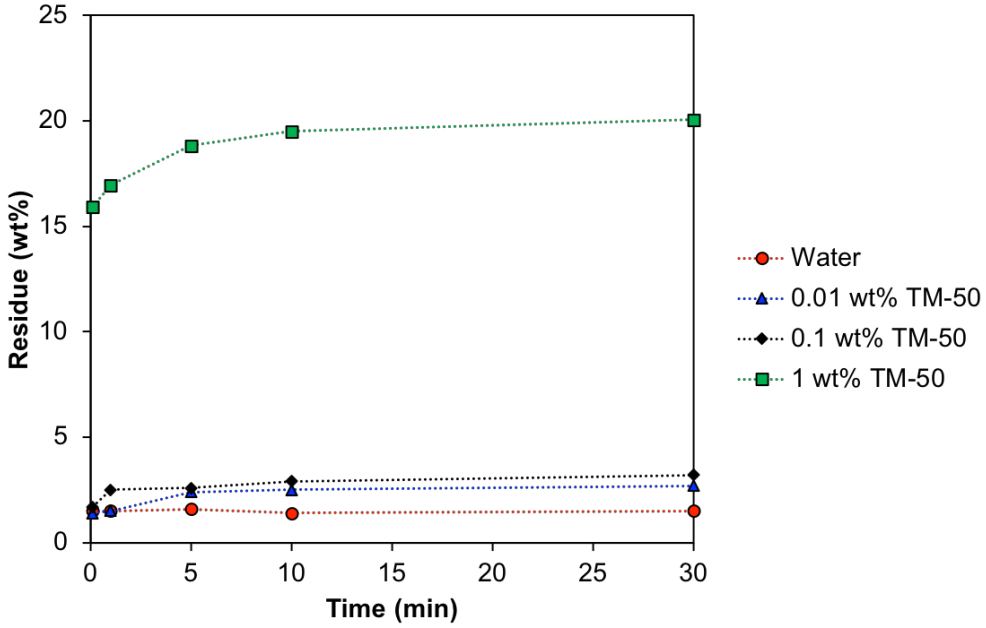

Figure C.7. Residue weight of PEO20 soaked in water, 0.01 wt% Ludox TM-50, 0.1 wt% Ludox TM-50 and 1 wt% Ludox TM-50.

The adsorption of silica nanoparticles onto the PEO20 nanofibers not only influences the physical crosslinking of PEO network chains themselves, but also has the potential to effectively 'glue' individual nanofibers to one another. Thereby, the morphology of PEO20 nanofibers following the adsorption of Ludox TM-50 was investigated using SEM, as shown in **Figure C.8**. Before soaking in silica nanoparticles, PEO20 nanofibers exhibited a smooth surface with uniform fiber size. Following a dip (1 second) in 0.1 wt% Ludox TM-50, PEO20-0.1-TM50 nanofibers at the surface of the mat exhibit a rougher surface and a small degree of fiber melding (i.e. gluing of

neighboring nanofibers) is apparent. As the soaking time increases to approximately 30 minutes, the surface of all nanofibers becomes more homogeneously rough and the degree of fiber melding increases. Above 30 minutes, where the adsorption of silica has reached an equilibrium state (no further evidence of weight change), the morphology of the nanofibers shows a highly melded surface. Furthermore, the effect of silica adsorption can be observed within the first several layers of the nanofiber scaffold, suggesting that silica has impregnated into the mat.

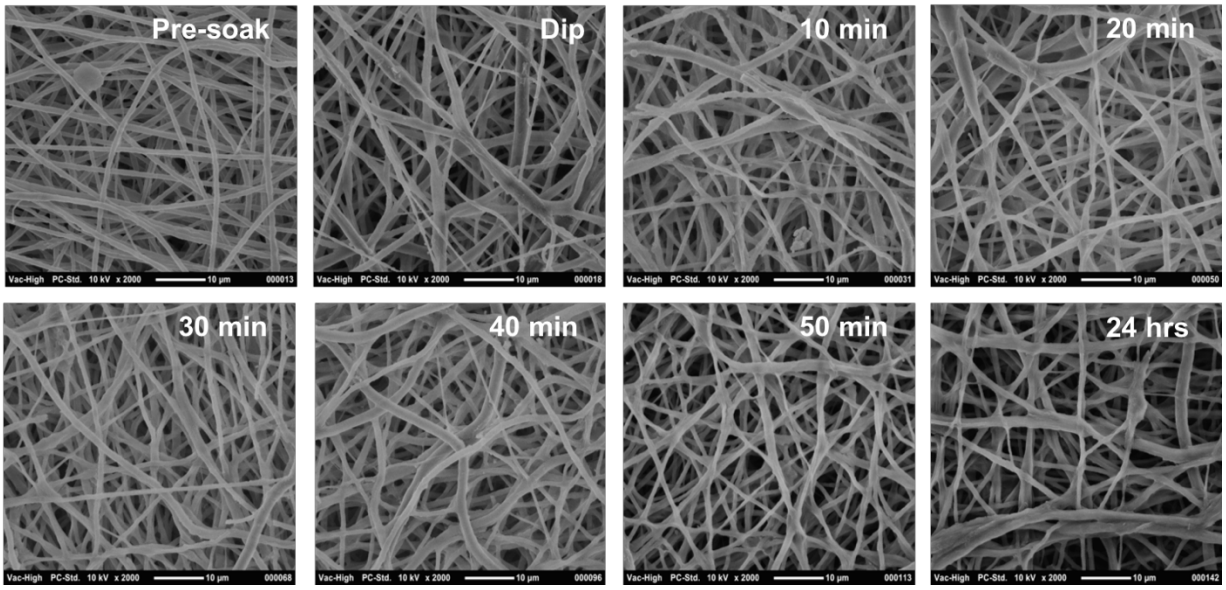

Figure C.8. SEM images of PEO20 soaked in 0.1 wt% Ludox TM-50 for various time periods.

From this analysis of silica adsorption with PEO20 over time, it is evident that an equilibrium concentration of silica and consistent nanofiber morphology is achieved by soaking PEO20 nanofibers in silica suspensions for at least 30 minutes. Thus, a soak time of 1 hour will be used for all subsequent experiments to ensure the equilibrium adsorption state has been achieved.

C.3.2.2 Variation in Silica Adsorption with Concentration

The influence of silica adsorption with PEO20 at the equilibrium adsorption state was investigated as a function of silica concentration and size. PEO20 nanofibers were placed in silica suspensions (TM-50, HS-40, or SM) diluted to 0.001 wt%, 0.01 wt%, 0.1 wt%, 1 wt%, and 10

wt% in water for 1 hour to achieve equilibrium adsorption. Following adsorption, PEO20 mats were washed in water to remove non-adsorbed silica and dried under vacuum. The weight change following silica adsorption was determined gravimetrically by measuring the mass of the dried PEO20 mats before and after adsorption. The weight change as a function of silica concentration is shown in **Figure C.9A**. As expected, for silica nanoparticle of all sizes the weight change increases with increasing concentration. As described previously, this may be attributed to an increase in the number of adsorption sites for PEO20 as the number of silica nanoparticles increases. At 1 wt% of silica and above in the soaking suspensions, the magnitude of weight change is influenced by the size of the nanoparticles. A slight increase in weight change is observed with increasing nanoparticle size. This is surprising due to the increased specific surface area (SSA) of the silica nanoparticles as the diameter decreases (see **Table C.1**), however, it likely implies slight variations in surface chemistry that arise during the production and stabilization of the nanoparticles.

The hydration properties of scaffolds used for tissue engineering play a key role in dictating a cell's ability to proliferate within the scaffold, mechanical properties, and the diffusion of materials (e.g. drugs, nutrients, waste) throughout the scaffold.[35] Because PEO is a highly hydrophilic polymer, a high hydration level is expected at equilibrium (as shown in Appendix B), however, this value is likely influenced by the presence of silica nanoparticles adsorbed to the PEO network chains. Thus, the equilibrium swelling degree of PEO20 modified with various concentrations of silica nanoparticles was determined by equilibrating the samples in water at 37 ºC for more than 24 hours. A temperature of 37 ºC was chosen to mimic biological conditions. After 24 hours, no weight change was observed in the samples with time. The equilibrium swelling degree was determined by weighing the wet nanofibers and comparing this to the dry weight using the following relation:

$$\text{Equilibrium Swelling Ratio} = \frac{w_{wet} - w_{dry}}{w_{dry}} \quad \textbf{(C.1)}$$

where w_{wet} is the weight of the swollen mat and w_{dry} is the weight of the dry mat. As shown in **Figure C.9B**, the equilibrium swelling degree decreases with increasing silica concentration. The increase in silica concentration results in an increase in PEO-silica specific interactions. Because the adsorption of PEO chains to the silica nanoparticle surface restricts the mobility of the polymer chain and causes a reduction in sites available for water absorption, the equilibrium swelling value decreases with increasing silica adsorption. Furthermore, a greater reduction in equilibrium swelling is observed with increasing nanoparticle size, which may be attributed to the total amount of silica adsorbed (**Figure C.9A**).

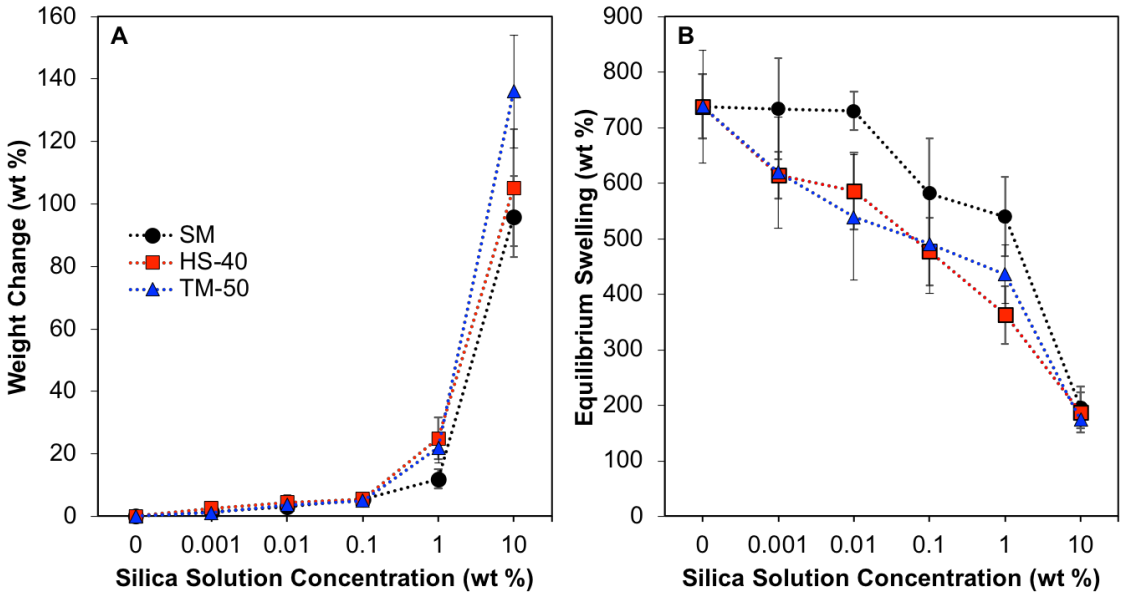

Figure C.9. Weight change (A) and equilibrium swelling (B) of PEO20 nanofibers equilibrated with various concentrations and sizes of silica nanoparticles.

As demonstrated in **Section C.3.2.1** , it is expected that the concentration of silica will affect the nanofiber morphology of PEO20 by adhering nanofibers to one another. SEM was

utilized to determine the nanofiber morphology of PEO20 scaffolds soaked in Ludox TM-50, as shown in **Figure C.10**. With increasing silica solution concentration, the nanofiber surface exhibits a rougher surface and the diameter of the nanofibers appears to increase in size. Furthermore, significant fiber melding occurs, especially at concentrations of 1 and 10 wt% silica. Similar morphologies were observed for PEO20 nanofibers soaked in Ludox HS-40 and SM solutions with increasing concentration. The 'gluing' of PEO20 nanofibers to one another will have significant implications on the mechanical properties of the scaffolds, which will be investigated in the section below.

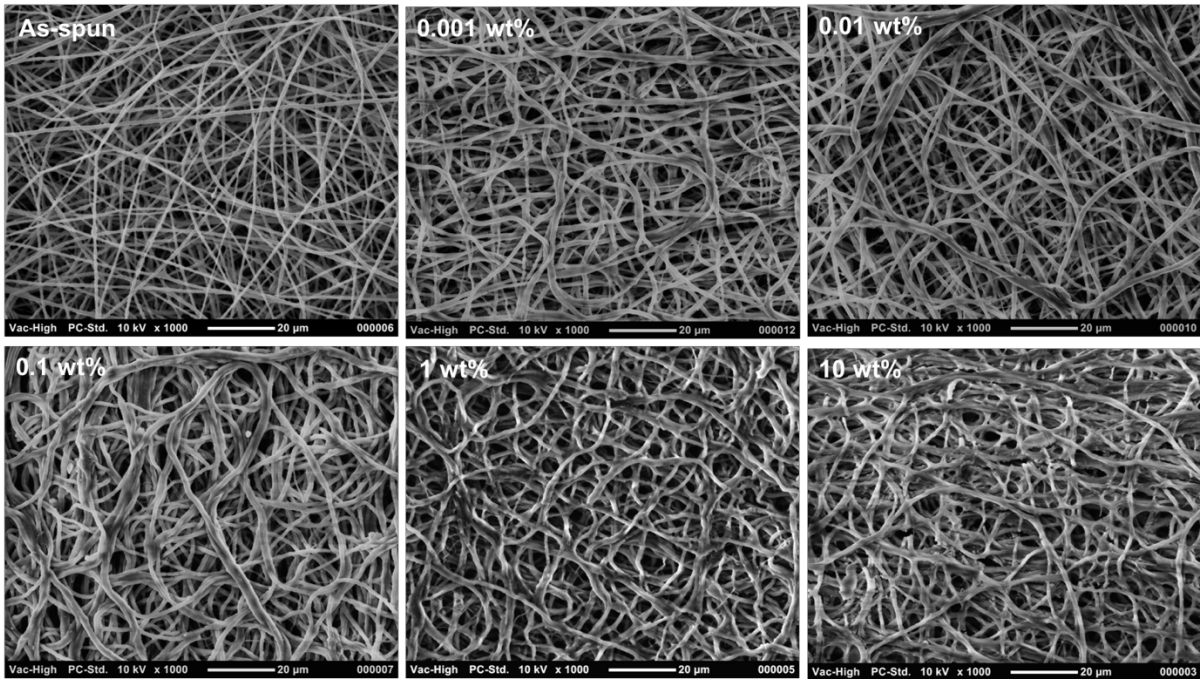

Figure C.10. SEM images of PEO20 scaffolds following the adsorption of Ludox TM-50 silica nanoparticles. The morphology as a function of the silica suspension concentration used during the PEO20 soak is displayed.

C.3.3 Tensile Properties of PEO Nanofibers with Adsorbed Silica

The adsorption of silica to PEO20 nanofibers not only introduces physical crosslinks to the network PEO chains, but also leads to fiber melding of the individual nanofibers to one another.

Tensile testing was performed on PEO20 modified with silica adsorption in both the dry state and the wet state (at equilibrium swelling) to determine the influence of adsorbed silica on the mechanical properties of PEO20. The representative stress vs. strain curves for PEO20 soaked in Ludox TM-50 solutions is shown in **Figure C.1**.

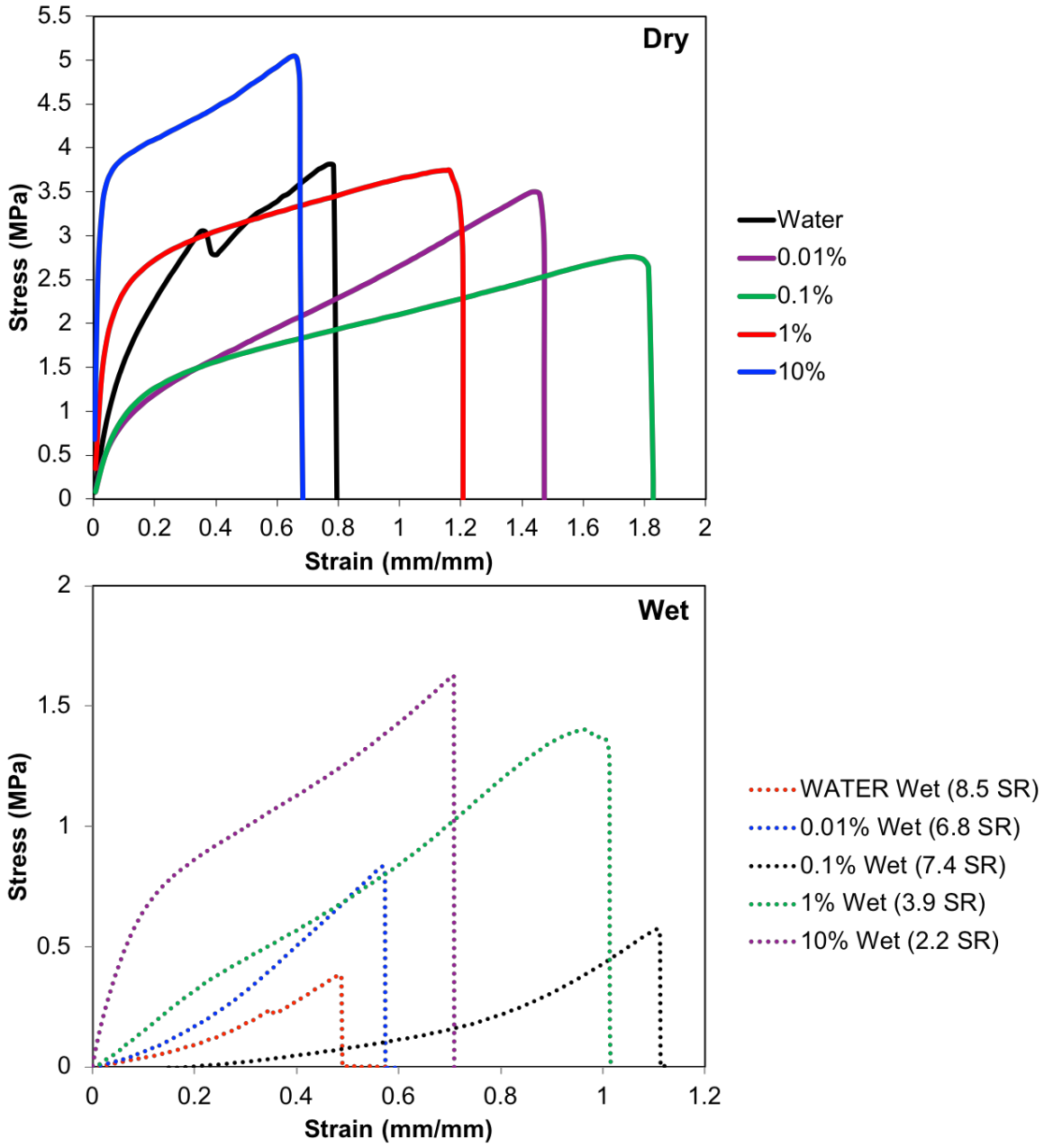

Figure C.11. Tensile properties of PEO20 nanofibers soaked in TM-50 solutions of variable concentration for one hour. Wet samples were swollen in water to their equilibrium swelling ratio (SR) prior to testing. Representative curves from five separate measurements are shown.

At low silica concentrations (i.e. ≤ 0.1 wt%), the stress vs. strain profiles of PEO20 are relatively similar, displaying a modulus and strength at break comparable to, but slightly less than that of PEO20 with no adsorbed silica. At these low concentrations, desorption of adsorbed PEO

network chains from the silica nanoparticle surface effectively dissipates stress when strain is applied to the PEO20 nanofibers, resulting in a lower modulus, lower tensile strength at break, and greater strain at break. When the silica concentration is raised to 1 wt% and above, however, the physical crosslinking caused by silica adsorption to numerous network chains dominates, and an increase in modulus and tensile strength is observed with increasing silica concentration. Similar results are observed for the hydrated PEO20-silica mats with the added effect of hydration further decreasing the mechanical properties.

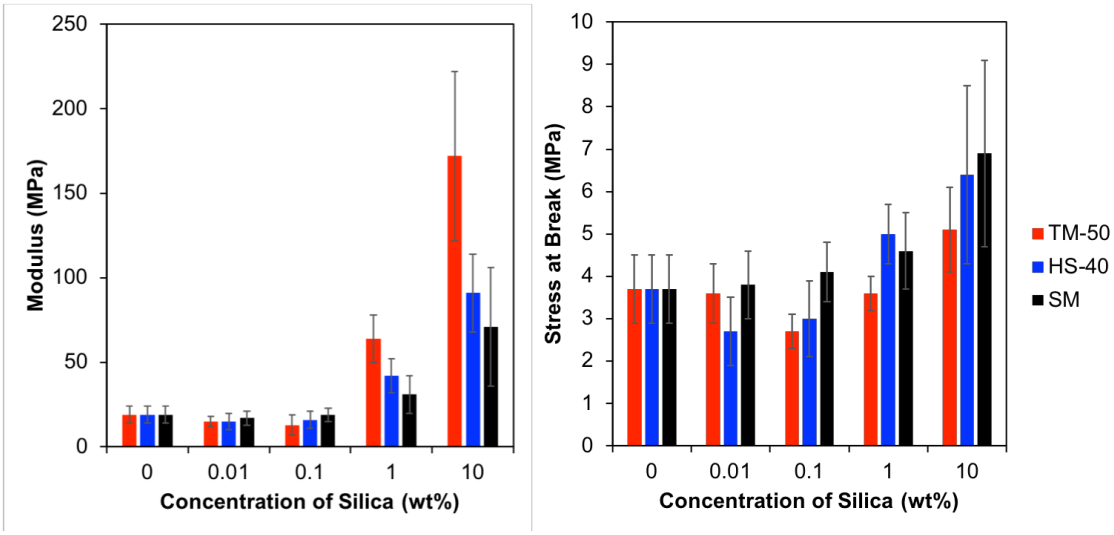

Figure C.12. Modulus and stress at break for dry PEO20 samples soaked in silica solutions of various concentrations and nanoparticle sizes.

The modulus and the tensile stress at break were determined from the stress vs. strain graphs of PEO20 soaked in Ludox TM-50, HS-40, and SM solutions and the results are displayed in **Figure C.12**. No observable difference in modulus is seen when soaking PEO20 nanofibers in water and in low concentrations of silica ($\leq$ 0.1 wt%). As the silica concentration is increased to 1 wt% and then 10 wt%, the modulus of the PEO20 nanofibers increases, suggesting an increase in physical crosslink density with greater silica adsorption. A larger number of silica nanoparticles results in a greater number of adsorbed PEO network chains and thereby a greater restriction in

PEO chain mobility, increasing the stiffness of the PEO20 nanofibers. The increase in modulus is dependent on the size of the silica nanoparticles and modulus increases with nanoparticle size. This is likely due to the greater number of adsorption sites per silica nanoparticle as the size increases, which restricts the mobility of a greater number of polymer chains. Furthermore, the stress at break is not considerably influenced by silica adsorption until high silica loading (10 wt%) where a greater stress at break is observed.

C.3.4 Stress Relaxation of PEO Nanofibers with Adsorbed Silica

It is well understood that the viscoelastic character of the extracellular matrix (ECM) of cells plays an integral role in regulating cell growth and tissue homeostasis through the dissipation of stress imparted by cell-generated forces.[36-39] Thus, polymeric tissue scaffolds seek to mimic the viscoelastic character of the ECM to ensure optimal cell spreading, proliferation, and differentiation. In general, increased cell spreading and proliferation is observed with increasing stress relaxation of the tissue scaffold.[39-40]

To determine the viscoelastic properties of the silica-modified PEO20 nanofibers, stress relaxation experiments were performed. PEO20 with various concentrations of adsorbed silica were subjected to 10% strain and the relaxation behavior was investigated over 10 minutes. The normalized stress (σ/σ_o) as a function of time for PEO20 with adsorbed Ludox TM-50, HS-40, and SM is displayed in **Figure C.13**.

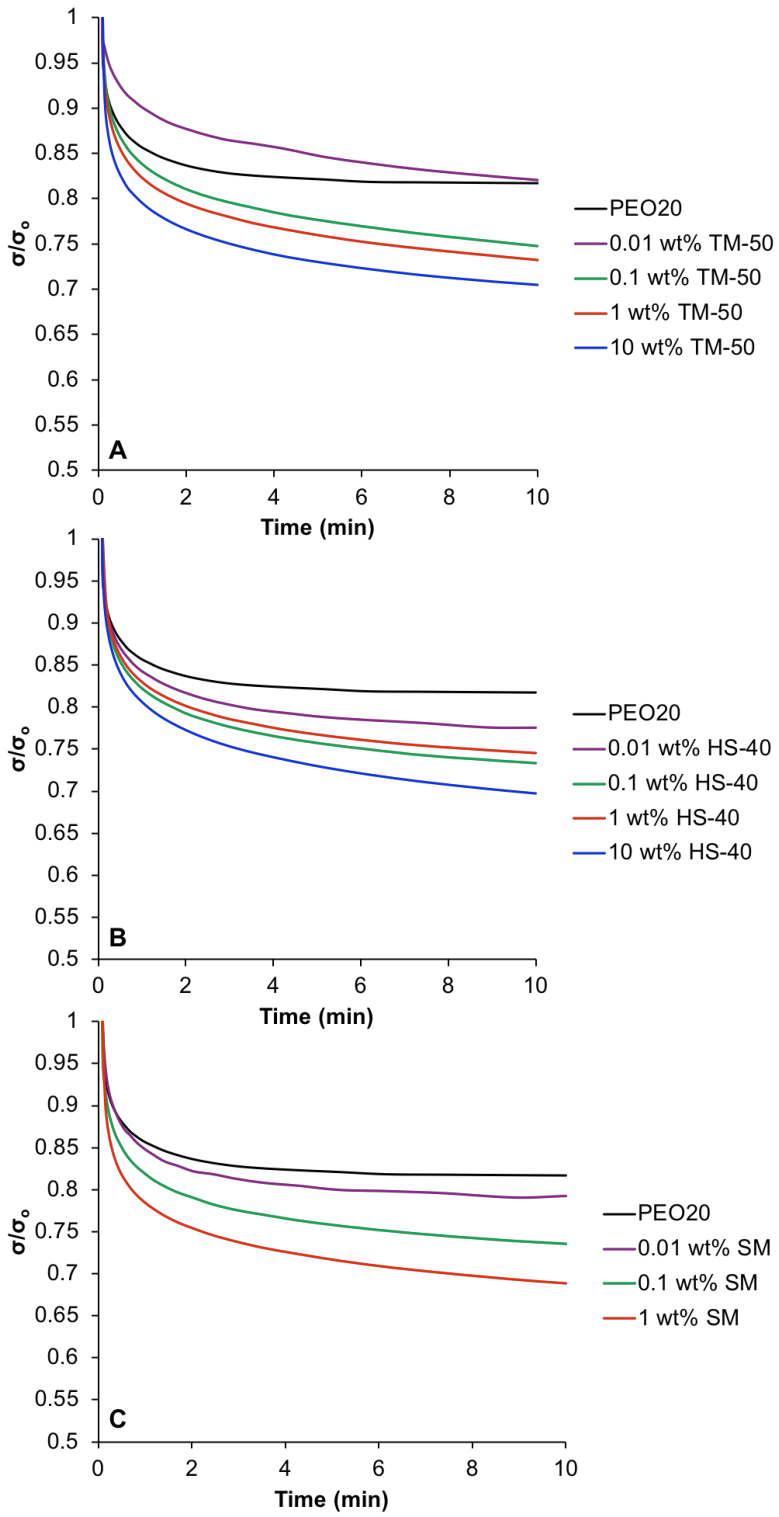

Figure C.13. Stress relaxation for PEO20 nanofibers with various concentrations of adsorbed silica for various silica nanoparticle sizes. PEO20 with adsorbed Ludox TM-50 (A), Ludox HS-40 (B), and Ludox SM (C) is investigated.

For PEO20 modified with silica of all sizes, stress relaxes more quickly and to a higher degree as silica concentration increases. For the PEO20 mats with no silica, the primary mechanism of stress relaxation is through the diffusive rearrangement of the polymer network chains.[41] Due to the covalent nature of the PETA crosslinks in PEO20, irreversible chain scission would be necessary to achieve further relaxation. The overall relaxation achieved is a function of the crosslink density, as the polymer chains are stretched to their maximum extent between the covalent crosslinks. With the adsorption of the PEO networks chains to the silica nanoparticles, an additional mechanism of stress relaxation arises. Because of the physical, reversible nature of PEO adsorption to silica, stress is dissipated through the desorption of monomers from the nanoparticle surface. In fact, stress-induced desorption of a single monomer unit has the ability to release the tension of the entire network chain segment of N/n monomers, where N is the number of monomers between *covalent* crosslinks and n is the number of adsorbed monomers per chain segment.[29] Thus, stress relaxation occurs more rapidly upon PEO20 adsorption to silica and with increasing silica concentration due to the increased ability of the PEO network chains to relax via detachment from the silica nanoparticle surface. The detachment of a monomer not only dissipates stress, but also yields an empty adsorption site upon which a PEO monomer from the same network strand or a different network strand may attach. Because the energy dissipated by the desorption of a monomer is much less than the free energy of adsorption, the physical network is readily reformed as stress is dissipated, maintaining the mechanical integrity of the physical network.

The degree of relaxation was estimated by noting the percent relaxation at 10 minutes with constant strain. The degree of relaxation as a function of silica concentration and size is shown in **Figure C.14A**. As noted with the stress relaxation profiles, the degree of relaxation increases with increasing nanoparticle concentration. The size of the nanoparticles does not appear to have any considerable influence on the degree of relaxation. In fact, when superimposed at identical silica

concentrations, the stress relaxation profiles of PEO20 with TM-50, HS-40, and SM silica nanoparticles are nearly superimposable, suggesting similar mechanisms of stress relaxation with increasing silica content.

It is important to note that although the normalized stress relaxes more quickly and to a greater degree within increased silica adsorption, the magnitude of the initial stress observed increases with silica concentration. As shown in **Figure C.14B**, silica concentrations of 1 wt% and above demonstrate a substantial increase in the initial stress from that of unmodified PEO20. This correlates well with the increase in modulus observed in **Figure C.12A** and validates the increase in network rigidity associated with increasing the number of physical crosslinks within the PEO20 nanofibers. Furthermore, at high silica contents the size of nanoparticles dictates the initial stress experience, with larger TM-50 nanoparticles exhibiting greater stress than smaller nanoparticles (HS-40, SM). Again, this is likely due to the increase in the number of adsorbed monomers on a single silica nanoparticle as the nanoparticle increases in size.

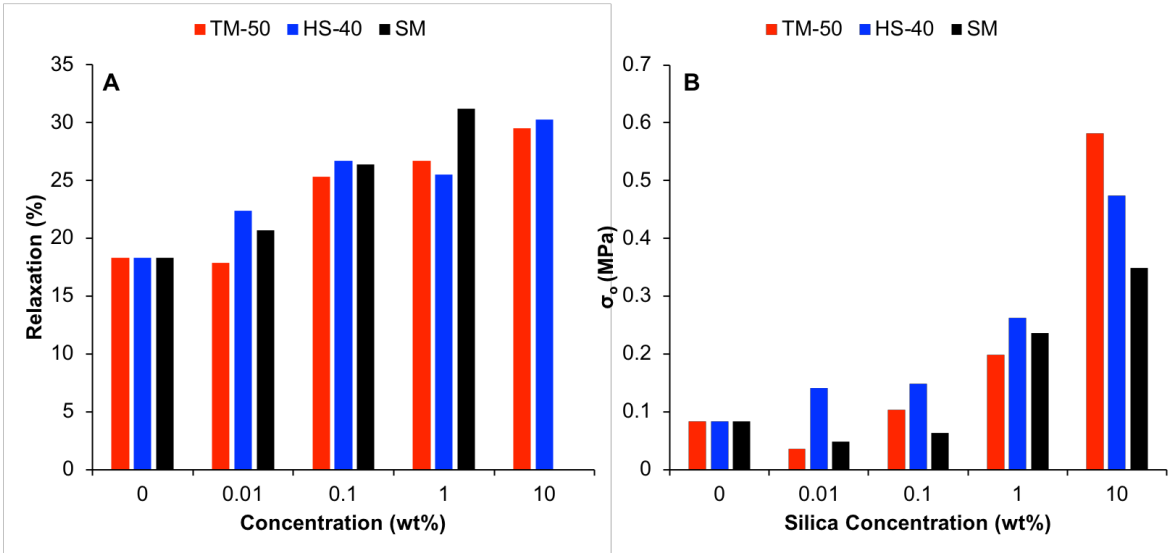

Figure C.14. Relaxation (A) and initial stress (B) of PEO20 soaked in various concentrations of silica dispersions.

C.3.5 Thermal Properties of PEO with Adsorbed Silica

PEO is a semicrystalline polymer that maintains a significant degree of crystallinity following the electrospinning and crosslinking process with PETA (See Appendix B). When in the dry state, polymer crystallinity influences the mechanical properties of the nanofibers by restricting polymer chain mobility and thereby increasing scaffold stiffness. Hydration in water has the potential to dissolve these crystallites and thus adsorption of PEO20 network chains to the silica nanoparticle surface may disrupt the length of crystallizable PEO chains and limit crystallizability when the nanofibers are dehydrated. To determine the influence of silica adsorption on the crystallizability of PEO20, DSC was performed. Hydrated PEO20 nanofibers were equilibrated in TM-50 silica suspensions of variable concentration for 1 hour and the resultant scaffolds were washed in deionized water and dried under vacuum. Dried scaffolds were heated in the DSC to 80 ºC and the resultant thermograms are displayed in **Figure C.15**.

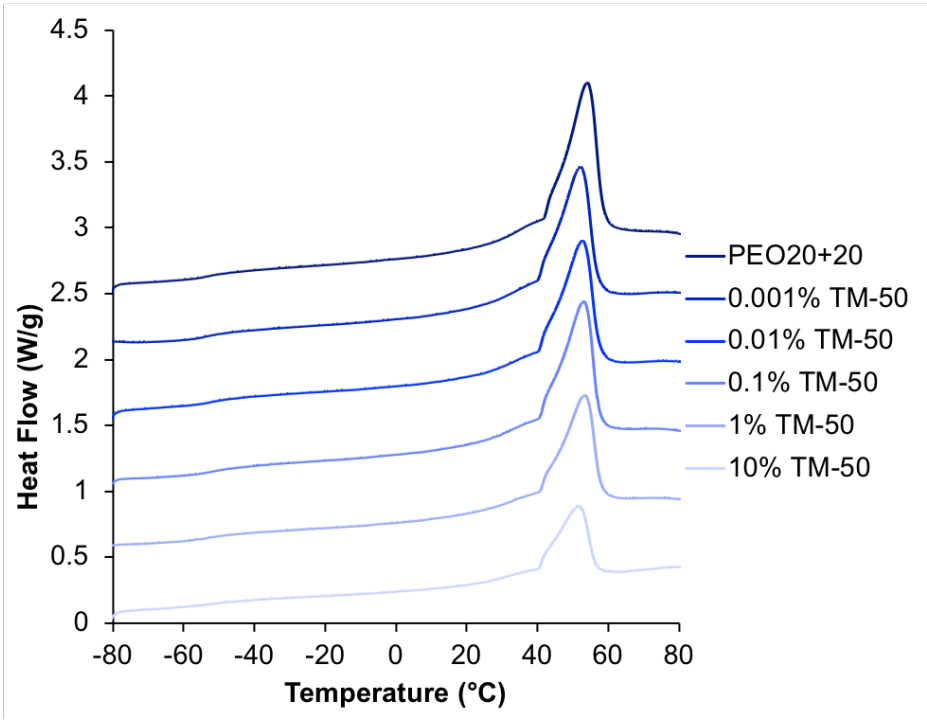

Figure C.15. DSC thermograms of the first heat of dried PEO20 nanofibers soaked in various concentrations of Ludox TM-50 silica.

The DSC thermograms of the PEO20 and silica-modified PEO20 mats display two clear thermal transitions – a broad glass transition (T_g) at approximately -50 ºC and a large endotherm at 53 ºC that may be attributed to the melting of PEO crystallites. No shift in T_g or the melting temperature (T_m) is observed with increasing nanoparticle concentration, however, the melting endotherm appears to decrease in magnitude with increasing concentration. While the smaller melting endotherm implies a decrease in crystallinity, it is important to note that the total mass of PEO is not consistent among the plotted samples. To normalize the enthalpy of melting to the actual mass of PEO20, the melting endotherm was integrated and divided by the mass ratio of PEO20 in each sample (PEO20 mass before adsorption/total mass following adsorption). Normalization of the enthalpy of melting reveals a constant value of approximately 55 J/g, independent of silica content. This implies that the crystallinity of the dried silica-modified PEO20

mats is unchanged from that of PEO20 itself. Upon hydration with water and soaking in aqueous silica suspensions, the crystalline domains likely persist and only PEO20 network chains within the amorphous domains are capable of adsorbing to the nanoparticle surface. This preserves the original crystalline architecture of the as-spun PEO20 samples.

Table C.2. Thermal properties determined from the DSC thermograms of PEO20 and silica-modified PEO20. Ludox TM-50 silica suspensions were used.

Sample	T_g (ºC)	T_{m1} (ºC)	ΔH_{m1} (J/g)	$\Delta H_{m1,\,norm}$ (J/g)	T_c (ºC)	ΔH_c (J/g)	T_{m2} (ºC)	ΔH_{m2} (J/g)	$\Delta H_{m2,norm}$ (J/g)
PEO20	-52	54	60	60	41	70	53	74	74
0.001 wt%	-54	52	55	56	40	65	52	72	73
0.01 wt%	-52	53	54	55	39	62	52	60	61
0.1 wt%	-53	53	54	55	41	66	52	65	67
1 wt%	-53	53	45	54	39	50	52	50	60
10 wt%	-50	52	28	56	37	31	50	32	64

To further investigate the effect of silica adsorption on the thermal properties of the PEO20 nanofibers, silica-modified PEO20 was crystallized by slow cooling (10 ºC/min) from the melt and subsequently reheated to 80 ºC. The DSC thermograms of the cooling and heating cycles and the quantitative properties determined from these thermograms are shown in **Figure C.16** and **Table C.2**, respectively. Similar to the results from the first heat of the samples, silica-modified PEO20 demonstrates minimal change in the T_g, T_m, and normalized melting enthalpy with increasing silica concentration. Heating into the melt does not impart any physical strain into the network system, and thus limited detachment of adsorbed PEO20 chains from the silica surface is expected. Thus, the non-adsorbed PEO chains previously imbibed in the crystallites can readily re-associate and crystallize upon cooling to form similarly sized crystalline lamella to that of the original PEO20.

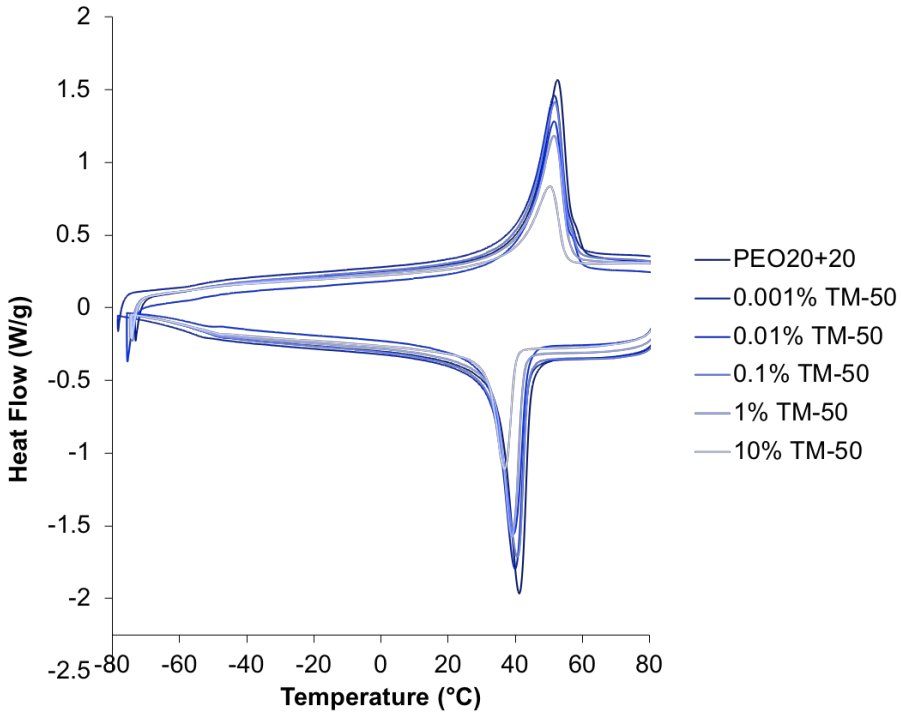

Figure C.16. DSC thermograms of the cooling of silica-modified PEO20 nanofibers from the melt and subsequent heating.

C.3.6 Degradation of Silica-Adsorbed PEO20 Over Time

For use in tissue engineering, the rate of degradation of the scaffold influences the ability cells to penetrate and overtake the scaffold over time. Controllable degradation is key so that the scaffold degradation rate matches the rate of tissue formation.[42] Typically, the degradation rate of tissue engineered scaffolds is investigated by monitoring the mass loss of the scaffolds over time.[43] To this end, PEO20 nanofiber mats (with and without adsorbed silica) were placed in phosphate buffered saline (PBS) at 37 ºC and the mass of the mats was monitored over several weeks. The mass loss of PEO20 and silica-adsorbed PEO20 (1 wt% Ludox TM-50) is shown in **Figure C.17**. PEO20 displays increased mass loss over time compared to PEO20-1-TM50. For both samples, degradation may occur by several means. First, the ester groups of the PETA crosslinker may undergo passive hydrolysis.[44-45] Because PETA is trifunctional, hydrolysis of multiple ester

linkages would be necessary to release a soluble PEO chain. Next, oxidative degradation of the PEO chains may occur (as described in Appendix B). The mechanism of oxidative degradation not only causes chain scission of the PEO polymer chains, but also results in formates, aldehydes, and esters as degradation products.[46] The esters may thereby undergo hydrolysis, similar to PETA. As shown in **Figure C.17**, the adsorption of PEO20 to silica slows down the mass loss of PEO20. Because degradation relies partially on hydrolysis, this change in mass loss may be attributed to the decrease in swelling upon silica adsorption (See **Figure C.9B**). Furthermore, adsorption of degradation products to the silica nanoparticles may slow mass loss over time by preventing their dissolution in solution. Thus, control of the degradation rate of PEO20 nanofibers may be achieved by regulating the amount of silica. It is also of interest to note that after 60 days in PBS, the mass loss of the PEO20 and PEO20-1-TM50 samples converged to a similar value of approximately 33 wt%.

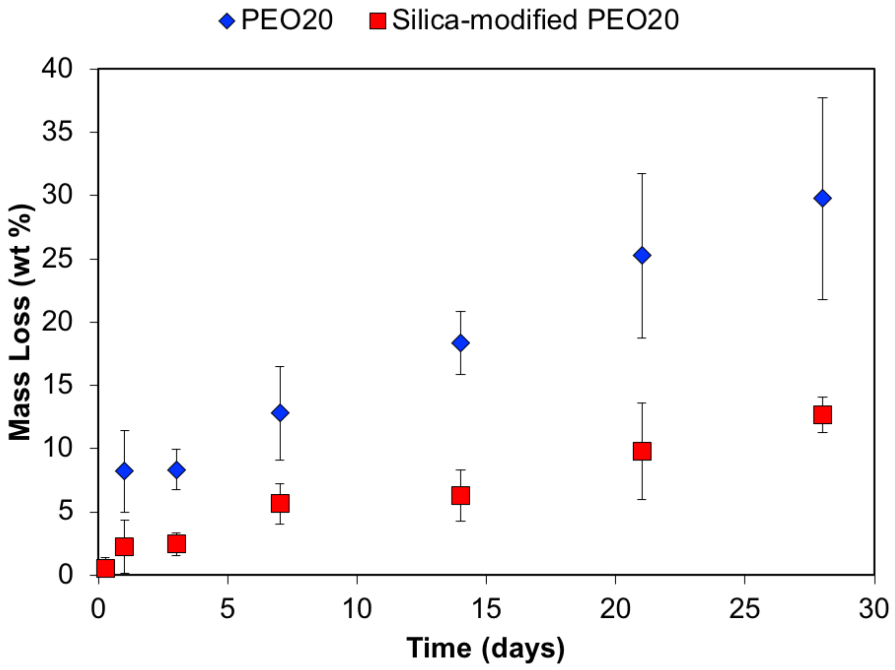

Figure C.17. Mass loss of PEO20 and silica-modified PEO20 (1 wt% TM-50).

The morphology of the nanofiber scaffolds throughout the degradation studies was also examined using SEM. The SEM images of PEO20 and PEO20-1-TM50 after 0, 3, 7, and 42 days are shown in **Figure C.18**. Within the first week of soaking in PBS, the PEO20 nanofibers appear to grow in size and look more distorted than their initial state. Furthermore, there is significant evidence of fiber melding over time, suggesting that degradation causes the fibers to become more soluble and merge together. The PEO20-1-TM50 mat does not display a drastic change in nanofiber morphology within the first week. After 6 weeks in PBS, both the PEO20 and PEO20-1-TM50 show noteworthy changes in nanofiber morphology. For both samples, nanofibers become significantly enlarged and a high degree of fiber melding is observed. In fact, the degree of fiber melding is so high that very limited porosity is observed in the scaffolds. It is also interesting that limited to no nanofiber breakage is observed for PEO20 or PEO20-1-TM50 over time; rather, nanofibers are merely distorted in shape and size. It is important to note that these degradation studies were performed by soaking the scaffolds in PBS over time with limited agitation and no interactions with cells. Forces exerted through the adhesion and growing of cells is anticipated to further alter the nanofiber morphology with time.

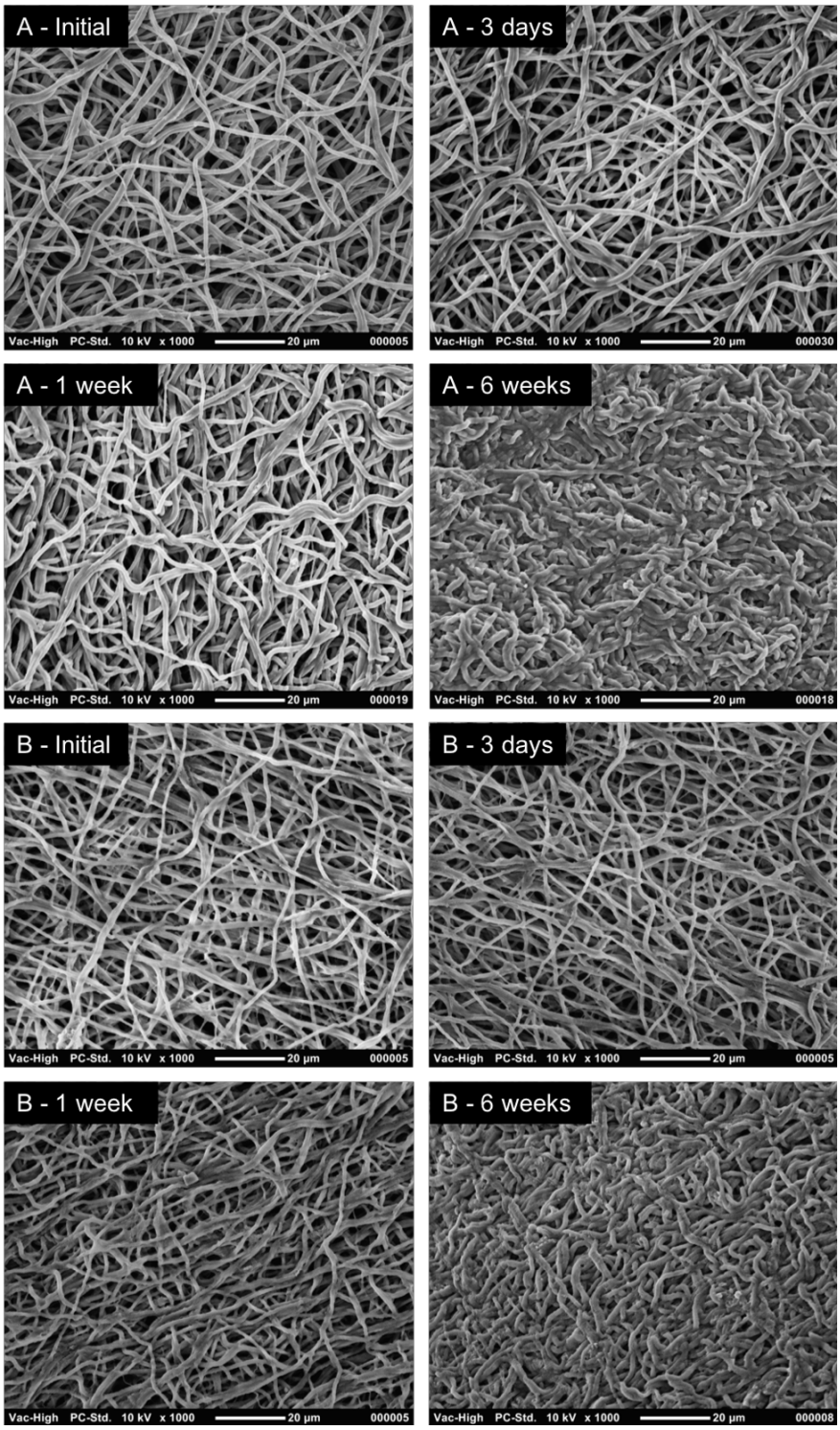

Figure C.18. SEM images of PEO20 (A) and PEO20-1-TM50 (B) after degradation in PBS at 37 ºC for 3 days, 1 week, and 6 weeks.

C.3.7 Cellular Adhesion and Growth on Silica-Modified PEO Nanofibers

Hydrogels made from PEO are considered nonadhesive to mammalian cells and proteins, and thus PEO is often modified chemically or physically to promote cell adhesion. Nanocomposites have recently been investigated to improve the biological and mechanical properties of PEO without chemically changing PEO. Nanocomposite hydrogels made from PEO and charged silicate demonstrated improved cell adhesion, proliferation, and spreading as the silicate concentration was increased.[47] Furthermore, silica photocrosslinked PEO gels with incorporated silica nanospheres enhanced initial cell adhesion, and resulted in enhanced cell spreading and increased metabolic activity than PEO itself.[28] Thus, the effect of the incorporation of silica into PEO20 nanofibers on cell adhesion and growth was investigated.

Adhesion of cells to the nanofibers was examined after sterilizing the scaffolds and equilibrating them in Dulbecco's Modified Eagle Medium (DMEM). Unsupplemented DMEM does not contain any proteins, lipids, or growth factors. Thus, supplemented DMEM was prepared by adding 10% fetal bovine serum (FBS), which contains many proteins and growth promoting factors. Adhesion was compared following equilibration in unsupplemented and supplemented DMEM by seeding HeLa cells at 25,000 cells/mL and allowing the cells to incubate at 37 ºC for 4 hours. Samples were then washed with PBS to remove any unadhered cells and cell viability was examined using the Cell Titer Glo® assay. Adhesion was determined as the percent viability relative to control HeLa cells seeded directly onto the well plate and the results are shown in **Figure C.20**. Studies in unsupplemented DMEM revealed a limited influence of silica nanoparticles on the initial adhesion of the HeLa cells. At all silica concentrations, little difference is observed in the percentage of cells adhered to silica-modified PEO20 and unmodified PEO20. When equilibrating in supplemented DMEM, however, an increase in adhesion is observed with increasing silica concentration. It is likely that proteins from the FBS are adsorbing to the silica

surface and promoting the adhesion of HeLa cells. The adhesion increases with increasing silica concentration because a larger number of proteins are capable of being adsorbed to the nanofiber scaffold. Thus, the silica nanoparticles indirectly promote the adhesion of cells by adsorbing adhesive proteins to their surface.

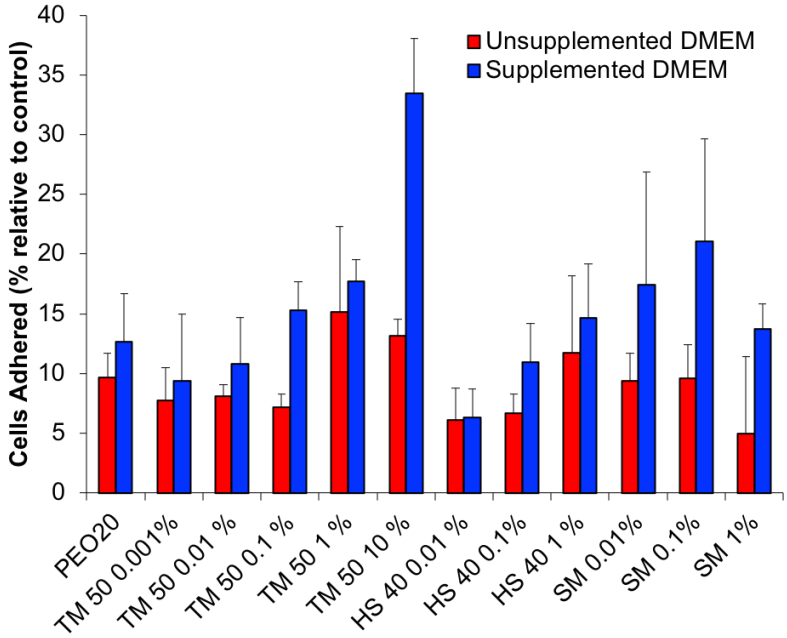

Figure C.19. Cell adhesion of PEO20 and silica-modified PEO20 nanofiber scaffolds after 24 hours in unsupplemented and supplemented DMEM.

The viability of cells seeded onto the scaffolds was also examined after 1, 3, and 7 days. The viability of HeLa cells relative to the control at each of these time periods is shown in **Figure C.20**. For PEO20, the showed a viability around half that of the control on days 1 and 3. PEO20 with low concentration of silica nanoparticles (< 0.1 wt%) showed a lower viability compared to PEO20 on day 1, however, a large increase in viability was noted on day 3. PEO20-TM50 and PEO20-SM at 0.1 wt% silica and above samples showed similar viability to PEO20 on day 1 and improved viability on day 3. When examining the full PEO20-TM50 series, it appears that viability increases with increasing silica concentration until 10 wt%, where cell viability begins to decrease. The highest viability of HeLa cells was observed on day 3 for PEO20-SM samples, suggesting that

smaller nanoparticles improve cell viability compared to larger nanoparticles. For all samples (PEO20 and silica-modified PEO20), a large decrease in viability was noted on day 7, suggesting that there are far less cells or fewer metabolically active cells than the control. It is plausible that a threshold may be reached at day 7 for the number of cells that can survive on the surface of the scaffold. The pores of the nanofiber mat may be too small for cells to penetrate, thus limiting cell growth. Furthermore, between 5 and 15 wt% mass loss is observed for the nanofiber mats within a week, and the degradation products may be cytotoxic. Further analysis of the degradation products is necessary to determine their influence on cell viability. Because a similar decrease in viability is observed for both PEO20 and silica-modified PEO20 at day 7, it is unlikely that the silica nanoparticles are contributing significantly to the loss of viability.

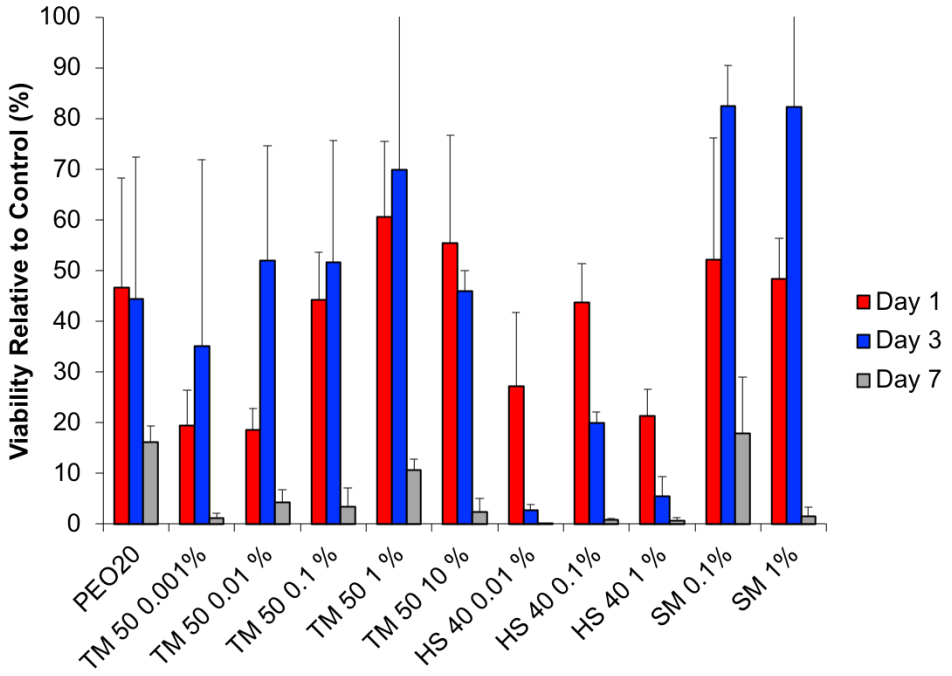

Figure C.20. Cell viability of HeLa cells seeded onto PEO20 and silica-modified PEO20 over one week.

The morphology of the HeLa cells adhering and growing on the PEO20 and silica-modified PEO20 nanofibers was also investigated using SEM. Cells adhered to the PEO20 scaffolds were fixed with 3.7% paraformaldehyde and slowly washed with PBS/ethanol solutions with increasing

ethanol content to dry out the cells. Scaffolds with cells were dried on the benchtop overnight and then sputter coated. SEM images were taken after days 1 and 3 of incubation and the effect of silica on the cell morphology was investigated. **Figure C.21** shows the SEM images of HeLa cells on PEO20 and PEO20-TM50 at various silica concentrations after 1 day of incubation. At this time, a low cell density is observed on both the PEO20 mat and the PEO20-TM50 mats at 0.1 wt% silica and below. A greater number of cells are observed on PEO20-TM50 with silica concentrations at 1 wt% and above, suggesting that an increased number of cells have attached to the scaffolds with more silica, consistent with the viability results above. For all samples, the HeLa have a round appearance which is attributed to the shape of adhering HeLa cells.[48] After 3 days of incubation, **Figure C.22** shows an increase in cell density and spreading for all samples compared to day 1. Again, the cell density increases with increasing silica concentration until 10 wt% silica, where the density decreases slightly. The cells are less rounded than day 1 and exhibit a more 'fried egg' morphology, demonstrating their increased spreading with time. Further SEM images of the modified silica PEO20 (including PEO20-HS40 and PEO20-SM) were taken on day 3, as shown in **Figure C.23**. Significant cell spreading and incorporation of the cells into the nanofibrous scaffold architecture is observed for all modified PEO20 samples, suggesting that silica adsorption to crosslinked PEO is a suitable scaffold for cell growth. Future cell studies should focus on the adhesion and proliferation of fibroblast cells on the nanofiber scaffolds to determine their efficacy for potential skin replacements.

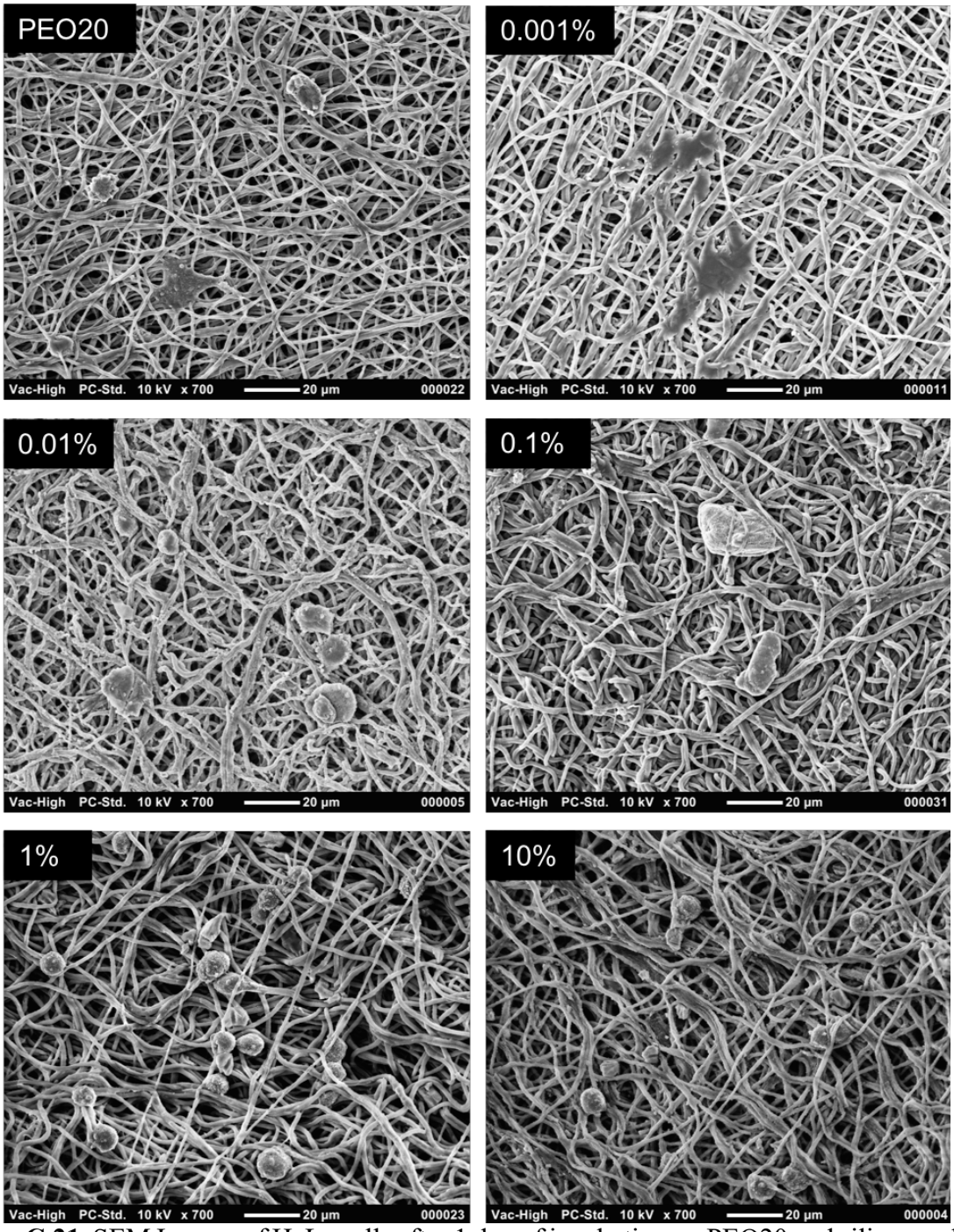

Figure C.21. SEM Images of HeLa cells after 1 day of incubation on PEO20 and silica-modified PEO20 (TM-50) at various silica contents.

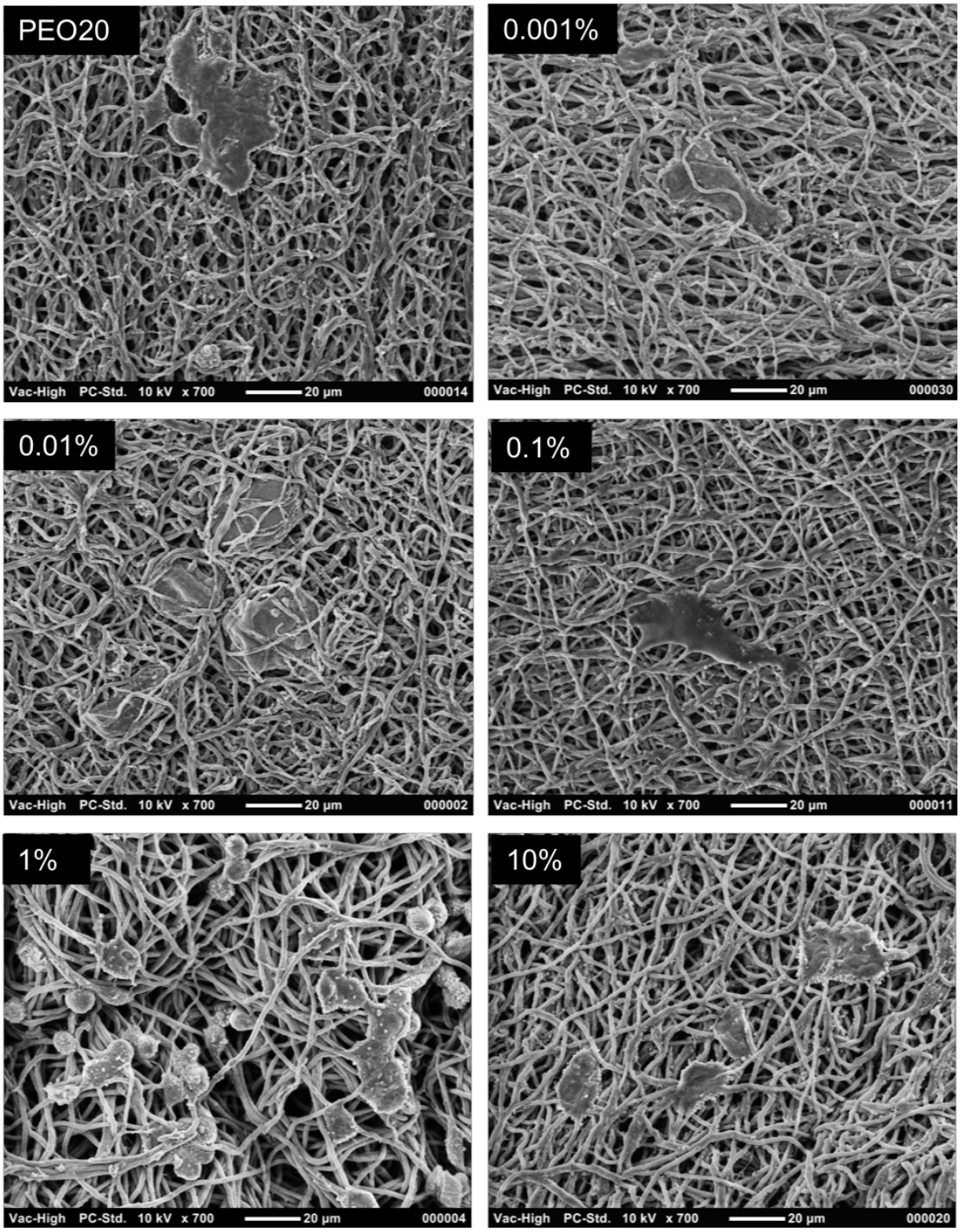

Figure C.22. SEM Images of HeLa cells after 3 days of incubation on PEO20 and silica-modified PEO20 (TM-50) at various silica contents.

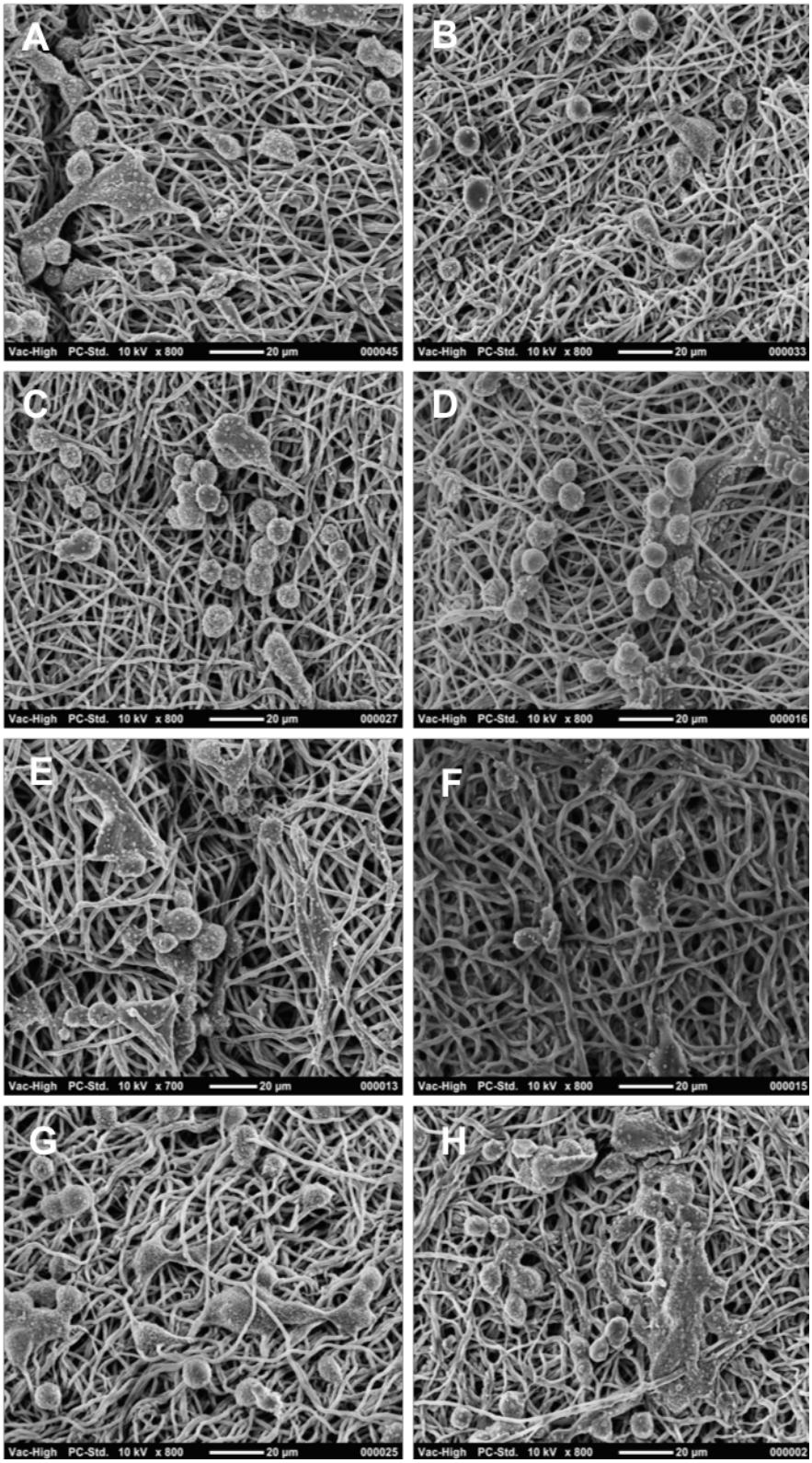

Figure C.23. SEM Images of HeLa cells after 3 days of incubation on PEO20 (A), PEO20-0.001-TM50 (B), PEO20-0.01-TM50 (C), PEO20-0.1-TM50 (D), PEO20-1-TM50 (E), PEO20-10-TM50 (F), PEO20-0.01-HS40 (G), and PEO20-0.01-SM (H) nanofibers.

C.3.8 Effect of Silica Adsorption on Crosslinked PEO with Variable PETA

While these studies have focused on the modification of PEO20 nanofibers with silica, it is also of interest to examine the effect of crosslink density on the adsorption of silica. PEO10, PEO20, and PEO30 samples were soaked in Ludox TM-50 solutions at concentrations of 0.1, 1 and 10 wt% and the change in mass was determined gravimetrically. The weight change following silica adsorption is shown in **Table C.3**. With increasing PETA concentration (i.e. increasing crosslink density), a decrease in weight change is observed upon soaking in silica solutions. Increasing crosslink density decreases the mobility of the PEO polymer chains and decreases the total number of PEO monomers capable of adsorbing to the surface of the silica nanoparticles. Thus, the concentration of silica nanoparticles may be tuned by silica concentration in solution as well as the chemical crosslink density.

Table C.3. Weight change of PEO10, PEO20, and PEO30 following adsorption of Ludox TM-50 at various concentrations.

Sample	Mass Gain Following Adsorption (wt%)		
	0.1 wt% TM-50	1 wt% TM-50	10 wt% TM-50
PEO10	7.1	27.4	236
PEO20	5.0	22.0	136
PEO30	0.7	2.2	20

The influence of crosslink density on the morphology of silica-modified PEO nanofibers was also examined using SEM. **Figure C.24** shows the SEM images of PEO10, PEO20, and PEO30 following a 1-hour soak in 0.1 wt% TM-50. PEO10 displays a high degree of fiber melding following adsorption to silica nanoparticles. Because of the greater silica content and greater amount of PEO capable of interacting with the silica, the silica nanoparticles readily act as adhesives between the individual nanofibers. The result leads to a substantial loss in porosity at the surface of the mats. As the PETA content increases, PEO20 and PEO30 maintain more of their native nanofiber architecture upon silica adsorption. The degree of fiber melding decreases with

increasing PETA content due to the decrease in silica content. PEO20 and PEO30 remain highly porous at the surface, unlike PEO20. Thus, modified PEO20 and PEO30 will be more suitable for a cell scaffold into which cells can penetrate.

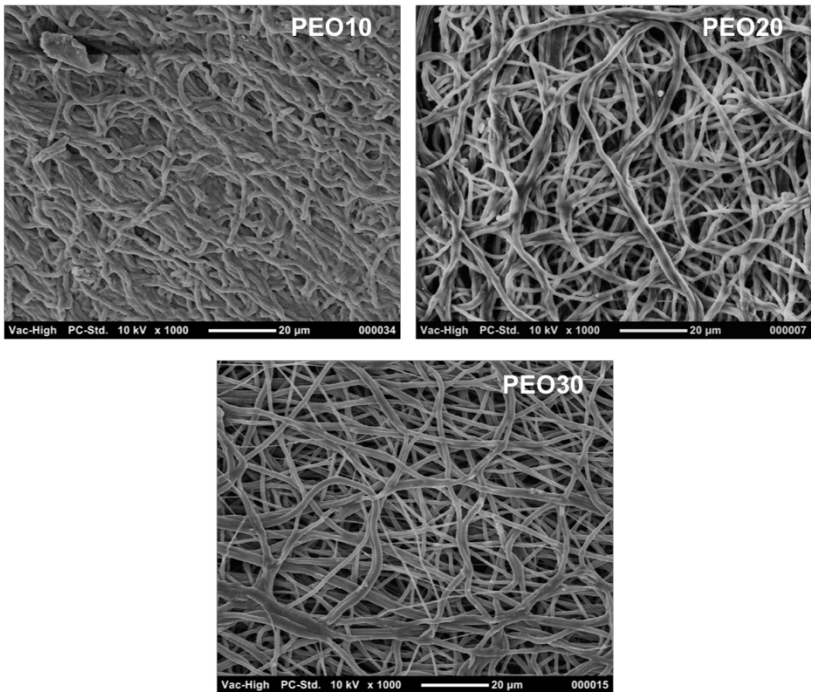

Figure C.24. SEM Images of PEO10, PEO20, and PEO30 following a 1 hour soak in 0.1 wt% TM-50.

As shown in **Section C.3.3** , the tensile properties of PEO20 are significantly altered upon the adsorption of silica nanoparticles. Thus, the tensile properties of PEO10 and PEO30 following soaks in Ludox TM-50 were also determined and compared to those of PEO20. The stress vs. strain curves of PEO10, PEO20, and PEO30 after soaks in various concentrations of Ludox TM-50 is shown in **Figure C.25**. For comparison, crosslinked PEO mats were also soaked in water to provide a control. At low silica contents (0.1 wt%), the effect of amount of silica adsorption is clearly evident. PEO10 shows a large increase in modulus and strength at break with silica adsorption. PEO20 exhibits a similar effect, although it is not as pronounced as for PEO10 due to a decrease in silica content adsorbed. PEO30, which does not adsorb a considerable amount of

silica when soaked in 0.1 wt% solutions, shows no considerable change in tensile properties from PEO30 mats soaked in water. As the concentration of the silica soak solution increases, further increases in moduli are observed for crosslinked PEO samples with variable PETA content.

To better quantify the tensile properties, the modulus of PEO10, PEO20, and PEO30 soaked in various concentrations of Ludox TM-50 were plotted, as shown in **Figure C.26**. For each PEO sample, the modulus increases with increasing silica concentration, as expected. The increase in silica content results in a higher degree of physical crosslinking between the PEO chains, restricting their mobility and increasing the modulus. The increase in modulus appears more dominant for PEO10, which adsorbs the greatest amount of silica at each soak solution concentration (see **Table C.3**).

Based on the changes in nanofiber morphology and tensile properties upon silica adsorption, it appears that crosslinked PEO samples containing higher PETA contents (≥ 20 wt%) are most suitable for use in tissue engineering scaffolds. PEO20 and PEO30 better maintain their nanofibrous architecture following the adsorption of silica, thereby providing an environment that mimics the ECM. The adsorption of silica occurs more gradually for PEO20 and PEO30 than PEO10 due to the greater crosslinking density, and thus smaller changes in the tensile properties can be achieved to closely match the mechanical properties of the native tissue.

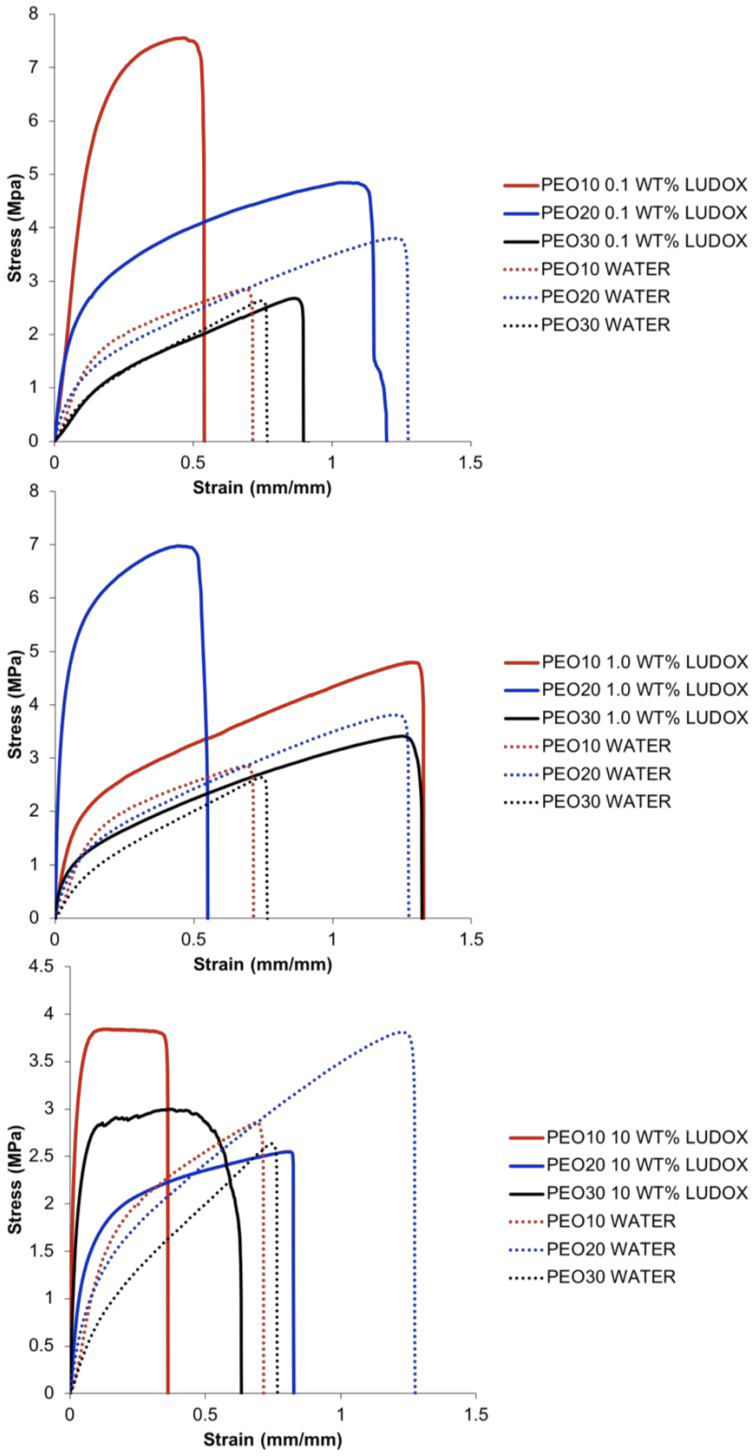

Figure C.25. Stress vs. strain curves of PEO10, PEO20, and PEO30 soaked in water, 0.1 wt% TM-50, 1 wt% TM-50, and 10 wt% TM-50 for 1 hour.

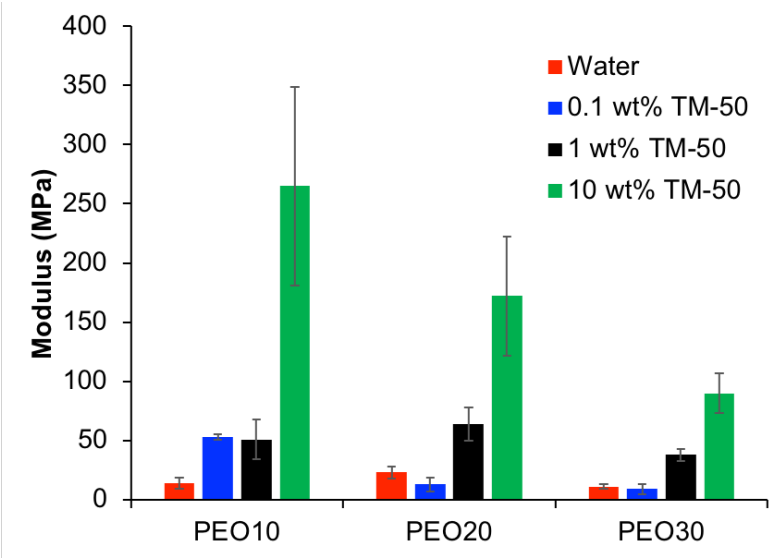

Figure C.26. Average modulus determined from stress vs. strain curves of PEO10, PEO20, and PEO30 soaked in water, 0.1 wt% TM-50, 1 wt% TM-50, and 10 wt% TM-50 for 1 hour.

C.4 Conclusions and Future Work

In this study, the effect of silica adsorption on the properties of crosslinked, electrospun PEO nanofibers was investigated. Silica suspensions were found to reproducibly adhere PEO20 nanofiber scaffolds to one another, and an increase in adhesive strength was found for increasing silica size and increasing concentration. Gluing junctions were easily repairable to full strength with light finger pressure after bringing the mats into contact with one another again.

Silica adsorption to the PEO20 scaffolds was also investigated by soaking PEO20 in silica suspensions of various concentrations. Equilibrium adsorption was found to occur after approximately 30 minutes and the silica content of PEO20 mats was found to increase with increasing silica concentration in the soaking suspensions. Equilibrium swelling in water was found to decrease with increasing silica content due to increased interactions of the PEO chains with the nanoparticles. Furthermore, the nanofiber morphology was altered through the adsorption of silica nanoparticles. Increasing silica content resulted in a rougher surface of the nanofibers and increased adhesion of nanofibers to one another, leading to fiber melding.

PEO20 nanofibers also displayed an increase in modulus and tensile strength at break with increasing silica contents. Stress relaxation experiments revealed the desorption process was successful in mitigating stress and PEO20 relaxed to a greater degree with increased silica content. Silica-adsorption was not found to alter the crystallinity of the nanofiber mats, suggesting that adsorption occurs with PEO chains within the amorphous domains of the PEO20 network. Degradation studies in PBS revealed a slower mass loss over time for silica-adsorbed PEO20 compared to unmodified PEO20 and swelling and melding of nanofiber morphology throughout degradation. Cell adhesion in supplemented DMEM revealed increased viability of HeLa cells with increasing silica concentration after 4 hours of incubation, suggesting that adsorption of growth-promoting factors from the media onto the surface of the silica may contribute to cell adhesion. Cells remained viable on silica-modified PEO20 scaffolds for several days and displayed increased spreading using SEM.

Overall, it was determined that silica adsorption to crosslinked PEO20 nanofibers is a facile method to manipulate mechanical properties, nanofiber morphology, degradation, and equilibrium swelling behavior. Control over the amount of adsorbed silica is easily achieved by varying the concentration of the silica suspension used for soaking the PEO20 mats or by varying the degree of chemical crosslinking (i.e. crosslinker concentration) of the PEO mats. Future work will focus on further methods to improve the bioactivity of the modified PEO scaffolds. Adsorption or covalent tethering of growth-promoting peptides to the silica surface may be investigated to further promote cell adhesion. Furthermore, future cell studies will investigate the adhesion and growth of fibroblast cells onto the PEO scaffolds and will investigate a more broad spectrum of cell properties, including cell viability, metabolic activity, and cell morphology.

C.5 References

1. Knop, K.; Hoogenboom, R.; Fischer, D.; Schubert, U. S., Poly(ethylene glycol) in Drug Delivery: Pros and Cons as Well as Potential Alternatives. *Angewandte Chemie International Edition* **2010,** *49* (36), 6288-6308.
2. Peppas, N. A.; Keys, K. B.; Torres-Lugo, M.; Lowman, A. M., Poly(ethylene glycol)-containing hydrogels in drug delivery. *Journal of Controlled Release* **1999,** *62* (1), 81-87.
3. Apicella, A.; Cappello, B.; Del Nobile, M. A.; La Rotonda, M. I.; Mensitieri, G.; Nicolais, L., Poly(Ethylene oxide) (PEO) and different molecular weight PEO blends monolithic devices for drug release. *Biomaterials* **1993,** *14* (2), 83-90.
4. Hoffman, A. S., Hydrogels for biomedical applications. *Advanced Drug Delivery Reviews* **2012,** *64*, 18-23.
5. Bryant, S. J.; Anseth, K. S., Hydrogel properties influence ECM production by chondrocytes photoencapsulated in poly(ethylene glycol) hydrogels. *Journal of Biomedical Materials Research* **2002,** *59* (1), 63-72.
6. Ma, L.; Deng, L.; Chen, J., Applications of poly(ethylene oxide) in controlled release tablet systems: a review. *Drug Development and Industrial Pharmacy* **2014,** *40* (7), 845-851.
7. Ruan, G.; Feng, S.-S., Preparation and characterization of poly(lactic acid)–poly(ethylene glycol)–poly(lactic acid) (PLA–PEG–PLA) microspheres for controlled release of paclitaxel. *Biomaterials* **2003,** *24* (27), 5037-5044.
8. Zalipsky, S., Functionalized poly (ethylene glycols) for preparation of biologically relevant conjugates. *Bioconjugate chemistry* **1995,** *6* (2), 150-165.
9. Bailon, P.; Palleroni, A.; Schaffer, C. A.; Spence, C. L.; Fung, W.-J.; Porter, J. E.; Ehrlich, G. K.; Pan, W.; Xu, Z.-X.; Modi, M. W.; Farid, A.; Berthold, W.; Graves, M., Rational Design of a Potent, Long-Lasting Form of Interferon: A 40 kDa Branched Polyethylene Glycol-Conjugated Interferon α-2a for the Treatment of Hepatitis C. *Bioconjugate Chemistry* **2001,** *12* (2), 195-202.
10. Lee, S.; Vörös, J., An Aqueous-Based Surface Modification of Poly(dimethylsiloxane) with Poly(ethylene glycol) to Prevent Biofouling. *Langmuir* **2005,** *21* (25), 11957-11962.
11. Desai, N. P.; Hubbell, J. A., Biological responses to polyethylene oxide modified polyethylene terephthalate surfaces. *Journal of Biomedical Materials Research* **1991,** *25* (7), 829-843.
12. Desai, N. P.; Hossainy, S. F. A.; Hubbell, J. A., Surface-immobilized polyethylene oxide for bacterial repellence. *Biomaterials* **1992,** *13* (7), 417-420.
13. Harris, J. M., New polyethylene glycols for biomedical applications. *Water-Soluble Polymers.* **1991**.
14. Swartzlander, M. D.; Barnes, C. A.; Blakney, A. K.; Kaar, J. L.; Kyriakides, T. R.; Bryant, S. J., Linking the foreign body response and protein adsorption to PEG-based hydrogels using proteomics. *Biomaterials* **2015,** *41*, 26-36.
15. Ngo, B. K. D.; Grunlan, M. A., Protein Resistant Polymeric Biomaterials. *ACS Macro Letters* **2017,** *6* (9), 992-1000.
16. Otsuka, H.; Nagasaki, Y.; Kataoka, K., Self-assembly of poly(ethylene glycol)-based block copolymers for biomedical applications. *Current Opinion in Colloid & Interface Science* **2001,** *6* (1), 3-10.
17. Keys, K. B.; Andreopoulos, F. M.; Peppas, N. A., Poly(ethylene glycol) Star Polymer Hydrogels. *Macromolecules* **1998,** *31* (23), 8149-8156.

18. Doytcheva, M.; Dotcheva, D.; Stamenova, R.; Tsvetanov, C., UV-Initiated Crosslinking of Poly(ethylene oxide) with Pentaerythritol Triacrylate in Solid State. *Macromolecular Materials and Engineering* **2001,** *286* (1), 30-33.
19. Zhou, C.; Wang, Q.; Wu, Q., UV-initiated crosslinking of electrospun poly(ethylene oxide) nanofibers with pentaerythritol triacrylate: Effect of irradiation time and incorporated cellulose nanocrystals. *Carbohydrate Polymers* **2012,** *87* (2), 1779-1786.
20. Wong, R. S. H.; Ashton, M.; Dodou, K., Effect of Crosslinking Agent Concentration on the Properties of Unmedicated Hydrogels (). *Pharmaceutics* **2015,** *7* (3), 305-319.
21. Elisseeff, J.; Anseth, K.; Sims, D.; McIntosh, W.; Randolph, M.; Langer, R., Transdermal photopolymerization for minimally invasive implantation. *Proceedings of the National Academy of Sciences* **1999,** *96* (6), 3104-3107.
22. Buxton, A. N.; Zhu, J.; Marchant, R.; West, J. L.; Yoo, J. U.; Johnstone, B., Design and Characterization of Poly(Ethylene Glycol) Photopolymerizable Semi-Interpenetrating Networks for Chondrogenesis of Human Mesenchymal Stem Cells. *Tissue Engineering* **2007,** *13* (10), 2549-2560.
23. Nuttelman, C. R.; Rice, M. A.; Rydholm, A. E.; Salinas, C. N.; Shah, D. N.; Anseth, K. S., Macromolecular Monomers for the Synthesis of Hydrogel Niches and Their Application in Cell Encapsulation and Tissue Engineering. *Progress in polymer science* **2008,** *33* (2), 167-179.
24. Zhu, J., Bioactive modification of poly(ethylene glycol) hydrogels for tissue engineering. *Biomaterials* **2010,** *31* (17), 4639-4656.
25. Lin, C.-C.; Anseth, K. S., PEG Hydrogels for the Controlled Release of Biomolecules in Regenerative Medicine. *Pharmaceutical Research* **2009,** *26* (3), 631-643.
26. Rose, S.; Prevoteau, A.; Elziere, P.; Hourdet, D.; Marcellan, A.; Leibler, L., Nanoparticle solutions as adhesives for gels and biological tissues. *Nature* **2014,** *505* (7483), 382-385.
27. Meddahi-Pellé , A.; Legrand, A.; Marcellan , A.; Louedec, L.; Letourneur, D.; Leibler, L., Organ Repair, Hemostasis, and In Vivo Bonding of Medical Devices by Aqueous Solutions of Nanoparticles. *Angew. Chem.* **2014,** *126* (25), 6487-6491.
28. Gaharwar, A. K.; Rivera, C.; Wu, C.-J.; Chan, B. K.; Schmidt, G., Photocrosslinked nanocomposite hydrogels from PEG and silica nanospheres: Structural, mechanical and cell adhesion characteristics. *Materials Science and Engineering: C* **2013,** *33* (3), 1800-1807.
29. Rose, S.; Prevoteau, A.; Elzière, P.; Hourdet, D.; Marcellan, A.; Leibler, L., Nanoparticle solutions as adhesives for gels and biological tissues. *Nature* **2013,** *505*, 382.
30. Netz, R. R.; Andelman, D., Neutral and charged polymers at interfaces. *Physics Reports* **2003,** *380* (1), 1-95.
31. Voronin, E. F.; Gun'ko, V. M.; Guzenko, N. V.; Pakhlov, E. M.; Nosach, L. V.; Leboda, R.; Skubiszewska-Zięba, J.; Malysheva, M. L.; Borysenko, M. V.; Chuiko, A. A., Interaction of poly(ethylene oxide) with fumed silica. *Journal of Colloid and Interface Science* **2004,** *279* (2), 326-340.
32. Zhang, Q.; Archer, L. A., Poly(ethylene oxide)/Silica Nanocomposites: Structure and Rheology. *Langmuir* **2002,** *18* (26), 10435-10442.
33. Rubio, J.; Kitchener, J. A., The mechanism of adsorption of poly(ethylene oxide) flocculant on silica. *Journal of Colloid and Interface Science* **1976,** *57* (1), 132-142.
34. Montarnal, D.; Capelot, M.; Tournilhac, F.; Leibler, L., Silica-Like Malleable Materials from Permanent Organic Networks. *Science* **2011,** *334* (6058), 965.
35. Stratton, S.; Shelke, N. B.; Hoshino, K.; Rudraiah, S.; Kumbar, S. G., Bioactive polymeric scaffolds for tissue engineering. *Bioactive Materials* **2016,** *1* (2), 93-108.
36. Mammoto, T.; Ingber, D. E., Mechanical control of tissue and organ development. *Development (Cambridge, England)* **2010,** *137* (9), 1407-1420.

37. Vogel, V.; Sheetz, M., Local force and geometry sensing regulate cell functions. *Nature Reviews Molecular Cell Biology* **2006,** *7*, 265.
38. Discher, D. E.; Janmey, P.; Wang, Y.-l., Tissue Cells Feel and Respond to the Stiffness of Their Substrate. *Science* **2005,** *310* (5751), 1139.
39. Chaudhuri, O.; Gu, L.; Darnell, M.; Klumpers, D.; Bencherif, S. A.; Weaver, J. C.; Huebsch, N.; Mooney, D. J., Substrate stress relaxation regulates cell spreading. *Nature Communications* **2015,** *6*, 6365.
40. Bauer, A.; Gu, L.; Kwee, B.; Li, W. A.; Dellacherie, M.; Celiz, A. D.; Mooney, D. J., Hydrogel substrate stress-relaxation regulates the spreading and proliferation of mouse myoblasts. *Acta Biomaterialia* **2017,** *62*, 82-90.
41. Bartenev, G. M.; Lyalina, N. M., Stress relaxation in crosslinked rubber-like polymers. *Polymer Science U.S.S.R.* **1970,** *12* (2), 420-429.
42. Hongbo, Z.; Li, Z.; Wenjun, Z., Control of Scaffold Degradation in Tissue Engineering: A Review. *Tissue Engineering Part B: Reviews* **2014,** *20* (5), 492-502.
43. Holy, C. E.; Cheng, C.; Davies, J. E.; Shoichet, M. S., Optimizing the sterilization of PLGA scaffolds for use in tissue engineering. *Biomaterials* **2000,** *22* (1), 25-31.
44. Li, S., Hydrolytic degradation characteristics of aliphatic polyesters derived from lactic and glycolic acids. *Journal of Biomedical Materials Research* **1999,** *48* (3), 342-353.
45. Woodard, L. N.; Grunlan, M. A., Hydrolytic Degradation and Erosion of Polyester Biomaterials. *ACS Macro Letters* **2018,** *7* (8), 976-982.
46. Morlat, S.; Gardette, J.-L., Phototransformation of water-soluble polymers. I: photo- and thermooxidation of poly(ethylene oxide) in solid state. *Polymer* **2001,** *42* (14), 6071-6079.
47. Schexnailder, P. J.; Gaharwar, A. K.; Bartlett II, R. L.; Seal, B. L.; Schmidt, G., Tuning Cell Adhesion by Incorporation of Charged Silicate Nanoparticles as Cross-Linkers to Polyethylene Oxide. *Macromolecular Bioscience* **2010,** *10* (12), 1416-1423.
48. Fairman, K.; Jacobson, B. S., Unique morphology of HeLa cell attachment, spreading and detachment from microcarrier beads covalently coated with a specific and non-specific substratum. *Tissue and Cell* **1983,** *15* (2), 167-180.